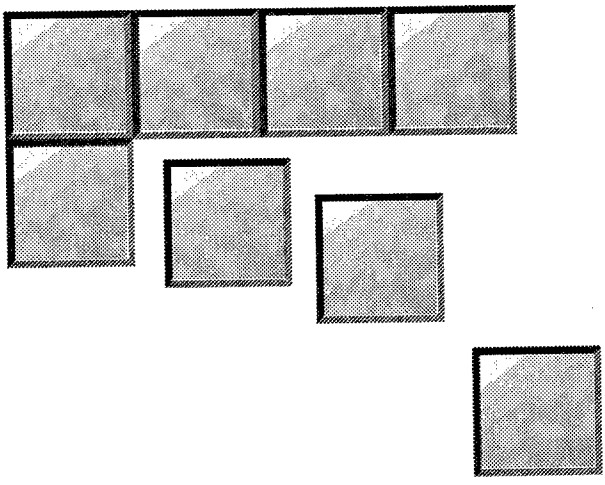
# Proceedings of
# 13th ARMY SYMPOSIUM ON SOLID MECHANICS



Edited by
Dr. Shun-Chin Chou
Dr. Fulton D. Bartlett Jr.
Dr. Thomas W. Wright
Dr. Kailasam Iyer

DISTRIBUTION STATEMENT A
Approved for public release;
Distribution Unlimited

**17-19 August 1993**
**Plymouth, Massachusetts**

# THIRTEENTH ARMY SYMPOSIUM ON SOLID MECHANICS PROCEEDINGS

DTIC QUALITY INSPECTED 4

19970710 071

*17-19 August 1993*

Plymouth Massachusetts

Edited by: *Dr. Shun-Chin Chou*
*Dr. Fulton D. Bartlett Jr.*
*Dr. Thomas W. Wright*
*Dr. Kailasam Iyer*

The findings in this report are not to be construed as an official Department of the Army position, unless so designated by other authorized documents.

Mention of any trade names or manufacturers in this report shall not be construed as advertising nor as an official endorsement or approval of such products of companies by the United States Government.

# PREFACE

This proceeding contains the papers presented at the 1993 Army Symposium on Solid Mechanics, held at Plymouth, Massachusetts, August 17-19, 1993. It was the thirteenth in a series of biennial symposia with an emphasis on solid mechanics research achievements relevant to defense system needs. The symposia series which began in 1966, has been sponsored by the Army Materials Technology Laboratory in its role as the US Army lead laboratory for solid mechanics research and exploratory development. In October 1992, the research laboratories under Army Materiel Command were reorganized, and the Army Research Laboratory (ARL) was established with 10 Directorates. The Materials Technology Laboratory became the Materials Directorate. This symposium is the first one organized under ARL with collaborations from three directorates, namely Materials Directorate, Vehicle Structures Directorate and Weapons Technology Directorate, and the Army Research Office which has the responsibility of managing Army's basic research programs.

The symposium is organized into nine technical sessions covering subjects from basic research to applications. A total of fifty seven (57) technical papers were presented by the contributors representing government laboratories, academic institutions, and industry.

The Symposium Organizers wish to thank Mr. Lawrence D. Johnson, Directorate Executive of Materials Directorate, Army Research Laboratory and Dr. George H. Bishop, Jr., Technical Director of Materials Directorate for their support and encouragement in organizing the symposium. The dedication and hard work of Mrs. Ann Baratta is gratefully acknowledged for handling all communication's related to the symposium. Finally the organizers wish to thank Mrs. Karen Wilcox, Materials Directorate Conference Coordinator, for her effort in arranging the setting for the symposium which really enhanced the interchange among participants, and her effort in publishing the proceedings. The administrative contributions of Ms. Lori Mantia of Universal Technology Corporation are also acknowledged.

S.C. Chou, ARL/MD
F.D. Bartlett, Jr., ARL/VSD
T.W. Wright, ARL/WTD
K. Iyer, ARO

# CONTENTS

**Symposium Committee** ..... 1

**Symposium Presentations** ..... 5

**Session I: Ballistics**

Prediction of Large Scale High Velocity Penetration Experiments on Ceramic Armor - *S.J. Bless, R. Subramanian, C.E. Anderson Jr. and D. Littlefield* ..... 9

Ballistic Performance of Ceramic Targets - *G.E. Hauver, P.H. Netherwood, R.F. Benck and L.J. Kecskes* ..... 23

Ballistic Penetration Phenomenology of High Symmetry Single Crystals - *P.W. Kingman and R.A. Herring* ..... 35

Ballistic Environment Simulation Facility - *A. Frydman and A. Abrahamian* ..... 47

Numerical Modeling of a Reactive Armor System - *W.L. Cheng* ..... 61

**Session IIA: Failure and Damage**

Accumulated Damage and Fracture of Composite Laminates Under In-Plane Loads - *I. Shahid and F.K. Chang* ..... 65

Small Crack Growth in Brittle-Matrix/Brittle-Fiber Composite Materials - *F.T. Patterson and M.P. Cleary* ..... 77

Process Damage in Polymers - *K. Mallick and D. Krajcinovic* ..... 89

Plastic Flow and Damage in a Tungsten Based Composite - *G. Bao, Z. Lin and K.T. Ramesh* ..... 101

Shear Bands in Pressure-Shear Plate Impact - *M. Zhou, R.J. Clifton and A. Needleman* ..... 117

Deformation and Failure of Tantalum and Tantalum-Tungsten Alloys Under Dynamic Tensile/Shear Loading - *D.H. Lassila, M.M. Leblanc and K.A. Winer* ..... 137

Viscoelastic Mode I Fracture Behavior in Nitrile Rubber Sheets - *C.J. Quigley, J.L. Mead and A.R. Johnson* ..... 139

**Session IIB: Composites**

Combined Tension and Bending Testing of Tapered Composite Laminates - *T.K. O'Brien, G.B. Murri, R. Hagemeier and C. Rogers* ..... 143

Ballistic Performance of Kevlar Composites in an Arctic Environment - *E.M. Lenoe and P.K. Dutta* ..... 155

Effect of Specimen Size on the Tensile Strength of Geometrically Scaled $[+\theta^\circ_n/-\theta^\circ_n/90^\circ_{2n}]s$ Composite Laminates - *K.E. Jackson and S. Kellas* ..... 167

Deformation and Failure of Tungsten Composites - *T.K. Ramesh* ..... 185
Composite Hull - *W.E. Haskell* ..... 187
Micromechanical Models for Textile Structural Composites - *B.V. Sankar and R.V. Marrey* ..... 189
Stress Concentration and Post Matrix Yield at Fiber Breaks in Hybrid Composites - *J.N. Rossettos and M. Olia* ..... 201

**Session III: Penetration Mechanics**

An Advanced Ceramic Model for Impact Dynamic Codes - *A.M. Rajendran* ..... 215
Dynamic Impact and Penetration of Thick Composite Laminate - *C.T. Sun and S.V. Potti* ..... 233
Axisymmetric Penetration of Thermoviscoplastic Targets - *R.C. Batra, X. Chen and Z. Peng* ..... 235
Perforation of HY-100 Steel Plates with Long Rod Projectiles - *S.J. Hanchak, B.S. Altman and M.J. Forrestal* ..... 247
A Conceptual Model to Predict Force-Time Histories in Steel Plates Due to Penetration by Tungsten Rods at Velocities of 1.5 to 2.5 Km/s - *S. Dhar, D.J. Grove and N.S. Brar* ..... 257
A Time-Dependent Model for Long-Rod Penetration - *J.D. Walker and C.E. Anderson Jr.* ..... 271

**Session IVA: Structural Application**

Aging Aircraft: Structural Integrity and Damage Tolerance - *R. Greif, D.Y. Jeong and P. Tong* ..... 285
Structural Optimization and Design Sensitivity of Composite Cylindrical Shells for Energy Absorption - *A. Chattopadhyay and J.M. Ferreira* ..... 311
Design and Fabrication of Thick Composite Cylinders Subjected to Axial Loads - *J. Tzeng, J. Bender, B. Burns and A. Alexander* ..... 327
Validation of Projectile Transient Response Models for the Study of Pressure Oscillations in Guns - *M. Berman, T. Li and D. Hopkins* ..... 329
Rebending, in Thick-Walled Tubing, due to a Radial Temperature Gradient - *B. Avitzur* ..... 341
Stress Reversal in Steel Wheels Subjected to High Performance Braking - *O. Orringer* ..... 353

**Session IVB: Numerical Analysis**

The Micromechanical Simulation of Ductile Failure with an Eulerian Finite Element Code - *D.J. Benson* ..... 357

Validation of A-Posteriori Error Estimators by a Computer-Based Approach - *T. Strouboulis, C.S. Upadhyay, S.K. Gangaraj and K. Copps* ..... 369
Toward the Application of an Adaptive Finite Element Method to the Simulation of Adiabatic Shear Bands - *J.W. Walter Jr.* ..... 407
Finite Element Modeling of Segmental Chip Formation in High Speed Orthogonal Cutting - *J. Hashemi, A.A. Tseng and P.C. Chou* ..... 419
Heat Transfer and Thermal Stress Analysis of Railroad Car Wheels During Stop-Braking and Quenching - *Y.H. Tang* ..... 431
The High Capacity Artillery Projectile - *J.M. Bender and B. P. Burns* ..... 433
Free Vibration and Impact Response of Laminated Composites Using a Layer-Wise Theory - *A. Nosier, R.K. Kapania and J.N. Reddy* ..... 445

**Session V: Ceramics/Glass**

Determination of Material Strength in Shocked Ceramics - *Y.M. Gupta* ..... 459
Dynamic Behavior of Ceramics Under Multiaxial Compression - *W. Chen and G. Ravichandran* ..... 461
Hydrodynamic Compressibility of High-Strength Ceramics - *D.E. Grady* ..... 469
Strength of Aluminium Nitride - *D.P. Dandekar, A. Abbate and J. Frankel* ..... 479
The Mechanical Behavior of a High-Purity Alumina Over the Strain Rate Range $10^{-4}$ - $10^{6}$ $sec^{-1}$ - *J.M. Staehler, W.W. Predebon and B.J. Pletka* ..... 493
Plate Impact Investigation of Failure Waves in Glass - *G.F. Raiser, R.J. Clifton, J.L. Wise, D.E. Grady and D.E. Cox* ..... 505

**Session VIA: Anisotropy and Heterogeniety**

Degree-of-Freedom Based Deterministic Model Reduction: Application to Laminates - *L.D. Flippen Jr.* ..... 509
Modeling Anisotropic Response of Titanium Polycrystalline Aggregates - *V.C. Prantil, J.T. Jenkins and P.R. Dawson* ..... 525
Voronoi Cell Finite Element Model for Random Micropolar Elastic-Plastic Heterogeneous Media - *S. Ghosh, S. Moorthy and Y. Liu* ..... 527
On the Coupling of Pressure and Deviatoric Stress in Hyperelastic Materials - *M. Scheidler* ..... 539

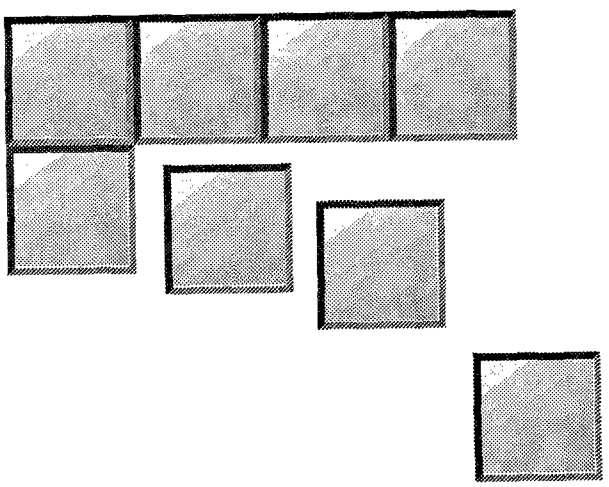
Modelling Substructural and Textural Anisotropy at Finite Strain - *M.P. Miller, D.L. McDowell and D.J. Bammann* ..... 551
End Effects in Anisotropic and Composite Structures - *C.O. Horgan and J.G. Simmonds* ..... 567

**Session VIB: Dynamic Behavior**

Experimental Evaluation of Strain, Strain-Rate and Temperature Dependance of Flow Stress at High Strain Rate - *S. Nemat-Nasser* ..... 581
Effect of Gas-Producing and Polymorphic Reactions on Stress Wave Propagation - *T.J. Ahrens and G. Chen* ..... 583
On the Strain and Strain-Rate Dependence of the Fraction of Plastic Work Converted to Heat and Full Field Measurements of the Dynamic Deformation Field Around a Growing Adiabatic Shear Band - *J.J. Mason, A.J. Rosakis and G. Ravichandran* ..... 595
Considerations in the Experimental Determination of Constitutive Parameters for Finite Strain Plasticity - *N.J. Huffington Jr.* ..... 609
High Strain Rate Behavior and Localization in Hafnium - *G. Subhash and G. Ravichandran* ..... 621
Split Hopkinson Bar Compression Screening Tests of High Density Penetrator Materials - *L.S. Magness Jr. and C. Lopatin* ..... 633

**Attendance List** ..... 645

# SYMPOSIUM COMMITTEE



# ARMY SYMPOSIUM ON SOLID MECHANICS

SYMPOSIUM COMMITTEE

*Dr. Fulton D. Bartlett, Jr.*
*Dr. Shun-chin Chou*
*Dr. Thomas W. Wright*
U.S. Army Research Laboratory

*Dr. Kailasam Iyer*
U.S. Army Research Office

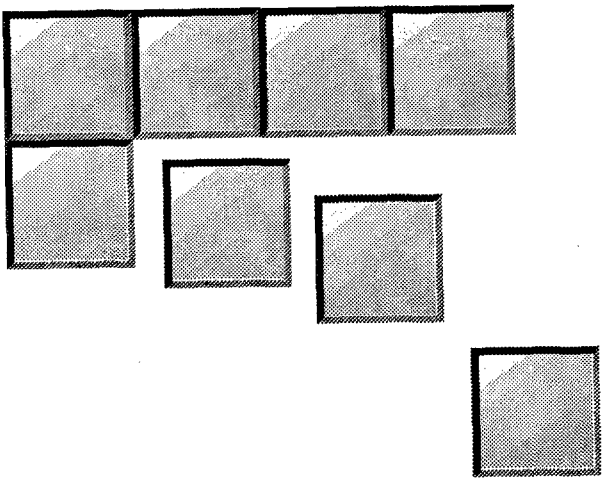
SYMPOSIUM COORDINATORS

*Karen Kaloostian*
*Ann Baratta*
U.S. Army Research Laboratory

SYMPOSIUM ADMINISTRATION

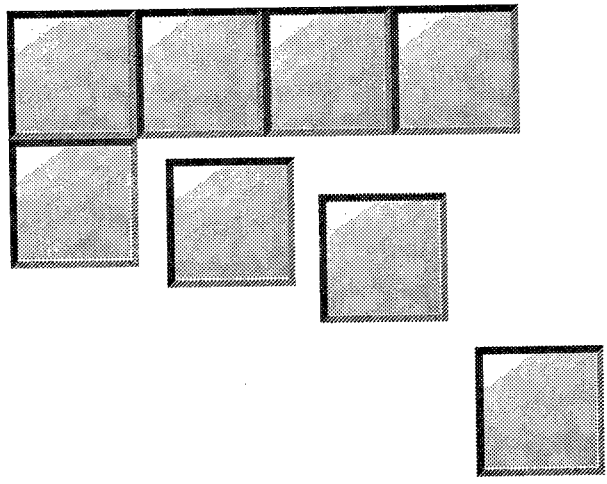
*Ms. Lori Mantia*
Universal Technology Corporation

# SYMPOSIUM PRESENTATIONS



# SESSION I:
# BALLISTICS

**Chairman:** *G. Bishop*
**Materials Directorate**
**Army Research Laboratory**



# Prediction of Large Scale High Velocity Penetration Experiments on Ceramic Armor

Dr. Stephen J. Bless*
Mr. Ravi Subramanian
Institute for Advanced Technology
The University of Texas at Austin
4030-2 W. Braker Lane
Austin, TX 78759-5329

Dr. Charles E. Anderson, Jr.
Dr. David Littlefield
Southwest Research Institute
6220 Culebra Road
P. O. Drawer 28510
San Antonio, TX 78228-0510

**ABSTRACT**—In December 1992, experiments were conducted in which 2.8 MJ L/D = 30 rods were shot at 1.775 and 1.8 km/s into ¾ scale ceramic armor targets containing 300 mm line-of-sight thickness of 99.5% alumina. These experiments were preceded by independent predictions using CTH and various analytical models. Parameters for the analyses were derived from several different relatively small scale laboratory penetration experiments. It turned out that all the predictions underestimated penetration at 1.775 km/s. The discrepancies are probably due to the inability of the analyses and the laboratory scale experiments to properly mimic the degradation that occurs ahead of the penetration in thick tiles struck by long rods.

## INTRODUCTION

Programs are under way in several countries to develop new gun and missile technologies which have the potential to substantially increase the striking velocity of projectiles on battlefields in the next century. Under contract from the Electric Armament Program Office of the U.S. Army Armament Research, Development and Engineering Center, the Institute for Advanced Technology (IAT) has been evaluating the potential for more efficient penetration of ceramic armor at higher impact velocities. Simple Tate modeling indicates that ceramics may be more vulnerable to hypervelocity attack [1,2]. On the other hand, Russians report that ceramics are very difficult to penetrate above their intrinsic failure speeds [3,4]. Theoretical work at IAT indicates that penetration resistance, $R_T$, may increase with impact velocity due to the pressure dependence of ceramic "flow stress" [5].

*Denotes Speaker

There are a great many design parameters associated with ceramic armor involving materials and geometry. There are also a large number of projectile parameters besides velocity, since we are ultimately interested in penetration concepts other than conventional long rods. Although development of military projectiles must be based on experiments that are close to the appropriate scale, practicalities dictate large roles for analysis, numerical simulation, and subscale testing.

Our initial approach to the study of ceramic armor has been to conduct a series of benchmark experiments at the largest feasible scale. The experiments were preceded by predictions using standard analytical and numerical techniques. Three benefits are expected: (1) an initial assessment of velocity effects on ceramic armor, (2) reference data for verifying fidelity of future smaller scale tests, and (3) assessments of predicting methodologies that might be used to reduce the number of needed experiments.

## DESCRIPTION OF EXPERIMENTS

### Projectiles

Projectiles were launched at 1.8 and 2.6 km/s with the G-04 two-stage light-gas gun at the Arnold Engineering Development Center (AEDC). The rod length to mass effective diameter ratio was chosen as 30, which represents the state of the art in fielded long rod penetrators. The energy of the projectile was kept constant at a nominal value of approximately 2.9 MJ. This energy was selected because it was the largest energy that could be launched with reasonable success probability at 2.6 km/s with the two-stage light-gas gun at the AEDC facility.

Projectiles were size scaled to keep the kinetic energy constant. The dimensions are summarized in Table 1, and Figure 1 shows the designs. The design of the superior grooves was modeled after those used by Silsby [6]. The material was Teledyne 91% tungsten swaged WHA (X27X). According to the purchase specifications, the density of these rods is 17.45 g/cm$^3$ (which we verified), the ultimate stress is 190 ksi, and the elongation is 10%.

The projectiles were gripped in full length sabots made from 7075T6 alloy aluminum that were EDM machined to mate with the

Table 1
**Projectile Parameters**

| | 1.775 km/s Test | 2.6 km/s Test |
|---|---|---|
| **Mass (g)** | 1830 | 850 |
| **Kinetic energy (MJ)** | 2.88 | 2.88 |
| **Length (mm)** | 494 | 384 |
| **Mass Effective Diameter (mm)** | 16.5 | 12.8 |

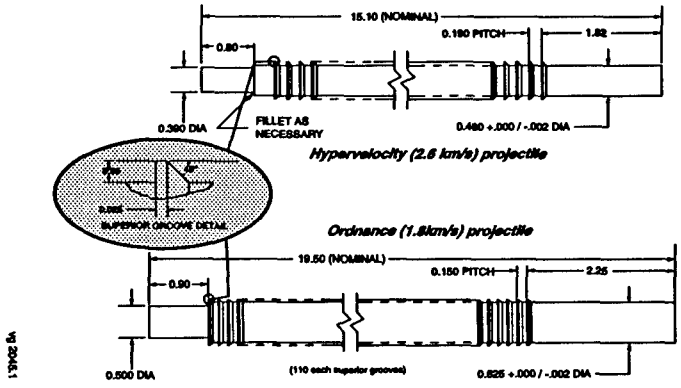



Figure 1. **Sketch of projectiles.**

superior grooves. There were nylon bore riders fore and aft. The sabots were designed to pivot behind the rod. Details of launch techniques for these rods are provided [7,8].

## Target Design

The targets were modeled after the ATM (armor technology module) target set developed by the Army Research Laboratory [9]. The scale was reduced from the ARL target dimensions because the penetrators were lower energy than the 6.8 MJ nominal "full scale" penetrator energy. Cube root energy scaling provided the scale factor of 75%.

The design of the ceramic target is shown in Figure 2. The ceramic tiles were Coors Porcelain 99.5% alumina (AD995). The interfaces between tiles were ground and matched by Coors. The RHA components were 269 BHN, except for the ceramic cover plate which was 300 BHN. The steel confinement was double-pass welded, after pre-heating the assembly to 250° Centigrade, into a box without the

rear confinement plate in place. The ceramic tiles were then potted in place with Epon 828 resin mixed with an equal mass of V-40 curing agent. The tiles were centered in the confinement box with six Isodamp C-1002 wedges per tile. Large voids in the epoxy introduced during mixing were removed by placing the mixed epoxy in a vacuum for approximately ten minutes.

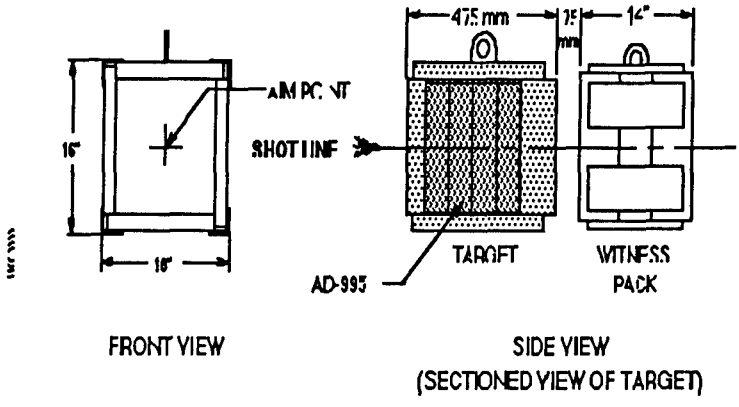



Figure 2. **Ceramic target design.**

After the rear confinement plate was lowered into place, a clamping pressure of approximately 5 psi was applied with a large weight and the excess epoxy was allowed to squeeze out around the rear confinement plate. The epoxy then cured for one week before the rear confinement plate was double-pass welded into place (without pre-heat), completing the target. The inside surfaces (against the ceramic) of both the front and rear confinement were surface ground, resulting in an epoxy-filled gap of less than 0.5 millimeters between the tiles and the front and rear confinement plates. The epoxy-filled lateral gap between the tiles and the steel side plates ranged from 5 to 10 mm. The areal density of the ceramic target, as measured along the shotline, was 253 g/cm$^2$.

## RESULTS OF EXPERIMENTS

Table 2 lists all of the experimental parameters and results. Figure 3 shows the craters that were produced in the witness blocks.

The ceramic targets were destroyed by the impacts, most corner braces failed, and the ceramic tiles were broken into pieces no larger than 30 mm across. The lateral confinement plates, however, were not noticeably bent. The damage to the cover plates was con-

Table 2
**Experimental Results**

| Shot Number | V, (Km/s) | Witness Pack DOP (mm) | Witness Pack Lr (mm) |
|---|---|---|---|
| 6864 | 2.59 | 77.5 | 8 |
| 6865 | 1.73 | 85.8 | 67 |
| 6866 | 2.60 | 71.0 | 5 |
| 6867 | 1.77 | 82.0 | 51 |

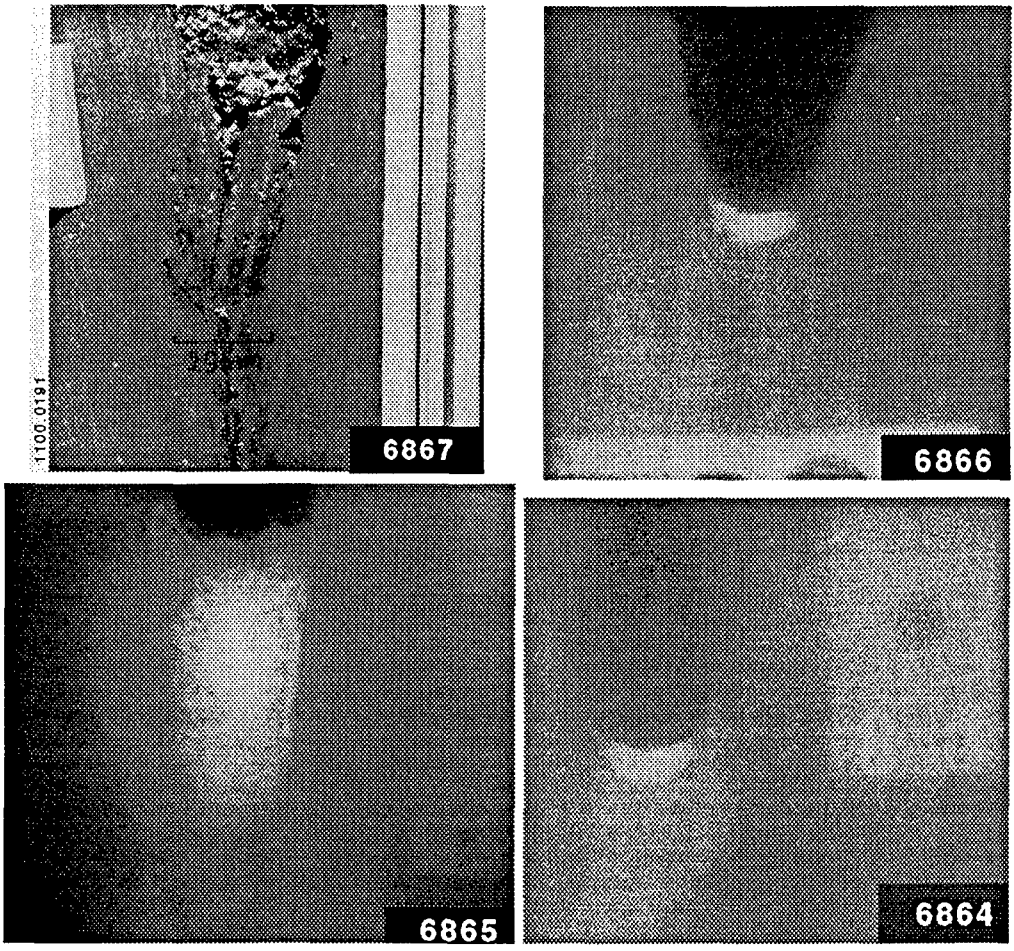



Figure 3. **Craters produced by residual penetrators.**

ventional for thick cover plate designs, i.e., there was a deeply undercut region in the cover plate at the interface between this plate and the ceramic. This undercut may indicate side flow of rod material during the initial stage of penetration into the ceramic [10]. This was true at both velocities. There were also circular imprints on the inside

of the coverplates which may provide evidence of the size of the fractured zone around the penetrator during the penetration. The diameter of this zone was about 150 mm at both velocities.

The differential efficiency of the ceramic element, $\Delta e_c$, can be computed from the equation:

$$\Delta e_C = \frac{W_{ref} - (W_{cp}+W_{bp}+W_r)}{W_C}$$

where W represents areal density, and subscripts ref, cp, bp, r, and c respectively, refer to penetration of same penetrator into RHA, cover plate, back plate, penetration in witness block, and ceramic element. For $W_{ref}$, we used a polynomial fit to high L/D (length/diameter) ratio WHA rods striking RHA:

$$W_{ref} = \rho_S L \sum_0^7 C_i V^i$$

where $\rho_s$ is steel density, L is rod length, V is velocity in m/s, and the coefficients $C_i$ are:

$C_0 = 30.1886$ $C_2 = 88.621$ $C_4 = 16.4003$ $C_6 = 0.31181$

$C_1 = -81.1852$ $C_3 = -50.3917$ $C_6 = 0.31181$ $C_7 = -0.01313$

The differential efficiency turns out to be $1.48 \pm 0.08$ and $2.02 \pm 0.02$ at impact velocities of 1.75 and 2.6 km/s, respectively. The ordnance velocity value is substantially lower than usually reported for good alumina in laboratory tests. For example, values of 2.5 have been reported ([11], [12]) for similar aluminas at ordnance velocities. We know of no high velocity $\Delta e_m$ data for the same alumina, but $\Delta e_m$ values computed from the alumina tests range from 1.8 to 1.9 over impact velocities of 2 to 2.5 km/s [13].

## PREDICTIONS

The predictions were all carried out and documented before test data were available. The predictions were based on the nominal impact velocities 1.775 and 2.60 km/s.

Two analytic models were used to predict the results of the ceramic armor testing: Tate and Walker/Anderson.

## Tate Model Predictions

Application of Tate modeling [14] to ceramics has become common practice [11,15,16], since the $R_T$ parameter is a convenient way to express effective penetration resistance. This is true, even though the penetration process in ceramics is considerably different from that which Tate assumed for metals.

IAT carried out the Tate model predictions with the properties Y=15 kbar for the rod, and $R_T$=55 kbar for RHA and 63 kbar for ceramic.

Selection of $R_T$=63 kbar was based on an analysis of DOP data by Woolsey [17] and Gooch [18], shown in Figure 4. Here, $R_T$ was computed from their data by assuming that the rod penetration velocity is constant, and by assuming:

$$\frac{L_r - L_o}{L_o} = \frac{P_{ref} - P_r}{P_{ref}}$$

where P is penetration. Woolsey's data are for WHA and Gooch's data are for DU. Nominally for RHA, Y=18 kbar, and for DU, Y=12 kbar. Considerable scatter can be seen. Our selection of $R_T$ = 63 kbar was based on the belief that the lower values of $R_T$ in the thickest tiles were most likely to represent the behavior of AD 995 in the ATM target. At the exit face of the RHA backing plate, a simple breakout model was used in which the target resistance decayed linearly to zero, beginning at a distance 4D from the free surface.

Using these parameters, the predictions of the Tate's model were: $P_R$ = 20.5 mm at V = 1.775 km/s and 47 mm at V = 2.60 km/s.

## Correction to Nominal Conditions

In order to compare the predictions with the data, it is necessary to account for the difference in velocity between the experiment and the predictions. This is especially important at ordnance velocity, when $\partial P/\partial V$ is relatively large for RHA.

This correction was made using Tate's theory [14]. A layered Tate model was used for the ceramic and steel. Interfaces were

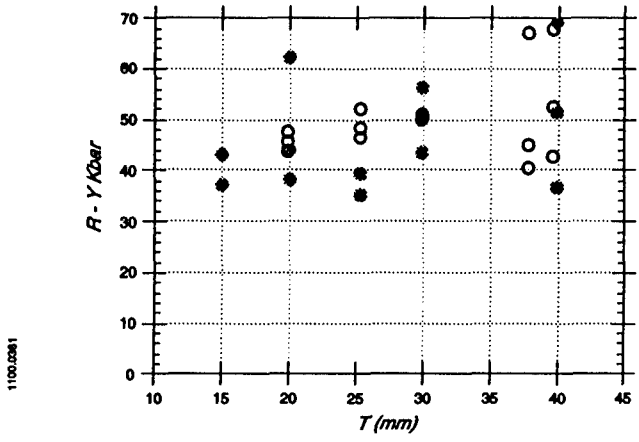



Figure 4. **R-Y from DOP data. Open circles [17] are for WHA rods closed circles [18] are for DU rods.**

ignored. The penetration resistance of the steel was taken as velocity dependent, following [19], $R_T = 92.5 - 25\ V_i$, where $V_i$ is impact velocity in km/s and $R_T$ is in kbar. For each experiment, $R_T$ for the ceramic was adjusted until the measured value of residual penetration was obtained. Then, using this same value of ceramic $R_T$, a new value of residual penetration was computed for the nominal velocities $V_n$, 1.775 and 1.80 km/s. Using this procedure, we obtained the results shown in Table 3.

The average value of $R_T$ that was derived for the AD995 in this process was 46 kbar at 1.775 km/s, and 60 kbar at 2.6 km/s. Penetrations (based on simple averages) are 97 mm and 75 mm, respectively.

Table 3
**Reference Residual Penetration**

| $V_i$ km/s | $V_n$ km/s | Shot | $P_r$ (adj.) mm |
|---|---|---|---|
| 1.73 | 1.775 | 6865 | 108 |
| 1.77 | 1.775 | 6867 | 87 |
| 2.59 | 2.60 | 6864 | 79 |
| 2.60 | 2.60 | 6866 | 71 |

At 1.775 km/s, the observed value of residual penetration greatly exceeds the Tate model pre-test prediction. The discrepancy is still unacceptable at 2.60 km/s, although much less. At 1.775 km/s, the disagreement mainly comes from the relatively low average $R_T$ value required to match the data. $R_T$ values are closer at 2.60 km/s. The calculation scheme used to derive $R_T$ from the data involves time stepping and is apparently more accurate than the constant penetration velocity assumption used in Figure 4.

**Walker/Anderson Model Predictions**

The Walker-Anderson model [20] is based on a more realistic description of the flow field around a long-rod penetrator than the Tate model. Importantly, it also includes transient effects at impact and at the end of penetration. The conceptual framework for the extent of plastic flow is built on ductile cavity expansion, and the application of the model to ceramics should be regarded as an empirical approach with parameters that are adjusted to fit experimental data.

The model was run with two different values for the flow stress of the failed ceramic. First, the model was run using 26 kbars (2.6 GPa) for the flow stress of the failed ceramic. The model results were essentially identical to the predictions of CTH using the Johnson-Holmquist model. However, comparison of the model predictions with position-time data taken with the PHERMEX facility at Los Alamos National Laboratory [21] indicated that the 26-kbar value was too "strong," and that a value of 12 kbars (1.2 GPA) was a more appropriate value. The second case, therefore, used the 12-kbar value to represent the flow stress of the failed ceramic material for the ceramic laminate target. The resulting predictions from the Walker-Anderson model for the ceramic laminate target were:

| V (km/s) | Strength (kbar) | $P_r$ (mm) | |
|---|---|---|---|
| 1.775 | 24 | 0 | (stopped at ceramic base) |
| 1.775 | 12 | 72 | |
| 2.60 | 24 | 47 | |
| 2.60 | 12 | 116 | |

The predictions with 24 kbar strength very substantially underestimate penetration at 1.775 km/s. Even the 12 kbar strength calculation underestimates the observed value. Thus, as with this Tate model, all predictions based on DOP testing seriously overestimated

the effective strength of the ceramic at ordnance velocity. In hypervelocity, the predictions bracketed the observed value.

## CTH Predictions

CTH calculations were performed using the Johnson-Holmquist model [22]. An independent evaluation of the parameters for the Johnson-Holmquist model has not been performed for 99.5%-pure $Al_2O_3$. Therefore, the depth-of-penetration (DOP) data from Woolsey [17] was used to "calibrate" the model constants. A parametric study was performed, and it was determined that the flow stress of the failed material was the most significant model parameter in these calculations. It was the only parameter that was varied in the calculations. The experimental data and the computational results are shown in Figure 5. It is clear from the scatter in the data, particularly for the thicker tiles, that several different values for the failed flow stress might be used. However, the 26 kbar value appears to represent the data reasonably well over the various tile thicknesses tested. Thus, for the CTH calculations, a value of 26 kbars (2.6 GPa) was used for the flow stress of the failed ceramic. The regular Johnson-Cook parameters were used for the tungsten and steel, and are listed in Table 4. The Johnson-Holmquist parameters are listed in Table 5. (Parameters are defined in Figure 6.)

Table 4. **Johnson-Cook Constitutive Parameters**

| | $Y_o$ (GPa) | B (GPa) | n (-) | C (-) | m (-) | $T_{melt}$ (K) | G (GPa) | ν (-) | Frac. Stress (GPa) |
|---|---|---|---|---|---|---|---|---|---|
| Tungsten | **1.51** | **0.177** | **0.12** | **0.016** | **1.00** | **1752** | **119** | **0.30** | **2.0** |
| 4340 Steel | **1.189** | **0.765** | **0.26** | **0.014** | **1.003** | **1793** | **77.6** | **0.29** | **2.0** |

$$\sigma_{eq} = \left(Y_O + B\epsilon_p^n\right)\left[1 + C\,ln\left(\dot{\epsilon}_p/\dot{\epsilon}_o\right)\right]\left(1 - T^{*m}\right) \quad \dot{\epsilon}_o = 1.0\,s^{-1} \quad T^* = \left(\frac{T - T_o}{T_m - T_o}\right) \quad T_o = 300°K$$

Table 5. **Johnson-Holmquist Model Parameters**

| $S_1$ (GPa) | $S_2$ (GPa) | $S_3$ (GPa) | $P_1$ (GPa) | $P_2$ (GPa) | T (TPa) | $C_6$ (-) | $C_3$ (-) |
|---|---|---|---|---|---|---|---|
| **3.91** | **5.58** | **2.59** | **1.4** | **7.3** | **-260** | **1.13** | **0.007** |

$$\sigma_{eq} = \sigma_o\left[1 + C\,ln\left(\dot{\epsilon}^p/\dot{\epsilon}_o\right)\right] \qquad \dot{\epsilon}_o = 1.0\,s^{-1}$$

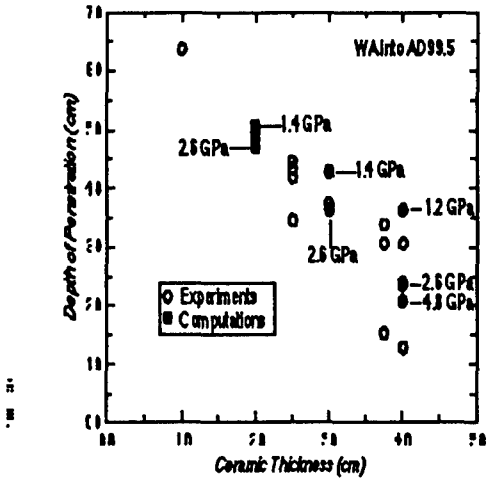



Figure 5. **DOP data [17] and CTH model calculations.**

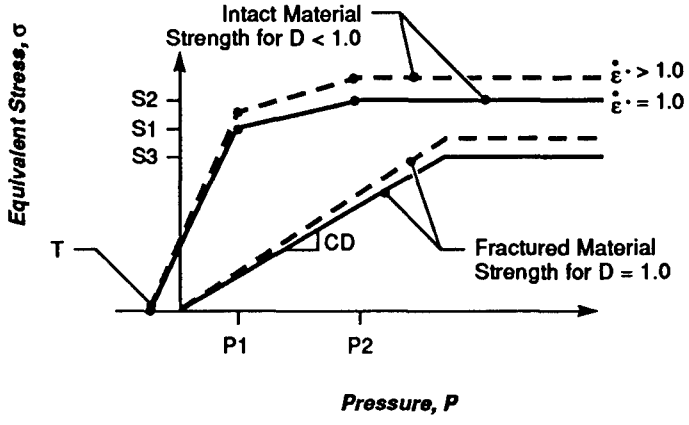



Figure 6. **Johnson-Holmquist Brittle Model.**

Figure 7 shows the results for final penetration depth at these two velocities. At 1.775 km/s the rod only reached the base of the ceramic; $P_R = 0$. At 2.60 km/s, $P_R = 18$mm. Both calculations very seriously underestimated the observed values.

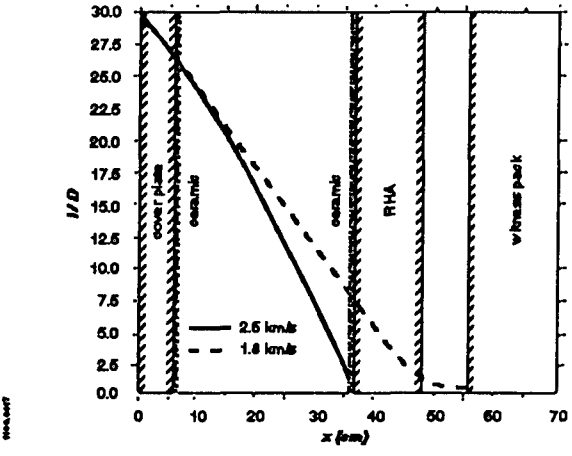



Figure 7. **CTH calculations for rod erosion.**

## DISCUSSION

All predictions of the ordnance velocity experiment were qualitatively wrong. Each prediction scheme was based on laboratory test results, and this test geometry represented a genuine extrapolation, in terms of tile thickness, rod length, tile shape (cube) and velocity. We show in [23] that the ability of these models to predict RHA penetration is excellent, so the discrepancies must be due to treatment of the ceramic component. The fact that predictions were more accurate at 2.6 km/s suggests that at higher velocity inertia dominates the material responses. Consequently, we think the failure of the predictions probably stem from two causes: (1) phenomena occur in the ATM target that are qualitatively different from those occurring in the tests used to calibrate the models; and (2) the physical description of ceramics in the models is incomplete.

The most accurate of the quasi empirical modules was the one that was calibrated against the Phermex experiments, which resembled the ATM target in that the tile was very thick. Thus, perhaps quasi empirical models can be used oas long as there is not too much extrapolation.

It should also be pointed out that the performance of the ATM target at 1.775 km/s, resulting in $\Delta e_c = 1.48$, was considerably less than achieved with newer laminated ceramic armor designs [24]. If such a target had been tested in this program, the prediction may have been much more accurate; nevertheless, the inability to predict the

experimental results clearly demonstrates the inadequacy of our constitutive treatment of ceramics.

## CONCLUSIONS

1. Analytical and numerical models for heavy ceramic armor cannot be relied upon for predicting performance for impact configurations that differ significantly from those from which the model parameters were derived.
2. Model scale experiments used for evaluating ceramic armor or for model calibration should more faithfully mimic real armor configurations.
3. More effort is needed to develop ceramic behavior models that incorporate all of the physical processes that control ceramic penetration resistance. This is very important if we are going to assess *a priori* designs the improve or optimize ceramic performance.

## ACKNOWLEDGMENTS

The work was supported by the U.S. Army Armament Research, Development and Engineering Center (ARDEC) under contract DAAA21-90-D-0009.

## REFERENCES

[1] S. Bless, Z. Rosenberg, and B. Yoon, "Hypervelocity Penetration of Ceramics," *Int. J. Impact Eng.* 5:165-171, 1987.

[2] S. J. Bless and C. E. Anderson, "Penetration of Hard Layers by Hypervelocity Rod Projectiles," to appear *Int. J. Impact Eng.*, 1993.

[3] A. A. Kozhushko, I. I. Rykova, A. D. Izotov, and V. B. Lazarev, "Strength and Fracture of Ceramic Materials in High-Velocity Deformation," Izvesiya Akademii Nauk SSSR, Neorganischeskie Materialy, Vol. 23, No. 12, 2078-2082, 1987.

[4] A. A. Kozhuskhko, I. I. Rykova, and A. B. Sinani, "Resistance of Ceramics to Penetration at Impact Velocities Above 5 km/s," *J. de Physique IV*, C3-117-C3122, 1991.

[5] Y. Partom, "Ceramic Armor Resistance to Long-Rod Penetration and its Dependence on Projectile Velocity," Inst. for Adv. Tech. Report IAT.R 0017, March 9, 1993.

[6] B. R. Sorensen, K. D. Kimsey, G. F. Silsby, D. R. Scheffler, T. M. Sherrick, and W. S. deRosset, "High Velocity Penetration of Steel Targets," *Int. J. Impact Eng.*, Vol. 11, 107 - 119, 1991.

[7] S. J. Bless, R. Subramanian, D. Orphal, T. Kiehne, and R. Watt, "Evaluation of a Ceramic Armor Target with Long Rods at Ordnance Velocity and Hypervelocity," 1993 TACOM Armored Vehicle Survivability Conference, Gaithersburg, MD, March 31-April 2, 1993.

[8] R. M. Watt, "Hypervelocity Impact Tests of Long Rod Penetrators Against Standard Single Technology Targets," AEDC-TSR-93-V6, June 1993.

[9] E. Rapacki, "Standard Single Technology Targets," Second Ballistics Symp. on Classified Topics, Laurel, MD, October 26-29, 1992.

[10] S. J. Bless, M. Benyami, L. S. Apgar, and D. Eylon, "Impenetrable Ceramic Targets Struck by High Velocity Tungsten Long Rods," Proc. Conf. Structures Under Shock and Impact SUSI 92, Portsmouth UK, 16-18 June 1992.

[11] B. L. Morris and C. E. Anderson, Jr., "The Ballistic Performance of Confined Ceramic Tiles," 1991 TACOM Combat Vehicle Survivability Symp., Gaithersburg, MD, April 15-17, 1991.

[12] S. Bless, J. Gonzalez, N. Brar, M. Alme, and C. Terry, "Ceramic Armor Design Study," Fifth TACOM Armor Coordinating Conference, Monterey, CA, March 7 - 9, 1989.

[13] M. Wilkins, J. Gibbons, V. Hohler, and M. Cozzi, "Ballistic Performance of ALN, SiC, and $Al_2O_3$ Ceramic Tiles Impacted by Tungsten Alloy Long Rod Projectiles," 1991 TACOM Combat Vehicle Survivability Symp., Gaithersburg, MD, April 15 -17, 1991.

[14] A. Tate, "Further Results in the Theory of Long Rod Penetration," J. Mech. Phys.Solids, 17:141, 1969.

[15] D. L. Orphal and R. R. Franzen, "Penetration of Confined B4C, AlN and SiC Targets by Tungsten Long Rods at 1.5 to 5 km/s," presented at 1992 Hypervelocity Impact Symp., Classified Proceedings, Austin, TX, 17-20 Nov. 1992.

[16] G. Hauver, "Variation of Target Resistance During Long Rod Penetration into Ceramics," 13th Int'l Symp. Ballistics, Stockholm Sweden, 1-3 June 1992.

[17] P. Woolsey, "Ceramic Materials Screening by Residual Penetration Ballistic Testing," 13th Int'l Symp. Ballistics, Stockholm Sweden, 1-3 June 1992.

[18] W. Gooch, "DOP Testing with DU Rods," private communication, 1991.

[19] C. E. Anderson, Jr., J. D. Walker, and G. E. Hauver, "Target Resistance for Long-Rod Penetration into Semi-Infinite Targets," Nuclear Engineering and Design 138, 93-104, 1992.

[20] J. D. Walker and C. E. Anderson, Jr., "A Nonsteady-State Model for Penetration," 13th Int. Symp. Ballistics, Stockholm Sweden, Vol. 3 9-16, June 1992.

[21] R. Skaggs, private communication, 1992.

[22] G. R. Johnson and T. J. Holmquist, "An Improved Computational Constitutive Model for Brittle Materials," High Pressure Science and Technology - 1993, Inst. of Physics, 1994.

[23] C. E. Anderson, Jr., S. J. Bless, D. Littlefield, and R. Subramanian, "Prediction of Large Scale Impact Experiments on Steel Targets," to be presented at the 14th International Symposium on Ballistics, Quebec, Canada, 26-29 September 1993.

[24] J. Prifti, P. Woolsey, W. A. Gooch, and W. J. Perciballi, "Advanced Ceramic/Metallic Amor Systems for the Defeat of Long Rod Penetrators (u)," Second Ballistics Symposium on Classified Topics, October 26-29, 1992.

# Ballistic Performance of Ceramic Targets

G.E. Hauver(*), P.H. Netherwood,
R.F. Benck, and L.J. Kecskes
WTD, ARL, APG, MD 21005-5066

## ABSTRACT

The resistance of a ceramic to penetration by a long tungsten-alloy rod, impacting at 1600 m/s, depends on the design and construction of the entire target. A ceramic in one target may offer little resistance to penetration, but in a different target configuration, the same ceramic may allow no penetration. Resistance to penetration depends on damage to the ceramic, and damage depends on target characteristics. Sources of damage were identified by direct observation, or were inferred by varying the design and construction of targets and evaluating the change in ballistic performance. Target modifications, introduced to reduce damage, were found to nearly double the penetration resistance routinely reported for a few common ceramics. This improved performance was found to be accompanied by an interval of time during which the ceramic could not be penetrated. With further modification of the target, the entire long-rod penetrator was consumed by extended lateral flow at the surface of the ceramic. Damage, suppression of damage, and target characteristics will be discussed.

## INTRODUCTION

Ceramic armor for defeating long-rod penetrators usually performs below expectations, and it is common to observe that increasing the thickness of ceramic fails to achieve a corresponding improvement in the resistance to penetration. This observation suggests that the ceramic is being damaged well ahead of the penetrating rod. Designs for ceramic targets which are used to evaluate the ballistic performance of ceramics are similar to designs for ceramic armor, so it is reasonable to expect the performance of these targets to be degraded by similar sources of damage. This study has examined damage in ceramic targets used for ballistic evaluations, and has explored ways to reduce the damage and increase the resistance to penetration.

## DAMAGE IN CERAMIC TARGETS

Damage in ceramic targets is illustrated by Fig. 1 which shows three simple target configurations, A, B, and C. The ceramic in these targets was Ebon-A, a hot-pressed, 99.8% pure aluminum oxide ceramic produced by CERCOM, Inc. Each target was impacted by a tungsten-alloy rod launched at a velocity of 1500 m/s. In target A, the ceramic was 6 mm thick and was bonded to steel backing by approximately 1 mm of epoxy. The average penetration resistance of the ceramic, interpreted by the Tate Model [1,2,3], was 2.3 GPa. In target B, the ceramic was much thicker, and flash-radiographic observations were necessary to measure the time interval for 6 mm of penetration. From this measurement, the average penetration resistance was determined to be 6.0 GPa. In target C, a 6 mm thickness of steel was bonded to the front of thick ceramic, and flash-radiographic observations were again necessary to determine the time interval for penetration to a 6 mm depth in the ceramic. For target C, the average penetration resistance was determined to be 12.3 GPa.

Average penetration resistances of 2.3 to 12.3 GPa, for 6 mm thicknesses of the same ceramic, can be explained qualitatively in terms of ceramic damage. In the case of target A, impact against bare ceramic produced a peak shock stress near 40 GPa, which is approximately four times the Hugoniot Elastic Limit of the ceramic. This shock wave produced severe damage in the vicinity of impact. The diverging shock wave attenuated rapidly, and the penetration resistance should have increased as the damage decreased. However, when the shock wave reflected at the low-impedance interface bond, it produced tensile damage at the back of the ceramic. This additional source of damage limited the average penetration resistance in target A to only 2.3 GPa. In the case of target B, the absence of a low-impedance interface bond eliminated this source of tensile damage just 6 mm from the impacted surface. With only impact damage, the average penetration resistance was 6.0 GPa. In the case of target C, a front steel plate permitted some attenuation of the impact shock before it arrived at the ceramic. The front plate also probably retarded the displacement of damaged ceramic. The result was a higher penetration resistance of 12.3 GPa.

The shock wave from impact propagates through the ceramic and into the surrounding confinement. Some reflections occur at interfaces, but the major reflections occur at free boundaries. Reflected waves return and interact in the central region of the target. Although the diverging shock wave attenuates rapidly, there frequently is evidence of damage by wave interactions. The upper two radiographs in Fig. 2 provide evidence of this damage. In these radiographs, central damage appears to begin as orthogonal zones, although only one zone of damage

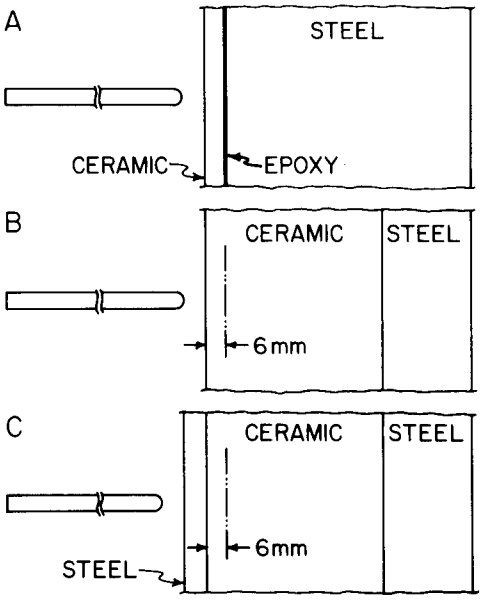



Fig. 1. Targets in which the ceramic sustains different damage.

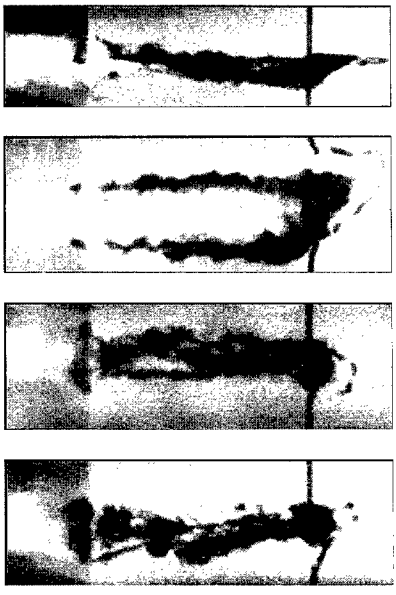


Fig. 2. Radiographs which show influences on the penetration.

persists to alter the penetration path deeper in the ceramic. The small, 75 mm square cross section of the confinement in this particular target was undoubtedly responsible for the unusually strong interaction. However, with a target this small, waves arriving at the free boundary have not attenuated to a level where wave traps are completely ineffective. The lower two orthogonal radiographs in Fig. 2 show the full penetration path in a similar target with wave traps at the boundaries. Here, wave interactions have been reduced, the penetration path is more symmetrical, and the penetration resistance has increased by approximately six percent.

Similar damage from wave interactions has also been observed in larger targets with a 127 mm square cross section. The dimensions of these larger targets precluded flash-radiographic observations during penetration, but a recovered target shown in Fig. 3 reveals damage zones under the front steel confinement. These orthogonal damage zones in the ceramic are aligned with surfaces of the free boundary. In later tests, this damage was eliminated by configuring free boundaries to disperse the reflected waves.

Damage from interacting waves can also be observed in acrylic targets similar to those once tested by Kolsky and his associates [4]. By using a small explosive

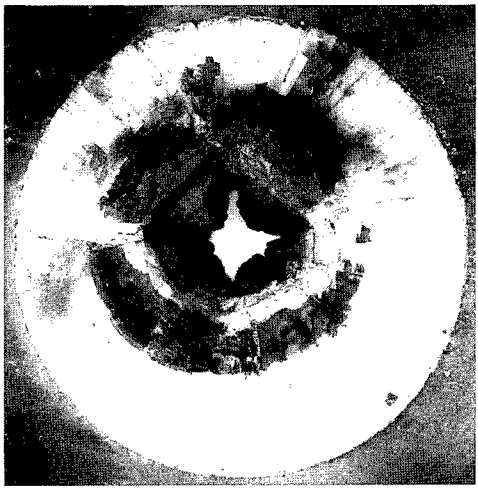


Fig. 3. Orthogonal damage zones in a ceramic target.

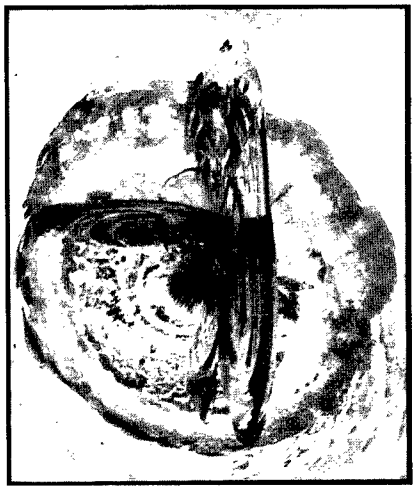


Fig. 4. Orthogonal damage in an acrylic block.

charge to shock an acrylic target with a square cross section, orthogonal damage is produced in the central region as shown in Fig. 4. Ceramic targets with a circular free boundary have been a special concern because the reflected wave converges to the central region. Consequently, similar tests were conducted using acrylic targets with a circular cross section. Targets from these tests are shown in Fig. 5. The target at the left in this figure was shocked at the axis, so the reflected wave converged to the axis where a damage zone developed. In a penetration test, the damage zone and the penetration path would coincide. The target at the center was shocked 10 mm away from the axis, so the reflected wave converged to a damage zone diametrically displaced by nearly 20 mm. These observations suggest that the scatter of data from penetration tests with ceramics may relate to the target geometry and the location of impact. The free boundary of the target at the right was configured with conical depressions. As a result, the reflected wave was dispersed and a central zone of damage is barely visible.

## SUPPRESSION OF DAMAGE

The target configuration shown in Fig. 6 includes a few features which reduce damage and increase ballistic performance above the values commonly reported. The steel side confinement is heated and allowed to shrink into contact with the ceramic core, producing a prestress of a few tenths of a GPa. This prestress cannot be varied greatly, and the available range of prestress produces little change in the ballistic performance. The main benefit is believed to result from the elimination of an epoxy bond at the peripheral interface. Although a shrink fit offers

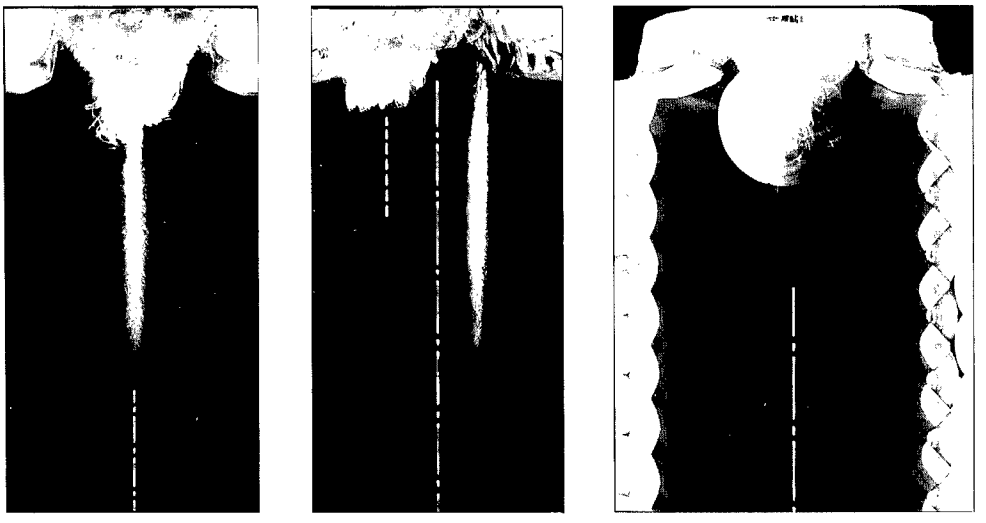


Fig. 5. Damage in acrylic targets with circular cross sections.

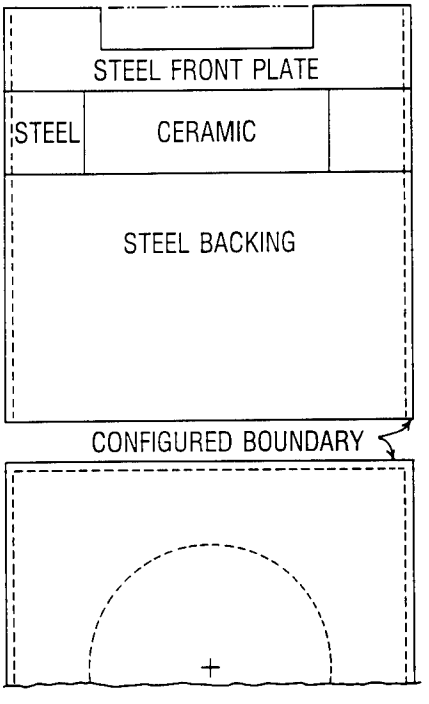



Fig. 6. Target configuration which reduces damage to the ceramic.

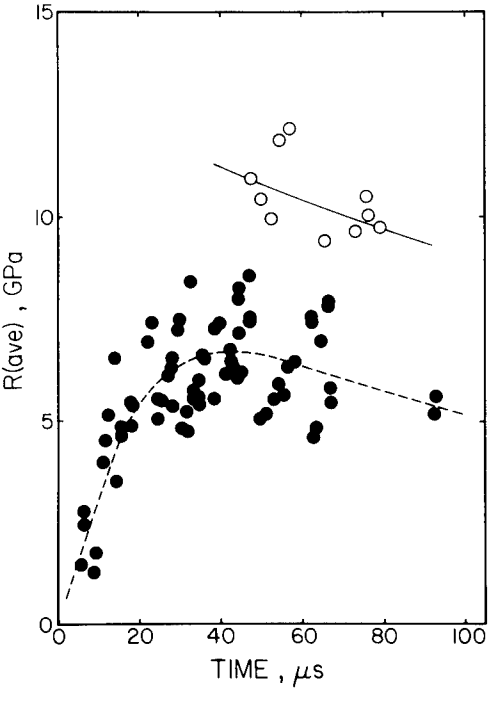



Fig. 7. Performance data for aluminum-oxide ceramics.

impedance benefits, the low strength of an epoxy interface layer could also be a consideration. The radial cracks, observed in Fig. 3, propagate to the periphery of the ceramic at a velocity of approximately 3000 to 4000 m/s, forming wedge-shaped blocks of ceramic which transmit force from the region where the penetrator interacts with the ceramic. Epoxy is more easily compressed or displaced than the steel confinement, and small increases in area at the periphery can have a significant influence on behavior at the center of the target. A small additional increase in performance occurs when epoxy at the back interface is replaced by braze. Outside surfaces of the target were also configured with conical depressions which, in an acrylic target, were found to disperse reflected waves and reduce the damage from wave interactions in the central region.

Aluminum oxide ceramics with a purity of 99%+ were evaluated in the target configuration of Fig. 6. The performance data from these tests are plotted as open circles in Fig. 7 and are represented by the continuous curve. In this figure, the average resistance to penetration serves as a measure of ballistic performance, and is plotted as a function of time. The apparent scatter of data along the continuous curve results from test variations such as prestress, bonding at the rear interface, mechanical clamping of the target laminations, and characteristics of the front steel confinement. These data indicate significantly higher ballistic performance than data from standard depth-of-penetration (DOP) tests [1,5,6]. The data from DOP tests are plotted as closed circles and are represented by the dashed curve.

## LIMITED LATERAL FLOW AT THE CERAMIC

Recovered targets were examined for evidence which might explain the higher performance in tests represented by the continuous curve in Fig. 7. Sectioned steel cover plates suggested an initial time interval during which the ceramic could not be penetrated. Fig. 8 shows two examples of residual penetrator material which has accumulated at one side of the penetration path, trapped between the steel cover plate and the ceramic. Judging by the volume of the depression in the steel plate, from 20% to 30% of the penetrator was consumed during this interval. An examination of the residue from this limited lateral flow provided details which were consistent with many of the microstructural observations by Bless, et.al. [7]. However, Fig. 9 shows a distinguishing feature of limited lateral flow. Near extremities of the flow, tungsten grains tend to pile up and deform, excluding the penetrator matrix. The displacement of matrix material results in the formation of matrix-rich zones as seen at the left of center in Fig. 9.

The target in Fig. 6 (and Fig. 8) is believed to have been poorly designed to accommodate material eroded from the penetrator. The upper plate in Fig. 8 was

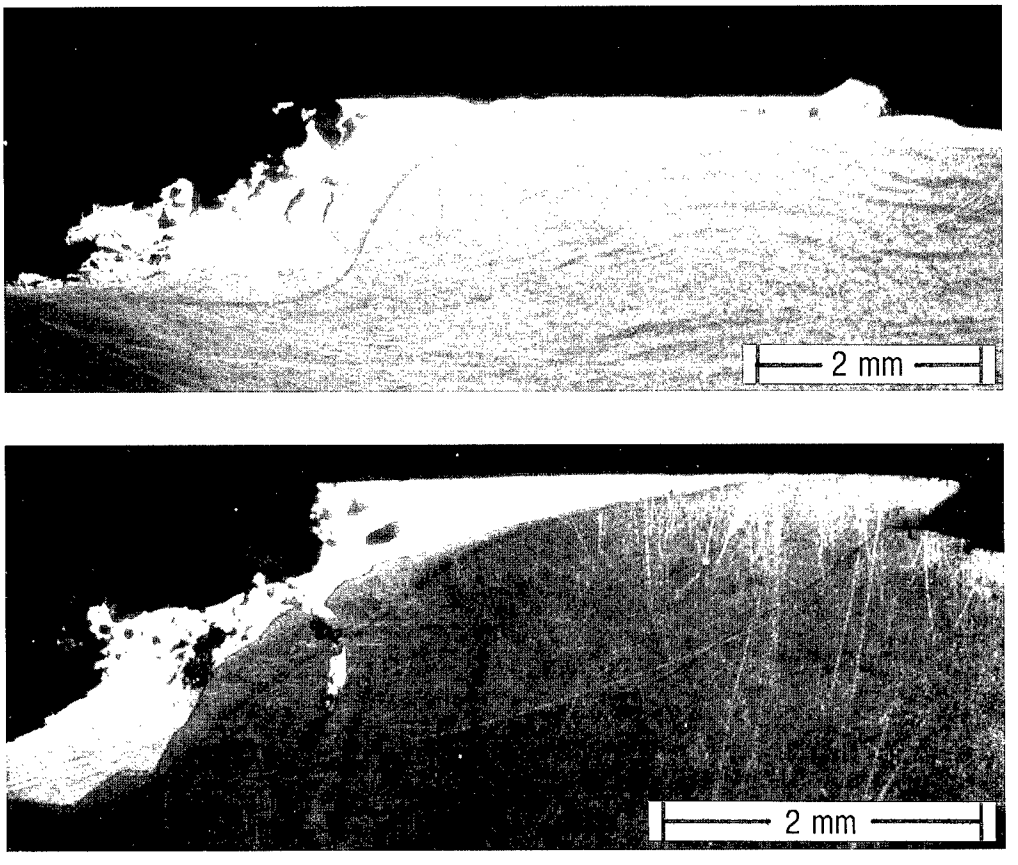



Fig. 8. Residues of limited lateral flow at the ceramic.

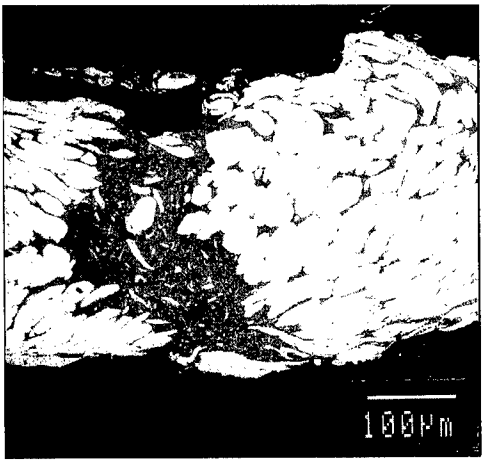



Fig. 9. Microstructure which occurs in limited lateral flow.

tightly clamped, the ceramic remained intact, and erosion products could flow only a limited distance into the interface. Consequently, the flow of incoming penetrator material changed from 90 degrees to 180 degrees, doubling the force at the axis of the rod. The state of damage at that time probably permitted penetration. The initial accumulation of erosion products in the lower plate of Fig. 8 caused the formation of an adiabatic shear band. A block of plate material, freed by this shear band, wedged into the interface and effectively blocked the lateral flow of erosion products. Again, the flow reversed, the axial force doubled, and penetration began.

The ability of a ceramic to temporarily resist penetration is also shown by the flash radiographs in Fig. 10. However, details of the eventual penetration are probably different from the explanation offered for Fig. 8. The target in Fig. 10 had a front plate of titanium alloy, 13 mm thick, which permitted appreciable attenuation of the shock wave from impact. However, the small 75 mm square cross section of the target permitted a strong tensile interaction in the central region which nearly coincided with the penetration time through the cover plate. The damage from this interaction probably allowed an early onset of penetration and ended the brief accumulation of rod material. Once penetration began, the granular flow of displaced ceramic particles eroded away much of the rod material in the center of the deposit, leaving only a residue as observed in Fig. 8.

## EXTENDED LATERAL FLOW AT THE CERAMIC

The target in Fig. 11 was introduced in an attempt to correct conditions believed to be responsible for limited lateral flow which prevented higher ballistic performance with the target in Fig. 6. This target configuration permits the examination of design variables which can be adjusted to minimize damage to the ceramic and better accommodate the lateral flow of erosion products. Since there is evidence that the impact shock is a source of damage, a shock attenuator was included at the front of the target.

The target in Fig. 11 contains ceramic with a diameter of 72.01 mm and a nominal thickness of 25 mm. Steel backing in the initial tests was RHA (rolled homogeneous armor) with a matching diameter, a thickness of 70 mm, and a hardness of 260 BHN. Steel backing with a higher hardness is one of the design variables. The ceramic and its steel backing were confined by ARMCO 17-4 PH steel with an inside diameter initially 0.13 mm less than the diameter of the core. Heating this confinement to 482 degrees C provided the clearance for assembly and left the confinement with a hardness of 420 BHN. In the initial design, the cover plate was AISI-4340 steel with a hardness of 450 BHN and a thickness of 9.5 mm. A 0.25 mm thickness of PTFE (polytetrafluoroethylene) was added between the steel cover and the ceramic to aid the accommodation of erosion

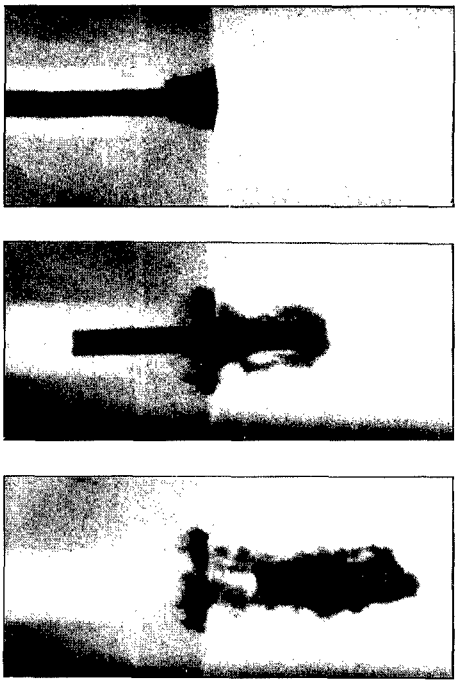


Fig. 10. Radiographs which show limited lateral flow.

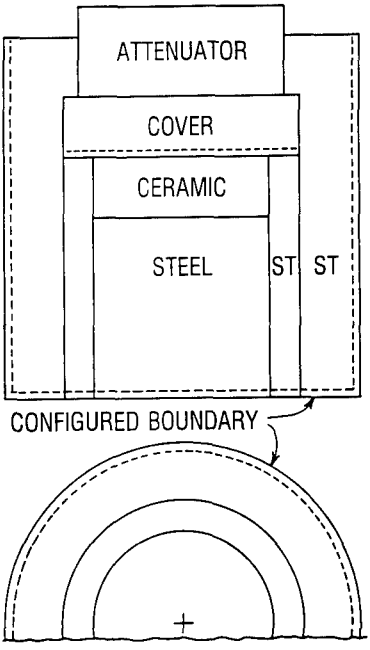



Fig. 11. Target introduced to achieve extended lateral flow.

products. The cover and the PTFE were bonded with Hysol 608 epoxy, and the PTFE was also bonded to the ceramic and its confinement. These components were placed in mild steel outer confinement using a second shrink fit. The shock attenuator is another test variable. Initially, it consisted of a 35 mm thickness of PMMA (polymethyl methacrylate) which reduced the shock stress at the ceramic to less than a few tenths of a GPa. The surface of the outer confinement was configured as a precaution, but this may not be necessary with an improved attenuator.

In an early test, the ceramic was hot-pressed TiC. A 93% tungsten-alloy penetrator, approximately 5 mm in diameter and 100 mm in length, was launched at 1600 m/s. After the test, the outer confinement was removed so that interior parts of the target could be examined. Photographs of the target interior are shown in Fig. 12. In this figure, (A) is the cover plate, viewed from the interface side. Erosion products abraded the plate as the flow moved radially away from the entrance hole. Some erosion products are fused to the surface of the plate near the periphery, but with the exception of this peripheral deposit, the interface side of the

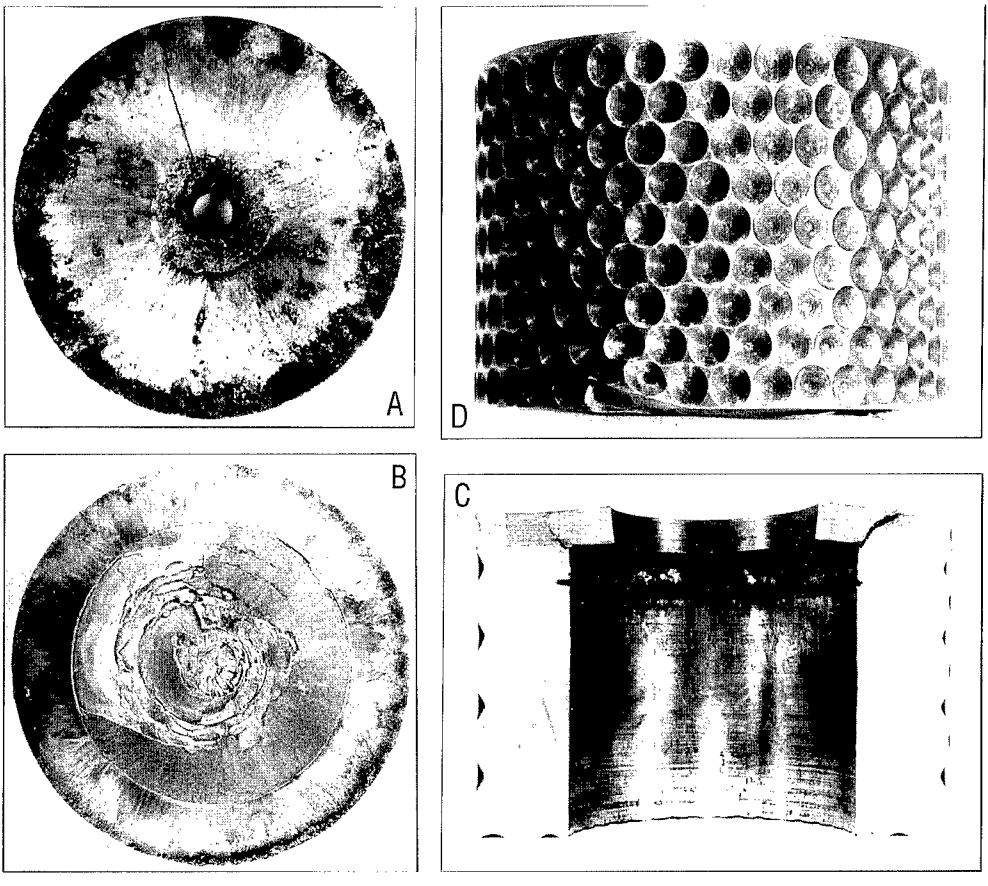



Fig. 12. Recovered target which shows extended lateral flow at the ceramic.

cover plate is almost bare. (B) is the corresponding surface of the ceramic. The central region exhibits the most severe damage, and material there was lost to a maximum depth of nearly 3 mm. However, the absence of radial flow lines where material is missing from the ceramic surface suggests that damaged material was separated from the surface after the rod was consumed and lateral flow ceased. In the next test, the ceramic sustained similar damage, but was found to be almost totally in place when the target was opened more carefully. Substantial areas of shallow damage (0.25-0.50 mm flaking) were suspected to result from thermal shock. (C) shows the inside of the outer confinement and the circumferential slot cut by erosion products which flowed radially through the interface. (D) shows the configured surface of the outer confinement.

Erosion products, fused near the periphery of the cover plate in a target from a different test, exhibited much of the microstructure identified by Bless, et.al. [7].

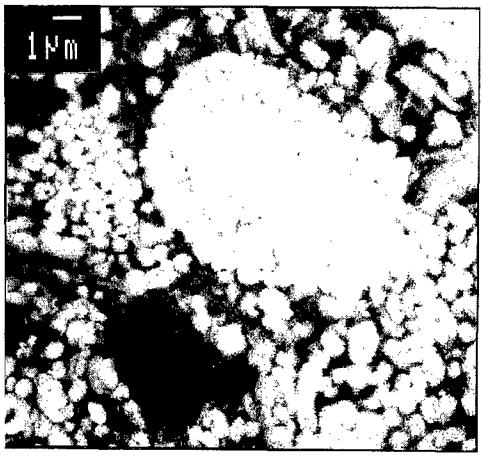



Fig. 13. Microstructure which occurs in extended lateral flow.

In particular, examination of a fragment revealed heavily deformed tungsten grains, intermixed with titanium diboride debris retained in the penetrator matrix. However, an additional structural feature of the tungsten grains should be noted. What appears as an agglomeration of submicron tungsten particles, in Fig. 13, is believed to result from the dissolution of tungsten into the molten matrix and the subsequent reprecipitation during rapid cooling. Although some of this tungsten appears to coat undissolved tungsten grains, a significant fraction appears as fine precipitates. If correct, this would support elevated temperatures during interface flow, as proposed in Ref. 7.

Test results indicate that there are limits within which extended lateral flow occurs. If target laminations separate freely after the penetrator arrives, the ceramic is not highly resistant to penetration. At the other extreme, if the steel/ceramic interface does not permit a flow of erosion products, the ceramic again is not highly resistant to penetration. Minimizing damage to the ceramic is suspected to be critical in initiating a lateral flow of erosion products, especially as the impact velocity increases. The controlled accommodation of erosion products is suspected to be critical in extending the duration of lateral flow at the ceramic. Current target design is addressing both issues in order to achieve maximum ballistic performance which is consistent with properties of the ceramic.

## CONCLUSIONS

The investigation of extended lateral flow at a ceramic is, clearly, work in progress. Although the result shown in Fig. 12 is encouraging, there is no reason to believe that the ballistic performance in this early test was optimum. The ballistic

performance of ceramics, and extended lateral flow in particular, is poorly understood at the present time. Many aspects of this phenomenon need to be investigated, including target design, velocity dependence, sensitivity to impact location, sensitivity to impact obliquity, and scaling. With refinements, velocity dependence should be found to correlate with ceramic properties. At present, the clearest conclusion is that ceramics are capable of much higher ballistic performance than is currently indicated by routine evaluation tests.

## REFERENCES


1. G.E. Hauver, P.H. Netherwood, R.F. Benck, W.A. Gooch, W.J. Perciballi and M.S. Burkins, "Variations of Target Resistance During Long-Rod Penetration into Ceramics," Proceedings of the Thirteenth International Symposium on Ballistics, Vol. 3, 257-264, National Defence Establishment, S-172 90 Sundyberg, Sweden, 1992.

2. A. Tate, "Theory for the Deceleration of Long Rods after Impact," J. Mech. Phys. Solids, 15, 387-399, 1967.

3. A. Tate, "Further Results in the Theory of Long Rod Penetration," J. Mech. Phys. Solids, 17, 141-150, 1969.

4. H. Kolsky, Stress Waves in Solids, Dover Publications, Inc., New York, 1963.

5. P. Woolsey, S. Mariano and D. Kokidko, "Alternative Test Methodology for Ballistic Performance Ranking of Ceramics," Proceedings of the Fifth Annual TACOM Armor Coordinating Conference, Monterey, CA, 1989.

6. V. Hohler and A. Stilp, Private Communication, Ernst-Mach-Institut, Freiburg, F.R.G., 1989.

7. S.J. Bless, M. Benyami, L.S. Apgar and D. Eylon, "Impenetrable Ceramic Targets Struck by High Velocity Tungsten Long Rods," Proceedings of the Second International Conference on Structures Under Shock and Impact, Portsmouth, UK, 16-18 June, 1992.

# Ballistic Penetration Phenomenology of High Symmetry Single Crystals

Dr. Pat W. Kingman*
Weapons Technology Directorate
Army Research Laboratory
Aberdeen Proving Ground, MD 21005-5066

Dr. Rodney A. Herring
Advanced Research Laboratory
Hitachi Limited
Hatoyama-machi, Hiki-gun, Saitama, Japan 350-03

## 1 Introduction

The material flow mechanisms which occur during ballistic penetration regimes and their role in influencing penetration behavior are not fully understood.

Penetration experiments at this laboratory in which tungsten single crystal rods of high symmetry orientations were fired into semi-infinite RHA targets showed that the penetration results were a strong function of crystallographic symmetry, and that the best performing orientation, the four-fold [100], exceeded current tungsten heavy alloy penetrators and was comparable to depleted uranium (1). Preliminary examination of recovered penetrators showed distinct differences in flow and failure patterns as a function of crystallography (1,2). The observed flow patterns are shown in Figure 1. These results are of fundamental interest because in single crystal experiments all variations in geometry, ballistic conditions, and such material parameters as density, grain size, etc. are eliminated: crystallography is the single variable. Since the overall macroscopic deformation geometry in all cases is eversion of the rod into a continuous tube possessing a pattern of scroll-like foliations on the inner

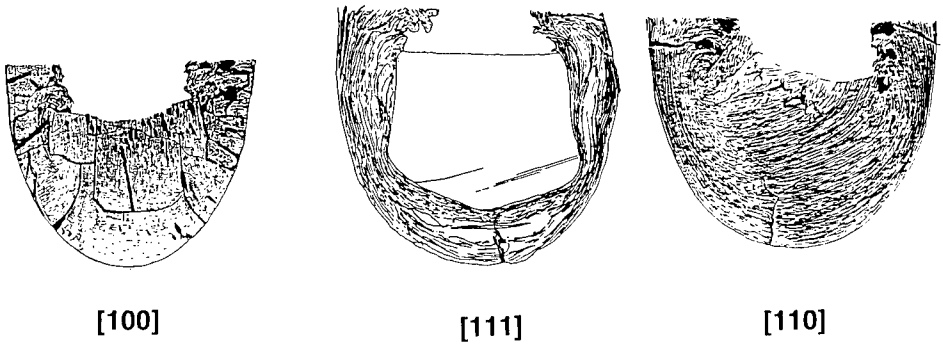



**Figure 1** Geometry and flow patterns around nose of penetrator.

surface, the large differences in penetration must therefore arise from the crystallography of the detailed processes operating in the initiation and continuation of material flow in the lattice.

Preliminary characterization of the flow patterns and fracture topography of the post-mortem specimens has been further extended and now provides a basis for better understanding the mechanisms which influence the penetration performance.

## 2 Experimental Approach

A synergistic approach was applied to characterization, utilizing optical metallography, scanning and transmission electron microscopy, and X-ray diffraction. The penetrators were embedded in semi-infinite RHA target blocks which were longitudinally sectioned. The residual back end of the penetrator, typically about one diameter (~6mm) in length, rested at the bottom of the penetration cavity surrounded by a thin layer of flowed material which extended back along the cavity walls to form a continuous back-extruded tube 1-3mm thick. Previous optical studies of these sections demonstrated the effects of crystallographic orientation on the general flow pattern during penetration and eversion (1,2), and provided a spatial reference frame for correlating micro-structural information. The large size of the steel target block sections limited scanning microscopy of the fracture surfaces to examination of separated fragments, generally from the back-extrusion tubes. The unpolished halves of the sectioned targets were cut up and prepared for transmission microscopy. Transverse and longitudinal TEM samples for each orientation were obtained by standard thinning techniques. X-ray diffraction pat-

terns of the polished metallographic sections were used to determine the crystal orientation and provide lattice information at intermediate resolution. To characterize the small, inhomogeneous residual penetrator samples still embedded in massive blocks, Laue back reflection was the only feasible method. Although the irradiated area is comparatively large (about half a millimeter), by making a series of small, incremental translations and comparing changes, the spatial resolution can be improved by about an order of magnitude. The target block was mounted in a special holder equipped with x and y micrometer translations. Once a reference point was established, relative positioning was extremely precise and reproducible, and could be correlated directly with optical macros.

Information from white-radiation diffraction is necessarily qualitative but nonetheless Laue patterns can provide a wealth of information about a deformed sample: orientation, lattice inhomogeneity (bending, substructure, etc.), recrystallization, grain size, preferred orientation, etc. This information was a major key in drawing together all of the observations into a coherent picture of the deformation process.

## 3 Results

### 3.1 Transmission Electron Microscopy

Dislocation arrangements were examined in samples of all three symmetry orientations, in both transverse and longitudinal sections, except for [110], where the only thinned sample obtained was transverse. More detailed discussion of the TEM results has been presented elsewhere (2), but the principal observations are summarized as follows.

The principal defect type observed was arrays of predominantly screw dislocations of the type b = 1/2<111>. All crystals contained dislocation networks, sub-boundaries, and recrystallized grains, but the detailed dislocation arrangements varied as a function of crystallographic orientation. Dislocations observed in the [100] and [111] crystals were networks of pure screws or mixed dislocations with a large screw component. Dislocations in the [110] penetrator were straight screw dislocations with short segments left by edge dislocations. Other types of defects, such as twins and stacking faults, were not observed. There was often extensive recrystallization, with freshly recrystallized material adjacent to heavily deformed structures. However, due to the extreme

inhomogeneity of the deformation, it was not possible to make direct correlation between the actual TEM observation area and the macro-structural flow pattern.

### 3.2 X-ray Diffraction

Observations for each orientation are summarized below.

*[110] Penetrator*

This residual penetrator was completely recrystallized except for a small region at one corner of the back end. The material in the etched band structure is polycrystalline, and Debye-Scherrer (D-S) rings from various regions showed a variety of substructures ranging from sharp, equiaxed recrystallized grains to broad cold-worked rings, generally with heavy texture. The few single crystal regions were distorted and ambiguous and thus no orientation information could be obtained. Further examination showed that the rear surface of the rod was a jumble of irregular surfaces, implying that the residual rod was cracked irregularly throughout as suggested by the cracks visible in the macro-section.

*[111] Penetrator*

Diffraction patterns showed the clearly-defined residual rod to be a single crystal, with little net lattice rotation except in the lobes near the front edge of the rod. Material in the flowed regions was primarily polycrystalline, with strong preferred orientation, but there were also included regions, primarily directly ahead of the residual rod, which were still single crystals, although severely bent and deformed; see Figure 2.



**Figure 2** Diffraction patterns from [111]: (L) residual rod, ( R) fragment embedded in recrystallized material ahead of residual rod.

*[100] Penetrator*

The most salient factor in the [100] X-ray results was the persistence of single crystal character throughout the entire head of the penetrator and well into the extrusion tube. Optical macros showed no clearly outlined rod remnant, as seen in the [111] penetrator, but instead there was an assemblage of blocky segments defined by large cracks, and throughout much of the sample on a smaller scale there occurred a semi-continuous network of fine, straight crack segments intersecting at right angles. In the central residual rod, these cracks were parallel and perpendicular to the rod axis, but in the peripheral flow regions they became respectively radial and parallel to the cavity interface.

X-ray analysis confirmed that the cracks were in all instances parallel to {100} cleavage planes. In the residual rod remnant, the diffraction pattern was always uniquely sharp and well-defined. Along the penetrator axis directly ahead of the residual rod the orientation was maintained and the spots were uniformly broadened without asterism; see Figure 3. A traverse across the sample directly below the rod rem-

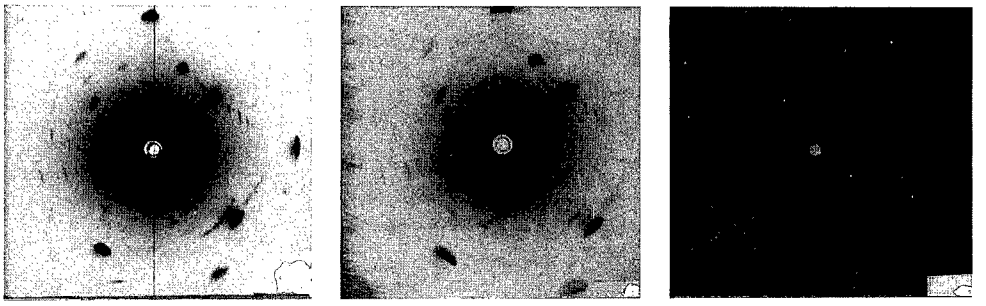


**Figure 3** Diffraction patterns from [100]: (L) residual rod, (C,R) material ahead of residual rod.

nant showed the lattice orientation changing continuously, corresponding with the reorientation of the {010} cleavage cracks, with surprisingly little asterism except in the vicinity of major cracks; see Figure 4. Numerous sequences throughout the sample demonstrated that single crystal reflections were obtained except in the vicinity of a few obvious inhomogeneities such as the severe, localized bands found near the back edges of the penetrator, where local recrystallization occurred. Single crystal patterns from the immediate vicinity of major cracks or similar inhomogeneities sometimes contained twisted, forked, or ginko-

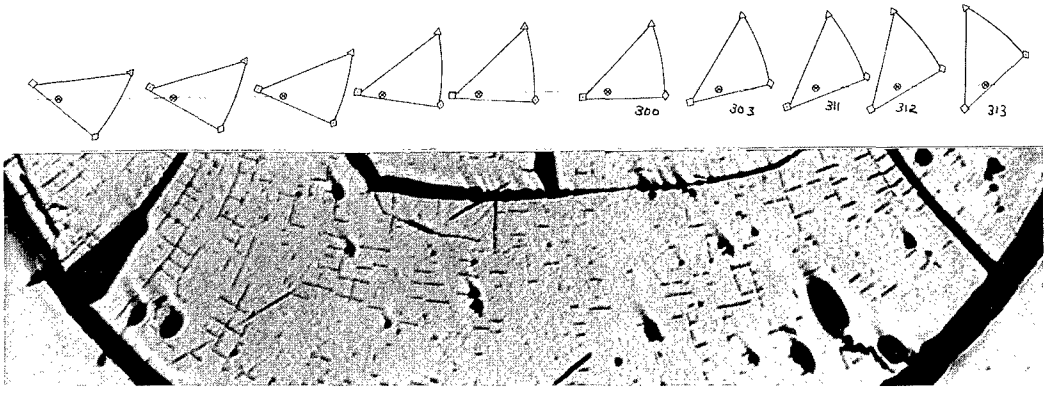



**Figure 4** Stereograms of diffraction patterns taken in sequence across [100] peripheral flow, correlating with cleavage cracks.

leaf spot shapes, indicating complex local bending, and superimposed D-S rings from recrystallization might be seen, but in many other instances uniform single-axis reorientation of the lattice occurred with a minimum of inhomogeneity; Figure 5. These Laue patterns contained uniform, continuously extended spots; when both ends of each spot were plotted, two crystal orientations related by a single axis rotation were represented, giving the limits of the continuous lattice rotation occurring within the irradiated area.

Since the observation surface is an axial plane of the penetrator, continuous lattice reorientation about the normal to the observation plane is consistent with radial material flow. Along the left edge of the penetrator this lattice rotation can be documented continuously from the nose back into the hollow extrusion tube for several rod diameters without discontinuity, until the single crystal spots finally disappear in textured D-S patterns. Along the right edge an orientation discontinuity occurs at a major crack near the residual rod, and a new orientation begins. Examination of a large fragment of another penetrator, which separated from the target block by fracturing away from a thin layer adhering to the cavity surface, clarified this discontinuity. Figure 6 shows the convex surface, partially covered with sheaf-like packets. X-rays of the packets showed broad single crystal reflections along with D-S rings. Seen in three dimensions these individual packets, defined by cleavage planes, appear to have sheared radially and also rotated in varying amounts about a normal axis, in agreement with the lattice rotations observed in the two dimensional axial surface of the first penetrator.

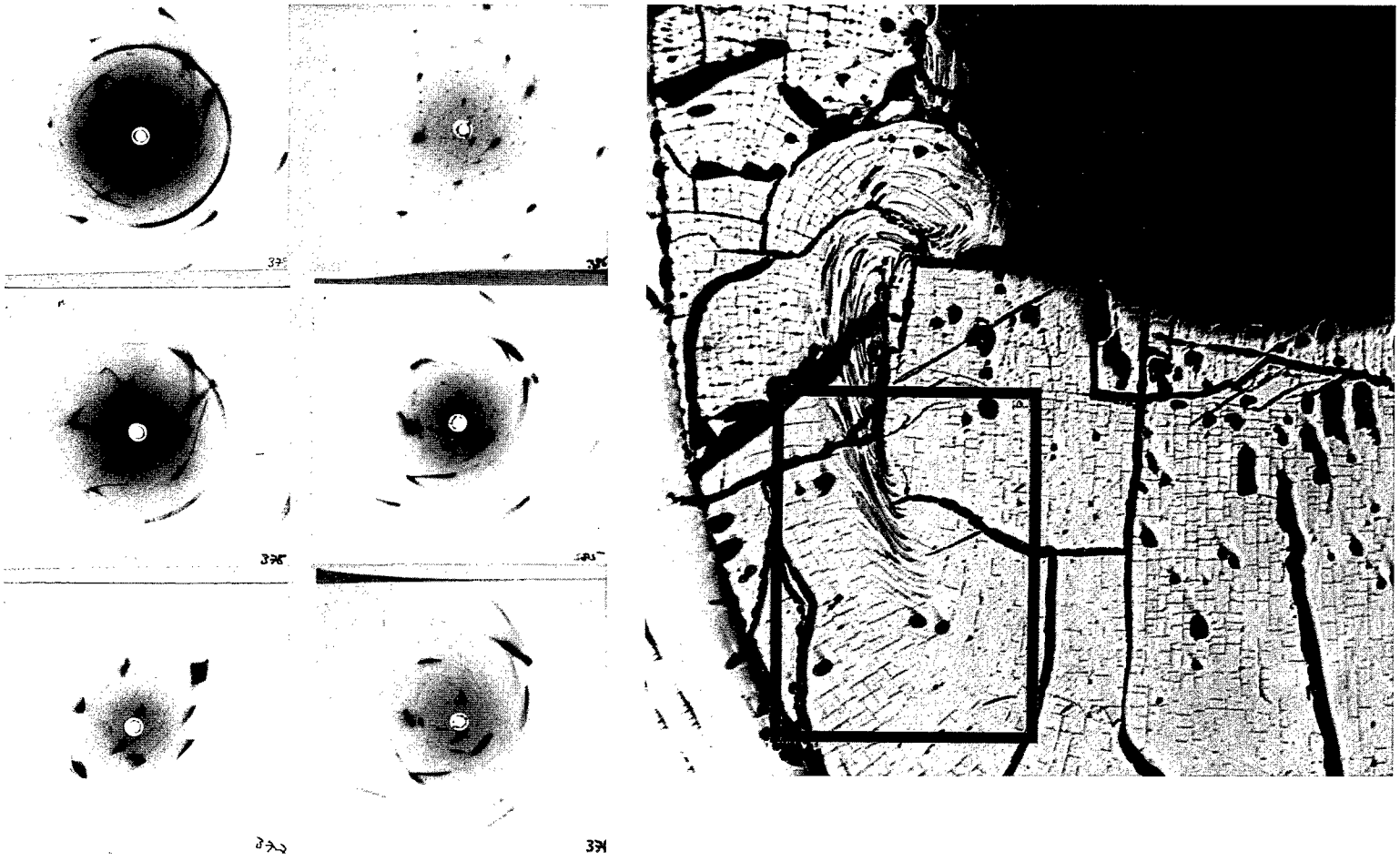


**Figure 5** Diffraction patterns from adjacent regions in [100] residual penetrator.

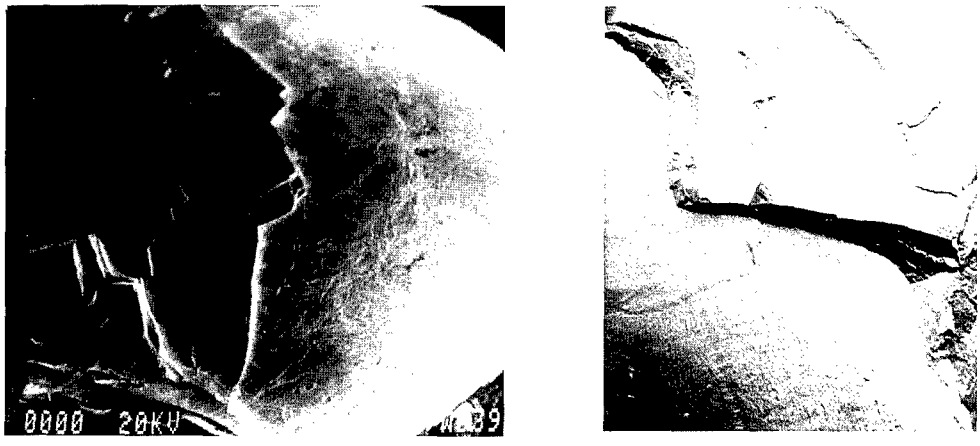



**Figure 6** Convex surface of separated [100] residual penetrator.

## 4 DISCUSSION

From these observations, it is evident that the microstructural processes operative in these three single crystal penetrators are quite different.

In the [111] rod, three <111> directions occur symmetrically at 70.5 degrees from the rod axis. Resolved shear stresses on these dislocations are thus relatively low, resulting in a high yield strength, while ample generation of dislocations available for interaction enhances work hardening. As well, screw dislocations will tend to move outward resulting in radial mass transfer toward the cavity walls. The well defined shape of the residual rod, with a blunt, low-angle nose and mushroom lobes, reflects this. The precise character of the few narrow bands etched in the residual is undefined, but the location and direction, along with the presence of large crystal fragments surrounded by heavily deformed and recrystallized material just ahead of the residual rod, suggests that separation of discrete material segments initiates with these bands. Additionally, the inner surface of the penetration tunnel is wavy and pocked, suggesting radial impingement of discrete segments of penetrator material as the blunt nose of the remaining rod forces these segments radially outward and then between the rod and the cavity wall. Diffusion gradients at the penetrator surface and iron-rich intrusions in cracks appear only in this sample, implying higher temperatures than for the other orientations. Eventually the crystal segments recrystallize, perhaps repeatedly, with a strong preferred orientation. All of these processes absorb a fraction of the total energy, which thus becomes unavailable for forward penetration. Thus the crys-

tallographic factors which lead to high yield strength, work hardening, and superior stress strain characteristics in unconfined conventional testing actually detract from penetration performance.

In the [100] penetrator, the material mechanisms are different. With four-fold symmetry, all four <111> directions are equally stressed, creating large numbers of dislocations able to react with one another. One possible reaction (3) is the Cottrell reaction:

$$\frac{1}{2}[\bar{1}1\bar{1}] + \frac{1}{2}[\bar{1}\bar{1}1] = [\bar{1}00] ,$$

which produces a sessile dislocation. This sessile dislocation is associated with the initiation of {100} cleavage cracks in bcc crystals oriented with a tensile stress axis along the [100] direction (4). Under hydrostatic stresses, cracks would not open at once, but could be nucleated as deviatoric stresses increase and material flow is initiated. It can also be reasonably speculated that early creation of a large distribution of these sessiles would inhibit subsequent work hardening. The smooth lamellar bending and shear and the relative absence of substructure, complex lattice distortion, and recrystallization evident in X-ray patterns from much of the peripheral flow region indicate that the work hardening expected from standard stress-strain behavior does not occur. In contrast to the [111] penetration profile, the [100] penetration tunnel is narrow and exceptionally smooth, and there is little evidence of interaction between the penetrator and the target material. Rather than discontinuously shedding finite material segments, the [100] rod is postulated to flow by a smooth continuous process in which small, finite lattice elements defined by cleavage cracks undergo a combination of lamellar bending and rigid rotation with little internal disturbance—a process which is highly energy efficient, thus allowing maximum partition of energy into forward motion, i.e. penetration. Such features as the etched deformation bands at the back ends of the sample, which contain heavily deformed and recrystallized material, seem likely to be a localized artifact rather than a primary deformation mode. The persistence of the rectangular crack pattern even through the curved foliations in the extrusion tube (Figure 5) is strong evidence that lamellar flow of finite entities with minimal lattice disruption is the continuing deformation mode and that continuous reorientation of defined entities was complete before recrystallization eventually occurred.

Again, standard stress-strain properties do not predict penetration

results, since the [100] yield and work hardening curves are similar to but lower than those for [111], while in ballistic penetration a highly efficient alternative material flow mechanism occurs, absorbing less energy and allowing the [100] penetrator to exceed the performance of the [111].

For the [110] orientation detailed conclusions are more difficult since the recrystallization is so extensive. In 2-fold symmetry, only two <111> directions are stressed and work-hardening dislocation reactions are unavailable. Classically, [110] bcc crystals have a high yield but do not work harden; at high impact velocities twins may occur. (5) The TEM, SEM, and X-ray results all indicate that the penetrator material has repeatedly recrystallized, deformed, and recrystallized again. The nature of the etched bands, which were entirely recrystallized with a strong preferred orientation, was not determined. The flow packets in the (110) extrusion tube were unique in having a completely non-crystallographic appearance; instead they resembled ductile, bifurcating fronds. It seems possible that multiple fractures occurred very early, and after yield ductile flow occurred with repeated recrystallization.

It is interesting to compare the observed modes occurring in single crystal rods with the work of Magness(6) and Magness and Farrand(7) in several materials. Magness interpreted these results in terms of the initiation of shear localizations, primarily adiabatic shear bands in the deforming penetrator. Figure 7, taken from Magness, shows sche-

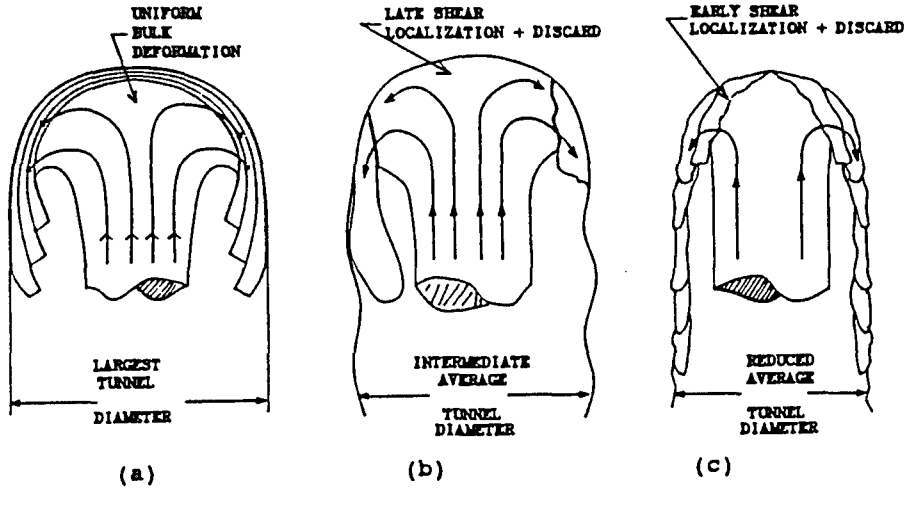



**Figure 7** Schematic of postulated flow modes, after Magness (6).

matically the flow patterns he identifies.

Mode (b), late shear localization and discard, leads to the mushrooming and wavy cavity profile resulting from non-steady flow which are associated with poor penetration performance, and are typical of polycrystalline tungsten. The [111] flow pattern resembles this model: some mushrooming and a wavy profile are definitely present, and the few narrow bands present may be sites for discontinuous material separation.

The penetration cavity of the [100] rod resembles mode (c), like that of the DU penetrators described by Magness. In the [100] case the chisel-shape profile is absent but the tip radius is still narrow and the geometry of the penetration tunnel resembles that of the early shear and discard model. It appears that the successful performance of this penetrator results from an extremely efficient flow mechanism initiated, like the adiabatic shear localizations observed in DU, early in the flow process, but on a much finer scale. This fine scale allows relatively smooth, continuous initiation of flow which is energetically efficient. Thus the deformation mode occurring in the [100] crystal is an alternative mechanism which extends the concept of penetration by early initiation of energy-efficient shear to a microscopic scale.

The characterization of the [110] flow is less obvious, but the shallower, wider cavity with relatively smooth walls may be consistent with the stable, uniform flow model (a), modified by anisotropy. Further information about the actual flow mechanisms would be needed to characterize this orientation.

## 5 CONCLUSION

Single crystal penetrator tests have shown that crystallography, which governs microstructural failure and flow mechanisms, is a strong determinant of penetration behavior. Additionally, as previously pointed out by Magness and others, classical quasi-static data do not necessarily imply similar performance in ballistic penetration. Finally, the excellent performance of the [100] single crystal penetrators has been shown to result from a unique deformation mode in which work hardening is suppressed and flow initiates at microscopic inhomogeneities which allow small but finite crystal entities to shear and flow with minimal internal deformation. This mode allows an energetically efficient uniform flow which maximizes the fraction of total energy partitioned into forward

penetration, resulting a deep, narrow, smooth walled penetration cavity similar to the geometry of "chisel nose" DU penetrators, but by a mechanism different from adiabatic shear. Single crystal experiments provide a unique opportunity to isolate the effects of crystal symmetry on microstructural deformation and study the basic material mechanisms involved. This understanding will lead to more effective processing to utilize and optimize the appropriate properties of existing materials and can ultimately define a basis for designing novel materials and composites in the future.

**References**

(1) Bruchey, W.J., E.J. Horwath, & P.W. Kingman "Orientation Dependence of Deformation and Penetration Behavior of Tungsten Single-Crystal Rods" in Tungsten and Tungsten Alloys, Recent Advances, A. Crowson & E. Chen, eds., TMS, Warrendale, Pa.

(2) Bruchey, W.J., R.A. Herring, P.W. Kingman, & E.J. Horwath, "Deformation Mechanisms in Tungsten Single Crystals in Ballistic Impact Experiments", in High Strain Rate Behavior of Refractory Metals and Alloys, Asfahnai et al, eds., TMS, Warrendale, Pa., 1992.

(3) Carrington, W., K.F. Hale, & D. McLean, "Arrangement of Dislocations in Iron", Proc. Roy. Sci. A, Vol 259, 1960, pp 203-227.

(4) Reed-Hill, R., "Physical Metallurgy Principles", van Nostrand, Princeton, N.J., 1964, pp 534-536.

(5) Vecchio, K., Private communication to P. Kingman.

(6) Magness, L.S., "Properties and Performance of KE Penetrator Materials", in Tungsten and Tungsten Alloys, Metal Powder Industries Federation, Princeton, N.J., 1992, pp 15-22.

(7) Magness, L S., and T.S. Farrand, "Deformation Behaviour and Its Relationship to the Penetration Performance of High-Density KE Penetrator Materials", Proceedings of the 1990 Army Science Conference, 1991, pp 465-479.

## Ballistic-Environment Simulation Facility

Mr. Abraham Frydman* and Mr. Ara Abrahamian

Army Research Laboratory
Weapons Technology Directorate, Mechanics and Structures Branch
2800 Powder Mill Road, Adelphi, MD 20783

Background: In the early 1940's, a group was formed at the National Bureau of Standards (NBS) in Washington, DC to develop fuzes for bombs, rockets, mortars, and grenades. This Ordnance Development Division, was headed by Harry Diamond, a pioneer radio engineer who developed the airborne weather radiosonde, ILS blind landing system, radio beacon system, and other navigation aids. Its major accomplishment was the radio Doppler proximity fuze. By 1951, the first large gas gun was in use and in 1953, the Division was transferred to the Army, renamed the Diamond Ordnance Fuze Laboratories (DOFL), and attached to the Office of the Chief of Ordnance. In 1962, DOFL became the Harry Diamond Laboratories (HDL), one of five laboratories of the Army Materiel Command. The ballistic facilities in DC were relocated to a specially designed research facility at Adelphi, MD in 1976. In the fall of 92, HDL was disbanded and the ballistic facility was transferred and became part of the Mechanics and Structures Branch (MSB) of the Weapons Technology Directorate of the ARL.

### Ballistic Simulation Methodology

Interior Ballistics: Setback (linear acceleration) is the prime acceleration of smooth bore munitions; while setback, angular acceleration, and centrifugal acceleration relate to rifled weapons. Ballistic simulators provide unique, in-house, laboratory operational evaluation of devices[1] that previously could be met only by expensive, time-consuming field tests. Simulation of actual firing conditions enables the devel-

[1] The word *device* represents any projectile or component that requires this type of test. When the simulators were at HDL, *device* refered to a fuze or fuze component.

oper to respond quickly and resolve R&D problems. Simulators are also used in production tests to efficiently screen out manufacturing flaws and to reduce the number of rounds required for field tests.

Chronology: The first setback simulator, built in 1951, tested the ruggedness of new proximity fuzes. An air gun was made from eight, 12' long, gun barrels, bored out to 4" ID, and was assembled using copper gasket seals. A 100 cubic foot, 125 psi air tank, supplied the propulsive force for a 20 lb. hardened steel bird[2] that housed the unit under study. The experiment, simulating setback conditions, occurred in a heavy-walled steel box where the bird impacted a lead target.[3] The device orientation in the bird was reversed relative to its orientation in the projectile so that the deceleration force at impact acted in the same direction as did the acceleration force due to weapon firing. The bird acceleration in the air gun was low to minimize effects on the device but achieve terminal velocities of a few hundred ft/sec. Bird weight and muzzle velocity were varied to control deceleration. Peak deceleration was determined by copper-ball accelerometry (a dent technique). This simple, inexpensive method was used until 1965. It is now known that for many devices, such tests were overly severe; a prevailing philosophy was *if it survives the air gun, it will survive anything.* The concept of the impact deceleration simulating the actual launch acceleration is still paramount although we are more advanced in terms of theory, instrumentation, data reduction and gas gun design and usage. We can simulate a wide range of unique ballistic environments that are especially applicable to many devices. With the advent of very high acceleration smooth bore guns, and, with the recent re-organization, the character of the ballistic experiments will change to accommodate higher accelerations, heavier birds, and an ability to measure structural response and performance of a device during impact.

Setback Test Methodology.: The concept of setback testing is mitigated momentum exchange. Initial bird velocity is still provided by low acceleration air or gas guns. A light aluminum or phenolic bird replaces the heavy steel bird and a crushable energy-absorbing target (mitigator) backed by a momentum exchange mass, MEM, replaces

---

[2]Bird will be used to refer to the projectile used in the simulation to distinguish it from the projectile used in the field.

[3]*Harry J. Davis, Impact Testing Using a Four-inch Air Gun and Lead Targets, Harry Diamond Laboratories, TR-1383 (April 1968).*

the lead (fig. 1). The mitigator may be expanded or wound aluminum honeycomb (fig. 2) or plywood; the MEM is either a solid metal mass or a more involved mass-spring system. The mass of the bird and the strength, density and shape of the mitigator determine the rise and magnitude of the deceleration pulse; (springs, affect pulse rise and fall) and proper selection of MEM assures that the bird will have zero velocity after the impact event (rather than rebound as would occur if the mitigator was against a rigid wall). This technique eliminates post-test damage and provides immediate access to inspect the tested item; a distinct advantage for chemical systems (e.g., power supplies).

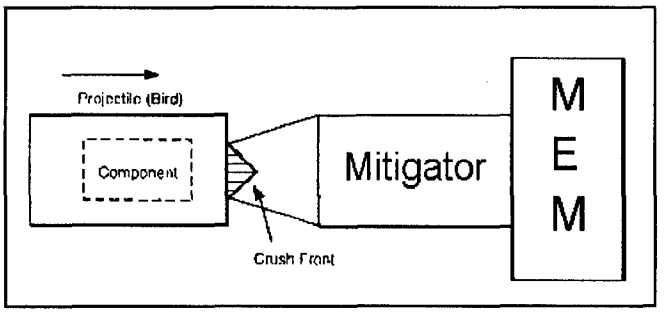



FIGURE 1. MITIGATED MOMENTUM EXCHANGE. The bird emerges from the gun, crushes the mitigator, and comes to rest as the MEM carries off the momentum.

An acceleration-time curve[4] for a flat nosed bird that impacts wound aluminum honeycomb is shown in fig. 3 along with a predicted curve. Typically, peak deceleration is ≈20 K-g but experiments range from 400 g to 100 K-g.

In the case of wood mitigators, the acceleration at the end of the pulse often increases as the wood compresses and stiffens (bottoms).

MSB currently has two 'setback only' simulators; a 4" simulator, utilizing the 4" gun discussed above, and a 7" simulator.[5] The 4" and 7" guns are typically used in the 'vacuum' mode. The bird is inserted into the gun breech up to a restraining pin. An O-ring in the breech provides a vacuum seal around the bird. A plastic dia-

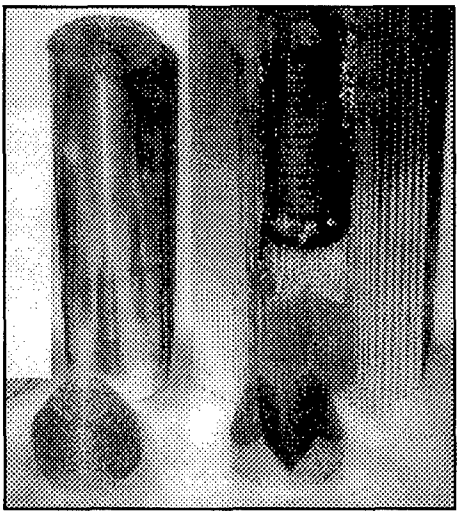


FIGURE 2. ALUMINUM HONEYCOMB

[4] *Irvin Pollin, Impact Pulse Shaping, Harry Diamond Laboratories HDL-TR-1710 (June 1975).*

[5] *Michael G. Otten, Development of a 7-in. Air Gun for Use in Interior Ballistic Simulation, Harry Diamond Laboratories HDL-TM-75-13, October 1975.*

phragm (one or two mil Mylar) covers the gun muzzle and is clamped against another O-ring. The gun is evacuated to ≈2 torr by a vacuum roughing pump. When the restraining pin is withdrawn, ambient air propels the bird down the gun, through the diaphragm and into the mitigator (which is set in a tube, or on rails concentric with the gun). The 4" gun is 96' long when used as a vacuum gun with muzzle speeds of 530 and 700 ft/sec for 5 and 3 lb. birds. This is ≈93% of the speed predicted by frictionless infinite-chambrage gun theory. The 4" gun has a second breech, ≈20' from the vacuum breech. The barrel between the breeches is pressurized with helium to increase muzzle speed.[6] The 7" gun is 304' long and uses vacuum only.

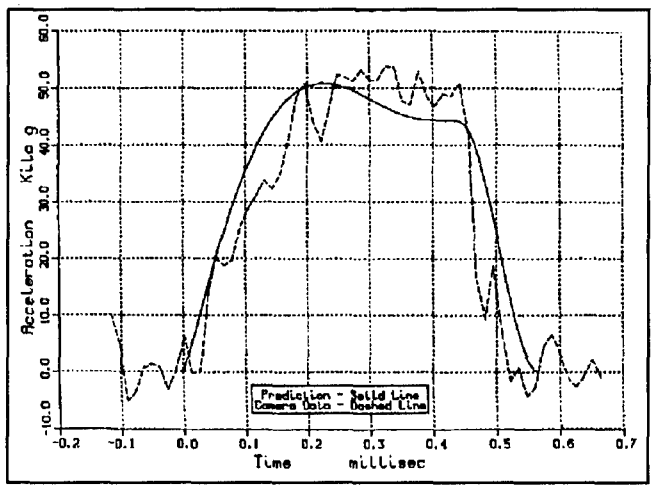


Figure 3. Typical Acceleration-Time Curve.

It is easy to install a temperature conditioned device in the bird just seconds before firing the gun (in the vacuum mode) because the rear of the bird is open to the room.

Instrumentation: Muzzle speed is measured by electro-optical techniques. Knowing the physical properties of the mitigators and by measuring the deformation of the mitigator after impact we can compute a post-impact predicted rigid-body deceleration-time curve based on this speed and crush.

Streak photography[7] in the 4" and 7" systems records the displacement-time curve of the bird during impact. Rotating drum cameras are used to avoid synchronization problems associated with rotating mirror cameras. The 4" simulator employs a camera built to photograph

---

[6]*Herbert D. Curchack, Optimized Breech Location in the Harry Diamond Laboratories 4-Inch Gas Gun, Harry Diamond Laboratories HDL_TR-1983 (April 1982).*

[7]*Donald J. Mary, Errors in Streak Photography Measurements Caused by Subject and Camera Misalignment, Harry Diamond Laboratories HDL-TR-1609 (August 1972).*

shock tube events and uses 2" wide film, one foot long. The 7" simulator uses a Cordin™ camera using 70 mm x 1 m film. Another Cordin camera is mounted in a portable fashion for use in special situations.

A pattern of stripes was designed (to optimize computer processing) and a master negative made. Prints from this negative are fastened to the bird with photographic mounting tape. A portion of a streak photograph of these stripes, taken with the HDL camera, is shown in fig. 4. The streak picture represents a displacement-time curve of the bird during impact. Originally the film was digitized manually on an optical densitometer and the results typed into a computer. This process was time consuming, tedious and restrictive as to the quantity of data that could practically be treated and was replaced by a precision, high resolution PDS 1010A densitometer with a special transport to handle 70-mm by 1-m film strips. A PDP-8/M computer processed more data in less time and increased the precision and accuracy of the data. (The PDP-8M was recently replaced by a 386 PC system.) A rasterscan program controls the densitometer and the film transport to record position and density values that is processed on a VAX computer using HDL generated code. This yields displacement, velocity, and acceleration vs. time records of the simulation. Because of the small capacity of the PDP-8M, the amount of data per scan was limited to densities above a threshold and much data were not used in determining bird motion. The PC based system is not limited in data collection, and new code will be written to increase precision and accuracy.

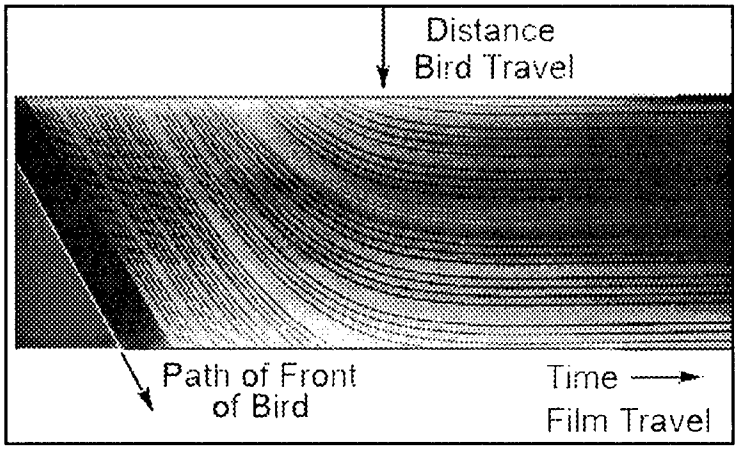



Figure 4. Streak Film Image of Impact.

Pre-impact velocities from film data agree with the optical measurements within 1%. Acceleration error on a good film (due to film reading imprecision) is about 100 g for 100 μsec reading intervals, 600

g for 50 μsec intervals, and increases significantly for smaller intervals.

Theory for honeycomb mitigators[8]: The conservation equations were solved to obtain the motions of the bird, mitigator, and MEM as functions of time. In order to do this, assumptions are made as to the behavior of aluminum honeycomb. These assumptions are valid for honeycomb up to ≈1100 ft/sec impact velocity. The assumptions are:

1) The mitigator crushes only at the impacted end.
2) The crush is columnar (fig 5).
3) The uncrushed mitigator behaves as if it is attached to the MEM.
4) The crushed mitigator behaves as if it is attached to the bird.
5) The crush front (the region that separates crushed and uncrushed mitigator) is short compared to the length of the mitigator.
6) The crush strength and density of the mitigator are uniform and constant along the mitigator length.

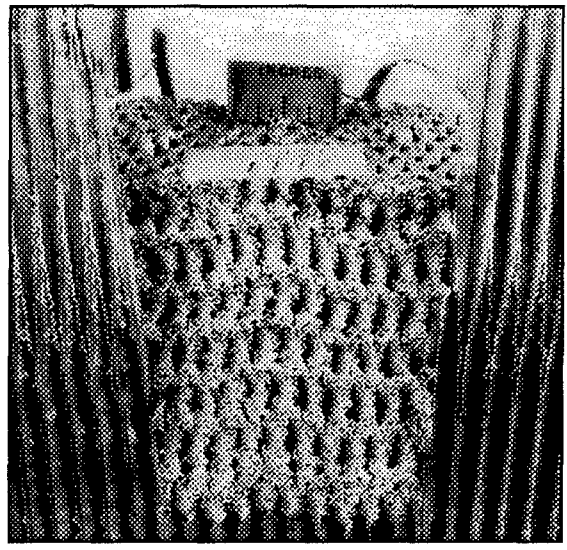


Figure 5. Mitigator section showing columnar crush.

Typical crush length vs. applied pressure curves (such as calibrations supplied by the manufacture) show that the initial crush pressure can exceed the rated crush pressure by 50% or more. This is due to the fact that the mitigator maintains its strength until the columnar folds are formed and only then does it start to crush. However, mitigators used in impact experiments are tapered so that the initial crush area is small compared to the major mitigator cross section, and crush starts close to the rated crush strength.

7) The mitigator is long enough so that there is always uncrushed mitigator. When the mitigator length is too short, *bottoming occurs and* the honeycomb behaves like a solid chunk of aluminum. This occurs in aluminum honeycomb at strains of ≈80%.

---

[8]*Irvin Pollin, Controlled, Long Duration, Impact Pulses, International Congress on Instrumentation in Aerospace Simulation Facilities (1979), 150-166.*

8) The energy associated with elastic waves is small compared to the energy dissipated by mitigator crush. Elastic waves are believed responsible for oscillations that appear in the measurements.

Using these assumptions, we formulate the problem as follows.

1) The equations of motion are required for only the bird and the MEM.
2) The bird gains mitigator mass as the mitigator crushes and the MEM loses an equal mass.
3) Newton's law for the bird, (the force on a body equals the rate of change of momentum) must contain a velocity multiplied by a time-rate-of-change of mass term (hydrodynamic force) as well as the mass times acceleration term. The hydrodynamic force does not apply to the MEM because the loss of mitigator mass does no work.
4) The event ends when the bird and MEM achieve the same speed. Actually, slight elasticity in the impact causes bird-MEM separation. Theory of this elastic foot has not been developed. The effect of the foot is to extend the fall time of the pulse by ≈50 μsec. Some experiments had railroad-springs in the MEM to increase the fall (and rise) time. These were easier to predict because the added elasticity 'swamped out' this foot.

Equation (1) is Newton's law for the bird; (2) Newton's law for the MEM; (3) is mass conservation for the mitigator; and, (4) is momentum conservation for the system

$$(m_b + m_c)\ddot{x}_b + \rho rs(\dot{x}_b - \dot{x}_m)^2 = -F \qquad (1)$$

$$(m_m + m_u)\ddot{x}_m = F \qquad (2)$$

$$m_h = m_u + m_c \qquad (3)$$

$$(m_b + m_c)\dot{x}_b + (m_m + m_u)\dot{x}_m = m_{b_0}\dot{x}_{b_0} \qquad (4)$$

where

$\dot{x}$ is velocity, and $\ddot{x}$ is acceleration (variables)

$m$ is the mass (variable)

$s$ is the mitigator area at the crush front (function of mitigator shape)

$\rho$ is the uncrushed-mitigator density (constant for a specific mitigator)

$r$ is the ratio of crush travel to bird travel (constant for a specific mitigator). It is a function of the ratio, $d$, of crushed mitigator density to uncrushed mitigator density, $r=1+1/d$ , ≈1.2 for honeycomb.

$F$ is mitigator dynamic crush force (constant for a specific mitigator))

and subscript

| | |
|---|---|
| *b* is for bird | *m* is for MEM |
| *h* is for honeycomb | *u* is for uncrushed honeycomb |
| *c* is for crushed honeycomb | *o* is for initial |

Equations 1 through 4 plus the area-distance relationship of the mitigator and the initial conditions are not solvable in closed form. They are integrable on the computer in timewise steps; holding slowly changing variables constant; updating them, and iterating.

Wood Mitigators: Wood mitigators are especially useful where a non-conducting mitigator is needed for electrical purposes. The only wood that has repeatable results is marine-grade plywood (plywood with neither knots nor voids on any ply). Such wood has a crush strength of ≈5000-psi, is considerably more elastic than honeycomb but will start to bottom at strains of ≈30%. No theory has been formulated for wood crush. Empirical results are used for predictions.

## ARTILLERY SIMULATORS[9]:

The artillery simulator extends the impact concept to simultaneous linear and angular accelerations as in projectiles fired from rifled barrels. The angular velocity achieved is maintained for a time representative of the flight time of the actual projectile while devices are electrically monitored. The technique is as follows:

Consider a hollow tube rotating about its longitudinal axis at a desired angular velocity. The bird enters the tube at a prescribed velocity. Within the tube, the bird stops its linear motion and accelerates its angular motion until it has acquired the angular velocity of the tube. Furthermore, during this process an electrical circuit is completed to continuously monitor a device within the bird. To do this we had to:

1) Provide the requisite linear velocity to the bird by use of a gas gun.
2) Construct a tube (spin-catcher) that can rotate at artillery angular velocity.
3) Use mitigated momentum exchange to decelerate the bird while minimizing the forces transmitted to the bearings
4) Provide electrical circuits from the bird to the spinning tube to remote instrumentation. This is accomplished by longitudinal or front-to-back electrical splitting of the tube while maintaining physical

---

[9] *Herbert D. Curchack, An Artillery Simulator for Fuze Evaluation, Harry Diamond Laboratories TR-1330 (November 1966)*

strength. Contacts on the bird are connected internally to the device and are centrifugally or spring activated to contact the electrically isolated sections of the tube. Each tube section is connected to a carbon-silver slip ring and to the instrumentation.

In addition to 2" and 3" laboratory artillery simulators at Adelphi, two 2" table-top simulators were built for on-line evaluation of fuze power supplies and have been supplied to power supply manufacturers.[10]

## SETBACK-DRAG SIMULATORS[11,12]

In the simulation of sequential setback and aerodynamic drag, the bird emerges from the air gun and impacts a mitigator located against a MEM as in setback-only experiments. This simulation occurs within an open-ended catch tube of circular cross section (fig. 6).

Drag simulation is obtained as follows: The bird and MEM are circular cylinders. The bird is a close fit with the inner wall of the catch tube, but the diameter of a

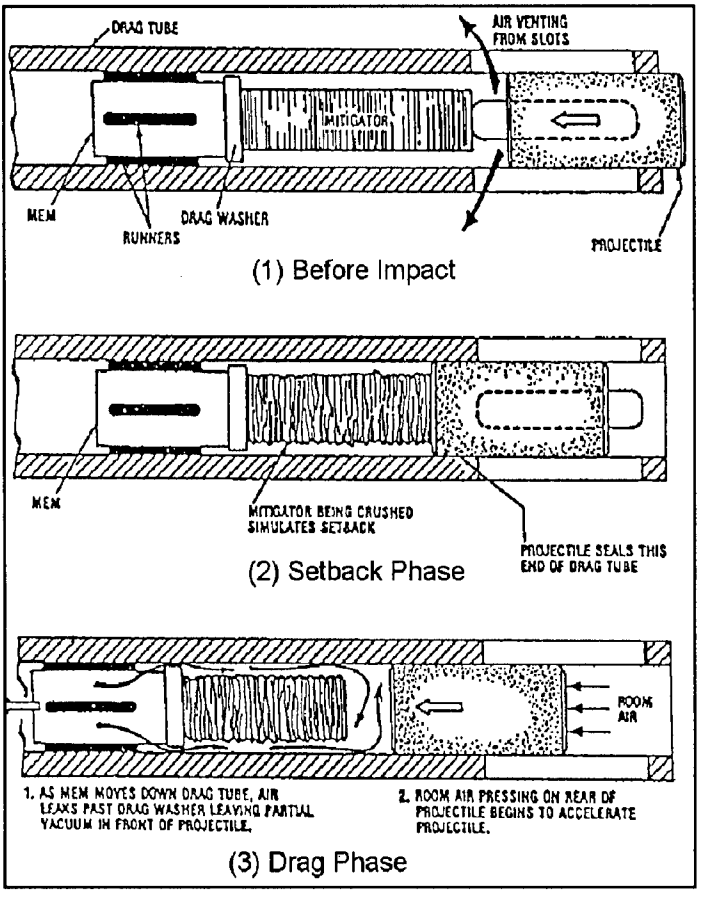



Figure 6. Setback-Drag Simulation.

---

[10] *Donald J. Mary, The High-Spin Tabletop Artillery Simulator, Harry Diamond Laboratories, HDL-TR-1900 (September 1979)*

[11] *Irvin Pollin, Simulation of Sequential Setback and Aerodynamic Drag of Ordnance Projectiles, Harry Diamond Laboratories HDL-TR-1811 (June 1977).*

[12] *Donald J. Mary, A Setback-Drag Simulator, Harry Diamond Laboratories, HDL-TR-1984 (February 1982)*

washer attached to the MEM is selected to obtain a desired clearance between it and the tube. (The mitigator diameter is much smaller than the washer diameter.) At the completion of setback, bird velocity is close to zero, and the bird momentum has been transferred to the MEM. The MEM motion increases the length of the cavity formed by the bird, MEM and tube, causing the pressure to drop. The pressure differential across the bird causes bird acceleration, or drag simulation. Drag is determined by the relative motions of the bird and the MEM, the cavity volume, the air leakage into the cavity around the washer, and the bird mass. MEM mass is much larger than bird mass so that little change in MEM speed occurs during drag simulation. Pressure buildup in the cavity before impact is avoided by slots in the catch tube (open to the atmosphere) that extend from the entrance of the tube to the impact location. The drag profile is insensitive to moderate variations of the initial cavity volume and pressure. Data of bird displacement vs. time are obtained by streak photography, from which setback and drag are determined. Drags of a 4 g to 80 g have been obtained.

Current capabilities: Table 1 shows present capabilities. The peak deceleration in these simulations is 100 K-g.

| Gun Configuration | | | Typical Conditions | | | |
|---|---|---|---|---|---|---|
| ID | Length | Driver | Spin | Payload | Speed | Relevance |
| (in.) | (ft) | | (rps) | (lb.) | (ft/s) | |
| 2 | 9 | Air | 300 | 1/2 | 150 | Power supply tests |
| 2 | 32 | Air | 150 | 1/2 | 300 | 4.2-in. mortar |
| | 32 | He | 150 | 1/2 | 1100 | Low-zone artillery |
| 3 | 12 | Air | -- | 1/2 | 200 | Hi-g rocket w/drag |
| 3 | 100 | Air | 300 | 1 | 575 | Low-zone 8" howitzer |
| 4 | 97 | Air | -- | 2 | 575 | High-zone mortar |
| | 61 | He | -- | 2 | 1100 | Med.-zone artillery |
| | 61 | He | -- | 10 | 1500 | Terminal ballistics |
| | 61 | He | -- | 1 | 4000 | Terminal ballistics |
| 7 | 304 | Air | -- | 7 | 850 | High-zone mortar |
| | | Air | -- | 2 | 1150 | Terminal ballistics |
| | | Air | -- | 1 | 1250 | Terminal ballistics |

Table 1. Some Capabilities Available at Adelphi, MD (1993)

## NEW WORK

New projects are directed towards extending payloads, pulse amplitudes, and pulse times in the simulators to values closer to actual gun characteristics; to improve the instrumentation by taking advantage of state-of-the-art computer and data-acquisition systems; to assess the structural response and performance of projectile components under test; and. to simulate liquid-propellant gun oscillations in projectiles.

Mitigation techniques: There are two major limits regarding the use of aluminum honeycomb as a mitigator. These are the maximum usable crush strength, and a bird impact velocity effect that causes the honeycomb to crush at both ends. We have reached both these limits, yet demands for higher payloads, g's and velocity require extending simulation capability. The cause of these limits and possible fixes are:

Strength: In order to obtain high g (>30 K-g) for payloads greater than 2 kgm, the strongest aluminum honeycomb that is available (nominal 8000 psi crush strength) is used. This material utilizes a large volume of foil in its construction. As the material crushes, each column interferes with an adjacent column and causes radially outward folds in the mitigator. This unpredictable folding is not incorporated in our model.

We have obtained two samples of stainless steel mitigators with crush strength of ≈20,000 psi. The model should hold for steel, as long as we can determine the various mitigator constants. Experiments will determine if stainless steel exhibits satisfactory crush.

Crush at both ends: As bird impact speed increases, the compressive elastic wave in the mitigator strengthens. Upon reaching the solid MEM, this wave reflects back into the mitigator and compression increases. At some critical velocity (≈1100 ft/sec), the reflected compressive force exceeds the crush strength and the mitigator starts to crush at the MEM in an unpredictable fashion. The elastic oscillations (that appear in the data), grow to be as great as the peak acceleration as a result of alternate crushing at the bird and MEM interfaces. Perhaps, we can match stress wave impedance at the MEM end, so that the elastic wave is transmitted rather than reflected.

Several other deceleration techniques have been proposed (e.g., pneumatic, frictive) but have yet to be explored.

## NEW INSTRUMENTATION.

Measurement of bird deceleration inferred from MEM acceleration.[13] An accelerometer in the MEM is easy to install and instrument because the MEM is initially at rest, and by impact end, achieves less than 10% of the bird velocity and less than 10% of the bird acceleration. Hence, by measuring MEM acceleration, and by using equations 1-4 from the equations of motion, we can infer bird acceleration. This method is inexpensive compared to the streak technique and would be useful at contractor sites. However, upon bird impact, the MEM 'rang' at its natural frequencies and swamped the rigid body signal. Once ringing was controlled, several shots supplied reasonable data. The project ended before completion because the sponsoring project was terminated because of an international arms' agreement.

Optical Telemetry. An infrared optical communication system is under development to monitor and transmit component data from a device shot in the artillery simulator to a receiver near the muzzle of the gas gun. The optical system is a true FM transmission system and the receiver has true FM demodulation/high-speed A/D, 16 bit resolution. The prototype transmitter has been repeatedly fired in the 4" simulator at 50 K-g and has performed successfully.

Onboard Recorder. A one channel onboard measure-record-store system is being validated for use in moderate to large caliber projectiles. It is designed for ±100 K-g shock, high-frequency (140-kHz) response, and samples at 1-mHz for 32 msec. A paramount application of the recorder is to characterize the structural oscillations in the bird during impact, so as to assess the feasibility of using simulators to reproduce the structural oscillations developed in projectiles fired from 155 mm RGLP guns. Prototype experiments at 15 K-g for 2.5 msec, 20 K-g for 2.0-msec (fig.7), and 45 K-g for 1.0 msec, show a good match exists between calculated and measured data. In some cases the peak-to-peak g due to structural oscillation exceeded 70 K-g. The

---

[13]*Herbert D. Curchack, Measurement and Calibration of Impact Tests, Summit Technologies - Final Report - Contract DAAL02-86-D-0021/DO-34 (Sep. 1990).*

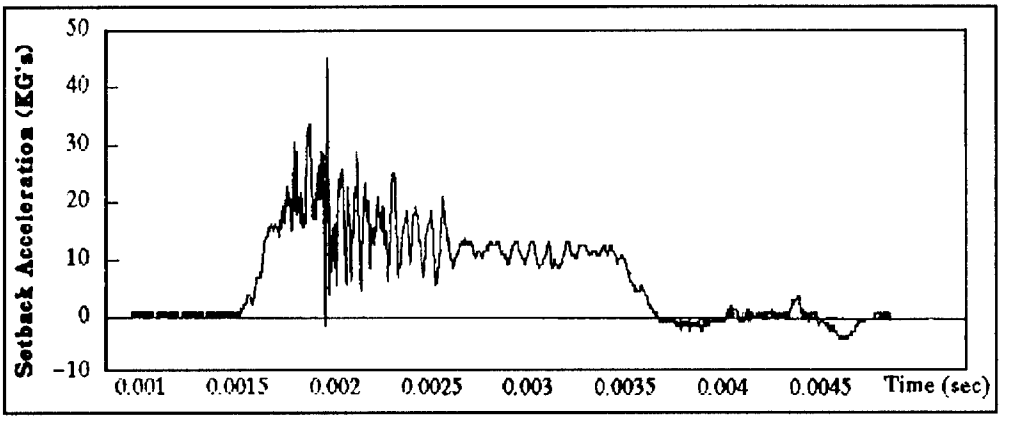



Figure 7. On-board Accelerometer Readout.

prototype is packed in a 3" OD by 4" long housing and weighs ≈2 K-gm. The main components are a ±100 K-g IES model-31 recorder and a ±200 K-g ENDEVCO piezo-resistive accelerometer. The next steps are to demonstrate repeatability, determine life at 20-30 K-g, and to reduce weight, size and cost.

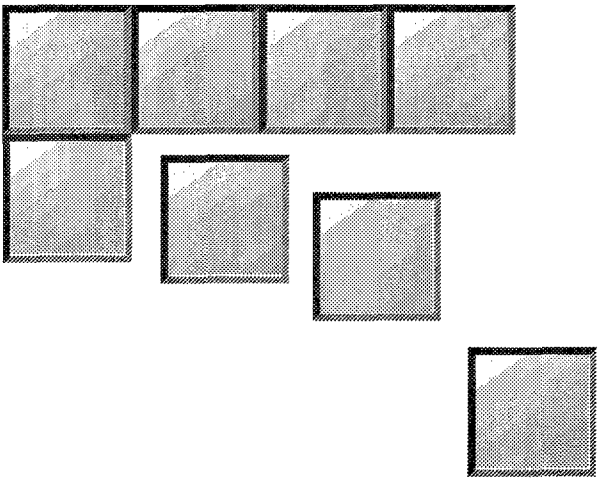
# Numerical Modeling of a Reactive Armor System

*W.L. Cheng*
FMC Corporation

"PAPER NOT AVAILABLE"

# SESSION IIA:
# FAILURE AND DAMAGE

**Chairman:** *Dr. B. Freund*
**Brown University**



# Accumulated Damage and Fracture of Composite Laminates Under In-Plane Loads

Dr. Iqbal Shahid and Dr. Fu-Kuo Chang*
Department of Aeronautics and Astronautics
Stanford University, Stanford, CA 94305

## ABSTRACT

A damage mechanism-based failure model has been developed for predicting accumulated damage and the response of organic matrix composite laminates resulting from in-plane tensile and shear loads. Fiber and matrix failure in the laminates were the primary concern of the study.

The proposed model comprises of a local and a global analysis. The local analysis based on a unit cell element was developed for establishing the relationship between the material properties of a ply in a laminate and damage. Damage accumulation criteria were proposed for predicting the extent of damage and the mode of failure in the laminate as a function of the applied loads. The global analysis based on a nonlinear finite element method was developed for calculating stresses and strains inside the laminate and predicting the damage state for a given loading condtion. A user-friendly computer code was developed based on the model. The predictions based on the model agreed very well with existing data.

## 1. INTRODUCTION

Damage in fiber-reinforced composite laminates can appear at an early loading stage and continue to accumulate inside the materials until the laminates can no longer sustain the applied loads. Therefore, the response of composites strongly depend upon not only the material properties but also on the extent and the type of the damage inside the materials. For laminates under tensile and shear loads, ply failure can be classified into three basic modes: matrix cracking, fiber breakage, and fiber-matrix shear-out. Matrix cracking is most likely associated with initial failure, and the fiber-matrix shearing and fiber breakage are related to the final failure of the laminates.

Studies on modeling of the response of laminated composites beyond initial failure have been reported in the literature [1 – 7]. However, the majority of these studies were primarily focused on matrix cracking failure in cross-ply laminates under a uniaxial load. In this paper, a dam-

age mechanism-based local-global failure model is proposed for predicting the failure and response of laminated composites subjected to combined in-plane tensile and shear loads. The model estimates the response of composite laminates from initial loading to final failure and predicts the extent of the damage inside the materials as a function of the applied loads. Due to space limitations, this paper only summarizes briefly the model. A detailed description of the model can be found in [8].

## 2. THE MODEL

Since the response of a laminated composite strongly depends upon the mode of failure and the extent of the damage in the laminate, the state of damage (the failure mode and the extent of damage) as a function of loads and the relationship between damage and the material properties must be established. Therefore, a damage mechanism-based local-global failure model is proposed which consists of three parts: 1) constitutive modeling, 2) damage accumulation prediction, and 3) stress analysis.

It was assumed in the model that each ply in a laminate with damage could still be treated as a continuous elastic layer with degraded material properties (the effective ply moduli and strengths). Hence, it is necessary to establish the relationship between the effective ply properties and damage to a ply in a laminate under consideration. A local analysis based on a unit cell element was proposed in the model to characterize the effective ply stiffness and strengths for a given state of damage.

In order to determine the constitutive equations of a ply in a laminate, the damage accumulated inside the laminate has to known. Hence, damage accumulation criteria were proposed to predict damage as a function of the applied loads. A global analysis based on a finite element method was developed in the model for calculating effective stresses and strains and predicting the state of damage in a laminate. A schematic of the local-global model is shown in Figure 1.

### 2.1 Constitutive Modeling

A unit cell element was selected as the representative element of a ply in a laminate for characterizing the effective stiffness and strengths of the ply in the laminate. For matrix cracking failure, the state of damage in a ply can be characterized by crack density $\phi$. Hence, a two-dimensional elasticity analysis for the unit cell was developed [8] for determining the ply effective stiffness and strengths as a function of crack density (see Figure 2). Within the unit cell, the analysis evaluates each ply one at a time for a given crack density in the ply and takes account of the constraining effects of the neighoring plies on the cracked ply. Accordingly, the ply constitutive equation including the effect of matrix cracking can be established for each ply in a laminate. It is worth mentioning that the effective ply stiffness due to matrix cracking may vary from ply to ply depending upon the ply orientation of the laminate and the thickness of

each ply in the laminate.

Corresponding to the effective ply stiffness, the effective strengths with respect to crack density are defined as the minimum stresses required to produce matrix cracks at crack density $\phi$. Therefore, using the unit cell element, the effective ply transverse tensile strength $Y_t(\phi)$ and shear strength $S(\phi)$ were obtained based on fracture mechanics combined with the aforementioned elasticity solutions [8]. The values of $Y_t(\phi)$ and $S(\phi)$ strongly depend upon the intralaminar fracture toughnesses $G_{Ic}$ and $G_{IIc}$ of the ply, respectively, and upon crack density as well as the ply thickness and the laminate ply orientation. It is noted that $Y_t(\phi)$ and $S(\phi)$ may also vary from ply to ply in the laminate.

As the load continues to increase, damage in other forms may develop which will eventually result in a substantial loss of the loading-carrying capability of the ply in relation to the applied load. Delamination, fiber breakage, and fiber-matrix shearing failure are assoicated with the final stage of laminate failure. Matrix cracking-induced delamination could significantly further degrade the ply properties and results in ultimate failure of the laminates. Therefore, the effect of such matrix cracking-induced damage on the material degradation must be taken into account for predicting the ultimate failure of the laminates.

## Matrix Cracking

It was assumed that the ply degradation due to additional damage could be characterized based on continuum damage mechanics [8]. As a result, the effective ply stiffness matrix due to matrix cracking and matrix crack-induced delamination is proposed as follows:

$$\begin{pmatrix} Q_{xx}^M & Q_{xy}^M & 0 \\ Q_{yx}^M & Q_{yy}^M & 0 \\ 0 & 0 & G_{xy}^M \end{pmatrix}_k = \begin{pmatrix} Q_{xx}(\phi) & Q_{xy}(\phi) & 0 \\ Q_{yx}(\phi) & Q_{yy}(\phi) & 0 \\ 0 & 0 & G_{xy}(\phi) \end{pmatrix}_k \begin{pmatrix} d_s & 0 & 0 \\ 0 & d_s & 0 \\ 0 & 0 & 1 \end{pmatrix}_k \tag{1}$$

where

$$d_s = e^{-\left(\frac{\phi}{\phi_o}\right)^{\eta}} \tag{2}$$

where the first matrix on the right-hand side is related to pure matrix cracking failure and the second matrix is associated with delamination resulting from matrix cracking. $\phi_o$ is the matrix crack saturation density of the k-th ply, and $\eta$ is a material parameter dictating the rate of stiffness degradation due to delamination failure. The value of $\eta$ is accordingly related to the interlaminar fracture toughnesses of the laminate.

### Fiber-Matrix Shearing Failure

Depending upon the loading condition, fiber-matrix shearing and fiber breakage may also occur after matrix cracking has been generated in the laminates. If the ultimate failure of the ply is primarily due to fiber-matrix shearing failure, additional degradation of shearing properties will be needed for predicting the ply's ultimate failure. Accordingly, the ply constitutive equation due to fiber-matrix shearing failure has the following expression [8]:

$$\begin{pmatrix} \bar{\sigma}_{xx} \\ \bar{\sigma}_{yy} \\ \bar{\sigma}_{xy} \end{pmatrix} = \begin{pmatrix} Q^M_{xx} & Q^M_{xy} & 0 \\ Q^M_{yx} & Q^M_{yy} & 0 \\ 0 & 0 & G^M_{xy} \end{pmatrix}_k \begin{pmatrix} 1 & 0 & 0 \\ 0 & 1 & 0 \\ 0 & 0 & d_s \end{pmatrix}_k \begin{pmatrix} \bar{\epsilon}_{xx} \\ \bar{\epsilon}_{yy} \\ \bar{\gamma}_{xy} \end{pmatrix} \tag{3}$$

where $\bar{\sigma}$ and $\bar{\epsilon}$ are the effective stresses and strains in local material coordinates. It was assumed that the rate of material degradation due to fiber-matrix shearing failure was also dictated by ply interface properties.

### Fiber Breakage Failure

Fiber breakage can also lead to catastrophic failure of the ply in the laminate. If the ultimate failure of the ply is due to fiber breakage, it was proposed that the stiffness degradation due to fiber breakage was associated with the extent of fiber failure area [8]. Hence, the ply constitutive equations due to fiber breakage failure can be expressed as follows:

$$\begin{pmatrix} \bar{\sigma}_{xx} \\ \bar{\sigma}_{yy} \\ \bar{\sigma}_{xy} \end{pmatrix} = \begin{pmatrix} Q^M_{xx} & Q^M_{xy} & 0 \\ Q^M_{yx} & Q^M_{yy} & 0 \\ 0 & 0 & G^M_{xy} \end{pmatrix}_k \begin{pmatrix} d_f & 0 & 0 \\ 0 & d_f & 0 \\ 0 & 0 & d_f \end{pmatrix}_k \begin{pmatrix} \bar{\epsilon}_{xx} \\ \bar{\epsilon}_{yy} \\ \bar{\gamma}_{xy} \end{pmatrix} \tag{4}$$

where

$$d_f = e^{-\left(\frac{A_f}{\delta^2}\right)^{\beta}} \tag{5}$$

where $A_f$ is the estimated fiber failure area, and $\delta$ is the fiber interaction length for a unidirectional composite under consideration. $\beta$ is a parameter which controls the rate of material degradation due to fiber failure.

It is to be noted that if the ply stress-strain relationships are nonlinear, the above constitutive equations can also be modified to accommodate the nonlinear relations.

## 2.2 Damage Accumulation Criteria

There are numerous ply failure criteria based on ply strengths that are available in the literature for predicting failure of a unidirectional ply. The ply strengths are frequently treated as material constants. As a result, they can only provide an estimate of the "first ply failure" of a laminate. The damage state in the first failed ply and failure of the subsequent plies in the laminate could not be determined.

In this model, the ply strengths in a laminate (the effective transverse tensile and shear strengths) are no longer constants, but are *in – situ* properties of the laminate. Their values vary from ply to ply in a laminate and depend upon the state of damage. Accordingly, by combining the effective ply strengths with the existing failure criteria, the damage state and the failure of subsequent plies in a laminate can be predicted. In this study, Hashin failure criteria [9] were adopted and modified for predicting failure of laminated composites.

### Matrix Cracking

For matrix cracking, the criterion has the following form [8]:

$$\left(\frac{\bar{\sigma}_{yy}}{Y_t(\phi)}\right)^2 + \left(\frac{\bar{\sigma}_{xy}}{S(\phi)}\right)^2 = e_M^2 \tag{6}$$

where $\bar{\sigma}_{yy}$ and $\bar{\sigma}_{xy}$ are the effective transverse tensile and shear stresses in each layer, respectively. Note that when $e_M^2$ reaches unity, matrix cracking failure corresponding to a crack density is predicted.

### Fiber-Matrix Shearing Failure

The criterion for predicting fiber-matrix shear-out failure can be described as follows [8]:

$$\left(\frac{\bar{\sigma}_{xx}}{X_t}\right)^2 + \left(\frac{\bar{\sigma}_{xy}}{S(\phi)}\right)^2 = e_S^2 \tag{7}$$

where $\bar{\sigma}_{xx}$ is the effective ply longitudinal stress in the fiber direction and $X_t$ is the longitudinal tensile strength of a unidirectional composite. Failure is predicted due to fiber-matrix shear-out when $e_S^2$ reaches unity.

### Fiber Breakage

The failure criterion has the following form [8]:

$$\left(\frac{\bar{\sigma}_{xx}}{X_t}\right) = e_F \tag{8}$$

Failure is predicted due to fiber breakage when $e_F$ reaches unity.

At $\phi = 0$, the ply strengths $Y_t(\phi = 0)$ and $S(\phi = 0)$ correspond to the initial damage of a ply under consideration. If the applied stress field satisfies one of the criteria, the initial damage is predicted and the mode of failure is identified. Both moduli and strengths of the failed ply have to be modified based on the predicted type and state of damage. The stresses would have to be recalculated and then be applied to the damage growth criteria with the new effective strengths corresponding to the next damage state. The procedure would be repeated until the laminate could no longer sustain any additional load. The final failure load is then predicted.

Accordingly, the major difference between the proposed modified criteria and the original Hashin criteria is that the present criteria can not only predict mode of failure, but also provide an estimate of the accumulated damage, both of which are needed for the constitutive equations (Eqs. (1-5).). It is to be noted that other failure criteria such as the Tsai-Wu criterion could also be adopted with a similar modification for predicting laminate failure.

### 2.3 Stress Analysis

A nonlinear finite element method was developed based on large deformation theory to calculate stresses and deformations of composite laminates under multiple in-plane loads [8]. The constitutive equations and the damage growth criteria were implemented in the analysis.

## 3. COMPUTER CODE

A user-friendly computer code, designated "PDCOMP," has been developed based on the study. For a given laminate under in-plane tensile and shear loads, the code can provide the following information:

1. Stiffness degradation as a function of the applied load.
2. The failure mode and the state of damage as a function of the applied loads in each layer.
3. The response of the laminate as a function of the applied loads.

The code can be obtained from F.K. Chang at the address given in the first page.

## 4. COMPARISONS

### 4.1 Laminates Without a Cutout

The measured and predicted responses of $[45/90/-45/90/45/90/-45/\bar{90}]_s$ and $[60/90/-60/90/60/90/-60/\bar{90}]_s$ laminates subjected to a tensile load are shown in Figure 3. The test data were taken from [10]. Because of the ply orientations, the response of the laminates was dominated by the matrix. Accordingly, a significant reduction was predicted by the model once matrix cracking initiated. The predictions based on the model agreed well with the test data.

The comparison between the measured and predicted in-plane shear strengths of cross-ply laminates is presented in Figure 4. The experimental shear strengths were measured from a rail shear fixture [11]. Apparently, the shear strength was very sensitive to the laminate ply orientation and thickness. The predictions based on the model correlated very well with the experiments.

For laminates under biaxial loads, the strength envelopes as a function of the biaxial stresses for AS4/3501-6 $[90/\pm 45/0]_s$ laminates were measured by Swanson et al. [12]. Figure 5 shows the comparison between the measured and the predicted strength envelopes. A good correlation between the predictions and the experiments was obtained. Interestingly, the laminates in the biaxial loading state could sustain higher stresses compared to a uniaxial loading state.

### 4.2 Laminates With a Cutout

The analysis has also been extended to study the response and failure of notched composite laminates. The measured and predicted ultimate strength of AS4/938 [45/90/ − 45/0/30/ − 30/0/ − 45/90/45] (denoted as "crown-1") composite laminates with a central slit and subjected to a uniaxial load is shown in Figure 6. The width (W) to the slit size (D) ratio was four. The test data were taken from [13]. The predictions based on the model agreed very well with the test data for a wide range of panel widths. Predictions based on the existing semi-empirical models are also shown in the figure [8]. The data at $W = 10$ inches was used to obtain constants needed in these models. The Mar-Lin model requires two constants, but the others need only one parameter.

## 5. CONCLUSIONS

A damage mechanism-based local-global failure model has been developed for predicting the failure and response of laminated composites subjected to tensile and shear loads. The model can estimate the damage accumulated inside the laminate in terms of matrix cracking, fiber-matrix shearing, and fiber breakage, and can also predict the residual stiffness of the laminates as a function of the applied load. The predictions from the

model compared favorably with the available experimental data.

## 6. ACKNOWLEDGEMENT

The authors are grateful for the financial support of the Army Research Office, Boeing Commercial Airplane Company, and the 1988 PYI award from the National Science Foundation.

## 7. REFERENCES

[1] Wang, A.S.D., Chou, P.C. and Lei, S.C., "A Stochastic Model for the Growth of Matrix Cracks in Composite Laminates," *Journal of Composite Materials*, Vol. 18, 1984, pp. 239–254.

[2] Laws, N. and Dvorak, G.J., "Progressive Transverse Cracking in Composite Laminates," *Journal of Composite Materials*, Vol. 22, 1988, pp. 901–916.

[3] Nuismer, R.J. and Tan, S.C., "A Theory for Progressive Matrix Cracking in Composite Laminates," *Journal of Composite Materials*, Vol. 22, 1988, pp. 307–321.

[4] Daniel, I.M. and Tsai, C.L., " Analytical/Experimental Study of Cracking in Composite Laminates Under Biaxial Loading," *ICCM*, Hawaii, 1991, 37-C-1–37-C-10.

[5] Talreja, R., " Modeling of Damage Development in Composites Using Internal Variable Concepts,"*Damage Mechanics in Composites, AD Vol. 12*, ASME Winter Annual Meeting, Boston, 1987, pp. 11–16.

[6] Allen, D.H., Harris, C. and Groves, S.E., "A Thermomechanical Constitutive Theory for Elastic Composites With Distributed Damage-I. Theoretical Development," *International Journal of Solids and Structures*, Vol. 23, 1987, pp. 1301–1318.

[7] "Damage Mechanics in Composites," *American Society of Mechanical Engineers*, AMD-Vol. 150, AD-Vol. 32, 1992, edited by D.H. Allen and D.C. Lagoudas.

[8] Shahid, I., "Progressive Failure Analysis of Laminated Composites Subjected to In-Plane Tensile and Shear Loads," Ph.D. Dissertation, Department of Civil Engineering, Stanford University, 1993.

[9] Hashin, Z., "Failure Criteria for Unidirectional Fiber Composites," *J. of Applied Mechanics*, Vol. 47, 1980, pp. 329-334.

[10] Kistner, M.D., Whitney, J.M. and Browning, C.E., "First-Ply Failure of Graphite-Epoxy Laminates," *Recent Advances in Composites in the U.S.A. and Japan,* ASTM STP 864, Philadelphia, 1985, pp. 44–61.

[11] Chang, F.K. and Chen, M.W.,"The In Situ Laminar Shear Strength Distribution in Graphite/Epoxy Laminates," *J. of Composite Mate-*

*rials,* Vol. 21, 1987, pp. 708-733.

[12] Swanson, S.R. and Christoforou, A.P. ,"Response of Quasi-Isotropic Carbon/Epoxy Laminates to Biaxial Stress," *J. of Composite Materials,* Vol. 20, 1986, pp. 457-471.

[13] Walker, T.H., Avery, W.B., Ilcewicz, L.B., Poe, C.C., Jr., and Harris, C.E. ,"Tension Fracture of Laminates for Transport Fuselage, PART I:Material Screening," Second NASA Advanced Composites Technology Conference, 1991.

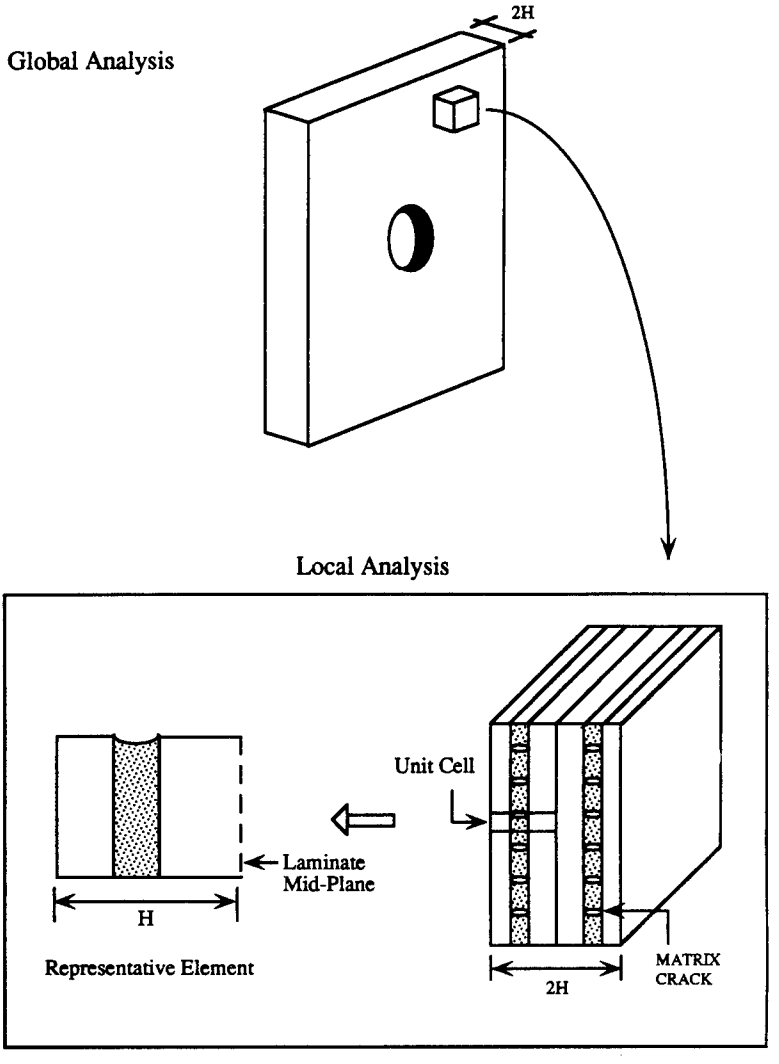



**Figure 1.** A schematic description of the proposed local-global failure model.

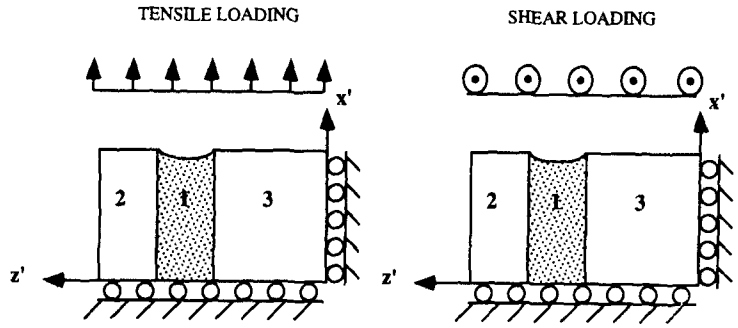



**Figure 2.** A unit cell element for analyzing matrix cracking.

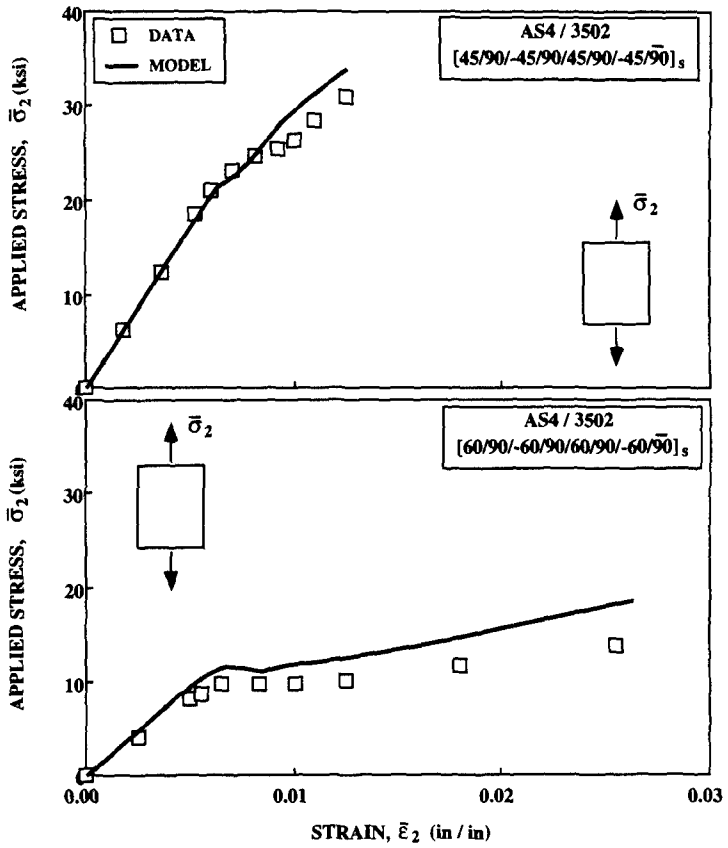



**Figure 3.** Comparison between the measured and the calculated effective strain distribution for $[45/90/-45/90/45/90/-45/\bar{90}]_s$ and $[60/90/-60/90/60/90/-60/\bar{90}]_s$, AS4/3502 composite laminates subjected to a uniaxial tensile load. Data taken from [10].

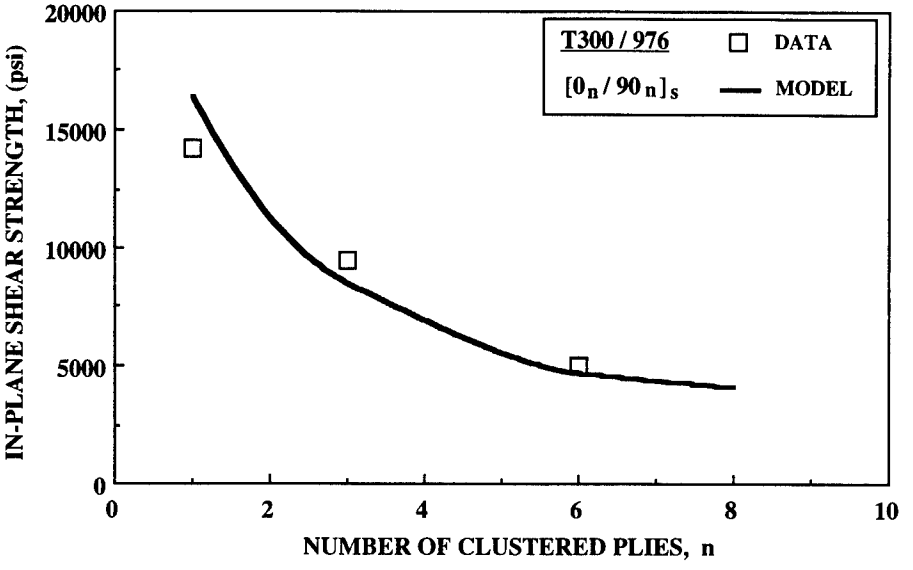



**Figure 4.** Comparison of rail shear strength of $T300/976$ between the prediction based on the model and the experiments. Data taken from [11].

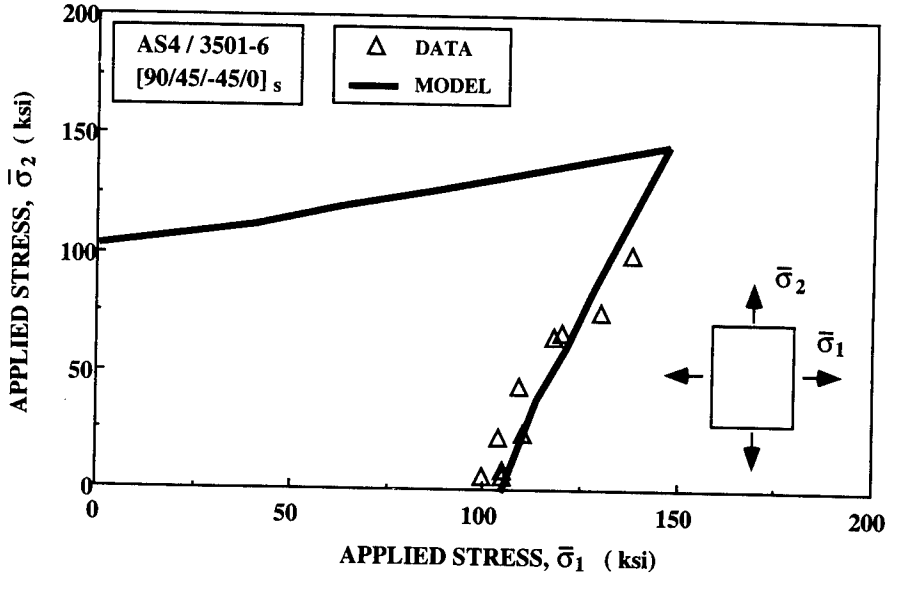



**Figure 5.** Comparison between the predicted strength and the test data for a $[90/\pm 45/0]_s$, AS4/3501-6 composite laminate subjected to bi-axial tensile loads. Data taken from [12].

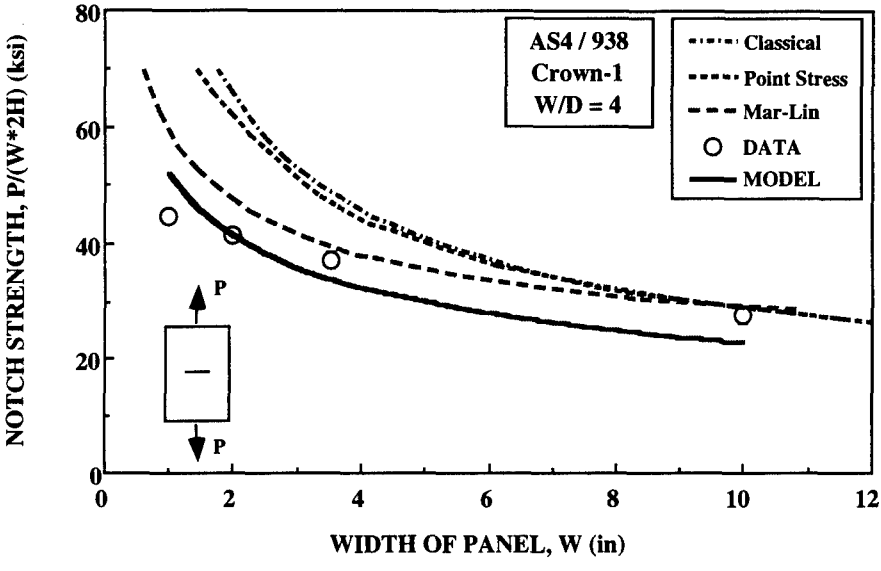



**Figure 6.** Comparison between the predicted strength and the test data for AS4/938 composite plates subjected to a uniaxial tensile load. Data taken from [13].

# Small Crack Growth in Brittle-Matrix/ Brittle-Fiber Composite Materials

Mr. Forrest T Patterson* and Dr. Michael P. Cleary
*Department of Mechanical Engineering,*
*Massachusetts Institute of Technology,*
*Cambridge, MA 02139-4307*

**Abstract.** An understanding of damage development in ceramic composite materials is critical to their successful application in high-temperature structural components. This paper develops the surface integral and boundary element hybrid (SIBEH) method for three-dimensional fracture analysis in composite media. Application to the problem of small crack growth in brittle composite materials is also discussed. The surface integral method models fractures as a piece-wise continuous distribution of displacement discontinuities. Using superposition, this technique is combined with classical boundary element methods to handle geometric boundaries, material interfaces, and thermal effects. Ultimately, the project will determine the applied stress required for crack initiation from inherent matrix flaws and identify micromechanical parameters which promote tough failure modes. Final results of this investigation will be useful in developing guidelines for the manufacture and design of inclusion toughened ceramic materials.

## 1. Introduction

For high-temperature structural applications, ceramic materials offer high strength, low weight, and good thermal properties. However, inherent brittle failure modes and notch sensitivity have precluded the use of ceramics in critical structural components. Though it presents formidable manufacturing challenges, the inclusion of ceramic fibers provides opportunities for increased material toughness and desirable failure modes through crack deflection, fracture bridging, and frictional interface slip [1-3]. For these reasons, ceramic materials reinforced with carbon and silicon carbide fibers are currently being tested for aircraft and automotive engine components.

Experimental observations show that ceramic composite materials initially fail at several points in the matrix and along the interfaces and that matrix cracks initiate from flaws with dimensions on the order of the fiber spacing. These small cracks propagate, coalesce, and form larger cracks, eventually leading to component failure [4,5]. The behavior of these initial fractures determines the active material toughening mechanisms and the component failure mode. Most importantly, this damage evolution is strongly influenced by micromechanical parameters such as the fiber-matrix interfacial properties. Therefore, an understanding of small crack behavior is necessary for the successful design of composite systems.

Previous investigations have demonstrated these phenomena and have analyzed the influence of microstructural parameters on the extension of 'large' cracks (i.e. crack length greater than several fiber spacings). By considering energy and crack-tip stresses, these analyses account for the effects of fiber bridging, frictional pullout, and interface debonding and have supported experimentally observed trends [6-10]. In addition, these investigations have identified microstructural parameters which significantly influence material toughness and have improved understanding of these mechanisms.

More recently, computational methods have been applied to 'small' matrix cracks (i.e. crack length on the order of the fiber spacing) to enhance understanding of the initiation and development of damage in brittle composite materials [11-18]. These numerical techniques can more accurately handle the geometrical effects and toughening mechanisms which dominate crack growth on this scale and which have limited the application of analytical models discussed previously. Though these techniques are more expensive, computational tools can be used to verify or adapt more elegant analytical models.

This investigation expands on previous analyses by developing the surface integral and boundary element hybrid (SIBEH) method to model the effects of proximal fibers and interfacial slip on three-dimensional matrix crack growth. This paper outlines the development of this general computational tool and discusses its application to small crack growth in fiber-reinforced ceramic composite materials.

## 2. The Surface Integral Method

The surface integral method models three-dimensional fractures in linear elastic materials as a piece-wise continuous distribution of displacement discontinuities. This technique resembles the indirect boundary element analysis in formulation. However, the technique derives from the more general concept that local material phenomenon

can be efficiently modeled with dipole distributions and is based on different fundamental solutions [19,20]. In various forms, the surface integral method has been used successfully to model arbitrary two- and three-dimensional crack growth, shear band formation in granular media, and interfacial slip in composite materials. [17,21-24]

The governing equations express the stress or displacement in the material surrounding the crack as a function of the dipole distributions:

$$\mathbf{t}(\mathbf{x}) = \mathbf{n} \int_{S_c} \overline{E}\, \gamma^{\mathbf{s}}(\mathbf{x},\zeta)\delta(\zeta)dA_\zeta \tag{1}$$

$$\mathbf{u}(\mathbf{x}) = \int_{S_c} \overline{E}\, \gamma^{\mathbf{d}}(\mathbf{x},\zeta)\delta(\zeta)dA_\zeta \tag{2}$$

where $\mathbf{t}(\mathbf{x})$ and $\mathbf{u}(\mathbf{x})$ represent the traction and displacement components at some point $\mathbf{x}$ in the media surrounding the fracture surface $S_C$. Each integrand combines material parameters $\overline{E}$, crack-face displacement distribution $\delta$, and a fundamental solution $\gamma$. The fundamental solutions give stresses and displacements due to infinitesimal tensile or shear crack openings, represented by a force multipole (a combination of dipoles) [23].

For many practical applications, an analytical representation for the crack-face displacements cannot be obtained. Therefore, the exact distribution is approximated in a piece-wise continuous manner by dividing the crack surface into subregions over which some local distribution is assumed. As in classical boundary element methods, the local distribution is defined by the crack-face displacements at specific points within each element, $\delta^\alpha$, and shape functions, $\eta^\alpha$. In this formulation, the integral relations in (1) become summations of integrals taken for each elemental region, $S_e$.

$$\mathbf{t}(\mathbf{x}) = \sum_e \mathbf{n} \int_{S_e} \overline{E}\, \gamma^{\mathbf{s}}(\mathbf{x},\zeta)\delta^{(\mathbf{e})}(\zeta)dA_\zeta \tag{3}$$

$$\delta^{(\mathbf{e})}(\zeta) = \eta^\alpha(\zeta)\, \delta^\alpha \tag{4}$$

To determine the crack-face displacement distribution, a collocation method can be employed in which the applied boundary conditions are enforced at a distinct number of points on the crack

surface [21]. This results in a linear system of equations relating the crack-face displacements and tractions:

$$\mathbf{C}_{IJ}\,\delta_J = \mathbf{t}_I \tag{5}$$

$$\mathbf{C}_{IJ} = \mathbf{n}\int_{S_e^{(J)}} \overline{E}\,\gamma^{s}(\mathbf{X},\zeta)\eta^{(J)}(\zeta)dA_\zeta \tag{6}$$

where the coefficient matrix terms $\mathbf{C}_{IJ}$ represent the traction forces **t** at collocation point I corresponding to unit crack-face displacements δ at collocation point J The integration in equation (6) is taken over the elements, $S_e^{(J)}$, enclosing point J.

The equation system expressed in (5) can be solved and the results combined with assumed local shape functions to obtain the approximate crack opening distribution. Stresses and displacements at points in the surrounding media can then be expressed as a function of the crack-face displacement distribution:

$$\mathbf{t}(\mathbf{x}) = \sum \delta_J \mathbf{n}\int_{S_c^{(J)}} \overline{E}\,\gamma^{s}(\mathbf{x},\zeta)\eta^{(J)}(\zeta)dA_\zeta \tag{7}$$

$$\mathbf{u}(\mathbf{x}) = \sum \delta_J \int_{S_c} \overline{E}\,\gamma^{\mathbf{d}}(\mathbf{x},\zeta)\eta^{(J)}(\zeta)dA_\zeta \tag{8}$$

In general, the integral equations in (6) can be handled using Gaussian quadrature. However, when the collocation points at which the displacements and tractions are evaluated coincide, the singularity of the fundamental solution makes the integral intractable. For these cases, subtraction of a rigid body motion transforms the integral so that it is defined in a Cauchy principal value sense and can be evaluated numerically [17,23]

Despite these complicated integration procedures and its limitation to linear elasticity, the surface integral method provides several advantages over conventional numerical techniques. Because the fundamental equations are based on multipole solutions (representing infinitesimal fracture events), the surface integral technique accurately captures the stresses singularities near the crack tip. Crack-face displacements and stress intensity factors can be determined with a limited number of low-order crack elements. More importantly, only the fracture surface need be discretized, reducing required degrees of freedom and simplifying crack growth logistics.

## 3. The SIBEH Method

To include the effects of component and model boundaries, the surface integral method can be combined with other numerical techniques using superposition. A hybrid concept combining the surface integral and finite element methods has been used to successfully model fractures in the presence of finite component boundaries, material interfaces, and thermal strains [17,19,23,24].

Development of the surface integral and boundary element hybrid (SIBEH) method is presented here for application to small crack growth in composite materials. The fracture model described above will be superposed with boundary element models of the surrounding matrix and proximal fibers. Although it results in fully-populated, coupled coefficient matrices, this formulation avoids the complicated volumetric finite element meshes required for this problem. In addition to the fracture surface, only the material interfaces, planes of symmetry, and loading surfaces will be discretized.

The governing equation of the boundary element method derives from Kelvin's point force elasticity solutions and relates boundary tractions and displacements [24]. After discretizing the boundary and approximating the tractions, **T**, and displacements, **U**, with local shape functions, $\eta$, a system of equations can be formulated with the general form:

$$\mathbf{H}_{IJ}\mathbf{U}_J = \mathbf{G}_{IJ}\mathbf{T}_J \tag{9}$$

$$\mathbf{H}_{IJ} = \delta_{IJ}c^{(J)} + \int_{S_e^{(J)}} \mathbf{p}^*(\mathbf{x},\zeta)\eta^{(J)}(\zeta)dA_\zeta \tag{10}$$

$$\mathbf{G}_{IJ} = \int_{S_e^{(J)}} \mathbf{u}^*(\mathbf{x},\zeta)\eta^{(J)}(\zeta)dA_\zeta \tag{11}$$

where $\mathbf{p}^*$ and $\mathbf{u}^*$ represent the fundamental boundary element solutions, $c^{(J)}$ is a geometric constant, and $S_e^{(J)}$ represents the boundary elements enclosing the point J. For simplicity, all domain integral terms, such as body forces, thermal strains, and local plastic flow, have been omitted from (9) for this development.

Stresses at points within the model can also be expressed as a function of the boundary values, $\mathbf{U}_J$ and $\mathbf{T}_J$, and derivative kernel functions $\mathbf{d}^*$ and $\mathbf{s}^*$ [25]:

$$\mathbf{t}(\mathbf{x}) = \sum \left\{ \mathbf{U}_J \int_{S_e^{(J)}} \mathbf{d}^*(\mathbf{x},\zeta)\eta^{(J)}(\zeta)dA_\zeta + \right. \tag{12}$$

$$\left. \mathbf{T}_J \int_{S_e^{(J)}} \mathbf{s}^*(\mathbf{x},\zeta)\eta^{(J)}(\zeta)dA_\zeta \right\}$$

The superposition process used to couple the surface integral and boundary element models is shown schematically in Figure 1. The problem of a cracked, finite body under applied crack-face and boundary tractions is solved by combining both techniques.

The surface integral method, shown in Figure 1b, models the fracture in an infinite homogeneous domain. Integral equations (5) relating the crack-face displacements and tractions at collocation points along the fracture surface are constructed as before. However, corrective tractions, $\mathbf{t}^*$, (evaluated along the image of the fracture in the boundary element model) must be subtracted from the applied tractions, $\mathbf{t}$, to ensure satisfaction of the boundary conditions.

$$[\mathbf{C}]\{\delta\} = \{\mathbf{t} - \mathbf{t}^*\} \tag{13}$$

The corrective tractions can be expressed in terms of the boundary element displacements and tractions using relation (12).

$$\{\mathbf{t}^*\} = [\mathbf{D}]\{\mathbf{U}^{be}\} + [\mathbf{S}]\{\mathbf{T}-\mathbf{T}^*\} \tag{14}$$

The boundary element method, shown in Figure 1c, models the finite, uncracked domain. In a similar fashion, the integral equations (9) can be constructed with the necessary subtraction of corrective surface traction $\mathbf{T}^*$ from the surface integral model and equations (3-4).

$$[\mathbf{H}]\{\mathbf{U}^{be}\} = [\mathbf{G}]\{\mathbf{T}-\mathbf{T}^*\} \tag{15}$$

$$\{\mathbf{T}^*\} = [\mathbf{A}]\{\delta\} \tag{16}$$

Displacements along the boundary of the original problem will be the sum of displacements from both models [22].

$$\{\mathbf{U}\} = \{\mathbf{U}^{si}\} + \{\mathbf{U}^{be}\} = [\mathbf{B}]\{\delta\} + \{\mathbf{U}^{be}\} \tag{17}$$

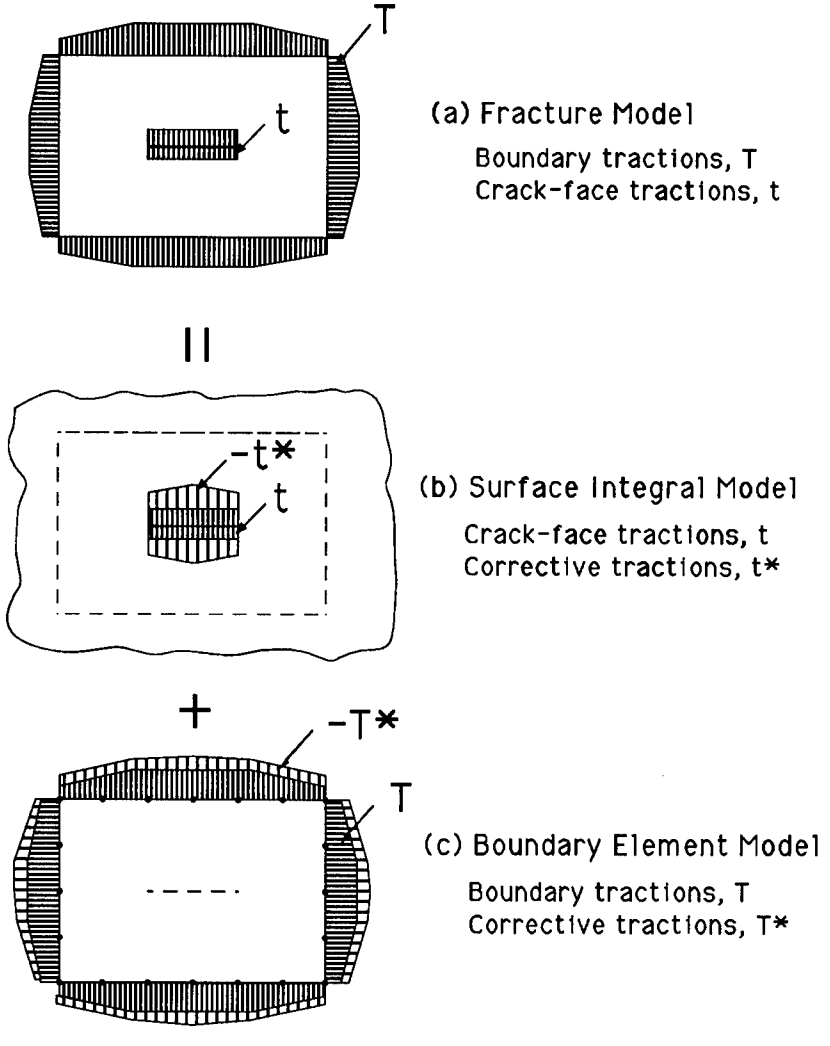



Figure 1. Surface Integral and Boundary Element Hybrid (SIBEH) Method

Combining (13-16) and substituting (17) gives the complete equation system, relating crack-face and boundary displacements to the applied tractions.

$$([\mathbf{C}]+[\mathbf{S}][\mathbf{B}])\{\delta\} - [\mathbf{S}]\{\mathbf{U}\} = \{\mathbf{t}\} - [\mathbf{D}]\{\mathbf{T}\} \qquad (18)$$
$$([\mathbf{G}][\mathbf{A}]-[\mathbf{H}][\mathbf{B}])\{\delta\} + [\mathbf{H}]\{\mathbf{U}\} = [\mathbf{G}]\{\mathbf{T}\}$$

Though developed for the case of applied tractions, the resulting system of equations can be also be used to solve mixed boundary value problems, after partitioning the matrices in (18) and rearranging terms.

By combining the crack modeling capabilities of the surface integral method with the versatility of the boundary element method, the SIBEH method provides an efficient tool for linear elastic fracture mechanics. The technique is particularly well suited for fracture propagation analysis, since only a limited number of the terms in equation (18) need to be recomputed as the crack surface is extended.

## 4. Application to Small Crack Growth in Brittle Composite Materials

The focus of this investigation is to determine the stresses required to propagate small matrix cracks in fiber-reinforced ceramic materials. In addition, the fiber stresses and interfacial slip are monitored to help identify optimum ranges for interfacial properties. A properly tailored interface should allow sufficient slip to protect fibers from excessive crack tip stresses and still provide frictional resistance for significant toughness and strength. These tasks are being accomplished using the SIBEH method outlined above.

For this investigation, a sample material consisting of lithium aluminosilicate reinforced with continuous silicon carbide fibers is being studied. Although the model developed is general, use of these specific material properties will facilitate comparison of results with published experimental data and application of the findings to a common material combination [4,5]. Both matrix and fiber materials are being modeled as isotropic, linear elastic solids.

Matrix crack initiation begins from penny-shaped flaws located within a hexagonal array of fibers (Figure 2), a situation identified experimentally as a common configuration for crack initiation [4,5]. The fracture is extended in a quasi-static manner from the initial flaw to a crack with radius spanning several fiber rows. To reduce the problem size, only the shaded portion of the problem shown in Figure 2 is modeled directly. Unit cells enclosed by symmetric boundaries and by uniform displacement loading planes have been constructed to handle the fracture at various stages of growth. For the case considered here of static tensile loading, additional reduction has been accomplished using symmetry about the fracture plane.

Since the crack is contained solely in the matrix material and along the interfaces, the fracture and surrounding media can be

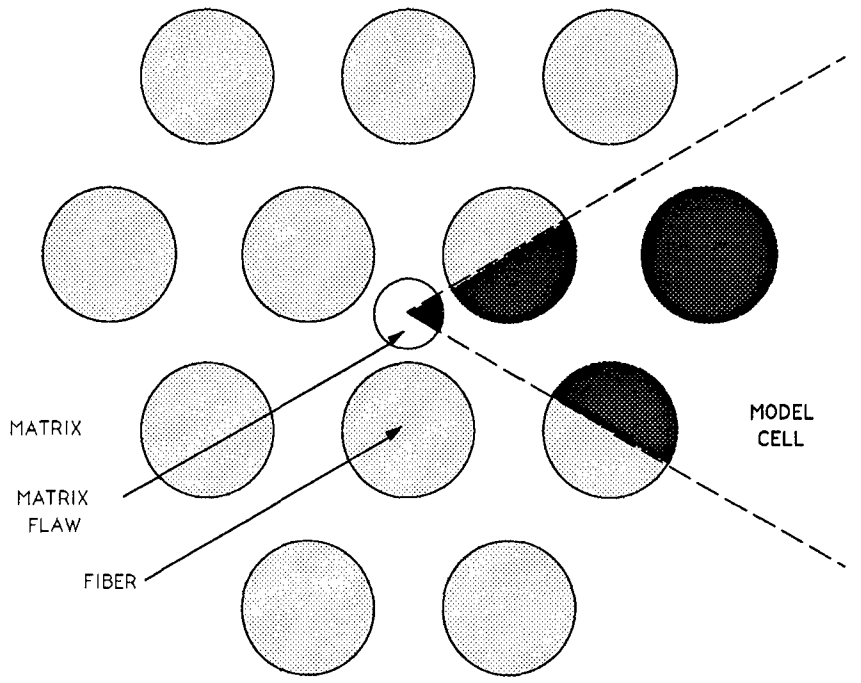



Figure 2. Crack Initiation in Fiber-Reinforced Composite Material;

modeled with the SIBEH method as outlined in Section 3 above. Fibers have been added to (18) as distinct boundary element regions and coupled with the matrix model by the variables at the interface [25]. Interfacial slip between regions is evaluated iteratively after each fracture growth step.

When traction conditions at any point along the interface are compressive with sub-critical shearing stresses, the fiber and matrix regions are linked by enforcing displacement equality and traction continuity at that node. For interfacial points at which the shear forces exceed the critical value or for which the normal stresses are tensile, appropriate traction conditions will be applied to both boundary element regions [17]. The interfacial conditions are summarized here:

$$\begin{aligned} &\text{(i) Bonding:} && \sigma_n < 0,\ \tau < \tau_{CRIT} \\ &\text{(ii) Frictional Slip:} && \sigma_n < 0,\ \tau > \tau_{CRIT} \\ &\text{(iii) Separation:} && \sigma_n < 0 \end{aligned} \qquad (19)$$

Other interfacial models such as Coulombic friction can easily be incorporated for cases in which constant shear conditions do not apply [26,27]. This approach models the three-dimensional crack-tip shielding (and related crack pinning) and approximates the effects of interfacial slip.

Several numerical and modeling issues are currently being addressed concerning the accuracy of the fracture model. Meshing of the surface integral model must accommodate variations in displacement and stress intensity factors. Similarly, the boundary element mesh on the symmetric and interfacial boundaries must capture the stress variation created by proximal and abutting cracks. This is being accomplished through both mesh and element refinement and will be evaluated with convergence tests and by comparison to analytical models.

On a more conceptual level, the SIBEH method is based upon material models (e.g. isotropy) and on geometric assumptions (e.g. matrix porosity and interface reaction zone) which will be less accurate at small scales. Although these are important assumptions on the scale of this investigation, the current model will provide an improved three-dimensional solution which can be used as a basis for further analyses and can be linked to existing analytical models.

Despite these issues, the SIBEH model provides an accurate and efficient method for modeling arbitrary fracture growth in composite media. With regard to ceramic composite failure, the technique will be used to improve analytical models by quantifying three-dimensional effects and to identify optimum interfacial properties for toughness and 'graceful' failure modes. Final results of this investigation will be useful in developing guidelines for the manufacture and design of toughened ceramics. In addition, the method developed can easily be extended to more general cases of three-dimensional fracture in composite media.

## Acknowledgments

The authors wish to express their thanks to the Air Force Office of Scientific Research for their support and to Professors W.D. Keat, M.C. Larson, and J.W. Hutchinson for their helpful discussions and insight.

## References


1. A.G. Evans, "Perspectives on the development of high-toughness ceramics", *J . Am. Ceram. Soc.*, 73[2]:187-206, 1990.
2. E.Y. Luh and A.G. Evans, "High-temperature mechanical properties of a ceramic matrix composite", *J. Am. Ceram. Soc.*, 70[7]:466-469, 1987.
3. K.M. Prewo, "Glass and ceramic matrix composites: Present and future", in *Mat. Res. Soc. Symp. Proceedings, v. 120*, pages 145-156, 1988.
4. R.Y. Kim and N.J. Pagano, "Initiation of damage in unidirectional brittle matrix composites", in *Proc. Fourth USA-Japan Conf. Composite Materials*, pages 799-812, Lancaster, PA, 1988. Technomic.
5. M.W. Barsoum, P. Kangutkar, and A.S.D. Wang, "Matrix crack initiation in ceramic matrix composites Part I: Experiments and test results", *Comp. Sci. Tech.*, 44:257-269, 1992.
6. M. He and J.W. Hutchinson, "Crack deflection at an interface between dissimilar elastic materials", Technical Report MECH-133, Harvard University, 1988.
7. J. Aveston, G.A. Cooper, and A. Kelly, "Single and multiple fracture", in *The Properties of Fiber Composites,* pages 15-26, Guildford, UK, 1971. National Physical Laboratory, IPC Science and Technology Press.
8. B. Budiansky, J.W. Hutchinson, and A.G. Evans, "Matrix fracture in fiber-reinforced ceramics", *J. Mech. Phys. Solids*, 34[2]:167-189, 1986.
9. D.B. Marshall, B.N. Cox, and A.G. Evans, "The mechanics of matrix cracking in brittle-matrix fiber composites", *Acta. Metall.*, 33[11]:2013-2021, 1985.
10. R.M. McMeeking and A.G. Evans, "Matrix fatigue cracking in fiber composites", *Mechs. of Mats.*, 9:217-227, 1990.
11. G. Meda and P.S. Steif, "A detailed analysis of cracks bridged by fibers Part II: Cracks of intermediate size", Carnegie Mellon University Report SM 93-6, August, 1993.
12. H. Gao and J.R. Rice, "A first-order perturbation analysis of crack trapping by arrays of obstacles", *J. Appl. Mech.*, 56:828-836, 1989.
13. N. Fares, "Crack fronts trapped by arrays of obstacles: Numerical solutions based on surface integral representation", *J. Appl. Mech.*, 56:837-843, 1989.
14. A.F. Bower and M. Ortiz, "A three-dimensional analysis of crack trapping and bridging by tough particles", *J. Mech. Phys. Solids*, 39[6]:815-858, 1991.

15. A.S.D. Wang, X.G. Huang, and M.W. Barsoum, "Matrix crack initiation in ceramic matrix composites Part II: Models and simulation results", *Comp. Sci. Tech.*, 44:271-282, 1992.
16. T.M. Mower, *Experimental Investigations of Crack-Trapping in Brittle Heterogeneous Solids*, PhD thesis, Massachusetts Institute of Technology, May, 1993.
17. M.C. Larson, *Theoretical and Experimental Analysis of Toughening in Brittle Matrix- Brittle Fiber Ceramic Composites with Frictional Interfaces*, PhD thesis, Massachusetts Institute of Technology, June, 1992.
18. G. Xu, *Three Dimensional Elastic Analysis of Crack Growth and Toughening Mechanisms of Brittle Matrix Composites*, PhD thesis, Brown University, May, 1994.
19. W.D. Keat, B.S. Annigeri, and M.P. Cleary, "Surface integral and finite element hybrid method for two- and three-dimensional fracture mechanics analysis", *Int. J. Fracture*, 36:35-53, 1988.
20. T.A. Cruse, *Boundary Element Analysis in Computational Fracture Mechanics*, Kluwer Academic Pub., 1988.
21. B.S. Annigeri and M.P. Cleary, "Surface integral finite element hybrid (SIFEH) method for fracture mechanics", Technical Report REL-82-21, Massachusetts Institute of Technology, 1982.
22. K.Y. Lam, *The Development of a Fully Three-Dimensional Simulator for Analysis and Design of Hydraulic Fracturing*, PhD thesis, Massachusetts Institute of Technology, June, 1984.
23. W.D. Keat, *Surface Integral and Finite Element Hybrid Method for the Analysis of Three Dimensional Fractures*, PhD thesis, Massachusetts Institute of Technology, June, 1989.
24. R.J. Bsaibes, *Analysis of Three-Dimensional Fractures Subject to Thermal Loading*, BS thesis, Massachusetts Institute of Technology, June, 1991.
25. C.A. Brebbia and J. Dominguez, *Boundary Elements: An Introductory Course*, McGraw-Hill Book Co., 1989.
26. D.B. Marshall and W.C. Oliver, "Measurement of interfacial mechanical properties in fiber-reinforced ceramic composites", *J. Am. Ceram. Soc.*, 70[8]:542-548, 1987.
27. T.P. Weihs and W.D. Nix, "Experimental examination of the push-down technique for measuring the sliding resistance of silicon carbide fibers in a ceramic matrix", *J. Am. Ceram. Soc.*, 74[3]:524-534, 1991.

# PROCESS DAMAGE IN POLYMERS

Mr. Kaushik Mallick and Dr. Dusan Krajcinovic*
Arizona State University, Tempe, AZ 85287-6106.

## Abstract

The objective of this paper is to address the basic issues in formulation of a rational analytical model and estimate the process induced damage in thermosetting resins. The basic premise of the model is that the large fluctuations of stresses and temperatures within the disordered gel are responsible for the nucleation and initial growth of microdefects.

## Introduction

Performance of polymer matrix composites is strongly affected by microdefects nucleated during the curing process. The size and density of these 'birth defects' depend on the chemistry of polymerization, thermal gradients in the matrix and the attendant stresses. Optimization of the curing process, i.e. minimization of the performance limiting birth defects, is an important task with far reaching consequences. The inherent complexity of the phenome-non, coupling exothermic chemical reactions, heat transfer and damage evolution defies easy solutions. This complexity is augmented by the disordered and evolving microstructure of the polymeric matrix and its effect on the local fluctuations of stresses.

The objective of this study is to provide an analytical model describing the coupled physico-chemical processes referred to as polymerization. More specifically, the analyses are focused on chemical reactions during which the crosslinks are formed and ruptured. Primary interest of this study centers on the influence of the inherent disorder of the incipient gel network on the rupture of crosslinks. An illustrative problem is considered in an attempt to replicate the dominant trends in mechanical behavior during the polymerization process of a generic thermoset resin.

## Polymerization of thermosetting resins

Polymerization is a complex process during which some of the colliding polyfunctional monomers endowed with sufficient kinetic energy react and form irregular three-dimensional networks. On the microscale the process is observed as a change in connectivity (related to the degree of cure) as the colliding monomers link into m-mers. On the specimen scale the material changes it phase from a viscous fluid to a glassy solid. The crosslinking reaction is exothermic and is accompanied by chemical shrinkage. Since the crosslinking is a random process the gel structure, temperature and stresses are random fields susceptible to large spatial and temporal fluctuations.

The initial stage of the polymerization process is governed by the formation of gel aggregates (nodules) at many locations by diffusion or reaction limited aggregation. Aggregates are dispersed in sol which is still a continuous phase. As reaction proceeds further the number of aggregates increases but their size remains approximately same (with diameter of 0.01 to 0.1 $\mu$m, Erath and Robinson, 1963). Finally the aggregates become sufficiently numerous to fill most of the space and are rendered immobile. The intrinsic linear length of the micro-structure is established by the liquid phase of the process.

The subsequent phase of the curing process is characterized by random bonding between the polymer aggregates. This process can be approximated by a bond percolation model (Martin and Wilcoxon, 1989). Individual aggregates behave as large renormalized monomers fixed in distinct sites of a 3-D lattice. Bonds connecting aggregates comprise of several polymer chains. As the reaction proceeds aggregate clusters of random sizes and shapes appear in the system. In contrast to the spatial correlation length $R$ (average radius of the aggregate) which remains constant, the connectivity correlation length $\xi$ (related to the average cluster radius) gradually increases and finally diverges at the connectivity threshold (Martin and Wilcoxon, 1989). The divergence in the average size of the clusters heralds the actual gel point of the material. This stage is discerned by a very steep increase of the viscosity of the system and the attendant immobilization of the curing mass. Hence, the actual gel point of the material can be identified with the rigidity percolation threshold of the renormalized lattice ($p=p_{ce}$) at which the polymer attains shear strength.

In gelation it is necessary to differentiate between two gel points. First defines the phase transition in connectivity within a single aggregate. Second is characterized by large changes in the physical macro-properties of the resin. Sol-to-gel transition is identified mea-suring shear moduli of the curing polymer (Adolf and Martin, 1990).

## Continuum model

Polymerization is a process that combines chemical reaction of cross-linking, heat transfer and deformation attributable to chemical and thermal shrinkage. The rate of change of the bond density $p$ is defined on the basis of the collision theory as

$$\frac{dp}{dt} = \frac{1}{t_o}\exp\left(-\frac{U_o}{k_b T}\right)(1-p) - \frac{1}{N}\sum_{i=1}^{N_t}\frac{1}{t_o}\exp\left(-\frac{U_o - \Phi_i}{k_b T}\right) \quad \text{for } p > p_{ce} \qquad (1)$$

where $t_o$, $k_b$, $U_o$, $p_{ce}$ and $\Phi_i$ are the atomic free vibration period, Boltzmann constant, activation energy, elastic percolation threshold (i.e. connectivity at sol to gel transition) and Helmholtz free energy in the i-th bond. Also $N$ and $N_t$ are the total number of links and the number of load carrying links respectively. Arrhenius term $t_o^{-1}\exp\left[-(U_o - \Phi_i)/k_b T\right]$ represents the probability that a bond will form (or rupture). The probability that a bond will rupture (second term on the right hand side of (1)) depends on the energy stored in the link. In the period following the sol to gel transition, forces in the bonds of the gel exhibit large fluctuations due to disordered geometry. This term can be rewritten as

$$\frac{1}{N}\sum_{i=1}^{N_t} t_o^{-1}\exp\left(\frac{U_o - \Phi_i}{k_b T}\right) = t_o^{-1}\exp\left(\frac{U_o}{k_b T}\right)\int_o^{\infty}\exp\left(\frac{\Phi}{k_b T}\right)\tilde{p}(\Phi)\,d\Phi \qquad (2)$$

assuming $U_o$ and $T$ to be constant. In (2) $\tilde{p}(\Phi)$ is the probability density function of free energy stored within individual links. Molecular bonds belonging to a highly stressed crosslink store significant magnitudes of free energy $\Phi$ and are prone to catastrophic failure under the effect of thermal energy fluctuations.

To illustrate the salient aspects of the problem consider a polymer slab of constant thickness $2h_o$ infinitely extended in the $(x, z)$ plane. The surfaces of the slab $y = \pm h_o$ are exposed to the autoclave temperature which does not change with respect to $x$ and $z$ coordinates. Accordingly, the temperature $T$ is a function of the time $t$ and coordinate $y$ (defining the position across the slab thickness) only. The heat conduction problem is therefore governed by the partial differential equation (Ciriscioli and Springer, 1990, Mallick and Krajcinovic, 1992a,b)

$$\frac{\partial\left(\rho C_p T\right)}{\partial t} = \frac{\partial}{\partial y}\left[K_T\frac{\partial T}{\partial y}\right] + \frac{\rho H_T}{2\sqrt{r}}\frac{\partial r}{\partial t} \qquad (3)$$

The second term on the right-hand side of (3) represents the heat liberated during the exothermic reactions. It is proportional to the degree of cure $\alpha = \sqrt{r} = \sqrt{(1-r_s)p + r_s}$, where $r$ is the density of inter-molecular bonds and $r_s$ a constant. $H_T$ is the total exothermic heat energy generated during the course of the reaction. The density $\rho$, thermal conductivity $K_T$ and the specific heat $C_p$ are assumed to be constant (independent of $p$ and $T$).

A number of experimental and analytical studies have been devoted in the past to the estimation of cure stresses in polymer matrix composites (Hahn and Pagano, 1976, Loos and Springer, 1983, Bogetti and Gillespie, 1989, etc.). These studies focused on the formulation of continuum phenomenological models needed to determine the evolution of the effective elastic moduli of the resin with the degree of cure. However, the elastic moduli of a crosslinking polymer are dependent on the time in a much more complex way. The complexity is attributed to two different but simultaneous phenomena: viscoelastic behavior of the polymer and changing connectivity of the network during polymerization. Beyond the gel point the network behaves as a viscoelastic solid. The viscoelasticity of polymers can be related to the dynamics of a single molecular chain and the interactions between adjacent chains. Long polymer chains, tangled up like spaghetti, must uncurl as they deform producing delayed elastic effects. Since the incipient gel is a self-similar structure, a change in the degree of cure results in a mere change in scale of the cluster size. Thus, with a suitable rescaling of time, it is possible to derive a universal relationship for the time-dependent viscoelastic behavior of the curing polymer referred to as the time-cure superposition principle (Adolf and Martin, 1990).

The boundary conditions in the present problem requires that all slab boundaries are free of transverse stresses i.e. $\overline{\sigma}_y(y = \pm h_o) = 0$. The only non vanishing macro-stresses $\overline{\sigma}_x$ and $\overline{\sigma}_z$ are equal to each other. The constitutive relationship of the material relating the average stresses $\overline{\sigma}_x (= \overline{\sigma}_z)$ to the eigenstrains $\overline{\varepsilon}^*$ is (Mallick and Krajcinovic, 1992a,b)

$$\frac{1}{2}\overline{\sigma}_x(y,t) + \int_o^t G_\infty(p_s)\left\{\frac{2}{3K(p_s)}\frac{d\overline{\sigma}_x(y,s)}{ds} + 3\frac{d\overline{\varepsilon}^*(y,s)}{ds}\right\}ds + \int_o^t \varepsilon_y^{eff}(s)\frac{dG_\infty(p_s)}{ds}ds$$
$$+ \int_o^t G_r(t-s,p_t)\left\{\frac{2}{3K(p_s)}\frac{d\overline{\sigma}_x(y,s)}{ds} + 3\frac{d\overline{\varepsilon}^*(y,s)}{ds}\right\}ds = 0 \qquad (4)$$

where

$$\varepsilon_y^{eff}(s) = \int_o^s \Gamma_r(s-u,p_u)\left\{\frac{2}{3K(p_u)}\frac{d\overline{\sigma}_x(y,u)}{du} + 3\frac{d\overline{\varepsilon}^*(y,u)}{du}\right\}du \qquad (5)$$

In (4) and (5) $G_r$ and $G_\infty$ are the relaxation and equilibrium components of the shear modulus respectively, $K$ the cure-dependent bulk modulus and $\Gamma_r$ a non-dimensional parameter defined as $\Gamma_r(t) = G_r(t) / G_r(0)$ (Martin and Adolf, 1990). In addition, $\bar{\varepsilon}^*$ is the isotropic eigenstrain in the material due to chemical shrinkage and thermal dilatation. During the chemical reaction of bonding two reacting monomers must reduce their distance in order to attain the equilibrium position. Since the molecules are restrained from moving, the molecular chain experiences chemical shrinkage (Trznadel and Kryszewski, 1992). The chemical shrinkage in the slab is assumed to be proportional to the number of formed crosslinks $p$ above the gel point. Consequently (Mallick and Krajcinovic, 1992a,b),

$$\bar{\varepsilon}^* = \bar{\varepsilon}_{th} - \bar{\varepsilon}_{sh} = \alpha_T (T - T_{ce}) - \bar{\varepsilon}_f (p - p_{ce}) / (1 - p_{ce}) \qquad (6)$$

where $\bar{\varepsilon}_f$ is the final shrinkage strain at the end of the cure ($p=1$), $\alpha_T$ the thermal expansion coefficient for the material and $T = T_{ce}$ at the elastic percolation threshold.

A system of three coupled integro-differential equations (1), (3) and (4), subject to obvious initial and boundary conditions, suffices for the determination of three unknown variables $\bar{\sigma}_x$, $T$ and $p$. The coupling occurs through probability of link forming and rupture in (1), heat liberated during chemical reaction (3) and connectivity dependent material properties and eigenstrains (4). However, the most prominent source of complexity is the fact that the rate of ruptured bars depend on local energy distributions ($\Phi_i$) which cannot be easily determined. To solve the problem and determine the number of links ruptured during curing it is necessary to compute spatial and temporal distribution of forces in the gel molecule.

## Force-displacement relationship in a polymer chain

Mechanical behavior of long polymer chains is in an essential manner dominated by its large scale (length). In order to establish the "stiffness" of the chain it suffices to consider only the change of conformation and its effect on the flexibility. During stretch a polymer chain passes through a sequence of a discrete equilibrium (minimum free energy) states each one of which corresponds to a particular conformation. In the course of the stretching process there is very little change in internal energy stored within the bonds. The change in the free energy is almost entirely attributed to the change in the probability of a particular conformation and the attendant change of the entropy.

Consider first a freely-jointed chain (neglecting valence angles and constraints of internal link rotations), consisting of $n$ links (segments) of length $\ell$, which is fixed at one end. The chain is formed by adding links in

a perfectly random fashion (random walk). The probability $\psi(r)dr$ that the other end will be found within the interval ($r$, $r$+d$r$) (see Meares, 1965) must therefore be Gaussian, i.e.

$$\psi(r) = 4\pi r^2 \left(\beta/\sqrt{\pi}\right)^3 \exp(-\beta^2 r^2) \tag{7}$$

where $r$ is the shortest distance between two ends, while

$$\beta = \frac{1}{\ell}\left(\frac{3}{2n}\right)^{1/2} \tag{8}$$

gives the reciprocal of distance $r$ at which $\psi(r)$ is maximum.

The entropy of a single, freely jointed chain is in statistical mechanics defined as

$$S = k_b \ln[\psi(r)] = C - \frac{3k_b}{2n\ell^2} r^2 \tag{9}$$

where $C$ is a constant. The force in the chain is then,

$$f = \left.\frac{\partial \Phi}{\partial r}\right|_T = -T\left.\frac{\partial S}{\partial r}\right|_T = 3\frac{k_b T}{n\ell^2} r \tag{10}$$

The linear force-displacement relation (10), with a temperature dependent "spring" constant, is derived assuming small displacements, i.e. that $r << n\ell/\sqrt{3}$ (Meares,1965). For larger displacements the probability density function $\psi(r)$ is defined in terms of the inverse Langevin functions rendering the force-displacement relation highly nonlinear. Results indicate that the linear expression (10) is highly accurate for fr $r / n\ell \le 0.3$ $r / n\ell \le 0.3$.

In actual chains the bonds do not rotate freely. Skipping the details of the derivation available in Meares (1965) it suffices to state that, in the linear range the expression (10) retains its validity if the parameters $n$ and $\ell$ are computed from an equivalent random chain. The influence of the crosslinking is a more complex problem which will not be discussed in this paper.

Force transmitted by a crosslinked network is derived from the free energy which combines competing influences of the internal energy and entropy. The relative significance of these two terms changes during the curing process. In an equilibrium (ordered) microstructure the internal energy term dominates. Parameters of an ordered solid can be derived from the properties of the constituent atoms. Parameters of dissipative (disordered) microstructures depend on the texture which is several orders of magnitude larger than constituent molecules. In the initial phase of the linking between two adjacent aggregates the developing network can be obviously classified as a disordered structure since its properties

depend on the chain length rather than on the constituent molecules. Consequently, the deformation of very flexible chains before crosslinking is governed by entropic elasticity discussed above. System is highly deformable and if the stress on the chain is maintained the chain reverts to the original (most probable) conformation converting the excess energy into heat. As the crosslinking progresses the bond between two adjacent aggregates transforms into a network characterized by a relatively small deformability. The relative importances of internal energy and entropy change at the expense of the entropy. Assuming deformation to be small it is assumed that the relationship between the force and the displacement remains linear (for small extensions) albeit with a changed "spring" constant. The new "spring" constant should be obviously determined from the crosslinked network (density of chains, crosslinks and the properties of individual chains). Thus, neglecting changes of the "spring constant" $k$ and using the force-displacement relation (10) free energy stored in the i-th link is

$$\Phi_i = kr_i^2 \tag{11}$$

## Distribution of the free energy in the network

As already stated the polymerization of a thermoset resin can be modeled by the bond percolation on a central-force lattice. The only non-zero temperature and stress gradients are directed along the thickness of the infinite slab and the tensile stresses can occur only in the $(x,z)$ planes. Thus, the slab can be approximated by a stack of independent lattices parallel to its mid-plane. Numerical simulations on a plane, square lattice were considered by Mallick and Krajcinovic (1992b). However, to preserve the actual distance between the nodes at 0.05 μm and be able to consider slabs 50 cm long the network should have $10^{14}$ nodes rendering simulations impossible.

The only reasonable manner to solve the problem must involve a scaling law allowing predictions for large lattice on the basis of the simulations performed on smaller lattices. The current problem is further complicated since the estimate of the rate at which the links rupture (1) requires knowledge of the distribution of forces (energies) in individual links (2). The complete histogram $n(f,L)$ of force distribution (signifying number of bonds subjected to force $f$ in a lattice of size $L$) exhibits a multifractal behavior. The statistical moments of the force distribution

$$[M]_m = \sum_i |f_i|^m = \int_o^\infty f^m n(f,L,p)df \propto L^{y(m)} \tag{12}$$

where the sum is taken over all links in the backbone of the gel. The distribution is multifractal since the exponents are a nonlinear function of $m$ (Hansen and Roux, 1988, Hansen 1990, etc.).

The derivation of the scaling law (12) for all statistical moments of the free energy distribution in the links of the gel backbone in the neighborhood of the percolation threshold and the off-critical states requires much more space than allotted to this paper. The result of this lengthy derivation for the case of a constant energy density ensemble is that the exponents (12) defining the force distribution near the percolation threshold were derived in form

$$y(m) \approx 0.75 + 0.51m + 0.87\exp(-0.676m) \tag{13}$$

It is important to notice that in (13) $y(0) = 1.62 = D_b$ (scaling for the backbone mass), $y(2) = 2$ (constant energy density) and $y(\infty) \rightarrow \infty$ (size effect).

In the off-threshold regime, i.e. for $p$ between $p_{ce}$ and 1 the scaling exponents were derived using the method discussed in Roux and Hansen, 1989) as

$$y(m) \approx 2 - \hat{x}[1.25 - 0.51m - 0.87\exp(-0.676m)] \tag{14}$$

$\hat{x} = \ln(\xi)/\ln(L)$ ,with $\xi$ being the correlation (coherence) length.

The statistical moments of the distribution of the free energy stored in the links of the lattice scale as

$$[M_m] = \int_o^\infty \Phi^m \tilde{p}(\Phi) d\Phi \propto L^{z(m)} \tag{15}$$

where

$$z(m) \approx \hat{x}[-1.25 + 1.03m + 0.87\exp(-1.35m)] \tag{16}$$

Finally, expanding the exponential function into a Taylor series the integral in (2) can be rewritten using the multifractal formalism in form of a convergent series

$$\int_o^\infty \exp\left(\frac{\Phi}{k_b T}\right)\tilde{p}(\Phi)d\Phi \approx \sum_{m=0}^{\infty} \frac{1}{m!}\left(\frac{\overline{\Phi}}{k_b T}\right)^m L^{z(m)} \tag{17}$$

## Numerical results

The computations are based on the properties of a commonly used epoxy resin, diglycidyl ether of bisphenol A (DGEBA). The parameters defining the physical properties of the resin are given in Mallick and Krajcinovic (1992a,b). The equations (1), (3), (4) are integrated

numerically. The space coordinate (y) is discretized by a finite element procedure to solve the nonlinear heat diffusion equations (3) coupled with the kinetic rate equation (1). The time ($t$) is discretized by a finite difference scheme to compute the stresses from the nonhomogeneous integral equation (4).

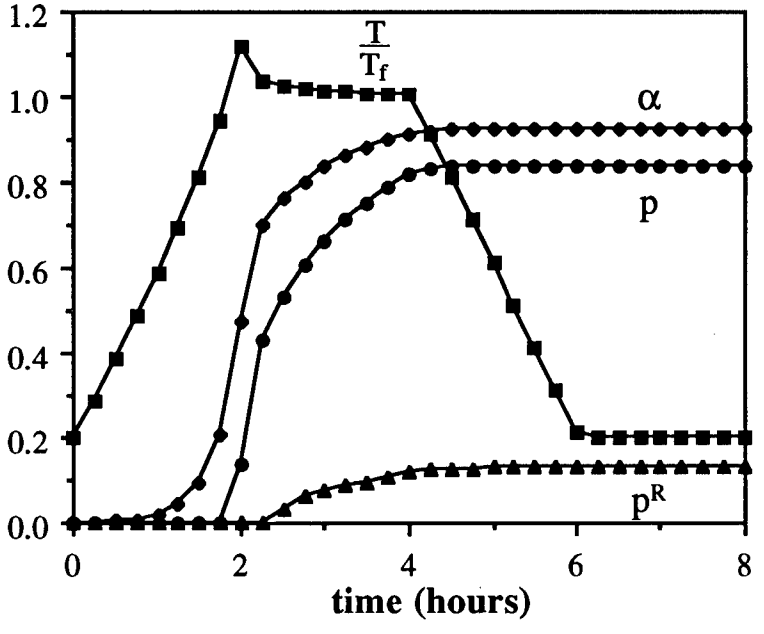



Fig.1 Time dependence of normalized temperature ($T/T_f$), degree of cure (a), density of crosslinks ($p$) and density of ruptured crosslinks ($p^R$) at the center of the slab (y=0).

The viscoelastic stresses ($\overline{\sigma}_x$) are computed for different cross-sections of the slab (Fig. 2). The stress at the center of the slab is significantly higher than that at the surface. All stresses in the slab decay to an equilibrium value near the end of the cure cycle.

## Summary and conclusion

A two-scale analytical model is formulated to estimate the effect of microstructural disorder on the nucleation of microdefects in thermosetting resins during cure. The physico-chemical processes during curing are defined by spatial and temporal changes in temperature, stress and crosslinking. The evolution of these three fields as a function of time and space are determined on the macro-scale by the equations of the heat diffusion (including the source term due to exothermic reaction), rate of chemical reactions (formation and rupture of individual crosslinks) and the viscoelastic deformation of the polymerizing media.

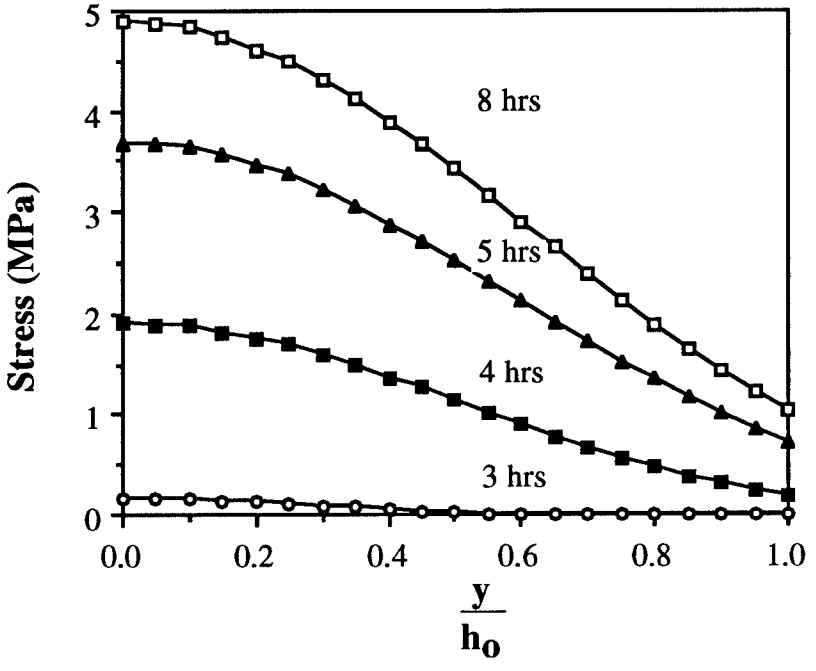



Fig.2 Spatial variation of viscoelastic stresses.

The objective of the study was to demonstrate that the knowledge of average values of stresses and temperatures during the process of gelation in thermoset resins are not sufficient to compute the process damage. The damage attributable to the curing process is directly and inherently related to large fluctuations in the stress fields and the level of microstructural disorder. To determine the stress concentrations it is necessary to consider the influence of the microstructural inhomogeneity on the spatial distribution of stresses. This is achieved by considering the self-similarity of the network structure during the course of gelation. Percolation theory provides the framework for performing quantitative analyses of the nature of the disorder statistics. The scaling laws derived from the multifractal consideration of the gel network define the influence of the size of the system on the growth rate of defects. The microscale and macroscale models are coupled through the connectivity variable defined as the fraction of existing crosslinks. The proposed formulation is applied to an initial boundary value problem to study the temporal and spatial curing of a slab of resin exposed to a specified autoclave cure cycle. The stress-strain law is derived on the basis of the time-cure superposition principle and relaxation-integral equations in terms of cure-dependent elastic moduli and shrinkage strains. Computations indicate that the magnitude of the stress is higher at the center of the slab and is responsible for higher density of defects in form of ruptured crosslinks.

## Acknowledgment

The research on which this paper is based was made possible by the research grant from the U. S. Army Research Office, Engineering Science Division, Structural Mechanics Branch to the Arizona State University.

## References

Adolf, D. and Martin, J. E. (1990) Time-Cure Superposition During Crosslinking. **Macromol.**, 23, 3700-3704.

Bogetti, T. A., and Gillespie, W., Jr. (1989) Process-Induced Stress and Deformation in Thick-Section Thermosetting Composite Laminates. in **21st International SAMPE Technical Conference,** Atlantic City, New Jersey.

Ciriscioli, P. R., and Springer, G. S (1990) **Smart Autoclave Cure of Composites**, Technomic, Lancaster, PA.

Erath, E. H. and Robinson, M. (1963) Colloidal Particles in the Thermosetting Resins. **J. Polym. Sc. C**, 65-76.

Hahn, H. T., and Pagano, N. J. (1976) Curing Stresses in Composite Laminates. **J. Comp. Matls.**, 10, 266-277.

Hansen, A (1990) Disorder in **Statistical Models for the Fracture of Disordered Media** (edited by H. J. Herrmann and S. Roux), 115-158, North Holland, Amsterdam, The Netherlands.

Hansen, A. and Roux, S. (1988) Multifractality in Elastic Percolation. **J. Stat. Phys.**, 53, 759-771.

Mallick, K. and Krajcinovic, D. (1992a) Cure Induced Inelastic Deformation in Thermosetting Polymers, AMD - Vol. 132, MD - Vol. 30, **Recent Advances in Damage Mechanics and Plasticity**, ASME 1992.

Mallick, K. and Krajcinovic, D. (1992b) Curing Induced Microcracks in Polymer Matrices, AMD - Vol. 150, AD - Vol. 32, **Damage Mechanics in Composites**, ASME 1992.

Martin, J. E. and Adolf, D. (1990) Constitutive Equation for Cure-Induced Stresses in a Viscoelastic Material. **Macromol.**, 23, 5014-5019.

Martin, J. E. and Wilcoxon, J. P. (1989) Spatial Correlations and Growth in Dilute Gels. **Phys. Rev. A**, 39, 252-258.

Meares, P. (1965) **Polymers**, D. Van Nostrand Company, Ltd., N.Y.

Roux, S. and Hansen, A. (1989) Off-Threshold Multifractality in Percolation. **Europhys. Lett.**, 8, 729-734.

Trznadel, M. and Kryszewski, M. (1992) Thermal Shrinkage of Oriented Polymers. **J.M.S - Rev. Macromol. Chem. Phys.C**, 32, 259-300.

# PLASTIC FLOW AND DAMAGE IN A TUNGSTEN BASED COMPOSITE

G. BAO*, Z. LIN and K. T. RAMESH

Department of Mechanical Engineering, The Johns Hopkins University, Baltimore, MD 21218

**Abstract**—A micromechanics study is carried out on the plastic flow and damage in a tungsten heavy alloy comprised of a continuous pure tungsten phase in a relatively soft tungsten-nickel-iron "matrix". The heavy alloy is modeled as a dual-phase composite, with the tungsten phase approximated by aligned, uniformly distributed and equal-sized particles. Stress-strain curves of the composite under uniaxial compression are computed numerically using several cell models representing different tungsten particle shapes. It is found that without damage the overall stress-strain behavior of the composite is essentially independent of the particle shape. However, the character of the local plastic deformation changes dramatically with the inclusion geometry. Two simple formulae are given that approximate the overall flow behavior of the undamaged composite in terms of the tungsten volume fraction and the behavior of the individual phases. For a composite sustaining debonding at W-W grain boundaries, a damage evolution model is proposed based on the Weibull statistics. It is shown that the stress-strain behavior of the alloy under quasistatic tensile loading is controlled by two competing trends – strain hardening and debonding softening – both evolve with the tungsten volume fraction and the applied strains.

## 1. INTRODUCTION

Tungsten "heavy alloys" are dual-phase metals that have a unique combination of mechanical and thermal properties: high strength, high density, moderate ductility and outstanding thermal conductivity. This suite of properties makes this class of materials attractive candidates for energy penetrators in advanced anti-armor systems [1]. Typically these materials have a relatively high tungsten content, providing the high strength and the high density; a comparatively ductile second phase provides the composite with some overall deformability.

Tungsten-nickel-iron (W-Ni-Fe) heavy alloys are usually fabricated by liquid phase sintering of mixtures of elemental powder containing 80-98 wt. % tungsten, nickel and iron [2, 3]. The resulting

microstructure consists of spheroidal body-centered cubic (bcc) grains of pure tungsten embedded within a face-centered cubic (fcc) W-Ni-Fe matrix. For the high tungsten contents that are of commercial interest, the tungsten particles coalesce to form a microstructure consisting largely of contiguous tungsten "grains," although the softer phase is still conventionally termed the "matrix" phase. The size of the tungsten grains is typically 30 - 60 μm, which allows the present study to remain within the framework of continuum plasticity theory.

This paper presents a micromechanics study of the plastic flow and damage in a tungsten-nickel-iron (W-Ni-Fe) alloy under uniaxial loading, with the intent of gaining some fundamental understanding of the deformation and failure in tungsten heavy alloys. In particular, the intent is to develop a predictive capability for the uniaxial stress-strain behavior of the composite using cell models. This study is one part of a more general investigation into the deformation and failure of dual-phase solids under quasistatic and dynamic loading. While this paper examines specifically the stress-strain behavior of a tungsten heavy alloy under quasi-static loading, the basic findings shed some light on more complex problems encountered in the processing and use of dual-phase alloys in general.

Theoretical study of deformation and failure of dual-phase, power-law hardening solids has attracted many researchers, simply because this class of solids embraces a wide range of engineering materials including metal alloys and composites. The microgeometry of a dual-phase solid is usually taken to be of the inclusion-matrix type, with the inclusion phase uniformly distributed in the matrix. Assuming perfectly bonded interfaces, the overall stress-strain behavior of a dual-phase solid can be predicted using either a Mori-Tanaka mean-field approach [7, 8], or a three-phase self-consistent model [9-10], or a dual-phase cell model [11, 12]. The overall stress-strain behavior of a composite sustaining a uniformly distributed damage can also be predicted using a dual-phase [13] or a three-phase [14] finite element cell model. The finite element cell models (which are used in the present work) have the advantage that local stress and strain distributions can also be calculated. These distributions are important in determining the initiation and development of localized deformations such as adiabatic shear localization.

There are several possible damage mechanisms in tungsten heavy alloys including cleavage of tungsten grains, void growth in the matrix, debonding at tungsten-tungsten (W-W) grain boundaries, and sliding at tungsten-matrix interfaces. It has been found that the interface between tungsten grains and the softer W-Ni-Fe matrix is usually

strong; few cracks have been observed at the tungsten-matrix interfaces or within the tungsten grains even at large plastic strains [4]. Bonding at the tungsten-tungsten grain boundaries, however, is relatively weak [5], causing debonding cracking to occur at W-W grain boundaries perpendicular (or nearly so) to the tensile loading direction. As a result, the plastic flow stress of a W-Ni-Fe alloy under tension has been found to be lower than that under compression. This paper examines first the composite behavior under compressive loading, since the tungsten heavy alloys are often used in penetration applications where the stress state is predominantly compressive with a superimposed shear. The effect of W-W grain boundary debonding on the tensile behavior of the composite is then probed using a Weibull-type damage model coupled with finite element cell model calculations.

This paper is organized as follows. Dual-phase cell model calculations are described in Section 2, with the emphasis placed on the comparison of results from cell models that represent different shapes for the tungsten particles. In Section 3, systematic predictions of stress-strain curves corresponding to uniaxial compression are presented. Two simple formulae that relate the overall composite behavior to the tungsten volume fraction and to the material characteristics of the individual phases are obtained. A damage evolution model is proposed in Section 4 linking the fraction of grain-boundary damage to tungsten volume fraction and the applied strains. Predictions are made for the tensile behavior of the alloy based on the damage evolution model. The implications of the basic findings in this work are briefly discussed in Section 5.

## 2. DUAL-PHASE CELL MODELS

From a microstructural viewpoint, tungsten heavy alloys are nearly ideal model materials. Due to the near spherical shape and the high volume concentration of the tungsten phase, the microgeometry of a W-Ni-Fe alloy is relatively regular, as shown schematically in Fig. 1a. For the purposes of this study, the tungsten heavy alloy is approximated as a dual phase composite comprised of aligned, uniformly distributed and equal-sized tungsten particles embedded in a W-Ni-Fe matrix; both matrix and tungsten grains are assumed to be isotropic. The tungsten particles form a continuous network and are assumed to be perfectly bonded to the matrix. It is also assumed that the particles are packed in a hexagonal array so that, by translating in all possible directions, a unit hexagonal cell consisting of a single, axisymmetric tungsten particle embedded in the tungsten-nickel-iron matrix can realize the whole composite body. The hexagonal cell is

further approximated by a cylindrical cell in order to form an axisymmetric cell model, which is computationally advantageous. The volume fraction of the particles, f, is taken to be the ratio of the particle volume to the cell volume. The axisymmetric cell shown in Fig. 1b is constrained such that the cylindrical surface remains cylindrical and the ends remain planar. For overall uniaxial stressing, the average normal stress on the ends is $\bar{\sigma}$, and the average normal tractions on the cylindrical surface and the shear tractions on the cylindrical sides and the ends are zero.

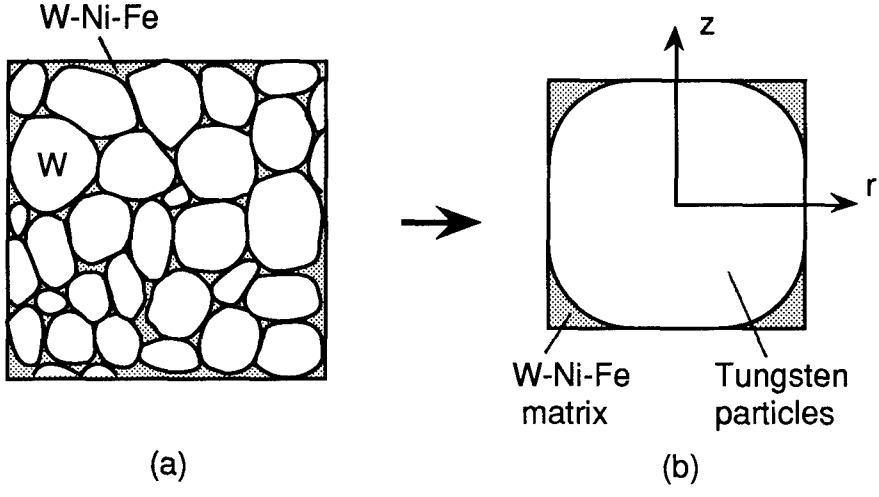



Fig. 1. The tungsten-nickel-iron heavy alloy in (a) is modeled by an axisymmetric cell in (b).

As with most metals, the uniaxial stress-strain behavior of each individual phase can be characterized by a power-law type relationship between the stress $\sigma$ and the axial strain $\varepsilon$. Specifically, the Ramberg-Osgood curve (Fig. 2)

$$\frac{\varepsilon}{\varepsilon_0} = \frac{\sigma}{\sigma_0} + \alpha_0 \left( \frac{\sigma}{\sigma_0} \right)^{n_0} \qquad (1)$$

is used for the tungsten phase. Here the stress exponent is $n_0 = 11.75$, $\alpha_0 = 0.132$, $\sigma_0 = 1$ GPa is the initial yield stress, $E_0 = 400$ GPa is the Young's modulus, and $\varepsilon_0 = \sigma_0/E_0$. The parameters used in equation (1) were evaluated using the quasistatic compression results in [15] on pure polycrystalline tungsten. Likewise, the plastic flow behavior of the softer W-Ni-Fe phase is described by the Ramberg-Osgood curve shown in Fig. 2:

$$\frac{\varepsilon}{\varepsilon_1} = \frac{\sigma}{\sigma_1} + \alpha_1 \left(\frac{\sigma}{\sigma_1}\right)^{n_1} \qquad (2)$$

Here $n_1 = 1.97$, $\alpha_1 = 20.7$, $\sigma_1 = 300$ MPa (the initial yield stress), $E_1 = 140$ GPa is the Young's modulus of the matrix, and $\varepsilon_1 = \sigma_1/E_1$. These latter material properties (except for the modulus) are obtained from the experimental data on a material with the matrix composition in [16]. It should be noted that the stress-strain behavior of the tungsten phase and the matrix phase in other W-Ni-Fe alloys may differ from that defined in (1) and (2). This is due to the fact that the alloys may be made using different processing routes, may have different ratios of nickel content to iron content, and may have experienced different heat treatments or prior thermomechanical processing. Further, direct measurement of the matrix properties as obtained in [16] is complicated by the difficulty of choosing an appropriate grain size for the comparison material. Nevertheless, the cell model developed here is rather versatile in that the plastic flow behavior of the two phases can be defined by any available stress-strain curves, and therefore it is potentially possible to deduce the behavior of the matrix from the measured behavior of the composite (using at least two known volume fractions) and the known behavior of the polycrystalline tungsten.

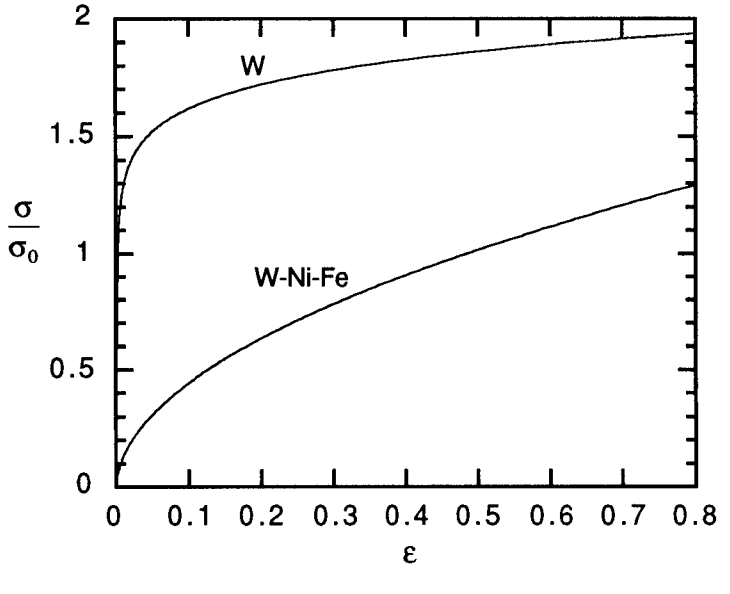



Fig. 2. Uniaxial stress-strain behavior of the hard tungsten phase and the relatively soft W-Ni-Fe phase.

To mimic the microgeometry of the dual-phase alloy, and more importantly, to reveal the influence of particle geometry, three different particle-matrix shapes (shown schematically in Fig. 3) are used in calculating the overall stress-strain curves of the composite. In the first approach, the junction between tungsten particles is taken to be spherical, and the resulting cell model A (Fig. 3a) consists of a soft spherical W-Ni-Fe "inclusion" surrounded by the hard pure tungsten phase. The second approach (cell model B) assumes that the isolated W-Ni-Fe phase is cusp-shaped as in Fig. 3b, with the concave surface generated by a quarter of a circle rotating around the z-axis. In both model A and model B, the W-Ni-Fe phase assumes the position of an "inclusion." The third cell model (model C) shown in Fig. 3c is constructed by putting a squeezed tungsten sphere (partly spherical, partly cylindrical) in the middle, with the W-Ni-Fe phase filling the rest of the space. Model B and model C can be viewed as interchanging the "inclusion" and "matrix" phases. In all three models, the tungsten phase is taken to be continuous, a close approximation to the real microstructure in tungsten heavy alloys containing high volume fractions of tungsten.

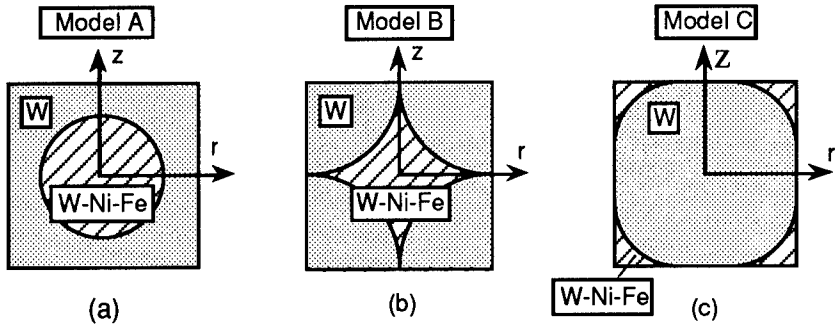



Fig. 3. Cell models for dual-phase alloys with different particle-matrix geometries. In (a) the softer W-Ni-Fe matrix is taken as spherical while in (b) it is assumed to be cuspid. In (c) the tungsten phase has the shape of a deformed sphere.

Fig. 4 presents the predicted overall composite flow stresses against applied strains for a tungsten heavy alloy with a tungsten volume fraction f = 0.94. The stress-strain curves for the pure tungsten phase and the W-Ni-Fe phase are also shown in Fig. 4 for comparison. The dashed lines represent the predictions using cell model A and C, while the solid line is that using cell model B. The small difference between the solid and dashed curves indicates that the effect of particle shape on the overall flow behavior of the tungsten heavy alloy is essentially negligible. This is in contrast to the behavior of ceramic-particle-reinforced metal matrix composites, where similar

computations show that the shape of the nearly rigid ceramic particles has a significant effect on the overall flow behavior of the composite [11]. This phenomenon, which appears to be manifested also in other tungsten-based composites with high tungsten volume fraction [17], may be attributed to the fact that the W-Ni-Fe phase is much softer than the hard tungsten phase which forms an essentially continuous network in the tungsten heavy alloys. At sufficiently large strains the morphology of the deformed composite (under uniaxial compression) is essentially controlled by the deformation of the tungsten grains themselves, with the matrix behaving as a space-filling medium.

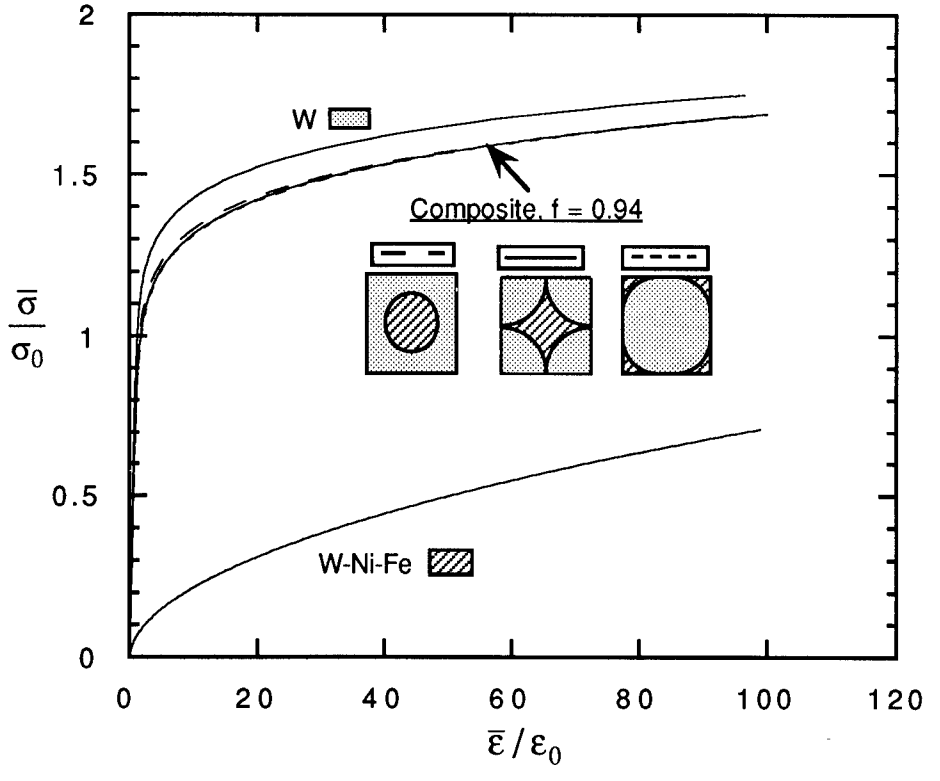



Fig. 4. Uniaxial stress-strain curves for a tungsten heavy alloy under compression obtained using two different cell models. The tungsten volume fraction is f = 0.94. Also shown are the stress-strain curves of the two individual phases.

The local behavior of a dual-phase solid is in general complex, since it is critically dependent on the size, shape and distribution of the individual phases. For instance, although the overall stress-strain behavior of a W-Ni-Fe alloy is essentially independent of the shape of the tungsten particles, as demonstrated in Fig. 4, the local stress and strain distributions are found to change quite dramatically with the particle shape [17]. Specifically, the local plastic deformation in the W-

Ni-Fe matrix phase in model C is more localized than that in model A where the soft W-Ni-Fe phase is spherical.

## 3. THE COMPRESSIVE BEHAVIOR

To benefit the users of tungsten heavy alloys, systematic finite element calculations are carried out to predict the overall stress-strain behavior under uniaxial compression. The plastic flow behavior of the tungsten and the W-Ni-Fe phases are defined by equations (1) and (2), respectively. The volume fraction of the tungsten particles is taken to be within the range $0.7 \leq f \leq 0.96$, a range that covers all of the useful W-Ni-Fe systems. Due to the fact that the major application of tungsten heavy alloys is as penetrator materials undergoing large plastic deformations, the maximum applied strain in the calculation is chosen to be 0.8. The shape of the softer W-Ni-Fe phase is taken to be spherical, since the geometry of tungsten particles appears to have little effect on the overall stress-strain behavior, as discussed in Section 2.

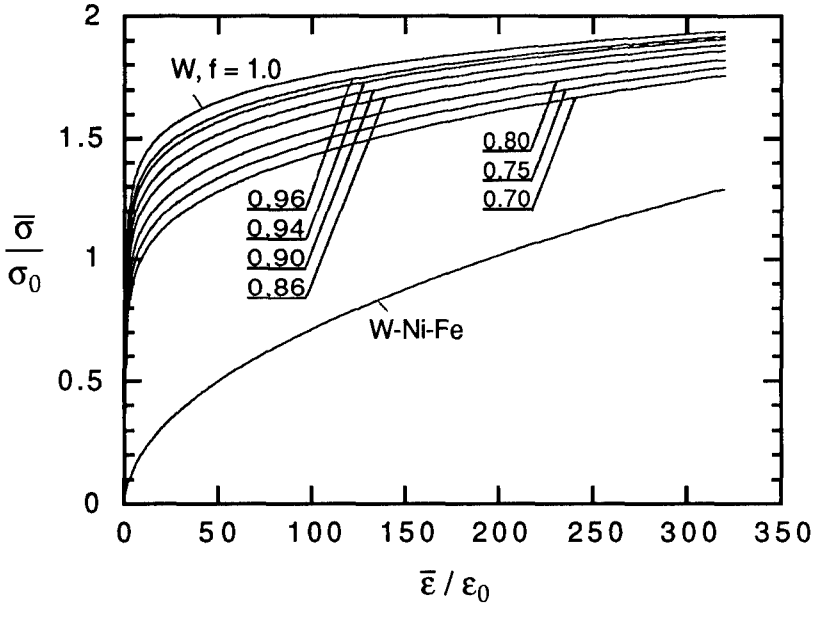



Fig. 5. Uniaxial stress-strain curves for a W-Ni-Fe heavy alloy under compression with applied strains up to 0.8. The tungsten volume fraction of the alloy is in the range $0.7 \leq f \leq 0.96$. The stress-strain curves of the two individual phases are shown for comparison.

Fig. 5 shows the predicted overall stress-strain curves for these heavy alloys with tungsten volume fractions f ranging from 0.7 to 0.96. The curves all have shapes similar to that of the tungsten phase owing

to its high volume fraction in the alloys. It is also evident that not only the flow stress but also the stress hardening exponent changes with f. This reflects the fact that the two phases undergoing plastic deformation have quite different hardening behavior.

The shape of the curves in Fig. 5 suggests that the overall uniaxial stress-strain behavior of the W-Ni-Fe alloys can be described by a relation of the Ramberg-Osgood type:

$$\frac{\bar{\varepsilon}}{\varepsilon_0} = \frac{\bar{\sigma}}{\bar{\sigma}_N} + \alpha\left(\frac{\bar{\sigma}}{\bar{\sigma}_N}\right)^n \tag{3}$$

where $\varepsilon_0$ is the same as that defined in (1), $\bar{\sigma}_N$ is a reference stress, a is the coefficient, and n is the stress exponent. Clearly, the parameters $\alpha$, n, and $\bar{\sigma}_N$ are functions of the tungsten volume fraction f, and of the material characteristics of the two phases. Guided by the formula given in (3), we find that within 2% error, the curves in Fig. 5 can be fitted by taking

$$\alpha(f) = \alpha_0 f + \alpha_1(1-f)\ , \tag{4a}$$

$$n(f) = n_0\left[a_0 + a_1(1-f) + a_2(1-f)^2 + a_3(1-f)^3\right], \tag{4b}$$

and

$$\bar{\sigma}_N(f) = \sigma_0\left[b_0 + b_1(1-f)^{1/2} + b_2(1-f) + b_3(1-f)^{3/2}\right]. \tag{4c}$$

For the particular material characteristics chosen here for the pure polycrystalline tungsten phase and the soft W-Ni-Fe phase, the corresponding values for the parameters $a_i$ and $b_i$ for use in eqn. (4) are given in Table I.

Table I. Values of the parameters $a_i$ and $b_i$ in eqn. (4)

| $a_0$ | $a_1$ | $a_2$ | $a_3$ |
|---|---|---|---|
| 1.0 | –3.535 | 9.788 | –11.437 |
| $b_0$ | $b_1$ | $b_2$ | $b_3$ |
| 0.976 | 1.246 | –4.018 | 2.8 |

Note that equation (4a) for $\alpha$ is just the rule of mixtures. The value of $\bar{\sigma}_N$ for $0.7 \le f \le 0.96$ is only slightly below or above unity. The expression for n in equation (4b), however, is markedly different from the rule of mixtures. The values of n given by (4b) are below the predictions of the rule of mixtures for $0.7 \le f < 1$, indicating that the softer W-Ni-Fe phase has a strong influence on the plastic flow

behavior of the alloys (although the shape of the soft "inclusion" has relatively little effect).

When the applied strains are large, the elastic strains in both phases can be neglected. Consequently, the stress-strain behavior of the tungsten phase and the W-Ni-Fe matrix phase can be approximated by pure power law relations

$$\frac{\sigma_w}{\sigma_0} = \left(\frac{\varepsilon_w}{\alpha_0 \varepsilon_0}\right)^{1/n_0} \tag{5a}$$

and

$$\frac{\sigma_s}{\sigma_1} = \left(\frac{\varepsilon_s}{\alpha_1 \varepsilon_1}\right)^{1/n_1} . \tag{5b}$$

In equations (5), $\sigma_W$ and $\varepsilon_W$ denote stress and strain in the tungsten phase and $\sigma_S$ and $\varepsilon_S$ are stress and strain in the soft W-Ni-Fe matrix phase.

A basic feature of the tungsten heavy alloys is that the tungsten phase forms a continuous "network"; the W-Ni-Fe phase is mostly isolated. Therefore, the average strains in the softer W-Ni-Fe phase can be taken to be the same as in the tungsten phase, i.e., $\varepsilon_w = \varepsilon_s = \bar{\varepsilon}$, where $\bar{\varepsilon}$ is the remotely applied strain. The average stress in the composite can be related to the stresses in the tungsten phase and the W-Ni-Fe phase by

$$\bar{\sigma} = f\sigma_w + (1-f)\sigma_s . \tag{6}$$

Combining equations (5) and (6) yields a simple formula for composite flow behavior at large strains

$$\frac{\bar{\sigma}}{\sigma_0} = f\left(\frac{\bar{\varepsilon}}{\alpha_0 \varepsilon_0}\right)^{1/n_0} + (1-f)\left(\frac{\bar{\varepsilon}}{\alpha_1 \varepsilon_1}\right)^{1/n_1} . \tag{7}$$

Equation (7) can be used to predict the overall stress-strain behavior of the tungsten heavy alloys as determined by the tungsten volume fraction and the characteristics of the individual phases. It is evident that at large strains, equation (7) gives fairly accurate predictions over a wide range of the tungsten volume fraction [17]. Equation (7) may also be used to extract the flow behavior of the matrix material from the measured stress-strain curves of the tungsten phase and the composite since measuring the matrix flow behavior under the appropriate microstructural constraints is rather difficult.

## 4. DEBONDING DAMAGE

The tungsten-tungsten grain boundaries in a W-Ni-Fe alloy formed during liquid-phase sintering are relatively weak, causing debonding to occur at relatively low applied strains [5]. The spatial distribution of the initial defects at W-W grain boundaries is likely to be quite uniform over a large volume of the alloy; the size of the defect, however, varies from place to place. Consequently, upon tensile stressing of the alloy, some of the W-W grain boundaries perpendicular to the loading direction are debonded first simply because they contain large initial flaws. Since the matrix is more ductile plus the tungsten-matrix interface is strong, the debonding crack often arrests once the whole contact area is completely debonded. The debonding-cracking process depends on many factors, especially the strength of the W-W grain boundary. To gain insight, in this study, the detailed debonding process at each individual grain boundary is neglected. Rather, a grain boundary is modeled as either perfectly bonded or completely debonded; the evolution of damage is therefore represented in term of the population of the debonded contacts.

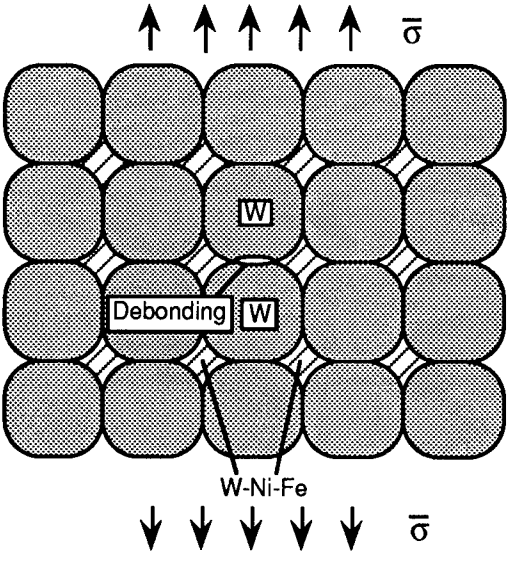



Fig. 6. Schematic of a tungsten-nickel-iron heavy alloy sustaining debonding damage at tungsten grain boundaries.

Assume that the equal-sized tungsten grains are aligned along the tensile loading direction (Fig. 6). Then each grain has six contact sites among which only two are perpendicular to the loading direction. Under uniaxial tensile stressing, the grain boundaries perpendicular to the loading direction can debond, while those parallel to the loading direction are unlikely to be debonded since they are subjected to

compression. To model the level of debonding damage quantitatively, we define a non-dimensional parameter $\rho$: the number of debonded grain boundaries over the total number of grain boundaries that are perpendicular to the loading direction. The parameter $\rho$ represents the population or fraction of debonded grain boundaries; it usually increases with the local stress level which is in turn controlled by the applied stress or strain. In addition, it increases with the contact area of W-W grain boundaries since the probability of having a sizable defect is larger when the contact area is larger. We thus propose a Weibull-type model linking $\rho$ to the area of a single W-W contact and the applied strain $\bar{\varepsilon}$

$$\rho = 1 - \exp\left[-\beta(\bar{\varepsilon} / \varepsilon_c)^m\right] \tag{8}$$

where $\varepsilon_c$ is a reference strain; m is a parameter similar to the Weibull modulus reflecting how rapidly $\rho$ changes with $\bar{\varepsilon}$; $\beta$ is a dimensionless parameter representing the contact area between two tungsten grains. Obviously, the damage model given by (8) is analogous to the Weibull statistics for brittle materials [18]. It gives the right trends: $\rho$ equals zero if $\beta$ or $\bar{\varepsilon}$ is zero; $\rho$ approaches unity when $\bar{\varepsilon}$ is large.

The nondimensional parameter $\beta$ is defined as the area A of a single contact between two tungsten grains normalized by $A_0$ the maximum cross-section area of a grain perpendicular to the loading direction. To obtain $\beta$ as a function of the tungsten volume fraction f, consider the tungsten grain depicted in Fig. 6. It consists of a cylinder of radius r and two identical spherical caps mimicking a "squeezed" sphroidal tungsten grain. The parameter $\beta$ is then given by

$$\beta = \frac{A}{A_0} = \frac{\pi b^2}{\pi r^2} = \left(\frac{b}{r}\right)^2 . \tag{9}$$

It can be shown that $\beta$ defined in (9) is related to the tungsten volume fraction f by

$$1.5f = 1 + 1.5\beta - \beta^{3/2} . \tag{10}$$

Note that for a fixed tungsten volume fraction, the total contact area is dependent on the grain size: the smaller the grain, the larger the total contact area. Such a size effect will not be considered in the present study.

To illustrate the practical significance of the damage model, the experimental data given in [5] was used to obtain m = 1.6, $\varepsilon_c$ = 0.077 taking f = 0.74 and the grain size $a_0$ = 35 μm. It is quite remarkable that the model predictions of ρ for the W-Ni-Fe alloy with three different tungsten volume fractions all agree well with the experimental data, as can be seen from Fig. 7. It is obvious that the damage model given in (8) captures not only the dependence of ρ on the applied strains $\bar{\varepsilon}$, but also that on the tungsten volume fraction f. It is true that the damage model proposed here is still an empirical one; nevertheless, it can be used to predict quite accurately the damage population ρ as a function of f and $\bar{\varepsilon}$. It can also be used in conjunction with the finite element cell model to predict the effect of damage on the tensile behavior of the alloy [19].

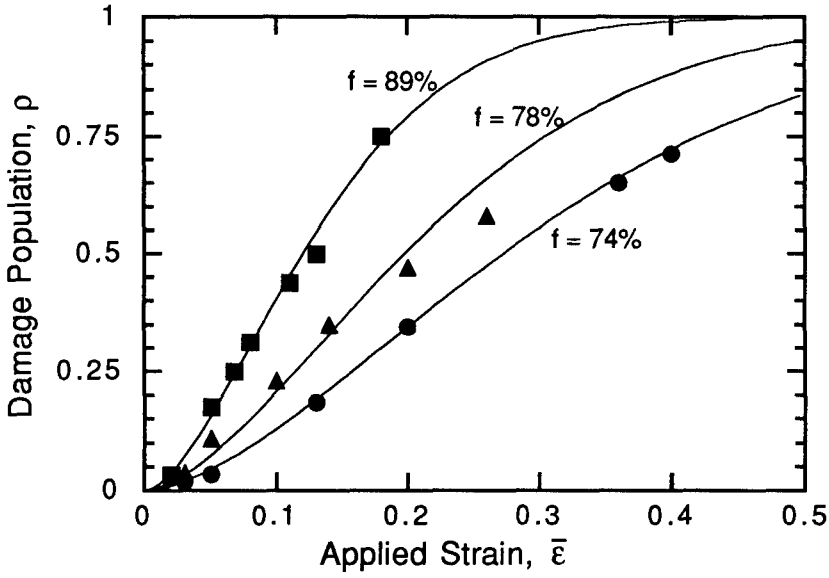



Fig. 7. Comparison between the model predictions of ρ using equation (8) and the experimental measurements shown as points. The solid lines are predictions for f = 0.74, 0.78 and 0.89 based on m = 1.6 and $\varepsilon_c$ = 0.077.

Based on the damage evolution law developed above, a finite element analysis was carried out for the composite tensile behavior using a three-phase cell model [19]. Shown in Fig. 8 are the overall tensile stress-strain curves of the debonding damaged tungsten heavy alloy for f = 0.86, 0.9 and 0.94 for applied strains $\bar{\varepsilon}$ up to 0.2. The corresponding stress-strain curves of the undamaged alloy are also displayed for comparison. These predictions show that the softening effect of debonding damage is more profound when the applied strains

$\bar{\varepsilon}$ and the tungsten volume fractions f are large. It is also clear that without damage, the overall plastic flow stress always increases with the applied strains $\bar{\varepsilon}$ and tungsten volume fraction f, a hardening behavior common to many composites. These two competing trends – hardening and softening – are exemplified by the curves with f = 0.94. It is worth noticing that a peak appears on the stress-strain curve of the damaged alloy with f = 0.94. Similar softening phenomena has been found in metals due to void growth and in metal matrix composites due to reinforcement cracking and debonding [14].

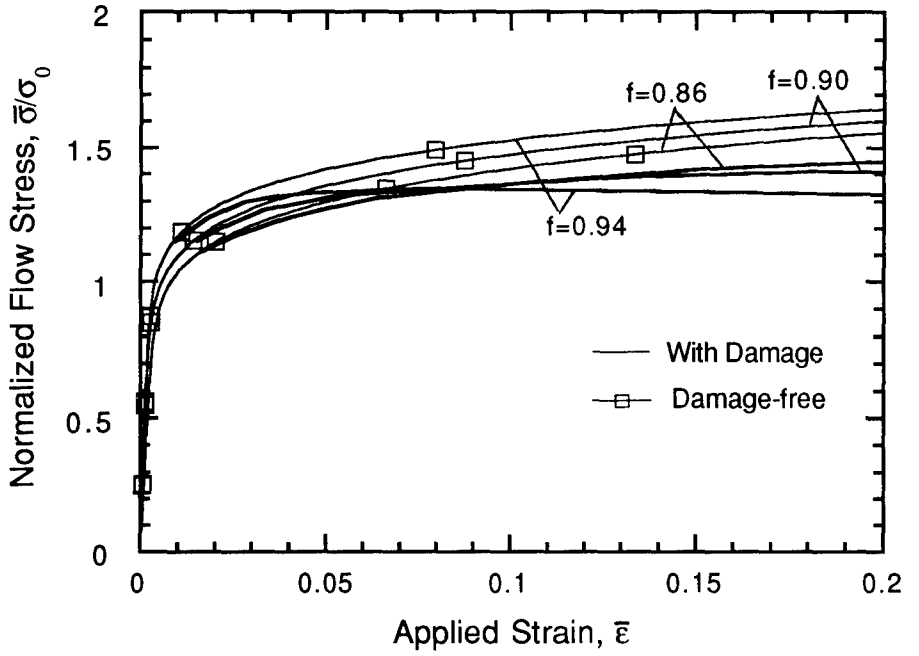



Fig. 8. Predicted stress-strain curves for the heavy alloy with progressive damage. Comparison of the curves with and without damage for f = 0.86, 0.90 and 0.94 indicates the two competing trends of strain- hardening and damage-softening.

## 5. CONCLUDING DISCUSSION

Tungsten heavy alloys are good candidate materials for making penetrators in advanced antiarmor systems. To achieve the high performance required in this application, the fundamental relation between material microstructure and thermomechanical properties needs to be established. Due to the complexities of the deformation and failure modes in tungsten heavy alloys under impact loading conditions, a general predictive model is yet to emerge.

To set the stage for a systematic micromechanics study, quasi-static plastic flow in tungsten composites under compression is

simulated since compressive failure is an important deformation and failure mode in penetrators. It is found that under compressive loading, the overall stress-strain behavior of the composite at large strains is essentially independent of the particle shape, although the local plastic flow behavior changes dramatically with the inclusion geometry. Two simple formulae are proposed to describe the overall flow behavior as determined by the tungsten volume fraction, and the flow behavior of both phases. To predict the tensile behavior of tungsten composites sustaining debonding at W-W grain boundaries, a damage evolution model is proposed based on the Weibull statistics. It is shown that the stress-strain behavior of the alloy under quasistatic tensile loading is controlled by two competing trends – strain hardening and debonding softening – both evolve with the tungsten volume fraction and the applied strains. It is recognized that the rate dependent plastic flow and thermal softening of the material are essential in determining the performance of a penetrator. The strategy represented in this work is the study of the very complicated subject via specific cases of systematically increasing complexity. Each step represents one important deformation and failure mechanism, and reflects one aspect of the true nature of the physical process.

To solve the actual initial-boundary value problem associated with penetration, constitutive expressions and failure criteria concerning the deformation and failure mechanisms in the material are essential. These mechanisms are controlled by microstructural features such as grain size, shape, and orientation, interface and grain boundary strength, dislocation density, and initial damage distribution. To gain more understanding of the fundamental relation between material microstructure and thermomechanical properties, mechanism-based micromechanics studies involving these phenomena are needed. The finite element cell models used here can be further developed to study this range of issues, including interface sliding, rate effects, and thermal softening. Experimental investigations and numerical simulations examining these issues in dual-phase materials are in progress.

## ACKNOWLEDGMENTS

Funding of this work was supplied in part by NSF through a Research Initiation Award (MSS-9210250) to G. Bao, and in part by the U.S. Army Research Office through Grant No. DAAL03-91-G-0079 to K. T. Ramesh.

## REFERENCES


1. T.W. Penrice, "Kinetic Energy Penetrators," in *Powder Metallurgy in Defense Technology*, **5**, compiled by Metal Powder Industries Federation, Princeton, pp. 11 (1980).
2. L.L. Bourguignon and R.M. German, *Int. J. Powder Metall.*, **24**, 115 (1988).
3. C. Lea, B.C. Muddle and D.V. Edmonds, *Metall. Trans.*, **14A**, 667 (1983).
4. R.S. Coates and K.T. Ramesh, *Mat. Sci. Eng. A*, **145**, 159 (1991).
5. B.H. Rabin and R.M. German, *Metall. Trans.*, **19A**, 1523 (1988).
6. T. Mori and K. Tanaka, *Acta Metall.*, **21**, 571 (1973).
7. G.J. Weng, *J. Mech. Phys. Solids.*, **38**, 419 (1990).
8. R.M. Christensen, *J. Mech. Phys. Solids.*, **38**, 379 (1990).
9. D.G. Taggart and J. Bassani, *Mech. Mat.*, **12**, 63 (1991).
10. G. Bao, J.W. Hutchinson and R.M. McMeeking, *Mech. Mat.*, **12**, 85 (1991).
11. G. Bao, J.W. Hutchinson and R.M. McMeeking, *Acta Metall. Mater.*, **39**, 1871 (1991).
12. T. Christman, A. Needleman and S. Suresh, *Acta Metall.*, **37**, 3029 (1989).
13. V. Tvergaard, *Mat. Sci. Eng. A*, **125**, 203 (1990).
14. G. Bao, *Acta Metall. Mater.*, **40**, 2547 (1992).
15. A.K. Zurek, P.S. Follansbee and D. Kapoor, "Strain rate and temperature effects in tungsten and tungsten alloys," in *High strain rate behavior of refractory metals and alloys*, compiled by R. Asfahani, E. Chen, and A. Crowson, TMS, Warrendale, PA, pp. 179 (1992).
16. R.L. Woodward, I.G. McDonald and A. Gunner, *J. Mat. Sci. Lett.*, **5**, 413 (1986).
17. G. Bao and Ramesh, *Acta Metall. Mater.*, **41**, 2711 (1993).
18. W. Weibull, *Ins. Vet. Ak. Handl.*, **151** (1939).
19. Z. Lin and G. Bao, "Damage in a tungsten composite due to debonding at W-W grain boundaries", submitted to *Acta Metall. Mater.*

# SHEAR BANDS IN PRESSURE-SHEAR PLATE IMPACT

M. Zhou*, R. J. Clifton and A. Needleman
Division of Engineering
Brown University
Providence, RI 02912

## Abstract

Pressure-shear plate impact is used to study dynamic shear banding in a two-phase microstructure at nominal shear strain rates up to $7 \times 10^5$ $s^{-1}$, under pressures of the order of 10 GPa. The material is a tungsten heavy alloy (WHA) which has a microstructure consisting of hard tungsten grains embedded in a soft matrix. Experiments and numerical simulations show that the two-phase alloy is more susceptible to shear banding than either of its constituent phases when tested separately. While the onset of shear localization depends on the grain distribution and volume fraction, the shear band width is found to be set by heat conduction and is insensitive to the grain volume fraction and the grain morphology.

## 1. Introduction

Dynamic plastic flow localization plays an important role in a wide range of applications including high speed machining, high rate forming, explosive welding and armor penetration. For example, the performance of tungsten heavy alloys (WHA) as materials used for penetrators of heavy armor has been understood to depend strongly on their resistance to the formation of shear bands. Excessive mushrooming of the projectiles, and the resulting reduction in penetrator performance have been associated with a relatively weak propensity for forming shear bands. Understanding the mechanisms through which shear strain localizes in these alloys is clearly important for improving the performance through revisions in materials design and processing.

At the high rates of straining found in these applications, thermal softening that occurs because of the heating due to plastic dissipation, together with the lack of time for heat conduction, provides the main driving force for localization. Controlled shear band development under well-characterized deformation conditions has been limited to nominal shear strain rates of the order of $10^3$ $s^{-1}$. These experiments involve small or no hydrostatic pressures. Much higher strain rates and higher pressures are present in applications in which shear band formation is believed to play a significant role. Higher strain rates delay the localization of shear strain through inertia effects and through enhanced material rate sensitivity. High hydrostatic pressures can suppress void nucleation and growth, thereby delaying the formation of shear band and prolonging the localized deformation after the bands form. The need to correctly understand and model shear banding at ultra-high strain rates calls for experimental studies that provide such conditions.

Pressure-shear plate impact of a thin foil specimen described by Clifton and Klopp (1985)[1] is an attractive means for conducting such studies. High rates and pressures are generated by sandwiching the specimen between two hard tungsten carbide plates. The specimen is subjected to simple shear at nominal shear strain rates between $10^5$ and $10^6$ $s^{-1}$, under pressures of the order of 10 GPa.

This study concerns the formation of shear bands in the two-phase microstructure of tungsten heavy alloys. These alloys are are characterized by the high density, high strength and toughness that they possess resulting from the composite microstructure of hard tungsten grains embedded in a ductile matrix such as the nickel-iron-tungsten (Ni-Fe-W) matrix used for the alloy studied in the current investigation.

There is an extensive literature on the one-dimensional problem of thermal softening induced localization in simple shear, *e.g.* Recht (1964)[2], Clifton (1980)[3], Wright and Walter (1987)[4], Bai (1982)[5], Merzer (1982)[6], Molinari and Clifton (1987)[7], Batra and Kim (1992)[8] and Shawki and Clifton (1989)[9]. Evidently, such formulations neglect the complex microstructural influence that in certain instances dominates the evolution of localized deformation. The composite microstructure of WHA calls for analyses that account for its microstructural heterogeneities. In the present paper, finite element calculations are carried out to model the pressure-shear impact experiments. The tungsten heavy alloy is modelled as a composite consisting of two phases, *i.e.* the hard tungsten grains and the soft matrix. The numerical calculation is carried out using a digitized microstructure of the actual alloy. In addition, calculations are carried out to simulate pressure-shear impact experiments on pure tungsten and a nickel-iron-tungsten alloy which are the constituents of the WHA composite. The coupled thermo-mechanical problem of dynamic finite deformation is formulated with full account of finite deformations, inertia, strain hardening, strain rate sensitivity, thermal softening and heat conduction.

## 2. Materials

Figure 1 shows the microstructure of a tungsten heavy alloy containing $93wt\% - W$, $4.9wt\% - Ni$ and $2.1wt\% - Fe$, before test. This is a typical structure for such an alloy, consisting of tungsten grains embedded in a matrix phase of nickel, iron and tungsten. The grains are nearly pure tungsten with a body-centered-cubic (BCC) lattice structure. The matrix is an alloy of nickel, iron and tungsten and has a face-centered-cubic (FCC) lattice structure.

In order to understand the effects of the two-phase microstructure or material inhomogeneity on the alloy's behavior, this investigation includes the determination of the response of the two constituent phases as well as that of the composite. To this end, pure tungsten and an alloy custom-made to match the the reported compositions of the matrix phase are studied along with the tungsten alloy. The matrix alloy contains $25wt\% - W$, $50wt\% - Ni$ and $25wt\% - Fe$.

More details including the microstructures of the tungsten and the matrix alloy can be found in Zhou (1993)[10]. All three materials are cross-rolled along two directions in the rolling plane after sintering. The thickness reduction is 8% in each direction.

## 3. Experiments

The configuration of the pressure-shear plate impact experiment for high strain rate deformation of a thin specimen is shown in Fig. 2, as described by Clifton and Klopp, (1985)[1]. The experiment involves the shearing of a thin foil specimen sandwiched between two hard tungsten carbide plates, which remain elastic during the experiment. The specimen, $50\mu$m to $200\mu$m in thickness, is subjected to simple shear for $2\mu$s at nominal shear strain rates between $10^5$ and $10^6$ $s^{-1}$, under pressures of the order of 10 GPa. Plane wave loading is achieved by the impact of the thin specimen, bonded to the front of a tungsten carbide flyer plate, with a stationary anvil plate. Combined pressure and shear loading is obtained by having the parallel impact faces inclined relative to the direction of approach. The impact is achieved on a 2.5 inch (63.5mm) light gas gun whose test chamber is evacuated to vacuum levels of about $100 \times 10^{-6}$ torr during experiments. Details of this experiment can be found in Clifton and Klopp, (1985)[1]. This experiment provides the simplicity of allowing the onset of shear localization and the development of a shear band to be interpreted from the stress-time and stress-strain profiles for plane wave loading under conditions for which the pressure history is well known. Because of the high normal pressure applied to the specimen this configuration provides a condition in which the effects of pressure on shear band formation can be investigated. Since the specimen has no free surfaces, shear band initiation and development are independent of a macroscopic geometrical defect parameter, which is important in analyses (Molinari and Clifton, 1987)[7] concerning other experimental configurations, such as the torsional Kolsky bar.

In order to obtain material response over a wide range of strain rates, torsional Kolsky bar experiments are conducted on the matrix alloy. In addition, data from similar experiments by Andrews *et al* (1992)[11] on a similar W-Ni-Fe alloy containing 93% $W$ are used along with pressure-shear impact results to obtain a complete understanding of the behavior of the WHA and the matrix alloy. Quasi-static torsional experiments are also conducted These two experiments involve the torsional deformation of a thin-walled tube specimen. The configuration for these experiments has been described by Duffy and co-workers, Hartley *et al* (1985)[12], Duffy *et al* (1971)[13] and Costin *et al* (1979)[14].

Tests at elevated temperatures of $200°C$ and $250°C$ were conducted to gain information on the temperature dependence of the stress-strain curves of the materials.

## 4. Experimental Results

Table 1 summarizes the pressure-shear plate impact experiments conducted on WHA, the matrix alloy and W. Each experiment is also called a "shot".

Table 1 Pressure-Shear Experiment on WHA, W and Matrix Alloy

| Shot # | Material Material | Projectile Velocity mm/$\mu$s | Skew Angle $\theta$, $^\circ$ | Normal Pressure p, MPa | Shear Stress MPa | Shear Rate $\times 10^5 s^{-1}$ | Specimen Thickness $\mu$m | Shear Band |
|---|---|---|---|---|---|---|---|---|
| 9109 | WHA | 0.181 | 21.5 | 8981 | 1100 | 0.14 | 1973 | No |
| 9201 | WHA | 0.188 | 22.0 | 9326 | 1300 | 1.2 | 201 | No |
| 9203 | WHA | 0.198 | 21.5 | 9831 | 1160 | 2.0 | 175 | No |
| 9205 | WHA | 0.205 | 21.5 | 10689* | 1350 | 3.9 | 78 | Yes |
| 9206 | WHA | 0.202 | 26.6 | 9629 | 1300 | 5.4 | 87 | Yes |
| 9207 | WHA | 0.213 | 22.0 | 10555 | 1350 | 4.0 | 89 | Yes |
| 9209 | WHA | 0.205 | 18.0 | 10430 | 1290 | 3.5 | 61 | No |
| 9211 | WHA | 0.205 | 21.5 | 10174 | 1250 | 6.5 | 57 | Yes |
| 9303 | WHA | 0.198 | 22.9 | 9748 | 1320 | 4.2 | 79 | Yes |
| 9204 | W | 0.193 | 22.0 | 9607 | 1340 | 1.2 | 195 | No |
| 9301 | W | 0.198 | 22.9 | 9733 | 1250 | 4.2 | 91 | No |
| 9302 | W | 0.206 | 22.9 | 10142 | 1320 | 2.5 | 151 | No |
| 9208 | Matrix | 0.200 | 18.0 | 10146 | 680 | 3.0 | 129 | No |
| 9212 | Matrix | 0.199 | 21.5 | 9910 | 780 | 9.0 | 55 | No |

* High pressure window of 1440 ns followed by low pressure window of 520 ns;

Figure 3 shows the stress-strain curves for the WHA at different strain rates obtained by pressure-shear impact, torsional Kolsky bar and quasi-static torsion. The results for the Kolsky bar and quasi-static torsion experiments were obtained by Andrews *et al* (1992)[11]. The alloy shows strain hardening at $\dot{\gamma} \sim 10^{-4}$ $s^{-1}$. On the other hand, the curves at dynamic strain rates show apparent softening of the material. This softening is attributed to the thermal softening of the material resulting from the heat generated by the plastic deformation. Two Kolsky bar experiments are shown. The defect parameter $\epsilon$, defined as the maximum wall thickness variation divided by the average wall thickness, apparently has a strong influence on the critical strain for shear localization. Figure 4 shows the deformed microstructure of the specimen corresponding to the pressure-shear curve in Fig. 3. The initial specimen thickness $h = 201\mu$m, the impact velocity $V_0 = 188$ m/s and the impact angle $\theta = 22°$. The grains show elliptically elongated shapes, demonstrating the shear deformation. No shear band is observed in this particular experiment (Shot 9201) even though the accumulated shear strain is comparable to what is seen in the tosional Kosky bar curves.

As the amount of shear strain is increased by reducing the specimen thickness, increasing the impact velocity and increasing the impact angle, shear bands form in the specimen. Figure 5 shows the stress-strain curves from three shots involving specimens $57 - 87\mu$m in thickness and impact angles of $18 - 26.6°$. Shear bands are observed in the two higher angle shots (Shots 9206 and 9211). Critical nominal shear strains at the onset of shear localization are between $1 - 1.5$. These values are significantly higher than what is shown in Fig. 3 for the torsional Kolsky bar experiments. The sharp downturn in the curves signifies the loss of stress-carrying capacity associated with the onset of shear localization. Since the late stages of the drop are very close to the end of the two-microsecond window of valid observation at the rear surface of the anvil, there is less certainty about the exact shape of the stress-strain curves at such late times.

Figure 6a shows the deformed microstructure after Shot 9205 which involves shearing under high pressure (10.7 GPa) for approximately $1.44\mu$s. After this period of shearing deformation the pressure on the specimen was reduced to a level for which no significant deformation occurred subsequently. The micrograph shows an emerging band at the center of the specimen. A neck has formed in the tear-drop shaped grain. The development of the band may involve further shearing of the tear-drop shaped grains and propagation into the neighboring materials on both sides of the putative band. Figure 6b shows the morphologies of a fully developed shear band in the specimen of Shot 9206. The intensely sheared region involves both the W gains and the matrix. The micrograph in Fig. 6b shows deep etching of the grains so that the structure of the deformed matrix and grains is clearly revealed. The grains form tear-drop shapes near the middle of the band. The shear band in Fig. 6b is $5 - 10\mu$m in width. This is in sharp contrast to the widths of approximately $100\mu$m reported for torsional Kolsky bar experiments, Andrews *et al* (1992)[11]. Also, the shear band in Fig. 6b shows more intense shear than observed in the torsional Kolsky bar experiments. Prolonged localized deformations occur in pressure-shear impact because the high pressure (9.62 GPa for Shot 9206) delays failure due to microvoids and microcracks. During the torsional Kolsky bar experiments, rupture occurs at relatively early stages of the localized deformation because of the absence of pressure.

Figure 7 (Shot 9207) shows a shear band that has led to the failure of the material through the center of the shear band. Ductile failure of the matrix, grain-matrix separation and grain fracture are visible. A fractograph of the ruptured shear band surface is shown in Fig. 8a for the specimen from Shot 9303, and Fig. 8b is the corresponding back-scattered electron image showing the two different phases. The dark areas are the matrix and the white regions are the grains. The surface morphology indicates intense shearing at the center of the shear band. Note the fractured grain at A. This suggests that grain fracture plays a part during failure. Dark strips on the grain surfaces, indicate grain-matrix contact before separation. In view of the high percentage of the fracture

surface that carrys the grain-matrix shear marks, grain-matrix separation appears to be the dominant failure mechanism. Some microcracks are seen on heavily sheared grains (grains A, B and C) in Fig. 8a. Grains A and C appear to have been fractured. Grain B probably has not fractured but has developed internal microcracks. Grains D, E and F have clean fracture surfaces with no indication of contact with the matrix before breaking. A combination of ductile rupture of the matrix, grain-matrix separations and grain fracture seems to be responsible for the failure of WHA inside a shear band.

Experiments were also conducted on pure tungsten and the matrix alloy. In contrast to the observed shear band formation in the case of WHA, neither the deformed microstructure of tungsten nor that of the matrix shows localized deformation, see Zhou (1993)[10]. The stress-strain curve for pure tungsten is shown in Fig. 9 along with the WHA curve from Shot 9206. Similar stress levels are observed for W and WHA. The tungsten curve does not show a sharp downturn that would indicate the loss of stress-carrying capacity due to localized deformation. The stress-strain curve for the matrix is also shown in Fig. 9. Note that there is no sharp downturn in this stress-strain curve signifying the onset of localized deformation. Furthermore, the curve shows strong strain hardening by the matrix during the pressure-shear impact experiment.

The above results demonstrate that the composite WHA is more susceptible to shear banding than either of its constituent phases when tested separately. This susceptibility suggests the role of material inhomogeneity in the formation of shear bands. The presence of different phases serves as a perturbation to the deformation that provides nonuniform fields for the development of shear bands. Full simulations will be carried out later to explore the role played by different microstructural aspects of this two-phase material. The calculations will confirm that the two constituent phases are indeed more resistant to shear banding than the composite WHA.

Figure 10 is a summary of the response of the matrix alloy obtained from quasi-static torsion, torsional Kolsky bar and pressure-shear plate impact. Unlike the WHA, the matrix alloy shows strain hardening under both quasi-static and dynamic conditions. This behavior indicates that the thermal softening due to plastic dissipation is relatively small and insufficient to overcome the strain hardening under these test conditions. This lack of strain softening can be explained as follows. While the matrix alloy has a specific heat three times that of the WHA, its flow stress is only about one half that of the WHA. For the same amount of plastic strain the temperature change would likely be only one third of that for the heavy alloy, considering a factor of two for the difference in the densities.

The strain rate sensitivities of the WHA and the matrix alloy are shown in Fig. 11. The flow stresses plotted correspond to a shear strain of $\gamma = 0.45$ for the matrix. It is noted that the matrix alloy exhibits a relatively lower strain-rate dependence of the flow stress. The WHA, on the other hand, shows a strong

strain-rate sensitivity at high strain rates. The flow stress levels of pure tungsten are found to be slightly higher those of the WHA.

Figure 12 shows the shear stress-strain curves of the matrix alloy at room temperature, $200°C$ and $250°C$, obtained from torsional Kolsky bar experiments. Significant thermal softening is seen in this temperature range. The experiments are limited to temperatures under $250°C$ to avoid significant expansions in the parts of the loading bars that experience heating together with the specimen. The temperature dependence of flow stresses for WHA, W and the matrix alloy are summarized in Fig. 13. The data for WHA are reported by Andrews *et al* (1992)[11], Bose, Sims and German (1988)[15], and O'Donnell and Woodward (1990)[16]. The solid lines are model characterizations which will be discussed in Chapter III. It is assumed that the materials lose all stress-carrying capacity when the temperature reaches their corresponding melting points. Tungsten shows a much lower rate of thermal softening than the matrix partly because of its high melting temperature (approximately 3600 K). The thermal softening behavior of WHA depends on the softening rates of both the tungsten grains and the matrix. There is a lack of data on the thermal softening behavior at high temperatures for all the materials studied.

## 5. Analytical Formulation

A convected coordinate, Lagrangian formulation of the field equations is used as, for example, in LeMonds and Needleman (1986), Needleman (1989), and Needleman and Tvergaard (1991). The coupled thermo-mechanical problem of dynamic finite deformation is formulated with full account of finite deformations, inertia, strain hardening, strain rate sensitivity, thermal softening and heat conduction. The equations that govern the coupled mechanical and the thermal processes are, respectively, the principle of virtual work and balance of energy, *i.e.*

$$\int_V \boldsymbol{\tau} : \delta \mathbf{E} dV = \int_S \mathbf{f} \cdot \delta \mathbf{u} dS - \int_V \rho \frac{\partial^2 \mathbf{u}}{\partial t^2} \cdot \delta \mathbf{u} dV, \tag{1}$$

$$\begin{aligned} \int_V \rho c_p \dot{T} \delta T dV = & \int_V \chi \boldsymbol{\tau} : \mathbf{D}^p \delta T dV + \int_S k(\mathbf{F}^{-1} \cdot \mathbf{F}^{-T} \cdot \frac{\partial T}{\partial \mathbf{x}}) \cdot \mathbf{n} \delta T dS \\ & - \int_V k(\mathbf{F}^{-1} \cdot \mathbf{F}^{-T} \cdot \frac{\partial T}{\partial \mathbf{x}}) \cdot \frac{\partial \delta T}{\partial \mathbf{x}} dV. \end{aligned} \tag{2}$$

In the above equations, $\boldsymbol{\tau}$ is the Kirchhoff stress ($\boldsymbol{\tau} = \det|\mathbf{F}|\boldsymbol{\sigma}$, with $\boldsymbol{\sigma}$ the Cauchy stress tensor and $\mathbf{F}$ the deformation gradient), $\mathbf{E}$ is Lagrangian strain, $\mathbf{f}$ is the traction on a surface in the reference configuration, $\mathbf{u}$ is the displacement, $\rho$ is the density in the reference configuration, $t$ represents time, $c_p$ is the specific heat, $T$ is temperature, $\xi$ is the portion of plastic work converted to heat, $\mathbf{D}^p$ is the plastic part of the rate of deformation, $k$ is the heat conductivity, $\mathbf{n}$ is the normal to a surface in the reference configuration, $\dot{(\ )}$ denotes $\partial(\ )/\partial t$, $(\ )^{-1}$ denotes inverse, and $(\ )^{-T}$ denotes inverse transpose.

The incremental stress-strain relation is written in terms of the Jaumann rate of Kirchhoff stress $\hat{\tau}$ and the rate of deformation $\mathbf{D}$ as

$$\hat{\tau} = \mathbf{L} : \left[\mathbf{D} - \mathbf{D}^p - \alpha \mathbf{I}\dot{T}\right], \tag{3}$$

where $\mathbf{L}$ is the elastic modulus tensor, $\mathbf{I}$ is the second order identity tensor, and $\alpha$ is the coefficient of thermal expansion. For an isotropically hardening, viscoplastic solid $\mathbf{D}^p$ is given by

$$\mathbf{D}^p = \frac{3\dot{\bar{\epsilon}}}{2\bar{\sigma}}\tau', \tag{4}$$

with $\dot{\bar{\epsilon}}$ being the equivalent plastic strain rate and

$$\tau' = \tau - \frac{1}{3}(\tau : \mathbf{I})\mathbf{I}, \qquad \bar{\sigma}^2 = \frac{3}{2}\tau' : \tau'. \tag{5}$$

The viscoplastic response of each of the constituent materials obtained experimentally for the strain-rate range of $10^{-4}$ s$^{-1}$ to $7 \times 10^5$ s$^{-1}$ is characterized by the following equations

$$\left.\begin{aligned} \dot{\bar{\epsilon}} &= \frac{\dot{\epsilon}_1 \dot{\epsilon}_2}{\dot{\epsilon}_1 + \dot{\epsilon}_2}, \\ \dot{\epsilon}_1 &= \dot{\epsilon}_0 \left[\frac{\bar{\sigma}}{g(\bar{\epsilon}, T)}\right]^m, \\ \dot{\epsilon}_2 &= \dot{\epsilon}_m \exp\left[-\frac{a g(\bar{\epsilon}, T)}{\bar{\sigma}}\right], \\ g(\bar{\epsilon}, T) &= \sigma_0 \left(1 + \bar{\epsilon}/\epsilon_0\right)^N \left\{1 - \beta\left[\left(T/T_0\right)^\kappa - 1\right]\right\}, \end{aligned}\right\} \tag{6}$$

where $\bar{\epsilon} = \int_0^t \dot{\bar{\epsilon}} dt$ is the equivalent plastic strain; $\dot{\epsilon}_0$ is a reference strain rate; $m$ and $a$ are rate sensitivity parameters, respectively, for strain rates below $10^3$ s$^{-1}$ and above $5 \times 10^4$ s$^{-1}$, $\sigma_0$ is a reference stress, $\epsilon_0$ is a reference strain, $N$ is the strain hardening exponent, $T_0$ is a reference temperature, and $\beta$ and $\kappa$ are thermal softening parameters. The function $g(\bar{\epsilon}, T)$ represents the stress-strain relation at a quasi-static strain rate of $\dot{\epsilon}_0$ and at temperature $T$. At room temperature $T_0$, $g(\bar{\epsilon}, T) = \sigma_0 \left(1 + \bar{\epsilon}/\epsilon_0\right)^N$.

After finite elment discretization, Eqns. (1) and (2) take the forms

$$\mathbf{M}\frac{\partial^2 \mathbf{U}}{\partial t^2} = \mathbf{R}, \tag{7}$$

and

$$\mathbf{C}\frac{\partial \mathbf{T}}{\partial t} = -\mathbf{K}\mathbf{T} + \mathbf{H}, \tag{8}$$

where **U** is the vector of nodal displacements, **T** is the vector of nodal temperatures, **M**, **C** and **K** are, respectively, the mass, the heat capacitance and the heat conductance matrices, and **R** and **H** are the mechanical and thermal force vectors. A lumped mass matrix is used in (7), for reasons of efficiency and accuracy, Krieg and Key (1973)[20]. Additionally, a lumped heat capacitance matrix is used in (8). In order to verify the accuracy of the integration of (8) with a lumped capacitance matrix, numerical results for a purely thermal problem involving non-uniform heat sources distributed on a rectangular area were compared with an analytical solution and good agreement was found.

Interested readers can find full descriptions of the formulation and the numerical implication in Zhou, Needleman and Clifton (1993)[21].

## 6. Numerical Results

Figure 14 shows the digitized microstructure used in the analysis. This microstructure is obtained from the actual alloy that was used in the impact experiments. This microstructure allows realistic simulations of the actual deformation.

In the numerical analyses, $\theta = 26.6°$, $V_0 = 202$ m/s and the specimen thickness $h = 87\mu$m, as in the experiment that led to the shear band in Fig. 6b. A square planar region, $87\mu$m $\times$ $87\mu$m, is used in the calculations. The mesh used in the simulations is an 80×80 uniform distribution of "crossed triangle" square elements.

The results at $2.0\mu$s after impact are shown in Fig. 15. The distributions of equivalent plastic strain (Fig. 15a), equivalent plastic strain rate (Fig. 15b) and temperature (Fig. 15c) indicate that a shear band has formed at the center of the specimen. The width of which is approximately $10\mu$m, which is consistent with the width of the band in the micrograph in Fig. 6b. Further calculations with microstructures with different grain shapes, grain arrangement, grain size, grain volume fraction and with adiabatic conditions assumed have shown that the length scale associated with heat conduction determines the shear band width in the circumstances considered, Zhou, Needleman and Clifton (1993)[21]. The largest equivalent plastic strain (Fig. 15a) in the shear band is 8 to 9 and the peak temperature (Fig. 15c) inside the band is approximately 1300 K, which is approximately 75% of the melting temperature of the matrix ($\approx$ 1750 K). In Fig. 15d, $g(\bar{\epsilon}, T)$ is a hardness function representing the effects of strain hardening and thermal softening (Eqn. 6). Clearly, the two phases have different hardness levels. Since more heat is generated inside the band, thermal softening inside the shear bands overcomes the strain hardening and the hardness decreases at higher rates than outside the band, as the temperature continues to increase. Consequently, $g(\bar{\epsilon}, T)$ is significantly lower inside the shear band than outside the band. Both the matrix and the grains are involved in the shear band. The tails of the tear-drop shapes are similar to those in the micrograph of Fig. 6b.

In addition, the overall shapes of the deformed grains resemble closely those observed in the micrograph of Fig. 6b.

The effects of heat conduction are assessed by comparing the calculated results with heat conduction with those for the corresponding adiabatic case. Figure 16 shows distributions of equivalent plastic strain, equivalent plastic strain rate, temperature and equivalent stress at $0.6\mu$s after impact for an adiabatic calculation. All other parameters correspond to the case in Fig. 15. Shear localization occurs much more rapidly when adiabatic conditions are assumed. Fully developed shear bands are found both at the center of the specimen and near the impact face, Figs. 16(a-d). The catastrophic process of coupled increases in temperature and strain continues until the temperature inside the band reaches the melting point and the matrix loses all stress-carrying capacity. In the adiabatic simulation this occurs shortly after $0.6\mu$s. Heat conduction, of course, stabilizes the deformation and delays the formation of shear bands. Additionally, there is a significant effect on the shear band width. In the adiabatic case in Fig. 16, the shear band width is $1 - 2\mu$m, which corresponds to a width of one to two quadrilateral elements. In contrast, the shear band width of $\approx 10\mu$m in the analyses accounting for heat conduction is much greater than the element size.

## 7. Discussion

To study the effect of material inhomogeneities, simulations were also carried out for impact experiments of pure tungsten and an alloy which has a similar composition as that of the matrix phase in the WHA composite. Figure 17 shows the distribution of the equivalent plastic strain rate across the specimen thickness, at $2\mu$s after impact, for pure tungsten and for the matrix. For comparison purposes, the corresponding strain rate distribution is also shown for the WHA simulation based on the digitized microstructure of Fig. 14. The curves for the digitized WHA microstructure represent averages over the $\xi^2$ direction. Neither the pure tungsten nor the matrix shows the formation of a shear band, but the WHA composite does. This behavior can be explained as follows. Pure tungsten has a much higher flow stress than the matrix. The high flow stress in tungsten causes high rates of heat generation, but, because of the high melting temperature of tungsten, thermal softening is not sufficiently strong to cause localization. Thus, in the composite, the inhomogeneities arising from the presence of the tungsten grains provide perturbations for initiating localization in the matrix at much earlier times. However, in order for a shear band to form the harder tungsten grains must undergo large deformations. The progressive thermo-mechanical coupling between the phases causes both of them to be involved in the formation of the shear band. Depending on grain morphology and volume fraction the band can occur either earlier or later than when localization would occur in the matrix alone.

A shear band width of about 10 $\mu$m has been obtained when heat conduction is considered (Fig. 15). This width agrees well with what is observed

experimentally, Fig. 6b. Further computations have shown that the shear band width is insensitive to changes in grain arrangement, grain shape, grain size and grain volume fraction, see Zhou, Needleman and Clifton (1993)[18]. On the other hand, a strong dependence on the thermal conductivity has been found. The dependence of the width on heat conductivity and strain rate was analyzed by Merzer (1982)[6]. The characteristic length set by heat conduction is $L^* = 2\sqrt{D^2 t^*}$ where $t^*$ is a time scale of the process and $D^2 = k/\rho c_p$ is the thermal diffusivity. Two time scales need to be considered: (1) the local characteristic time associated with the formation of a shear band; this characteristic time determines the width of the band; and (2) the duration of the experiment over which the conduction of heat into the flyer and anvil takes place; this characteristic time strongly influences the location of the shear band relative to the interfaces. For the present study $D^2 = 4.91 \times 10^{-5}$ m$^2$/s, $\bar{t} = 1/\dot{\gamma} = 2.89 \times 10^{-7}$ s for the development of a shear band, with $\dot{\gamma}$ the shear strain rate inside it. Therefore, $\bar{L} = 2\sqrt{D^2 \bar{t}} \approx 7.5\mu$m. Thus, the width of the shear band correlates well with the characteristic length set by heat conduction. The duration of the experiment is $\hat{t} = 2.0 \times 10^{-6}$ s. The length scale for heat conduction through the boundaries is $\hat{L} = 2\sqrt{D^2 \hat{t}} \approx 19.8\mu$m. This length is consistent with Fig. 15c, where heat conduction significantly influences the temperature distribution over approximately 1/5–1/4 of the specimen thickness near each of the two boundaries. This influence of heat conduction is clearly demonstrated by the difference between the results of Fig. 15 (with heat conduction) and Fig. 16 (without heat conduction). Heat conduction into the anvil effectively prevented one of shear bands in Fig. 16 (the one that is approximately $10\mu$m away from the impact face) from forming in Fig. 15. This indicates that heat conduction directly influences the formation of shear bands by preventing the localization from occurring near the impact face where the shearing rates are high initially.

Indeed, heat conduction plays an important role in dynamic shear band development in the pressure-shear plate impact experiment. It contributes to sustaining the stress carrying capacity and to stabilizing the deformation. Furthermore, it sets the length scale for the width of the shear band (note that when heat conduction is accounted for the shear band width is clearly not set by the mesh) and influences the location of the region where localized deformation takes place.

The analyses here have been carried out in a two-dimensional plane-strain context. The assumption of plane strain deformations is appropriate for the pressure-shear plate impact experiments over the time interval considered. The main limitation of the two-dimensional framework is associated with modelling the material microstructure in terms of cylindrical grains. On the other hand, a full three-dimensional analysis would require substantially greater computational resources. Also, the tungsten grains have been modelled as elastically isotropic and in the plastic range, as isotropically hardening Mises solids. Any effects of elastic anisotropy, or of plastic flow occurring on discrete slip systems has been neglected. Nevertheless, key features of the observed phenomenology

of shear localization in tungsten heavy alloys under pressure-shear plate impact are reproduced by the computations.

## Acknowledgement

This research is supported primarily by the Army Research Office. The computational work is supported by the NSF MRG on "Micro-Mechanics of Failure-Resistant Materials". Computations were performed at the San Diego Supercomputer Center.

## References

1. Clifton, R. J. and Klopp, R. W., (1985), *Metals Handbook*, Vol. 8, Amer. Soc. Metals, Metals Park, 9th ed., pp. 230-239.
2. Recht, R.F., (1964), *J. Appl. Mech.*, **86**, pp. 189-193.
3. Clifton, R.J., (1980), *Material Response to Ultra-High Loading Rates*, NMAB-356, National Materials Advisory Board (NRC), Washington, D.C., Chap. 8.
4. Wright, T.W. and Walter, J.W., (1987), *J. Mech. Phys. Solids*, **35**, No. 6, pp. 701-720.
5. Bai, Y.L., (1982), *J. Mech. Phys. Solids*, **30**, No. 4, pp. 195-207.
6. Merzer, A. M., (1982), *J. Mech. Phys. Solids*, **30**, No. 5, pp. 323-338.
7. Molinari, A. and Clifton, R.J., (1987), *Trans. of ASME, J. Appl. Mech.*, **54**, pp. 806-812.
8. Batra, R.C. and Kim, C.H., (1992), *Int. J. Plasticity*, **8**, pp. 425-452.
9. Shawki, T.G. and Clifton, R.J., (1989), *Mech. Mat.*, **8**, pp. 13-43.
10. Zhou, M., (1993), Brown University Ph.D. Thesis, Providence, RI.
11. Andrews, E.W., Bower, A.F. and Duffy, J., (1992), *Proc. Symposium on Shear Bands and Viscoplastic Theories, 29th Annual Technical Meeting of the Soc. for Engng Sci.*, Sep. 14-16, La Jolla, CA.
12. Hartley, K. A., Duffy, J. and Hawley, R. H., (1985), *Metals Handbook*, Vol. **8**, ASM, 1985, pp. 218-228.
13. Duffy, J., Campbell, J. D. and Hawley, R. H., (1971), *J. Appl. Mech.*, Vol. **38**, pp. 83-91.
14. Costin, L. S., Crisman, E. E., Hawley, R. H. and Duffy, J., (1979), *Proc. 2nd Conf. on Mech. Properties of Materials at High Rates of Strain*, ed. by J. Harding, The Institute of Physics, London, pp. 90-100.
15. Bose, A., Sims, D. and German, R. M., (1988), *Metall. Trans. A*, Vol. **19A**, pp. 487-494.
16. O'Donnell, R. G. and Woodward, R. L., (1990), , *Metall. Trans. A*, Vol. **21A**,. M., (1982), *J. Mech. Phys. Solids*, **30**, No. 5, pp. 323-338.
17. LeMonds, J. and Needleman, A., (1986), *Mech. Mat.*, **5**, pp. 339-361.
18. Needleman, A., (1989), *J. Appl. Mech.*, **56**, pp. 1-9.
19. Needleman, A. and Tvergaard, V., (1991), *Int. J. Frac.*, **49**, pp. 41-67.
20. Krieg, R.D. and Key, S.W., (1973), Transient Shell Response by Numerical Time Integration, *Int. J. Numer. Meth. Engng.*, **7**, pp. 273-286.
21. Zhou, M., Needleman, A. and Clifton, R. J., (1993), Submitted to *J. Mech. Phys. Solids.*

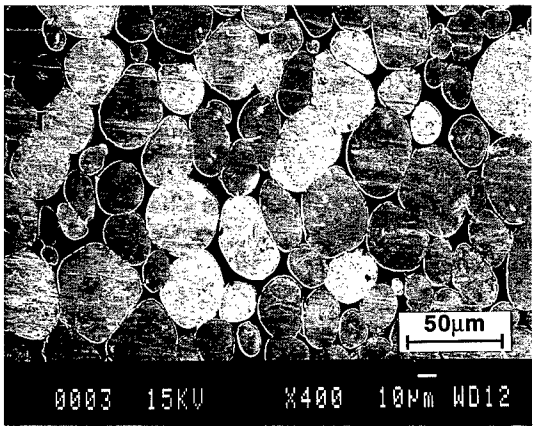



Fig. 1 MICROSTRUCTURE OF THE WHA USED IN THE EXPERIMENT

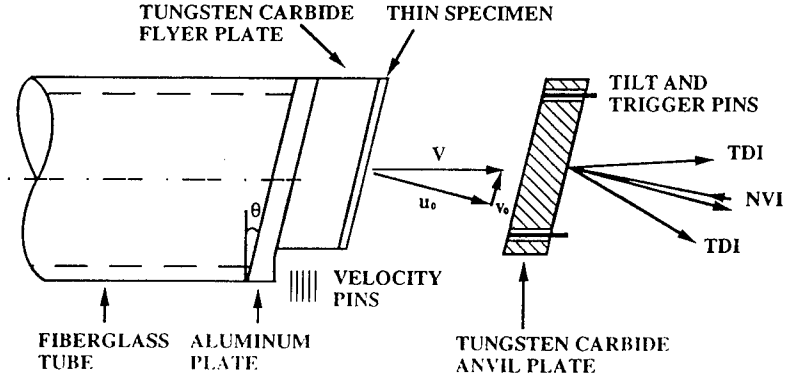



Fig. 2 CONFIGURATION OF THE PRESSURE-SHEAR PLATE IMPACT EXPERIMENT OF A THIN SPECIMEN

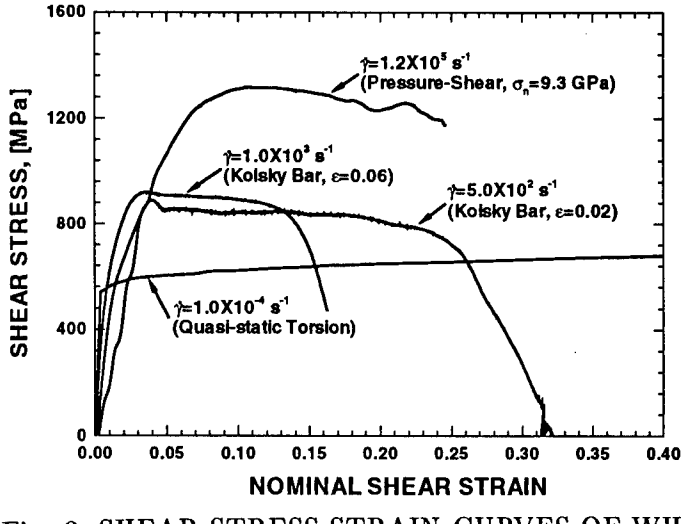



Fig. 3 SHEAR STRESS-STRAIN CURVES OF WHA

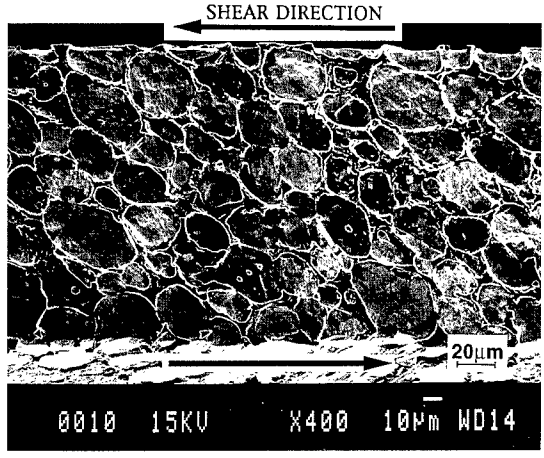



Fig. 4 DEFORMED MICROSTRUCTURE OF WHA AFETR SHOT 9201

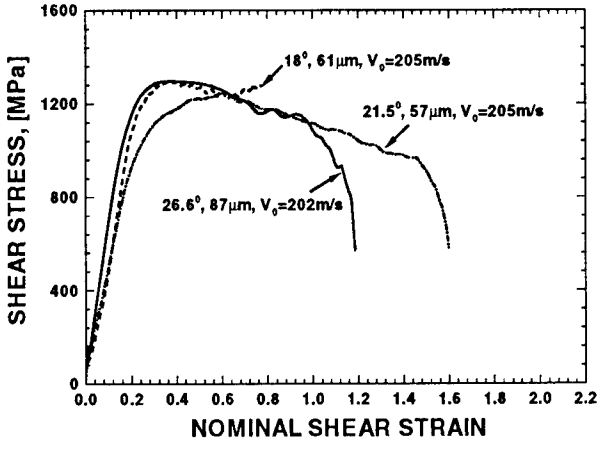



Fig. 5 DYNAMIC SHEAR STRESS-STRAIN CURVES OF WHA OBTAINED BY PRESSURE- SHEAR PLATE IMPACT

(a) SHOT 9205

(b) SHOT 9206

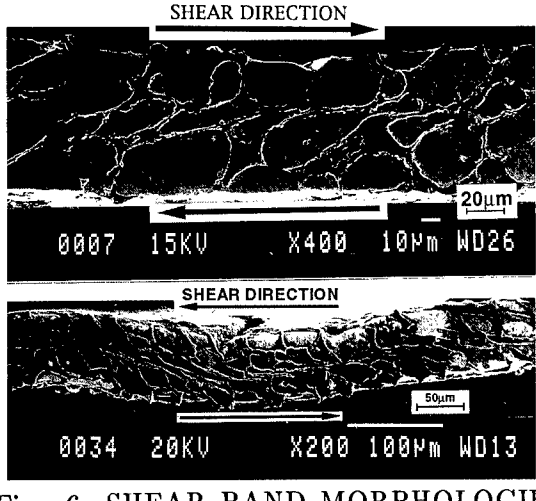



Fig. 6 SHEAR BAND MORPHOLOGIES

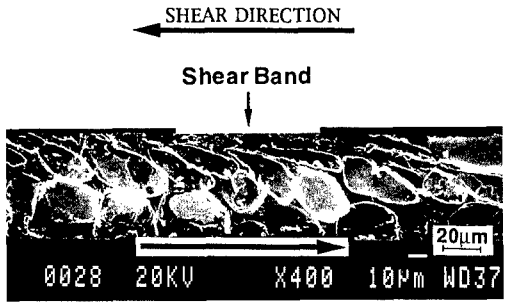
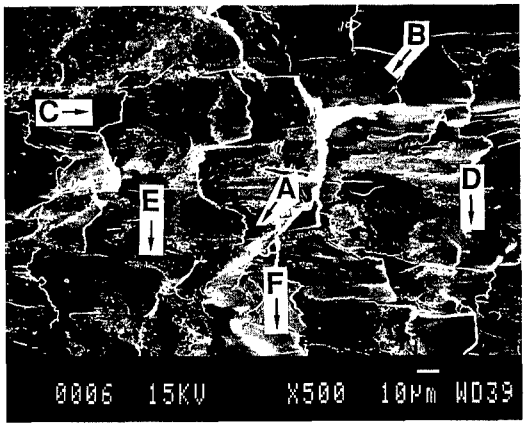



Fig. 7 SHEAR BAND MORPHOLOGY AFTER SHOT 9207

(a)




(b)

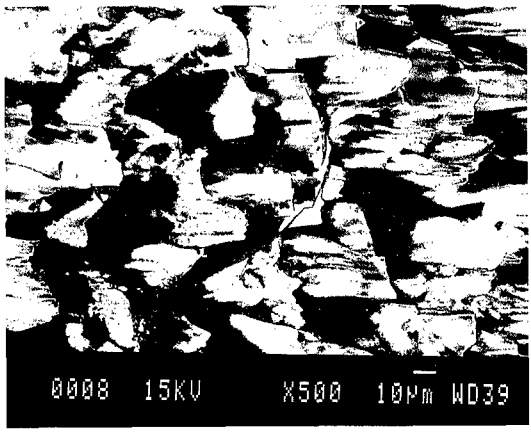



Fig. 8 FRACTOGRAPHS OF THE SHEAR BAND SURFACE AFTER SHOT 9303 (a) MORPHOLOGY OF SHEAR BAND SURFACE; (b) BACK-SCATTERED ELECTRON IMAGE OF THE SAME AREA

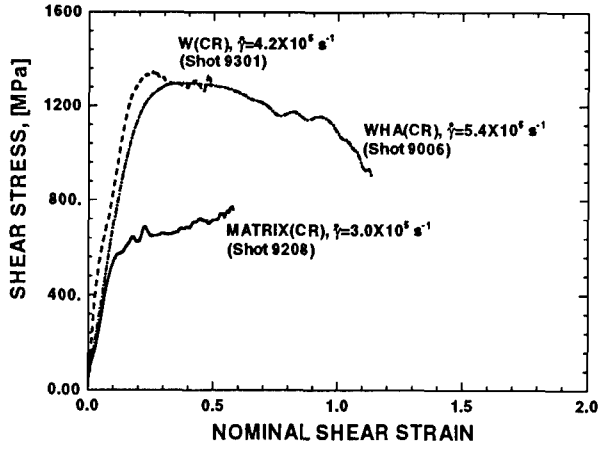



Fig. 9 DYNAMIC SHEAR STRESS-STRAIN CURVES OF WHA, W AND MATRIX ALLOY OBTAINED BY PRESSURE-SHEAR PLATE IMPACT

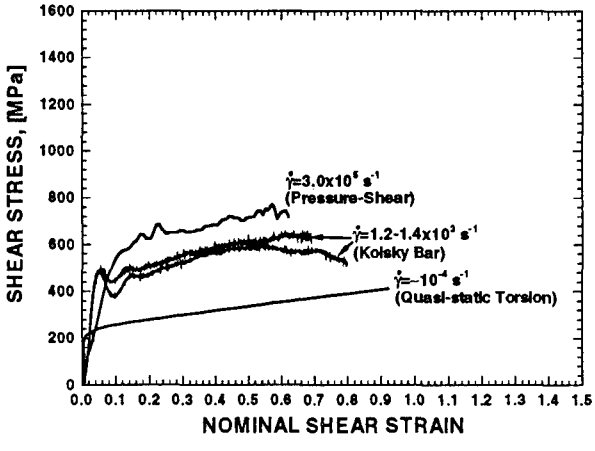



Fig. 10 SHEAR STRESS-STRAIN CURVES OF MATRIX ALLOY

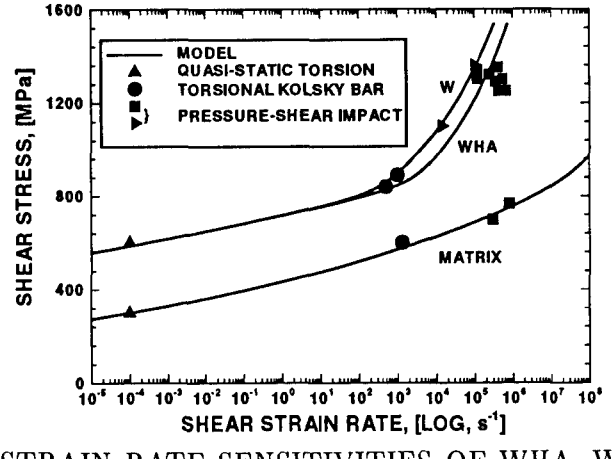



Fig. 11 STRAIN RATE SENSITIVITIES OF WHA, W AND MATRIX ALLOY

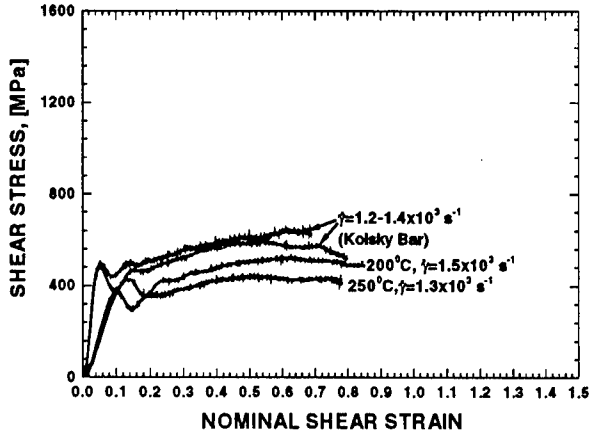



Fig. 12 STRESS-STRAIN CURVES OF MATRIX ALLOY AT DIFFERENT TEMPERATURES

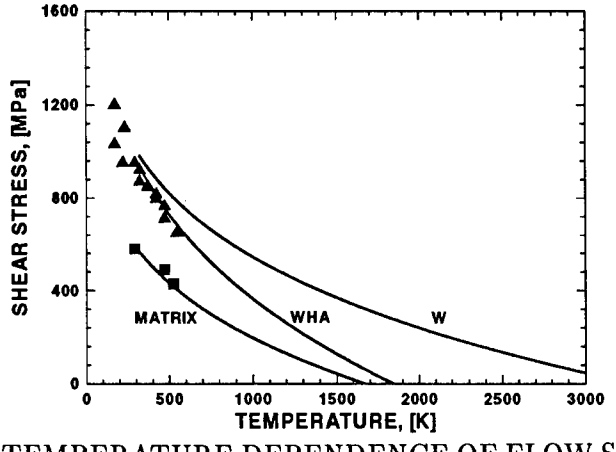



Fig. 13 TEMPERATURE DEPENDENCE OF FLOW STRESS FOR WHA, W AND MATRIX ALLOY

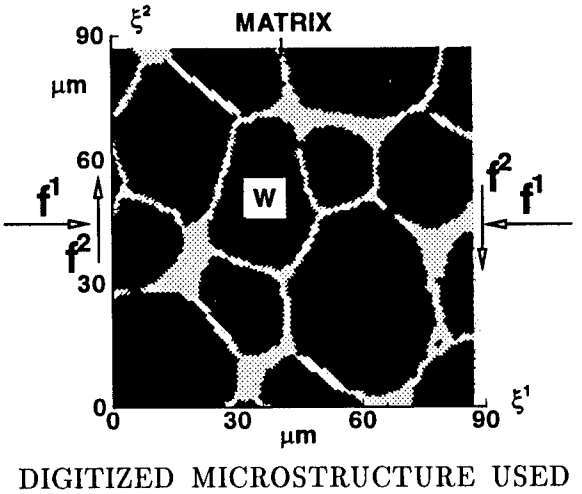



Fig. 14 DIGITIZED MICROSTRUCTURE USED IN THE ANALYSIS

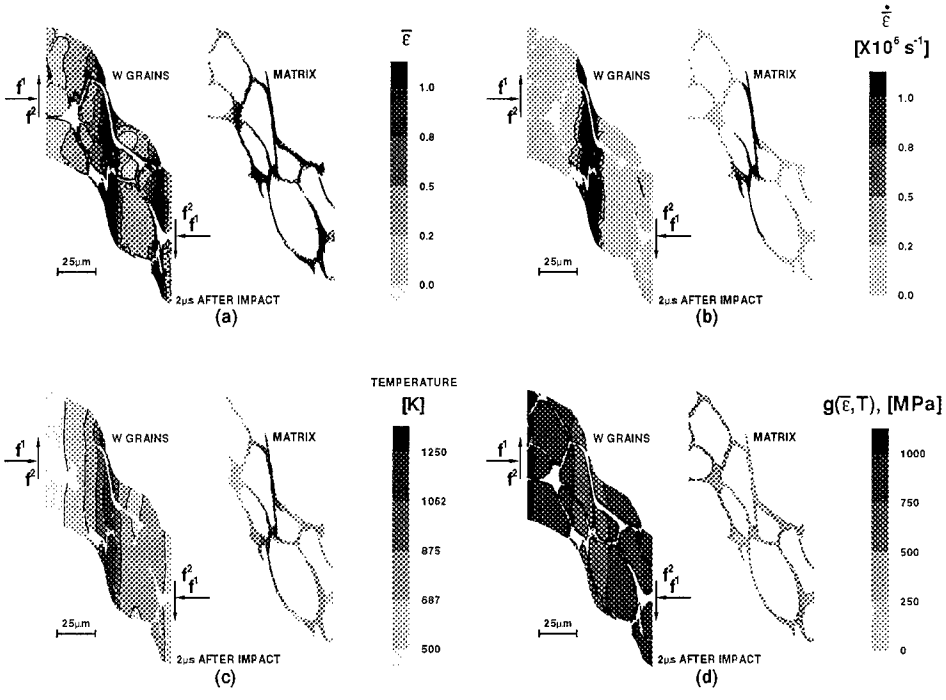



Fig. 15 CALCULATED DISTRIBUTIONS AT 2$\mu$s AFTER IMPACT OF: (a) EQUIVALENT PLASTIC STRAIN, (b) STRAIN RATE, (c) TEMPERATURE AND (d) HARDNESS $g(\bar{\epsilon}, T)$

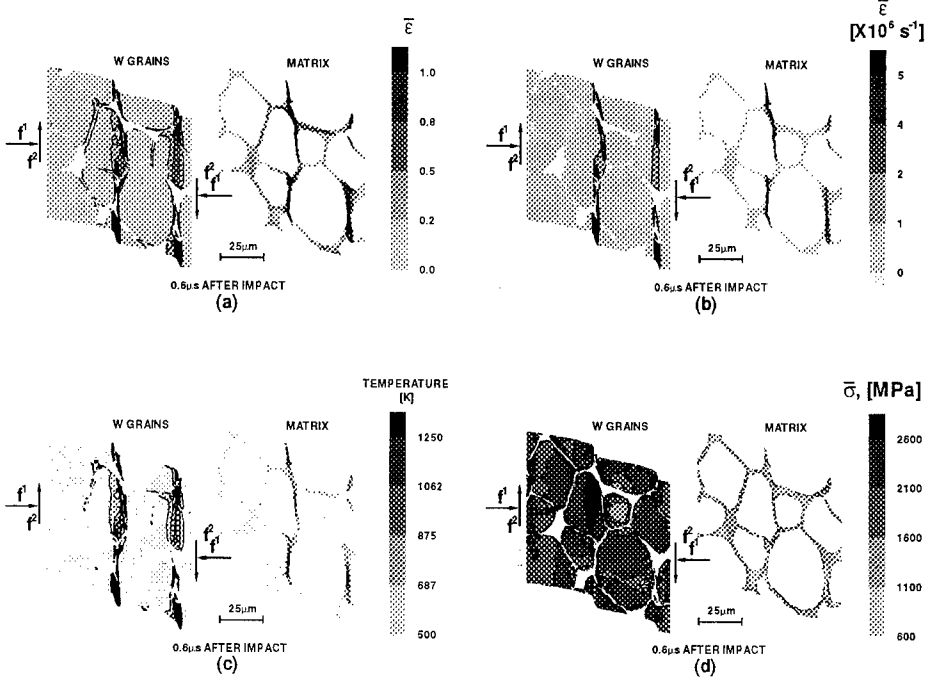



Fig. 16 CALCULATED DISTRIBUTIONS AT 0.6$\mu$s AFTER IMPACT OF: (a) EQUIVALENT PLASTIC STRAIN, (b) STRAIN RATE, (c) TEMPERATURE AND (d) EQUIVALENT STRESS $\bar{\sigma}$ WITH ADIABATIC CONDITIONS ASSUMED

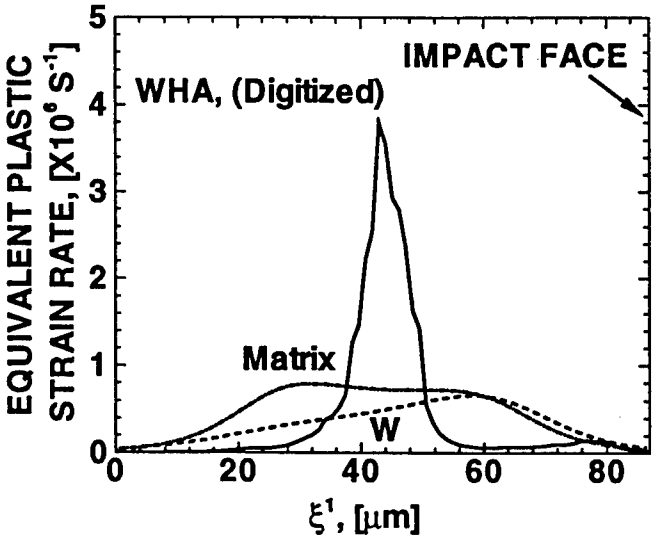



Fig. 17 CALCULATED DISTRIBUTIONS OF $\dot{\bar{\epsilon}}$ ACROSS SPECIMEN THICKNESS at 2$\mu$s AFTER IMPACT FOR WHA, W AND MATRIX ALLOY

# Deformation and Failure of Tantalum and Tantalum-Tungsten Alloys Under Dynamic Tensile/ Shear Loading

*D.H. Lassila, M.M. Leblanc and K.A. Winer*
Lawrence Livermore Laboratory

"PAPER NOT AVAILABLE"

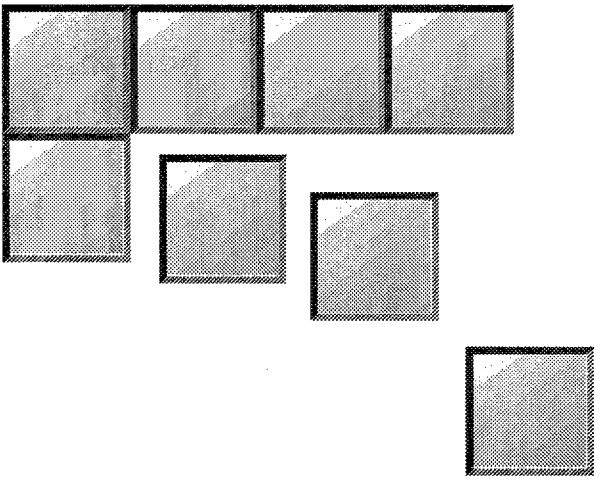
# Viscoelastic Mode I Fracture Behavior in Nitrile Rubber Sheets

*C.J. Quigley, J.L. Mead and A.R. Johnson*
Materials Directorate, ARL

"PAPER NOT AVAILABLE"

# SESSION IIB: COMPOSITES

**Chairman:** *Dr. B. Burns*
**Weapons Directorate**
**Army Research Laboratory**



# Combined Tension and Bending Testing of Tapered Composite Laminates

Dr. T. Kevin O'Brien*
Ms. Gretchen B. Murri
Army Research Laboratory
Vehicle Structures Directorate
NASA Langley Research Center
Hampton, Virginia 23681

Mr. Rick Hagemeier
Aerospace Engineering Department
Wichita State University
Wichita, Kansas 67208

Mr. Charles Rogers
Bell Helicopter Textron
Fort Worth, Texas 76101

Hingeless and bearingless composite rotor hubs are currently being designed and manufactured to reduce weight, drag, and parts count as well as to improve the aerodynamic performance of military and civilian helicopters. To achieve the required performance in the flexure region of the hub, the stiffness of the composite flexbeam is varied by dropping (terminating) internal plies. These dropped plies create discontinuities in the beam that initiate delaminations under the combined centrifugal force (CF) tension and cyclic bending loads experienced by the hub during service. Recently, studies have been conducted to ascertain the delamination durability of tapered laminates under cyclic tension loads [1,2]. The purpose of this study was to develop a tapered beam coupon analysis for combined tension and bending loading that could be used to identify configurations with the surface strain distribution similar to a full scale hub. Linear and non-linear tapered laminate configurations were investigated for two different glass/epoxy materials.

## Analysis of Linear Taper Flexbeam Coupon

A beam element used at Bell Helicopter [3] was incorporated in the computational mechanics testbed (COMET) finite element code [4] at the Langley Research Center (LaRC). This beam element is a modified Euler-Bernolli beam that includes additional terms in the element stiffness matrix to incorporate the non-linear effects of a constant membrane force on the flexural stiffness. Hence, nodal

forces are given by $\{F\} = [k]\{u\}$ , where $[k] = [k]_A + [k]_B$ , and where

$$[k]_A = \frac{2EI}{L^3}\left[f(1,L,L^2)\right] \tag{1}$$

$$[k]_B = \frac{P}{60L}\left[f(1,L,L^2)\right] \tag{2}$$

where EI is the flexural rigidity of the beam of length, L, P is the membrane load, and $[f(1,L,L^2)]$ represents a matrix whose terms are either constants or linear or quadratic functions of L only [3]. This element captures the influence of a constant membrane force on transverse bending deflections, without requiring an iterative non-linear solution scheme.

The constant membrane force is consistent with the load control arrangement on a combined axial tension and bending (ATB) hydraulic load frame that was recently designed and built at LaRC to test composite laminates [5] .In the ATB machine, the axial load cell is incorporated in the top grip that rotates with the thin portion of the tapered laminate as the transverse load is applied. Hence, a constant membrane load may be maintained while the flexbeam coupon is subjected to cyclic bending.

By modeling tapered flexbeam laminates with the appropriate ATB boundary conditions and loadings, the ability of candidate flexbeam coupon configurations to simulate the response of full scale rotor hub components may be assessed. Initially, variations on the linear tapered laminate configurations previously tested under cyclic tension [1,2] were analyzed. Figure 1 shows one half of the thickness of the linear tapered specimens, consisting of internal core plies that run the length of the beam, the dropped plies, and the external belt plies that transform through the taper angle, $\alpha$, between the thick and thin regions.

Section properties were calculated at locations A, B', C, C', D, D', E and F, using a laminated plate theory code for tapered laminates that specified not only the in-plane angle for each ply, but the out-of-plane taper angle, $\alpha$, as well [1]. The code uses the appropriate lamina properties (Table 1) for each section to calculate the [A], [B], and [D] (axial, coupling, and bending) stiffness matrix terms as well as the engineering moduli and Poisson's Ratio ($E_x, E_y, G_{xy}, \nu_{xy}$) for that location. All of the primed sections (B', C', D') had two ply thicknesses of isotropic resin modeled to replace the dropped plies in the unprimed sections (A,C,D) at the same location. The belt ply properties in sections B', C, C', D, D', and E were transformed through the taper angle of 5.71 degrees. The equivalent bending

stiffness, EI, at each location was calculated as $b/d_{11}$, where b is the specimen width and $d_{11}$ is the first term of the inverse bending stiffness matrix. Two section properties were calculated at the ply drop associated with the transition from the thick to tapered region (sections A & B'), at each of the tapered region ply drops (sections C & C' and D & D'), and at the juncture point between the thin and tapered region (sections E & F). The element bending stiffness, EI, for each plydrop region in the tapered section was calculated from section properties using a weighted average:

$$EI = \frac{(EI)_{left} - (EI)_{right}}{\ln\left(\frac{(EI)_{left}}{(EI)_{right}}\right)} \qquad (3)$$

Three configurations with the same width (1.0 in.), total length (3.5 in.), and the same taper length (0.5 in.) but different thin and thick region lengths were analyzed (fig.2). These consisted of (a) equal thin and thick region lengths of 1.5 inches, corresponding to the configuration used previously for tension fatigue studies [1,2], (b) a short (0.5 inch) thick region and a long (2.5 inch) thin region, and (c) a zero-length thick region. Configurations (b) and (c) are more typical of rotor hub flexbeams than configuration (a).

Figure 3 shows a sketch of a linear tapered laminate coupon plus the ATB loading apparatus and the corresponding finite element model. The bottom grip is modeled as a rigidly clamped boundary that reacts both the axial load and the bending moment. The thick, tapered, and thin regions of the laminate are modeled using the beam elements described earlier. The beam elements in the thin and thick region were 0.5 inches long, whereas the beam elements in the tapered region were one third of this length. This corresponded to one beam element for each of the three unique ply drops in the tapered region. Also included in the model are the top grip, load cell, and pin assembly where the loads are applied in the ATB machine. The top grip, load cell, and pin assembly are modeled as isotropic beams using an axial modulus for stainless steel and a moment of inertia corresponding to the dimensions of each cross section. This combination of top grip, load cell, and pin assembly is two orders of magnitude more rigid than the tapered composite laminate, and hence, has no significant contribution to the flapping angle, $\theta$.

Figure 4 shows the moment distributions for a unidirectional S2/SP250 glass/epoxy laminate corresponding to the three configurations in fig. 2 with an applied axial tension load, P, of 8000 lbs and a transverse load, V, of 1000 lbs. For a one inch wide coupon,

these loads correspond to typical CF tension and cyclic bending loads experienced in bearingless rotor hubs. The moments in the tapered region (indicated by solid symbols) are greater the closer the taper is to the bottom grip.

Figure 5 shows the distribution of tensile stresses on the surface of the tapered laminate associated with the axial, bending, and combined loads for configuration (b). Surface stresses due to bending were calculated in the outermost zero degree ply for each unique section of a unidirectional S2/SP250 glass/epoxy tapered laminate using the expression derived by Whitney [6]

$$\sigma_x^k = (Q_{11}^k S_{11b} + Q_{12}^k S_{12b} + Q_{16}^k S_{16b}) \frac{Mz}{I} \qquad (4)$$

where $$S_{ijb} = \frac{d_{ij} t^3}{12}$$

For the outermost zero degree plies of the linear tapered laminates, this reduces to

$$\sigma_x = 19h\,(Q_{11}d_{11} + Q_{12}d_{12})M \qquad (5)$$

$$\sigma_x = 13h\,(Q_{11}d_{11} + Q_{12}d_{12})M \qquad (6)$$

$$\sigma_x = \frac{t}{2}(Q_{11\alpha}d_{11\alpha} + Q_{12\alpha}d_{12\alpha})M \qquad (7)$$

for the thick, thin, and tapered regions, respectively, where h is the average ply thickness and t is the section thickness. The subscript $\alpha$ indicates that the unidirectional properties have been translated through the 5.71 degree taper angle. In the thick and thin regions, laminated plate theory equations 5&6 yield the same result as isotropic beam theory for unidirectional laminates. However, in the tapered region eq(7) deviates from the beam theory for unidirectional laminates due to the taper angle translation in the belt plies.

As shown in fig.5 for a unidirectional S2/SP250 glass/epoxy tapered laminate, the surface stress due to the membrane load is greatest in the thin region, decreases through the tapered region, and is lowest in the thick region. The surface stress due to bending and the total surface stress within the taper region are greatest at the juncture point.

Figures 6 shows the distribution of tensile strain on the surface of a unidirectional S2/CE9000 glass/epoxy tapered laminate associated with the combined tension and bending loads

for configuration (b). The maximum surface strains in the tapered regions occurred at the ply drop location nearest the juncture point followed by the juncture point.

Linear Taper Configuration Experiments

Experiments were conducted in the ATB machine on S2/CE9000 unidirectional glass/epoxy tapered laminates using configuration (b). The axial load was applied first, followed by the transverse load. The transverse displacement at the top grip point, v, was measured using a DCDT mounted to the load frame. The rotation at the top grip point, $\theta$, was measured using a digital protractor mounted on the top grip. Surface strains were measured using strain gages mounted in the thick, tapered, and thin regions.

Figure 6 compares the measured maximum surface strains to the analytical predictions for the S2/CE9000 unidirectional glass/epoxy tapered laminates. Predicted strains were close to, but slightly exceeded, the measured values.

Analysis of Non-linear Tapered Configuration

In order to achieve a more uniform surface strain distribution on the flexbeam, internal plies may be dropped in a staggered pattern to achieve a non-linear taper. A finite element model was conducted for a non-linear tapered flexbeam configuration (fig.7) loaded in the ATB test machine. The model had a 6.5-inch gage length between the top and bottom grip, with a 0.5-inch thick region emanating from the bottom grip before the taper began, and a 5 inch non-linear tapered region. The thick region had a $[45/\text{-}45/0_5/(45/\text{-}45)_6/45/0_4/(\text{-}45/45)_6/\text{-}45/45/\text{-}45/0_2/(45/\text{-}45)_6/45/0_4/(\text{-}45/45)_6/\text{-}45/0_3/45]_s$ layup. The zero-degree unidirectional plies were continuous throughout the beam length. Most of the 45 and -45 degree plies were dropped in a staggered pattern along the tapered region length until a uniform thin region was achieved with a $[45/\text{-}45/0_9/45/\text{-}45/0_9/45]_s$ layup. The tapered region was modeled as four equivalent uniform thickness beams with element properties estimated from eq(3). The equivalent uniform thickness beams had lengths corresponding to the distance between points where the zero-degree plies transition from straight plies to curved plies following the surface contour (see fig.7).

The moment distribution was generated using the beam element described previously and S2/SP250 glass/epoxy lamina properties from Table 1. The moment distribution is shown in fig. 8 for the non-linear tapered beam with an applied axial tension load, P, of 8000 lbs and a transverse load, V, of 1000 lbs. The stresses in the

surface 45-degree plies due to the axial, bending, and combined loads were calculated using eq(4). As shown in fig.9, the combined axial and bending stress in the surface 45 degree plies is greatest shortly after the taper begins just inboard of the thin region. The surface strains in the 45-degree plies are shown in fig.10. The maximum strain is on the order of 1.0%, which is well below the 2.5 to 3.0 % failure strain of the S2 glass fiber. Hence, these non-linear tapered laminates are good candidate test coupons for examining the delamination durability of the composite flexbeam in the full scale rotor hub.

## Summary

A simple beam element used at Bell Helicopter was incorporated in the Computational Mechanics Testbed (COMET) finite element code at the Langley Research Center (LaRC) to analyze the response of tapered laminates typical of flexbeams in composite rotor hubs. This beam element incorporated the influence of membrane loads on the flexural response of the tapered laminate configurations modeled and tested in a combined axial tension and bending (ATB) hydraulic load frame designed and built at LaRC. The moments generated from the finite element model were used in a tapered laminated plate theory analysis to estimate axial stresses on the surface of the tapered laminates due to combined bending and tension loads. Surfaces strains were calculated and compared to surface strains measured using strain gages mounted along the laminate length. The strain distributions correlated reasonably well with the analysis. The analysis was then used to examine the surface strain distribution in a non-linear tapered laminate. Results indicate that simple finite element beam models may be used to identify tapered laminate configurations best suited for simulating the response of a composite flexbeam in a full scale rotor hub and studying their delamination durability.

## References

1. G.B. Murri, S.A. Salpekar, and T.K. O'Brien, "Fatigue Delamination Onset Prediction in Unidirectional Tapered Laminates," *Composite Materials: Fatigue and Fracture (Third Volume), ASTM STP 1110*, 1991, pp.312-339.

2. G.B. Murri, T.K. O'Brien, and S.A. Salpekar, "Tension Fatigue of Glass/Epoxy and Graphite/Epoxy Tapered Laminates," *J. of the American Helicopter Society*, Vol.38, No.1, Jan. 1993, pp.29-37.

3. J.R. Brooks, "Finite Element Analysis of Beams with Variable Midplane Forces," M.S. Thesis, U.of Texas at Arlington, May, 1971.

4. C.B. Stewart, "The Computational Structural Mechanics Testbed User's Manual," NASA TM-100644, Oct. 1989.

5. , M.R. Gardner, R.S.Young, and T.K. O'Brien, "Hydraulic Load Frame for Combined Axial Tension and Bending Loads (ATB Test Machine), Patent disclosure on file with Langley Research Center Patent Office, NASA Case LAR 14848-1.

6. J.M. Whitney, C.E. Browning, and A. Mair, "Analysis of the Flexure Test for Laminated Composite Materials," *Composite Materials: Testing and Design (Third Conference), ASTM STP 546*, 1974, pp.30-45.

Table 1 - Glass/Epoxy Lamina Properties

| | S2/SP250 | S2/CE9000 | Neat Resin |
|---|---|---|---|
| $E_{11}$ x $10^6$ Psi | 6.60 | 7.12 | 0.595 |
| $E_{22}$ x $10^6$ Psi | 2.10 | 2.46 | 0.595 |
| $G_{12}$ x $10^6$ Psi | 0.88 | 1.10 | 0.224 |
| $\nu_{12}$ | 0.275 | 0.303 | 0.330 |

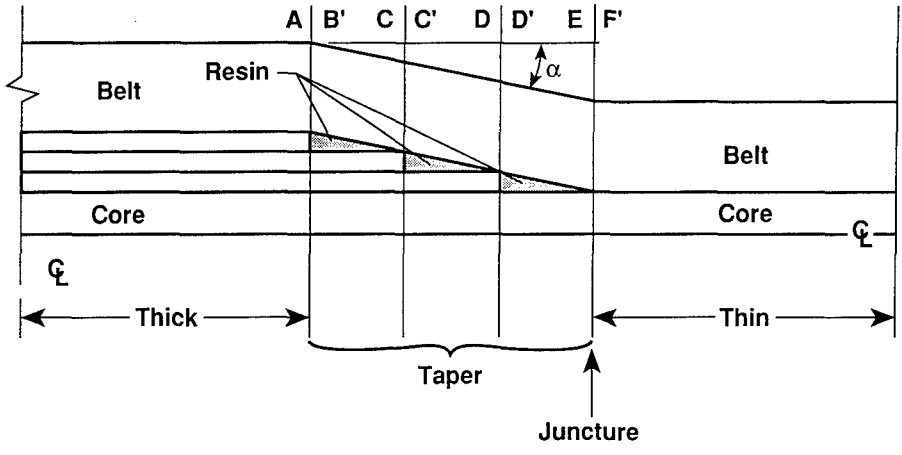



Fig.1 Linear Tapered Sections

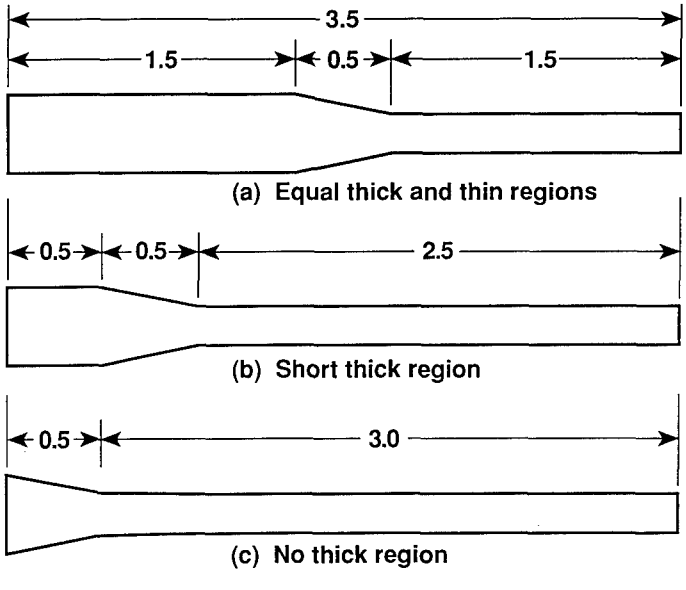



Fig.2 Linear Taper Configurations

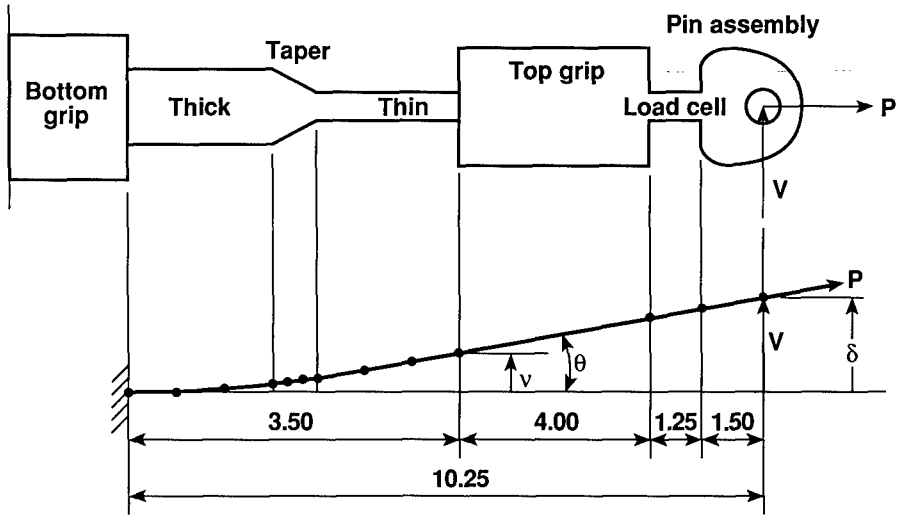



Fig.3 Test Configuration and Finite Element Model

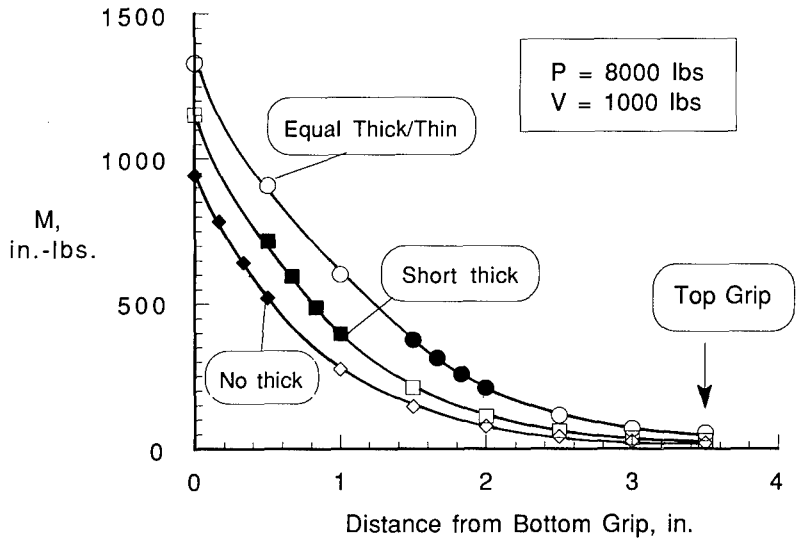



Fig.4 Moment Distributions in S2/SP250 Linear Tapered Laminate

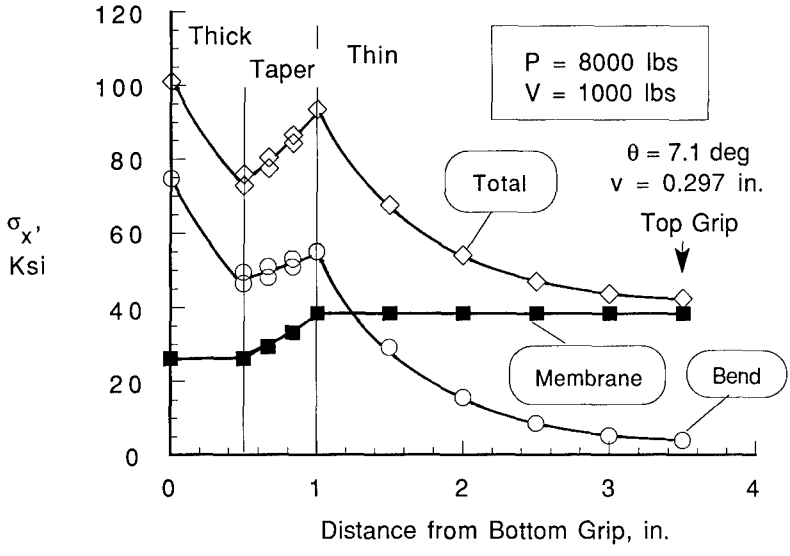



Fig.5 Surface Stress Distributions in S2/SP250 Linear Tapered Laminate

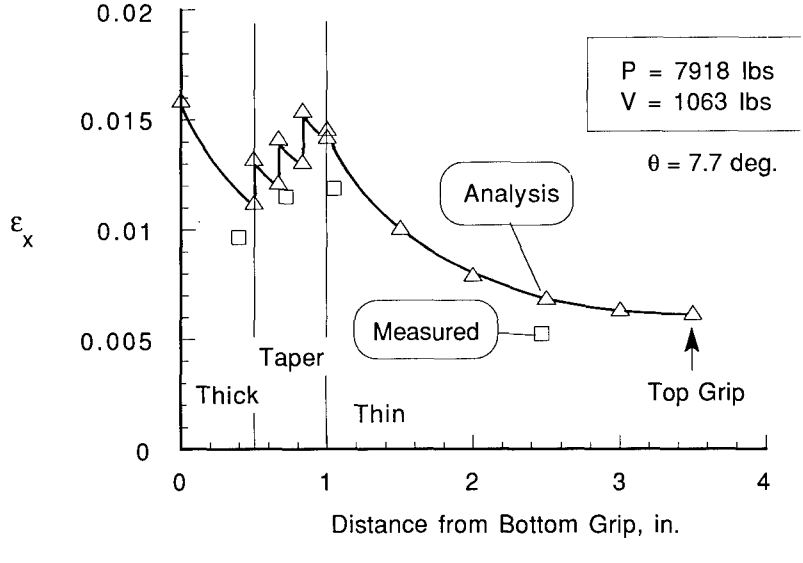



Fig.6 Surface Strain Distributions in S2/CE9000 Linear Tapered Laminate

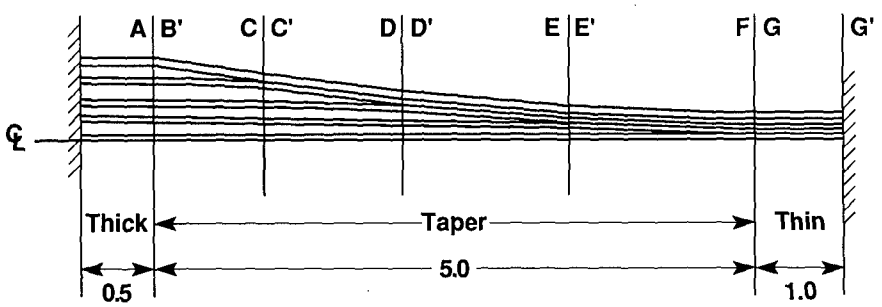



Fig.7 Non-linear Tapered Flexbeam Configuration

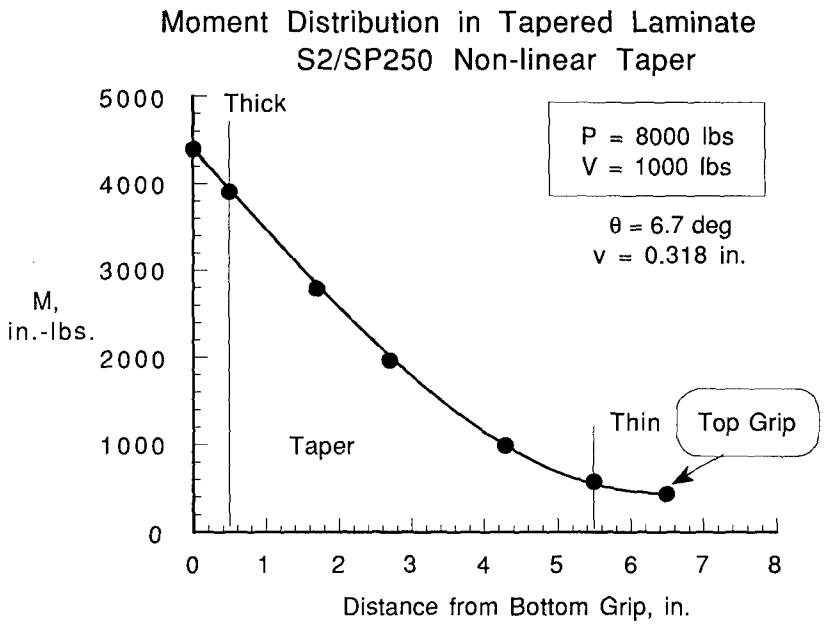



Fig.8 Moment Distributions in S2/SP250 Non-linear Tapered Laminate

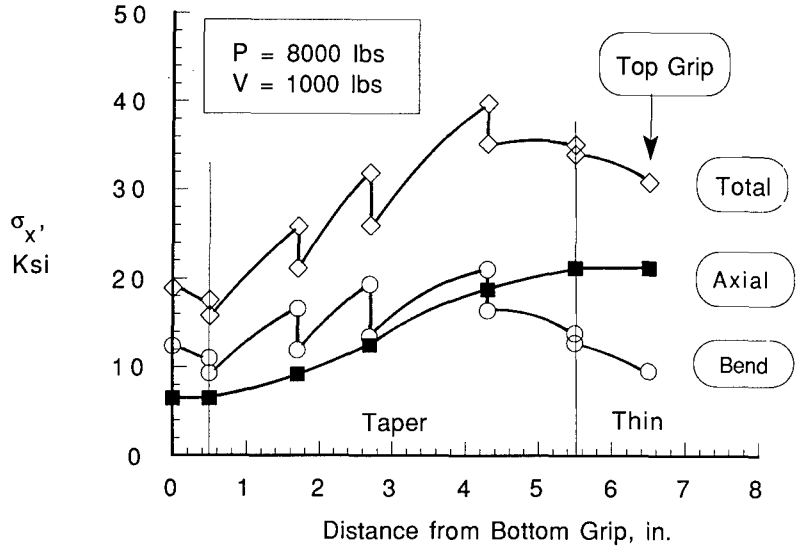



Fig.9 Surface Stress Distributions in S2/SP250 Non-linear Tapered Laminate

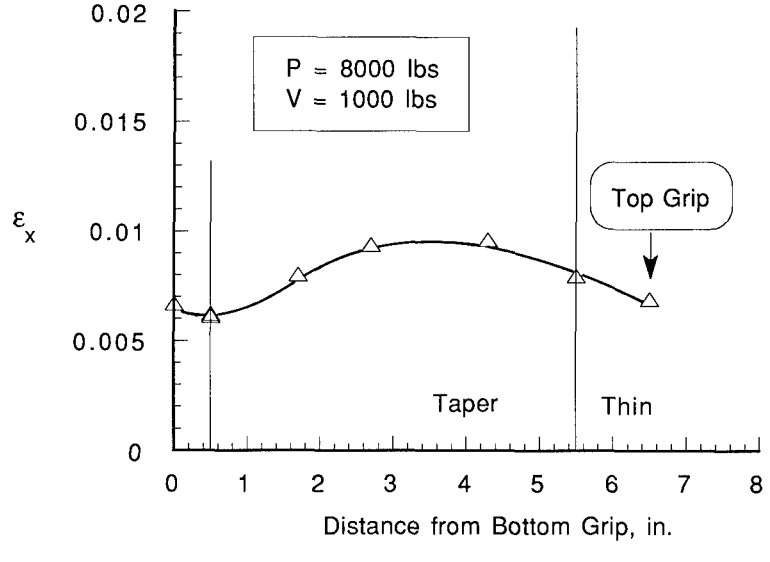



Fig.10 Surface Strain Distributions in S2/SP250 Non-linear Tapered Laminate

# BALLISTIC PERFORMANCE OF KEVLAR COMPOSITES IN AN ARCTIC ENVIRONMENT

Dr. Edward M. Lenoe *
Department of Civil & Mechanical Engineering
US Military Academy
West Point, New York 10996-1792
Dr. Piyush K. Dutta
Materials Research Engineer
US Army Cold Regions Research & Engineering Lab
Hanover, New Hampshire 03755

## Abstract

Kevlar composites are used by the United States Army for ballistic protection against small arms fire and fragmentation munitions. Typical applications include infantrymen's Kevlar helmets, and back face spall liner plates for combat vehicle armor. While such composites are widely used, they had not been evaluated for extremes of Arctic environments. Therefore this paper presents results of an investigation of the effects of Arctic environment on the performance of Kevlar composites. Standard issue Kevlar/epoxy helmets and 12 inch square plates of Kevlar/epoxy spall liners were subjected to 100 thermal cycles between +60 and -60 degrees centigrade to simulate exposures to several months of an Arctic environment. Tension tests were performed before and after such exposure. Ballistic tests, were also conducted on the same materials. Severe thermal cycling, over extended periods of time, can induce microcracking. Such microcracking can effect the performance of composite materials. As expected, reduction of strength, changes in stress-strain curve and different ballistic failure modes were observed.

## Introduction

Kevlar composites have been qualified for a wide range of aerospace applications, and effects of severe environments have been routinely evaluated. But many United States (US) Army applications use relatively thick sections of composites, particularly for armor. Accordingly it was prudent to investigate the influence of Arctic weather on representative ballistic protection materials. Two type of composite applications were chosen for evaluation, namely helmets and spall liners as used for infantry fighting vehicles.

A dozen helmets were provided by the US Army, Natick Laboratory. These had been fabricated according to MIL-H-444099A, dated 22 December 1986, Military Specification, Helmet, Ground Troops and Parachutists. The standard ballistic protection helmet consists of a laminated, coated aramid cloth shell with a replaceable suspension assembly, headband and chin strap. Helmet shells are formed in complex molds, under high pressure, using either "pinwheel" preforms or a combination of pinwheel preforms and specified number of rectangular fabric panels. The pinwheels are continuous, integral pieces of fabric, which may be cut up to within 2 1/2 inches of the center, leaving an uncut area measuring a minimum of 5 inches across in any direction. There may be no more than 8 legs in any pinwheel and no less than 19 layers of fabric. The purpose of the preform is to facilitate formation of the complex, doubly curved helmet. Ballistic limits, V50, for these helmets must be no less than 2000 feet per second (fps), when tested according to MIL-STD-662, which necessitates firing a .22 caliber fragment simulating projectile weighting 17 $\pm$ .25 grains.

Two types of representative spall plates were provided by US Army Research Laboratory, Materials Directorate, Watertown, Massachusetts. Plates were 12 inch square panels, at 2.0 and 2.9 pounds per square foot (psf) respectively. The heavier, thicker panels were used for mechanical properties testing, whereas both thicknesses were used in ballistic testing. The Watertown laboratory also supplied us with prototype Spectra helmets of the same configuration as the issue models.

## Ballistic Performance

Researchers at US Army, Natick Laboratory brought to our attention reports of the ballistic performance of Kevlar helmets. As just mentioned, the Kevlar helmet in the US Army's inventory is designed to stop 17 grain fragments at speeds up to 2000 fps. However in Operation Just Cause more than a dozen soldiers reported that their helmet was able to defeat small arms fire at point blank range. One hypothesis was that oblique impacts enhanced performance of the Kevlar composite and we were asked to investigate.

Accordingly, Kevlar polyester panels of 2 and 2.9 pounds per square foot (psf) areal density were tested at 0.45 and 90 degree obliquities at ranges of 17 and 25 yards. Threats were standard military ball, full metal jacket (FMJ) 5.56, 7.62 and 9mm rounds. The desired angles of obliquity were achieved by mounting the plates in hinged frames and setting the desired angle using a plumb bob, liquid bubble level, and protractor. Weapons were fired from a sturdy, aligned bench rest. In addition to experiments on square plates, three types of helmets were also tested at point blank range, namely Kevlar and Spectra epoxy helmets and World War II steel helmets with nylon reinforced composite liners. The various helmets were held onto thin plywood panels via rubber bungee cords, and mounted in the target frames with the plywood panels perpendicular to the bullet trajectory. In this way by aiming at the crown of the helmets, or at different distances from the helmet center, varying degrees of projectile impact angle could be achieved.

Throughout military history, armies have sought better helmets, and the helmet is an important piece of equipment for the US Army. On a routine basis, the head is the only protected part of a soldier's anatomy. Although the Army has ballistic protective vests, these are not worn universally in battle. The Kevlar composite helmet replaced the W.W.II "steel pot" in 1978, although it is not widely issued. The M1 steel helmet was adopted by the US Army in June 1941. Originally it had a cotton reinforced plastic liner. In March of 1961 the cotton liner was replaced by nylon to raise the ballistic limit by 10 to 15%. In the original ballistic tests, Kevlar composite was found to be at least 60% better than the steel pot, for various size fragments. Of course it is considerably more expensive. Titanium helmets had also been studied, but rejected due primarily to cost.

The first ballistic tests were conducted using the 2.0 psf composite plates. Initial threats used were 5.56, 7.62 and 9mm rounds, fired at zero obliquity. The plates were subsequently set at angles of 45 and 60 degrees, and the entire series repeated with 2.9 psf panels. The 5.56 and 7.62 threats defeated all targets fired upon, the change in impact angles did not help. With metal armor the increase in angle of obliquity is treated as if the projectile has to penetrate a thicker target, increasing target thickness using cosine of the impact angle. Of course this is an extremely simplified viewpoint. With angled impact, wave propagation is no longer symmetric, and complex asymmetric wave interaction occurs. The local wave phenomena is far more complex in anisotropic, laminated composites. As the angle of impact increased from 0 to 45 to 60 degrees, the volume of material damaged increased and so did the exit damage. Much more frayed and cut Kevlar yarn occurred in the exit zone for 60 degree impacts.

In the flat panel tests the 9mm, 124 grain full metal jacket projectile was defeated by both 2.0 and 2.9 psf plates at zero degree obliquity. These 9mm rounds did not penetrate but were trapped in the composite, causing a slight bulge on the rear surfaces of the panel.

On completion of the panel experiments, the three types of helmets were ballistically tested, using the same threats. Shots were fired at the center and radially across the helmets to evaluate obliquity effects. The 5.56 and 7.62mm projectiles defeated all three types of helmet, regardless of the impact angle. Similarly to the flat panel tests, the Kevlar composite helmet defeat the 9mm, 124 grain FMJ bullets. The W.W.II helmet, with nylon reinforced liner did not, but the prototype Spectra composite helmet did defeat the 9mm threat.

Examination of photos of helmets from survivors of Operation Just Cause indicated that a number of the impacts were glancing or grazing hits, and several were oblique impacts where the projectile had been deflected away from the head. According to our experiments the survivors were very fortunate that these were glancing impacts. In our ballistic testing if it was a fair hit, at reasonably small angle, in the majority of cases the projectile was deflected towards the wearers head. In only one out of ten hits was the bullet deflected away.

Let us briefly consider kinetic energy (KE) of the different threat. The 17 grain fragment at 2000 fps has a KE of 151 foot pounds, whereas the 124 grain 9mm projectile has a KE of 333 foot pounds. Since the composite helmets stopped the 9mm round at this velocity and KE, a higher KE would be required to penetrate at point blank range. Considering that the pistol threat was defeated, one can suppose that the 5.56 and 7.62 bullets might be defeated when their impact energies dropped to near 333 foot pounds, or some slightly higher energy. According to published values for a 55 grain, 5.56mm grain bullet at 814 meters the velocity drops to 1556 fps, and the KE will be 333 foot pounds. The possibility of defeating the 5.56 and 7.62mm threats was explored by long range shooting. Both projectiles clearly penetrated 2.9 psf Kevlar composites at 200 meters. However several rounds of each of these threats were stopped by the composite panels at 300 meters, in our field tests. It is desirable to precisely measure the ballistic limit of the helmet for several of these threats. Hopefully we will accomplish this in the near future.

## Arctic Environment Effects on Helmet Ballistic Performance

Thus far it had been demonstrated that the Kevlar helmets could stop 9mm 124 FMJ bullets at point blank range. Now it was desired to investigate whether thermal cycling to representative Arctic temperatures had a detrimental effect on ballistic resistance. Accordingly, several helmets were subjected to 100 thermal cycles of an hour duration each, ranging from -60 to +60 degrees Celsius. Subsequently one helmet was tested ballistically at room temperature and one was shot in a cooled insulated box. This second helmet was packed in place using polystyrene "peanuts" and chilled via liquid nitrogen. At impact this helmet was cooled to -100 Celsius according to an implanted thermocouple. Both room temperature and supercooled helmets stopped the 9mm 124-grain FMJ round at point blank range. There was a difference in behavior. In the room temperature test the projectile was trapped in the helmet and only a slight resulting bulge was visible on the interior surface. At -100 C the bullet was trapped and flattened by the cooled, rigid layers and ejected out through the surface, flat as a pancake!

The thermally cycled helmets were also tested using a steel cruciform sabot projectiles in the 9mm pistol. In this case the lighter, harder projectile impacted at velocities of 1835 fps. This potent round easily penetrated the helmets.

## Determination of Mechanical Behavior

### Specimen Preparation and Preconditiong

Woven Kevlar fiber composite panels for this portion of the study were fabricated at the Army Research Laboratory (ARL), materials Directorate, Watertown, Massachusetts. Laminated plates were produced by wet lay-up using thermosetting polyester resin matrix and square weave Kevlar fabric with equal number of fibers along two orthogonal directions. Three twelve-inch square plates, with thicknesses of 0.445, 0.465 and 0.307 inches respectively, were selected for evaluation. The thinnest plate was reserved for later determination of ballistic limit velocity, V50.

Specimen dimensions were chosen for convenience with 0.75 as nominal width so that at least ten specimens could be obtained from each plate after some loss and wastage in the cutting process. Initial efforts to cut these specimens at Cold Regions Research and Engineering Lab (CRREL) were quickly abandoned in favor of the more experienced machinists at the ARL, Watertown. Machining Kevlar composite is a formidable challenge to the inexperienced, and the ARL facility had suitable machines and protection systems from dust and fumes. The specimens were cut using a diamond coated saw at a slow cutting feed (0.5 in/min) with continuous cooling fluid. The resulting specimen had reasonably smooth, clean edge surfaces.

One intact plate and ten selected specimen were thermally cycled between -60 and +60 degrees centigrade for 100 times in order to simulate exposure to a severe Arctic environment. This was accomplished in a liquid nitrogen cooled computer controlled thermal cycling chamber in which the specimens were kept in racks, and cooling or warming air, depending on which cycle had been activated, would circulate in the chamber with unhindered access to specimen surfaces. Each temperature cycle was programmed for one hour, so that at the end of, say the warming cycle, the cooling cycle would

automatically begin. Thermocouple records indicated it took about 10 minutes to reach specified temperature (-60°C).

## Tensile Testing

In order to prevent failure or cracking within the tensile machine grips, each specimen was prepared with end tabs at both ends. The tabs were made of 1/4 inch thick polycarbonate, each approximately 3 inches long and bonded with a quick setting adhesive. A servo-hydraulic machine using hydraulic grips was used for tensile testing. Each specimen was carefully aligned using bubble levels, and load was applied at a constant displacement rate of 0.005 in/min. Extensometers were mounted at mid gage section to measure average displacement and to allow calculating strain. Individual load-displacement curves were recorded via an X-Y plotter. Both the thermally cycled batch A specimens and the uncycled batch B specimens started producing a cracking sound when the applied load reached close to 85 to 90% of the failure load. All specimens failed in the gage portion, away from the end tab grips, although there was a general difference in overall failure location between batch A and B specimens as discussed later. Typically the failure zone spread through the thickness and over a length of approximately two inches, showing extensive damage by delamination, matrix cracking and interply failures.

## Observed Tensile Response

Figure 1 illustrates the sturdy grips, extensometer and tensile specimen used. Note the 12 inch long, nominal 5/16 thick and 3/4 inch wide Kevlar polyester specimens had 3 inch long, 1/4 thick polycarbonate bonded tabs for load transfer. Experimental results are summarized in Figures 2 and 3. Figure 2 presents tensile data for the as received, 2.9 psf Kevlar composite. The average tensile strength was 57,432 psi with standard deviation of 2,636 and with values ranging from 52,285 to 62,044. Average failure strains were .0194, ranging from .015 to .024 in/in. Modulus was estimated as a "secant" modulus via failure stress. Average "secant" modulus was 3,021,865 psi. Figure 3 illustrates behavior of the specimens which were exposed to 100 cycles of -60 to +60 degrees C. Now the average tensile strength was 52,946 psi, ranging from 48,542 to 56,057 psi. Total strain to failure was .0213, ranging from .0170 to .0265 in/in.

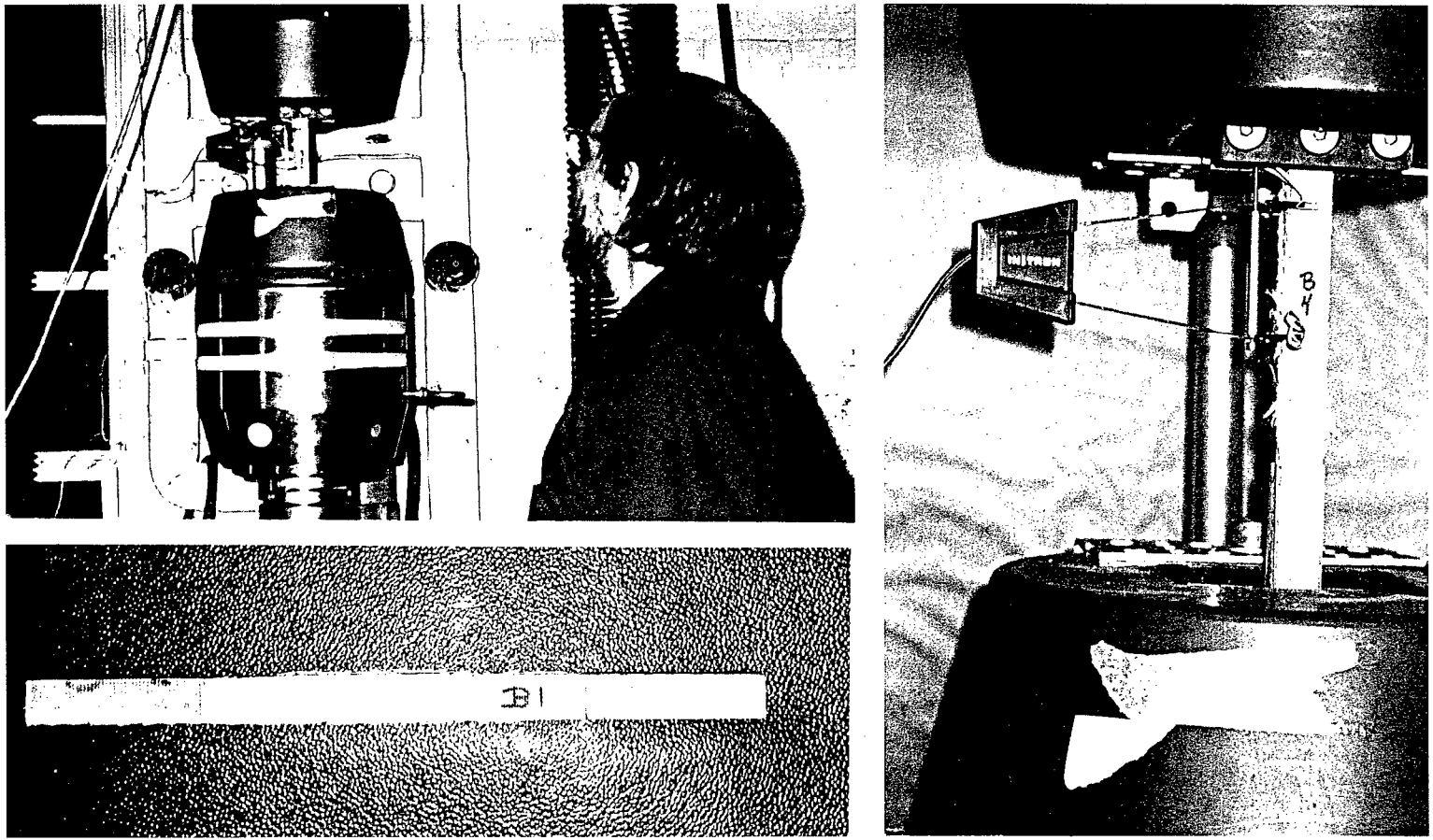


FIGURE 1. GRIPS,EXTENSOMETER AND SPECIMEN

ROOM TEMPERATURE DRY SAMPLES

| SAMPLE # | DENSITY (lb/in cub) | AREA ( in sq ) | FAILURE LOAD ( lbf ) | FAILURE STRAIN ( in/in ) | FAILURE STRESS ( psi ) | SECANT MODULAS ( psi ) |
|---|---|---|---|---|---|---|
| B - 1 | 0.044 | 0.35 | 20800 | 0.0200 | 59710 | 2985520 |
| B - 2 | 0.042 | 0.36 | 20800 | 0.0160 | 57316 | 3582254 |
| B - 3 | 0.041 | 0.37 | 20800 | 0.0155 | 55570 | 3585187 |
| B - 4 | 0.043 | 0.32 | 18800 | 0.0220 | 58690 | 2667728 |
| B - 5 | 0.042 | 0.37 | 21200 | 0.0195 | 57463 | 2946845 |
| B - 6 | 0.042 | 0.36 | 21200 | 0.0195 | 59005 | 3025894 |
| B - 7 | 0.042 | 0.36 | 19600 | 0.0210 | 54480 | 2594279 |
| B - 8 | 0.041 | 0.37 | 21600 | 0.0210 | 57961 | 2760065 |
| B - 9 | 0.042 | 0.34 | 21200 | 0.0240 | 62045 | 2585189 |
| B - 10 | 0.038 | 0.37 | 19200 | 0.0150 | 52285 | 3485687 |
| AVERAGE | 0.042 | 0.36 | 20520 | 0.0194 | 57453 | 3021865 |
| STD DEV | 0.002 | 0.02 | 913.02 | 0.002820 | 2636 | 376952 |

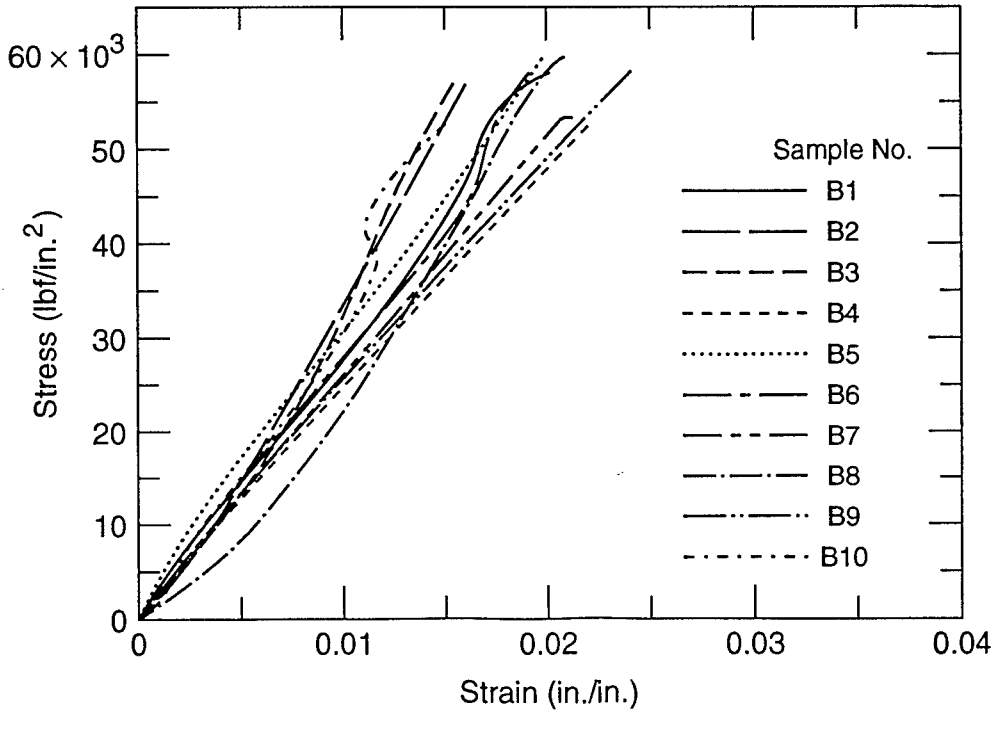



FIGURE 2. TENSILE RESPONSE: AS RECEIVED SPECIMENS

THERMALLY CYCLED BETWEEN -60 TO +60 DEGREES C 100 TIMES (DRY SAMPLES)

| SAMPLE # | DENSITY (lb/in cub) | AREA ( in sq ) | FAILURE LOAD ( lbf ) | FAILURE STRAIN ( in/in ) | FAILURE STRESS ( psi ) | SECANT MODULAS ( psi ) |
|---|---|---|---|---|---|---|
| A - 1 | 0.042 | 0.34 | 18000 | 0.0180 | 52723 | 2929047 |
| A - 2 | 0.039 | 0.36 | 20000 | 0.0265 | 56057 | 2115345 |
| A - 3 | 0.042 | 0.35 | 18400 | 0.0205 | 53210 | 2595607 |
| A - 4 | 0.043 | 0.34 | 18000 | 0.0170 | 52985 | 3116754 |
| A - 5 | 0.043 | 0.34 | 17600 | 0.0195 | 51734 | 2653040 |
| A - 6 | 0.041 | 0.35 | 18800 | 0.0250 | 53541 | 2141626 |
| A - 7 | 0.042 | 0.35 | 18000 | 0.0190 | 51871 | 2730042 |
| A - 8 | 0.042 | 0.34 | 18400 | 0.0235 | 53775 | 2288314 |
| A - 9 | 0.042 | 0.35 | 16800 | 0.0175 | 48542 | 2773829 |
| A - 10 | 0.043 | 0.34 | 18800 | 0.0260 | 55021 | 2116184 |
| AVERAGE | 0.042 | 0.35 | 18280 | 0.0213 | 52946 | 2545979 |
| STD DEV | 0.001 | 0.01 | 801.00 | 0.003473 | 1928 | 342390 |

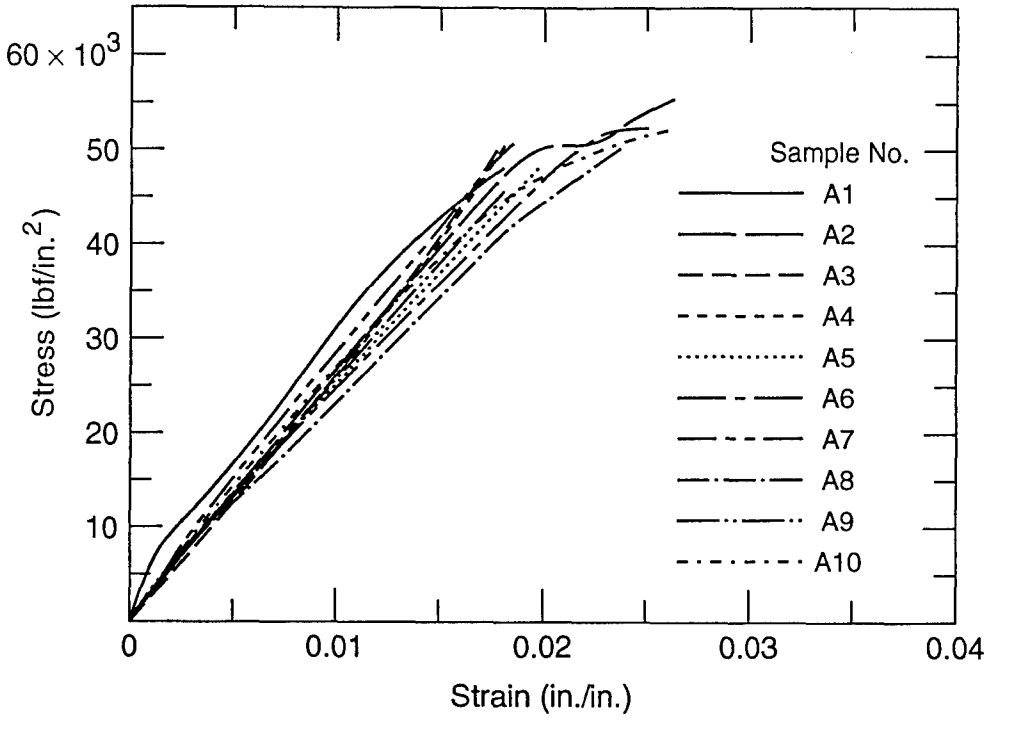



FIGURE 3: TENSILE RESPONSE: COLD CYCLED SPECIMENS

Secant modulus averaged 2,545,979 psi. It was observed that cold temperature cycling resulted in decrease in tensile strength, increase in failure strain and decrease in average secant modulus. Examination of the failed tensile specimen revealed that much more extensive interlaminar cracking occurred in the cold-cycled composite. Furthermore, the cycled samples all failed near the mid portion of the gage section whereas the unexposed specimens failed in 5 out of 10 cases near to the end tabs. Refer to the stress-strain curves shown in Figures 2 and 3. Note that the unconditioned composite tended to have concave upward curvature, while the thermally cycled specimens behaved either more linearly or had concave down curvature!

## Summary

Kevlar composite helmets performed satisfactorily in defeating 9mm 124-grain FMJ bullets at point-blank range after 100 cycles between -60 and +60C. However when tested at -100C, failure modes changed and the composite did not trap the projectile, but suffered more delamination and deflected the round outward. Our ballistic performance results are qualitative, and it is suggested the V50 ballistic limits be determined for the as-received and exposed composite to obtain quantitative data. Tensile strength and secant modulus of Kevlar/polyester composite decreased observably after thermal cycling, probably due to the effect of microcracking and interface damage from thermal cycle-induced stresses. The stress-strain response was affected after cold cycling: changing from a concave up to concave down curvature and larger damage zones occurring, which results in an apparent progressively decreasing modulus. Total strain to failure increased and the composite exhibited more extensive delamination and microcracking after 100 cycles of exposure. It is likely that the stress strain curvature observed is a function of location of the failure zone with reference to the extensometer measuring position. If the failure zone is located right between the nominal 1 1/2 inch extensometer averaging length then the curve would tend to be concave down and reversed if failure is occurring outside the extensometer position. One matter for conjecture: why did the unexposed specimen tend to fail near end tabs, outside the extensometry location? Were their fabrication induced residual stresses near the plate extremities which induced failures towards the sample ends? Thermal cycling could have changed the residual stress distribution and failure zone location.

Finally it is suggested that additional data should be gathered on currently fielded representative spall liners. And in conduct of tensile tests, the strain measuring procedures must be improved to obtain more realistic effective composite modulus estimates.

## Acknowledgment

The authors gratefully acknowledge the generous support of: Stan Waclawic, US Army Natick Lab, who provided helmets and reports on Operation Just Cause; Dr. Joseph Prifit, ARL, Materials Directorate, who donated Spectra helmets and spall plate liners; Dr. Margaret Roylance, MIT and consultant to ARL, who gave much appreciated advice on tensile testing and arranged for specimen machining; and Mr. Robert Pasternack, ARL, who performed the tensile testing. We also thank Captain William Haight and the Cadets at the US Military Academy who performed the ballistic evaluation.

# Effect of Specimen Size on the Tensile Strength of Geometrically Scaled $[+\theta°_n/-\theta°_n/90°_{2n}]_s$ Composite Laminates

Dr. Karen E. Jackson*
U.S. Army Vehicle Structures Directorate, ARL
M.S. 495 NASA Langley Research Center
Hampton, VA 23681-0001

Dr. Sotiris Kellas
Lockheed Engineering and Sciences Company
144 Research Drive
Hampton, VA 23666-1339

## Abstract

An experimental program was conducted to investigate the effect of outer ply constraint on the tensile strength of geometrically scaled composite graphite-epoxy coupons having a core of 90° plies located at the midplane of the laminate. The specific laminate stacking sequences were $[+\theta°_n/-\theta°_n/90°_{2n}]_s$, where n=1, 2, 3, and 4, corresponding to 1/4, 1/2, 3/4, and full-scale sizes. The outer ply orientations were varied from 0° to 90°, in 15° increments. Results of the tensile tests indicate a scale effect in strength with a trend of decreasing strength with increasing specimen size for ply level scaled coupons. The magnitude of the strength scale effect is a function of the outer ply constraint. In general, fiber dominated [0°/90°] cross ply laminates and the pure 90° laminates showed only a minor scale effect, while all other lay-ups exhibited a significant size dependency in strength.

## Introduction

Scale model testing of composite structures has been an active topic of research in recent years. Ultimately, the goal of this research is to develop the scaling laws that would permit data generated on

coupon-size specimens to be "scaled up" to predict full-scale structural behavior. The behavior, or property, of interest might be stiffness, strength, coefficient of thermal expansion, natural vibration frequency , or failure mechanism, etc. A scale effect, then, is defined as the dependence of a material property on specimen size. For example, if two composite coupons are built such that one specimen is scaled geometrically to be 1/2 the size of the other specimen, and both specimens are constitutively scaled, then the ratio of tensile strengths of the two coupons should be equal to 1.0. If the ratio of strengths is not equal to 1.0, then a scale effect is present.

Sub-scale composite structures can be fabricated using several approaches, due to the inhomogeneity of the material itself and the layered construction. Ideally, a true scale model composite structure would be fabricated from a microscopically scaled pre-preg material having scaled fiber diameters. Since this technique is not feasible, two other macroscopic scaling approaches are used, the ply level and sublaminate level scaling techniques. In ply level scaling, the baseline, or model, stacking sequence is "scaled up" by increasing the number of plies for each angular orientation in the baseline laminate stacking sequence. Thus, plies of similar orientation are blocked together. In the sublaminate level scaling approach, the baseline stacking sequence is treated as a sublaminate which is repeated to "scale up" the thickness of the full-scale laminate. Sublaminate scaled specimens have dispersed plies, as opposed to blocked ply groups in ply level scaled specimens.

Previous research [1-4] has shown that the strength of ply level scaled composite tensile coupons is dependent on specimen size. Specifically, sub-scale models can exhibit significantly higher failure stresses than their full-scale counterparts. Conversely, research [4,5] has shown that geometrically scaled tensile coupons fabricated using the sublaminate approach exhibit increasing strength with increasing specimen size. The magnitude of the size effect is dependent on the laminate stacking sequence, and is influenced by the type of damage initiated in the laminate and the manner in which the damage propagates. Matrix dominated laminates containing 90° core plies were found to be particularly size dependent [1], largely due to the presence of transverse matrix cracks which develop in the 90° plies and serve as sites of delamination, or as stress concentrations in neighboring plies. Thus, an experimental program was conducted to highlight the effect of outer ply constraint on the tensile strength of geometrically scaled composite coupons having a core of 90° plies located about the midplane of the laminate.

This study differs from previous research [6] on laminate or ply thickness effects in tensile strength of composites in that the coupons

are geometrically scaled in all three dimensions. While thickness has been shown to be the most important scaling dimension in determining laminate strength [4,5], it is difficult to isolate scaling effects using specimens with distorted geometry. For example, if the in-plane dimensions of two coupons are the same, but the thicknesses are different, then the effects from factors such as edge stresses and specimen volume are not scaled. Consequently, the conditions for similitude are not satisfied.

Also, this study is different from previous research [7-12] on the effect of ply constraint on the in situ strength of 90° core plies in the sense that the ratio of outer ply thickness to the thickness of 90° core plies is constant for all ply level scaled coupons. In most of the earlier work on this topic, the thickness ratio is altered for different specimens by increasing the number of core plies relative to the number of constraint plies. For this case, the change in thickness ratio affects the initiation of transverse matrix cracking in the 90° plies due to the increased core thickness and the reduced in ply constraint. Various analysis techniques [7,8,10,11] have been developed to model this effect which are typically based on energy methods. However, when these analyses are applied to ply level scaled tensile coupons with constant thickness ratios, they yield critical stress ratios for initiation of transverse cracking of $\lambda^{-1/2}$, where $\lambda$ is the scale factor (1/4, 1/2, 3/4) between the model and full-scale coupon. Thus, the analyses predict the same trend, regardless of the stiffness or constraint provided by the outer plies of the laminate. Results of this experimental study will show the effect of constant thickness ratio (thickness of 90° core plies to thickness of constraint plies) on the tensile response and strength of scaled composite coupons.

## Experimental Program

Specimens were fabricated from AS4/3502 graphite-epoxy pre-preg composite material. Four different size coupons were constructed with in-plane dimensions of 0.5*n x 5.0*n inches, where n=1, 2, 3, 4 corresponds to 1/4, 1/2, 3/4, and full scale factors, respectively. The laminate stacking sequences were chosen to be $[+\theta°_n/-\theta°_n/90°_{2n}]_s$ where $\theta$ ranged from 0° to 90° in increments of 15°, and n varied from 1 to 4. In addition, a set of unidirectional coupons, $[0°]_{8n}$, and a set of quasi-isotropic, $[+45°_n/-45°_n/0°_n/90°_n]_s$, coupons were tested. Laminates fabricated in this manner are scaled at the ply level since the specimen thickness is increased by blocking several plies of similar angular orientation together. In addition, a set of 1/2 scale specimens were fabricated having a $[(+\theta°/-\theta°/90°_2)_2]_s$ laminate stacking sequence

where θ varied from 0° to 90° in 15° increments. These coupons were fabricated by repeating a sublaminate group and are, thus, scaled on a sublaminate level. The sublaminate level specimens were included to examine the effect of thickness scaling technique on the initial response and mode of failure as compared to the ply level scaled specimens. One specimen of each size and lay-up was examined using dye penetrant x-ray technique to determine the initial damage state. Five data channels were recorded for each specimen including load, displacement, strain from gages applied at the midspan of the coupon, and strain from an extensometer. Tensile load was applied to the coupon by a load test machine through mechanical wedge-type grips. The grip distance was scaled as 0.075*L, where L is the gage length of the coupon. Also, a thin piece of abrasive cloth was placed around the grip area of the test specimen for improved friction. All coupons were loaded until ultimate tensile failure.

## Results

Approximately 250 tests were performed on ply level scaled composite coupons, including six replicate tests of each size and laminate stacking sequence. Initial modulus and strength data for each lay-up and specimen size were averaged and the results listed in Table 1. The modulus and strength data for the ply level scaled coupons were normalized by the full-scale value, corresponding to n=4, for each laminate family and plotted versus size n=1,2,3, as shown in Figures 1 and 2, respectively. If no size dependencies were observed, all data would fall on the horizontal line drawn at 1.0 in each plot. It is evident that the variation in initial modulus with size is small, for most laminates within ± 5 to 10%. Since this scatter is approximately the same as the specimen-to-specimen variation, it is reasonable to conclude that there is no size effect in initial tensile response, or modulus. The size dependency on ultimate strength is much larger. In general, the strength of sub-scale coupons is significantly greater than the strength of the full-scale prototype, in some cases by as much as a factor of two. The size effect is less pronounced in the unidirectional [0°], cross ply [0°/90°], and pure [90°] laminates. However, when the angle, θ, of the surface plies has a value other than 0° or 90°, a large size effect is observed. For these laminates, the constraining effect of the neighboring ±θ plies and the ply thickness of the 90° core become the primary factors controlling damage initiation and propagation.

No size effects were observed in initial tensile modulus based on the method of increasing the thickness, either by blocking the plies (ply level scaling) or by repeating a sublaminate group (sublaminate level scaling), for the 1/2 scale specimens. However, large differences

were found between the two methods of scaling with respect to strength. As shown in Figure 3, the normalized strength of the 1/2 scale coupons with distributed plies was, in general, higher than the comparable ply level scaled coupons with blocked plies. In fact, when compared to the 1/4 ply level scaled specimens, the 1/2 scale sublaminate specimens exhibit an increase in strength with size, the opposite effect shown by the ply level 1/2 scale specimens. This phenomenon has been previously studied by Kellas, et al., [4,5], and can be explained by the influence of outer ply constraint on the 90° core plies for specimens having lay-ups similar to the ones tested in this study [5].

Stress versus strain plots of ply level scaled coupons from each laminate family are shown in Figure 4. A typical specimen of each size and laminate type was chosen for a comparison of tensile stress-strain response. For these plots, it is important to note that both stress and strain scale as 1.0, i.e., the stress and strain states in both the full-scale and sub-scale coupons of a specific laminate family should be the same. Consequently, all scaled coupons for a given laminate type should exhibit the same response, regardless of specimen size. The results depicted in Figure 4 indicate that for most laminate families, the response curves for specimens of different sizes are not coincident. In fact, all of the laminate families show differences in response as a function of specimen size, prior to ultimate failure, with exception of the unidirectional [0°] and transverse [90°] stacking sequences. The unidirectional coupons exhibit an ultimate failure mode of fiber fractures and longitudinal splitting. Any intermediate damage prior to ultimate failure does not alter the response curve. Likewise for the transverse coupons, [90°]8nT, ultimate failure occurs when the tensile stress reaches the point to cause unstable crack growth in the matrix. No other intermediate failure mechanisms are possible for these coupons. Results for all other ply level scaled laminate families indicate a scale effect in damage initiation and propagation, as well as in ultimate failure. Typically, full-scale specimens exhibit the first indications of damage, such as a sudden loss of stiffness, followed by the next smaller sized specimen, and so on, as shown in Figure 4. Previous research [5] on damage evaluation in sublaminate scaled tensile coupons has shown a delay in transverse cracking and delamination onset for increasing specimen size.

## Discussion of Results

Testing for this project is yet to be completed. Thus far, only information on the stress/strain response and ultimate failure of $[+\theta_n/-\theta_n/90_{2n}]s$ geometrically scaled laminates was generated under

continuous tensile load until catastrophic faiilure. No evaluation techniques were used to determine the damage state of the coupons at intermediate load levels. Data such as stress at damage initiation and stress at onset of delamination in the scaled specimens will be obtained during the second phase of this research project. Consequently, the discussion of results will focus on ultimate strength data. In addition, comments will be made concerning analytical approaches used to predict first ply failure and delamination onset for the class of laminates considered.

Initial Damage Evaluation The damage evaluation of virgin specimens using dye-penetrant x-ray technique indicated that transverse matrix cracks were present in the 90° core plies of ply level scaled $\theta = 0°$ and 15° half-scale coupons, in the $\theta = 0°$, 15°, and 30° three-quarter scale coupons, and in the $\theta = 0°$, 15°, 30° , 45° and quasi-isotropic full-scale coupons. None of the 1/2 scale sublaminate coupons were damaged initially. The pre-existing matrix cracks developed from residual stresses in the coupons. Ideally, within the assumptions of lamination theory, all ply level scaled specimens within a laminate family should experience the same residual stress state. However, none of the one-quarter scale coupons showed any cracking prior to loading. Thus, a scale effect in the initial state of the cured specimens is observed. It is expected that as the undamaged specimens are loaded, the applied stresses combined with the residual stresses will produce matrix cracking. The specimens with pre-existing matrix cracks did not exhibit any significant change in initial stress/strain response due to the presence of the cracks, as shown in Figure 4. Previous research by Kellas and Morton [1] has shown that the pre-existing matrix cracks in 90° core plies can influence the damage mechanism of larger size coupons, as compared with the smaller scaled coupons, and, in this manner, contribute to the strength scale effect.

Scale Effects in Stiffness The stress/strain responses shown in Figure 4 indicate that all scaled specimens within a laminate family exhibit the same initial response curve, and, thus have the same initial stiffness. However, as mentioned in the previous section, some of the 1/2, 3/4, and full-scale coupons are damaged initially. Obviously, the pre-existing matrix cracks have little influence on the initial stiffness which is determined primarily by the outer plies of the laminate and the transverse constraint imposed by the 90° plies which is not affected by cracking.

Scale Effects in Ultimate Strength Some of the results shown in Figure 2 are typical of data obtained from previous studies on scale effects in the tensile strength of composite coupons. For example, in the reference by Kellas and Morton [1], strength data is presented for

$[+30°_n/-30°_n/90°_{2n}]_s$ scaled lay-ups fabricated from the same AS4/3502 material used in this study. The normalized strengths from both sets of data are nearly identical. The unique contribution of this study, however, is that a complete and systematic set of scaled coupons of a certain class of laminates was tested under tensile load until failure. Previous research on cross plied laminates in which the number of 90° core plies is increased relative to the number of constraint plies has demonstrated that as the absolute size of the 90° layer increases, the stress required to cause transverse cracking is lowered [8-12]. This observation correlates with the data obtained in this study.

Failure Analysis The tensile strength data generated from tests on geometrically scaled coupons illustrate the need for a size dependency in failure criteria for composite materials. Currently, many of the stress and strain based criteria, such as maximum stress, maximum strain, and tensor polynomial, do not account for size effects, and, consequently, cannot be used to predict the failure of scale model composite structures. Analytical techniques which have been used to predict the strength scale effect including a Weibull statistical model [13-15], and a fracture mechanics model [16] will be discussed.

*Weibull Statistical Approach* Weibull statistical models are based on the concept that for a given volume of material a certain number of defects exist with a probability that a critical defect is present. As the volume increases, the probability that a critical flaw size exists in the material also increases. The critical flaw size is the size of defect which will initiate failure in the material at a certain load or stress level. The Weibull model uses an empirical value, the shape parameter, $\beta$, which is a measure of the variability, or scatter, in the strength of the material, itself. Ideally, $\beta$ is a material property and may be determined from many tests on a single specimen configuration, or from specimens of two different sizes. Thus, knowing the value of $\beta$, a prediction of strength for a given volume of material can be made. The Weibull statistical criterion is given by Equation 1 for specimens which have different volumes, such as scaled specimens,

$$\frac{(S^{ult})_m}{(S^{ult})_p} = (V_p/V_m)^{1/\beta} \qquad (1)$$

where the subscripts m and p refer to model and prototype, respectively, V is volume, and $S^{ult}$ indicates ultimate strength. Values of $\beta$ have been determined previously [15] for 90° transverse coupons

of AS4/3501-6 material to be 7.63. In this study, values of $\beta$ were determined using the ultimate tensile strength of 1/4 and 1/2 scale laminates fabricated of AS4/3502 material for all of the ply level coupons. The $\beta$ values ranged from 4.1 to 75.8. The value for unidirectional coupons was 16.3. Clearly, the definition of a critical flaw size for composite materials is a complex issue and the presence of a defect will have a different outcome depending on fiber orientation for unidirectional composites, and stacking sequence for laminated composites. Moreover, in the case of scaled laminated composites which do not exhibit the same mode of failure, the definition of a critical flaw size may also depend on specimen size.

Since the Weibull statistical approach assumes that the failure events which happen in specimens of different size fabricated of the same the material are self-similar, it is inappropriate to apply this technique for most composite laminates which tend to fail in a complex, progressive mode. For many laminates, the 1/4 and 1/2 scale coupons fail in a similar mode, but a different failure mechanism may occur in the 3/4 and full-scale coupons of the same laminate family. Thus, the shape parameter determined from the 1/4 and 1/2 scale specimens is not valid for other laminates in the same family. The Weibull approach would be expected to correlate best for composite laminates whose failures represent basic material behavior and are generally statistical in nature, such as fiber fractures in unidirectional coupons [0°], or transverse matrix cracking in purely 90° coupons. However, the shape parameters obtained from these types of laminates do not apply to other, more complex laminates.

An additional problem with the Weibull approach is in the choice of critical volumes when the technique is used to predict flexural strength using data gathered on tensile coupons. For that case, what critical volume of the stressed beam should be chosen? This issue was discussed by O'Brien, et al., [15] and their suggestion is that "for a non-uniform stress field with finite stress concentrations, the maximum tensile stress and the total volume of material stressed in tension should be used in a scale law for transverse tensile strength to predict matrix cracking or delamination". This method may prove successful for 90° and/or 0° laminates, but is not recommended as a predictive methodology for the ultimate strength of other laminates with more complicated failure modes.

*Fracture Mechanics Approach* The analytical techniques used to predict the stress at damage initiation, and stress at onset of delamination, will be discussed with respect to scaled laminates in which the ratio of constraining plies to 90° core plies is the same for all coupon sizes within a laminate family. The following equation was used by Flaggs, et al., [8] to determine the in situ transverse failure strain of

a 90° core ply as a function of its thickness, and the extensional stiffness of the adjacent constraining plies.

$$(\varepsilon_2)_{cr} = [bE_\theta m/(d^2 bE_\theta + d^3 E_2)]^{1/4} \qquad (2)$$

where $(\varepsilon_2)_{cr}$ is the critical failure strain in the 90° core ply
b is the thickness of the constraining plies
$E_\theta$ is the stiffness of the constraining plies
m is $G_{23}(G_{Ic})^2/(E_2)^3$
d is the thickness of the 90° ply
$E_2$ is the transverse modulus of the 90° ply

If a dimensional analysis is performed on Eq.2 and , assuming that the critical strain energy release rate, $G_{Ic}$, is a material property and, therefore, scales as 1.0, the critical strain to cause transverse failure of the 90° plies scales as $\lambda^{-1/2}$, where $\lambda$ is the scale factor. This is true for all laminates regardless of the orientations of the constraining plies. Thus, without empiricism, Eq. 2 is not laminate specific for ply level scaled specimens, although, in general, the correct trend of decreasing failure strain with increasing size is predicted.

A closed form equation for determining the critical strain energy release rate has been developed by O'Brien [17] which incorporates the critical strain at delamination onset, and the stiffness change caused by delamination of the composite laminate. The equation has the form:

$$G_c = (\varepsilon_d)^2 t_L/2(E-E^*) \qquad (3)$$

where $G_c$ is the critical strain energy release rate, $\varepsilon_d$ is the critical strain at the onset of delamination, $t_L$ is the thickness of the laminate, and $(E-E^*)$ is the change in stiffness between the total laminate and the delaminated laminate. Equation 3 can be solved for the critical strain at delamination onset for ply level scaled laminates. The critical strain energy release rate, $G_c$, is now assumed to be a known material property, and the change in modulus may be analytically predicted using lamination theory. Ideally, for ply level scaled laminates, the delamination site should occur at the same location and, consequently, the $(E-E^*)$ parameter is the same for ply level scaled coupons. A dimensional analysis of this equation indicates that the critical strain at delamination onset scales in proportion to $\lambda^{-1/2}$, where $\lambda$ is the scale factor. Thus, the equation for prediction of delamination onset is not laminate specific for ply level scaled specimens, i.e., it predicts the

same $\lambda^{-1/2}$ trend regardless of the lay-up of the ply level scaled coupons. Equation 3 was used successfully to predict the trend of increasing strength with specimen size for sublaminate scaled tensile coupons in Reference [5]. For sublaminate level scaled coupons, the $(E-E^*)$ parameter is not identical for scaled specimens. Consequently, the stiffness parameter contributes to the ratio of critical delamination onset strains for scaled specimens.

## Conclusions

A study was conducted to examine scale effects in the tensile strength of a class of laminates having a core of 90° transverse plies located at the midplane of the laminate. The lay-ups were $[+\theta°_n/-\theta°_n/90°_{2n}]s$, where n=1, 2, 3, and 4, corresponding to 1/4, 1/2, 3/4, and full-scale factors. The outer ply orientations were varied from 0° to 90°, in 15° increments. Specimens were both geometrically and constitutively scaled. Results indicate that initial modulus is independent of specimen size. However, the first damage event and the ultimate failure are influenced by specimen size. The trend is that strength decreases as specimen size increases. The magnitude of the strength scale effect is determined by the laminate stacking sequence. In general, fiber dominated lay-ups and pure 90° transverse ply lay-ups exhibited the smallest effect, while all other laminates showed a significant influence of specimen size on strength.

Analytical techniques such as Weibull statistical and fracture mechanics based approaches were discussed with respect to the strength scale effect. Both techniques are capable of predicting a size dependency in failure events or strength. However, the Weibull approach requires an empirical shape parameter which is dependent on the laminate stacking sequence and is not a material property. The fracture mechanics approach predicts the same trend for all ply level scaled composite coupons, regardless of stacking sequence, and thus, is not laminate specific.

## Further Research

A study is planned in which a set of specimens similar to the ones used in this study are examined for initial damage, then loaded to a stress level of interest, removed from the test machine and evaluated for damage growth, and so on, as a means of understanding the influence of specimen size on damage initiation and propagation. In this manner the damage events may be thoroughly characterized and a predictive model may be developed for failure of composite laminates which incorporates the effect of specimen size.

## References

1. Kellas, S. and Morton, J.: "Strength Scaling in Fiber Composites," NASA CR 4335, November 1990.

2. Jackson, K. E..: "Scaling Effects in the Flexural Response and Failure of Composite Beams," *AIAA Journal*, Vol. 30, No. 8, August 1992, pp. 2099-2105.

3. Jackson, K. E.; Kellas, S.; and Morton, J.: Scale Effects in the Response and Failure of Fiber Reinforced Composite Laminates Loaded in Tension and in Flexure," *Journal of Composite Materials*, Vol. 26, No. 18, !992, pp. 2674-2705.

4. Kellas, S. and Morton, J.: "Scaling Effects in Angle-Ply Laminates," NASA CR 4423, February 1992.

5. Kellas, S.; Johnson, D.; Morton, J.; and Jackson, K. E.: "Scaling Effects in Sublaminate-Scaled Composite Laminates," 34th SDM Conference Proceedings, April 19-21, 1993, La Jolla, CA.

6. Crossman, F. W.; and Wang, A. S. D.: "The Dependence of Transverse Cracking and Delamination on Ply Thickness in Graphite/Epoxy Laminates," *Damage in Composite Materials*, ASTP STP 775, Ken Reifsnider, editor, American Society for Testing and Materials, 1982, pp. 118-139.

7. Parvizi, A.; Garret, K. W.; and Bailey, J. E.: "Constrained Cracking in Glass Fibre-Reinforced Epoxy Cross-Ply Laminates," *Journal of Materials Science*, Vol. 13, 1978, pp. 195-201.

8. Flaggs, D. L..; and Kural, M. H.: "Experimental Determination of the In Situ Transverse Lamina Strength in Graphite/Epoxy Laminates," *Journal of Composite Materials*, Vol. 16, 1982, pp. 103-116.

9. Laws, N. and Dvorak, G. J.: "Progressive Transverse Cracking in Composite Laminates," *Journal of Composite Materials*, Vol. 22, October 1988, pp. 900-916.

10. Bailey, J. E.; Curtis, P. T.; and Parvizi, A.: "On the Transverse Cracking and Longitudinal Splitting Behavior of Glass and Carbon Fibre Reinforced Epoxy Cross Ply Laminates and the Effect of Poisson

and Thermally Generated Strain," Proceedings of the Royal Society, London, A. 366, 1979, pp. 599-623.

11. Caslini, M.; Zanotti, C.; and O'Brien, T. K.: Study of Matrix Cracking and Delamination in Glass/Epoxy Laminates," Journal of Material Sciences, Vol. 13, 1978, pp. 195-201.

12. Chan, W. S.; and Wang, A. S. D.: "A Study on the Effects of the 90° Ply on Matrix Cracks in Composite Laminates," Proceedings of 27th Structures, Structural Dynamics and Materials Conference, San Antonio, TX, May 19-21, 1986, Technical Papers. Part I, New York, AIAA, pp. 689-694.

13. Weibull, W.: "A Statistical Distribution Function of Wide Applicability," *Journal of Applied Mechanics*, Vol. 18, 1951, pp. 293-297.

14 Bullock, R. E.: "Strength Ratios of Composite Materials in Flexure and Tension," *Journal of Composite Materials,* Vol. 8, April 1974, pp. 200-206.

15. O'Brien, T. K.; and Salpekar, S. A.: "Scale Effects on the Transverse Tensile Strength of Graphite Epoxy Composites," NASA TM107637, June 1992.

16. Atkins, A. G. and Caddell, R. M.: "The Laws of Similitude and Crack Propagation," *International Journal of Mechanical Sciences*, Vol. 16, 1974, pp. 541-548.

17. O'Brien, T. K.: "Characterization of Delamination Onset and Growth in a Composite Laminate," *Damage in Composite Materials*, *ASTM STP* 775, K. L. Reifsnider, Ed., American Society for Testing and Materials, 1982, pp. 140-167, New York, 1975.

Table 1. Summary of experimental data from tensile tests on ply level and sublaminate level scaled composite coupons. Modulus and maximum strain values were determined from back-to-back strain gages applied at the midspan of the coupons.

| LAY-UP | n=1 | | | n=2 | | | n=3 | | | n=4 | | |
|---|---|---|---|---|---|---|---|---|---|---|---|---|
| | Modulus msi | Strength psi | Max Strain % | Modulus msi | Strength psi | Max Strain % | Modulus msi | Strength psi | Max Strain % | Modulus msi | Strength psi | Max Strain % |
| $[0]_{8n}$ | 19.94 | 221603 | 1.14 | 19.84 | 195095 | 1.029 | 19.72 | 206865 | 1.013 | 20.31 | 194363 | 0.95 |
| $[02_n/90_{2n}]s$ | 10.75 | 122978 | 1.19 | 10.34 | 118850 | 1.122 | 10.20 | 111615 | 1.074 | 10.68 | 109674 | 1.014 |
| $[+15_n/-15_n/90_{2n}]s$ | 9.47 | 65042 | 0.726 | 9.16 | 46978 | 0.541 | 9.06 | 39335 | 0.446 | 8.83 | 33925 | 0.393 |
| $[+30_n/-30_n/90_{2n}]s$ | 6.09 | 39087 | 0.824 | - | 25051 | 0.542 | 6.03 | 22705 | 0.441 | 5.83 | 20199 | 0.395 |
| $[+45_n/-45_n/90_{2n}]s$ | 3.25 | 20329 | 0.843 | - | 12260 | 0.497 | 3.01 | 11493 | 0.577 | 2.85 | 11475 | 0.503 |
| $[+60_n/-60_n/90_{2n}]s$ | 1.93 | 9533 | 0.521 | 1.77 | 7661 | 0.443 | 1.79 | 6489 | 0.357 | 1.86 | 4881 | 0.287 |
| $[+75_n/-75_n/90_{2n}]s$ | 1.57 | 6345 | 0.417 | 1.48 | 6160 | 0.513 | 1.51 | 5158 | 0.334 | 1.47 | 4498 | 0.303 |
| $[90]_{8n}$ | 1.56 | 5689 | 0.366 | 1.46 | 5535 | 0.383 | 1.48 | 5521 | 0.377 | 1.47 | 5359 | 0.375 |
| $[+45_n/-45_n/0_n/90_n]s$ | 7.66 | 90165 | 1.418 | 7.52 | 81681 | 1.274 | 7.59 | 67253 | 1.025 | 7.40 | 54215 | 0.846 |
| $[(0_2/90_2)_2]s$ | | | | 10.74 | 126340 | 1.174 | | | | | | |
| $[(\pm15/90_2)_2]s$ | | | | 9.29 | 65903 | 0.725 | | | | | | |
| $[(\pm30/90_2)_2]s$ | | | | 6.07 | 49241 | 0.953 | | | | | | |
| $[(\pm45/90_2)_2]s$ | | | | 3.24 | 28122 | 1.286 | | | | | | |
| $[(\pm60/90_2)_2]s$ | | | | 1.88 | 13196 | 2.38 | | | | | | |
| $[(\pm75/90_2)_2]s$ | | | | 1.51 | 6100 | 0.406 | | | | | | |

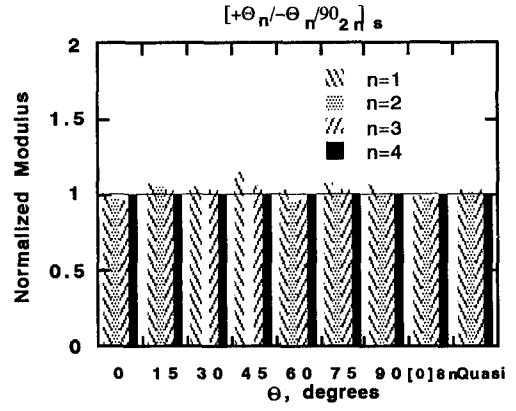



Figure 1. Normalized Modulus versus specimen size for ply level scaled composite tensile coupons. Sub-scale modulus values (n=1,2,3) have been normalized by the full-scale value (n=4) for each laminate family.

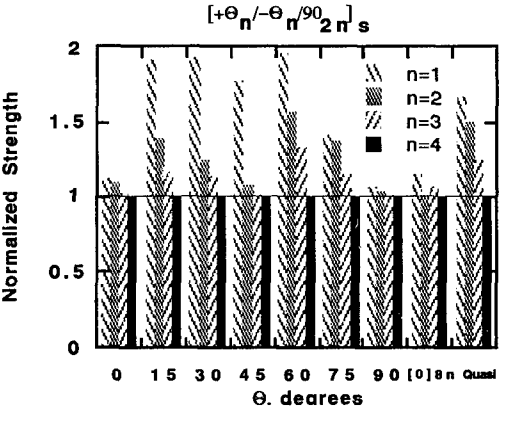



Figure 2. Normalized strength versus size for ply level scaled composite tensile coupons. Sub-scale strength values (n=1,2,3) have been normalized by the full-scale value (n=4) for each laminate family.

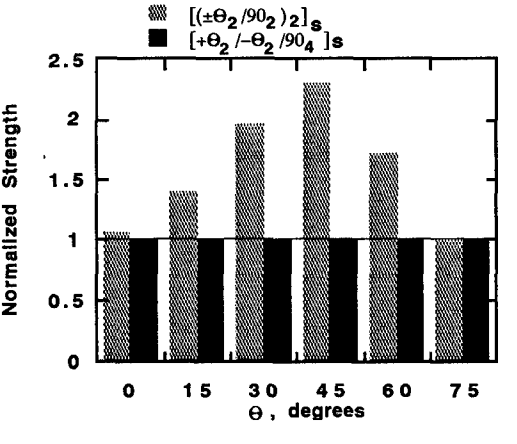



Figure 3. Normalized Strength versus angular orientation (θ) for ply level and sublaminate level 1/2 scale tensile coupons. Strength data were normalized by the ply level values for each lay-up.

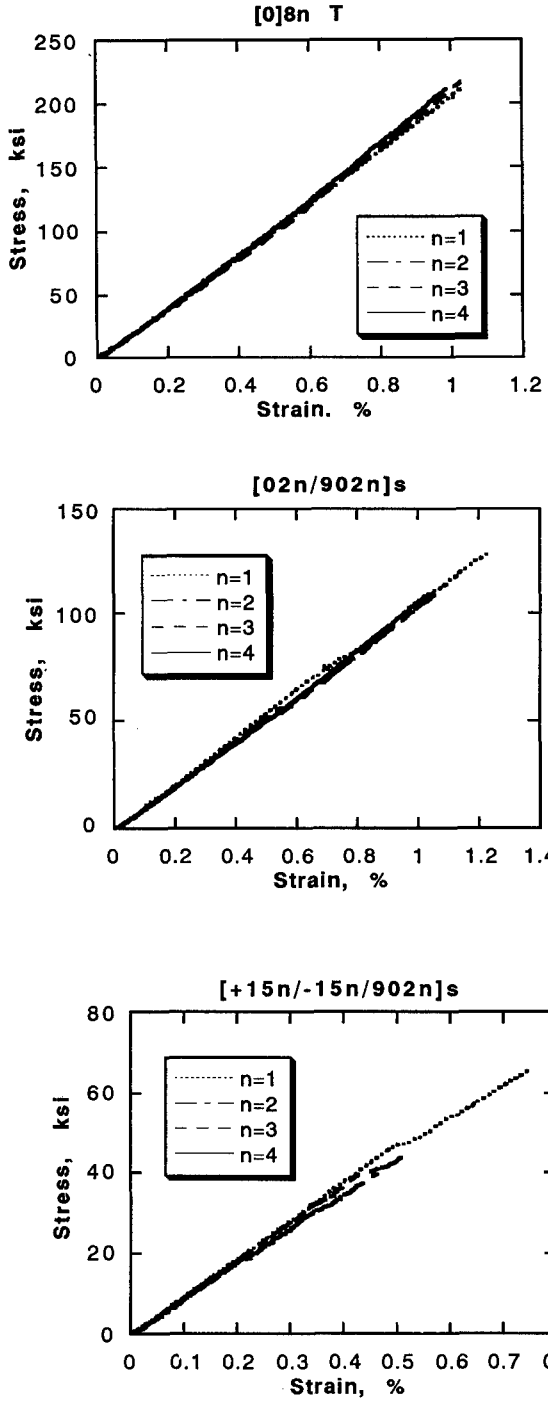
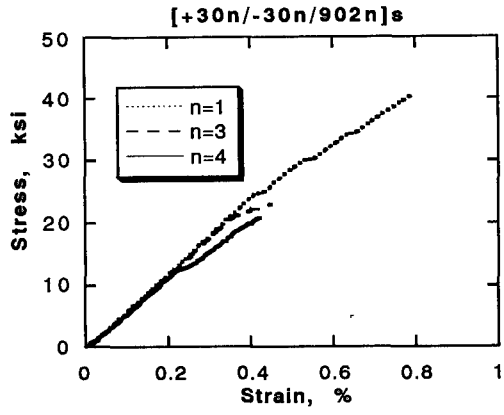
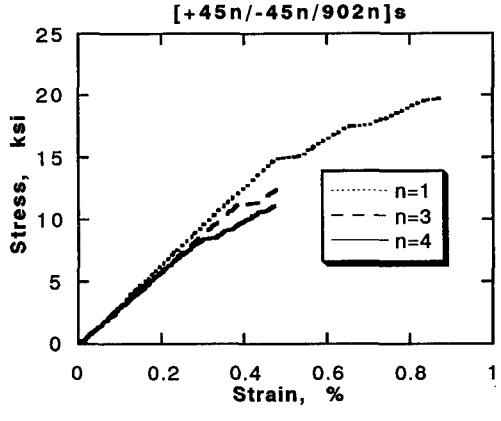



Figure 4. Stress vs. Strain plots of ply level scaled tensile coupons



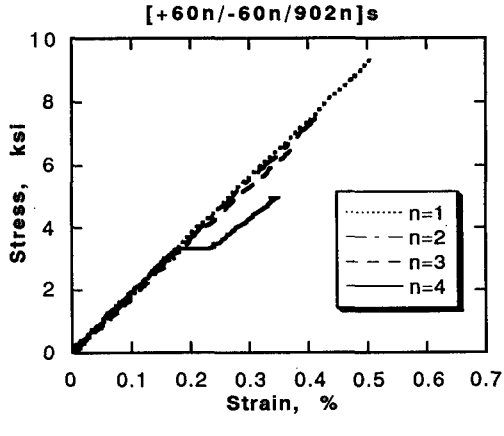




Figure 4. (cont.) Stress vs. Strain plots of ply level scaled tensile coupons

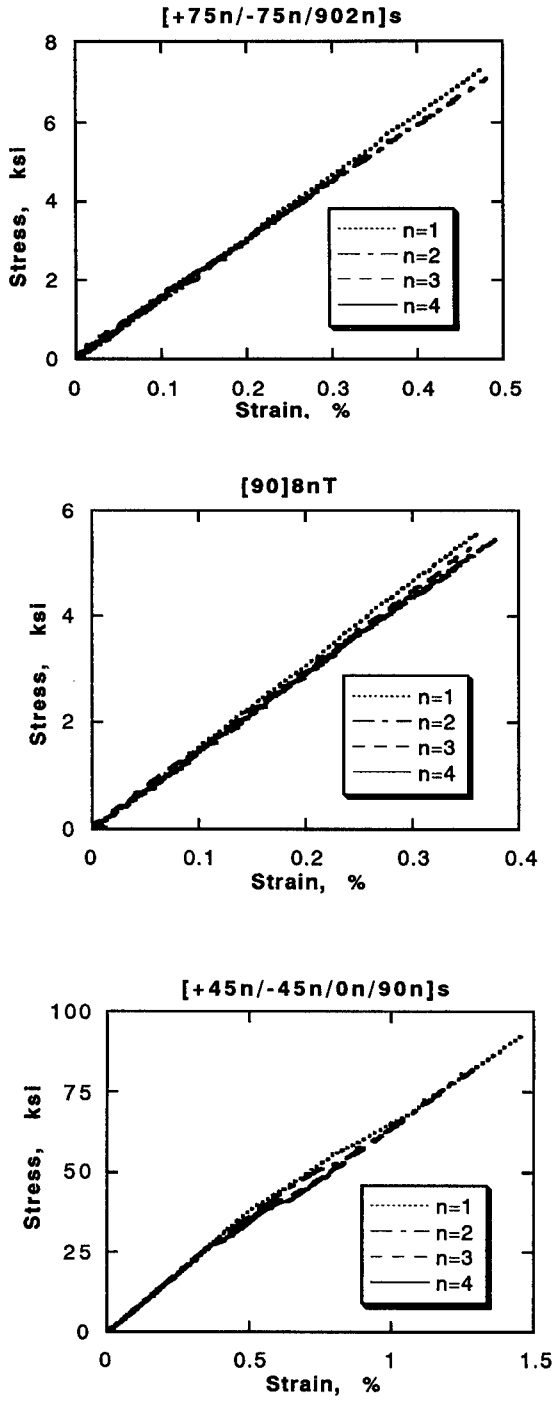



Figure 4. (completed) Stress vs. Strain plots of ply level scaled tensile coupons

# Deformation and Failure of Tungsten Composites

*T.K. Ramesh*
The Johns Hopkins University

"PAPER NOT AVAILABLE"

# Composite Hull

*W.E. Haskell*
Materials Directorate, ARL

"PAPER NOT AVAILABLE"

# Micromechanical Models for Textile Structural Composites

B.V. Sankar*, Associate Professor
R.V. Marrey, Graduate Student
Department of Aerospace Engineering,
Mechanics & Engineering Science
231 Aerospace Building, University of Florida
Gainesville, FL 32611-2031

## ABSTRACT

Finite element procedures for micromechanical analysis of textile structural composites are described. A method for predicting the engineering strength properties of textile composites is presented. In thin textile composites the stress gradients through the thickness are significant, and hence it is suggested that they may be modeled as homogeneous plates rather than homogeneous continua. Procedures for determining the plate stiffness properties and plate coefficients of thermal expansion are given. The failure envelope for a thin textile composite beam is described in the space of force and moment resultants instead of the stress space. Difficulties in finite element mesh generation are discussed, and a novel decomposition scheme is suggested so that regular elements can be used in micromechanical analyses.

## 1. INTRODUCTION

Recent developments in composites manufacturing technology are concerned with fabrication of near-net shape preforms, and introducing the matrix material using processes such as Resin Transfer Molding. Textile processes such as weaving and braiding can turn large volumes of yarn into dry preforms at a faster rate, thus reducing the cost and the cycle time. Unlike laminated structures, the three-dimensional woven or braided composites do not posses the weak plane of delamination, and have greater through-the-thickness strength, increased

impact resistance and fracture toughness. With the development in the aforementioned technologies, there is a need for developing efficient micromechanical analysis tools for predicting the thermomechanical, electromagnetic and other transport properties of these materials. Estimates of strength can also be made from micromechanical analyses.

## 1.1 Micromechanical Models

The micromechanical analyses for textile composites can be broadly classified into three categories: mechanics of materials type models[1-5], energy based approach, and finite element analysis of the unit cell[6-13]. All of the above models recognize that there is a representative volume element in the composite material, and they attempt to model the material as a homogeneous, but anisotropic - usually an orthotropic - material. In the mechanics of materials type models, the yarns are approximated as simple structural elements, *eg.*, beams, plates, laminates etc., and their deformation behavior is assumed to be governed by the corresponding structural constitutive relations. The kinematics is also simplified to a great extent, and a relation between the overall deformation of the unit-cell and the average forces are derived. The energetic approach is similar to the previous one, except that the strain energy in the unit-cell is evaluated based on some assumed displacement field, which is usually an oversimplification of exact displacements. The elastic constants are derived by equating the strain energy in the approximate model and the homogeneous composite. Mostly energy based approaches provide bounds for the homogeneous properties, and can be used as a check for experimental observations or other theoretical models.

The third method is the rigorous micromechanical analysis of the unit-cell, which often requires the use of numerical methods such as the finite element method, and also uses the exact three-dimensional constitutive relations for the yarn and the matrix material. Micromechanical models, in general, assume that unit-cells exist in all three dimensions, and determine the apparent homogeneous properties at a scale much larger than the dimensions of the unit-cell, but comparable to the dimensions of the structural component. The average stresses at a point at the structural scale will be called macrostresses. The actual stresses at a point at the continuum level will be called the microstresses. Another inherent assumption in micromechanical analyses is that the macrostresses do not vary rapidly so that they can be assumed to be nearly constant within a unit-cell. However the microstresses within the unit-cell are bound to have significant variations

because of discontinuities in the properties of the constituent materials. The objective of any micromechanical model is to predict the homogeneous properties of the composites, for example, elastic constants that relate the macrostresses to the macrostrains.

## 1.2 Stress Gradient Effects

The methods explained in the previous section assume that unit-cells exist in all the three directions in the textile composite. This will be true in the case of thick textile composites. However there are many applications in which thin composites are used. In fact, in order to take advantage of the properties of composites, the structures have to be made of thin plate like members with stiffeners for load transfer. In such cases there will be fewer unit cells in the thickness direction. Thus the free surface effects will be predominant. There will be severe stress gradients through the thickness, and they will have an influence on the apparent stiffness and strength of the structure. In such situations it will be useful to define the constitutive relations in a form that captures the effects of the through-the-thickness gradients. Plate theories provide a framework for achieving this. In other words, the textile composite can be approximated as a homogeneous plate (or shell) rather than a homogeneous continuum. Another advantage to this approach is that most of the structural analysis procedures and codes use plate models, and require plate properties as input. Then it is natural to provide the homogeneous plate properties of the textile composite. A similar situation exists even in thick textile composites near the free surface. If numerical methods are used for structural analysis, then the interior of the composite can be modeled as a homogeneous continuum, and the portions near the free surfaces as plates. The strength theories can also be modified so that they can be expressed in the space of force and moment resultants.

## 1.3 Scope of the Paper

In this paper the procedures for determining the thermo-mechanical properties of textile structural composites using the finite element micromechanical analysis of the unit-cell are described. The focus will be on the stress gradient effects described above, methods for determining them and their effects on the composite properties. The properties we have considered are: (a) Stiffness properties characterized by constitutive relations; (b) Coefficients of thermal expansion; and (c) Engineering strength properties. The residual stresses due to curing of the composite are also computed, and the differences between thin and

thick composites are discussed. Difficulties in FE mesh generation are discussed. A novel decomposition scheme is presented, in which regular elements can be used to obtain accurate results.

## 2. FINITE ELEMENT ANALYSIS OF THE UNIT-CELL

A detailed account of finite element procedures for determining the elastic constants, CTE's and failure envelopes can be found in References 10-13. In the following sections the essential principles governing the formulation are described.

### 2.1 Elastic Constants

In this paper a rectangular parallelepiped is considered as the unit-cell and the composite will be modeled as orthotropic in the macroscale. The length of the unit-cell in the $x_i$ direction is $L_i$. Our objective is to derive a macroscale constitutive relations in the form:

$$\sigma_i = C_{ij}(\epsilon_j - \alpha_j \Delta T), \qquad (i,j=1,2,...6) \tag{1}$$

where $\sigma_i$ and $\varepsilon_j$ are the macroscale stresses and strains respectively; $C_{ij}$ is the orthotropic stiffness matrix; $\alpha_j$ represents the macroscale CTE's and $\Delta T$ is a uniform temperature change. A macroscopically homogeneous deformation can be represented as :

$$u_i = H_{ij} x_j , \qquad i,j=1,2,3 \tag{2}$$

where $H_{ij}$ are the displacement gradients. The unit-cell of the composite is modeled by 3-D solid finite elements. The unit cell is subjected to deformations corresponding to Eq. (2) in the macroscale. The average macrostresses required to create each deformation are computed from the FE model. Continuity of microstresses across the unit-cell surfaces then requires that traction be equal and opposite at corresponding nodes on opposite faces of the unit cell. Similarly the displacements have to be continuous too. The periodic traction boundary conditions to be imposed on a pair of opposite faces (*e.g.*, $x_1=0$ and $x_1=L_1$) are:

$$F_i(L_1,x_2,x_3) = -F_i(0,x_2,x_3), \qquad (i=1,2,3) \tag{3}$$

$$u_i(L_1,x_2,x_3) - u_i(0,x_2,x_3) = H_{i1}L_1, \quad (i=1,2,3) \qquad (4)$$

The above boundary conditions are enforced by using multipoint constraint elements. The average stresses at the macroscopic level can be found by two methods. In the first method, the macroscopic stresses are assumed to be equal to the volume-averages of the corresponding microstress components in the unit-cell. In the second method, the macroscopic stresses are computed by averaging the nodal forces on each face of the unit cell[10]. In order to predict the orthotropic stiffness matrix $C_{ij}$, we choose $H_{ij}$ such that only one component of the strain is nonzero. The corresponding macroscopic stresses for $\Delta T=0$, are computed using one of the procedures indicated above. Substituting the values of the stresses and strains in the constitutive relation, Eq. (1), the stiffness coefficients in the column corresponding to the nonzero strain can be calculated. This procedure is repeated for other strain components to obtain all the stiffness coefficients, from which the orthotropic elastic constants of the material can be determined.

2.2 Thermo-Mechanical Properties

The textile composite, in general, will have six macroscale CTE's. To compute them we choose $H_{ij}$ such that all components of strain are zero, *i.e.*, $H_{ij}=0$. Then the composite constitutive relation will reduce to

$$\sigma_i = - C_{ij}\alpha_j \Delta T, \qquad i,j=1,2,...,6 \qquad (5)$$

From the finite element results, the macroscopic stresses are computed for an arbitrary temperature difference $\Delta T$, which are then substituted in Eq. (5) to obtain the CTE's. The residual thermal stresses due to the curing process are obtained by superposing stresses due to two load cases as explained below. In the first load case the macroscopic deformations of the unit cell are set to zero, *i.e.*, the composite is constrained from contracting in the macroscale, and a uniform temperature change is applied to all elements ($\epsilon_i=0$, $\Delta T=-T_0$, where $T_0$ is the curing temperature). Since the cured composite is supposed to undergo free contraction, the forces required to restrain the contraction in the first problem are removed by reversing the same. This can be accomplished by imposing deformations such that $\epsilon_i=-\alpha_i T_0$. The microstress distribution within the unit-cell obtained from each load case are added to obtain the residual stresses due to curing.

## 2.3 Strength Modeling

There are many failure criteria or strength theories for unidirectional fiber composites. This for example includes maximum stress theory, maximum strain theory, and Tsai-Hill theory. Even though failure of a material is a very complex phenomenon, engineering strength theories such as the above have been found to be useful in design. Our approach is similar to that used by Dvorak *et al*[14]. A state of homogeneous deformation is applied to the unit cell as explained in §2.1. Assuming linear elastic behavior, microstresses can be computed for any arbitrary state of macrostrains. We also assume that the failure behavior of the matrix material and the yarn are known. The textile composite is assumed to have failed, if there is failure in any one of the finite elements, either matrix or the yarn or at the yarn-matrix interface. By varying the macrostresses using a numerical simulation, failure envelopes can be obtained for the idealized homogeneous material.

# 3. STRESS GRADIENT EFFECTS

One method of overcoming the difficulties in modeling thin textile composites (see §1.2) is to compute the structural stiffness properties (*eg.*, [A], [B] and [D] of the plate) directly from the unit cell analysis instead of the continuum stiffness properties. In the case of strength predictions, the failure envelopes can be developed in terms of the force and moment resultants instead of stresses. In the following we illustrate these concepts for the case of a plain weave textile composite beam.

## 3.1 Beam Stiffness Coefficients

Consider a textile composite beam in the *xz*-plane with unit cells repeating in the *x*-direction. On the macroscale, the beam is assumed to be homogeneous and the beam behavior is characterized by the following constitutive relation:

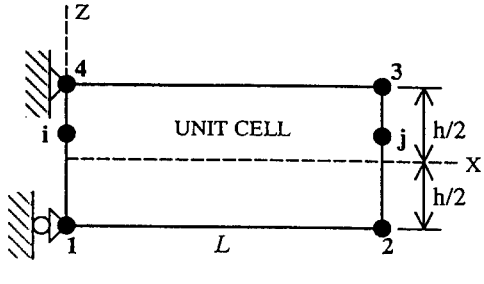
$$\lfloor P\ M\ V \rfloor^T = [K]\left[\lfloor \epsilon_0\ \kappa\ \gamma_0 \rfloor^T - \lfloor \alpha_P\ \alpha_M\ \alpha_V \rfloor^T \Delta T\right] \qquad (6)$$

where $P$, $M$ and $V$ are the axial force, bending moment and transverse shear force resultants respectively; [K] is the symmetric matrix of beam stiffness coefficients; $\varepsilon_0$, $\kappa$ and $\gamma_0$ are the midplane axial strain, curvature and transverse shear strain respectively; $\alpha_P$, $\alpha_V$ and $\alpha_M$ respectively are the thermal expansion, shear and bending coefficients. The detailed procedure for evaluating [K] is given in Sankar and Marrey[10]. However the principles involved are described briefly for the

sake of completion. In order to find the beam stiffness [K], three linearly independent deformations are applied to the unit cell, namely, (i) unit axial strain; (ii) unit curvature with a transverse deflection such that the shear strain vanishes; (iii) unit transverse shear strain. The periodic displacement boundary conditions for the three unit deformations are given in the table in Fig. 1. The temperature change, $\Delta T$, is assumed to be zero. For each case, the axial force $P$, the bending moment at the center of the unit cell $M_c$, and the shear force $V$ are computed from the nodal forces. By substituting the values of $P$, $M_c$ and $V$ in Eq. (6), one can evaluate the stiffness coefficients. The procedure for determining the beam thermal expansion coefficients is very similar to that given in §2.2.

### 3.2 Strength Models for a Textile Composite Beam

In this section we construct a failure envelope for a textile composite under a general combination of loads. For a textile composite beam, the failure envelope is constructed in the space of the three force resultants P, M and V. The textile composite beam is assumed to be in the 1-3 plane with unit-cells repeating in the 1 direction. Three linearly independent deformations are applied to the unit- cell as explained in §3.1. For each deformation the six microstresses, $\sigma_i$ (i=1,...,6), are computed at the center of each element. The influence coefficient $a_{jk}^{(i)}$ (j=1,...,6; k=1,2,3), is defined as the $j^{th}$ microstress for the $k^{th}$ deformation at the center of the $i^{th}$ element. For an arbitrary combination of loads, P, M and V, on the textile beam, the microstresses can be found by superposition of macro-deformations. The composite is assumed to have failed if there is failure in any one of the finite elements in the unit-cell. By varying P, M and V using a numerical simulation, the failure envelope can be plotted.




| Type of deformation | $u(L,z)-u(0,z)$ | $w(L,z)-w(0,z)$ |
|---|---|---|
| unit axial strain | $L$ | $0$ |
| unit curvature | $Lz$ | $-L^2/2$ |
| unit shear strain | $0$ | $L$ |

Fig. 1. Unit-cell boundary conditions for a beam

# 4. FINITE ELEMENT MESH GENERATION

## 4.1 Homogeneous Elements

By homogeneous elements we mean finite elements which are made up of only one material. This distinction has become important in the wake of the concept of inhomogeneous elements introduced and studied in detail by Foye[6]. More on inhomogeneous elements will be given in subsequent sections. Traditionally finite element models use elements that are homogeneous. In the context of textile composites, it means that the yarn and the matrix are modeled by separate elements. This is indeed preferable because the stresses at the yarn-matrix interface can be computed accurately. However meshing-especially the interstitial matrix region- becomes very difficult. The Node Migration Method developed by the authors is described in the next section.

## 4.2 Node Migration Method

The unit-cell is meshed with tetrahedral solid elements in an arbitrary fashion. This will be called the primitive mesh. The elements are identified as homogeneous or inhomogeneous. Then the nodes of the inhomogeneous elements are moved to the interface by using an heuristic algorithm. In each inhomogeneous element the node closest to the interface is allowed to migrate to the interface first. After each cycle, some elements will transform into homogeneous elements. Then the process is repeated until all the elements become homogeneous. The mesh thus generated is called the intermediate mesh.

The intermediate mesh will have some elements distorted due to node migration. This distortion can be removed by subjecting the mesh to an annealing process[15], by which the distortions concentrated near the interfaces in the first-stage mesh are distributed among other elements also.

## 4.3 Inhomogeneous Elements

Inhomogeneous elements in micromechanical analyses were studied in detail by Foye[6]. The advantage of using inhomogeneous elements is that mesh generation can be very simple. For example, the unit-cell can be discretized into rectangular parallelepipeds. The stiffness matrix of inhomogeneous elements represent smeared properties of the two phases determined by the numerical integration scheme. Thus the solution will be approximate in the interface regions. Foye has developed a modified method to evaluate the stiffness matrix of

inhomogeneous elements called Replacement Elements, which predict better stresses than the conventional inhomogeneous elements.

The problem with inhomogeneous elements is that they cannot represent the jump in strains that can occur at the yarn-matrix interface. In fact there are three strain components that can be discontinuous at the interface, but the corresponding stresses must be continuous. Such a behavior cannot be represented by inhomogeneous elements which assume a continuous strain fields within the element. This problem can be resolved by decomposing the displacement field into two parts: a displacement field $\{q_1\}$ that produces a strain field continuous everywhere in the unit-cell, and the second one $\{q_2\}$ that has a strain discontinuity at the yarn-matrix interface. The field $\{q_2\}$ can be assumed to be such that the displacements are identically equal to zero everywhere in the matrix and at the interface, and exist only in the interior of the inclusions. Thus one can use inhomogeneous elements for solving the first set of displacements. The second set of displacements exists only in the inclusions, and they can be solved by discretizing only the inclusion. However the issue is determining the decomposition $\{q\}=\{q_1\}+\{q_2\}$. The condition for the decomposition is that the jump in interfacial stresses should be equal and opposite in the two problems, since the interfacial stresses are continuous in the given problem.

4.4 Stiffness Matrix of Inhomogeneous Elements

A method for computing [K] of a unit-cell containing inhomogeneous elements is as follows. The elasticity matrix [C] can be divided into two parts, $C=C_1+C_2$, where $C_1$ is equal to that of matrix everywhere in the unit-cell, and $C_2$ exists only in the yarn and equal to the difference between the yarn and matrix stiffnesses. The strain energy in the unit-cell can be evaluated as:

$$U=\left(\frac{1}{2}\right)q^T\int_{\Omega} B^T C_1 B dv\, q + \left(\frac{1}{2}\right)q^T\int_{\Omega_y} B^T C_2 B dv\, q \qquad (7)$$

The first integration is performed in the entire domain of the unit-cell, and regular elements, *eg.*, rectangular parallelepipeds, can be used. The second integration is performed within the inclusion. A different mesh can be used for this integration. Since the inclusion is a simply-connected domain, FE meshing is not a problem. The two stiffness matrices cannot be added directly, because they are referred to different

set of nodal displacements. A transformation matrix T between the two sets of meshes have to be found such that

$$[K]=[K_1]+[T^T][K_2][T] \tag{8}$$

## 5. RESULTS AND DISCUSSION

The methods discussed in §2 and §3 were verified by considering homogeneous and bimaterial beams for which exact solutions are known, and applied to a plain weave textile composite beam[10-13]. The dimensions of the unit-cell and yarn architecture were taken from Ref. 8. The length and height of the unit-cell were 3.6 and 1.8 mm respectively. The yarn was modeled as a transversely isotropic material: $E_L$=159 GPa, $E_T$=10.9 GPa, $G_{LT}$=6.4 GPa, $\nu_{LT}$=0.38. The matrix was an isotropic material with E=3.5 GPa and $\nu$=0.35. The unit-cell and their deformations are shown in Fig. 2. The nonzero values of the [K] in SI units were: $K_{11}$ ($A_{11}$) = $27.76\times10^6$, $K_{22}$ ($D_{11}$) = 5.41, and $K_{33}$ ($A_{55}$) = $8.14\times10^6$. From $K_{11}$ the Young's modulus $E_x$ of the textile beam may be calculated as 15.42 GPa. If this is used to compute the flexural stiffness as $D_{11}=E_x h^3/12$, one will obtain $D_{11}$ = 7.5 Nm, where as the actual $D_{11}$ is 5.41 Nm. Similar observations can be made with regard to other stiffness coefficients[10]. This example illustrates the usefulness of computing the beam stiffness directly from the micromechanical analysis. The CTE's for the textile beam were computed as[12] $\alpha_P=12.6\times10^{-6}$ and $\alpha_M=-24.12\times10^{-6}$. These values could not have been obtained from the continuum CTE's of the same material.

Figures 3 and 4 depict the strength of the beam in the force and moment resultants space[13]. The solid lines refer to the continuum hypothesis. The symbols denote beam micromechanical analysis. Both methods used the same failure criteria for the matrix and the yarn. However one can see from the figure that modeling the textile composite as a homogeneous continuum leads to more conservative strength estimates. More results for various methods described in this paper can be found in Refs. 10-13. Examples for the Node Migration Method can be found in Ref. 15.

ACKNOWLEDGEMENT

This research is supported by a grant from NASA Langley Research Center (NAG-1-1226) to the University of Florida. Mr. Wade C. Jackson is the grant monitor.

## REFERENCES


[1]Ishikawa, T. and Chou, T. W., *J. Comp. Mater.*, **17** (1983), 92-104.
[2]Ishikawa, T. and Chou, T. W., *J. Mater. Sci.*, **18** (1983) 2260-8
[3]Ishikawa, T. & Chou, T. W., *AIAA J.* **21** (1983) 1714-21
[4]Yang, J. M. & Chou, T. W., *(ICCM VI).* **5** (1987), 579-588
[5]Ma, C. L., Yang, J. M. & Chou, T. W., *ASTM STP 893.* (1986) 404-21
[6]Foye, R.L., *NASA CR-189597*, February 1993
[7]Whitcomb, J. D., *ASTM STP 1110.* (1991) 417-38
[8]Yoshino, T. & Ohtsuka, T., *Bull. JSME,* **25-202** (1982) 485-92
[9]Dasgupta, A., Bhandarkar, S., Pecht, M., and Barker, D., *Proc. Am. Soc. Composites. V Tech. Conference.* (1990) 1001-10
[10]Sankar, B. V. and Marrey, R. V., *Composites Science and Technology (in press)*
[11]Sankar, B. V. and Marrey, R. V., *Technical Note CAC-TN-92-01, Center for Advanced Composites. University of Florida.*
[12]Marrey, R.V. and Sankar, B.V., *Proc. Am. Soc. Composites. VIII Tech. Conference (1993).* (in press).
[13]Marrey, R.V. and Sankar, B.V., *ASME Winter Annual Meeting (1993)*, (in press).
[14]Dvorak, G.J., Rao, M.S.M. and Tarn, J.Q., *J. Comp. Materials*, Vol. 7, 1973, pp. 194-216.
[15]Marrey, R.V. and Sankar, B.V., *Technical Report AeMES TR-93-1-03*, University of Florida, Gainesville.

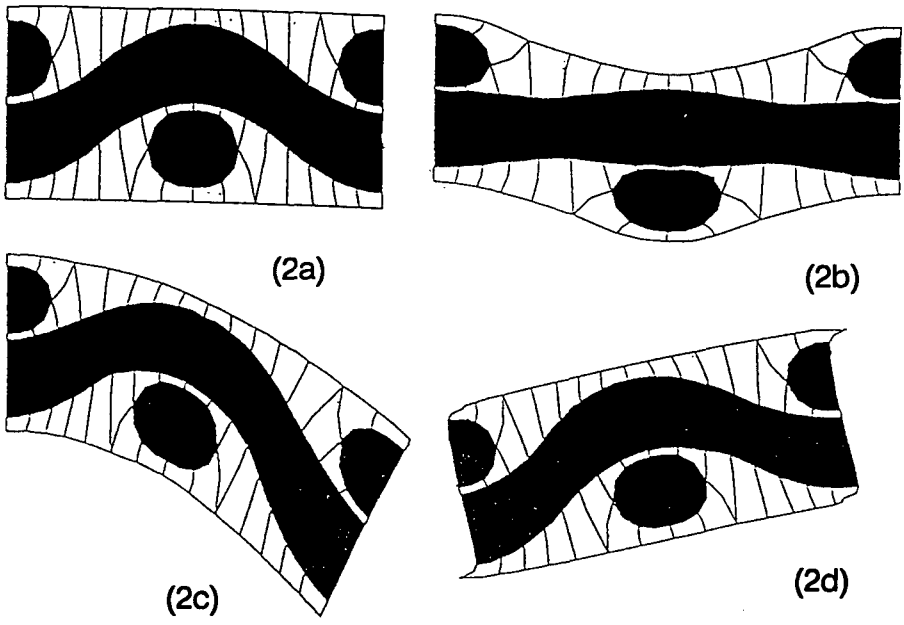




**Fig. 2. Deformations in a unit-cell: (a) Undeformed; (b) axial extension; (c) pure bending; (d) transverse shear**

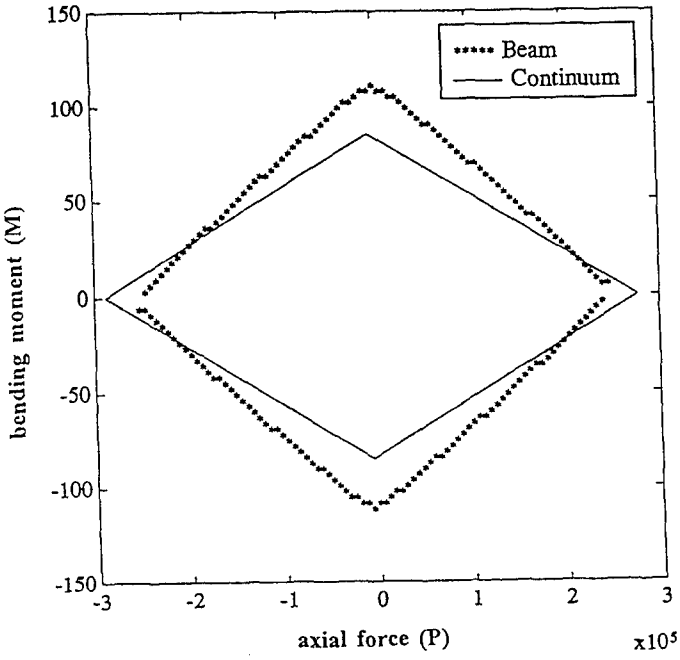



Fig. 3. Comparison of failure envelopes based on matrix failure

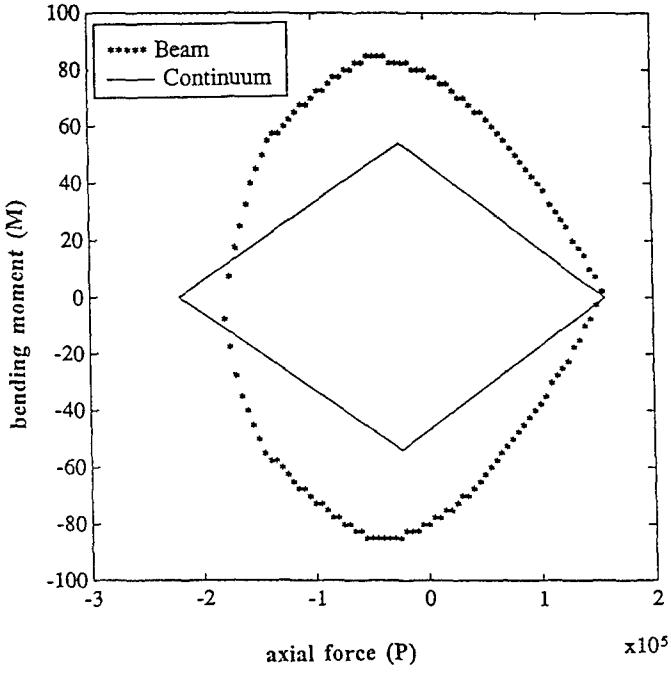



Fig. 4. Comparison of failure envelopes based on yarn failure

# Stress Concentration and Post Matrix Yield at Fiber Breaks in Hybrid Composites

Prof. John N. Rossettos* and Dr. Massoud Olia
Department of Mechanical Engineering
Northeastern University,Boston MA 02115-5096

## Abstract

The post matrix yield problem is formulated for a finite width hybrid composite monolayer,which contains an alternating arrangement of high modulus (HM) and low modulus (LM) fibers. The difference in the axial stiffness of such fibers has an important effect on the growth of the yield zone and stress concentration. Whether the broken fibers are LM or HM , and whether they are edge or internal breaks makes a difference. A material parameter, which relates the load required to break a fiber to the load to yield the matrix,is defined, and allows definition of a unique stress concentration factor which considers matrix yielding.

## Introduction

Hybrid composites, where more than one type of fiber is contained in a common matrix,provide a means to develop an optimum balance between stiffness and strength. In the analysis of failure mechanisms,the stress concentration which occurs near fiber breaks, together with the level of matrix yielding, are important cosiderations. The fiber load concentration determines a load sharing rule, which is used in statistical models of strength prediction as discussed by Fukuda(1985), and Zhu etal(1989). To date, load sharing rules have been based on an elastic matrix response at the fiber break. Matrix yielding can have an important effect on such rules, especially for metal matrix composites.

In the present work, the problem of matrix yielding at fiber breaks is formulated for a finite width hybrid composite monolayer. The shear lag model, which continues to be useful even in cases of relatively stiff matrices [Reedy(1984);Rossettos(1987)] is used. It is assumed that the matrix yields in an elastic -perfectly plastic sense

only in the matrix bay between the last fiber break(in a series of fiber breaks) and the adjacent intact fiber. This assumption is suggested by the results given by Dvorak and Bahei-El-Din(1988), and Goree and Gross(1979), and its validity is checked aposteriori by the present results.

The hybrid parameter,R,which appears in the equations,and first introduced by Fukuda and Chou(1983), is the ratio of the axial stiffness of the low modulus(LM) to the high modulus(HM) fibers. They indicated the presence of a hybrid effect where the high modulus fibers can sustain higher loading and elongation than when they exist alone in a non-hybrid composite. An eigenvector expansion approach is used here to solve the system of equations, and is very convenient for finite width geometry, edge breaks, arbitrary values of R and other practical configurations. The extent of the yielded region as a function of applied load, and the fiber stress concentration near the yielded region are determined, and the infinite sheet results of Hedgepeth and Van-Dyke(1967) are approached as the total number of fibers is increased, and when R=1. The results show how matrix yielding reduces the stress concentration (SCF). The effects of the hybrid parameter,R, are indicated, and depend strongly on the number of broken fibers and whether the broken fibers are HM or LM. The SCF for elastic matrix behavior is compared with that of a yielding matrix,for a different number of fiber breaks,and involves the introduction of a material parameter which is a measure of the fiber breaking strength compared to the matrix yield strength.

## Analysis

In the lamina analysis,we consider a finite width sheet consisting of 2q+1 fibers parallel to the x-axis or load direction(see Fig.1). The center fiber is the zeroeth,and the fibers above it are numbered so that n equals 1 to q. Below it they are numbered -1 to -q. There is an alternating arrangement of HM and LM fibers, where one or more fibers are broken in a continuous manner at x=0. The axial load and displacement in the nth fiber are denoted by $p_n(x)$ and $u_n(x)$. In what follows, asterisks will also denote quantities related to LM fibers. Force equilibrium is based on the shear lag model where fibers take the axial load and the matrix is in pure shear, and involves a force balance between the varying fiber load, $dp_n/dx$ , and the shear in the matrix on either side of the fiber. For instance, the shear force per unit length between the nth and n+1 th fiber, where the nth fiber is HM, is $Gh(u^*_{n+1} - u_n)/d$. It is $Gh(u_n - u^*_{n-1})/d$ between the nth and n-1 th fiber; d is the distance between fibers and h is the sheet thickness.

The resulting equilibrium equations for HM and LM fibers are,respectively, given by

$$EA\frac{d^2u_n}{dx^2}+(\frac{Gh}{d})(u^*_{n+1}-2u_n+u^*_{n-1})=0 \qquad \text{(n=0,2,4,..)} \qquad \text{(1a)}$$

$$E^*A^*\frac{d^2u^*_n}{dx^2}+(\frac{Gh}{d})(u_{n+1}-2u^*_n+u_{n-1})=0 \qquad \text{(n=1,3,5,...)} \qquad \text{(1b)}$$

where EA and G are the fiber extensional stiffness and matrix shear modulus. It is noted that in Eqs.(1), n=0 is an HM fiber. The equations are easily written when n=0 is an LM fiber instead. The fiber load-displacement relations are

$$p_n=EA\frac{du_n}{dx} \quad , \quad p^*_n=E^*A^*\frac{du^*_n}{dx} \qquad (2)$$

To proceed further, we consider the symmetrical case as indicated in Fig.1 where x=0 is an axis of symmetry, and the fiber breaks are symmetrical about the n=0 break. The extent of the matrix yield region is given by x=a, and yielding is assumed to occur in the matrix between the last fiber break and the first intact fiber. The matrix yields in an elastic-perfectly plastic sense when the shear stress $\tau$ reaches the yield value, $\tau_c$. The right half of Fig.1 is then divided into regions I and II where the extent of region I is that of the yield zone. Appropriate boundary and continuity conditions will need to be applied to these regions. Eqs.(1) hold throughout region II, but in region I they hold for all fibers except fibers N and N+1, where n+N is the last broken fiber which is next to an intact fiber(n=N+1) Force equilibrium of these two fibers contains a constant shear, $\tau_c$, above fiber N and below fiber N+1, so that these two equations will differ from Eqs.(1). In what follows, due to symmetry, we will consider only positive values of n including n=0. When fiber breaks occur at the edge of the lamina, the same approach is used. For instance, if there are three breaks at say the n=q,q-1,andq-2 fibers, then the yield zone will occur in the matrix between the q-2 and q-3 fibers. The other matrix bays in region I, in all edge break cases studied , are tested to confirm that in fact yielding does not occur there(ie.the shear stress is less than the yield value $\tau_c$.

Nondimensional fiber loads,$P_n$, and displacements,$U_n$, are next defined by

$$(p_n, p^*_n) = p(P_n, P^*_n) \;\; ; \;\; (x,a) = \sqrt{\frac{EAd}{Gh}}(\xi, \alpha)$$

$$(u_n, u^*_n) = p\sqrt{\frac{d}{EAGh}}(U_n, U^*_n); \quad R = \frac{E^*A^*}{EA} \tag{3}$$

The quantity p is the HM fiber load ar infinity(ie.,far from the damaged region), $\xi$ is a dimensionless coordinate in the x direction and $\alpha$ is the nondimensional extent of the yield region (Fig.1). With Eqs.(3), Eqs(1) and (2) become

$$U_n'' + U^*_{n+1} - 2U_n + U^*_{n-1} = 0 \qquad (n = 0,2,4,\ldots)$$

$$RU^{*''}_n + U_{n+1} - 2U^*_n + U_{n-1} = 0 \qquad (n = 1,3,5,\ldots) \tag{4}$$

and

$$P_n = U_n', \; P^*_n = RU^{*'}_n, \quad (\;)' = \frac{d(\;)}{d\xi} \tag{5}$$

For edge fibers which are say,HM fibers,we also have

$$U_q'' + U^*_{q-1} - U_q = 0 \qquad (n = q) \tag{6a}$$

$$U_{-q}'' + U^*_{-q+1} - U_{-q} = 0 \qquad (n = -q) \tag{6b}$$

As indicated, Eqs.(4) and (6) hold in region II, but in region I they hold for all fibers except fibers N and N+1, where n=N is the last broken fiber which is next to an intact fiber(n=N+1). For instance ,in Fig.1, N=2. Since we will be dealing with symmetry about fiber n=0, we need only consider positive values of n. Therefore,in region I,where yielding occurs, the equations for fibers N and N+1 (if fiber N is say an LM fiber) are given by

$$RU^{*''}_N + U_{N-1} - U^*_N - T = 0 \tag{7a}$$

$$U_{N+1}'' + U^*_{N+2} - U_{N+1} + T = 0 \tag{7b}$$

If there is only one broken fiber(N=0) and is HM, then from symmetry, the matrix yields on either side of the n=0 fiber and Eq.(7a) is replaced by

$$U_o'' - 2T = 0 \tag{8}$$

where the nondimensional shear,T,is defined by

$$T = \sqrt{EAdh/G}(\tau/p) \tag{9}$$

In Eqs.(7,8), T is a constant where the shear stress, $\tau$ , in Eq.(9) has the yield value, $\tau_c$. With the nondimensionalization in Eq.(3) it is seen that T can also be written in terms of dimensionless displacements in the yield region between fibers N and N+1 (where N is say LM) by

$$T = (U_N^* - U_{N+1})_{\xi=\alpha} \tag{10}$$

## Boundary Conditions and Solution Procedure

The boundary conditions associated with the system of equations given by Eqs.(4),(6a) and (7), in the symmetric case, will be given by using subscripts I and II to refer to solutions in regions I and II respectively. In region I, we have at $\xi$=0

$$U_{In} = 0 \ (unbroken\ fibers); P_{In} = 0 \ (broken\ fibers) \tag{11}$$

Since all fibers are continuous at $\xi = \alpha$, we also have

$$U_{In}(\alpha) = U_{IIn}(\alpha) \quad ; \quad P_{In}(\alpha) = P_{IIn}(\alpha) \tag{12}$$

Note that in Eqs.(11) and (12) starred quantities to be used for LM fibers have not been specified. Once a specific configuration has been selected appropriate conditions can be written in a straightforward manner. If a uniform strain is assumed far from the fiber break region, then the following must also hold for nondimensional quantities at $\xi = \infty$,

$$P_n = 1, \ P_n^* = R, \ \ U_n' = U_n^{*\prime} = 1 \tag{13}$$

The system of equations, namely Eqs.(4).(6a) and (7a,b), are then written in matrix form for region I as

$$\mathbf{U}'' - \mathbf{L}\mathbf{U} = \mathbf{0} \tag{14}$$

where $\mathbf{L}$ is banded and $\mathbf{U}^{\mathbf{T}} = \left[U_q, U^*_{q-1}, \ldots U_2, U^*_1, U_o\right]$. In the case of one central break, Eq.(8) can be solved separately and the system(Eqs.14) will consist of the remaining equations. A solution to Eq.(14) is assumed in the form $\mathbf{U} = \mathbf{R}e^{\lambda\xi}$. The resulting eigenvalue problem , $(\mathbf{L} - \lambda^2\mathbf{I})\mathbf{R} = \mathbf{0}$, in region I leads to eigenvalues, $\lambda_i^2$,and eigenvectors, $\mathbf{R}^i$, and the solution to $\mathbf{U}$ can be written as the expansion,

$$\mathbf{U}_I = \sum_{i=1}^{q+1} \mathbf{R}^i (B_i e^{\lambda_i \xi} + C_i e^{-\lambda_i \xi}) + \mathbf{U}_{Ip} \tag{15}$$

where $\mathbf{U}_{Ip}$ represents the particular solution involving the constant $T$. In region II,where Eqs.(4) and (6a) hold, the eigenvalue problem leads to eigenvalues, $\beta_i^2$, and eigenvectors, $\mathbf{Y}^i$. The $+\beta_i$ are discarded to satisfy Eq.(13) at $\infty$ and the solution is given by

$$\mathbf{U}_{II} = \sum_{i=1}^{q+1} D_i \mathbf{Y}^i e^{-\beta_i \xi} + \mathbf{U}_{IIp} \tag{16}$$

where $\mathbf{U}^T_{IIp} = \left[\xi, \xi, \ldots \xi\right]$ is added to again satisfy the conditions at infinity(Eqs.13). The constants, $B_i, C_i \; and \; D_i$ are then determined by using the boundary and continuity conditions.

Now, in order to find a relation between the dimensionless extent of the yield zone, $\alpha$, and the applied load,p, we proceed as follows . First note that the dimensionless shear quantity,T, is given by Eq.(10) in terms of displacements. By selecting values of the quantity $\alpha$, the defined boundary value problem yields solutions for the displacements, $\mathbf{U}$, and the value of T corresponding to the $\alpha$ value selected. In the solution process, Eq.(10) is an additional equation which is added to the system of equations(Eqs.14). The value of load, p, which just starts matrix yielding (at $\tau = \tau_c \; and \; \alpha = 0^+$) is denoted by $p_{\lim it} = p_L$ , with its corresponding value, $T_{\lim it} = T_L$,where $T$ is defined by Eqs.(9) and (10). We therefore have,

$$T_L = \sqrt{EAdh/G}\left(\tau_c / p_L\right) = \left(U^*_{I,N} - U_{I,N+1}\right)_{\xi=0^+} \tag{17a}$$

where subscript $I$ denotes solutions in region I. Also, the value of $T$ for arbitrary $\alpha$ and $p$ is given by

$$T = \sqrt{EAdh/G}\,(\tau_c/p) = (U^*_{I,N} - U_{I,N+1})_{\xi=\alpha} \tag{17b}$$

If Eq.(17a) is divided by Eq.(17b) we obtain

$$\frac{T_L}{T} = \frac{p}{p_L} = \frac{(U^*_{I,N} - U_{I,N+1})_{\xi=o^+}}{(U^*_{I,N} - U_{I,N+1})_{\xi=\alpha}} \tag{18}$$

Eq.(18) allows calculation of $p/p_L$ for different values of $\alpha$, where $p$ is the applied load beyond initial yield.

## Results and Discussion

In the results to follow, $P/P_L$ is the ratio of the post yield applied load to the applied load which just starts matrix yielding, R is the ratio of axial stiffness of low modulus(LM) to high modulus(HM) fibers, and the nondimensional extent of the matrix yield zone, $\alpha$, is defined in Eqs.(3).

In Fig.(2) the extent of the yield region, $\alpha$, is plotted against $P/P_L$ for different values of the parameter R in the case of 5 center breaks. As indicated, the LM,HM notation is used to represent the n=0 fiber. It is seen that the growth of the yield zone with applied load is reduced markedly as the hybrid parameter,R, decreases from unity, and also depends on whether the first intact fiber is LM or HM. For instance in Fig.(2) for $P/P_L$=5, a 40% reduction in $\alpha$ can be obtained when R=1/6(HM). Note that the smaller values of R mean a greater difference in the moduli of the HM and LM fibers.

The stress concentration factor (SCF) near fiber breaks is exhibited in Figs.(3) and (4). It is calculated by finding the maximum load in the adjacent intact fiber next to a series of fiber breaks (SCF is a load concentration factor). It turns out that it occurs at the end of the yield zone. If the first intact fiber is LM, then the SCF is given by $p^*_n/p^* = P^*_n/R$ if use is made of the nondimensionalization in Eqs.(3), and it is noted that $p^*$ is the load in the LM fiber at infinity for uniform strain conditions(i.e., far from the break region). If the first intact fiber is HM, then the SCF is given by $p_n/p = P_n$. Nondimensional loads are calculated from displacements using Eqs.(5).

In Fig.(3), the SCF is plotted against R at a fixed load level given by $P/P_L$=1.5, for the cases of one and five center breaks. The sensitivity of SCF to R is clearly shown, with the five breaks case leading to a higher stress concentration than the one break. While the SCF increases for the intact LM fibers it decreases for the HM fibers as R gets smaller. A greater hybrid effect is therefore indicated for the smaller values of R, where the LM fibers take on more of the load. Fig.(4) shows a similar plot involving three edge breaks with a correspondingly greater sensitivity of the SCF to the hybrid parameter,R.

Now, in order to compare the SCF for elastic matrix behavior with that of a yielding matrix, it is convenient to define the parameter $L_c$ by

$$L_c = p_{nc}/p_L \tag{19}$$

where $p_{nc}$ is the fiber critical load. It is seen that $L_c$ is a measure of the breaking strength of the fiber relative to the yield strength of the matrix.

Since the relation between the load ratio,$P/P_L$, and the yield zone, $\alpha$, can be determined for a given configuration(i.e.,Fig.2), and as indicated previously, the SCF can also be related to a given value of $\alpha$, the following relations can be established.

$$\frac{p}{p_L} = \left(\frac{p}{p_n}\right)\left(\frac{p_n}{p_L}\right) = \frac{p_n/p_L}{SCF} \tag{20}$$

where $p_n$ is the maximum load in the first intact fiber n. Suppose $\alpha$ (with corresponding $p/p_L$) is such that $p_n$ equals $p_{nc}$, the value for fiber breakage..By definition, $p_{nc}/p = SCF_c$. Therefore at $\alpha = \alpha_c$ (when $p_n = p_{nc}$ ), Eqs.(19) and (20) give

$$SCF_c = \frac{L_c}{(p/p_L)_c} \tag{21}$$

Note that $SCF_c$ actually defines the load concentration factor just before fiber breakage and gives a unique value for a given $L_c$. It is plotted against the number of broken fibers, r, in Fig.(5) for different values of $L_c$. The corresponding elastic case is also plotted for comparison. In Fig.(5), R=1 and there are 15 total fibers. If R is not equal to one ,Eq.(21) would still apply for HM fibers. For LM fibers we would have $SCF_c^* = SCF_c/R$. It is clear that the higher the fiber strength(i.e.,

higher $L_c$ ), the lower the $SCF$ since more yielding takes place before fiber breakage.

## References


Dvorak G.J.,and Bahei-El-Din,Y.A., 1988, "Fracture of Fibrous Metal Matrix Composites", Proc.of ASME Symposium-Mechanics of Composite Materials-1988 AMD-Vol.92, Dvorak,G.J.,and Laws,N.,Eds., pp.37-52.

Fukuda, H., and Chou, T.W., 1983, "Stress Concentrations in a Hybrid Composite Sheet", ASME J. of App. Mech. Vol.50, pp.845-848

Fukuda,H., 1985, "Load Concentration Factors in a Chain- of- Bundles Probability Model", Recent Advances in Composites in the United States and Japan, ASTM STP 864, Vinson J.R.,and Taya M., Eds., Am. Soc. Test. Mat., Philadelphia, PA, pp.5-15.

Goree,J.G.,and Gross,R.S.,1979, "Analysis of a Unidirectional Composite Containing Broken Fibers and Matrix Damage," Engng. Fracture Mech. Vol.13, pp. 563-578.

Hedgepeth,J.M., and Van Dyke, P., 1967, "Local Stress Concentrations in Imperfect Filamentary Composite Materials", J. Comp. Mater. Vol. 1, pp. 294-309.

Reedy, E.D., Jr., 1984, " Fiber Stresses in a Cracked Monolayer: Comparison of Shear-Lag and Finite Element Predictions", J. Comp. Mater., Vol.18,pp.595-607.

Rossettos, J.N., and Shishesaz, M., 1987, "Stress concentration in Fiber Composite Sheets Including Matrix Extension", Trans. ASME, J. of App. Mech. Vol. 54, No. 3, pp. 723-725.

Zhu,Y., Zhou, B., He,G., and Zheng,Z., 1989, "A Statistical Theory of Composite Materials Strength", J. Comp. Mater. Vol. 23, pp. 280-287.

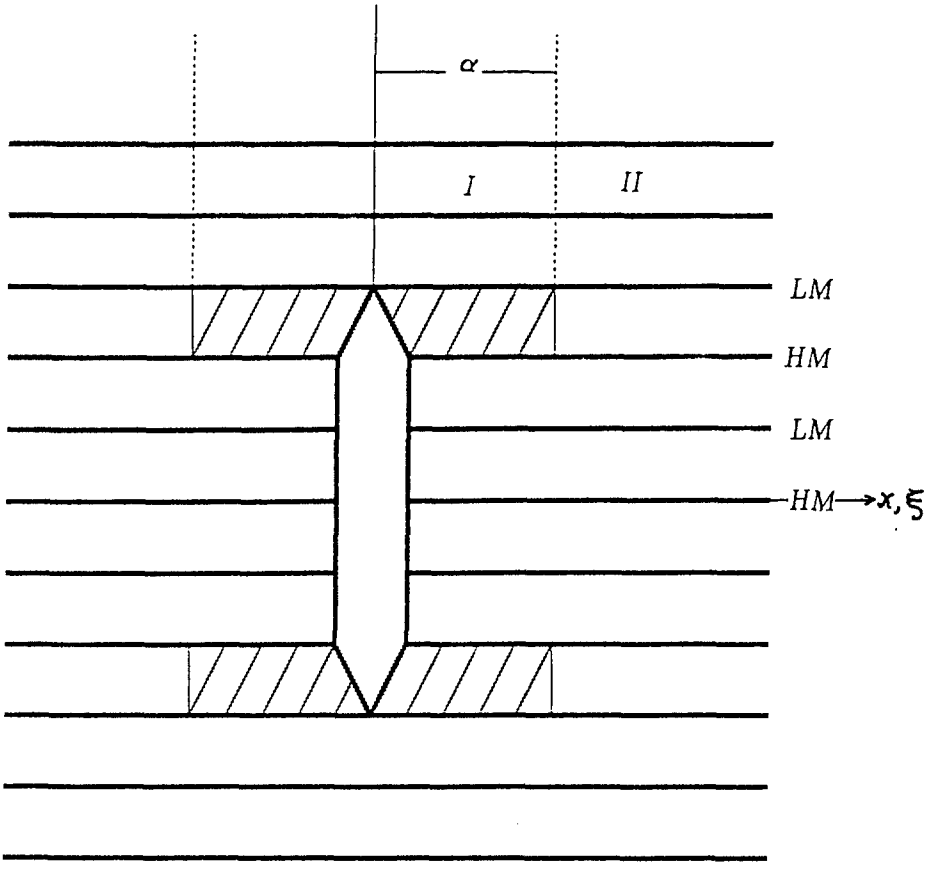



Figure 1. Geometry and Notation

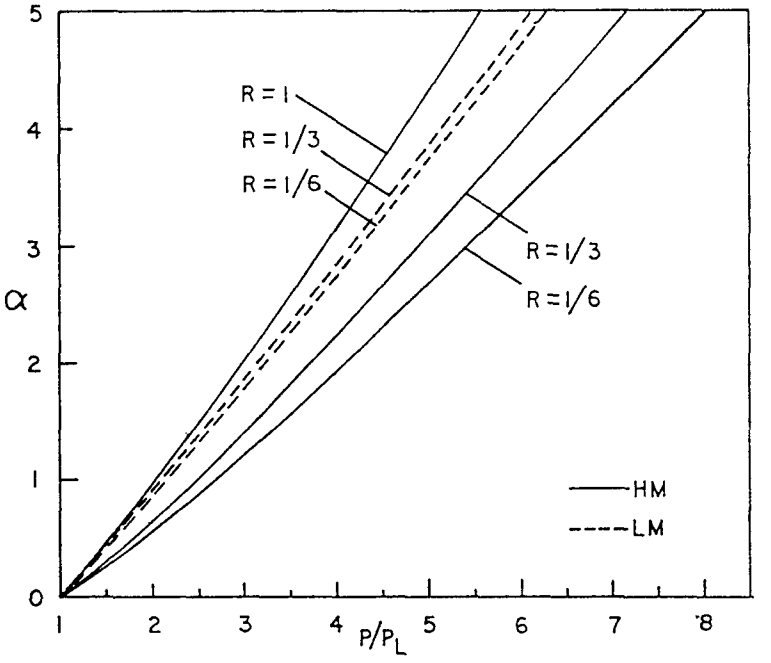



Figure 2. Extent of yield zone, $\alpha$, vs. load ratio, $P/P_L$; 15 fibers; 5 center breaks.

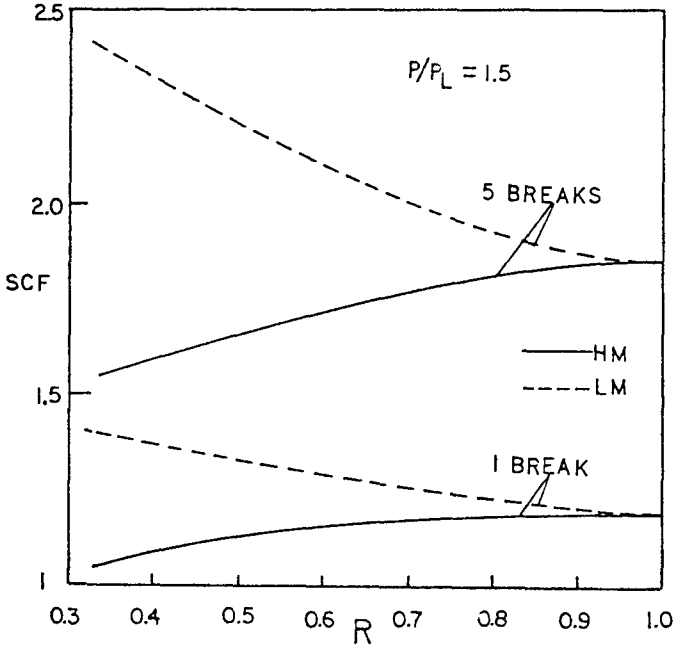



Figure 3. SCF vs. R 15 fibers; center breaks. SCF shown for intact(LM or HM) fibers adjacent to last break.

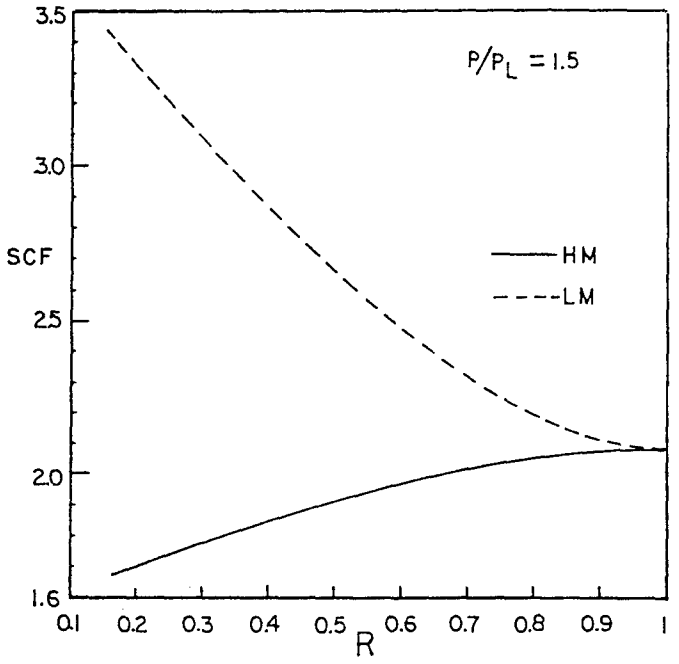



Figure 4. SCF vs. R 15 fibers; 3 edge breaks. SCF shown for intact(LM or HM) fibers adjacent to last break.

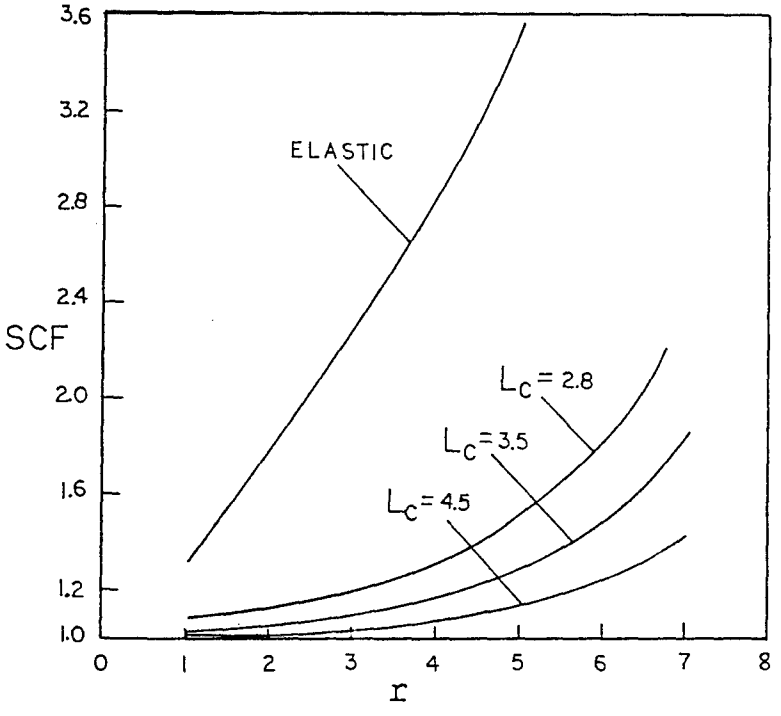
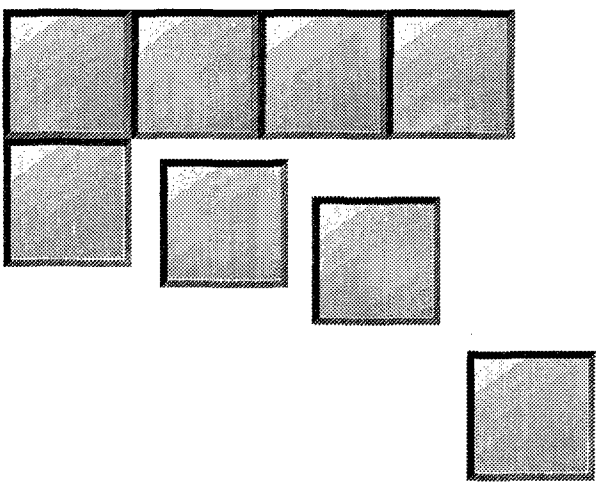



Figure 5. SCF vs. r (number of breaks) for 15 fibers;R=1; various $L_c$

# SESSION III:
# PENETRATION MECHANICS

**Chairman:** *Dr. C. Anderson*
**Southwest Research Institute**



# An Advanced Ceramic Model for Impact Dynamic Codes

Dr. A.M. Rajendran
Materials Directorate
Army Research Laboratory
Watertown, MA 02172-0001

## Introduction

Recently, Rajendran [1,2] reported a continuum mechanics based three dimensional constitutive model to describe the complex behaviors of ceramic materials. This model incorporates the effects of microcracks, porosity, and plastic flow on strength and stiffness of the ceramic materials. Damage is defined in terms of an average crack density and is treated as an internal state variable. The microcracks are assumed to be present prior to loading. This scalar damage model incorporates the effects of different damage processes under tension and compression using fracture mechanics based fracture criteria.

This paper describes the application of the ceramic model to a problem in which a steel projectile impacts a layered ceramic target. The main objectives are: 1) to establish generality of the model constants and 2) to demonstrate the model's ability to predict the measured stress history under multi-axial loading conditions. The center portion of the target in a ballistic test initially experiences one dimensional strain, and later multi-axial strains due to the release waves.

In the experiment [3], the shock stresses were measured using embedded manganin stress gauges at two locations inside the target. The measured stress history is influenced by the various shock/release waves: elastic-plastic shock waves, release waves from the edges of the projectile-target, and release and fracture waves due to ceramic fracturing. Therefore, the modeling of a ballistic experiment under such complex wave interactions is useful in the ceramic model validation.

## The Ceramic Model

Conventionally, the impact behavior of a material is described through a strength model and an equation of state. The strength model describes the variation of strength with respect to strain rate, temperature, and pressure. The strength is expressed through the von Mises stress, $\sqrt{3J_2}$ where $J_2$ is the second invariant of the stress deviators. Therefore, the strength model involves the calculation of the deviatoric part $(S_{ij})$ of the stress tensor $\sigma_{ij}$. The bulk (volumetric) behavior of the material is described by the equation of state. This involves the calculation of the pressure (mean stress) part of the stress tensor.

### Constitutive Relationships

The total strain is decomposed into elastic and plastic strains as,

$$\varepsilon_{ij} = \varepsilon_{ij}^{e} + \varepsilon_{ij}^{p} \quad , \tag{1}$$

where the elastic strain consists of the elastic strain of the intact matrix material $(\varepsilon_{ij}^{m})$, and the strain due to crack opening/sliding $(\varepsilon_{ij}^{c})$,

$$\varepsilon_{ij}^{e} = \varepsilon_{ij}^{m} + \varepsilon_{ij}^{c}. \tag{2}$$

Since the strain components due to microcracking are elastic, these strains are completely recoverable upon unloading. The plastic strains are calculated from viscoplastic flow equations. When voids (pores) present in the ceramic, the strain components due to pore collapse are assumed to be permanent and are calculated from Gurson's pressure dependent plastic flow equations [4]. The constitutive relationships for the microcracked material are given as follows:

$$\sigma_{ij} = M_{ijkl}(\gamma)\ \varepsilon_{kl}^{e} \tag{3}$$

The elements of the stiffness matrix $M_{ijkl}$ is based on the derivation of Margolin [5,6]. $M_{ijkl}$ is described in details by Rajendran [1,2]. The elements of this stiffness matrix is degraded with respect to a crack density parameter, $\gamma$, which is defined in a later section.

The total stress is decomposed into deviatoric stress and pressure components:

$$\sigma_{ij} = S_{ij} + P\delta_{ij} \tag{4}$$

The elastic stress-strain relationship between the deviatoric stresses and the corresponding deviatoric strains is given by,

$$S_{ij} = 2G(e_{ij} - e_{ij}^{p}) \tag{5}$$

where, $e_{ij}$ are the total deviatoric strains, $e_{ij}^{p}$ are the deviatoric plastic strains, and $G\ (=R_g\overline{G})$ is the degraded shear modulus due to microcracking and pores. $\overline{G}$ is the microcrack degraded shear modulus and $R_g$ is the Mackenzie's shear modulus correction factor [7] for porosity. The equation of state is described by the following modified Mie-Gruneisen relationship,

$$P = R_k \left[ \overline{P}_H(1 - 0.5\Gamma\mu) + \Gamma\rho_o(I - I_o) \right] \tag{6}$$

where,

$$\overline{P}_H = (\overline{K}/K)(\beta_1\mu + \beta_2\mu^2 + \beta_3\mu^3) \tag{7}$$

$\mu\ \left(=1-\frac{V}{V_0}\right)$ is the elastic volume compressibility (strain) and $\beta_1$, $\beta_2$, and $\beta_3$ are the empirical parameters. $\overline{K}$ is the effective bulk modulus of the microcracked material. $\Gamma$ is the Mie-Gruneisen parameter, $\rho_o$ is the material's initial density, $I_o$ is the initial value of internal energy, and $I$ is the current internal energy.

The Mackenzie's correction factor $R_k$ is given in References 7 and 8. $R_k\overline{K}$ is the degraded bulk modulus due to pores and microcracks. In the absence of voids and microcracks, Equation 6 reduces to the Mie-Gruneisen equation of state for the undamaged, flawless material.

## Definition of Damage

In the ceramic model, microcrack damage is measured in terms of a dimensionless microcrack density $\gamma$, where,

$$\gamma = N_0^* \, a_{max}^3 \tag{8}$$

$N_o^*$ is the average number of microflaws per unit volume in the ceramic which is a model constant. $a_{max}$ is the maximum microcrack size which is treated as an internal state variable. Microcrack extends when the stress state satisfies the Griffith's criterion [9].

As the microcracks extend, $\gamma$ increases and the stresses relax. In the model, $N_o^*$ is assumed to be constant. Therefore, the increase in $\gamma$ is due to increase in the crack size. The microcracks are assumed to exist prior to any loading. Therefore, the initial crack density $\gamma_0$ is determined from the relationship (8) using the values for the two material constants: $N_0^*$ and $a_0$ (initial value of $a_{max}$). The microdamage (microcrack size) will not increase until the generalized Griffith criterion (Margolin [10] and Dienes [11]) is satisfied either under shear or under tensile loading. Note that the shear loading could occur under both tensile and compressive pressures. The microdamage rate is zero until the applied strain energy release rate $G_I$ exceeds a critical value $G_C$.

## Damage Growth Model

The damage evolution equation is derived from fracture mechanics based relationship for a single crack propagation under dynamic loading conditions. An evolution law for the state variable $a_{max}$ is described through a strain energy release based microcrack growth rate law of the form

$$\dot{a}_{max} = n_1 C_R \left[ 1 - \left( \frac{G_c}{G_I} \right)^{n_2} \right] \tag{9}$$

Note that $\dot{a}_{max} = 0$ , *when* $G_I < G_c$ . $C_R$ is the Rayleigh wave speed, $G_c$ is the critical strain energy release for microcrack growth, and $G_I$ is the applied strain energy release. The model constants $n_1$ and $n_2$ can be used to limit the microcrack growth rate. $n_1$ and $n_2$ are damage growth constants. Since the crack growth based damage rates are different under tensile and compressive loadings, these constants will be assigned different values.

When the crack density reaches a critical value of 0.75 (see reference 1), the model assumes that the microcracks have coalesced, leading to pulverization of the ceramic. Henceforth, the material has no strength in tension, and its compressive strength follows a Mohr-Coulomb law, as in

$$Y = \alpha_p + \beta_p P \tag{10}$$

where $Y$ is strength, $P$ is compressive pressure, and $\alpha_p$ ( = 0) and $\beta_p$ ( = 1.0) are model constants for the pulverized material.

## Model Parameters Determination

There are six constants in the ceramic model to describe the microcracking behavior: $K_{IC}$, $\mu$, $N_0^*$, $a_0$, $n_1$, $n_2$. The preliminary set of the model constants is determined from split Hopkinson bar (SHB) and plate impact experimental data. The constants $\mu$ and $a_0$ were calibrated to reproduce the static and SHB compressive strength data.

To assure generality of the model constants, manganin gauge measured stress data from the bar-on-bar impact experimental configuration was also considered. The best suitable values for the constants are obtained based on the model's ability to reproduce the experimental data from SHB, plate impact, and bar-on-bar impact configurations. Rajendran [1] and Rajendran and Grove [12] reported this model determination scheme and determined the model constants for AD85 ceramic. The corresponding constants are given in Table 1.

The value for $K_{IC}$ is obtained from fracture mechanics hand books. With lack of any microscopic measurements, a large value for

the number of flaws in the ceramics $N_o^*$ has been arbitrarily assumed. Therefore, the initial estimates for the crack growth indices $n_1$ and $n_2$ were calibrated to reproduce the stress profile measurements in a bar (uniaxial stress state) and in a plate (one dimensional strain state). $n_1^+$ is set to one for AD85 ceramic.

Table 1. Model Constants for AD85 Ceramic

| Symbol | Value | Description |
|---|---|---|
| $K_{IC}$ | $3\ MPa\sqrt{m}$ | static fracture toughness |
| $\mu$ | 0.72 | Coefficient of friction |
| $N_o^*$ | $1.83 \times 10^{10}\ m^{-3}$ | Microcrack density (numbers/volume) |
| $a_o$ | $58 \times 10^{-6}\ m$ | Initial microcrack size |
| $n_2$ | 0.07 | Crack growth rate power index |
| $n_1^+$ | 1.0 | Tensile crack growth rate index |
| $n_1^-$ | 0.1 | Compressive crack growth rate index |

The crack propagation speed under shear modes is relatively lower than under mode I and therefore, a value of 0.1 is assumed arbitrarily for $n_1^-$. For $n_2$, a value of 0.07 was determined based on the model's ability to reproduce the rod-on-rod experimental data. The model parameters estimation scheme requires a trial and error basis of adjusting the crack growth indices between different experimental configurations. Unfortunately, there is no one set of unique values for the impact damage model parameters. At the best, a best suitable set of values can be successfully determined through a trial and error basis of reproducing a varieties of experimental configurations.

## Modeling the Ballistic Impact Pressure Measurements

Vincent and Chang [3] conducted instrumented ballistic experiments on ceramic targets. A schematic of the target configuration is shown in Figure 1. Two manganin gauges were embedded into the

target assembly: the first (top) gauge is placed between the front ceramic and the isodamp, and the second (bottom) gauge is placed between the back face of the isodamp and the second ceramic. This second ceramic is backed by a thick aluminum plate. The top gauge measurements seemed to be valid only for a very short time (< 2 microseconds). The ceramic material that surrounding this top gauge is destroyed by the cracked ceramic. However, the bottom gauge survived during the measuring period (about 8 to 10 microseconds). This gauge is protected by the intact second ceramic and isodamp. However, the bottom gauge is also destroyed eventually. Unfortunately, from these destructive tests, it is not possible to determine the timings of events such as the onset of microcracking or growth of macrocracks. Therefore, the different events which might occur inside the target during the projectile penetration can indirectly only be related to the various features of the stress gauge signal. The data from the two gauges are shown in Figure 2. The pulse duration and amplitudes are sensitive to the shock response of the ceramics, isodamp, and projectile.

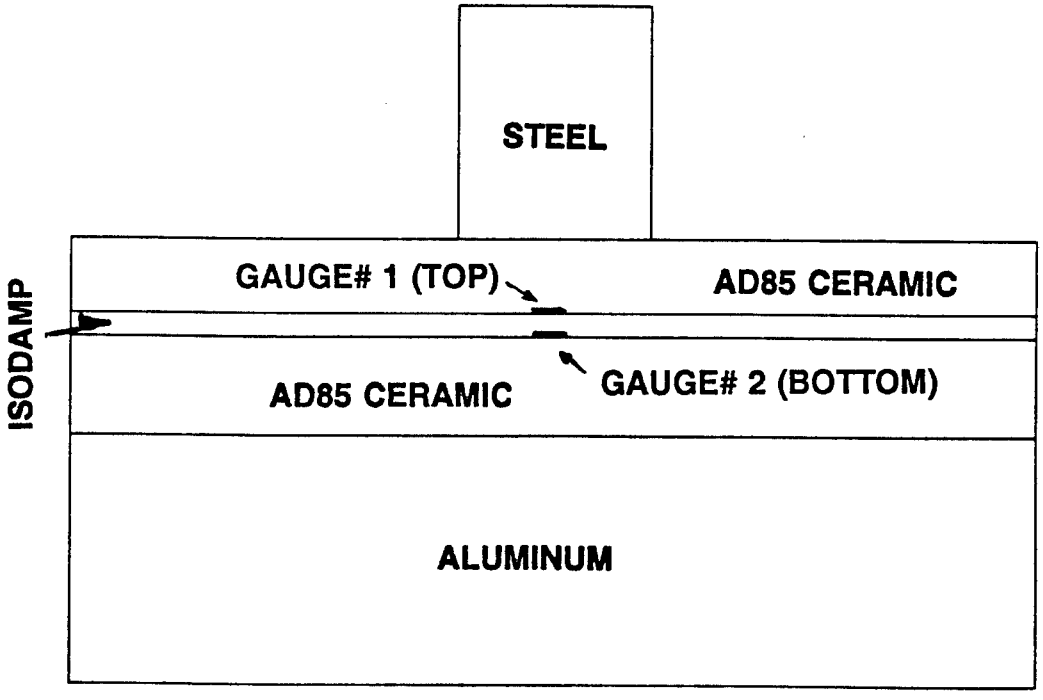



Figure 1. A Schematic of the Instrumented Ballistic Experiment.

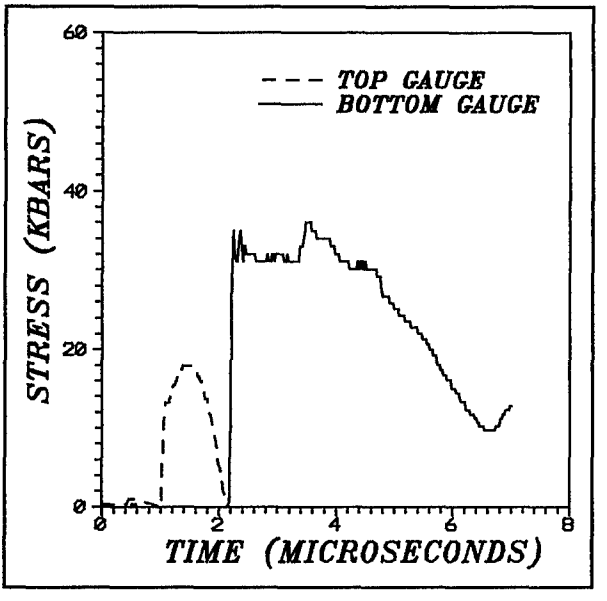



Figure 2. Manganin Gauge Measured Stress Histories in a Ballistic Experiment.

## Simulation Results and Analyses

The steel and aluminum were respectively modeled using the HY100 steel and 2024-T351 aluminum models in the 1986 version EPIC-2 library [13]. The isodamp was modeled as an elastic-perfectly plastic solid with a dynamic yield strength of 0.4 GPa.

Table 2. Material constants for isodamp and AD85 ceramic

| Material Constants | AD85 | Isodamp |
|---|---|---|
| Density (gm/cm$^3$) | 3.42 | 1.29 |
| Shear Modulus (GPa) | 108 | 0.5 |
| $\beta_1$ (GPa) | 188 | 3.9 |
| $\beta_2$ (GPa) | 188 | 16.3 |
| $\beta_3$ (GPa) | 0 | 42.0 |
| $\Gamma$ | 1.0 | 0.738 |

The material density, shear modulus, and EOS constants for isodamp and AD85 ceramics are given in Table 2. To understand the effects of various deformation processes in the ceramic material on the calculated stress histories (at the gauge locations), a number of simulations of the ballistic experiment were performed. For this purpose, the following cases were considered: 1) elastic, 2) elastic-plastic (Case EP), 3) elastic-cracking (Case EC), and 4) elastic-plastic-cracking (Case EPC).

These various cases were simulated by properly adjusting the model parameters. For instance, the cracking is eliminated by setting the initial crack size $a_0$ to zero. The plastic flow is eliminated by setting the strength model constant $C_1$ to a large number. To suppress plastic pore collapse, the void content, $f_0$ is set to zero.

**Grid and Time Step**

The EPIC-2 simulation of the ballistic experiment idealized the projectile-target configuration as an axi-symmetric geometry. In Figure 3, the calculated stress histories at the bottom gauge location are compared for two different meshes.

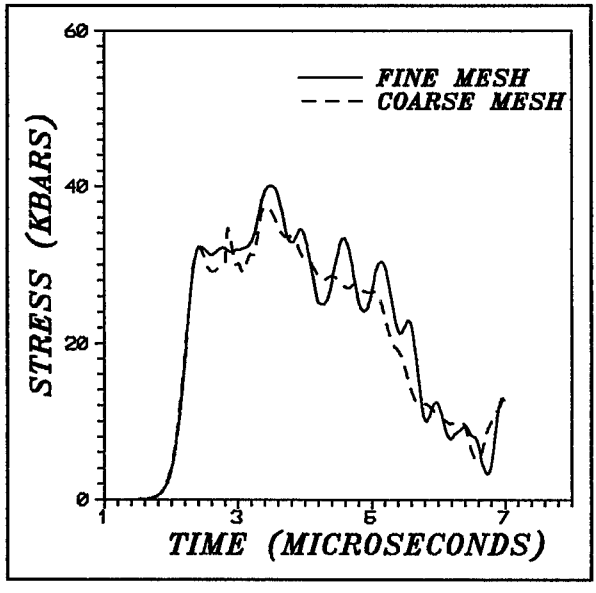



Figure 3. Effects of Mesh on Stress History.

A slight mesh effect on the stress histories can be seen from the plot. However, the overall shape and stress levels for the two meshes were practically the same. The element size for the ceramic in the coarse mesh was twice the element size for the isodamp.

In the EPIC code, one of the parameters that controls the time step size is the "ssf" parameter. The time step can be controlled by setting values between 0.1 and 0.9 for ssf. It is also possible to examine the time step effects through a parameter which controls the maximum allowable time step. The results for the ssf = 0.1 (small time step) and 0.9 (large time step) are compared in Figure 4. The stress-time histories are similar, except for some minor stress oscillations. These results provide sufficient confidence in the numerical results. One of several other code parameters, such as the maximum allowable time step, can also influence the numerical results; however, the proper choice of these time step related code parameters produce similar and repeatable results.

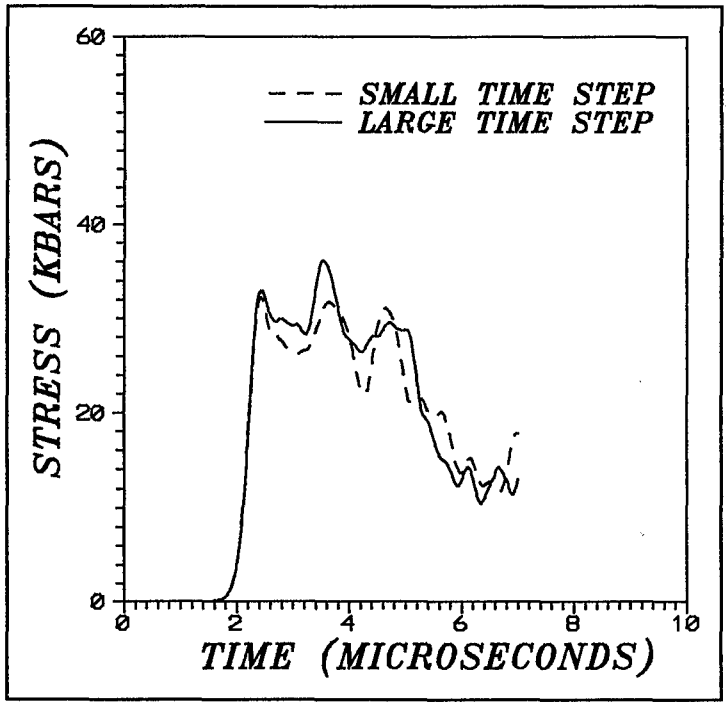



Figure 4. Effects of Time Step on Stress History.

**Elastic (Case E)**

The simplest stress-strain relationship is the Hooke's law for an elastic material. Since ceramic is a brittle solid, it is proper to begin the analysis with an elastic description. The inelastic strains due to both microcracking and plastic flows were suppressed in the elastic simulation. Therefore, the shear and bulk moduli were not degraded and the ceramic remained intact under impact loading. The strength of the ceramic was unlimited. Therefore, failure was not allowed in the elastic case.

The results from this case is presented in Figure 5. The bottom stress gauge signal is compared with the simulation in Figure 5. As can be seen from this figure, the calculated stress levels are higher and the loading duration is lower when compared to the data. These results clearly indicate that a simple elastic assumption is inadequate for describing the complex impact behavior of ceramics.

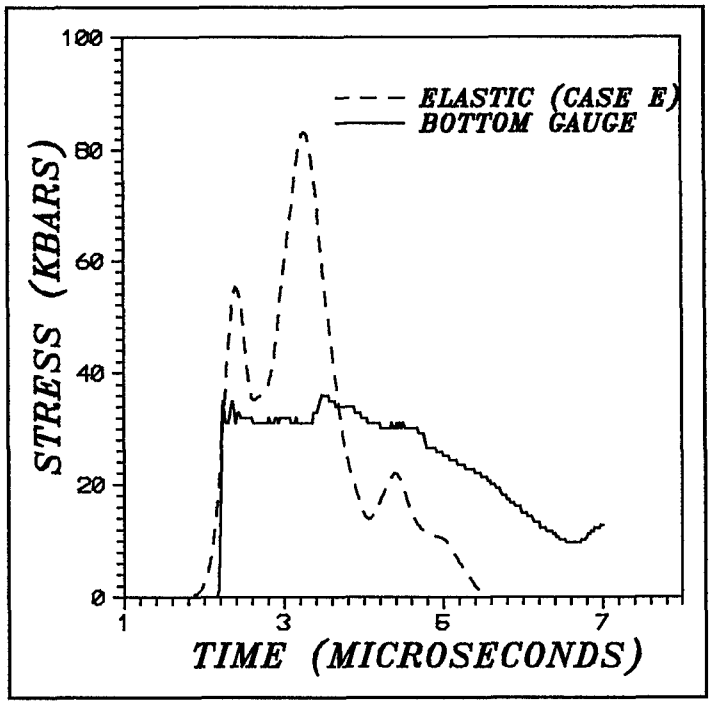



Figure 5. A Comparison Between Bottom Gauge Data and Case E. The Ceramic Behavior is Assumed Elastic.

## Elastic-Plastic (Case EP)

In the elastic-plastic simulation, the impact behavior of ceramic was described through the strain rate dependent strength. An initial value of zero for the microcrack size eliminates microcracking in the calculation. The initial porosity was also set to zero, so that pore collapse would not occur.

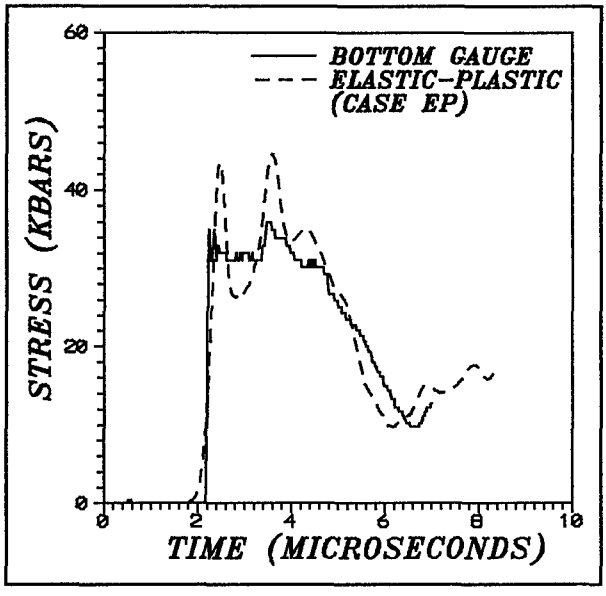



Figure 6. A Comparison Between Bottom Gauge Data and Case EP. The Ceramic Behavior is Assumed Elastic-Plastic (No Cracking).

When the ceramic behavior is described by an elastic-plastic model, the model comparison with the bottom gauge data improved significantly as shown in Figure 6. It appears that limiting the ceramic compressive strength to finite values through a yield surface could improve the model prediction. With lack of any microstructural evidence to prove macroplastic flows in the brittle ceramic under impact loading conditions, it is premature to conclude that AD85 ceramic deforms plastically like a metal just because the elastic-plastic model reproduced the experimental measurements. There is also a possibility to cap or limit the ceramic strength due to microcracking and crushing. Though the matching is good, the absence of certain salient features in the simulation indicates elastic-plastic idealization alone may not reproduce

all the features. It appears that the matching between the simulation and experiment can be significantly improved by limiting the ceramic strength to finite values.

**Elastic-Cracking (Case EC)**

This case examines the effect of microcracking on the stress profile. In the simulation, a very large value was assumed for the strength to eliminate the plastic flow. The strength was affected by the elastic moduli degradation and was allowed to relax through microcracking only. The pore collapsing was also suppressed in the simulation.

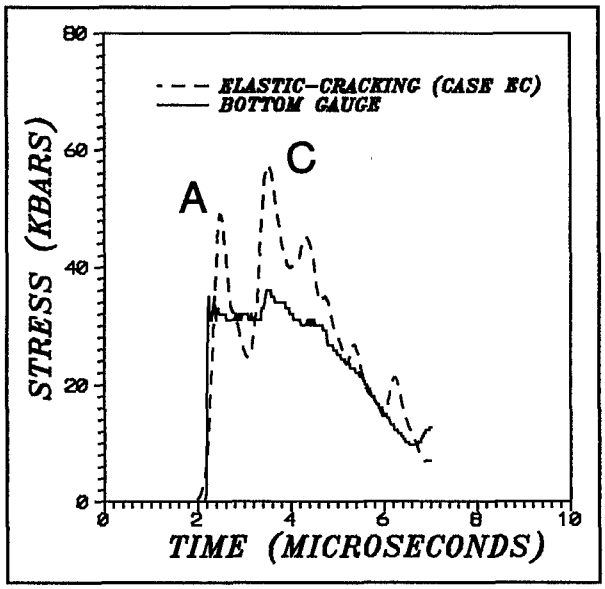



Figure 7. A Comparison Between Bottom Gauge Data and Case EC. The Ceramic Behavior is Assumed Elastic-Cracking (No Plastic Flow).

Figure 7 compares the calculated stress history from the Elastic-Cracking case and the bottom gauge data. The two stress peaks (at points A and C) were present as in Cases E and EP. The stress levels are instantaneously higher compared to the gauge data. The stress history during loading and unloading matched with the data some what in an average manner. The results from the Case EP (elastic-plastic) compared with the data relatively better than this elastic-cracking case.

## The Full Ceramic Model (Case EPC)

To further investigate the effects of inelastic deformations on the stress history, the elastic-plastic-cracking case with pore collapse was considered. In other words, the full features of the ceramic model were used to describe the impact behavior of AD85 under Case EPC.

The ballistic impact experiment of Vincent and Chang [3] was simulated using the ceramic model constants in Table 1. A 10 percent porosity content and an initial flaw size of 0.058 mm were used in the simulation. Figure 8 compares the model and the bottom gauge data.

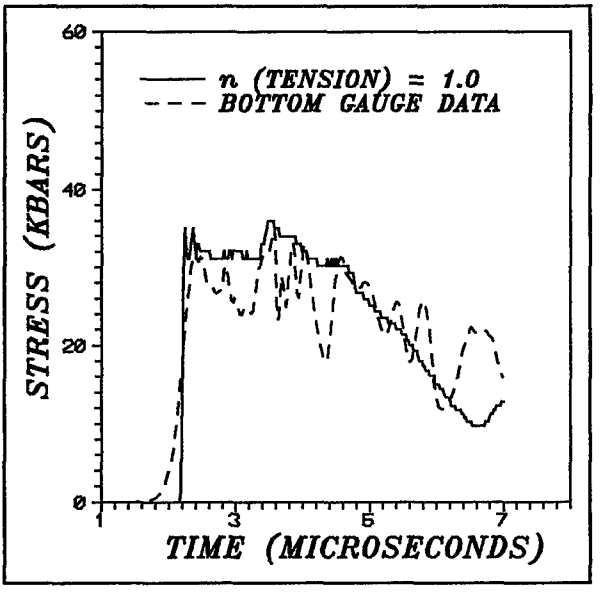



Figure 8. A Comparison Between The Ceramic Model (With Tensile $n_1$ = 1) and Bottom Gauge Data.

The model showed lower stress level and slightly a higher pulse duration compared to the data. The damage levels with respect to time and position indicated an excessive tensile damage in the top ceramic layer. An examination of the damage contours showed emanation of Herzian cracks and fracture conoid. Several regions of the top ceramic plate had pulverized. Since the ceramic model degraded the strength and stiffness due to microcracking, the microcrack-induced damage respectively lowered the stress level and increased the pulse duration.

To reduce the tensile damage, the tensile crack growth factor $n_1^+$ was reduced to a value of 0.1 and the simulation was repeated. In fact, a sensitivity study based on values between 0.1 and 0.5 showed very similar stress profiles. The computed stress history at the bottom gauge location is compared with the data in Figure 9. The model reproduced the experimental data extremely well.

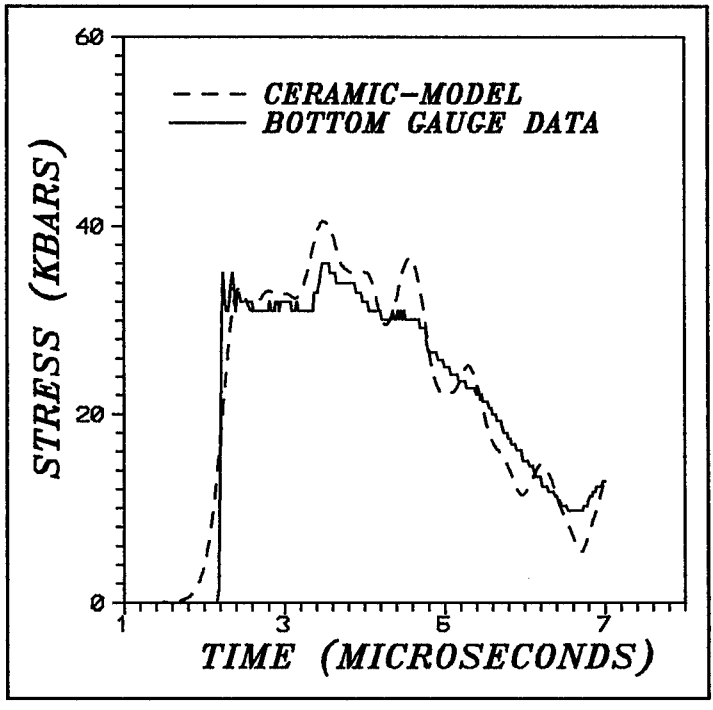



Figure 9. A Comparison Between the Ceramic Model (With Tensile $n_1$=0.1) and Bottom Gauge Data.

The model prediction significantly improved for $n_1^+$ values between 0.1 and 0.5. Since this parameter indirectly controls the amount of stress relaxation in the model, a reduced value for this parameter accordingly increased the calculated stress amplitude. These results indicate that the model prediction based on both brittle microcracking and plastic flow matched the experimental measurements extremely well. The ceramic model not only matched the stress amplitude and the time duration, it also reproduced most of the salient features of the measured stress signal.

## Summary

Recently, Rajendran [1,2] reported the development of an advanced ceramic model. This ceramic model has been implemented into the 86 version of the EPIC-2 code and successfully used to model the impact behavior of AD85 ceramic under different impact test configurations, such as the plane plate impact and rod-on-rod tests. The stress-strain states under these two configurations are fairly simple. In the plate impact test, the strain is one dimensional and in the rod-on-rod test the stress is one dimensional. There are seven model constants: $K_{Ic}$, $\mu$, $N_0^*$, $a_0$, $n_1^+$, $n_1^-$, $n_2$. The fracture toughness value is taken from fracture mechanics hand books. The rest of the constants were determined from the experimental data. For this purpose, the manganin gauge measured stress histories from the plate impact and rod-on-rod impact experiments were employed.

The present work demonstrated the applicability and generality of the ceramic model under relatively complex stress-strain states. The idea is to employ the AD85 constants, determined from the plate impact and rod-on-rod impact tests data, to successfully describe the AD85 ceramic behavior under an entirely different experimental configuration. The three dimensional stress-strain state under this target configuration is fairly complex due to shock wave interactions. The calculated stress history matched the measured stress history data extremely well. When a value of 1 was employed for $n_1^+$, the ceramic exhibited extensive damage and the simulated stress profile did not match with the experiment; however a value of 0.1 for $n_1^+$ predicted the data successfully. In summary, the ceramic model constants, estimated from the standard one dimensional impact tests data, reproduced the multi-axial experimental data well.

## References

1. Rajendran, A.M., **"High Strain Rate Behavior of Metals, Ceramics, and Concrete,"** WL-TR-92-4006, Air Force Report, Wright-Patterson Air Force Base, Ohio 45433-6533, April 1992.

2. Rajendran, A.M., **"Modeling the Impact Behavior of AD85 Ceramic Under Multi-Axial Loading,"** ARL-TR-137, May 1993.

3. Vincent, P.M. and Chang A.L., **"Ballistic Impact Pressure Pulse Measurement,"** 41st Meeting of Aeroballistic Range Association, Oct 22-25, 1990.

4. Gurson, A.L., **"Porous Rigid-Plastic Materials Containing Rigid Inclusions - Yield Function, Plastic Potential, and Void Nucleation,"** Adv. Res. Strength Fract. Matls., 2a, Tablin, D.M.R., ed., Pergamon Press, NY, 1977.

5. Margolin, L.G., **"Elastic Moduli of a Cracked Body,"** Int. Journal of Fracture, 22, pp. 65-79, 1983.

6. Margolin, L. G., **"Microphysical Models for Inelastic Material Response,"** International Journal of Engineering Science, **8-10**, 22, 1171-1179, 1984.

7. Mackenzie, J. H.,**"The Elastic Contents of a Solid Containing Spherical Holes,"** Proc. Phys. Soc., **2**, 63, 1950.

8. Johnson, J.N., **"Dynamic Fracture and Spallation in Ductile Solids,"** J. Appl. Phys., 52 (4), p. 2812, 1981.

9. Griffith, A. A., **"The Phenomena of Rupture and Flow in Solids,"** Phil. Trans. of Royal Soc. of London, 221, 163-198, 1920.

10. Margolin, L.G., **"A Generalized Griffith Criterion for Crack Propagation,"** Engineering Fracture Mechanics, Vol. 19 Vol. 30, pp. 539-543, 1984.

11. Dienes, J. K., **"Comments on 'A Generalized Griffith Criterion for Crack Propagation,' by L. G. Margolin"** - a Technical Note, Eng. Fracture Mechanics, **3**, 23, 615-617, 1986.

12. Rajendran, A.M., and Grove, D.J., **"Modeling The Impact Behavior of AD85,"** 24th Int. SAMPE Tech. Conf. Proceedings, Allied-Signal Inc., Publishers, Oct 1992.

13. Johnson, G. R. and Stryk, R. A., **"User Instructions for the EPIC-2 Code,"** AFATL-TR-86-51, Eglin Air Force Base, Fl, 1986.

# Dynamic Impact and Penetration of Thick Composite Laminate

*C.T. Sun and S.V. Potti*
Purdue University

"PAPER NOT AVAILABLE"

# Axisymmetric Penetration of Thermoviscoplastic Targets

Dr. R. C. Batra*, Dr. Xingju Chen, and Mr. Z. Peng
Department of Mechanical and Aerospace Engineering
and Engineering Mechanics
University of Missouri-Rolla
Rolla, MO 65401-0249 USA

## ABSTRACT

Axisymmetric deep penetration of a strain- and strain-rate hardening but thermally softening target by a fast moving hemispherical nosed rigid rod has been analyzed numerically by using the finite element method. The finite element mesh is refined adaptively whenever one of its elements has been severely distorted. Sixteen tests of Forrestal *et al.* involving the penetration of steel rods of radii 2.54 mm and 3.555 mm into aluminum targets have been simulated. The computed depth of penetration is found to correlate well with the test findings.

The perforation of a thermoviscoplastic plate by a rigid flat-nosed cylindrical projectile has also been studied. It is found that a shear band forms near the target/penetrator interface.

## INTRODUCTION AND GOVERNING EQUATIONS

We refer the reader to the review articles by Backman and Goldsmith [1], Jonas and Zukas [2], and Anderson and Bodner [3] for a description of the different physical mechanisms involved in the penetration and perforation processes, and a discussion of a number of engineering models. The recent book [4], edited by Zukas, provides extensive discussions of engineering models, experimental techniques, analytical models, and numerical simulation of perforation. Different computer codes used to study the penetration problem, and their

relative advantages and disadvantages have been surveyed by Zukas [4].

Here we study an axisymmetric penetration problem in which a rigid cylindrical hemispherical-nosed penetrator impacts a deformable target at normal incidence. We use a fixed set of cylindrical coordinates with z-axis coincident with the axis of symmetry of deformations and pointing into the target and the origin at the top surface of the undeformed target. We employ the Lagrangian or the referential description of motion to study the thermomechanical deformations of the target. The balance laws of mass, linear momentum, and internal energy are supplemented by the following constitutive relations.

$$\underset{\sim}{\sigma} = -p(\rho,\theta)\underset{\sim}{1} + 2\hat{\mu}\underset{\sim}{D}, \qquad \underset{\sim}{T} = \frac{\rho_0}{\rho}\underset{\sim}{\sigma}(\underset{\sim}{F}^{-1})^T, \tag{1,2}$$

$$2\hat{\mu} = \frac{\sigma_0}{\sqrt{3}I}\left(\frac{\psi}{\psi_0}\right)^n (1 + bI)^m(1 - \nu\theta), \tag{3}$$

$$2\underset{\sim}{D} = \text{grad}\underset{\sim}{v} + (\text{grad}\underset{\sim}{v})^T, \quad \tilde{\underset{\sim}{D}} = \underset{\sim}{D} - \frac{1}{3}(\text{tr}\underset{\sim}{D})\underset{\sim}{1}, \quad 2I^2 = \text{tr}(\tilde{\underset{\sim}{D}}^2), \tag{4,5,6}$$

$$p = p_H\left(1 - \frac{\Gamma\mu}{2}\right) + \Gamma\rho\,(e - e_o), \quad p_H = \frac{\rho_o\, c_o^2\, \eta}{(1 - s\eta)^2}, \tag{7,8}$$

$$\eta = 1 - \frac{\rho_o}{\rho}, \quad \mu = \frac{\rho}{\rho_o} - 1, \quad \underset{\sim}{Q} = -k\frac{\rho_0}{\rho}\text{grad}\theta(\underset{\sim}{F}^{-1})^T, \tag{9,10,11}$$

$$\dot{e} = c\dot{\theta} + \dot{\rho}p/\rho^2, \quad \dot{\psi} = \frac{\text{tr}(\underset{\sim}{\sigma}\underset{\sim}{D})}{\sigma_0\left(\frac{\psi}{\psi_0}\right)^n}. \tag{12,13}$$

Here $\underset{\sim}{\sigma}$ is the Cauchy stress tensor, T the first Piola-Kirchhoff stress tensor, $\sigma_0$ the yield stress of the target material in a quasistatic simple tension or compression test, $\psi_0$ the strain at yield, n the strain-hardening

exponent, m the strain-rate hardening coefficient, $\nu$ the coefficient of thermal softening, $\theta$ the temperature rise of a material particle, $\rho$ the present mass density of a material particle whose mass density in the reference configuration is $\rho_0$, e the specific internal energy, k the thermal conductivity, and c the specific heat. The internal variable $\psi$ may be associated with an equivalent plastic strain; its evolution is given by equation (13). Equation (7) is the Mie-Gruniesen equation of state. The material parameters n, b, m, $\Gamma$, $\mu$, $c_0$, s, k, and c are taken to be independent of the temperature.

We assume that the target is initially at rest, is stress-free, has a uniform mass density $\rho_0$ and a uniform temperature $\theta_0$. The initial velocity of the rigid penetrator is $v_0$ in the positive z-direction, and at time $t = 0$ it just impacts the top surface of the target at normal incidence.

For boundary conditions we take the target/penetrator interface to be smooth and neglect the heat transfer between the two, take all bounding surfaces of the target to be traction free, and regard them except the top one, where convective heat transfer between it and the surroundings is considered, to be thermally insulated. Due to the axisymmetric nature of deformations, boundary conditions following from the symmetry of deformations are applied on the axis of symmetry.

## NUMERICAL SOLUTION AND RESULTS

We use the updated Lagrangian formulation [5] of the problem to get its approximate solution. In the solution of the problem by the finite element method we employ the lumped mass matrix obtained by the row-sum technique, and use three quadrature points to numerically integrate various quantities over an element. The coupled nonlinear ordinary differential equations obtained by the Galerkin method are integrated with respect to time t by using the forward difference method. The time step used is small enough to satisfy the Courant condition and restrictions imposed on it by the slideline algorithm employed to account for the contact conditions at the target/penetrator interface.

After every time increment, the coordinates of node points are updated and elements in the finite element mesh are checked for excessive distortion. If either one of the interior angles of a triangular element is less than 15° or the ratio of its altitude to the base is less than 0.12, then the element is considered to have been severely

distorted, and the mesh is refined so that finer elements are generated in the region adjoining the target/penetrator interface and the element size increases gradually as one moves away from this surface. The values of the nodal variables at the newly generated nodes are obtained by first determining to which element in the old mesh the node belongs, and then by interpolating from the values at the nodes of that element. Additional information regarding the mesh refinement and the slideline algorithm may be found in Ref. [6].

## RESULTS FOR THE DEEP PENETRATION OF ALUMINUM TARGETS

We assign following values to material parameters for the 6061-T651 aluminum targets used in the ballistic experiments of Forrestal *et al.* [7].

$$\sigma_0 = 276 \text{ MPa}, \quad n = 0.051, \quad \psi_0 = 0.004,$$

$$b = 10000 \text{ sec}, \quad m = 0.01, \quad \nu = 0.00153/^\circ\text{C},$$

$$\rho_0 = 2710 \text{ kg/m}^3, \quad c_o = 5041 \text{ ms}^{-1}, \quad s = 1.420 \qquad (14)$$

$$\Gamma = 2.0, \quad k = 120 \text{ Wm}^{-1}{}^\circ\text{C}^{-1},$$

$$c = 875 \text{ Jkg}^{-1}\,^\circ\text{C}^{-1}, \quad \theta_a = 22^\circ\text{C}, \quad h = 20 \text{ Wm}^{-2}\,^\circ\text{C}^{-1}.$$

For these values of material parameters the stress-strain curve in a quasistatic compression test mimics well that given by Forrestal *et al.* Here $\theta_a$ denotes the ambient temperature and h the heat transfer coefficient between the top surface of the target and the surroundings.

In the ballistic experiments of Forrestal *et al.*, a 20-mm smooth-bore powder gun launched T-200 maraging steel hemispherical nosed cylindrical rods impacting 6061-T651 aluminum targets at normal incidence. They observed that the major penetration mechanism was ductile hole growth, and their post-test observations revealed that penetrators remained essentially undeformed. Thus, it is reasonable to regard the penetrator as a rigid body, and our model should simulate well their tests.

Preliminary computations for a few test conditions indicated that a thin layer of the target material adjoining the target/penetrator interface melted before the penetration process was completed. According to our constitutive hypotheses (1) and (3), when $\theta = 1/\upsilon$ = melting temperature of the material, $\hat{\mu} = 0$, and the material behaves like an ideal fluid and cannot support any shear stresses. To alleviate this problem, for $\theta > 0.955\ \theta_m$, equation (3) was modified to

$$2\hat{\mu} = \frac{0.045\,\sigma_0}{\sqrt{3}\,I}\left(\frac{\psi}{\psi_0}\right)^n (1 + bI)^m ,$$

where $\theta_m$ is the melting temperature of the target material.

Figure 1 provides a comparison of the computed depth of penetration with that found experimentally for a penetrator of radius 3.555 mm. Similar results were obtained for a penetrator of radius 2.54 mm. The curve depicts the computed penetration depth normalized by the penetrator length versus the impact speed and reveals that the computed penetration depth matches well with that found experimentally for low impact speeds but the two differ for higher values of the impact speed. The discrepancy between the two sets of results for high striking speeds could be due to frictional forces at the target/penetrator interface and the dependence of parameters for the target material upon the temperature. Dynamic effects such as recovery and recrystallization have also been neglected. We note that the test data for the range of temperatures, strains and strain-rates encountered in a typical penetration process is not available in the open literature. Also, in the tests and hence in our simulations, the target length equalled four to five times the penetration depth for low impact speeds and only twice the penetration depth for higher speeds. Thus, support conditions at the back surface may affect more the penetration depth at high impact speeds than at low speeds. We took the back surface to be traction free in every case.

In Figures 2a and 2b we have plotted contours of the temperature rise and the hydrostatic pressure in the deforming target region when the penetrator has been slowed down to 39.5% of its initial impact speed of 1.009 km/s. The temperature rise at a material point is indicative of the accumulated plastic deformation there. The nondimensional temperature is to be multiplied by 116.4°C to obtain the corresponding

dimensional value. These temperature contours suggest that the temperature of target particles adjoining the target/penetrator interface has reached close to the melting temperature of the material, and only a thin layer of the target material has undergone severe plastic deformations. This explains at least partially the observation reported by Forrestal *et al.* that a thin layer of the target material normal to the target/penetrator interface underwent microstructural changes. From the spacing between the contours of the temperature rise one can estimate the temperature gradient along the normal to the contours. The temperature gradient at points on the target/penetrator interface and perpendicular to it is quite sharp at points in the vicinity of the penetrator nose and drops off significantly as one moves away from the penetrator nose.

The contours of the hydrostatic pressure scaled by $\sigma_0$ indicate that peak values in excess of 9 $\sigma_0$ occur in a small region around the penetrator nose tip. Along any radial line the pressure drops off rapidly at target particles near the penetrator nose, and the rate of drop of the pressure decreases slowly as one moves away from the penetrator nose. We note that immediately after the impact the peak hydrostatic pressure near the nose tip exceeded 30 $\sigma_0$.

## RESULTS FOR THE PENETRATION OF RHA STEEL PLATES

We now study penetration of long rigid cylindrical rods 6 mm in diameter into 12 mm thick rolled homogeneous armor (RHA) steel circular plates 36 mm in diameter and supported at the back surface by rigid annular supports with an inner diameter of 24 mm. The bounding surfaces of the plate except those in contact with the penetrator and the back support are taken to be traction free and thermally insulated. Also all contact surfaces are taken to be smooth, and boundary conditions of no inter-penetration of the plate material into the penetrator and vice-a-versa are applied at all contacting surfaces. It is assumed that the penetrator speed $v_0$ stays constant which will be approximately valid for a long penetrator. Constitutive relations (3) and (7) are replaced by

$$2\hat{\mu} = \frac{\sigma_0}{\sqrt{3}\dot{\gamma}} (1 + B \ell n \dot{\gamma}) (1 - \nu\theta), \quad p = K\mu,$$

and we assigned following values to different parameters in order to

compute results.

$\sigma_0$ = 1500 MPa, $\rho_0$ = 7800 kg/m$^3$, c = 477 J/kg°C, $v_0$ = 25 m/s.

K = 302 GPa, B = 0.016, $\nu$ = 6.67 $\times$ 10$^{-4}$/°C, k = 38 W/m°C.

For a flat nosed penetrator, Figures 3 and 4 depict in the deformed shape of the plate, the distribution of the velocity field at times t = 48 $\mu$s and 288 $\mu$s after impact, and contours of the temperature rise at t = 432 $\mu$s. It is clear that the temperature rise at plate particles adjoining the periphery of the penetrator nose is quite high and significant temperature rise occurs in a narrow region encompassing the newly generated plate surface and extending towards the back surface of the plate. Recalling that the heat generated is because of the plastic deformations of material, one can conclude from the contours of the temperature rise that a narrow annular region of the plate is intensely deformed. It is confirmed by the plots at different times and given in Fig. 5 of the second invariant of the strain-rate tensor at particles situated on a radial line coincident with the flat penetrator nose. The velocity distribution (*cf.* Fig. 3) in the deforming plate region suggests that for t $\geq$ 192 $\mu$s, the plate material directly ahead of the flat surface of the penetrator nose moves essentially as a rigid body and is being sheared from the remainder of the plate which is essentially at rest. Even though the mesh was adaptively refined with finer mesh generated in the severely deforming region and coarser elements elsewhere, one can not estimate accurately the width of the shearing layer or equivalently the band-width.

## CONCLUSIONS

We have studied the deep penetration of aluminum targets by fast moving steel rods, and the penetration of RHA steel plates by long rigid rods. In each case, the target/penetrator interface is taken to be smooth and the target material to exhibit strain-rate hardening and thermal softening. For the penetration of aluminum targets by steel rods, the computed depth of penetration is found to match well with that determined experimentally by Forrestal *et al.* For the penetration of steel plates, the material ahead of the flat surface of the penetrator nose is found to move rigidly with the velocity of the penetrator and is sheared from the remainder of the plate which is essentially undeformed. Most

severe deformations of the plate material occur in a narrow region adjoining the interface between the plate and the mantle of the rigid penetrator.

ACKNOWLEDGEMENT: This work was supported by the U.S. Army Research Office grant DAAL-03-92G-0315 to the University of Missouri-Rolla.

## REFERENCES

1. M. E. Backman and W. Goldsmith, The mechanics of penetration of projectiles into targets, *Int. J. Engr. Sci.* 16, 1-99 (1978).
2. G. H. Jonas and J. A. Zukas, Mechanics of penetration: analysis and experiment, *Int. J. Engr. Sci.* 16, 879-903 (1978).
3. C. E. Anderson and S. R. Bodner, The status of ballistic impact modelling, Proc. 3rd TACOM Armor Coordinating Conf., Feb. 17-19, 1987, Monterey, CA.
4. J. A. Zukas (ed.), High Velocity Impact Dynamics, John Wiley and Sons, Inc., New York (1990).
5. K. J. Bathe, Finite element procedures in engineering analysis, Prentice-Hall, Englewood Cliffs, New Jersey (1982).
6. X. Chen and R. C. Batra, Deep penetration of thick thermoviscoplastic targets by long rigid rods, pending publication.
7. M. J. Forrestal, N. S. Brar and V. K. Luk, Penetration of strain-hardening targets with rigid spherical-nosed rods, *J. Appl. Mechs.* 58, 7-10 (1991).

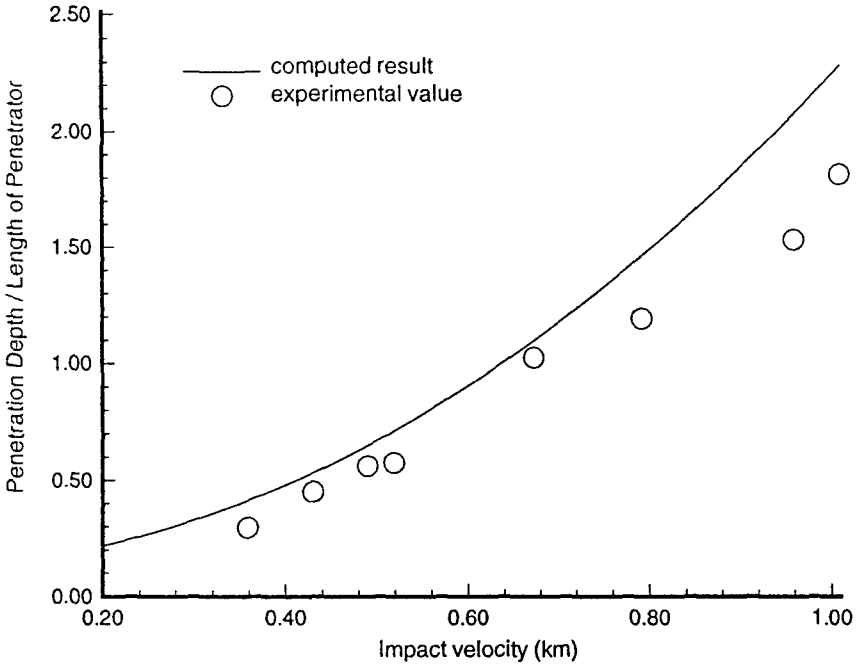



Fig. 1 Normalized penetration depth versus impact speed.

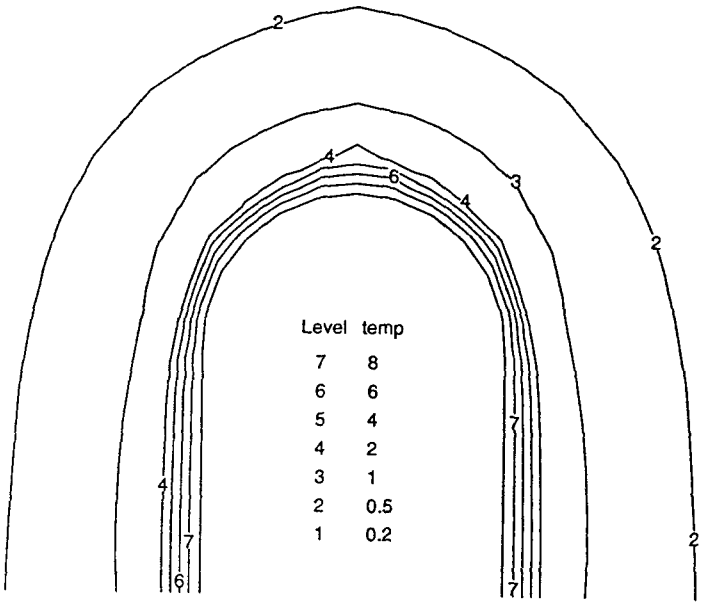



Fig. 2a Contours of nondimensional temperature rise in the deforming target region when penetrator speed = 0.395 $v_0$.

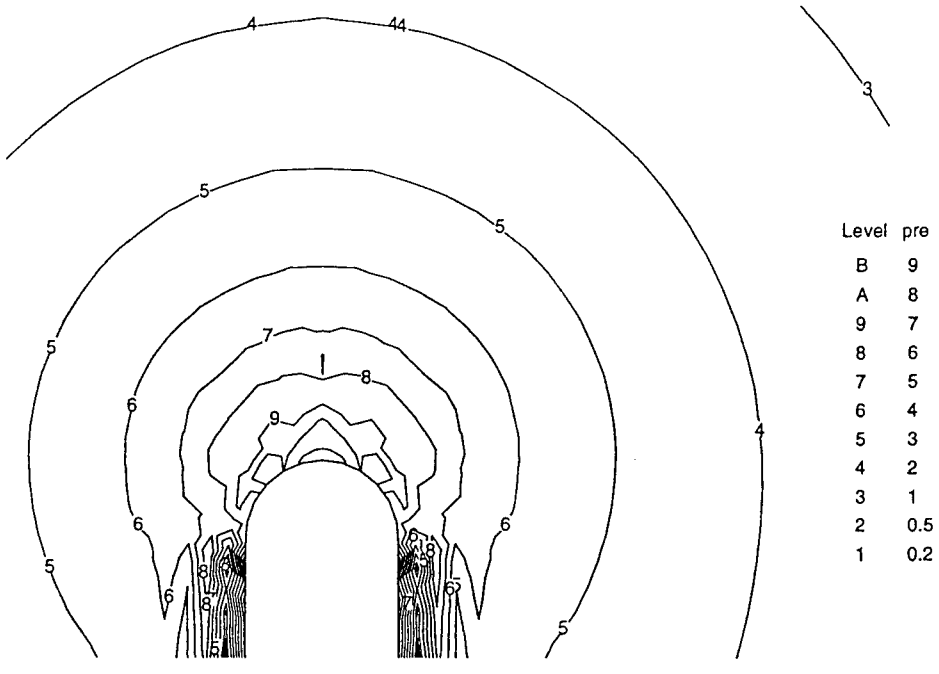



Fig. 2b Contours of nondimensional hydrostatic pressure ($p/\sigma_0$) in the deforming target region when penetrator speed = 0.395 $v_0$.

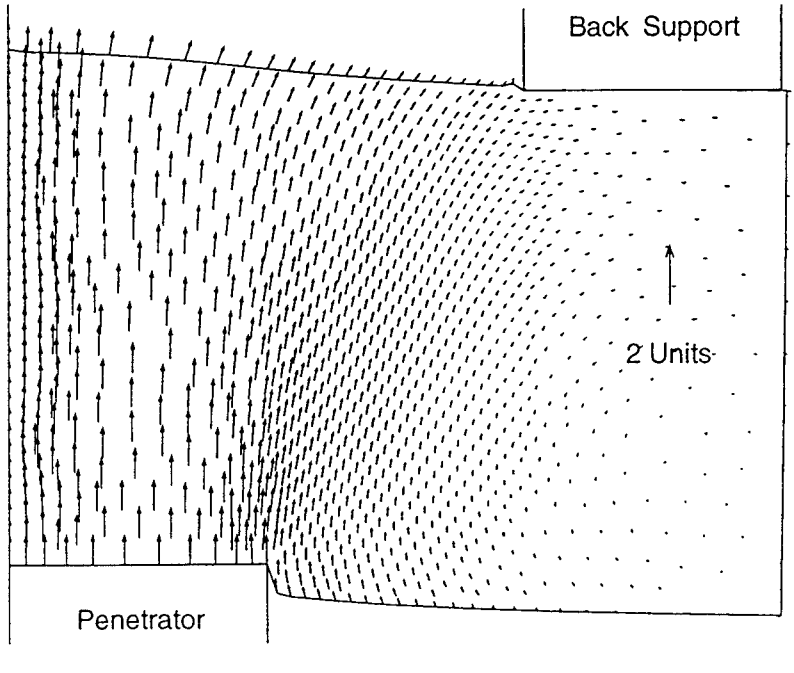



Fig. 3 Distribution of the velocity field in the deformed plate at t = 48 $\mu$s after impact.

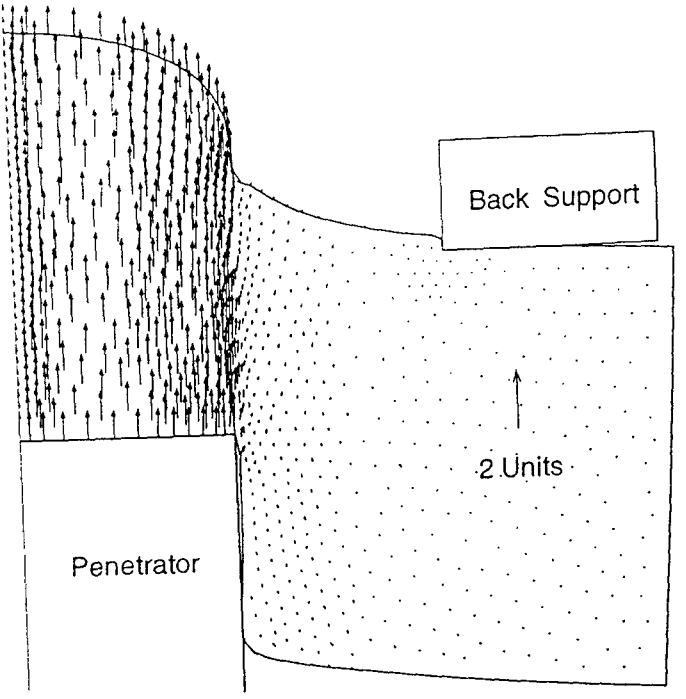



Fig. 3 (continued) Distribution of the velocity field in the deformed plate at t = 288 $\mu$s after impact.

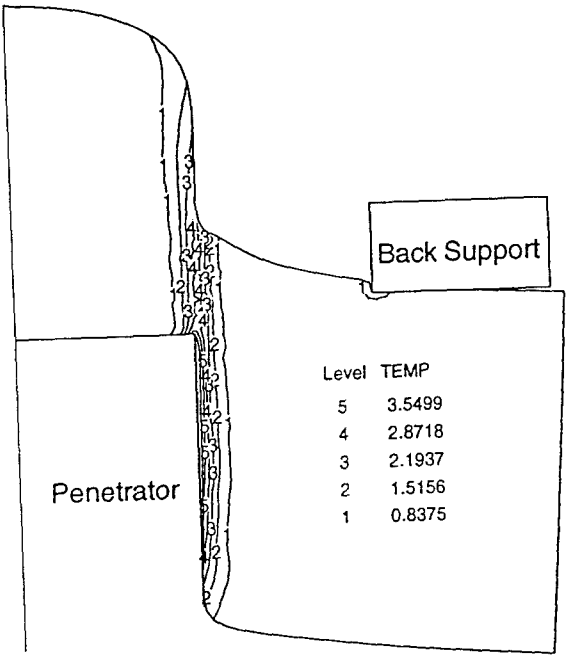



Fig. 4 Contours of nondimensional temperature rise in the deformed plate at t = 432 $\mu$s after impact.

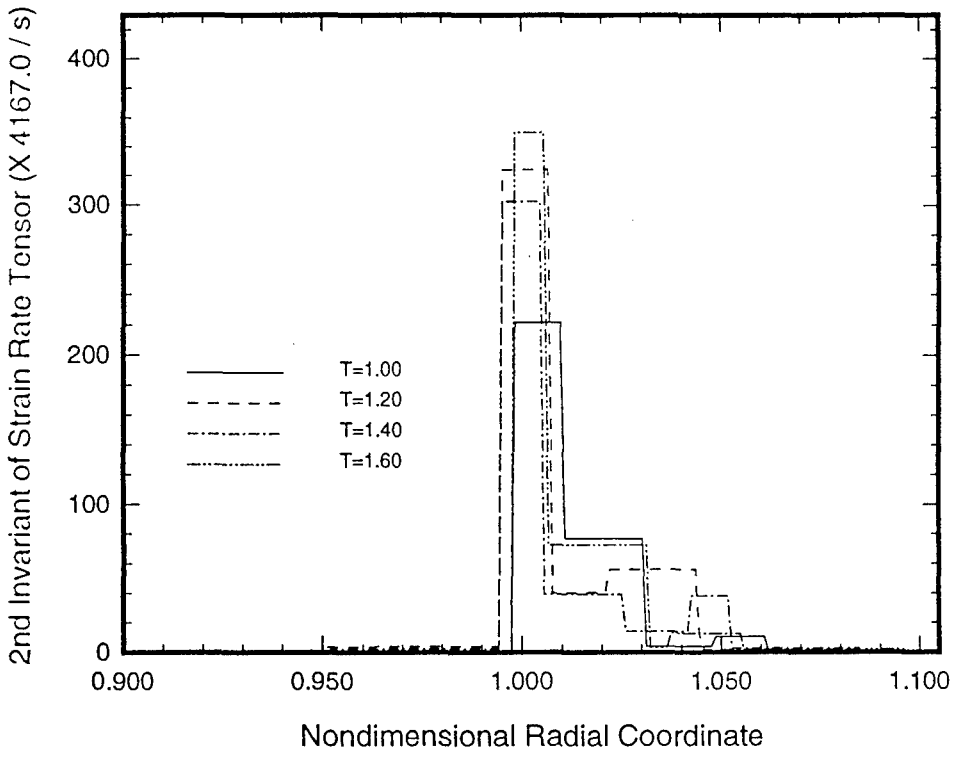



Fig. 5 Distribution, at different times, of the second invariant of the strain-rate tensor in the plate material situated on a radial line in the flat nose of the penetrator. The nondimensional times need to be multiplied by 240 $\mu$s to obtain time after impact. The radial coordinate is nondimensionalized with respect to the penetrator radius of 6 mm.

# Perforation of HY-100 Steel Plates with Long Rod Projectiles

Mr. Stephen J. Hanchak
Impact Physics Laboratory
University of Dayton Research Institute
Dayton, OH 45469-0182

Dr. Brad S. Altman
Advanced Munitions, Dept. 9723
Sandia National Laboratories
Albuquerque, NM 87185-5800

Dr. Michael J. Forrestal*
Advanced Munitions, Dept. 9723
Sandia National Laboratories
Albuquerque, NM 87185-5800

## Abstract

We conducted perforation experiments with 4340 steel, rod projectiles and HY-100 steel, target plates at striking velocities between 80 and 370 m/s. Projectiles were machined to nominally 30-mm-diameter and 281-mm-length so they could be launched from a 30-mm-powder gun without sabots. The target plates were rigidly clamped at a 305-mm diameter and had a nominal thickness of 10.2 mm. In addition to measuring striking and residual projectile velocities, we obtained back surface framing camera data that showed clearly the plate deformation and plug ejection process. An Imacon 792 camera provided up to 20 frames per experiment with an interframe time duration of 10 μs. Our modeling work is in progress, but we present a beam model that exhibits the features observed in the experiments.

## Introduction

We conducted a series of perforation experiments to investigate the ballistic performance of HY-100 steel plates. The experiments were instrumented with diagnostics that provided striking velocity, impact time, and residual velocity. In addition, an Imacon 792 camera photographed the rear surface deformation and plug ejection of the plate. At this time, we have not completed the analytical model for the

plate deformation (bending) and plug ejection (shear localization), but we present a beam model that contains these observed features.

## Perforation Experiments

We performed a set of perforation experiments with 4340 steel rod projectiles that impacted 10.4-mm-thick HY-100 steel (MIL-S-16216J-AM#1) plate targets at normal incidence. The rods were machined to fit in a 30-mm-diameter powder gun and launched without sabots. The rods had nominal 281-mm-length and 1.58-kg-mass.

Several machining steps were performed on the plates in preparation for testing. The plates were blanchard ground on both surfaces to provide a smooth, slag-free, flat surface. Eight equally spaced 22.2-mm-diameter holes were drilled on a 381-mm-diameter bolt circle to allow the plates to be sandwiched between, and bolted to, the test fixtures. The plates were installed with a clamping system that had an inner clamp diameter of 305mm.

We varied the striking velocity, $V_s$, between 78m/s and 370m/s. Table 1 shows the shot parameters and test results for the 10.4-mm-thick HY-100 plates. Figute 1 shows that this range of striking velocities determined accurately the ballistic limit velocity $V_{bl}$ and the residual rod velocities $V_r$.

Table 1: Shot parameters.

| Shot # | $M_{pr}$(kg) | h(mm) | $V_s$(m/s) | $V_r$(m/s) | $V_p$(m/s) | $\phi$(mm) | $M_{pl}$(kg) |
|---|---|---|---|---|---|---|---|
| 1-0149 | 1.594 | 10.5 | 78 | 0 | 0 | 0 | 0.000 |
| 1-0179 | 1.558 | 10.5 | 82 | 0 | 0 | 0 | 0.000 |
| 1-0194 | 1.559 | 10.5 | 105 | 0 | 0 | 0 | 0.000 |
| 1-0196 | 1.557 | 10.5 | 114 | 0 | 0 | 0 | 0.000 |
| 1-0195 | 1.558 | 10.4 | 125 | 80 | 80 | 30.5 | 0.054 |
| 1-0176 | 1.557 | 10.5 | 126 | 84 | 104 | 30.5 | 0.055 |
| 1-0148 | 1.583 | 10.5 | 127 | 98 | 112 | 30.3 | 0.056 |
| 1-0147 | 1.583 | 10.2 | 162 | 142 | 164 | 30.5 | 0.056 |
| 1-0178 | 1.556 | 10.5 | 163 | 138 | 163 | 30.7 | 0.057 |
| 1-0175 | 1.556 | 10.4 | 165 | 141 | 163 | 30.7 | 0.057 |
| 1-0191 | 1.558 | 10.5 | 207 | 168 | 210 | 31.1 | 0.059 |
| 1-0146 | 1.582 | 10.5 | 258 | 232 | 268 | 31.2 | 0.066 |
| 1-0192 | 1.558 | 10.4 | 261 | 233 | 269 | 31.8 | 0.064 |
| 1-0177 | 1.559 | 10.5 | 263 | 234 | 273 | 31.8 | 0.065 |
| 1-0180 | 1.559 | 10.5 | 318 | 284 | 335 | 32.6 | 0.063 |

| | | | | | | | |
|---|---|---|---|---|---|---|---|
| 1-0193 | 1.557 | 10.5 | 322 | 289 | 335 | 32.6 | 0.067 |
| 1-0145 | 1.582 | 10.2 | 370 | 333 | 389 | 33.1 | 0.062 |

h = plate thickness, $V_s$ = striking velocity, $V_r$ = rod residual velocity, $V_p$ = plug residual velocity, $\phi$ = hole diameter, $M_{pr}$ = projectile mass, $M_{pl}$ = plug mass after perforation.

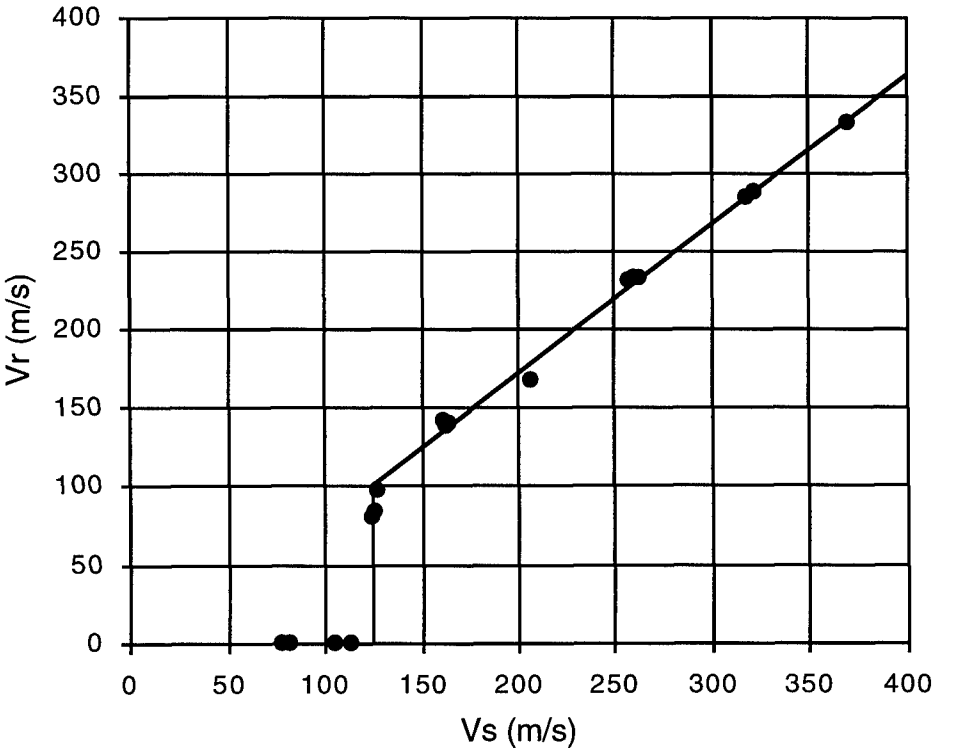



Figure 1: Rod striking velocity versus rod residual velocity data.

Striking velocity was determined by the rod interrupting two continuously monitored laser beams during free-flight prior to striking the plate. Impact time was measured by a time-of-arrival gage cemented to the front surface of the plate. The signal from the time-of-arrival gage triggerred the Imacon 792 camera that monitored the rear surface of the plate. The first frame in Figures 2 and 3 is at 5μsec from impact with all subsequent frames at 10μsec intervals. Figures 2 and 3 show the rear surface deformation recorded by the Imacon camera for shots 1-0191 ($V_s$=207 m/s) and 1-0193 ($V_s$=322 m/s) respectively. A fiduciary length was placed behind the rear surface of the plate to provide a known length scale. The photographs show the early time

plate deformation and late time plug ejection. We also see a cloud of material forming just after plug ejection. We believe this to be a combination of the time-of-arrival gage and compressed air that are trapped between the rod and the plate at the time of impact.

Residual velocity was determined by the plug and rod combination exiting the rear surface of the plate and interrupting two continuously monitored laser beams during free-flight.

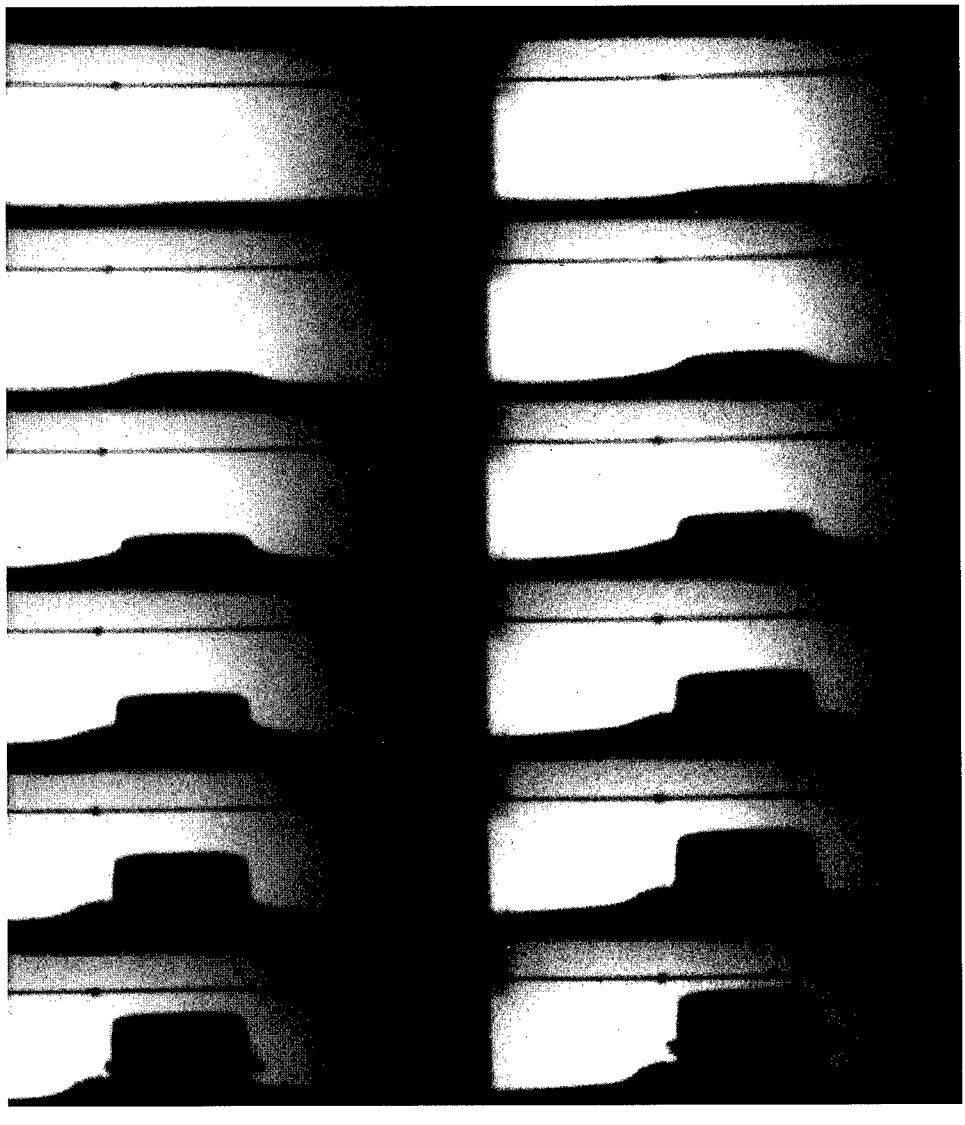


Figure 2: Dynamic deformation of rear surface of plate showing bending and plug ejection; $V_S$=207 m/s.

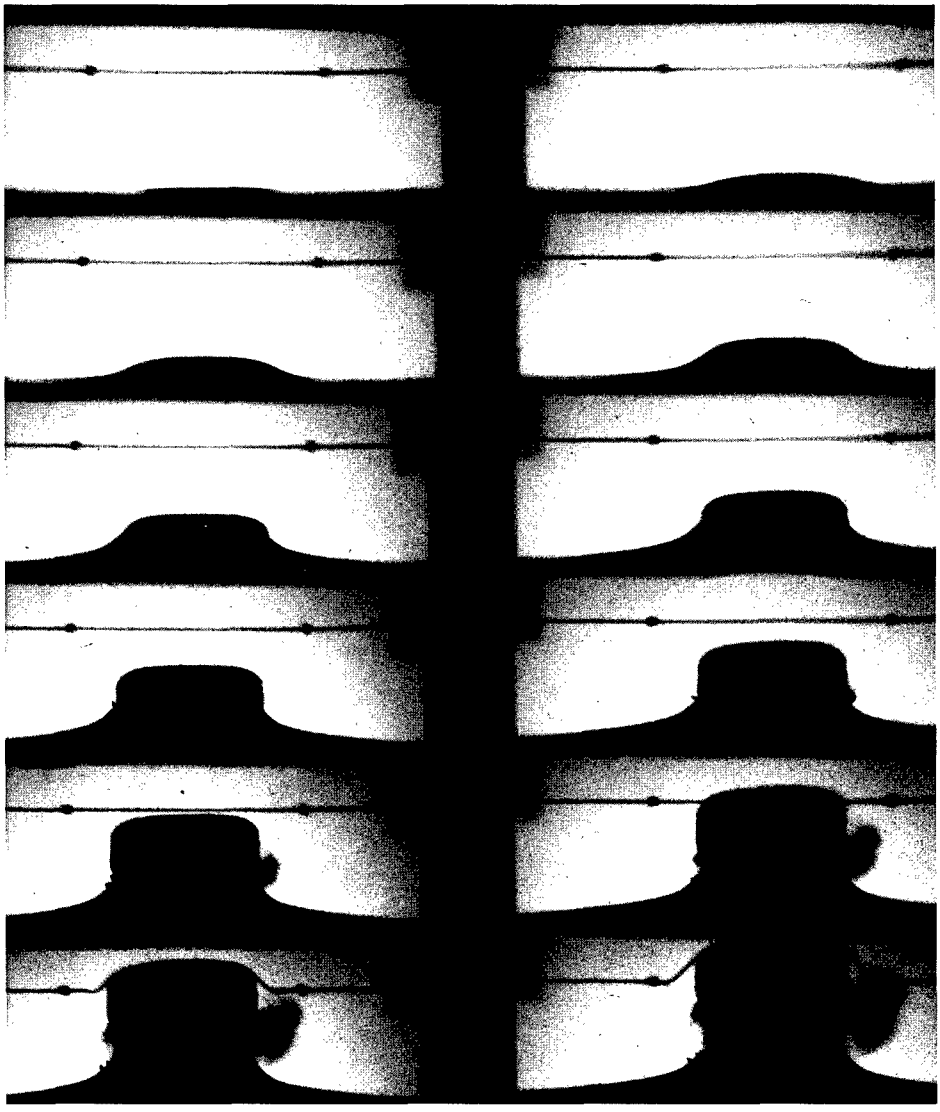


Figure 3: Dynamic deformation of rear surface of plate showing bending and plug ejection; $V_S$=322 m/s.

Beam Model

The photographs in Figures 2 and 3 led us to conclude that the major mechanisms for plate perforation are plate bending and shear localization. To start our modeling, we consider the simpler beam perforation problem. We start with the rigid plastic beam analysis presented by Jones [1] and Symonds [2] and extend their results to predict ballistic limit velocity $V_{bl}$ and residual velocity $V_r$. We model an infinitely long beam with rectangular cross-section struck by a rigid rod (nondeforming) with rectangular cross-section. Figure 4 defines the problem geometry.

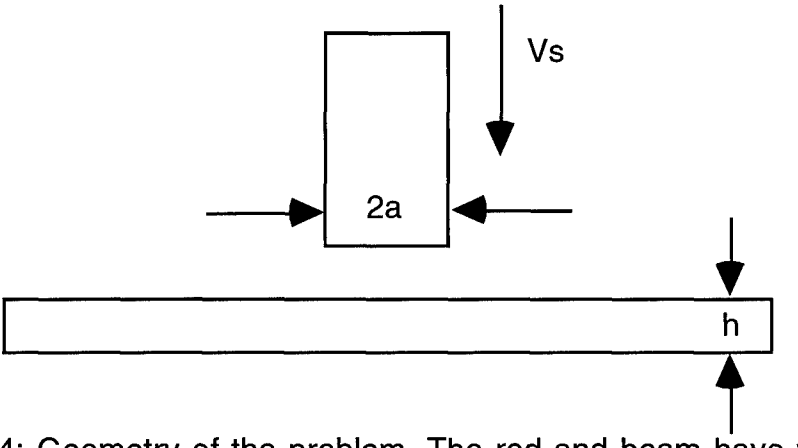



Figure 4: Geometry of the problem. The rod and beam have width b into the page.

Following the rigid plastic beam analysis of Symonds [2], we take the velocity profiles shown in Figure 5 as

$$\dot{w} = \dot{W}_o \qquad -a \le x \le 0 \quad , \tag{1a}$$

$$\dot{w} = \dot{W}_1\left(1-\frac{x}{\lambda}\right) \qquad 0 \le x \le \lambda \quad , \tag{1b}$$

$$\dot{w} = 0 \qquad x > \lambda \quad . \tag{1c}$$

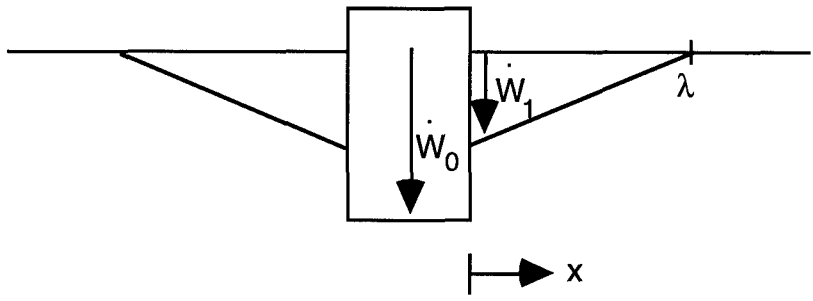



Figure 5: Diagram of velocity distribution.

We now write the equations of dynamics for the beam section $-\lambda<x<\lambda$. There are fully plastic moments, $M_0$, at $x=\pm\lambda$ while the shear forces, $Q_0$, are zero at $x=\pm\lambda$. The equation for lateral momentum is

$$(G+2am)\ddot{W}_0+2\int_0^{\lambda} m\,\ddot{w}\,dx=0 \quad , \tag{2}$$

where G is the mass of the rod and m is the mass per unit length of the beam. The equation for angular momentum of the beam section $0<x<\lambda$ is

$$2M_o=\int_0^{\lambda} m\,\ddot{w}\,x\,dx \quad . \tag{3}$$

The equation for the lateral momentum of the rod and plug is

$$(G+2am)\ddot{W}_o=-2Q_o \quad . \tag{4}$$

We integrate these equations subject to the initial conditions $\dot{W}_o(t=0)=V_s$, $\dot{W}_1(t=0)=0$, $W_1(t=0)=0$, and $W_o(t=0)=0$. After some mathematical manipulations we obtain

$$W_o(t)=\frac{GV_st}{G+2am}-\frac{Q_ot^2}{G+2am} \quad , \tag{5}$$

$$W_1(t)=\frac{{Q_o}^2t^2}{6mM_o} \quad , \tag{6}$$

$$\lambda = \frac{6M_o}{Q_o} \quad . \tag{7}$$

For a Tresca yield criterion with tension yield stress $\sigma_o$, the plastic bending moment and shear force are

$$M_o = \frac{bh^2\sigma_o}{4} \quad , \quad Q_o = \frac{bh\sigma_o}{2} \quad . \tag{8a,b}$$

The rod perforates the beam when

$$W_o(t_p) - W_1(t_p) = h \quad , \tag{9}$$

with residual rod velocity

$$V_r = \dot{W}_o(t_p) \quad , \tag{10}$$

where $t_p$ is defined as the time of perforation.

Figures 6a,b illustrate the displacement and velocity versus time histories for $V_s$=$V_{bl}$. When $V_s$=$V_{bl}$ we satisfy the conditions for perforation: $W_o - W_1 = h$ and $\dot{W}_o = \dot{W}_1$ at t=$t_p$. If the striking velocity is less than $V_{bl}$, then the condition $\dot{W}_o = \dot{W}_1$ is reached before $W_o - W_1 = h$ and the plate will not be perforated. For striking velocities higher than $V_{bl}$ the plate will be perforated and the condition $\dot{W}_o > \dot{W}_1$ will hold. For all $V_s \geq V_{bl}$, the residual rod/plug velocity is

$$V_r = \dot{W}_o(t_p) \quad . \tag{11}$$

We note that at the ballistic limit($V_s$=$V_{bl}$) the residual velocity is finite. This result is observed experimentally in Figure 1. From equations 5,6,8,and 9 the ballistic limit velocity is

$$V_{bl}^2 = \left(1+\frac{2am}{G}\right)^2 \frac{2bh\sigma_o}{3m}\left[1+\frac{3mh}{G+2am}\right] \quad . \tag{12}$$

For long rod penetrators and thin plates the term 2am/G is small compared to unity and may be neglected. The ballistic limit velocity for long rods and thin plates is

$$V_{bl}^2 \cong \frac{2bh\sigma_o}{3m} + \frac{2bh^2\sigma_o}{G} \quad . \tag{13}$$

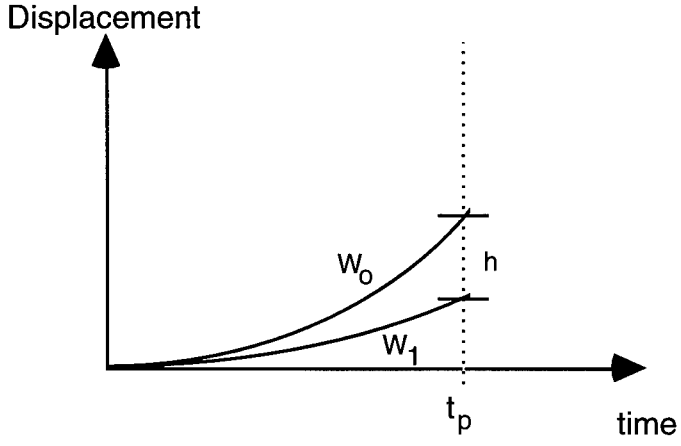



Figure 6: (a) Displacement versus time profile for $V_s=V_{bl}$.

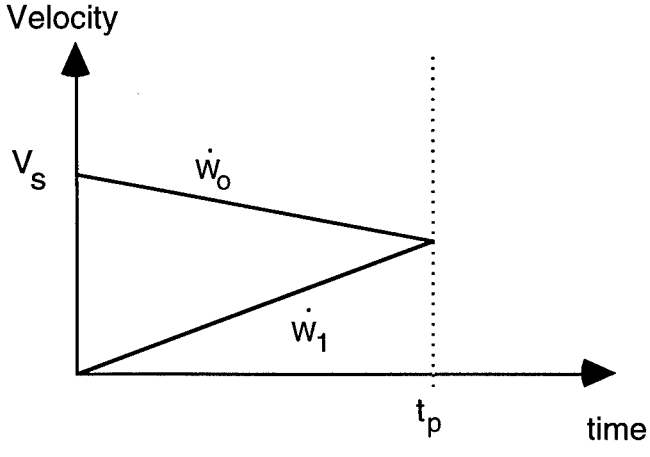



Figure 6: (b) Velocity versus time profile for $V_s=V_{bl}$.

## Summary

We conducted a series of perforation experiments with 4340 steel rod penetrators perforating HY-100 steel plates and present a

beam model that includes bending and shear localization. The beam model predicts a non-zero residual velocity at the ballistic limit velocity which is in agreement with our experimental observation for plates.

## Acknowledgments

This work performed at Sandia National Laboratories is supported by the U.S. Department of Energy under Contract DE-AC04-76DP00789

## References

[1] N. Jones, 1989, Structural Impact, Cambridge University Press, Cambridge, pp. 237-246.

[2] P. S. Symonds, 1968, Plastic shear deformations in dynamic load problems, Engineering Plasticity, eds. J. Heyman and F. A. Lechie, Cambridge University Press, Cambridge, pp. 647-664.

# A CONCEPTUAL MODEL TO PREDICT FORCE-TIME HISTORIES IN STEEL PLATES DUE TO PENETRATION BY TUNGSTEN RODS AT VELOCITIES OF 1.5 TO 2.5 KM/S

S. Dhar, D.J. Grove* and N.S. Brar
University of Dayton Research Institute
300 College Park
Dayton, Ohio 45469-0120

## ABSTRACT

A two-dimensional analytical model has been proposed to predict the force-time history in an isotropic plate due to penetration by a projectile. Mathematical expressions are formulated to describe the shape and radial expansion attributes of the local cavity during penetration. This paper outlines the concepts of the contact zone and cavity expansion in the target plate. Six penetration experiments were performed in 4340 steel plates by long tungsten rods (L/D = 11) at velocities in the range of 1.5 to 2.5 km/s. These experiments were then simulated using the EPIC91 Research Code. From the experiments, cavity radius, terminal velocity and reduction in rod length are compared with the finite element simulations. The simulated cavity radius, cavity depth, cavity expansion velocity, and force time history are compared with that obtained from the cavity expansion model. The results are encouraging.

**Key Words:** local cavity, global cavity, contact zone, cavity growth, cavity expansion.

**1.0 BACKGROUND.** The penetration process has been modeled by Tate [1,2], Hanagud and Ross [3], Awerbuch and Bodner [4] and Ravid and Bodner [5]. The above models are one dimensional and consider a rigid projectile, and a compressible [3] or incompressible [1,2,4,5] target. At low striking velocities all the models sufficiently describe the penetration and perforation parameters, even though the modelling concepts are different. The behavior at the projectile and target interface, where erosion occurs, is controlled by the hydrodynamic pressure, resistance of the target, and strength of the projectile. Tate [6] approximated the projectile strength and target resistance for a compressible target assuming spherical cavity shape. Forrestal et al [7] approximated the projectile strength and target resistance for a

compressible target, and a low cavity (spherical) expansion velocity. Rosenberg et al [8] described cylindrical cavity expansion in an infinite medium. For a hypervelocity case these models may be conservative.

We have proposed a two-dimensional model [9] to describe the penetration and perforation. The theoretical work is based on contact zone and cavity expansion approximation. In the contact zone model erosion behavior at the projectile and target interface is indirectly taken into account by considering a thin melt layer, which is formed due to generation of frictional heat. In the dynamic cavity expansion model, the concepts are taken from Hanagud and Ross [3], except for the material model.

**1.1 Model Concept.** To analytically calculate the loading history in the target, the impact or penetration event is described through contact zone and cavity expansion models [9]. The projectile is assumed to be a flat-end cylinder (rod) that impacts a homogeneous, isotropic target plate at normal incidence. Immediately upon impact, the projectile begins to penetrate the target. As the penetration proceeds, the projectile's nose remains in constant contact with the target and a cavity forms inside the target. This contact zone defines the target's local cavity and is schematically shown Fig. 1. In this figure *(r,z,θ)* and *(r ',z ',θ)* are

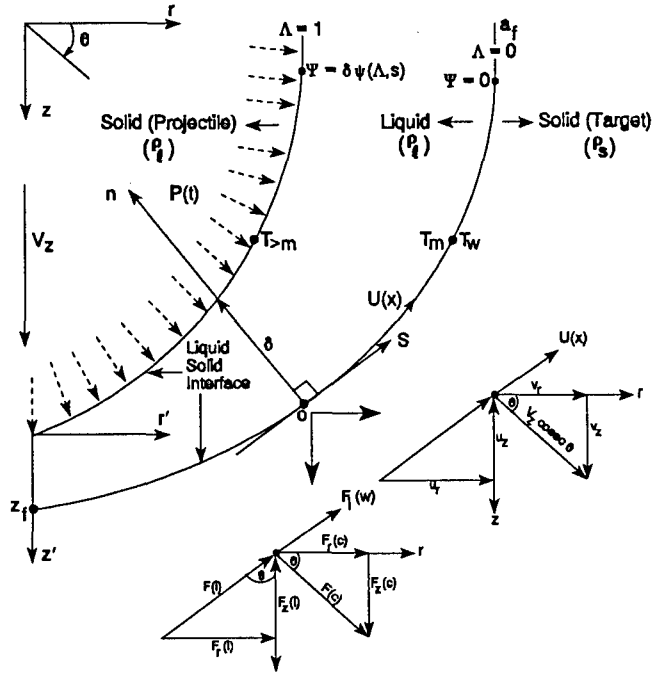



Figure 1 Schematic Representation of Mechanics of Cavity Formation.

the initial and moving axisymmetric coordinates. The $z'$ coordinate moves with the projectile nose and has velocity $V_z(t)$. At time $t = 0^-$, the velocity $V_z(0^-) = 0$; at time $t = 0^+$, the velocity $V_z(0^+) = V_s$, the striking velocity, and at time $t = t_f$, the velocity $V_z(t_f) = V_f$ is the exit velocity or the terminal velocity. The terminal value of the penetration depth $z_f$, may be obtained from the equation of motion for a projectile of density $\rho$ and the deforming radius $R(r,z)$ ($\rho_p \pi R^2(r,z) dV/dt = -F_c - F_i$ ) that is penetrating the target material in the vertical direction. The compressive force, $F_c$ , and the shearing or frictional force, $F_i$ , together decide the dynamic force resisting penetration along the vertical direction.

In the hypervelocity model, we consider that a very thin melt or vapor layer ($\delta$) is formed due to sliding friction between the projectile surface and the cavity wall. The temperature at the wall ($T_w$ ) will vary from melting point ($T_m$ ) to evaporation point ($T_{>m}$ ). The melt layer is assumed to be incompressible. We introduce a stream function $\psi = \psi(s,n)$ in two dimensional flow such that $v_\alpha = -\varepsilon_{\alpha B \gamma} \psi_{,B}$. The stream line coordinates in Fig. 1 are $s$ and $n$, where $s$ is along the contour of the cavity and $n$ is the normal to the tangent of the cavity surface. The origin, $O$, may be placed at an arbitrary point on the contour. The angle between the element of the contour and the direction of the velocity $V_z(t)$ of the penetrating projectile is denoted by $\theta(x)(=\pi/2 - x/R(r,z))$, where $x$ is the distance measured along the s coordinate and $R(r,z)$ is the radius of the deforming projectile. We make an assumption that the projectile ($0^+ \le t \le t_f$ ), is impinging at a constant velocity, $V_z$, on a contour of the cavity, and the points of the contour may move along it at a velocity, $U(x)$. In other words, keep the points on the contour in the target fixed, and vary the points on the contour of the projectile. Now the stream coordinate $n$ is non-dimensionalized with the thickness of the melt layer ($\Lambda = n/\delta$). The new stream function is then represented by $\psi = \psi\delta(x,\Lambda)$, where $\psi$ represents the rate of increase in the surface area and $\Lambda$ takes the value from 0 ($n = 0$) to 1 ($n = \delta$). At $\Lambda = 0$, $\psi = 0$ and at $\Lambda = 1$, $\psi = \psi\delta(x,\Lambda)$. The flow and temperature distribution in the melt layer are assumed to satisfy the usual equations of motion and heat balance based on thin-layer theory. The excess force of pressure and the frictional force in the direction of motion yield the resistance to the forward surface of the projectile. The forces of pressure and the frictional forces add up in the radial direction to cause cavity expansion. The above description defines the formation of the local cavity. During the entire penetration event, an infinite number of these local cavities are formed. This process can be approximated by the formation of a finite number of cavities.

**1.2 Cavity Model Approximation.** Recall that the target's local cavity is defined as that part of the global cavity in which radial expansion is occurring, i.e., in the immediate vicinity of the nose of the penetrating rod. Based on Mathieu's function [10], the following function has been has been formulated to describe the shape of these local cavities.

$$a(z) = \begin{cases} a_f\left[1 - K^*\left(1 - \dfrac{z}{z_f}\right)^2\right]^{\alpha} & , \quad Z^* < z \le z_f \\ \left(\dfrac{C_R}{\dot{z}_{int}}\right) z & , \quad 0 \le z \le Z^* \end{cases} \tag{1}$$

where the local cavity radius *a(z)* varies between *0* (at the base of the cavity) and $a_f$, the characteristic final (maximum) cavity radius. Also, $z$ is the local cavity depth, $z_f$ is the characteristic final (maximum) cavity depth, $C_R$ is the Rayleigh wave speed, $\dot{z}_{int}$ *(*$V_z$ *)* is the projectile/target interface velocity (assumed constant for complete penetration), and $\alpha$ is the calibration parameter. In Eqn. (1), the two expressions and their first derivatives (with respect to $z$) must be equal to each other at $Z^*$, i.e., the cavity shape function is smooth and continuous. For an arbitrary $\alpha$ *(0* $< \alpha \le$ *1)*, this condition can be satisfied by uniquely determining the parameters $K^*$ and $Z^*$ through an iterative numerical scheme. Fig. 2 illustrates the cavity shape function for various values of $\dot{z}_{int}$ and $\alpha$. Assuming that $\dot{z} = \dot{z}_{int}$, the partial derivative of the shape function *a(z)* with respect to time, $a(z,t)_{,t}$, provides the following expression for the local cavity's radial expansion velocity:

$$a(z,t)_{,t} = \begin{cases} \left(\dfrac{2\alpha a_f K^*}{z_f}\right)\left(1 - \dfrac{z}{z_f}\right)\left[1 - K^*\left(1 - \dfrac{z}{z_f}\right)^2\right]^{\alpha-1} \dot{z}_{int} & , \quad Z^* < z \le z_f \\ C_R & , \quad 0 \le z \le Z^* \end{cases} \tag{2}$$

The radius of the cavity is typically 2-3 times the radius of the projectile.

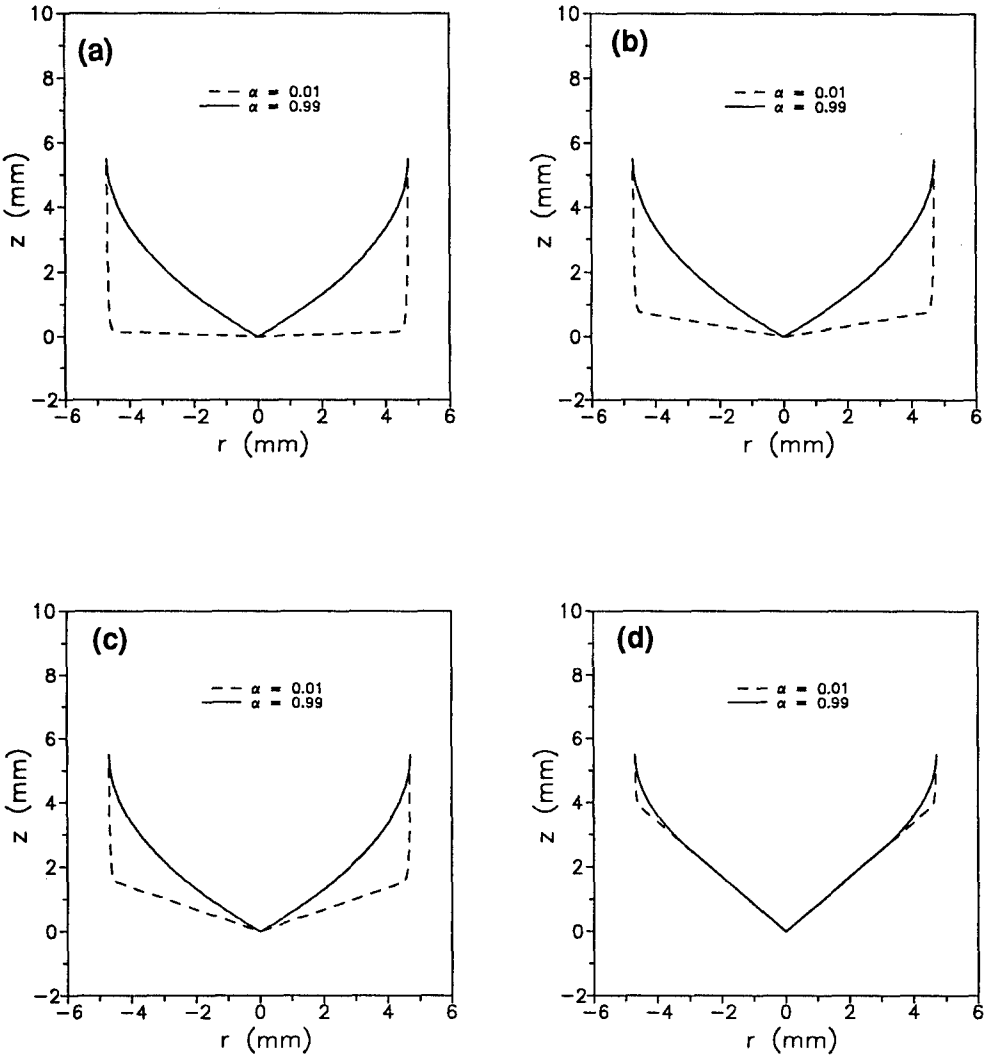



Figure 2 Local Cavity Shape Function for Various Values of $\dot{z}_{int}$ and α: (a) $\dot{z}_{int}$ = 0.1 mm/μsec; (b) $\dot{z}_{int}$ = 0.5 mm/μsec; (c) $\dot{z}_{int}$ = 1.0 mm/μsec; and, (d) $\dot{z}_{int}$ = 2.5 mm/μsec.

## 2.0 EXPERIMENTAL ANALYSIS.

**2.1 Description of Projectiles and Targets.** The tungsten projectiles, 0.195-in in diameter and 2.15-in long (L/D ≈ 11 and mass ≈ 18.8g), were prepared from as-received tungsten alloy rods. The tungsten alloy (WN307F, swaged and aged) had a density of 17.67 g/cm$^3$ (99.6% of the theoretical density) and a Rockwell hardness ($R_c$) of 44.6. The 4340 steel target plates, with a

12-in nominal diameter were sliced from a 12 inch cold-rolled round stock with thicknesses ranging from 1 to 4 inches. The hardness of these as-received plates was about 22. Both surfaces of the plates were turned to make them flat and parallel. The plates were subsequently heat treated to a hardness ($R_c$) of about 30.

**2.2 Two Stage Gas Gun Launch and Results.** Projectiles were launched using the 50/20 mm two stage gas gun at the University of Dayton Research Institute, to velocities up to about 2.7 km/s. Projectile velocities were measured to within 0.5% accuracy using time-of-flight measurements between four laser-photodetector stations located along the range center line. Preimpact yaw and pitch of the projectile were measured with an orthogonal set of flash x-rays triggered by a delayed pulse from the laser beam. Penetrator exit velocity and residual length were monitored by a second set of orthogonal flash x-rays mounted behind the target plate.

Table 1 summarizes the data on impact velocity, preimpact penetrator inclination, and residual velocity and length of the penetrator from the six experiments. Photographs of the penetrator, target configuration, residual length of the penetrator, and of the front and rear surfaces of the shot target plates are shown in Fig. 3. The target plates were then cut parallel to the hole made by the penetrator during the penetration process to expose the cavity outline. The surface area near the cavity was milled to clean up the saw cut marks. Photographs of the cavity profile from shot 4-1529 are shown in Fig. 3.

TABLE 1. SUMMARY OF PENETRATION DATA

| Shot No. | Penetrator (Rod) Mass (g) | Target Thick. (in.) | Impact Vel. (km/s) | Rod Inclination (°) | | | Residual Velocity[a] (km/s) | Residual Rod Length (in.) |
|---|---|---|---|---|---|---|---|---|
| | | | | Pitch | Yaw | Total | | |
| 4-1529 | 18.7242 | 2.532 | 2.02 | 0 | 0.75L | 0.75 | 1.31 | 0.24 |
| 4-1566 | 18.8131 | 2.505 | 1.60 | 12.25U | 11L | 16.5 | Partial | Penetration |
| 4-1567 | 18.7850 | 2.007 | 2.02 | 6D | 2R | 6.3 | 1.64, 1.63[b] | 0.29, 0.30[b] |
| 4-1568 | 18.7852 | 2.514 | 2.66 | 3U | 3L | 4.2 | 2.25 | 0.34 |
| 4-1569 | 18.8055 | 1.005 | 2.02 | 4U | 10R | 10.8 | -[c] | 0.46, 0.32, 0.25, 0.28[d] |
| 4-1570 | 18.8133 | 4.090 | 2.06 | 3.5D | 7.25R | 8 | Partial | Penetration |

[a] Residual velocity measured at the apparent fragment center of gravity (± 0.03 km/s)
[b] Residual rod broke into two pieces
[c] Only one view of residual rod obtained
[d] Residual rod broke into four pieces

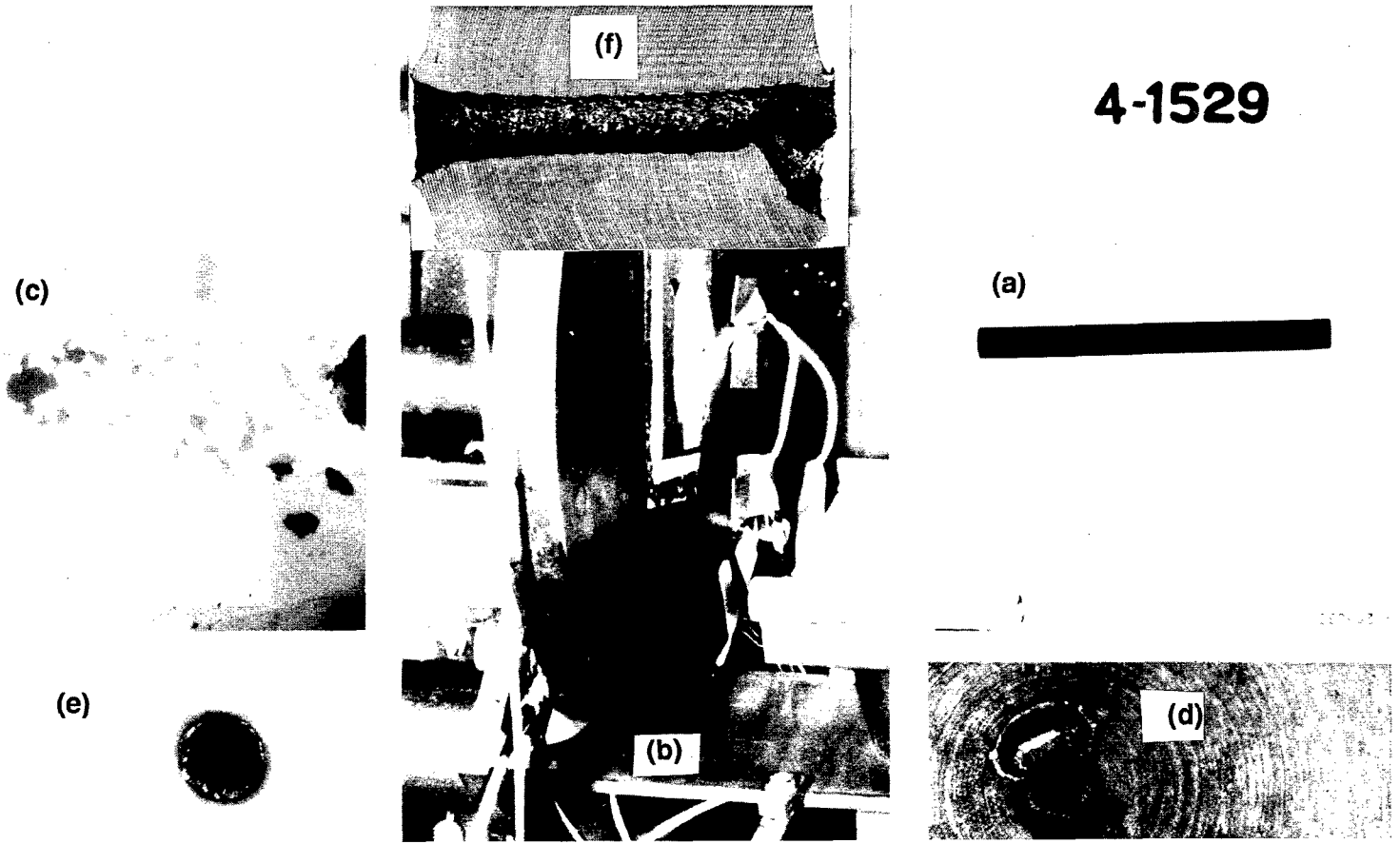



Figure 3 Photographs of the (a) Penetrator; (b) Target Configuration; (c) Residual Length of Penetrator; (d) Front Surface of the Shot; (e) Rear Surface of the Shot; and, (f) Cavity Profile.

**3.0 FINITE ELEMENT SIMULATIONS.** The 1991 version of the EPIC Research Code (EPIC91R) [11] was used to simulate all six penetration experiments. A baseline 2D axisymmetric finite element grid was created for each experimental configuration. All elements were generated in a crossed triangle arrangement. Elements on the rod/plate interface were eroded (eliminated) when their equivalent plastic strain exceeded an erosion strain criterion of 1.5. In all the simulations, the target plates were modeled without restraints.

**3.1 Calibration With Experiments .** Shot 4-1529 was chosen for the initial calibration of the finite element simulations, since it was the "best" shot in terms of preimpact rod inclination (pitch and yaw). The calibration objectives were to match the following experimental data: (1) the length of the exiting projectile, (2) the velocity of the exiting projectile, and (3) the dimensions of the cavity in the target plate. The first simulation of shot 4-1529 employed the Johnson-Cook strength and fracture models to describe the material behavior in both the tungsten rod and the steel plate. Reasonable agreement with shot 4-1529 was finally obtained by preventing damage growth (DAM=0) and thermal softening (M=0) in modeling the material behavior of the tungsten rod. Maintaining the above material behavior restrictions, the remaining five shots were simulated. Tables 2 and 3 compare the simulation results with the experimental measurements. Fig. 4 shows the final grid plots from the calibrated simulations.

TABLE 2. COMPARISON OF EXPERIMENTAL AND SIMULATION RESULTS FOR CAVITY DIAMETERS

| Shot Number | CAVITY DIAMETER (mm) | | | | | |
|---|---|---|---|---|---|---|
| | Entry | | Middle | | Exit | |
| | Exp. | Sim. | Exp. | Sim. | Exp. | Sim. |
| 4-1529 | 10 | 13 | 9.75 | 9.5 | 11.75 | 14 |
| 4-1566 | 6 | 11.5 | -- | 8 | -- | -- |
| 4-1567 | 11.5 | 13.5 | 10.5 | 9.5 | 12 | 14 |
| 4-1568 | 15 | 15.5 | 13.5 | 11 | 16 | 19 |
| 4-1569 | 11 | 13.5 | 10 | 10 | 11.5 | 15.5 |
| 4-1570 | 12 | 12.5 | 10 | 7.5 | -- | -- |

TABLE 3. COMPARISON OF EXPERIMENTAL AND SIMULATION RESULTS FOR ROD EXIT DATA

| Shot Number | Sim. Impact Velocity (km/s) | Preimpact Rod Inclination (°) | | Exit Velocity of Rod (km/s) | | Dimensionless Exit Length of Rod (Final/Initial) | |
|---|---|---|---|---|---|---|---|
| | | Exp. | Sim. | Exp. | Sim. | Exp. | Sim. |
| 4-1529 | 2.00 | 0.75 | 0.0 | 1.31 | 1.49 | 0.111 | 0.178 |
| 4-1566 | 1.60 | 16.5 | 0.0 | --- | --- | --- | --- |
| 4-1567 | 2.00 | 6.3 | 0.0 | 1.64 | 1.74 | 0.273 | 0.356 |
| 4-1568 | 2.66 | 4.2 | 0.0 | 2.25 | 2.42 | 0.157 | 0.280 |
| 4-1569 | 2.00 | 10.8 | 0.0 | --- | 1.89 | 0.606 | 0.662 |
| 4-1570 | 2.00 | 8.0 | 0.0 | --- | --- | --- | --- |

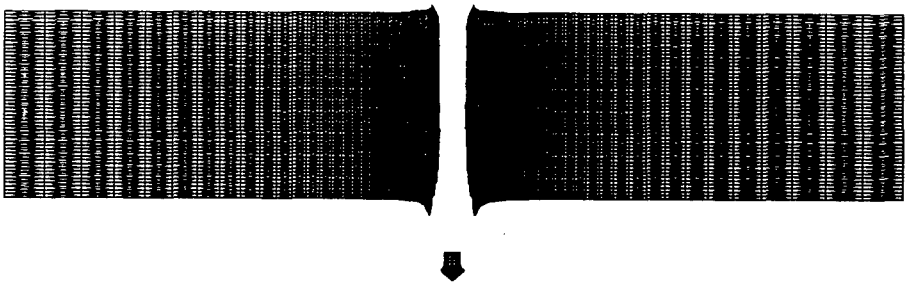


Figure 4 Final Grid Plot From Simulation of Shot 4-1529 (Baseline Grid).

**3.2 Force-Time History From Simulation.** Methods to obtain accurate time histories of the forces exerted on the targets from the above simulations were investigated. In one approach, the net system force exerted during a time step was determined by dividing the change in axial momentum by the time step $(\Delta M_z / \Delta t)$. However, the resulting force-time history profile became extremely noisy after the first few microseconds; this was probably due to the simulated erosion process. To eliminate this noise problem, the simulated time history of the target plate's axial momentum was first approximated with a fifth-degree polynomial. The net axial force exerted on the target at any time could then be calculated from the polynomial's first derivative $(dM_z / dt)$. The dashed line in Fig. 5 shows the smoothed axial force-time history that was computed from the simulation of shot 4-1529.

**3.3 Simulated Cavity Formation in the Target Plate.** The EPIC91R code was modified accordingly to produce additional output pertaining to the rod/plate interface velocity and the local cavity's shape and radial expansion characteristics. Output data from the EPIC simulation of shot 4-1529 were used to analyze the characteristics of local cavity expansion and growth in the target plate. The simulated local cavity shape data from 20 equally spaced axial locations throughout the thickness of the target plate were used to calibrate the parameters in the local cavity shape function (Eqn. (2)). The data and the cavity shape function are superimposed in Fig. 6. In this figure, the horizontal axis indicates radial distance from the axis of symmetry and the vertical axis represents local cavity depth. The cavity shape function parameters are: $a_f = 4.7$ mm, $z_f = 5.5$ mm, $\dot{z}_{int} = 1.15$ mm/μsec, $C_R = 2.94$ mm/μsec, $\alpha = 0.35$, $K \approx 1.245$, and $Z \approx 0.86365$ mm. Local cavity expansion occurs in the radial direction and cavity growth occurs in the axial direction. The characteristics of the cavity's radial expansion were determined by examining the simulated time histories of cavity radii for 20 equally spaced axial locations throughout the target thickness. The data from these profiles, superimposed in Fig. 7, exhibit a distinctive pattern. Initially, upon arrival of the penetrating rod, the radial expansion rate is highest. The expansion rate gradually decreases to zero (at about 4.5 μsec) as the rod passes and the cavity has expanded to its maximum radius (about 4.7 mm). The solid line in Fig. 7 represents a characteristic radial expansion history for the local cavity. This curve, based on the assumptions of constant local cavity shape and rod/plate interface velocity, was plotted from Eqn. (1) by varying the local cavity depth $(z)$ from $0$ to $z_f$ as a function of time.

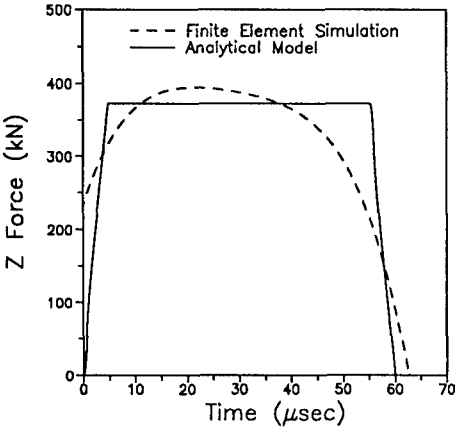



Figure 5 Force-Time Histories.

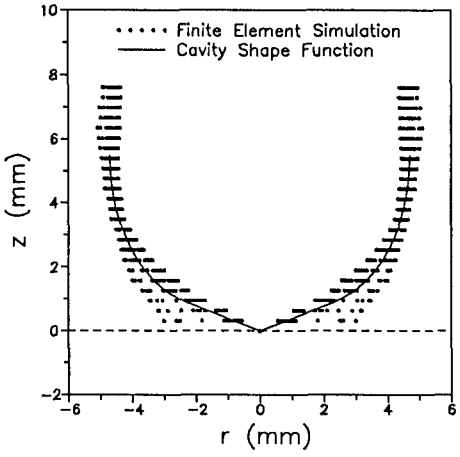



Figure 6 Cavity Shape Function With Cavity Shape Data.

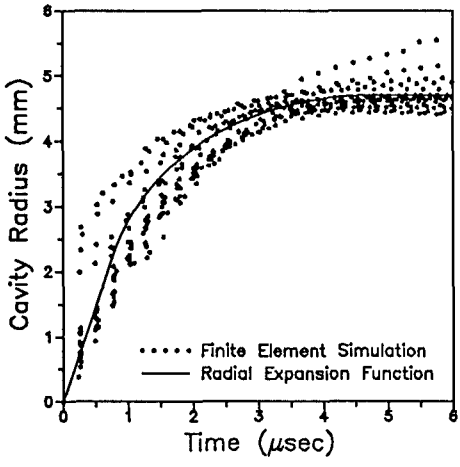



Figure 7 Radial Cavity Expansion -Time History.

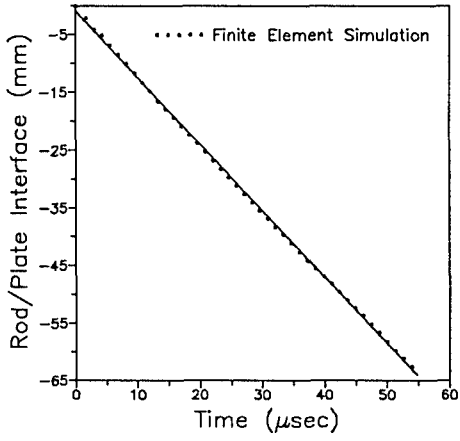



Figure 8 Cavity Growth - Time History.

Cavity growth in the axial direction was also examined through a time history plot of the simulated axial rod/plate interface position, shown in Fig. 8. This curve, essentially a straight line, suggests a relatively constant rod/plate interface velocity ($\approx$ 1.2 km/s) during the penetration process. A constant interface velocity assumption may be reasonable for complete penetration. In the case of partial penetration, however, the rod/plate interface velocity may be constant during most of the penetration event, but eventually this velocity must decrease to zero.

**4.0 APPROXIMATE ANALYTICAL FORCE-TIME HISTORY.** An analytical force-time history was computed for shot 4-1529. At any time during the penetration event, the instantaneous force exerted on the local cavity can be determined from the product of the total pressure on the local cavity and the surface area of the local cavity. The time history of pressure was computed based on the penetration model described in [9], and the surface area of the local cavity was determined from the characteristic cavity shape function. During the penetration event, the static pressure on the local cavity is constant and the dynamic pressure is a function of the local cavity's radial expansion rate. The following assumptions were made: (a) the melt layer was ignored *($\delta = 0$)*, (b) the interface velocity was constant, (c) the static pressure was based on the finite element analysis, (d) a simplified form of the dimensionless dynamic pressure was employed ($\bar{P}_D = \beta \dot{a}^2$, where $\beta$ is a constant), and (e) the local cavity shape was uniform throughout the penetration event.

Within the local cavity, the radial expansion rate decreases from a maximum at the base to a minimum (zero) at the top; the dynamic pressure also varies along the wall of the local cavity. Because of the assumption of constant local cavity shape, the calculated distribution of dynamic pressure also remained constant throughout the penetration. The local cavity shape function (Eqn. (1)) does not lend itself to an analytical expression for evaluating the cavity's surface area. Instead, a numerical integration technique (e.g., the trapezoidal rule) was necessary to compute the surface area as a function of cavity depth. The local cavity's surface area varies with time. At the beginning of the rod penetration event, there is no cavity, so the surface area is zero. As the penetration proceeds, the local cavity grows until it reaches its maximum depth ($z_l$) and surface area. The surface area of the local cavity then remains constant until the global cavity depth equals the target plate's thickness. Finally, the local cavity's surface area decreases to zero as the projectile exits the target. Calculation of the analytical force-time history requires the constants used to describe the local cavity shape *($a_f$, $z_f$, $\dot{z}_{int}$, $C_R$, $\alpha$, $K$, and $Z$)*, the thickness of the target plate, the static pressure, and the parameter $\beta$ (used to compute the dimensionless dynamic pressure). The solid line in Fig. 5 represents the analytical force-time history that was computed for shot 4-1529. In this calculation, the constants given in Section 3.3 were used to describe the shape of the local cavity. The target plate was 63.5 mm thick and the dynamic pressure parameter *($\beta$)* was set to 0.1 $\mu sec^2/mm^2$. To preserve the simulated total impulse, a static pressure of 2.08 GPa was assumed. Note that this loading history has an idealized profile due to

the simplifying assumptions mentioned above. As the figure indicates, the salient features of the analytical calculation compare reasonably well with the force-time history calculated from the simulation of shot 4-1529.

**5.0 DISCUSSION.** A methodology has been established for the analytical prediction of the force-time history in a 4340 steel plate due to penetration by a long tungsten rod at velocities in the range of 1.5 to 2.5 km/s. The forcing function shown in Fig. 5 was not a prediction. To predict force-time histories, an efficient solution technique must be devised. Once this solution algorithm has been translated to computer code, the following items can be predicted to describe the cavity formation during the penetration event: (a) distribution of the melt layer thickness, (b) pressure distribution on the melt layer surface, (c) static and dynamic pressure, shear stress along the cavity wall, (e) axial cavity growth rate, and (f) stress and strain distributions in the target during the penetration process. The force-time history in the target can then be accurately predicted, along with the penetration depth and amount of momentum transferred. In Figs. 6 and 7 the scatter could be due to the initial erosion phase of the flat end of the projectile. As Fig. 2 indicates, this could be modeled by varying the parameter $\alpha$ as a function of global cavity depth. Small values of $\alpha$ could be used to model the initial projectile nose shape (cylindrical), and then $\alpha$ could be increased to account for the erosion phase during which the projectile's nose becomes pointed.

## ACKNOWLEDGEMENTS

This work is being supported by the U.S. Army Research Laboratory, Aberdeen Proving Ground, Maryland under the Contract DAAA15-92-K-0001, with Mr. Michael Sivack as the program monitor. Mr. Andy Piekutowski and Mr. Kevin Poormon designed the launch techniques on the two stage light gas gun. Mr. Chuck Blair and Mr. Robert Gooding performed the shots. Mr. Ed Strader assisted with the recording the data from force transducers and Mr. Richard Tocci helped with the processing x-ray films and the prints. The authors thank Profs. Joseph P. Gallagher and Joseph E. Saliba for their suggestions and comments. The authors greatly appreciate the efforts of Ms. Marylea Barlow, who prepared this manuscript.

## REFERENCES

[1] Tate, A., J. Mech. Phys. Solids, Vol. 15, pp. 287-399, (1967).
[2] Tate, A., J. Mech. Phys. Solids, Vol. 17, pp. 141-150, (1969).
[3] Hanagud, S. and Ross, B, AIAA J., Vol. 9(5), pp. 905-911, (1971).
[4] Awerbuch, J. and Bodner, S. R., Int. J. Solids Struct., Vol. 10, pp. 671-684, (1974).
[5] Ravid, M. and Bodner, S. R., Int. J. Engng Sci., Vol. 21(6), pp. 577-599, (1983).
[6] Tate, A., Int. J. Engng Sci., Vol. 28(9), pp. 599-612, (1986).
[7] Forrestal, M. J. and Luk, V. K., J. Apple. Mech., Vol. 55, pp. 1-5, (1988).
[8] Rosenberg, Z., Marmor, E. and Mayseless, M., Int. J. Impact Engng., Vol. 10, pp. 483-486, (1990).
[9] Grove, D. J., Dhar, S., Brar, N. S. and Saliba, J. E., Rept. UDR-TR-93-60, Contract DAAA15-92-K-0001, July 1993, UDRI, Dayton, Oh.
[10] Abramowitz, M., and Stegun, I. A., Handbook of Mathematical Functions, National Bureau of Standards, Applied Mathematics Series, 55, (1964).
[11] Johnson, G. R. and Stryk, R. A., "User Instructions for the 1991 Version of the EPIC Research Code," Alliant Techsystems Inc., Air Force Report WL/MN-TR-91-53, October 1991.

# A Time-Dependent Model for Long-Rod Penetration

Dr. James D. Walker and Dr. Charles E. Anderson, Jr.*

Southwest Research Institute
P.O. Drawer 28510
San Antonio, TX 78228-0510

## ABSTRACT

The one-dimensional, quasi-steady-state, modified Bernoulli theory of Tate is often used to examine long-rod penetration into semi-infinite targets. In general, the time histories of penetration predicted by the Tate model are in good agreement with those computed from numerical simulations. However, discrepancies exist between the model and numerical simulations both at the beginning and at the end of penetration. From insights provided by numerical simulations, assumptions are made concerning the velocity and stress profiles in the projectile and the target. Using these assumptions, the time-dependent, cylindrically-symmetric, axial momentum equation is explicitly integrated along the centerline of the projectile and target to provide the equation of motion. Predictions of this one-dimensional, time-dependent penetration model are in good agreement with results from experiments and numerical simulations.

## INTRODUCTION

A one-dimensional model, proposed by Tate [1], has become the standard reference for long-rod penetration of thick targets in the velocity regime where the projectile erodes as it penetrates the target. The model assumes that the projectile is rigid, except for a thin region near the target-projectile interface where erosion is occurring, and the interface (penetration) velocity is found by a modified version of the Bernoulli equation [1]:

$$\frac{1}{2}\rho_p(v-u)^2 + Y_p = \frac{1}{2}\rho_t u^2 + R_t \qquad (1)$$

In this equation $\rho_p$ and $\rho_t$ are the projectile and target densities, v is the speed of the rear of the projectile, $u$ is the penetration speed, $Y_p$ is the strength of the projectile, and $R_t$ is defined as the target resistance in the one-dimensional formulation. Physically, the penetration event is not one

dimensional. Thus, in a one-dimensional model, some artificial means must be invoked to account for lateral confinement by the target. This is the role of $R_t$ in Eq. (1).

It has been demonstrated in Ref. [2], by comparison with numerical simulation, that the Tate model represents a reasonably accurate picture of the time history of long-rod penetration, as seen in Fig. 1. The figure depicts the penetration velocity and tail velocity along the centerline for a L/D=10 tungsten-alloy long rod impacting a steel target at an initial impact velocity of 1.5 km/s. The Tate model predicts similar qualitative and quantitative behavior as a detailed time-dependent numerical simulation, with only a few discrepancies. The Tate model does not account for the transient phase at the beginning of penetration, and there are two differences near the end of the penetration event. The analytical model predicts that the rear of the projectile decelerates too late and too rapidly at the very end of penetration, and it predicts that the projectile is fully eroded, with final length of the projectile being zero. It was argued in Ref. [2] that this is a consequence of the model not explicitly accounting for a finite region of projectile deceleration.

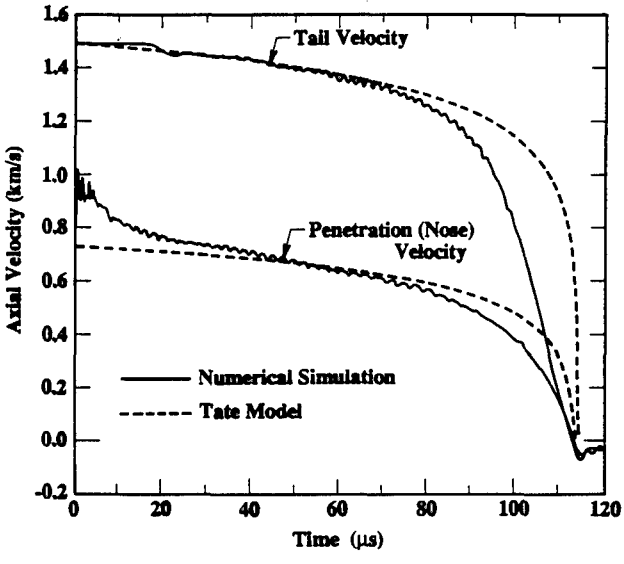



**Fig. 1. Penetration and Tail Velocities**

Due to the experience with the Tate model, and recognizing that the Bernoulli equation can be obtained from a momentum balance, the axial momentum equation has been more carefully examined. A series of assumption have been made, many of which were motivated by analysis of the results of numerical simulations. From this, a penetration model has been developed that includes transient effects. It appears to better model the early and late-time behaviors seen in long-rod penetration. A desire was to retain the overall simplicity of Tate's model. As will be seen, this new model gives Tate's original model upon taking a certain limit.

## MOMENTUM BALANCE

The axisymmetric projectile and target will be assumed to lie along the $z$ axis. The location of the interface between the projectile and the target is denoted $z_i(t)$, with $z_i(0) = 0$. The rear of the projectile is denoted

$z_p(t)$, and $z_p(0) = -L_o$, where $L_o$ is the initial length of the projectile. The velocity along the centerline in the projectile and target is written $u_z(z)$. With these definitions, the interface velocity $u$ and the velocity v of the back end of the projectile are given by:

$$u = \frac{dz_i}{dt} = u_z(z_i) \qquad (2a) \qquad\qquad v = \frac{dz_p}{dt} = u_z(z_p) \qquad (2b)$$

A central theme of the model presented in this paper is the use of the momentum balance along the $z$ axis. The $z$ component of the momentum equation along the centerline simplifies to:

$$\rho \frac{\partial u_z}{\partial t} + \frac{1}{2}\rho \frac{\partial (u_z)^2}{\partial z} - \frac{\partial \sigma_{zz}}{\partial z} - 2\frac{\partial \sigma_{xz}}{\partial x} = 0 \qquad (3)$$

We now integrate the momentum balance equation along the centerline over the target and projectile, or $[z_p(t), +\infty]$. Since the target material for large $z$ is not participating in the penetration event, $u_z(+\infty) = 0$ and $\sigma_{zz}(+\infty) = 0$. Also, the rear surface of the projectile is a free surface and hence stress free, so $\sigma_{zz}(z_p) = 0$. Assuming that the change in density in both the target and projectile is negligible (so that the density terms can be pulled out of the integral), and using the definitions in Eq. (2), then integration of Eq. (3) gives:

$$\rho_p \int_{z_p}^{z_i} \frac{\partial u_z}{\partial t} dz + \rho_t \int_{z_i}^{+\infty} \frac{\partial u_z}{\partial t} dz + \frac{1}{2}\rho_p u_z^2 \Big|_{z_p}^{z_i} + \frac{1}{2}\rho_t u_z^2 \Big|_{z_i}^{+\infty}$$

$$- \sigma_{zz}\Big|_{z_p}^{+\infty} - 2\int_{z_p}^{+\infty} \frac{\partial \sigma_{xz}}{\partial x} dz = 0 \qquad (4)$$

To integrate the equation further, assumptions must be made concerning the velocity profile $u_z(z)$ and the shear stress behavior, $\sigma_{xz}$.

## THE MODEL

Additional physics or mechanics usually need to be incorporated to make a model more realistic. The following assumptions are made based on the examination of numerical (hydrocode) simulations of long-rod impacts:

1) A velocity profile along the centerline in both the projectile and the target is specified.

2) The back end of the projectile is decelerated by elastic waves, with a magnitude proportional to the yield strength of the projectile. These waves reflect off the rear of the projectile, and this free surface reflection decelerates the rear of the projectile. At the front of the projectile, they reflect off the plastic zone rather than the target-projectile interface.

3) A shear behavior in the target material is specified. As will be seen, this is not independent of assumption 1.

### *Assumption 1: A Velocity Profile in the Projectile and Target*

Figure 2 shows the velocity profile along the centerline, from a numerical simulation, of a tungsten long-rod projectile penetrating a semi-infinite steel target. The velocity in the projectile is constant over most of the projectile length, save for a small region near the target-projectile interface. This velocity profile will be approximated by a bilinear expression. With $s$ equal to the extent of the plastic zone along the axis, the velocity in the projectile may be written as:

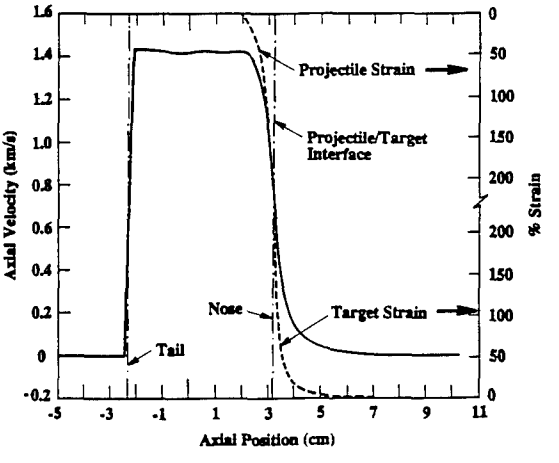



**Fig. 2. Centerline Velocity Profile**

$$u_z(z) = \begin{cases} u - \dfrac{\mathrm{v}-u}{s}(z - z_i) & (z_i - s) \le z < z_i \\ \mathrm{v} & z_p \le z < (z_i - s) \end{cases} \tag{5}$$

The behavior of the velocity in the target is more complicated. Velocity fields in numerical simulations have a spherical behavior, and due to this, a spherically motivated velocity profile is used [3]. Letting $r(z) = z - z_i(t) + R$, where $R$ is the *crater* radius, the following form of the velocity along the centerline of the target is assumed:

$$u_z(z) = \begin{cases} \dfrac{u}{\alpha^2 - 1}\left[\left(\dfrac{\alpha R}{r(z)}\right)^2 - 1\right] & R \le r(z) < \alpha R \\ 0 & \alpha R \le r(z) \end{cases} \tag{6}$$

The profile displays a similarity to that displayed from the numerical simulation. The velocity profile in the target is only over a finite domain, with furthest extent of $z = z_i + (\alpha - 1)R$. In some sense, $\alpha R$ can be viewed

as the extent of the plastic zone in the target. Finding $\alpha$ is nontrivial. In the example section a couple of approaches for doing this will be presented.

Equation (4) requires the integral of the partial of velocity with respect to time. Performing the differentiation of Eqs. (5) and (6) and then integrating gives:

$$\int_{z_p}^{z_i} \frac{\partial u_z}{\partial t} dz = \dot{v}(L-s) + \dot{u}s + (v-u)u + \left(\frac{\dot{v-u}}{s}\right)\frac{s^2}{2} \tag{7}$$

$$\int_{z_i}^{+\infty} \frac{\partial u_z}{\partial t} dz = \int_{R}^{\alpha R} \frac{\partial u_z}{\partial t} dr = \dot{u}R\frac{\alpha-1}{\alpha+1} + \dot{\alpha}\frac{2Ru}{(\alpha+1)^2} + u^2 \tag{8}$$

The dot represents differentiation with respect to time; the dot over [(v - *u*)/*s*], in Eq. (7), implies that the whole term is differentiated with respect to time.

***Assumption 2: The Deceleration of the Rear of the Projectile***

The projectile is decelerated by elastic waves. Finely-zoned numerical simulations clearly show the "step" deceleration of the rear of the projectile—see Fig. 1. In order to keep the model simple, the average momentum behavior of the projectile is described by the velocity profile, Eq. (5), and a second equation is written to describe the deceleration of the rear of the projectile.

When the elastic compressive wave reflects from the rear free surface of the projectile, it returns in tension. The change in particle velocity at the rear surface of the projectile is $\Delta v = -2c\sigma_p/E_p$ where $c$ is the elastic bar wave speed $(E_p/\rho_p)^{1/2}$, and $\sigma_p$ is the flow stress of the projectile. The elastic-plastic interface is a boundary because of the nonlinear material response of the plastically flowing material. Thus, the compressive wave travels from the elastic-plastic interface, reflects as a tensile wave off the free surface at the rear, and returns to the elastic-plastic interface, where it reflects as a compressive wave, and the cycle continues. The travel time of the wave is the distance divided by the wave speed. Due to erosion and change in the size of the plastic zone, the distance of the return trip is less. If $\Delta t$ is the time of the round trip of the wave, then

$$c\Delta t = L - s + L - \int_0^{\Delta t} (v-u)dt - \left(s + \int_0^{\Delta t} \dot{s}dt\right) \tag{9}$$

The equation of motion for the rear of the projectile is then given by:

$$\frac{dv}{dt} \approx \lim_{\Delta t \to 0} \frac{\Delta v}{\Delta t} = -\frac{\sigma_p}{\rho_p (L-s)}\left[1+\frac{(v-u)}{c}+\frac{\dot{s}}{c}\right] \tag{10}$$

***Assumption 3: The Assumed Stress Behavior in the Target***

This is actually the central and most difficult part of all penetration models. The fundamental question being addressed at this point is, "How does the target strength resist penetration?" The idea behind what is done here is as follows. Let us first suppose that the three-dimensional flow fields in the target can be determined. Then, if the target is behaving in a perfectly plastic manner, the stresses can be calculated from the von Mises flow rule. These stresses are then used to calculate the stress term in Eq. (4).

First, assuming we know the flow field ($u_x$, $u_y$, $u_z$), considerable algebra produces the gradient of the shear stress:

$$\left.\frac{\partial s_{xz}}{\partial x}\right|_{x=0} = \frac{\frac{1}{3}Y_t}{|\partial u_z/\partial z|}\left(\frac{\partial^2 u_z}{\partial x^2}-\frac{1}{2}\frac{\partial^2 u_z}{\partial z^2}\right)\Bigg|_{x=0} \tag{11}$$

Here, $Y_t$ is the target flow stress and incompressibility of the flow has been used in the derivation. It is expected that $\partial u_z/\partial z < 0$, i.e., the velocity of the flow field in the target decreases monotonically as one moves into the target away from the projectile nose. Thus, the absolute value in the denominator can be replaced with $-\partial u_z/\partial z$. This gives:

$$\int_R^{\alpha R}\left.\frac{\partial s_{xz}}{\partial x}\right|_{x=0} dr = \frac{Y_t}{6}\ln\left|\frac{\partial u_z}{\partial z}\right|_{r=R}^{r=\alpha R} - \frac{Y_t}{3}\int_R^{\alpha R}\left(\frac{\partial^2 u_z}{\partial x^2}/\frac{\partial u_z}{\partial z}\right)\Bigg|_{x=0} dr \tag{12}$$

The first term on the right hand side can be evaluated by taking the derivative of Eq. (6) and then evaluating at the limits. To evaluate the integral in Eq. (12) requires information about the flow field.

Incompressible flows can be obtained from the curl of a vector potential, since the divergence of the curl of any vector field is zero. Since the flow in the target around the projectile nose has a spherical quality to it, it is easiest to create a potential that produces such flow fields in spherical ($r$, $\varphi$, $\theta$) geometry. In particular, a potential that gives rise to the type of material motion seen in the numerical calculations is $\vec{A} = f(r)\sin(\theta)\hat{e}_\phi$ [3]. Taking the curl of this potential gives the flow field. The axial velocity $u_z$ is given by $u_z = u_r\cos\theta - u_\theta\sin\theta$.

Again, after considerable algebra, we have the simple result that the integrand of the right hand side integral of Eq. (12) is equal to $2/z$; therefore, the whole integral becomes:

$$\int_R^{\alpha R} \left.\frac{\partial s_{xz}}{\partial x}\right|_{x=0} dz = \frac{Y_t}{6}\ln\left(\frac{1}{\alpha^3}\right) - \frac{2Y_t}{3}\ln(\alpha) = -\frac{7}{6}\ln(\alpha)Y_t \qquad (13)$$

What is truly remarkable about this result is that few assumptions on the flow field have been made: 1) the flow field is monotonically decreasing along the axis, and 2) that it have a certain reasonable spherical behavior. From these assumptions follow the result that the shear term in the momentum balance only depends on the extent of the flow field ($\alpha$) and the slopes of the velocity at the front end and back end of the flow field.

### The Extent of the Plastically Flowing Zone in the Projectile

The extent of plastic flow in the projectile is defined by the length $s$ at the front of the projectile. The determination of $s$ is based on the following observation from numerical simulations: the slope of the velocity profile along the centerline is often smooth at the material interface, e.g., Fig. 2. In other words, the velocity profile is not only continuous, the first derivative along the axis also appears to be continuous. Assuming this, it is possible to derive an expression for $s$, as well as for its time derivative. Equating the slopes from Eqs. (5) and (6) at $z = z_i$ gives:

$$\frac{u - \mathrm{v}}{s} = -2\frac{u}{\alpha^2 - 1}\frac{\alpha^2}{R} \qquad (14)$$

From Eq. (14) we can solve for $s$ and the time derivative of Eq. (14), both of which are needed in Eq. (7):

$$s = \frac{R}{2}\left(\frac{\mathrm{v}}{u} - 1\right)\left(1 - \frac{1}{\alpha^2}\right) \quad (15a) \qquad \left(\frac{\dot{\mathrm{v}} - \dot{u}}{s}\right) = \frac{4}{(\alpha^2 - 1)R}\left\{\frac{\alpha^2 \dot{u}}{2} - \frac{u\alpha\dot{\alpha}}{\alpha^2 - 1}\right\} \quad (15b)$$

## THE MOMENTUM BALANCE EQUATION

If the terms obtained in the previous paragraphs are inserted into the original momentum balance, Eq. (4), we obtain

$$\rho_p \dot{\mathrm{v}}(L - s) + \dot{u}\left\{\rho_p s + \rho_t R\frac{\alpha - 1}{\alpha + 1}\right\} + \rho_p\left(\frac{\dot{\mathrm{v}} - \dot{u}}{s}\right)\frac{s^2}{2} + \rho_t\dot{\alpha}\frac{2Ru}{(\alpha + 1)^2}$$

$$= \frac{1}{2}\rho_p(\mathrm{v} - u)^2 - \left\{\frac{1}{2}\rho_t u^2 + \frac{7}{3}\ln(\alpha)Y_t\right\} \qquad (16)$$

The deceleration of the tail of the projectile is given by Eq. (10), and the time rate of change of the length of the projectile is the difference between the penetration speed and the tail speed:

$$\dot{\mathrm{v}} = -\frac{\sigma_p}{\rho_p(L-s)}\left\{1+\frac{\mathrm{v}-u}{c}+\frac{\dot{s}}{c}\right\} \quad (17) \qquad \dot{L} = -(\mathrm{v}-u) \quad (18)$$

Equations (16-18) completely determine the model. The initial penetration velocity $u$ may be obtained, for example, from the Rankine-Hugoniot shock jump conditions.

It is informative to take a certain limit of the above equations. If the two measures of spatial extent $R$ and $s$ are allowed to go to zero, i.e., $R \to 0$ and $s \to 0$, and the Young's modulus for the projectile is allowed to become very large, so $c \to \infty$, then Eqs. (16-18) become:

$$-\rho_p \dot{\mathrm{v}} L + \frac{1}{2}\rho_p(\mathrm{v}-u)^2 = \frac{1}{2}\rho_t u^2 + \frac{7}{3}\ln(\alpha)Y_t \qquad \dot{\mathrm{v}} = -\frac{\sigma_p}{\rho_p L} \qquad \dot{L} = -(\mathrm{v}-u) \quad (19)$$

These equations are Tate's original model with the target resistance given by $R_t = (7/3)\ln(\alpha)Y_t$; and the projectile strength $Y_p$ is identified with the flow stress, i.e., $Y_p = \sigma_p$. Thus, if the refinements in representation of the velocity profiles are removed, Tate's model results. The new model predicts, at the very minimum, an $R_t$ that varies with the extent of the plastic flow zone and the flow stress $Y_t$ of the target. An alternate view is that the second, third, and fourth terms in Eq. (16), along with $(7/3)\ln(\alpha)Y_t$, define an time-varying $R_t$, as suggested in [4].

## EXAMPLES

The behavior of the model will be demonstrated with a few examples. This will also be an opportunity to discuss the problem of determining $\alpha$. Although the original intent of the model was for long-rod eroding penetration problems, examining rigid penetration allows us to focus on target response, and hence on $\alpha$. For rigid-body penetration, $\mathrm{v} = u$, which simplifies Eqs. (16-18). The round circles in Fig. 3 are experimental points of $L = 7.47$ cm, $D = 0.71$ cm hard steel projectiles impacting 6061-T651 aluminum targets [5]. The dashed curve has $Y_t = 350$ MPa and a constant $\alpha = 10.7$, which is the value of $\alpha$ obtained from a cylindrical cavity expansion calculation in the $u \to 0$ limit (see [5-7] for a discussion of the cavity expansion technique—$\alpha$ is equal to the elastic-plastic interface velocity divided by the cavity expansion velocity). A constant $\alpha$ underpredicts the depth of penetration as a function of velocity at velocities

above 1 km/s (this is also apparent in the next example). A velocity-dependent $\alpha$ results from the cylindrical cavity expansion solution when compressible plastic response is included. The equation for $\alpha$ is:

$$(\rho_t u^2 + Y_t)\sqrt{K_t - \rho_t \alpha^2 u^2} = Y_t \left(1 + \frac{\rho_t \alpha^2 u^2}{2G_t}\right)\sqrt{K_t - \rho_t u^2} \qquad (20)$$

where $K_t$ and $G_t$ are the bulk and shear modulus of the target, respectively. The solid curve used Eq. (20) and a target flow stress of $Y_t$ = 380 MPa. Agreement between the experimental values and the model is good.

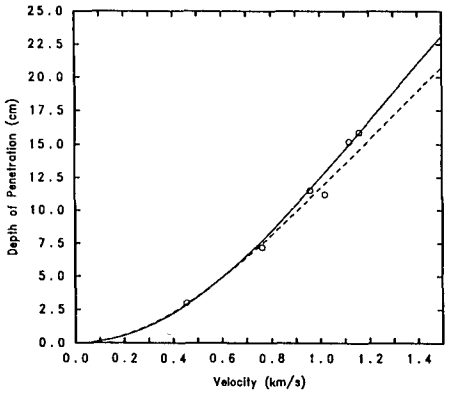



**Fig. 3. Steel into Aluminum**

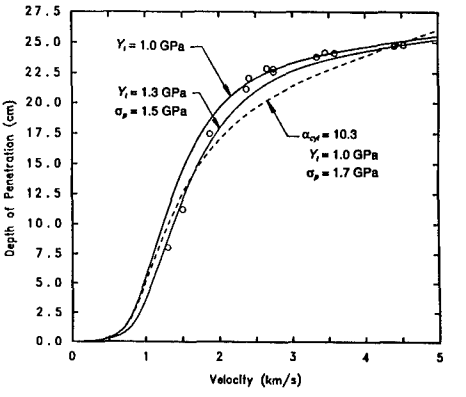



**Fig. 4. Tungsten into Steel**

The data points in Fig. 4 are from $L/D$ = 22.9, with $L$ = 15.58 cm, tungsten projectiles into a steel target [8]. The dashed curve is with a constant $\alpha$ = 10.3, $Y_t$ = 1 GPa, and $\sigma_p$ = 1.5 GPa. The depth-of-penetration versus velocity curve calculated with constant $\alpha$ does not have a rapid enough increase in penetration in the 1 to 2 km/s region. This again implies the need to use a variable $\alpha$, and in fact, it was the serious discrepancy of penetration into steel that led to the development of Eq. (20). The solid curves calculated $\alpha$ from Eq. (20), the upper with $Y_t$ = 1 GPa and $\sigma_p$ = 1.5 GPa, and the lower with $Y_t$ = 1.3 GPa and $\sigma_p$ = 1.7 GPa. The strength values used are in the range of values for these materials after work hardening.

Equation (20) requires an additional modification to increase the stiffness of the bulk modulus $K_t$ with increasing velocity. If this is not done, $\alpha$ will go below 1.0 as the velocity continues to increase, since at some point the rate of cavity expansion is faster than the low pressure elastic wave speed. Physically, the bulk modulus, and thus the elastic sound speed, increases with material compression; and increases in penetration

velocity increases material compression. Therefore, a procedure for estimating $K_t$ as a function of the penetration velocity must be devised. A heuristic argument for how $K_t$ increases with increasing penetration velocity follows. Under uniaxial strain conditions, the shock velocity is related to the particle velocity by the equation $u_s = c_o + k u_p$, where $c_o$ is the bulk sound speed, $k$ is the dependent slope. The ambient bulk modulus $K_o$ is given by the product of the density and the square of the sound speed: $K_o = \rho_o c_o^2$. Therefore, we relate the dynamic bulk modulus with the shock velocity:

$$K_t \approx \rho_o u_s^2 = K_o\left(1 + k\frac{u_p}{c_o}\right)^2 \tag{21}$$

Equation (21) is for one-dimensional impact. We are concerned here with cylindrical cavity expansion, and the geometric divergence would suggest that Eq. (21) is probably too stiff with penetration velocity, so the square root of the term within the parenthesis is taken:

$$K_t \sim K_o\left(1 + k\frac{u_p}{c_o}\right) \tag{22}$$

Figure 5 shows the dependence of $\alpha$ on penetration velocity, $u$. It should be noted that Fig. 5 [i.e., Eq. (20) in conjunction with Eq. (22)] states that the extent of the plastic zone decreases with increasing penetration velocity. The extent of the plastic zone actually increases with increasing penetration velocity, however, the crater radius grows at a faster rate than the plastic zone size. This conclusion has been verified through numerical simulations [9].

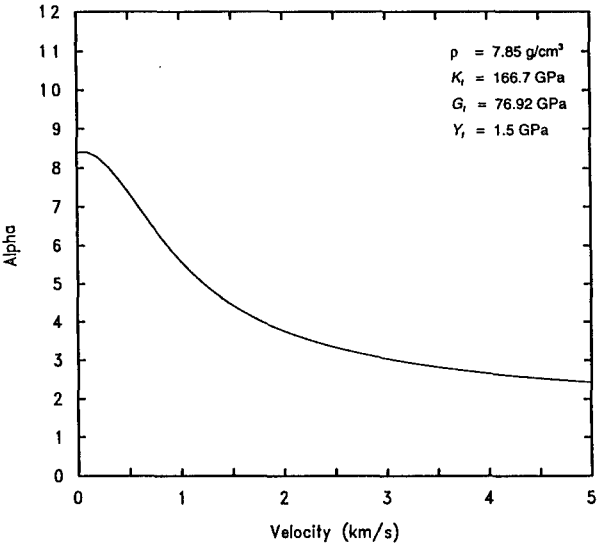



**Fig. 5. $\alpha$ versus Penetration Velocity (Steel Target)**

Although the assumption of nearly constant density—incompressibility—is still valid, compressible effects, as measured by $\alpha$, cannot be ignored in the resistance of the target material to penetration. The decrease in $\alpha$ with velocity from Eq. (20) is due to compressibility in

the assumed plastic response, and strongly suggests that compressibility of the target needs to be taken into account in penetration models for these higher velocities.

This eroding penetration example brings up another issue. When the penetration is rigid, the crater diameter is equal to the projectile diameter. In eroding flow, the crater diameter is a function of the impact velocity. An expression for crater diameter was obtained from the measured crater diameters in experiments [8]. In particular, $R = R_p(1 + 0.2869V_o + 0.1457V_o^2)$ was used, where $V_o$ is the initial striking velocity in km/s and $R_p$ is the radius of the projectile. $R$ is calculated from the initial impact velocity and is held constant throughout the calculation.

Although the method being used to calculate $\alpha$ has some virtues, the research on this topic is not complete. The original motivation for the model was to match the velocity profiles seen in the target and projectile. If the model were working well, one would think that there should be good agreement with the time-dependent interface and rear projectile velocities. These velocities are displayed versus time in Fig. 6. The solid curves are from the numerical simulation described in Fig. 1. The dashed curve is from the model, with $\alpha$ from Eq. (20), $Y_t$ = 1.2 GPa, and $\sigma_p$ = 1.5 GPa (chosen to match the 7 cm depth of penetration). The agreement is better than that seen in Fig. 1 with the Tate model, but certainly not perfect.

If a linear interpolation in time is used to calculate $\alpha$, taking $\alpha$ from 2 to 20 in 100 μs, then the dot-dash curve in Fig. 6 results. Here $Y_t$ = 1 GPa and $\sigma_p$ = 1.5 GPa. The interface velocity agreement is remarkable, and such a time dependent $\alpha$ has the intuitive appeal of a plastic field that grows steadily with time. The $\alpha$ from Eq. (20) does grow steadily in time, since $\alpha$ is a monotonically decreasing function of $u$. However, for much of the penetration event it maintains roughly the same value since the interface velocity is nearly constant. More work needs to be done on calculating the extent of the plastic zone in the target, even though the cylindrical cavity expansion approach seems to work well for matching experimental depths of penetration.

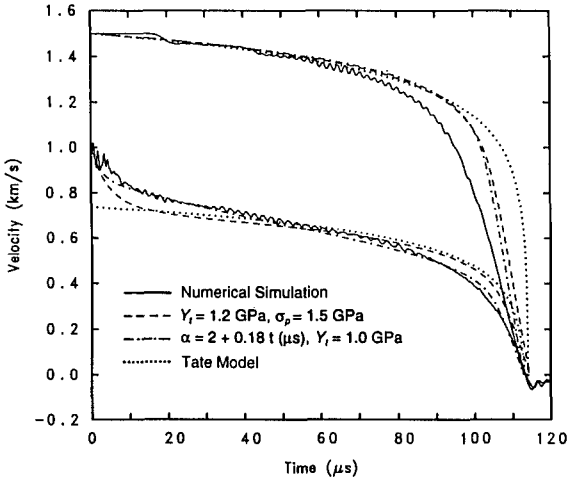



**Fig. 6. Penetration and Tail Velocities**

## SUMMARY

A penetration model has been presented that includes transient effects. The model has been shown to agree with both rigid and eroding projectile penetration data. Part of the model requires the calculation of the extent of the plastic zone in the target, and although techniques were presented, this is still considered an open problem.†

## REFERENCES


1. A. Tate, "A Theory for the Deceleration of Long Rods after Impact," *J. Mech. Phys. Solids* **15**, 387-399 (1967).

2. C. E. Anderson, Jr. and J. D. Walker, "An Examination of Long-Rod Penetration," *Int. J. Impact Engng.*, **11**(4), pp. 481-501 (1991).

3. J. D. Walker, "On Hemispherical Flow Fields for Dynamic Plastic Flow," in preparation.

4. C. E. Anderson, Jr., J. D. Walker, and G. E. Hauver, "Target Resistance for High-Velocity Long-Rod Penetration," in ***Computational Impact Mechanics***, W. K. Liu, T. Belytschko, and T. Aizawa (editors), Elme Press International, to be published.

5. M. Forrestal, K. Okajima, V. K. Luk, "Penetration of 6061-T651 Aluminum Targets with Rigid Long Rods," *J. Appl. Mech.*, **55**(4), pp. 755-760 (1988).

6. M. J. Forrestal, V. K. Luk, and N. S. Brar, "Perforation of Aluminum Armor Plates with Conical-Nose Projectiles," *Mechanics of Materials*, **10**, pp. 97-105 (1990).

7. M. J. Forrestal and V. K. Luk, "Dynamic Spherical Cavity-Expansion in a Compressible Elastic-Plastic Solid," *J. Appl. Mech.*, **55**, pp. 275-279 (1988).

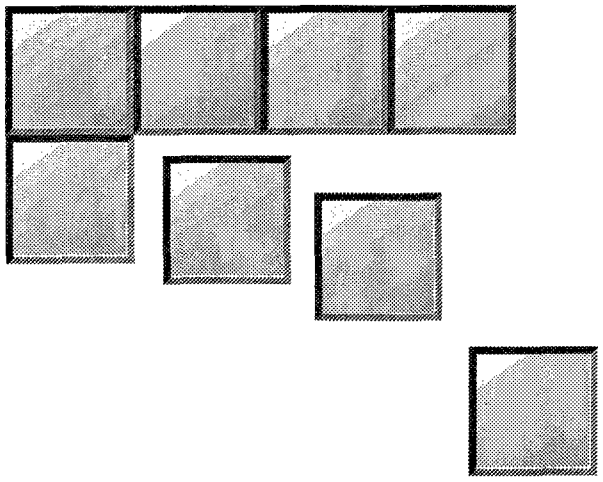
8. G. F. Silsby, "Penetration of Semi-Infinite Steel Targets by Tungsten Long Rods at 1.3 to 4.5 km/s," *Proceedings of the 8th International Symposium on Ballistics*, Orlando, FL, 23-25 October (1984).

9. C. E. Anderson, Jr., D. L. Littlefield, and J. D. Walker, "Long-Rod Penetration, Target Resistance, and Hypervelocity Impact," *Int. J. Impact Engng.*, **14** (1-4), in publication (1993).


†The model was first presented at the *13th International Symposium on Ballistics*, Vol. 3, pp. 9-16, Stockholm, Sweden, 1-3 June 1992. The model has been applied to a fairly large range of impact problems over the past year, and has consistently yielded good results. A more detailed paper is in preparation.

# SESSION IVA:
# STRUCTURAL APPLICATION

**Chairman:** *Dr. M.J. Shuart*
**NASA Langley**



# Aging Aircraft: Structural Integrity and Damage Tolerance

**Robert Greif[1]*, David Y. Jeong, and Pin Tong[2]**
**U.S. Department of Transportation**
**Volpe National Transportation System Center**
**Cambridge, MA 02142-1093 USA**

## Introduction

Damage tolerance is the characteristic of an aircraft structure that enables it to retain its required residual strength after the structure has been damaged. The term "Widespread Fatigue Damage" (WFD) is commonly used to refer to a type of multiple cracking that degrades the damage tolerance capability of an aircraft structure. Degradation is defined when the residual strength of the structure is reduced below the design limit load or when a change in the inspection program is required to insure the desired level of safety. Multiple cracking has been observed in several airplanes that have been in service for sometime.

The Federal Aviation Administration Technical Center (FAATC) has initiated a research program to investigate the effect of WFD on the structural integrity of aging airplanes. Two areas of this research effort are discussed in this paper. One area is the application of the hybrid finite element technique to analyze the residual strength of riveted stiffened panels. Results from this analysis (1) have shown that some multiple crack configurations may not reduce the residual strength of an aircraft structure below the allowable limit load defined by current damage tolerance regulations. That is, all multiple crack geometries may not be considered to be WFD. In the current work, this concept is quantified for a panel with specific multiple crack configurations. The hybrid technique has also been used to analyze stresses in a stiffened panel with a lap joint configuration simulating an aircraft fuselage. Another area of research involves laboratory testing of flat panels with multiple cracking (2). These tests were implemented by Foster-Miller, Inc., under contract with the Volpe National Transportation Systems Center.

---

[1]Also, Tufts University, Medford, MA 02155 USA.

[2]Also, Hong Kong University of Science and Technology, Kowloon, Hong Kong.

Details of the tests were designed by FractuREsearch, Inc. Test data are used to verify proposed criteria for multiple crack linkup. A generally accepted criterion for linkup of multiple cracks is necessary to determine the residual strength of aircraft structures containing multiple cracking. Various hypotheses for linkup of multiple cracks are discussed in this paper, including fast fracture associated with critical stress intensity factor and plastic zone interaction. Particular emphasis is given to a linkup criterion, proposed by Swift (3) and Tong et al (1), which assumes that a lead crack will linkup with smaller, collinearly aligned cracks when the ligament stress reaches the yield strength of the material.

## Hybrid Finite Element Analysis

An efficient computer code has been developed to analyze the related concepts of WFD, multiple site damage (MSD) and reduction of residual strength. This code is based on the principles of the hybrid finite element technique. The first application of this technique to damage tolerance analysis was done by Tong (4) in 1984. A typical aircraft structural element involves a panel with multiple cracks, as shown in Figure 1, which is connected to stiffeners by rivets and loaded by in-plane remote stresses $\sigma^o$ (representing fuselage hoop stresses). The panel also is subjected to concentrated loads which simulate the interaction of the rivet with the rivet hole surface. The entire domain for the problem can be treated as a single hybrid element, commonly called a "super element".

A hybrid variational function can be written (Ref. 1), in terms of an integral over the rivet surfaces as well as the crack surfaces $\Gamma_k$, in the form

$$\pi_p = t\left[\sum_k \int_{|z-z_k|=\epsilon} (T_i\bar{u}_i - \frac{1}{2}T_iu_i)ds + \sum_k \int_{\Gamma_k} \frac{1}{2}T_iu_i ds - \int_{\partial A_\sigma} T_i^o\,\bar{u}_i\,ds\right] \quad (1)$$

where t is the panel thickness, $\partial A$ is the boundary of the element, and $\bar{u}_i$ are the displacements at the element boundaries. $T_i(=\sigma_{ij}\nu_j)$ and $\sigma_{ij}$ are respectively the boundary tractions and stresses, $T_i^o$ are the prescribed tractions on $\partial A\sigma$, the boundary for which stress is known. The surfaces of the rivet holes are located at $|z - z_k| = \epsilon$ where $\epsilon$ is rivet radius. The quantities $\bar{u}_i$ and $u_i$ are separate displacement fields which are independent functional variables of $\pi_p$. The Euler equations for the element can be derived through the first variation of the functional $\pi_p$. In equation (1), we

have assumed that $\sigma_{ij}$ satisfies the equilibrium conditions and the traction free conditions at the crack surface.

The solution within the panel element can be found in terms of the complex stress functions $\phi(z)$ and $\psi(z)$ associated with the complex variable theory of elasticity. Using linear superposition, the stress functions are constructed from three different functions, representing three separate physical problems

$$\begin{aligned} \phi(z) &= \phi_1(z) + \phi_2(z) + \phi_3(z) \\ \psi(z) &= \psi_1(z) + \psi_2(z) + \psi_3(z) \end{aligned} \tag{2}$$

*Problem 1* is for an uncracked uniform skin subject to uniform remote stress. *Problem 2* represents the uncracked skin subject only to concentrated loads at $z_k$, the rivet locations. For this problem, the stress functions, $\phi$ and $\psi$, have logarithmic singularities at $z_k$. *Problem (3)* represents the cracked skin subject to arbitrary crack-face traction. For this problem, Chebyshev polynomials are used to represent the crack stresses as suggested by Gladwell and England (5).

One advantage of the variational approach to this problem is the ease with which additional structural elements can be included into the procedure. For a stiffened panel as shown in Figure 1, the stiffeners are represented by the bending and stretching energy of beams, and the rivets are represented by springs. The potential energy for the beams is

$$\pi_s = \sum_{\text{all stiffeners}} \left\{ \frac{1}{2} \int EA \left[ \frac{d}{dy} \left[ v_s - c \frac{dw}{dy} \right] \right]^2 dy + \frac{1}{2} \int EI \left[ \frac{d^2 w}{dy^2} \right]^2 dy - \left( v_s \sigma^o_{yy} A \right)_{y \to \infty} + \left( v_s \sigma^o_{yy} A \right)_{y \to \infty} \right\} \tag{3}$$

where w and $v_s$ are respectively the flexure and longitudinal deflections at the panel and stiffener interface and 2c is the stiffener height. The complementary energy for the rivets is

$$\pi_r = \sum_k \left[ (v_s - \bar{v})_k F^k - \frac{1}{2} \alpha (F^k)^2 \right] \tag{4}$$

where $F^k$ is the force on the rivet at $z_k$ and $\alpha$ is the rivet compliance coefficient. The hybrid variational functional $\pi$ for the entire panel with skin cracks and riveted stiffeners is the sum of the expressions from equations (1), (3), and (4). The independent fields in $\pi$ are the stiffener deflections, the stress function $\phi$ and the $N$ Chebyshev coefficients, $b_n$. In the finite element formulation, the independent variables are the nodal values of the stiffener deflections, the forces $(X_k, Y_k)$ at $z_k$ and Chebyshev coefficients $b_n$. The final form of the matrix equation to be solved is

$$[H] \left\{ \begin{array}{c} \underline{P} \\ \hline \underline{b}_n \\ \hline \underline{u}_s \end{array} \right\} = \{R\} \tag{5}$$

where $\underline{P}$ is a column of rivet forces, $\underline{b}_n$ is a column of Chebyshev coefficients for each crack, and $\underline{u}_s$ represents the nodal values of the stiffener deflections. The forcing function {R} in equation (5) is derived from the work done by rivet forces and stiffener axial force through the displacements of problem 1.

The stress intensity factors $K_j (j = I, II)$ can be evaluated at the crack tips from $\phi_3'(z)$, which may also be written as

$$K_I - iK_{II} = -\sqrt{\pi a} \sum_{n=1}^{N} b_n \qquad at\ x = +a \tag{6}$$

which shows the direct relationship of Chebyshev coefficients to the stress intensity factors. We also define the stress concentration factor in the stiffener as

$$(SCF)_s = \max \left( \frac{\sigma_o}{\sigma_{yy}^o}, \frac{\sigma_I}{\sigma_{yy}^o} \right) \tag{7}$$

where $\sigma_o$ and $\sigma_I$ are respectively the outer and inner flange stresses of the outer stiffener, and $\sigma_{yy}^o$ represents the far field stiffener stress.

A useful way to describe the damage tolerance capability of an aircraft structure is the ability of a stiffened panel to arrest a fast fracture. This is usually expressed in terms of the residual strength of the stiffened panel. The residual strength diagram is based upon the critical stress intensity factor $K_c$ (fracture toughness). The residual strength based upon skin fracture can be written in the form

$$\sigma_c = K_c / \beta \sqrt{\pi a} \qquad (8)$$

For a thin skin $K_c$ can be a function of skin thickness and is usually determined experimentally. In the case of multiple cracks, the residual strength can also be defined based on net section yielding of the ligaments between cracks. The residual strength of the skin is then the lower bound of the strength defined by $K_c$ or net section yielding. The residual strength of the stiffeners is related to the far field stress that leads to stiffener failure at its ultimate strength.

Residual strength diagrams based upon skin failure ($K_c = 120\ ksi\sqrt{in}$) or stiffener failure $\sigma_u = 82$ ksi are shown in Figures (2-4). As depicted by the logo in the upper right hand corner of the figures, the physical problem represents a main crack centrally located about a broken stiffener (as in Figure 1) with outlying smaller fatigue cracks near intact frames located twelve inches from the central stiffener. In Figure 2, the outlying cracks are located symmetrically around the frames while Figures 3 and 4 involve cases where the center of these cracks are located on the outside and inside of these frames, respectively. Superimposed in dotted lines are the results for the single crack. These single crack results are useful for understanding the MSD situation, since the initial three crack problem will become a single crack problem after the main central crack links up with the outlying cracks.

Consider the case of Figure 2 with a far crack of length $2a_2 = 3$ inches. Assuming the main crack propagates due to fatigue loading, it will linkup with the outer crack before $a_1$ reaches 10.5 inches. Since the stress intensity factor at the tips of the main crack becomes very large just before linkup, the corresponding residual strength accordingly approaches zero and linkup can occur at a very low load. Of course, this does not imply that the entire stiffened panel is unsafe. Rather, we must analyze the residual strength diagram for the new *single* crack of total length 27 inches ($a_1 = 13.5$ inches) which is formed by the linkup. As shown in Figure 2, the new value of

residual strength is controlled by the stiffener strength curve at point C. The original single crack residual strength of 24.71 ksi at point A has been reduced by 21.5% to point C due to the multiple cracks situation and the linkup of the cracks. If the linkup occurs at a load below the value at point C, the crack will be arrested after the linkup. But if the linkup load is larger than the value at C, the crack will continue to propagate after the linkup and the panel can be unsafe. The value at C is the residual strength of the stiffened skin for this case. If the value at C is below the design limit load, the case is a widespread fatigue damage configuration.

A similar study can be made for Figure 3 in which the center of the outlying crack is located on the far side of the frames with the distance between crack centers $d_c$ = 13 inches. For the 3 inch far crack, the main crack linkup occurs for a central crack half length ($a_1$) less than or equal to 11.5 inches. This immediately produces a single crack of total length 29 inches ($2a_1 + 2a_2$) which throws extra load onto the frames. The panel residual strength is now controlled by the stiffener strength at C, which is 28.6% below the original single crack residual strength at A, and also 9.1% below the point C of Figure 2.

A different result is obtained in Figure 4 where the center of the small cracks are located on the inside of the frames. For $a_2$ = 3 inches, linkup produces a single crack of length 25 inches and the subsequent load taken up by the stiffener is less than in the previous cases. The residual strength point C is higher than for the single crack residual strength point at A. Therefore, linkup in this case does not decrease the residual strength of the panel.

The cases analyzed in Figures 2-4 can be used to examine the damage tolerance capability of an aircraft structure. One measure of whether these cases represent WFD (or its subset MSD) is the effect of multiple cracks and linkup on residual strength. MSD occurs in a structure when the simultaneous presence of cracks, at similar structural details located in a common area, linkup to produce a residual strength which is less than the required residual strength based on the presence of a single crack. In Figures 2 and 3, the residual strength has been lowered to B or C, due to the presence of outlying cracks. In Figure 4, the residual strength is unchanged by crack linkup. This relationship between residual strength and the position of the outlying cracks is depicted in Figure 5, which amplifies the important relationship of MSD to inspection. For the cases considered, the critical size of the central crack is still quite large. As an example, if the design limit load in Figure 3 is 20 ksi, the critical size for linkup is $2a_1$ = 19 inches. It is likely that such a

crack can be detected visually or by other means. Conversely, the critical values for outlying cracks can be quite small. If the structure is to be protected from possible failure resulting from sudden external impact damage which produces a critical central crack, it is necessary to detect cracks of sizes based on the critical values of outlying cracks, and consequently visual inspection may not be adequate.

Although the preceding interpretation is relatively straight forward, note that the MSD definition refers to the required residual strength. This required strength is related to the design limit load which is 110 percent of normal operating pressure plus the aerodynamic pressures in lg flight for the fuselage, or generally 1.5 times the design operating load for transport category airplanes (6,7). As a consequence of the present definition, the occurrence of multiple cracks is not MSD if the linkup of these cracks does not result in the reduction of residual strength below the design limit load. Therefore, in Figures 2 and 3, if point A coincides with the design limit load, all multiple crack cases are MSD because the residual strength, B or C, of the structure with cracks as shown is below A. On the other hand, if the design limit load is between points B and C, then the case with $a_2 = 1.5$ inches is MSD and the case with $a_2 = 1.0$ inches is not. If the design limit load is below C, none of the cases are MSD.

**Riveted Lap Joint**

Another important application of the hybrid finite element technique is to the analysis of riveted lap joints. This configuration was an important factor in the 1988 Aloha incident, and is located along a longitudinal lap joint fastened with three rows of rivets as depicted in Figure 6 for a rivet pitch of 1 inch. The failure in this incident was precipitated by the linkup of small fatigue cracks emanating from adjacent rivet holes in a fuselage lap joint. The solution for riveted lap joint problems can be determined by using the complex variable theory of elasticity in conjunction with an appropriate hybrid variational function.

The first basic problem that must be understood is the riveted lap joint without any skin cracking. Although simplified one dimensional (bar) models of this problem have been developed (8), the first rigorous two dimensional elasticity solution was developed by Tong, Greif and Chen (9) in 1992.

The solution for the (uncracked) riveted lap joint may then be found by summation over all rivets, including the rivet force in terms of the relative

displacement of the top and bottom panels, and enforcing overall equilibrium. The final result for rivet forces is presented in Figure 6 for an all aluminum system with 1 inch rivet pitch and 0.04 inch skin thickness. Although the rivet forces predicted by Swift (8) are within 5%, the present more accurate solution technique is crucial for eventual analysis of the problem of the rivet lap joint with cracks.

Another problem of importance is the solution of the riveted lap joint with several rivets missing (or failed). This problem provides insight into the load redistribution caused by the loss of rivets and is an essential ingredient for the analysis of a lap joint with cracks emanating from rivet holes. A typical problem is shown in Figure 7 for the case of a single missing rivet. The solution for this case can be obtained by applying an external load to the missing rivet positions and solving the system using the hybrid finite element method. Superposition of the resulting rivet loads with those for the intact lap joint shown in Figure 6 then produces the final result with zero rivet force at appropriate rivet positions.

A hybrid variational function for the lap joint can be written as

$$\pi_p = \pi_u + \pi_l + \frac{1}{2} \sum_n k_n \left[ \{(\bar{u}_n)_u - (\bar{u}_n)_l\}^2 + \{(\bar{v}_n)_u - (\bar{v}_n)_l\}^2 \right] \qquad (9)$$

where summation is over all rivets (except for missing rivets), the subscripts u and l refer to the upper and lower panels of the lap joint, respectively, and $\pi_u$ and $\pi_l$ are similarly the functionals for each panel. The functional $\pi_u$ can be written as

$$\pi_u = t \left[ \int_{\partial A} (T_i \tilde{u}_i - \frac{1}{2} T_i u_i) \, ds - \int_{\partial A} r_u T_i ds - \sum_k p_k \tilde{u}_k \right] \qquad (10)$$

where $\partial A$ is taken over the boundary and all rivet holes, $r_u$ represents rigid body motion of the top panel, and $p_k$ are the known external loads applied at the appropriate missing rivet locations. A similar functional can be derived for the $\pi_l$ associated with the lower panel. Substituting these relations into equation (9), a matrix equation can be formed in which the rivet loads connecting the lap joint are the unknowns.

A solution for the case of a lap joint with a single rivet missing is shown in Figure 7 for a 15 ksi far field stress. The most notable feature is the localized nature of the redistribution of the rivet load. The rivet (row 2)

directly under the missing rivet is the most affected, and increases in load by 25%. It also should be noted that the redistribution of load is confined to two rivet spacing (2 inches) along the rivet row (x-axis). After about two rivet spacing, the rivet loads may be approximated by their asymptotic values as shown in Figure 7. Similar variational functions may be constructed for the lap joint in which cracks extend from the rivet holes, by including Chebyshev polynomials to represent equivalent crack stress. This will be reported on at a later date.

**Experimental and Analytical Investigation of Multiple Crack Linkup**

A test program was designed to investigate the residual strength of flat, unstiffened panels containing multiple cracking. The flat panels were 20 inches in width and 0.040 inch in thickness. Twelve flat panels were tested with a variety of multiple crack configurations. The test program included a series of small coupon tests to determine basic mechanical properties of the panel material, 2024-T3 aluminum. Values of yield strength were found to vary between 44 and 52 ksi, depending on grain orientation and skin thickness. Similarly, values for ultimate tensile strength varied between 64 and 67 ksi. A detailed description of the experimental phase of this work can be found in Reference (2).

An objective of the flat panel tests was to examine the validity of proposed criteria for the linkup of multiple cracks. One criterion for multiple crack linkup has been proposed by Swift (3) and Tong et al (1), who hypothesized that a lead crack will linkup with smaller, collinearly aligned cracks when the stress in the ligaments between crack tips reaches the yield strength of the material. This linkup criterion is shown schematically in Figure 8, and can be mathematically expressed as

$$r_p(a) + r_p(b) = L \qquad (11)$$

where $r_p$ (a) and $r_p$ (b) refer to the extent of the plastic zones ahead of two adjacent cracks and L is the distance between the crack tips or the ligament length. In Figure 8, the lead or main crack has a total length of 2a and the length of the smaller crack is 2b. Conventionally, the extent of crack tip plasticity can be estimated using the following equations which have been attributed to Irwin (10) and Dugdale (11), respectively

$$r_p = \frac{1}{2\pi}\left(\frac{K_I}{\sigma_p}\right)^2 \quad (Irwin) \qquad r_p = \frac{\pi}{8}\left(\frac{K_I}{\sigma_p}\right)^2 \quad (Dugdale) \quad (12)$$

where $\sigma_p$ is the yield strength of the material and $r_p$ is the extent of the plastic ahead of the crack. Also, $K_I$ is the stress intensity factor which can be written as

$$K_I = \beta(a)\sigma_o \sqrt{\pi a} \quad (13)$$

where $\beta$(a) is a geometric correction factor to account for crack interaction and $\sigma_o$ is the remote stress.

Using the foregoing relationship for crack linkup based on ligament yield and the Irwin and Dugdale formulas, a modified residual strength diagram can be derived as shown in Figure 3 based on a yield stress of 50 ksi. As can be seen, for certain combinations of stress and crack length, the residual strength may be more susceptible to ligament yielding rather than skin fracture. For example, if $K_c = 120\ ksi\sqrt{in}$, $\sigma_p = 50\ ksi$, it follows from the Irwin formula in equation (12) that $r_p = 0.92$ inch. In other words, at the condition for skin fracture based on the Irwin criteria, the yield zone at the crack tip will exceed 0.92 inch. In this case, yielding of the entire ligament is likely to occur before skin fracture if the ligament size is within about one inch. The ligament size is sensitive to $K_c$. For example if $K_c$ is 80 rather than $120\ ksi\sqrt{in}$, the critical ligament size is about one-half of the value previously calculated.

The Irwin and Dugdale formulas should be regarded as first order approximations of the extent of crack tip plasticity because each equation is derived from extracting the first term of a series expansion. For instance, the Irwin equation is based upon the singular term of the series expansion for the stress distribution ahead of a crack tip:

$$\sigma_{11} = \sigma_o \frac{\sqrt{a}}{\sqrt{2r}} = \frac{K_I}{\sqrt{2\pi r}} \quad (14)$$

where a is half of the crack length and r is the distance from the crack tip.

This approximation can be compared to the exact distribution of stress ahead of the tip of a single crack as given in Reference 12:

$$\sigma_{11} = \sigma_o \frac{r + a}{\sqrt{r^2 + 2ar}} \tag{15}$$

Figure 9 shows the ratio of the approximate to exact stress distribution for a single crack. The approximate stress solution underestimates the actual stress by 20% at a distance of 0.3 times the half-crack length from the crack tip.

Clearly, more accurate estimates of crack tip plasticity can be achieved if the nonsingular terms are included in the solution of the stress distribution ahead of the crack tip. In addition, a plastic zone correction as shown in Figure 10 should be included to satisfy equilibrium. When the nonsingular terms are retained in the solution of stress ahead of the crack tip, Tong (13) has shown that the plastic zone size may be estimated from the relation

$$r_p = \frac{1}{2\pi}\left(\frac{K_I}{\sigma_p - \sigma_o}\right)^2 \frac{1}{1 + \dfrac{K_I}{(\sigma_p - \sigma_o)}\sqrt{\pi a}} \tag{16}$$

Thus, an expression for multiple crack linkup can be derived by combining equations (11), (13), and (16):

$$\sigma_o^2 \left\{ \frac{\beta^2(a)a}{\sigma_p - \sigma_o\,[1 - \beta(a)\,]} + \frac{\beta^2(b)b}{\sigma_p - \sigma_o\,[1 - \beta(b)]} \right\} = 2\,L\,(\Delta a)\,.\,(\sigma_p - \sigma_o) \tag{17}$$

where L(Δa) is the distance between cracks which is a function of stable tearing. That is, the effect of stable tearing should be included in the prediction of multiple crack linkup.[1] The amount of stable crack extension due to a given applied stress can be calculated using R-curve data. Stable tearing affects linkup by reducing the distance between cracks and increasing the stress intensity correction factor due to crack interaction. If stable tearing is included, the calculation of linkup stress by equation (17) requires an iterative procedure because the amount of stable extension depends on the applied stress.

---

[1] In the present analysis, stable extension of the lead crack only has been considered. Stable tearing of the smaller or secondary cracks has been neglected.

A typical correlation between test data and analysis based on equation (17) is shown in Figure 11 for a five crack configuration. The schematic at the bottom of the diagram indicates the symmetric geometry of a lead crack with two smaller cracks ahead of each crack tip. The figure also compares predictions from the linkup criterion based on plastic zone size and from the conventional fracture criterion based on critical stress intensity factor. A yield strength of 50 ksi was assumed. Better agreement between test results and predictions of linkup is achieved with the plastic zone criterion than with the fracture criterion. For the geometry shown in Figure 11, the first linkup is predicted within 5% of the experimental value when equation (17) is used. Other correlations between other test results and analyses have shown that differences between experimental data and linkup predictions become larger as the ligament length increases.

Although a yield strength of 50 ksi was assumed in the current calculations, it is important to note that linkup predictions can vary by 20% since the yield strength was experimentally observed to vary between 44 and 52 ksi. Figure 12 compares experimental results with linkup predictions for the upper and lower bound values of yield strength using equation (17).

## Conclusions

Two areas of research regarding the structural integrity and damage tolerance of aging aircraft were discussed in this paper.

The hybrid finite element method is used to construct residual strength diagrams for stiffened structures with multiple cracks. Such residual strength diagrams are needed for damage tolerance evaluation. The results from the hybrid technique demonstrate the relationship between location of smaller outlying cracks, with a main central crack, relative to a stiffener and residual strength after linkup. In addition, the relationship between design limit load and residual strength was discussed. The occurrence of multiple cracking is not considered to be MSD if the linkup of these cracks does not result in the reduction of residual strength below the design limit load. The hybrid finite element method is also used to derive rigorous solutions for several riveted lap joint problems. Rivet loads predicted by this technique for an uncracked lap joint were found to agree within 5% for simplified methods. The hybrid technique was also used to calculate rivet loads for cases where rivets have failed or are missing. Results show that the redistribution of rivet load is confined to two rivet spacings (or 2 inches for the configuration analyzed) when a single rivet is missing from the lap joint.

Correlations between testing and analysis of panels with multiple cracks are presented. Analyses based on a proposed criterion for multiple crack linkup are shown to provide reasonable estimates when compared to actual test data. This proposed criterion for multiple cracks assumes that a lead crack will linkup with a smaller collinear crack when the stress in the entire ligament between cracks reaches the yield strength of the material The analyses are also based on using a new equation to estimate the extent of crack tip plasticity. Nonsingular terms in the solution of stress near the crack tip are retained in the derivation of this new equation. The accuracy of the linkup predictions, which includes the effect of stable tearing, are found to depend on the ligament length. Correlations between flat panel test data and analysis can be achieved within 10% if the ligament length is 0.5 inch or less. Results of correlations between flat panel experiments and analysis show that linkup of multiple cracks is controlled by ligament yielding rather than skin fracture. In addition, results suggest that the plastic zone criterion for multiple crack linkup, as proposed by Swift (3) and Tong et al (1), is reasonable.

## Acknowledgement

This work was supported by the U.S. Department of Transportation, Federal Aviation Administration Technical Center (FAATC), Atlantic City, NJ.

## REFERENCES

1. Tong, P., Greif, R. and Chen, L., "Residual Strength of Aircraft Panels with Multiple Site Damage," *Proceedings of the International Workshop on Structural Integrity of Aging Airplanes*, Atlanta Technology Publications, Atlanta, GA, pp. 200-216, 1992.

2. Thomson, D., "Residual Strength of Flat and Curved Fuselage Panels with and without Widespread Fatigue Damage," in preparation.

## REFERENCES (Cont.)


3. Swift, T., "Damage Tolerance Capability" Specialists Conference on Fatigue of Aircraft Materials, Delft University of Technology, October 1992.

4. Tong, P., "A Hybrid Finite Element Method for Damage Tolerance Analysis," *Computers & Structures*, Vol. 19, pp. 263-269, 1984.

5. Gladwell, G., and England, A.H., "Orthogonal Polynomial Solutions to Some Mixed Boundary Value Problems in Elasticity Theory," *Q.J. Mechanics and Applied Mathematics*, Vol. XXX, pp. 174-185, 1977.

6. "Damage Tolerance and Fatigue Evaluation of Structure," FAR 25.571 and FAA AC 25.571.1, FAA Airworthiness Requirements, 1978.

7. "Airplane Damage Tolerance Requirements," Military Specification, MIL-A-83444 USAF, 1974.

8. Swift, T., "Repairs to Damage Tolerant Aircraft," *Structural Integrity of Aging Airplanes*, Springer-Verlag, pp. 433-483, 1991.

9. Tong, P., Greif, R., and Chen, L., "Two Dimensional Elasticity Solution for a Riveted Lap Joint," 1992.

10. Irwin, G.R., "Analysis of Stresses and Strains Near the End of a Crack Traversing a Plate," *Journal of Applied Mechanics*, Vol. 24, pp. 361-364, 1957.

11. Dugdale, D.S., "Yielding of Steel Plates Containing Slits," *Journal of the Mechanics and Physics of Solids*, Vol. 8, pp. 100-108, 1960.

12. Paris, P.C. and Sih, G.C., "Stress Analysis of Cracks," *Fracture Toughness Testing and Its Applications, ASTM STP 381*, American Society for Testing and Materials, Philadelphia, PA, pp. 30-81, 1964.

13. Tong, P., "Solution of Stress Distribution Ahead of Crack Tip for Multiple Cracks," Private communication, April 1993.

Figure 1. Cracked stiffened panel with multiple cracks

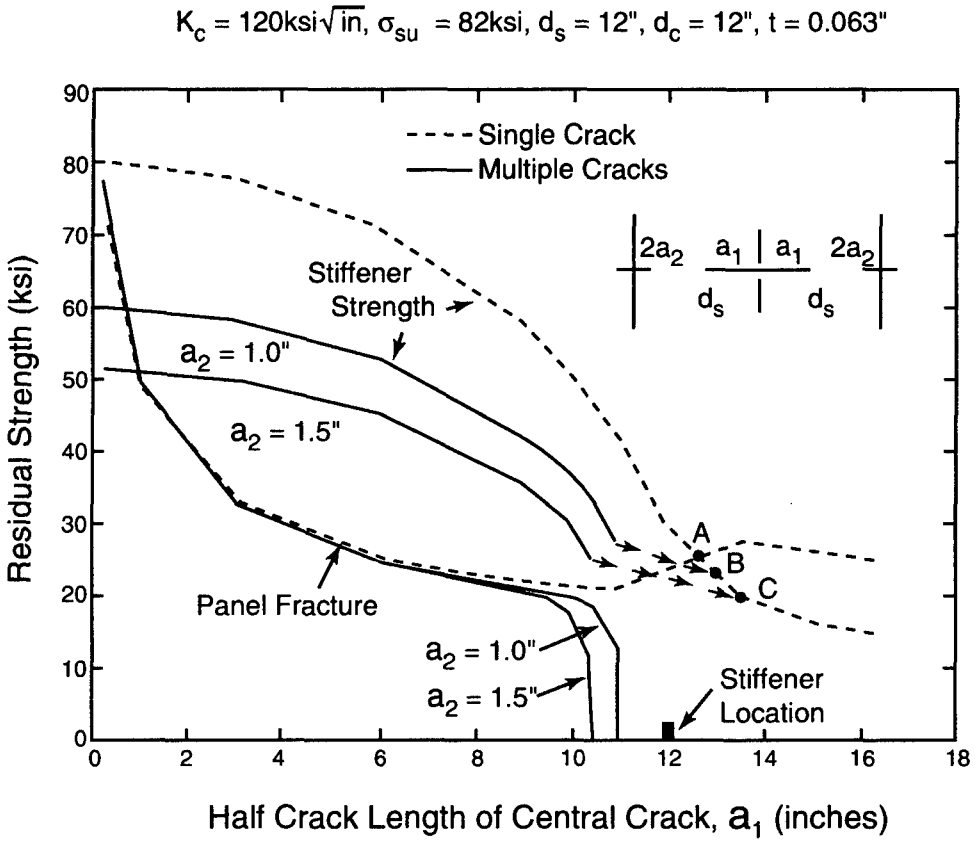



Figure 2. Residual strength diagram for stiffened panel with outlying cracks centered *over* frame

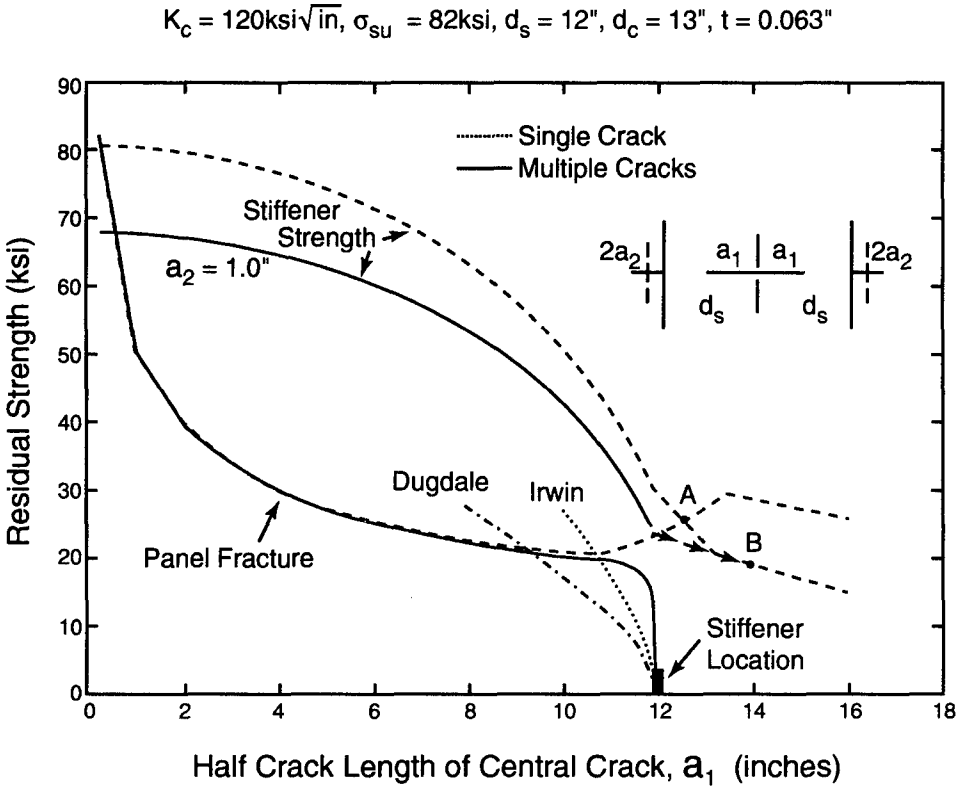



Figure 3. Residual strength diagram for stiffened panel with outlying cracks centered one inch *outside* frame

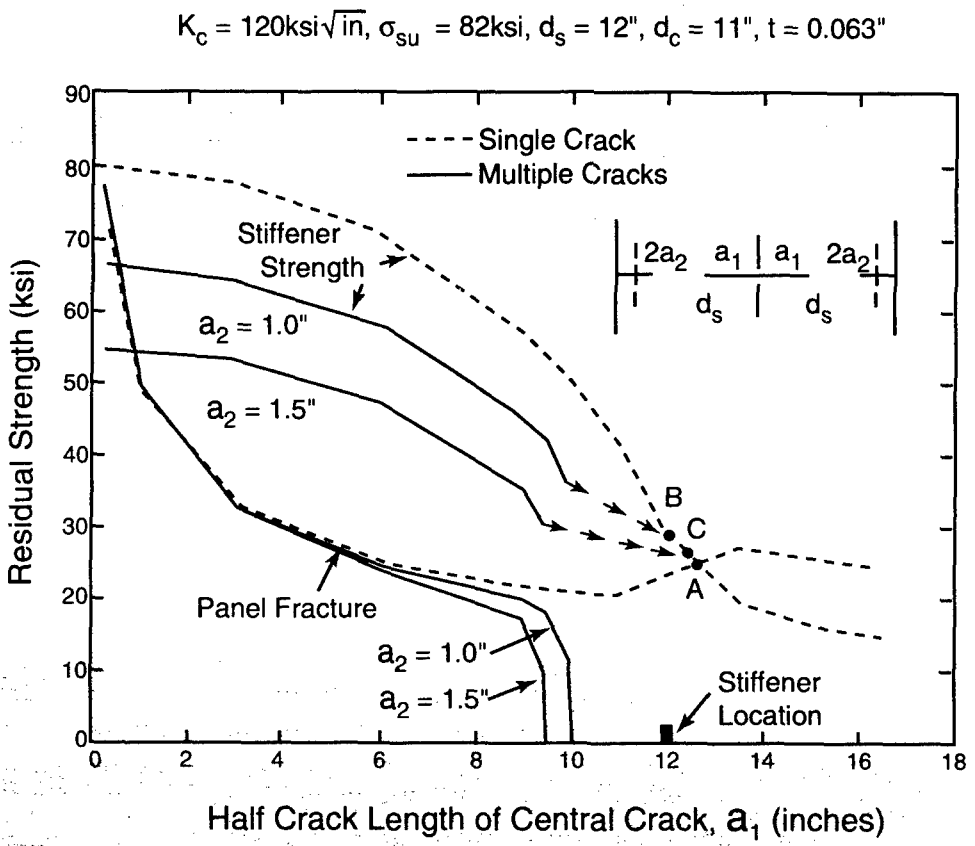



Figure 4. Residual strength diagram for stiffened panel with outlying cracks centered one inch *inside* frame

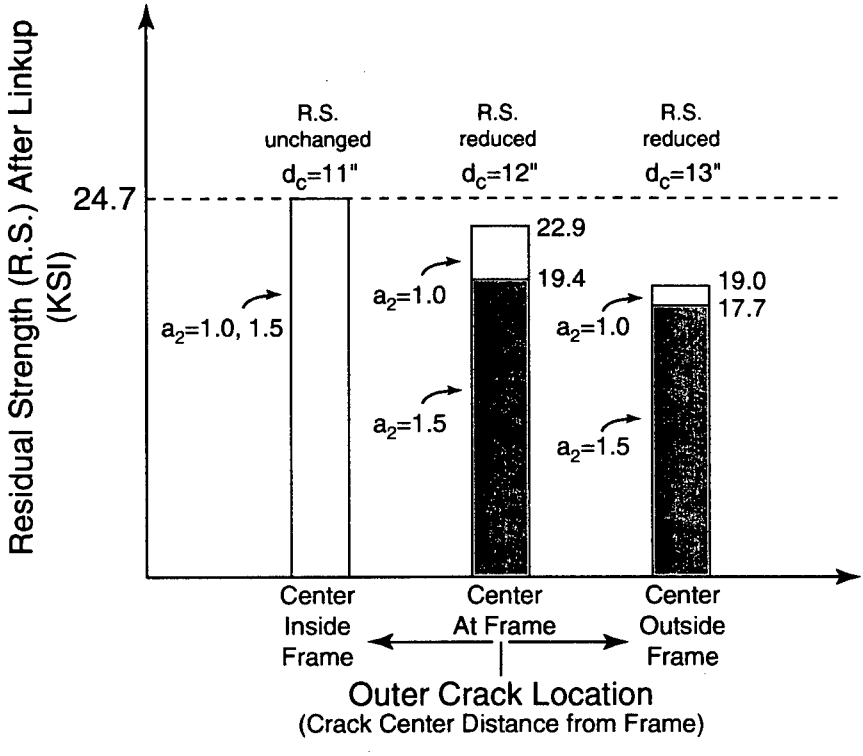
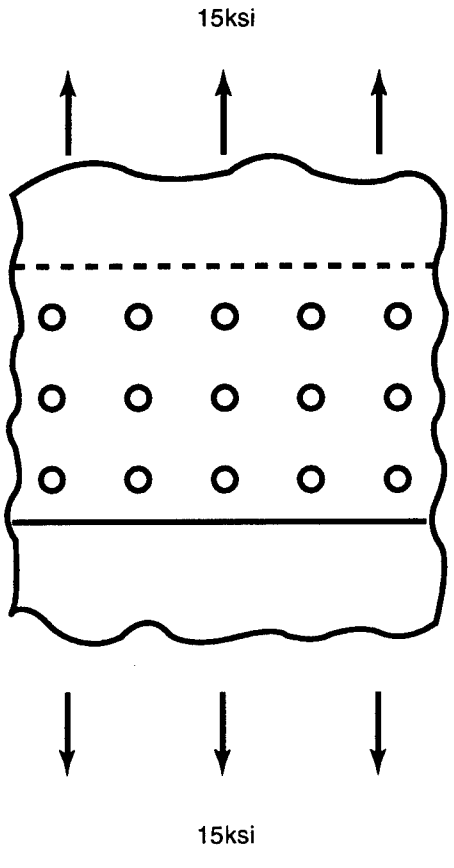



Figure 5. Relationship between residual strength and location of outlying cracks




| Row | Rivet Load (lbs) (2-D) | (1-D) |
|---|---|---|
| 3 | 216 | 220 |
| 2 | 168 | 160 |
| 1 | 216 | 220 |

Figure 6. Rivet forces for an intact lap joint

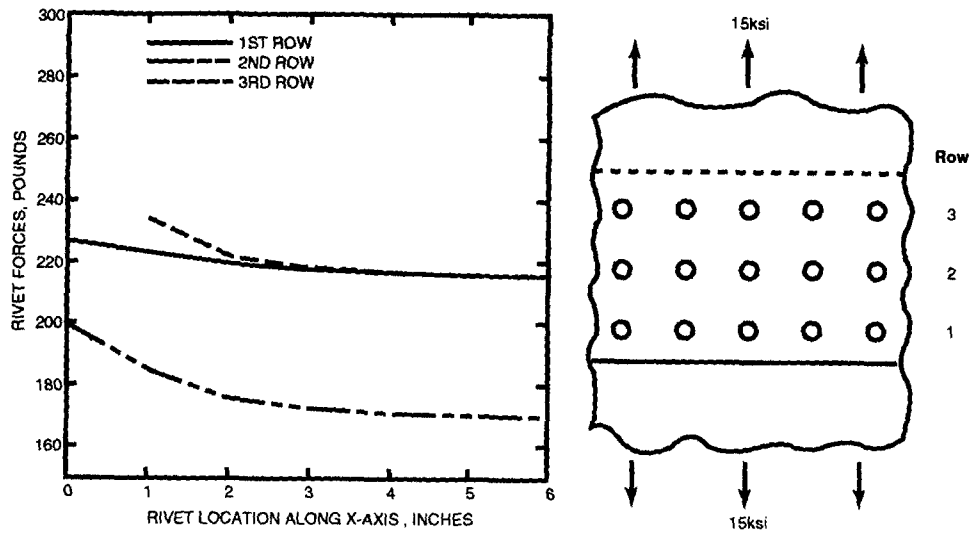



Figure 7. Rivet forces for a lap joint with a missing rivet

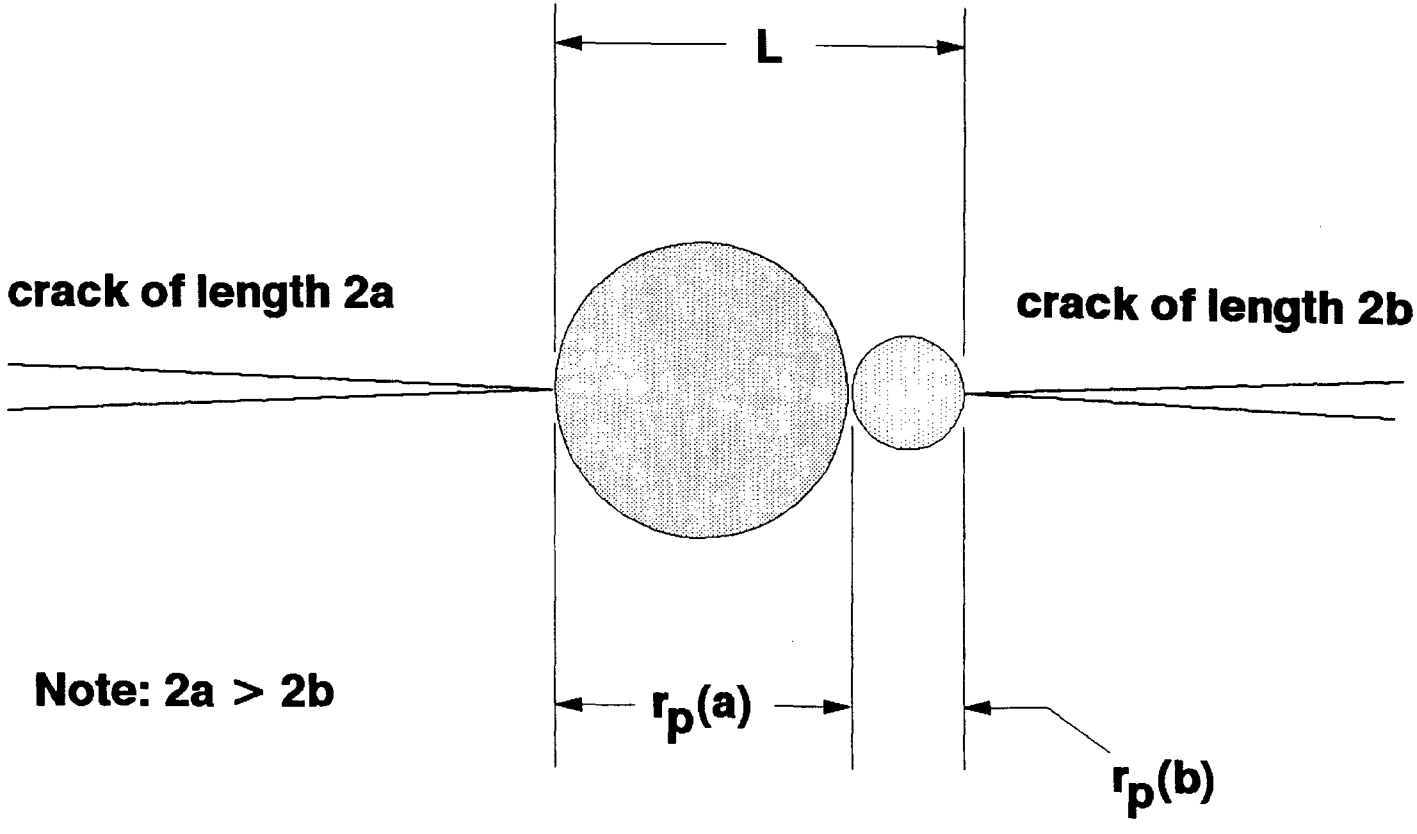



Figure 8. Schematic diagram of plastic zones ahead of neighboring cracks

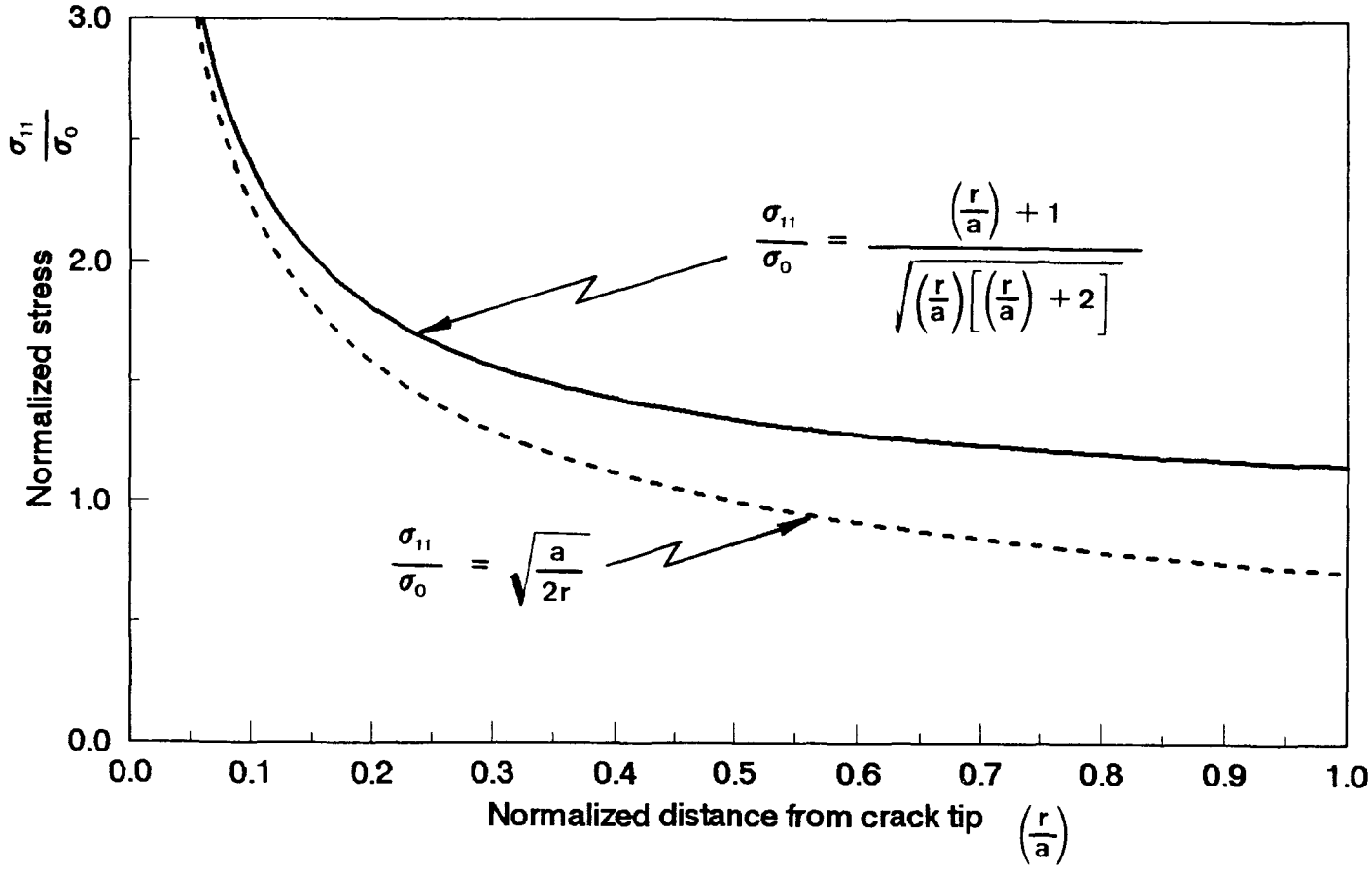



Figure 9. Comparison of stress distributions ahead of crack tip

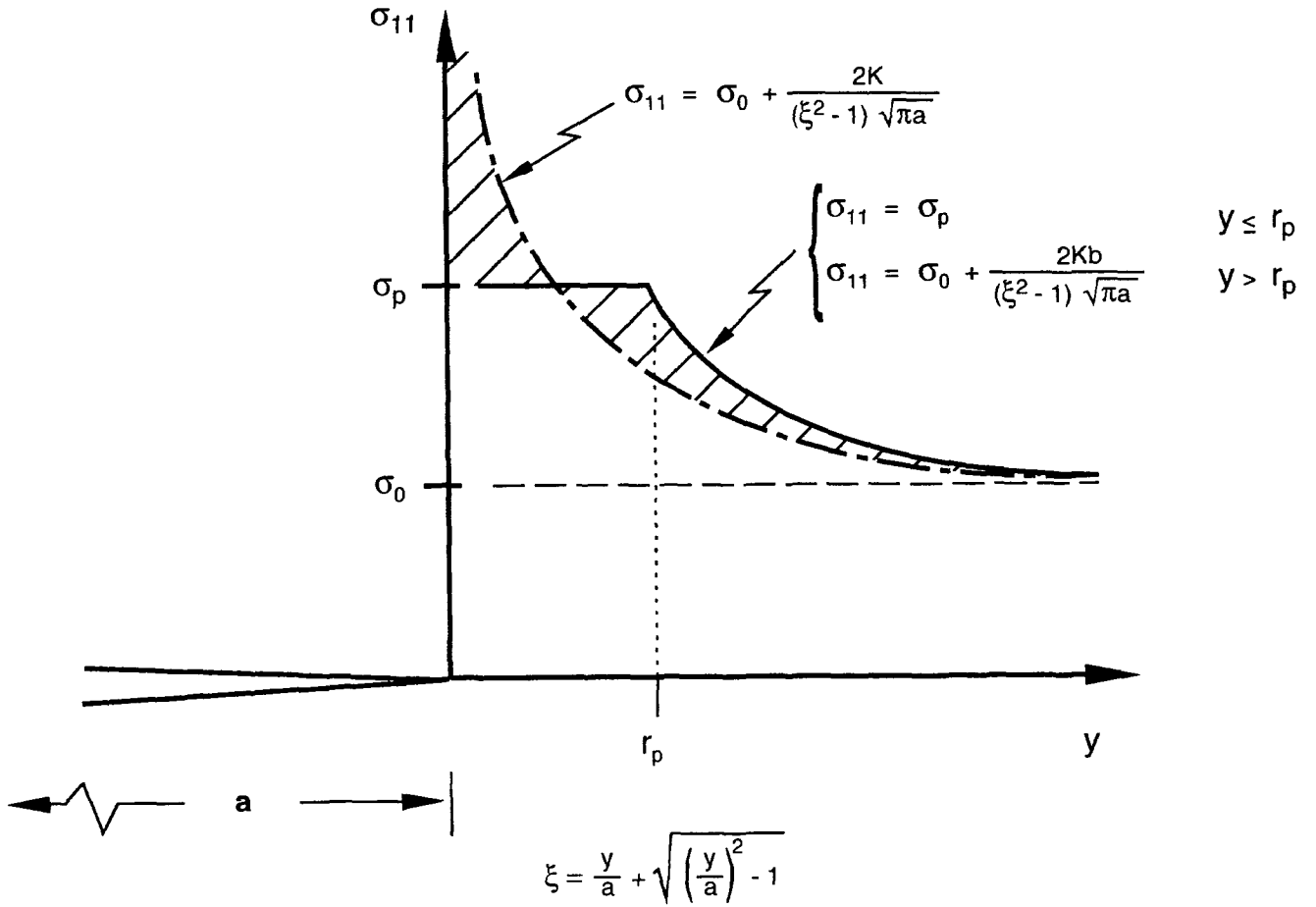



Figure 10. Modified stress distribution ahead of crack tip

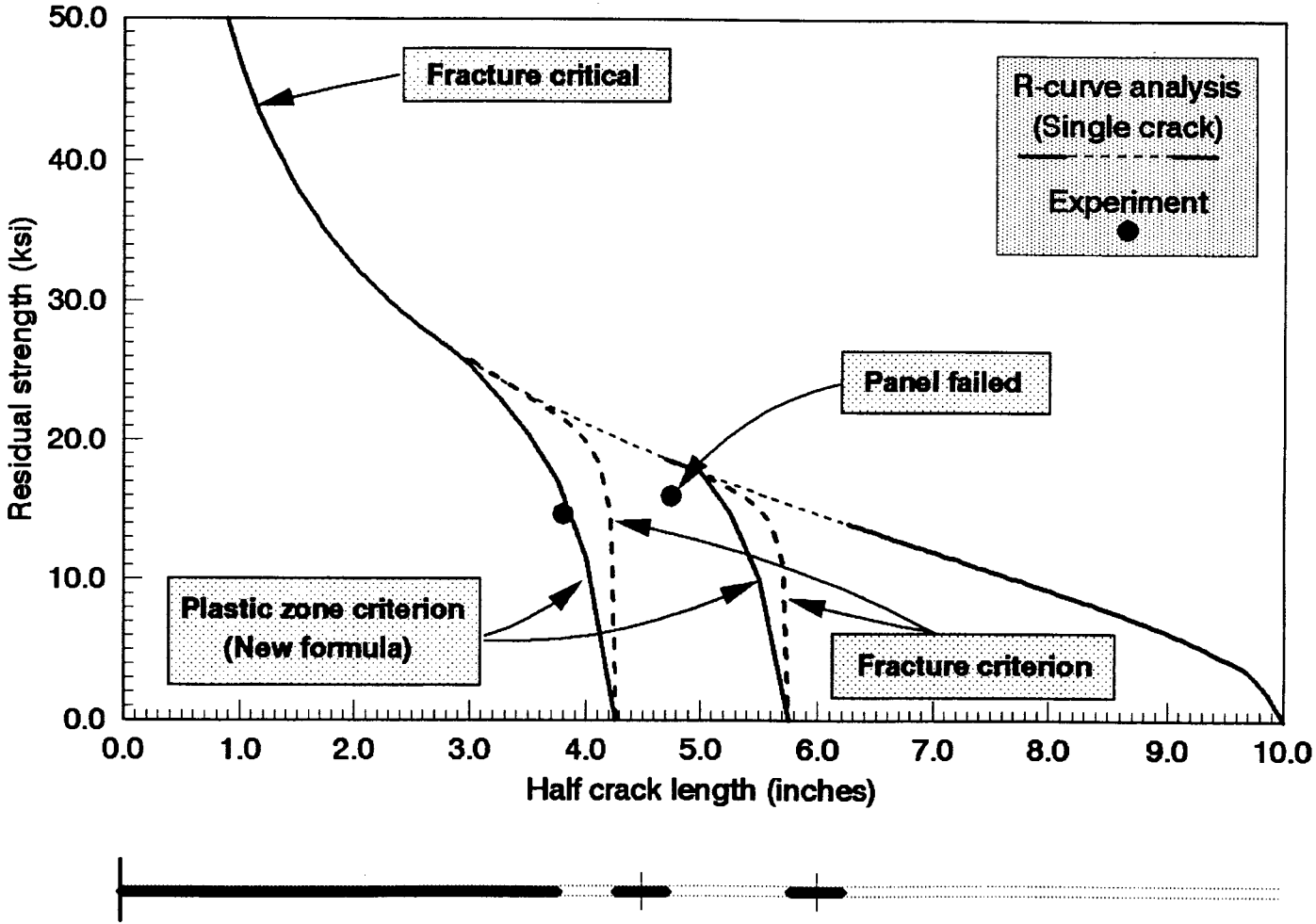



Figure 11. Typical residual strength correlation between test and analysis for flat panel with five cracks

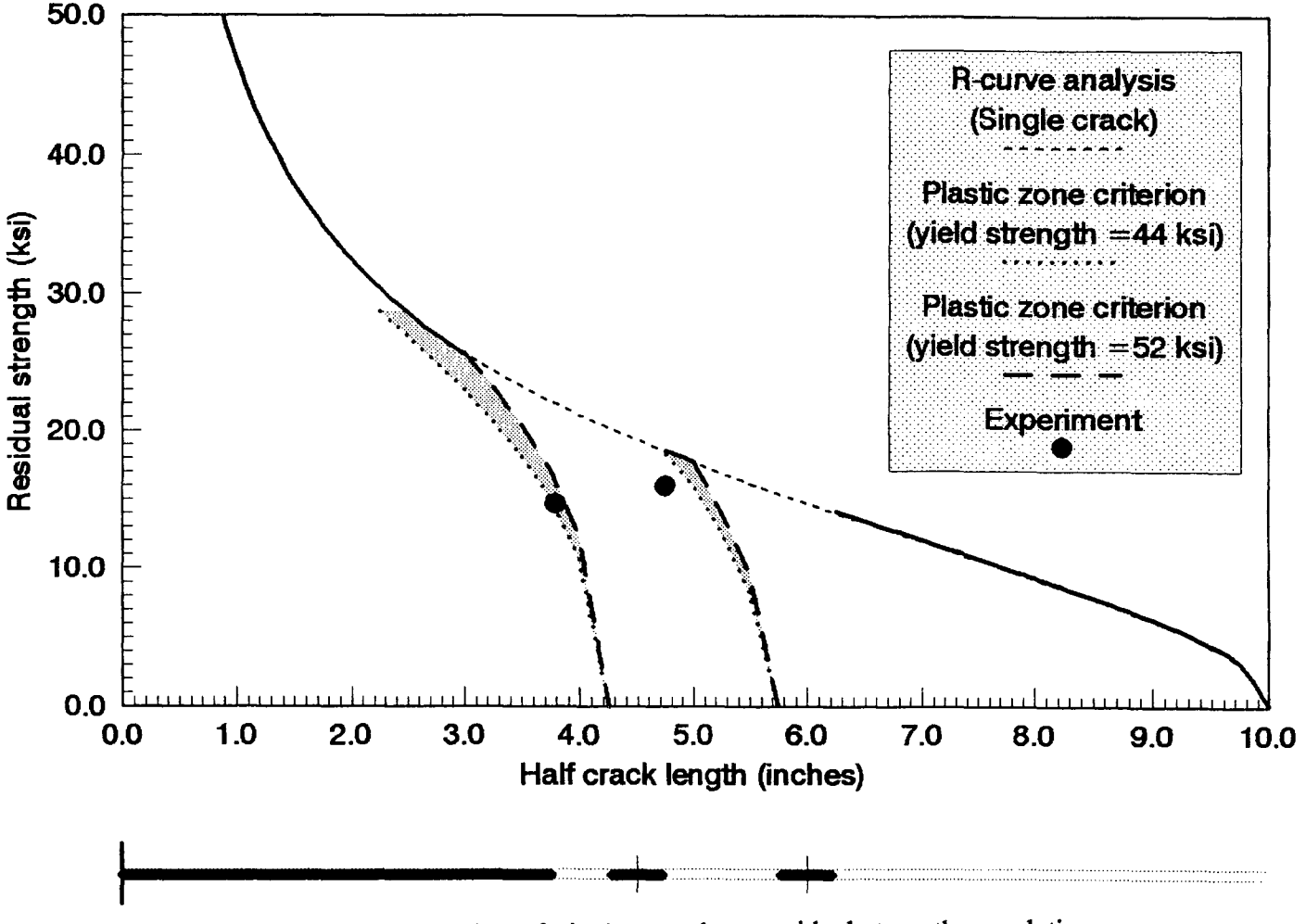



Figure 12. Effect of yield strength on residual strength correlation

# Structural Optimization and Design Sensitivity of Composite Cylindrical Shells for Energy Absorption

Dr. Aditi Chattopadhyay*
Assistant Professor

Mr. Jay M. Ferreira
Graduate Research Associate

Department of Mechanical and Aerospace Engineering
Arizona State University
Tempe, Arizona 85287

## Abstract

Composite cylindrical shells are being used more extensively for structural applications in both rotary- and fixed-wing aircraft where low weight and high strength are important design issues. This paper addresses the energy absorption capability of such shells, under axial compressive loading. A design optimization procedure is developed to improve the energy absorption by maximizing the buckling and post buckling characteristics of the shells. The sensitivity of both geometric and material properties is investigated by studying thin-walled shells of several thicknesses, made of different types of orthotropic laminates. Constraints are imposed on the longitudinal, normal and in-plane shear stresses of each ply by utilizing a failure criteria. Design variables include shell diameter and ply orientations. The optimization is performed using the nonlinear programming method of feasible directions. A two point exponential approximation is also used to reduce computational effort. Results are presented for Graphite/Epoxy, Glass/Epoxy and Kevlar/Epoxy composite cylindrical shells with symmetric ply arrangements.

## Introduction

The role of composite materials in structural applications has extensively increased over the past decade due to their reduced-

weight and high-strength capabilities. Composites have found widespread use primarily in aerospace and automotive vehicles. Therefore, passenger survivability, in the event of an accident, will inturn be greatly influenced by the performance of the structural composite components. To help assure passenger safety and survivability in accidents, the military and the government have been setting crashworthy standards that newly developed land and air vehicles must meet. In order to better adhere to crashworthy design requirements, it is necessary to maximize the amount of energy that vehicle structural components can absorb. Research in the area of crashworthy analysis and design has primarily been experimental in nature (Sen et. al., 1985; Farley, 1986, 1989) due to the complexities involved in the modeling and analysis of structures subject to impact type loading.

A commonly used structural component found in vehicles is the shell. Specifically, the shell of revolution or cylindrical shell has found the most wide spread use in the design of vehicles. Since shells are ideal for carrying many different types of loads, composites can be used to optimize the shell's structural performance to best suit a particular loading configuration. For crashworthy applications, it is also important to improve the shell's energy absorbing capabilities. This requires the determination of optimum material and geometric characteristics for efficient buckling and post buckling deformations.

The ability to improve the energy absorbing characteristics of composite cylindrical shells allows for the implementation of structural optimization techniques as a tool for improving the pre- and post-failure deformation process. Structural optimization has become an efficient means of expediting design in several disciplines. An extensive amount of work has been done in developing optimization procedures to bring the state of the art to a very high level (Schmit, 1981; Vanderplaats, 1982). In the past, conventional design procedures typically used the designer's experience and trial-and-error methods. Today, with the availability of sophisticated computing resources, it is possible to easily and effectively use optimization at various stages of design.

Although a significant amount of work has been done in the area of structural optimization, a great majority of this work has been limited to isotropic materials where the design variables are generally size, shape and topology. With the emergence of fiber-reinforced composites, it is now possible to consider design parameters related to material properties, either at the ply or laminate level. Due to the importance of the problem, there has been some effort at using structural optimization procedures for design with composites in recent years (Fukunaga et al., 1991; Gurdal et al., 1991; Hirano, 1983;

Kicher et al., 1971; Nshanian et al., 1983; Onada, 1985; Pederson, 1991; Vanderplaats et al., 1989; Zimmermann, 1989; ).

The application of design optimization for improved buckled configurations has been studied. Although a considerable effort has been devoted in improving pre-failure performance of a structural member, post-failure performance and the problem of improving its energy absorption characteristics using formal optimization procedures has not been addressed in much depth. To date, very few published research are available in this area. Lust (1990) presented a structural design optimization methodology for automobiles, which considers design criteria associated with both linear elastic and crashworthiness (nonlinear) conditions. By simultaneously considering both elastic and crashworthy criteria, more mass efficient structural designs were obtained. A scaling factor was utilized in approximating the nonlinear crashworthy constraints. Bolukbasi (1991) developed a preliminary design optimization methodology for rotorcraft. This procedure minimized the system weight of a helicopter while maintaining a specific level of crash protection. Crash response analysis tools and parametric subsystem weight analyses were employed in the optimization.

The goal of this research is to use design optimization procedures to maximize the energy absorbing capability of axially compressed composite cylindrical shells with constraints on the individual ply stresses and the critical buckling load. Additionally, a sensitivity analysis is performed to examine energy absorption with respect to material constitutive properties and geometry.

## Problem Description

This investigation addresses the use of formal optimization techniques and sensitivity analysis to maximize the energy absorption of axially compressed thin-walled composite cylindrical shells. The goal is to maximize the area under the force-deflection curve (Fig. 1) by using geometric and material design variables. A study is also conducted to examine the sensitivity of energy absorption with respect to material constitutive properties. Constraints are imposed on the in-plane material-axis stresses of each ply and the critical buckling load. A structural analysis procedure, based on laminate and shell theory, is used for the buckling and post buckling analyses. The nonlinear programming method of feasible directions combined with a two-point exponential approximation method is used for the optimization. Five cylindrical shells made of Gr/Ep, Gl/Ep and K/Ep with two, four, six, eight and 10 ply symmetric and unsymmetric lay-ups are investigated.

## Structural Model

A geometric illustration of a typical composite cylindrical shell considered in this study is presented in Fig. 2. The initial or reference cylinders all have a length, L, of 50 inches, an inner radius, R, of 10 inches (L/R=5) and ply orientations of alternating ±30°. A ±30° lay-up scheme was chosen because it is a typical configuration used in industry. The total number of plies used to make up the wall thickness, t, is varied in each specimen. The plies are numbered starting from 1 through to the final ply in the laminate, with the first ply being the outer most one. A value of 0.01 inch is used for the thickness of each ply. A total of 30 cylindrical shells are analyzed which include 10 shells of Graphite/Epoxy (Gr/Ep), Glass/Epoxy (Gl/Ep) and Kevlar/Epoxy (K/Ep) with two, four, six, eight and 10 ply symmetric and unsymmetric orthotropic laminates, respectively. The properties of these constituent materials are presented in Vinson and Sierakowski, 1987.

## Analysis and Optimization

This section presents a brief description of the analysis procedures followed by a formulation and implementation of the optimization problem.

### *Laminate Analysis*

Classical laminate theory (Vinson et al., 1987) is used to analyze the individual material-axis ply stresses of the cylindrical shells. The constitutive relations provided by this theory relate strains and curvatures to the resultant forces and moments. These equations are solved for mid-plane strains and curvatures to evaluate the individual ply stresses in the shell wall.

### *Failure Analysis*

Material failure occurs in a composite cylindrical shell if the longitudinal, transverse or in-plane shear stress of a ply in the shell wall exceeds its strength. Therefore, to avoid this problem, the individual ply stresses are constrained. The interaction failure criterion presented by Tsai and Wu (1971) is used in this research. This failure theory is chosen because it allows a more comprehensive formulation of a design constraint in the optimization formulation, since all three lamina stresses are combined into a single equation.

*Buckling and Post buckling Analysis*

The critical buckling load and post buckling curves (Fig. 1) are evaluated in this research using analytical formulations. The critical buckling load is derived using a Donnell-type linear stability analysis. A Navier type solution is used to solve for the stability relation. The post buckling behavior of the cylindrical shells is evaluated using von Karman-Donnell large displacement relations and the principle of stationary potential energy.

*Optimization Formulation*

The objective is to maximize the energy absorbing capability of axially compressed cylindrical shells. Constraints are placed upon the material-axis ply stresses, at the critical buckling load. A constraint is additionally placed upon the critical buckling load to control its magnitude. The shell mean radius and ply orientations are used as design variables.

Since this problem addressed in this research is one of maximizing energy absorption, the objective function is defined as the negative of the area under the load deflection curve. This allows the application of the techniques of minimization to produce a maximum. The formal optimization problem is mathematically posed as follows:

Minimize:

$-F(\phi_i)$ $\quad i = 1,..., NDV$ (objective function)

where

F is the area under load-deflection curves OA and BC (Fig. 1),

subject to:

$g_j(\phi_i) \leq 0$ $\quad j = 1,..., NCON$ (constraints)

$\phi_{iL} \leq \phi_i \leq \phi_{iU}$ (side constraints)

where $\phi$ is the design variable vector, NDV is the number of design variables, NCON is the total number of constraints and subscripts L and U refer to lower and upper bounds imposed on the design variables. Side constraints are imposed on the design variables to avoid unrealistic designs.

*Optimization Implementation*

The optimization process is initiated by defining all the necessary preassigned parameters (e.g., shell length and wall thickness) for the problem. Next, the design variables are initialized and the structural analysis is performed. The objective function (the numerically integrated area under the force deflection curve) and constraints are evaluated followed by a sensitivity analysis. The optimizer consists of the nonlinear programming technique (the method of feasible directions) as implemented in the computer-code CONMIN (Vanderplaats, 1973) and a two point exponential approximation method (Fadel et al., 1990). The approximate analysis is used to reduce the computational effort involved in using exact analysis for several evaluations of objective function and constraints necessary within CONMIN. To reduce possible errors in the approximations, move limits, defined as the maximum fractional change of a design variable value, are imposed as upper and lower bounds on the design variables, $\phi_i$. Convergence is based upon the objective function value over three consecutive cycles, where a cycle comprises a complete analysis and optimization. A convergence tolerance of 0.005 is used.

## Results

Results obtained using the above optimization procedure are presented in this section. The results of the optimization are compared against a reference (baseline) design. The material and number of plies are varied to investigate their sensitivity on the energy absorption. A total of 30 cylindrical shells are analyzed which include 10 shells of Graphite/Epoxy, Glass/Epoxy and Kevlar/Epoxy with two, four, six, eight and 10 ply symmetric and unsymmetric orthotropic laminates, respectively. Optimum configurations for maximum energy absorption are obtained within 4-13 cycles in each case. Results for the cylindrical shells made of symmetric laminates are presented below. Cylindrical shells made of unsymmetric laminates displayed similar trends.

The results of the optimization for the cylindrical shells made of symmetric orthotropic laminates are summarized in Table 1 and Figs 3-5. Each of the cylindrical shells are subjected to a compressive strain of 10%. Constraints are placed upon the in-plane stresses and the critical buckling load. The buckling load constraint is used to control the magnitude of the critical buckling load. Table 1 presents the critical buckling load, minimum stable post buckling load and specific energy absorption capability of both the reference and the optimum shells. It also lists the ratio of the minimum stable post

buckling load to the classical buckling load. The table indicates that Gr/Ep shells are able to absorb the maximum energy and display the highest buckling loads in both the reference and the optimum shells, followed by the Gl/Ep and the K/Ep shells. The values of the critical buckling loads are all close to or equal to the upper bounds imposed on them (i.e. the constraints are nearly critical). This is due to the fact that the energy absorption can be increased by increasing the critical buckling load. The optimization procedure, therefore, is greatly influenced by the load limiting constraint and convergence is reached after this constraint becomes active. The ratios of the minimum stable post buckling load to the critical buckling load for the reference and optimum cylindrical shells display an expected trend. The minimum stable post buckling loads exhibit a mean value of approximately 18% of their respective critical buckling load's magnitude. This is in good agreement with previous experimental results. Another interesting trend is also observed about this ratio. It is seen that for each group of shells made of the same material, the value of the ratio is highest for the 2- and the 10-ply cases. The smallest value occurs in the 6-ply case for all reference shells and in the 4-ply case for all optimum shells. The behavior of these ratios is highly nonlinear and no conclusion can be drawn at this point.

The percent increase in specific energy absorption of the shells, from reference to optimum, are presented in Figs 3-5. Figure 3 shows an improvement of the energy absorption capability for the Gr/Ep shells. The maximum increase (66%) occurs in the 8-ply shell and the 2-ply shell has the lowest overall increase (19%). Similarly, the K/Ep shells display a maximum and a minimum increase of 60% and 23%, respectively, in the 8- and the 2-ply cases (Fig. 4). The overall increase in energy absorption are the lowest for the Gl/Ep shells. In this case, the 6-ply shell shows the maximum increase in buckling load (37%) and the 2-ply shell once again yields the lowest increase (18%), as shown in Fig. 5. Since a global minimum cannot be guaranteed in most nonlinear optimization problems, such as these, no conclusion is drawn regarding this nonlinear change of optimum energy absorption with changes in the number of plies, due to possible convergence to local a minimum. The energy absorption capability of both the reference and the optimum shells increase, with the number of plies, almost linearly. As with the optimum buckling load obtained from the first part of the study, this is expected because the wall thickness plays a direct role in supporting the loads and in determining the amount of energy the shell can absorb.

Table 2 presents the design variable values for the reference and the optimum shells made of Gr/Ep. Shells made of Gl/Ep and K/Ep displayed similar trends. The shell radius is allowed to change by

±25% and the plies are allowed to vary between ±90° during optimization. Only half of the ply orientations ($\theta_i$) are presented, due to the conditions of symmetry. For all cylindrical shells, the radii decrease from their initial value of 10 in., in the reference, shells to a value of 7.5 in. (design variable lower bound) in the optimum shells for all three materials. This increases the slenderness ratio (L/R) from 5 to 6.67 and reduces the shell diameter to wall thickness ratio (D/t) and suggests that an increase in the energy absorption capability is also attributed to changes in these ratios. Sen et. al. (1985) and Farley (1986) have shown experimentally that a decrease in the ratio D/t is associated with increased energy absorption. It is also interesting to note that although the decrease in the radius reduces the circumferential area, the buckling load (which is directly proportional to circumferential area) and the energy absorption increases for all shells. This suggests that the ply orientations play a major role in energy absorption, as shown by Farley (1989). It must be noted that the radius and thus the surface area decrease thereby reducing the weight of the shell, without weight being used as a constraint. The optimum shells therefore support higher buckling loads and absorb more energy while being lighter than the respective reference shells. Table 2 also indicates that the ply angles closer to the mid-plane of the shell wall decrease in magnitude (from their reference value) and those nearer the outer surface increase in magnitude. This trend is due to the fact that the Tsai-Wu constraint criterion is more satisfied by the stress configurations that result from these ply orientations.

The reference (baseline) design and optimized designs are all feasible, i.e. designs satisfying all the constraints. Stress constraints all stay within their respective bounds during the optimization process and, as a result, a consistent monotonique increase in the objective function values (energy absorption) is noted in the investigation.

## Concluding Remarks

An optimization procedure has been developed to address the problem of maximizing the energy absorbing capability of composite cylindrical shells subjected to axial compressive loading. A sensitivity analysis is performed to study the effect of total number of plies and material constituent properties on the buckling load. The shell radius and ply orientations are used as design variables. Constraints are imposed on the longitudinal, transverse and shear in-plane ply stresses and on the critical buckling load. The optimization is performed using the method of feasible directions. A two-point exponential approximation method is used to reduce the

computational effort. Results are presented for shells made of Gr/Ep, Gl/Ep and K/Ep orthotropic laminates with five different wall thicknesses. The procedure yields improvements in the energy absorbing capabilities for all shells. Optimum energy absorption configurations are obtained within 4-13 cycles. The following observations are made from this study:

(1) The convergence was primarily governed by the load limiting constraint imposed on the critical buckling load.

(2) Optimization increased the energy absorption capability, from the reference values, for all the composite cylindrical shells. The highest percent increases were obtained with Gr/Ep shells, followed by K/Ep and Gl/Ep. These results agreed well with previous experimental findings.

(3) The ratio of the minimum stable post buckling load to the critical buckling load agreed well with previous analytical and experimental work.

(4) In the optimum configurations, ply orientations nearer the wall mid-plane decreased in magnitude and those farther away increased in magnitude. The radius reduced, thereby increasing the slenderness ratio, indicating that shells of smaller radii are more efficient for energy absorption.

(5) Reductions were obtained in the shell weights, although weight was not used as a constraint in the optimization formulation.

(6) The magnitudes and the nature of the stresses in each ply changed significantly, from reference to optimum, and with changes in wall thicknesses. Gr/Ep and K/Ep displayed the most significant changes.

## Acknowledgment

This research was sponsored in parts by grants from the Army Research Office, Grant Number DAAHOH-93-G-0043 and the National Science Foundation, Grant Number MSS-9209961.

## References


Bolukbasi, A. O. (1991). Crash-resistant rotorcraft preliminary design optimization. *Proc. 47h Annual Forum of the American Helicopter Society,* Phoenix, AZ, May 1991.

Fadel, G. M., Riley, M. F. and Barthelemy, J. F. (1990). Two-point exponential approximation method for structural optimization. *Structural Optimization*, **2**, 117-124.

Farley, G. L. (1986b). Effect of specimen geometry on the energy absorption capability of composite materials. *Journal of Composite Materials*, **20**, 390-400.

Farley, G. L. (1989d). Energy absorption capability of composite tubes and beams. Ph.D. Dissertation, Virginia Polytechnic Institute and State University, Blacksburg, Virginia.

Fukunaga, H. and Vanderplaats, G. N. (1991). Stiffness optimization of orthotropic laminated composites using lamination parameters. *AIAA Journal*, **29**(2), 641-646.

Gurdal, Z. and Haftka, R. T. (1991). Optimization of composite laminates. NATO / DFG ASI, *Optimization of Large Structural Systems,* Lecture Notes, Berchtesgaden, Germany, September, 1991,**1**, 200-215.

Hirano, Y. (1983). Optimization of laminated composite cylindrical shells for axial buckling. *Trans. Japan Society for Aeronautical and Space Sciences*, **26**, 154-162.

Kicher, T. P. and Chao, T. L. (1971). Minimum weight design of stiffened fiber composite cylinders. *Journal of Aircraft*, **8**(7), 562-568.

Lust, R. V. (1990). Structural optimization with crashworthiness constraints. *Third Air Force/NASA Symposium On Recent Advances in Multidisciplinary Analysis and Optimization*, San Francisco, CA, Sept., 1990.

Nshanian, Y. S. and Pappas, M. (1983). Optimal laminated composite shells for buckling and vibration. *AIAA Journal*, **21**(3), 430-437.

Onada, J. (1985). Optimal laminate configurations of cylindrical shells for axial buckling. *AIAA Journal*, **23**(7), 1093-1098.

Pederson, P. (1991). Optimal orientation of anisotropic materials. NATO / DFG ASI, *Optimization of Large Structural Systems,* Lecture Notes, Berchtesgaden, Germany, September, 1991,**1**, 168-200.

Schmit, L. A. (1981). Structural synthesis - its genesis and development. *AIAA Journal*, **19**(10), 249-1263.

Sen, J. K. and Dremann, C. C. (1985). Design development tests for composite crashworthy helicopter fuselage. *SAMPE Quarterly,* **17**(1), 29-39.

Tsai, S. W. and Wu, E. M. (1971). A general theory of strength for anisotropic materials. *Journal of Composite Materials*, **5**, 58-80.

Vanderplaats, G. N. (1973). *CONMIN - A Program for Constrained Function Minimization.* User's Manual. NASA TMX-62282.

Vanderplaats, G. N. (1982). Structural optimization - past, present and future. *AIAA Journal*, **20**, 992-1000.

Vanderplaats, G. N. and Weisshaar, T. A. (1989). Optimum design of composite structures. *Journal for Numerical Methods in Engineering*, **19**, 437-448.

Vinson, J. R. and Sierakowski, R. L. (1987). *The Behavior of Structures Composed of Composite Materials.* Kluwer, Dordrecht.

Zimmermann, R. (1989). Optimization of axially compressed fiber composite cylindrical shells. *Proc. International Seminar Organized by Deutsche Forschungsanstalt fur Luft- und Raumfahrt (DLR)*, Bonn, June 1989.

Table 1. Energy absorption and buckling loads of the reference and optimum cylindrical shells made of symmetric laminates

| | No. of plies | Reference | | | | Optimum | | | |
|---|---|---|---|---|---|---|---|---|---|
| | | $Nx_{cr}$ (lb/in) | $Nx_{min}$ (lb/in) | $\frac{Nx_{min}}{Nx_{cr}}$ | Energy (lb-in/lb) | $Nx_{cr}$ (lb/in) | $Nx_{min}$ (lb/in) | $\frac{Nx_{min}}{Nx_{cr}}$ | Energy (lb-in/lb) |
| Gr/Ep | 2 | 118.1 | 22.7 | 0.192 | 8285.3 | 152.2 | 27.1 | 0.178 | 9876.2 |
| | 4 | 479.7 | 90.2 | 0.188 | 14909.1 | 1086.3 | 160.7 | 0.148 | 20681.3 |
| | 6 | 1155.5 | 203.5 | 0.176 | 21575.8 | 2415.2 | 372.1 | 0.154 | 31848.4 |
| | 8 | 1961.6 | 383.1 | 0.195 | 28090.9 | 4292.3 | 755.4 | 0.176 | 46727.2 |
| | 10 | 3128.5 | 638.2 | 0.204 | 38345.4 | 6450.6 | 1257.8 | 0.195 | 60712.7 |
| Gl/Ep | 2 | 94.9 | 18.2 | 0.192 | 4803.2 | 122.2 | 21.7 | 0.178 | 5699.5 |
| | 4 | 385.6 | 64.9 | 0.168 | 10035.7 | 520.3 | 83.2 | 0.160 | 12571.4 |
| | 6 | 839.8 | 140.9 | 0.167 | 12238.1 | 1271.1 | 230.3 | 0.181 | 16738.1 |
| | 8 | 1549.4 | 268.6 | 0.173 | 15500.3 | 2191.4 | 385.6 | 0.176 | 19714.3 |
| | 10 | 2447.4 | 428.1 | 0.174 | 18085.7 | 3386.7 | 612.9 | 0.181 | 24014.3 |
| K/Ep | 2 | 52.0 | 10.3 | 0.198 | 4424.5 | 70.4 | 13.6 | 0.193 | 5465.3 |
| | 4 | 211.9 | 40.7 | 0.192 | 6850.3 | 508.7 | 73.7 | 0.145 | 9350.2 |
| | 6 | 496.8 | 93.9 | 0.189 | 10166.7 | 1157.1 | 180.8 | 0.156 | 15933.3 |
| | 8 | 860.9 | 170.1 | 0.197 | 13675.5 | 1914.2 | 344.2 | 0.180 | 21925.3 |
| | 10 | 1395.3 | 276.1 | 0.198 | 16160.2 | 2726.2 | 556.1 | 0.204 | 24040.5 |

Table 2. Comparison of design variables for the Gr/Ep shells made of symmetric laminates

| | Reference | Optimum | | | | |
|---|---|---|---|---|---|---|
| | | 10 plies | 8 plies | 6 plies | 4 plies | 2 plies |
| Mean radius (in) | 10.0 | 7.5 | 7.5 | 7.5 | 7.5 | 7.5 |
| $\theta_1$ (degrees) | 30.0 | 52.4 | 51.3 | 47.8 | 51.0 | 39.9 |
| $\theta_2$ (degrees) | -30.0 | -26.7 | -51.3 | -14.3 | -16.6 | |
| $\theta_3$ (degrees) | 30.0 | 16.8 | 17.1 | 14.3 | | |
| $\theta_4$ (degrees) | -30.0 | -16.6 | -17.1 | | | |
| $\theta_5$ (degrees) | 30.0 | 16.3 | | | | |

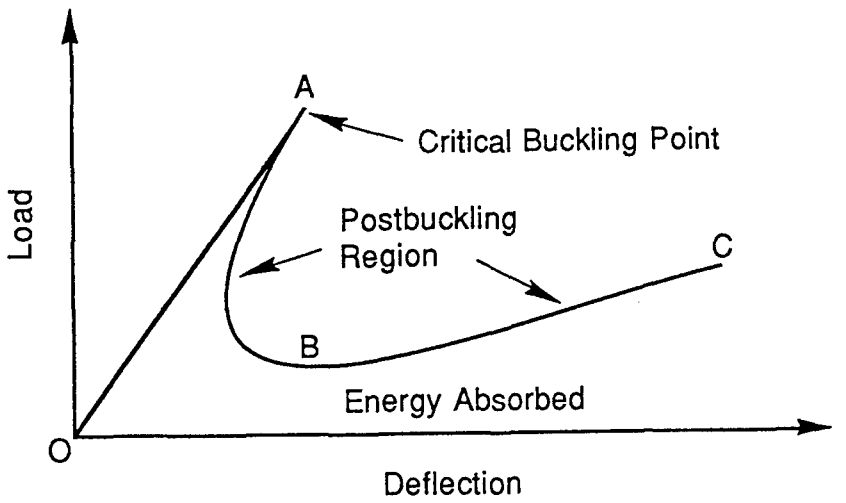



Fig. 1. Typical load-deflection graph of an axially compressed cylindrical shell.

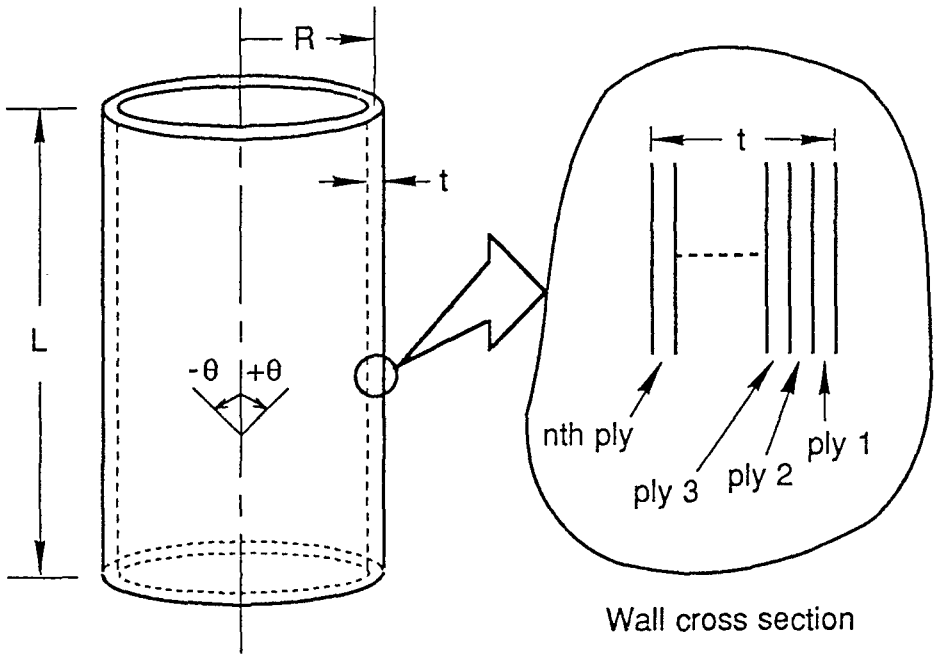



Fig. 2. Composite cylindrical shell geometry and notation.

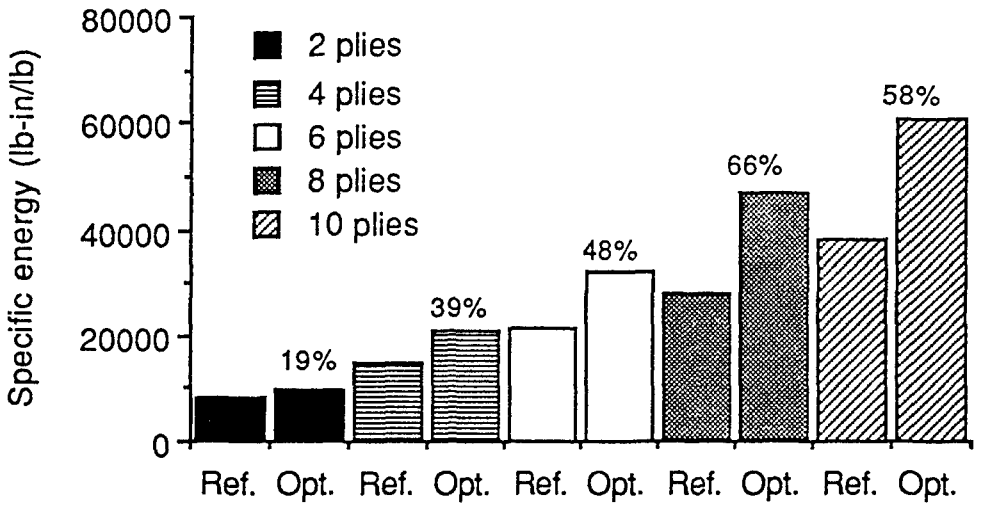



Fig. 3. Comparison of energy absorption for Gr/Ep cylindrical shells made of symmetric laminates.

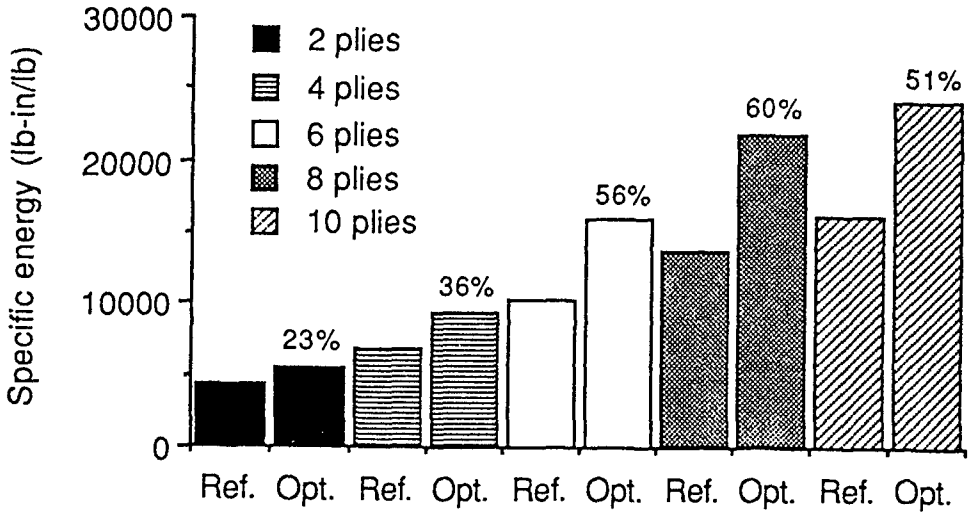



Fig. 4. Comparison of energy absorption for K/Ep cylindrical shells made of symmetric laminates.

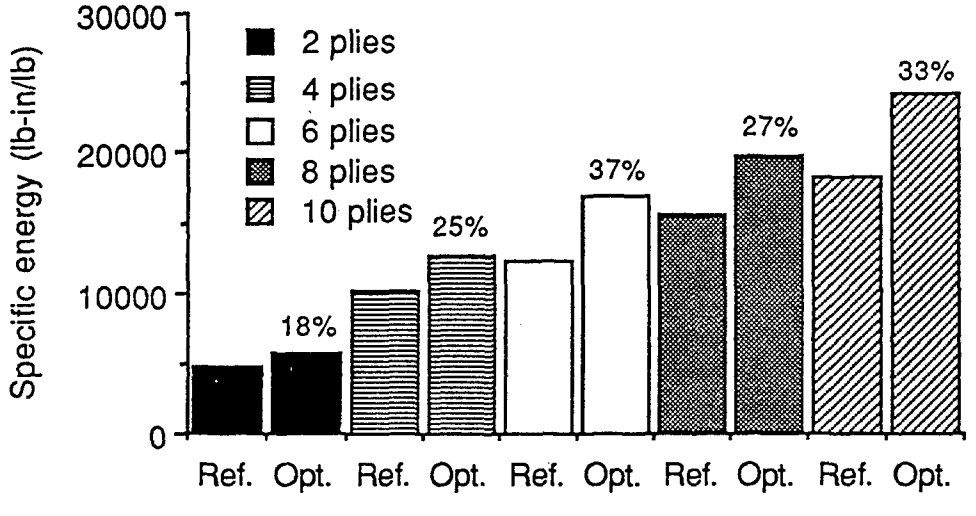



Fig. 5. Comparison of energy absorption for Gl/Ep cylindrical shells made of symmetric laminates.

# Design and Fabrication of Thick Composite Cylinders Subjected to Axial Loads

*J. Tzeng, J. Bender and B. Burns*
Weapons Technology Directorate, ARL

*A. Alexander*
Custom Analytical Engineering System Inc.

"PAPER NOT AVAILABLE"

# Validation of Projectile Transient Response Models for the Study of Pressure Oscillations in Guns

Morris Berman
Ting Li
U.S. Army Research Laboratory
2800 Powder Mill Road
Adelphi, Maryland 20783-1145

David Hopkins*
U.S. Army Research Laboratory
Aberdeen Proving Ground, Maryland 21005-5066

## INTRODUCTION

The U.S. Army is currently developing an Advanced Field Artillery System. This system uses liquid propellant (LP), as opposed to conventional solid propellant, for projectile propulsion. The characteristic base pressure history of solid propellant is a smooth curve. With LP, the low frequency components of the curve remain unchanged, however a high frequency oscillation is also present (Fig. 1). Projectile components such as fuzes are designed to survive a

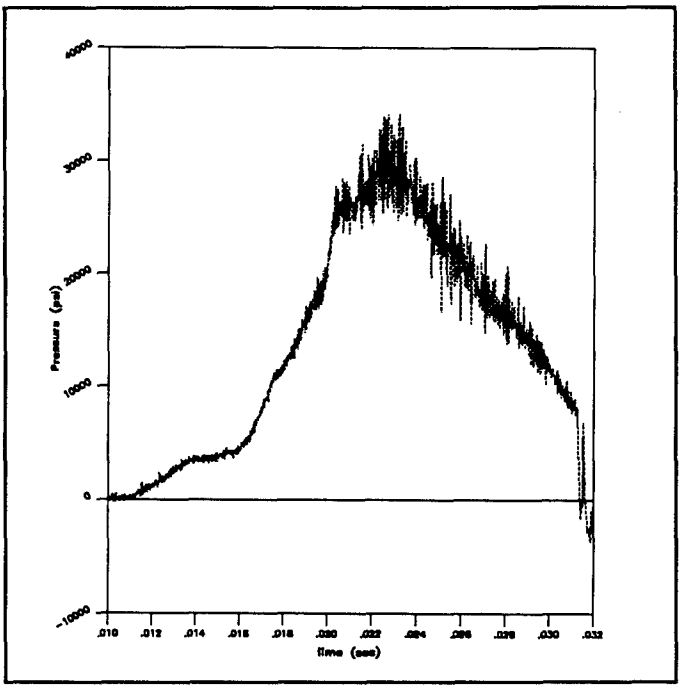



**Figure 1.** LP Pressure-Time History

certain vibrational environment [1]. The introduction of LP guns may therefore change the environment in which such components must function.

One means of quantifying the effect of the RLPG combustion environment on the current projectile inventory is to conduct an extensive firing test involving all munitions of interest. Alternatively, finite element (FE) techniques can be used to generate a model of the projectile. While this is a fairly standard approach [2-5], it has not been common practice to demonstrate apriori that the FE model appropriately approximates the dynamics of the projectile. Experimental modal analysis (EMA) can be used to determine a projectile's dynamic characteristics. These characteristics can then be compared with the corresponding FE model's characteristics to determine the accuracy of the modeled dynamic behavior. After validation, the FE model can used to determine the effect of the LP envirionment upon the projectile. This approach is used in this paper to validate an FE model of the PXR6353 instrumented projectile. This model is then used to determine the probable response of this particular projectile to an actual RLPG pressure-time history.

## BACKGROUND

The basic goal of dynamic analysis is the determination of the dynamic response of a structure to a defined forcing function. For complex structures this often entails the development of an appropriate FE model. The discretized FE model yields a system of n equations describing the dynamic behavior of the structure. These equations can be written in the form

$$M\ddot{x}(t) + C\dot{x}(t) + Kx(t) = f(t) \tag{1}$$

where **M**, **C**, and **K** are the mass, damping and stiffness matrices, **f**(t) is a defined forcing function, and **x**(t) is the response. For linear structural analysis **M**, **C**, and **K** are symmetric and time invariant. Equation 1 can be rewritten in the Laplace domain as

$$s^2 M X(s) + s C X(s) + K X(s) = F(s) \tag{2}$$

This equation represents an eigenvalue problem. For lightly damped structures, it is not unusual to neglect the damping and instead consider undamped free vibration response. The non-trivial solution of this problem is given by

$$|s^2 M + K| = 0 \tag{3}$$

Solution of equation 3 yields n natural frequencies, $s_n=j\omega_n$, and n modal vectors $\Psi_n$. These can be used in a normal mode analysis to solve the forced vibration problem given by equation 1. Also, the predicted natural frequencies and mode shapes can be compared with the corresponding experimentally determined quantities to determine the appropriateness of the FE model.

The experimental determination of the natural frequencies and modal vectors constitute EMA [6]. As with FE analysis (FEA), EMA starts with a system of equations written as in equation 2. However, **M**, **C**, and **K** are now unknown. Instead, the response, **x**(t), and the applied load, **f**(t), vectors are the known quantities. Accordingly, equation 2 is rewritten as

$$B(s)\ X(s) = F(s) \tag{4}$$

where $\mathbf{B}(s)=\mathbf{M}s^2+\mathbf{K}$.
The transfer function **H**(s) is then defined as

$$H(s)=[B(s)]^{-1} \tag{5}$$

Therefore, equation 4 can be expressed as

$$H(s)\ F(s) = X(s) \tag{6}$$

The transfer function **H**(s) relates the input to the system, **F**(s), to the output, **X**(s). In component form, equation 6 relates the input at some point q to the output at a point p by the relation

$$H_{pq}(s) = \frac{X_p}{F_q} \tag{7}$$

These elements of **H**(s), $H_{pq}$, are assumed to have the form

$$H_{pq} = \sum_{r=1}^{n} \left( \frac{Q_r\ \Psi_r\ \Psi_r^T}{s-s_n} + \frac{Q_r^*\ \Psi_r^*\ \Psi_r^{*T}}{s-s_n^*} \right) \tag{8}$$

where $Q_r$ is a scaling factor, $\Psi_r$ is the rth modal vector, and $s_r=j\omega_r$ is the $r^{th}$ pole. This representation is based upon a simple one degree-of-freedom oscillator [7].

Assumptions in the derivation of equation 1, and consequently equation 6 imply that the entire transfer function matrix **H**(s) can be reconstructed by measuring the transfer functions, equation 7, of a single row or column of **H**(s). To increase accuracy though it is

common practice to measure several rows or columns. These data are then used to determine the natural frequencies and modal vectors by curve fitting the data. Also, if multiple modes at a single frequency are to be resolved, then multiple rows or columns must measured. Agreement between the predicted and measured natural frequencies, $\omega_r$, and the corresponding mode shapes $\Psi_r$ is an indication of the accuracy of the FE model.

## ANALYSIS

The PXR6353 projectile is a very complex structure. In order to provide an accurate baseline for the validation of the FE model, simpler sub-structures were also analyzed. As a result, five configurations of the PXR6353 projectile were analyzed using EMA.

The first configuration consisted of the complete projectile with all internal components. The internal components were then removed and the projectile was re-analyzed. The remaining three configurations consisted of sub-components of the projectile (Fig. 2). Table 1 summarizes the tested configurations.

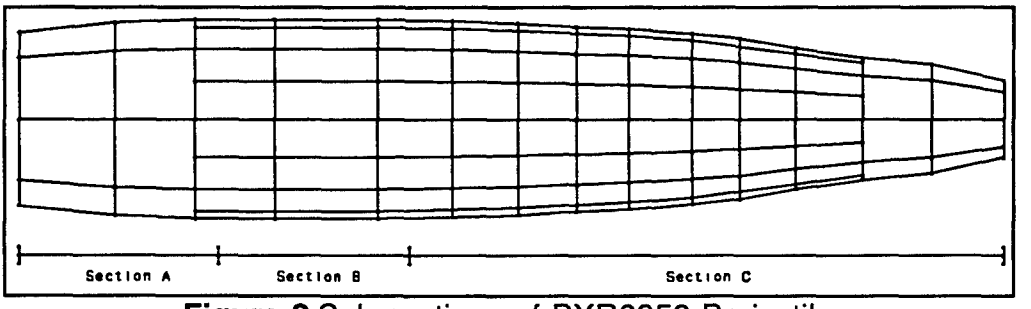



**Figure 2.**Sub-sections of PXR6353 Projectile

**Table I.** PXR6353 Configurations

| Configuration | Description | Excitation |
|---|---|---|
| 1 | Whole, with Internal Components | Shaker |
| 2 | Whole, without Internal Components | Hammer |
| 3 | Section A | Hammer |
| 4 | Section B | Hammer |
| 5 | Section C | Hammer |

Both shaker and hammer excitation methods were utilized. The shaker method of excitation provided a flat energy distribution from 1

to 10 kilohertz. However, the hammer excitation technique proved unable to excite natural frequencies above 8,000 Hz. This frequency limitation is evident in Figure 3 which shows the frequency content of a typical hammer impact used in this analysis. Response sensors were placed to measure the response in 2 degrees of freedom (DOF) at each measurement point. When using the hammer technique, the only response DOF obtainable was collinear with the direction of impact. As a result, only the radial DOF was measured in the analyses utilizing the hammer technique.

Assuming a linear structure, reciprocity indicates that the frequency response functions (FRF) generated by the hammer technique are the same as the FRF generated using the shaker method for a given configuration.

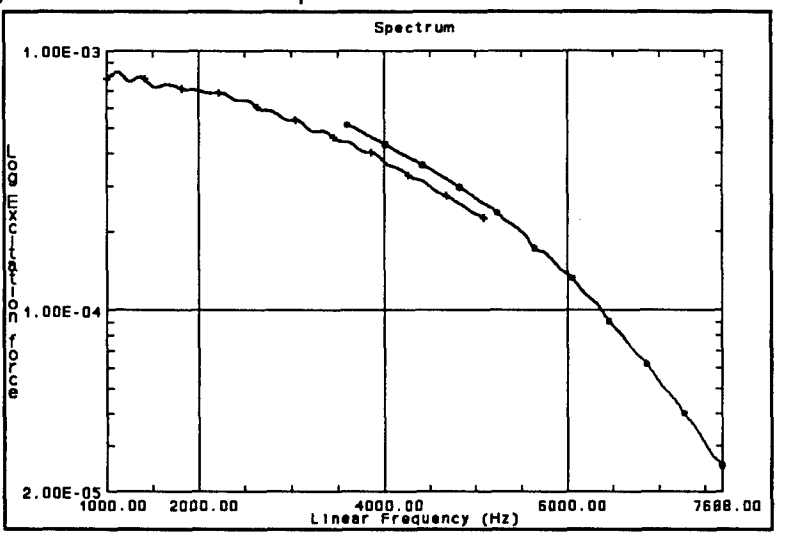



**Figure 3.** Hammer Impact Frequency Content

## RESULTS

The first configuration consisted of the entire projectile, complete with all internal components. Based on the expected frequency content from the preliminary FE analysis results, the shaker method of excitation was chosen. Because of a loose connection between sections B and C, and the presence of potting wax, the data from this test was very inconsistent and difficult to analyze.

Three modes, though, were extracted from the data. Modes 1 and 2 formed a double bending mode. Both modes flex in the same direction in the Z-X plane (Fig. 4). The undeformed geometry is indicated by the dashed line in these figures. However, in the Z-Y plane, they deflect in opposite directions. Mode 3 was an ellipsoidal radial mode (Fig. 5).

The projectile was then disassembled. The ballast, accelerometer

mounting units, potting wax and telemetry housing were removed from sections A and B. Disassembly of Section C was impossible without damaging the projectile. After reassembly, all fasteners were tightened to the torques specified by the engineering drawings.

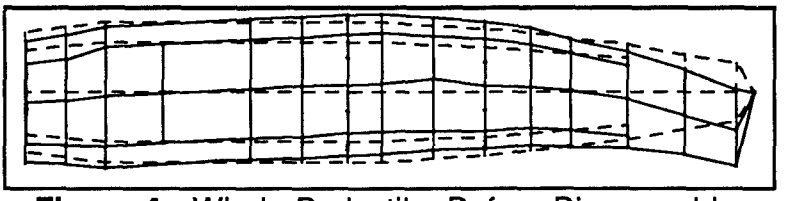


**Figure 4.** Whole Projectile, Before Disassembly, Representative Shape for Modes 1 and 2, Z-X Plane

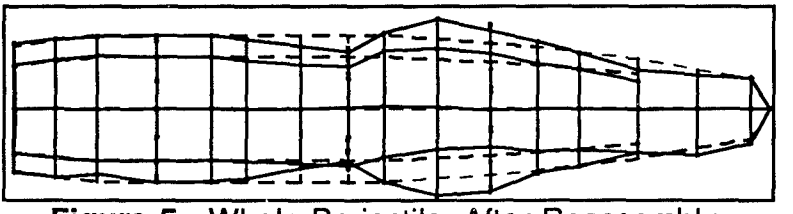


**Figure 5.** Whole Projectile, After Reassembly, Mode 2

**Table II.** Whole Projectile Modal Parameters

| | Mode Number | Frequency (hertz) | Damping (% critical) | Description |
|---|---|---|---|---|
| Before Disas-sembly | 1 | 568 | 9.05 | Bending |
| | 2 | 656 | 7.81 | Bending |
| | 3 | 3369 | 2.34 | Breathing |
| After Reas-sembly | 1 | 842 | | 1st Bending |
| | 2 | 866 | | 1st Bending |
| | 3 | 1759 | 1.567 | 2nd Bending |
| | 4 | 1786 | 1.035 | 2nd Bending |
| | 5 | 2109 | 0.478 | Elliptical, 1 Wave |
| | 6 | 2117 | 0.344 | Elliptical, 2 Waves |
| | 7 | 2122 | 0.333 | Elliptical, 2 Waves |
| | 8 | 3657 | 0.569 | Elliptical, 2 Waves |
| | 9 | 3659 | 0.493 | Elliptical, 2 Wave |

The first two modes extracted for the reassembled projectile were very similar to mode 1 of configuration 1. These modes were very highly damped and noisy. These two conditions resulted in a very inaccurate estimate of modal damping. Therefore, no damping values are given for these two modes.

The next two modes were very similar to a free-free beam's 2nd bending mode (Fig. 6). However, the primary plane of deflection is different for the two modes.

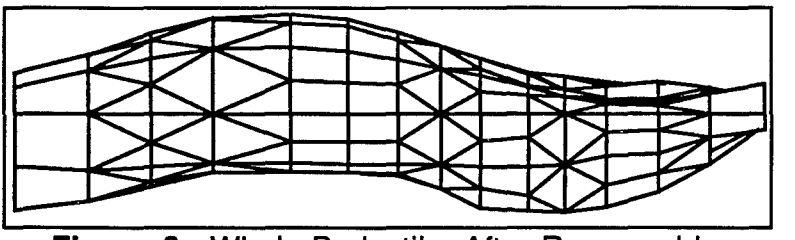


**Figure 6.** Whole Projectile, After Reassembly, Modes 3 and 4

The remaining 5 mode shapes which were extracted were elliptical breathing modes. Three representative shapes of these modes are shown in Figure 7. Mode 5 has a single axial wave and is a single root. Modes 6 and 7 and modes 8 and 9 are double roots and have two axial waves. A modal analysis of the FE model was not performed on either of the complete projectile configurations. A summary of modal parameters extracted for both configurations appears in Table II.

The projectile was then disassembled into the three sections mentioned. Section A consisted of the boat-tail and forward motor body of the projectile. The hammer excitation technique was utilized to analyze this section.

Three modes were extracted for this section of the projectile. The cross-section of modes 1 and 3 is elliptical and the cross-section of mode 2 is triangular (Fig. 8). Although both modes 1 and 3 have similar cross-sections, mode 1 has a single axial wave and mode 3 has two axial waves (Fig. 9).

These results of the EMA were then used to validate the FEA model created from the engineering drawings of this projectile.

The mass of the FE model of section A is 7,424.1 g while the actual mass is 8,065. This mass difference is primarily due to the absence of the rotating band in the FE model. If this band is included, the FE model's mass increases to 7,935. This 1.6% error was judged to be an acceptable error. Table III summarizes the FE and EMA modal parameters. The FEA predicted frequencies are in good agreement with the experimentally determined frequencies.

Section B consisted only of the body section. The hammer method was chosen for this section. Mode shapes 1 and 2 were extremely similar to mode shapes 1 and 2 of section A.

Modes 3 and 4 form a double mode with a shape very similar to section A's mode 3 (Figure 8). The ellipse of mode 3 is rotated 46

degrees from the ellipse of mode 4.

The FE model's mass for this section is 11,024.2 g, while the actual mass is 10,735 g. Transverse through-holes in the base of section B which were not included in the FE model account for the 2.7% mass difference. These holes occur in a very rigid section of the structure, so their exclusion has minimal effect on the predicted natural frequencies. Table III shows the predicted frequencies in good agreement with the measured frequencies.

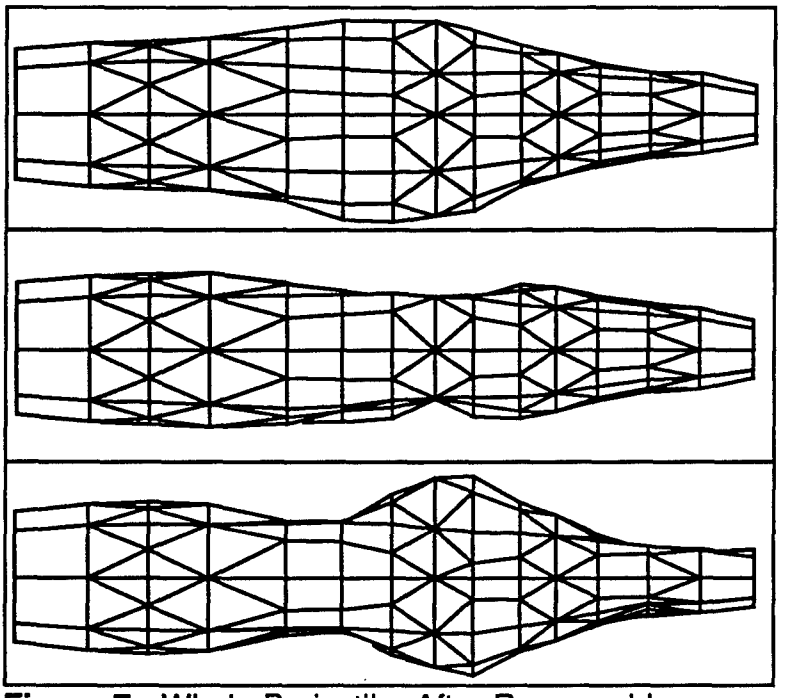


**Figure 7.** Whole Projectile, After Reassembly, Modes 5 (top), 6 (middle) and 8 (bottom)

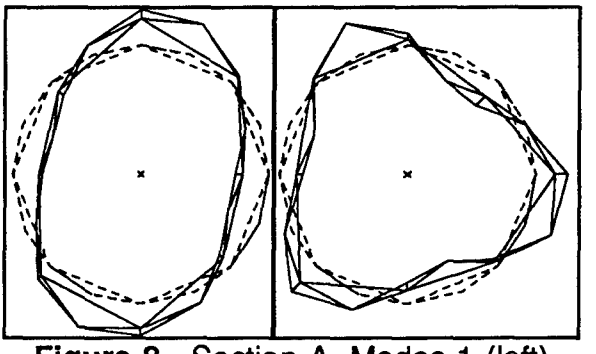


**Figure 8.** Section A, Modes 1 (left) and 2 (right)

Section C, the most complex section, consisted of the antenna section and all parts between the antenna section and the nose. The mode shapes of section C exhibited the same general displacement motion as sections A and B. However, since section C has a major internal division at the fifth axial station, the mode shapes exhibited a localization. Mode 1 shows motion only in the antenna section and mode 2 shows motion only in the windshield section. Only mode 3 exhibits simultaneous motion in both the antenna and windshield sections (Fig. 10). The cross-section of all three modes was elliptical.

The mass estimate for the FE model of this section (10,033 g) is within 2.6% of the measured mass (10,007 g). This agreement is fortuitous since disassembly of section C to determine exactly

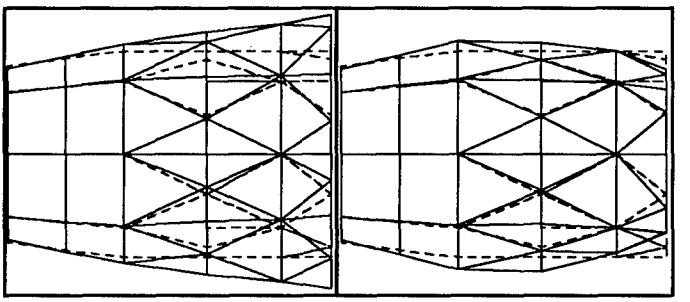


**Figure 9.** Section A, Modes 1 (left) and 3 (right)

**Table III.** EMA and FEA Modal Results

| | Mode | Frequency (Hz) | | | % Error | | Damping (%) |
|---|---|---|---|---|---|---|---|
| | | EMA | FEA | | | | |
| | | | 2D | 3D | 2D | 3D | |
| Section A | 1 | 1823 | 1941 | 1966 | 6.5 | 7.8 | 0.145 |
| | 2 | 4265 | 4748 | 4900 | 11.3 | 14.9 | 0.087 |
| | 3 | 5489 | 5717 | 5820 | 4.2 | 6.0 | 0.232 |
| Section B | 1 | 1897 | 1957 | 1984 | 3.2 | 4.6 | 0.207 |
| | 2 | 4679 | 4902 | 5075 | 4.8 | 8.5 | 0.142 |
| | 3 | 6111 | 6199 | 6332 | 1.4 | 3.6 | 0.122 |
| Section C | 1 | 1613 | 1696 | 1731 | 5.1 | 7.3 | 0.246 |
| | 2 | 3448 | - | 2508 | - | -27.0 | 4.00 |
| | 3 | 4034 | 4225 | 4345 | 4.73 | 7.7 | 0.583 |

which internal components were present was impossible. Despite the excellent mass estimate, the frequency estimates were not as accurate. In particular, the second frequency is in error by -27.3%. It has been determined that section C had been previously fired and sustained some internal damage. Therefore, it is highly unlikely that the FE model represents the actual internal boundary conditions. A summary of these results is also given in Table III.

Finally, a non-linearity survey was performed on section B. A shaker outputting a broad band random signal from 1,000 to 10,000 hertz was used to excite the structure. Six levels of excitation were

used. The shaker was placed at one end of section B in the radial direction.

Most modes were linear and similar to the first peak in Figure 11 with minimal dispersion. A few modes, such as those represented by the second peak in Figure 11, show the presence of non-linearity. Section B is a very simple, single piece structure and was expected to be very linear.

Based on the acceptance of the individual sections as valid models, a complete FE model of the PXR6353 round was generated by reassembling these validated models of sections A, B and C and adding the parts which were excluded for the EMA. A transient analysis was then performed using the Dyna3D FEA software [8] on a Cray X-MP.

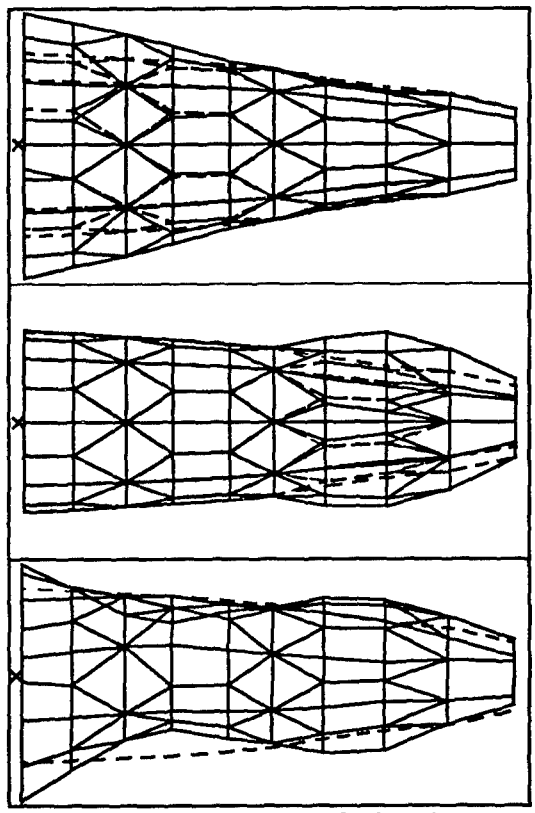


**Figure 10.** Section C, Modes 1 (top), 2 (middle) and 3 (bottom)

The pressure-time history shown in Figure 1 was used as the force input for a 20 Khz bandwidth simulation. Figures 12 to 14 show the vibrational response of the projectile from this simulation for three

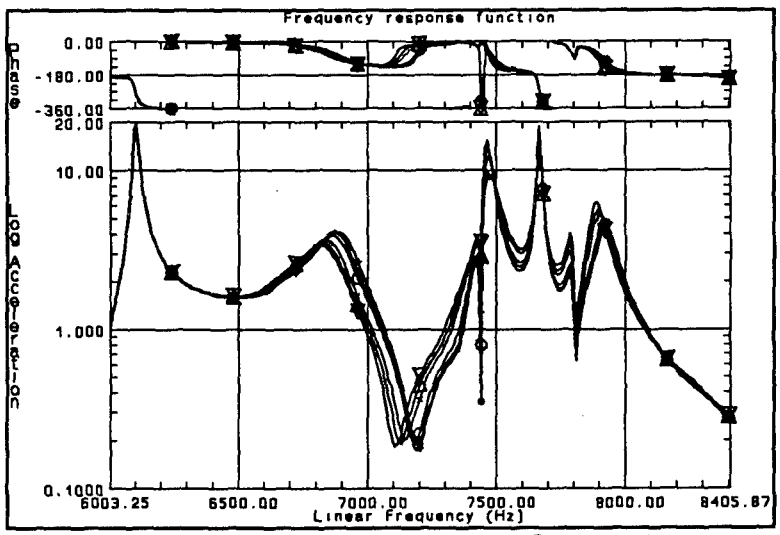



**Figure 11.** Non-Linearity of Section B

different locations within the structure. The overall acceleration amplitudes agree well with the experimentally measured results.

## SUMMARY and CONCLUSION

An FE model was generated for the PXR6353 instrumented artillery projectile. The predicted modal frequencies and mode shapes were in good agreement with the experimentally obtained frequencies. Linearity of the structure was established through a linearity study of one configuration. A transient analysis was then performed on the FE model utilizing a typical pressure-time curve as the force input. The analysis showed good agreement with experimentally obtained data.

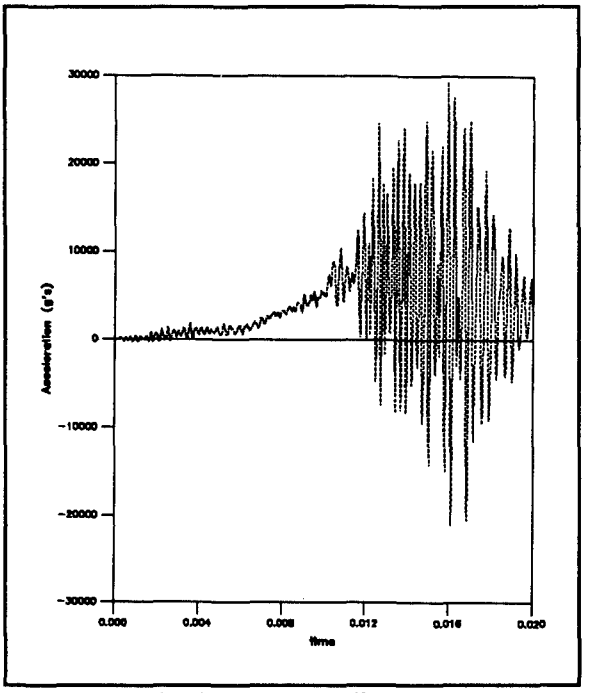



**Figure 12.** Vibration History at Nose

## REFERENCES


1) Bender, James M. and Burns, Bruce P., Dome Bases for Expellable-Munitioned and Saboted Projectiles, U.S. Army BRL-MR-3391, Aberdeen Proving Ground, MD, October, 1984.
2) Kaste, R.P. and Wilkerson, S.A., An Improved Sabot Design and DYNA3D Analysis for the XM900E1 Kinetic Energy Projectile, U.S. Army BRL-TR-3359, Aberdeen Proving Ground, MD, June 1992.
3) Rabern, D.A. and Bannister, K.A., Finite Element Models to Predict the Structural Response of 120-mm Sabot/Rods During Launch, Proceedings of the 6th U.S. Army Symposium on Gun Dynamics, Tamiment, PA, May 1990.
4) Rabern, D.A., Numerical Simulation of Gun-Launched Kinetic Energy Projectiles Subjected to Asymmetric Projectile Base Pressure, 13th International Symposium on Ballistics, Stockholm,

Sweden, June 1992.
5) Sorensen, Brett R., Finite Element Optimization of a Sabot for Use with Tungsten or Uranium Penetrators, 13th International Symposium on Ballistics, Stockholm, Sweden, June 1992.
6) Ewing, D.J., Modal Testing: Theory and Practice, John Wiley and Sons, Inc., New York, 1984.
7) Allemang, Randall J., Vibrations: Analytical and Experimental modal Analysis, Structural Dynamics Research Laboratory Report, UC-SDRL-SN-20-263-662, University of Cincinnati, Cincinnati, OH, 1992.
8) Hallquist, J.O. and Benson, D.J., DYNA3D User's Manual, Lawrence Livermore National Laboratory Report, UCID-19592, Rev.2, 1986.

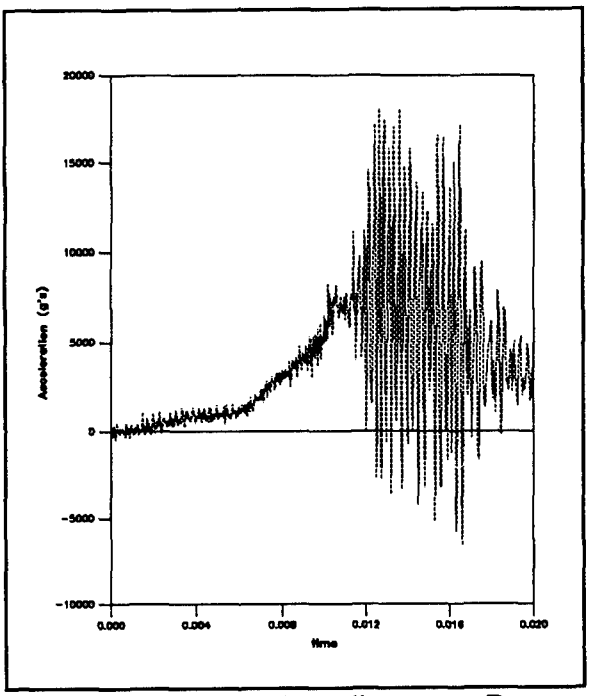



**Figure 13.** Vibration History at Base

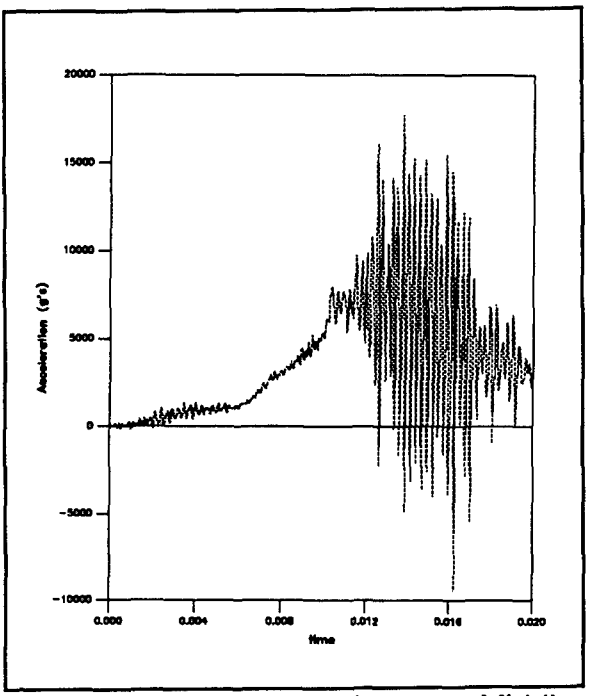



**Figure 14.** Vibration History at Middle

**Rebending, in Thick-Walled Tubing,**
**due to a Radial Temperature Gradient**

by
Boaz Avitzur

**Abstract:**

Thick-walled tubes often bend if and when they undergo heat-treatment. When precision is important and machining follows the heat-treatment, a *straightening* step precedes the machining process, to secure the alignment of the tube on the lathe. This *straightening* operation leaves the tube with a residual stress pattern, which is not axisymmetric. Therefore, each machining step causes a *re-bending*, resulting from the removal of stressed material, and it changes the overall residual stress distribution pattern. Thus, each machining step is being followed by a re-*straightening* step.

Similarly, subjecting a previously *straightened* thick-walled tube to an in-service through-wall temperature gradient, relaxes the residual stresses (left by the *straightening* process) in a non-axisymmetric fashion and thus leads to *re-bending* (even though the thermal gradient is axisymmetric). Such in-service temperature gradients are experienced by tubes in heat-exchangers, in chemical reactors as well as in rapid-firing gun tubes.

This work focuses on the calculation of *re-bending* due to an axisymmetric through-wall temperature gradient, in previously *straightened* thick-walled tubes. Other mechanisms of bending and/or *re-bending* under through-wall temperature gradient notwithstanding, this work accounts for *re-bending* due to relaxation of residual stresses associated with thermal variations in the material's Modulus of Elasticity. The temperature gradient and the material's Modulus of Elasticity dependency on temperature are to be provided by the user.

The post-*straightening* residual stress distribution pattern is being calculated by a previously developed computer program which guides the numerically controlled *straightening* process

**Introduction:**

Shafts and beams (or beam-like products) often call for tight tolerances in their alignment. Misalignment might occur during rolling and/or forging or extrusion operations. Furthermore, if and when the manufacturing processes, of a beam-like product, include Heat-Treatment and/or welding then a further misalignment occurs. When the resulting misalignment exceeds the allowable level (of misalignment) then a *'straightening'* operation follows. The allowable tolerances in the product's misalignment is being dictated by the functions of the product (as in the case of a rotating shaft or the side members of a rail-road car) and/or by the process that follows (such as turning on a lathe).

Very often, the *'straightening'* operation entails bringing certain points, along the beam's axis, into alignment with the product's *end-points*. This is being done by bending the beam, beyond its *elastic limit*, with the point to be *'corrected'* deviating from the beam's alignment in the opposite direction. When processed properly, the elastic *recovery*, after

removing the bending load, will bring the point of interest within the desired alignment, with the two *end-points*. Associated with the recovery, from bending into the *elastic-plastic* region, there is a residual stress distribution pattern, retained in the effected region of the beam.

That, indeed, the *post-bending* beam contains a non-symmetric pattern of residual stresses can be manifested by cutting the beam along its neutral axis. The two halves of the beam will then bend (curve). The distribution of such retained stresses can be computed by gradually removing thin layers of the (stressed) beam's outer layers and then calculating the (pre-machining) stresses, in that layer, from the curvature of bending of the remaining beam [1]. Such a ***re-bending*** also occurs when the ***'straightening'*** operation is being followed by machining. If that ***re-bending*** exceeds the tolerances allowed for the next operation and/or in the final product, another ***'straightening'*** operation will follow.

*Re-bending*, of a previously straightened beam, will also occur when the beam is being subjected to a non-uniform temperature distribution, through the effected regions. (The *elasto-plastically* deformed cross-sections, of the beam [2]). In this case, the ***re-bending*** is being attributed to the relaxation of the ***residual stress pattern***, due to the temperature dependency of the material's Modulus of Elasticity. According to Underwood and O'Hara, this can effect the accuracy of gun tubes. In such cases, the anticipated through-the-wall temperature gradient is basically axisymmetrical. Therefore, bending due to variations in thermal expansion (per se) should be ruled-out.

**Analysis:**

***Re-bending moment:***

For the sake of the calculations, involved in this work, the stress-strain relation of the beam's material, is assumed to be symmetrical (in tension and in compression) with a linear rate of strain-hardening. At any cross-section, subjected to a bending moment, M, greater than its elastic limit ,$M_e$ there will be an *elastic-plastic* interface at a distance $\eta = H - h$ from the beam's neutral axis. $\eta$ decreases as M increases. In a beam, whose cross section is symmetrical with respect to its neutral axis, two such stress distributions are being represented, schematically, by solid lines in figure#1. The corresponding moment being;

$$M = 2\int_{o}^{H} b\,\sigma_{xx}\,dy = 2\int_{o}^{\eta} b\,\sigma_{xx}\,dy + 2\int_{\eta}^{H} b\,\sigma_{xx}\,dy \qquad (1)$$

where $\sigma_{xx}(y)$ follows the solid line in figure #1. Upon a removal of the load, the stress will recover, elasticity, with $\sigma_{xx}(y)$ following the dashed line, – – – – – –, in figure #1, for a recovery moment, $M_r$, that equals the original moment (eqn. #1). The retained stress distribution, described by the dash-dot lines, – · – · – · –, (in figure #1) yields a net of zero moment. Associated with the non-zero retained stress distribution there is a strain $\varepsilon_{xx} = \sigma(y)/E$, in the range $-\eta \le y \le \eta$. $\varepsilon_{xx}(y)$ represents the retained strain. However, this is not the case in the ranges $y < -\eta$ and $y > \eta$. If, however, the ***modulus-of-elasticity*** is temperature dependent and the beam is being subjected to a temperature gradient

(symmetrical with respect to the beam's neutral axis) between it's neutral axis and its outer most fibers, then

$$\int bE(y)\varepsilon_{xx}(y)dy \neq 0 \qquad (2)$$

(not equals zero) any more. Yet, in the absence of external forces

$$\int b\sigma_{xx}(y)dy = 0 \qquad (3)$$

where $\varepsilon_{xx}(y)$ represents the *pre-heating strain*, while $\sigma_{xx}(y)$ reflects the retained stress distribution. The difference between the integrals in eqn. (2) and in eqn. (3);

$$\Delta M = 2\int bE_T(y)\varepsilon_{xx}(y)dy - 2\int b\sigma_{xx}(y)dy = 2\int b[E_T(y)/E - 1]\sigma_{xx}(y)dy \qquad (4)$$

is the moment being released by the thermal gradient. This moment results in the *re-bending* of the beam. Upon equalization of the temperature (distribution) such as upon cooling of the rapid-firing gun tube, the beam will return to the shape that it had prior to the establishment of the subject *temperature gradient*. Namely, it will *re-straighten* itself.

***Background:***

The *straightening* operation is usually done by a vertical press while the beam is resting (horizontally and freely) on two vertical supports. Thus, the cross-sections over the resting points are subjected to a zero moment. This moment increases, gradually, towards the pressing point (or points) exceeding the cross-sectional *elastic limit* only on a limited range, of the beam's total length. Within this *elastic-plastic region*, the plastically deformed depth of penetration varies continuously. Thus, the pattern and magnitude of the *residual stress* distribution varies continuously, from point to point, along the effected range of the beam's length.

Experience shows that no two beams have the same *misalignment*. Furthermore, historically, the *straightening* operation was done by *trial and error*. In such cases, regardless of whether the trial and error is a manual process or if it is being done electronically, it does not provide the operator with the stress distribution, required for the calculation of the residual stress distribution that prevails after the removal of the *straightening* load and which is the basis for the calculation of *the thermally induced re-bending*, discussed here.

At least since the late 1950's, efforts are being made to replace the *trial and error* approach (to beam *straightening*) by a numerically controlled operation [3]. Tadjbakhsh's work was followed by that of L. R-L. Wang [4], which developed a computer program designed to predict the load and the total deflection under such a load, required in order to remove a specific *misalignment* in a (circular and concentrically hollowed) beam. Prof. Wang, in his derivation of the core equations used in the subject computer program, followed the classical work by Seely and Smith [5] Unfortunately, Seely and Smith approach, to *elastic-plastic* problems, was developed for *elastic-perfectly plastic* materials only. Indeed, upon testing Wang's [4] computer program, Wang and Goodheim [6] concluded that the *straightening*

operations, which were guided by Wang's computer program, failed short of the desired tolerances. They suggested 6 different factors, which were not included in the derivations of the equations used in the pertinent computer program, as possible causes for the computer program's failure to attain a more reliable recommendations. The material's rate of strain-hardening being one of these six missing factors.

Shortly there-after, Avitzur [7] derived equations that account for a linear material's strain-hardening. Many years later, Avitzur's computer program (which is based on these equations) was tested [8] and was found to be successful. The subject computer program was designed to calculate the stress distribution that prevails, in the beam, while under the *straightening* load, as well as the residual stresses (that prevail) after the removal of the load. It is this residual stress distribution which is being used as a basis for the calculations of *re-bending*, under a through-wall temperature gradient.

**Calculations:**

Conventionally, the misalignment is being measured as the deviation, $\delta$ , of a point (at a distance $L_c$ from one end of the beam) from the straight line connecting the two ends of the beam. Associated with such a deviation, one may compute the angle $\theta_0$, between (see fig# 3) two tangents to the 'corrected' bend. The angle $\theta_0$ can be approximated as;

$$\theta_0 = \tan^{-1}(\delta / L_c) + \tan^{-1}(\delta / (L - L_c)) \qquad (5)$$

Avitzur's [8,9,10] computer program computes the exact angle $\theta_0$ for any set of straightening variables.

Avitzur [9,10] applied his computer program to an hypothetical circular beam (shown in figure #2) and made of an hypothetical material (having a Yield Strength of $\sigma_0$ = 95,000 psi and a Modulus of Elasticity of E = 11,000,000 psi) to correct a deviation of $\delta$ = 0.500 inch at a distance of $L_c$ = 102.0 inches from the beam's left end. The subject beam, though hypothetical, contains features such as cylindrical and tapered segments and an abrupt change in the beam's outer diameter. Features which are characteristic to gun-tubes. To test the capabilities of the subject computer program, the two supports were assumed to be at different distances from the beam's wider end. i.e. $L_l$ = 24.0 inches or $L_l$ = 36.0 in. and $L_r$ = 188.0 in. or $L_r$ = 168.0 in., with the load being applied at $L_p$ = 98.0 inches from the wider end of the beam and near an abrupt change in the beam's cross-section. The recommended load and the corresponding deflection-under-load (to attain the same correction of $\delta$ = 0.500 inch at a distance of $L_c$ = 102.0 inches) were calculated accordingly. Figure #4 displays the shape of the correction in the beam's alignment (with a biased scale, for the depth of bending, as compared to the scale of its axial length) relative to its end points, and the depth of penetration of the *elastic-plastic* interface (while under load). Notice the skewed shape of the *elastic-plastic* interface, due to the abrupt change in the beam's cross-section in the vicinity of the maximum moment. The *normalized* "Retained Deflection" vs. Beam's Length, as measured between the supports, is shown in fig. #5, for comparison with the same "Retained Deflection" vs.Beam's Length, as measured between the beam's ends, fig. #4.

**Results:**

For the purpose of this work, an equilibrium temperature gradient (given by equation (6));

$$T_{(r)}=T_{(b)}+(T_{(a)}-T_{(b)}) \cdot (\log(r/b) / \log(a/b)) \qquad (6)$$

is being assumed. A simple minded dependency of the Modulus of Elasticity on temperature, led to a radial distribution of the Modulus of Elasticity given by equation (7);

$$E_{Tr} = E_{Tb} + (E_{Ta} - E_{Tb}) \cdot (\log(r/b) / \log(a/b)) \qquad (7)$$

The Modulus of Elasticity, at the bore was assumed to be $E_{Ta}$ = 9,000,000 psi with $E_{Tb}$ = 11,000,000 psi at the tube's O.D.. The variations in the required load and in the shape of the *elastic-plastic* interface, due to different locations of the two supports (for the *straightening* operation) manifest themselves in variations in the amount of *re-bending* (due to a through-wall temperature gradient). However, for the three sets of supports that were studied by Avitzur [10], the angle $\Theta$ of *re-bending*, is about 3% of the corrected (*straightened*) angle $\Theta_0$ This seems to be a very small portion of the original bend. However, when a high precision at a long distance from the gun's muzzle is required, this might be a significant bend[2].

The above values, for *re-bending*, were obtained for a temperature gradient at equilibrium.This is never the case with a rapid firing gun-tube. However, equation (6), of this study, can be replaced by any pertinent temperature gradient or even by a time-dependent temperature gradient. The same holds true for equation (7), correlating the Modulus of Elasticity with temperature [2,11]

**Conclusions:**

Thick-walled tubes, that were previously *straightened*, do *re-bend* when subjected to an axisymmetrical, through-wall, temperature gradient. Such a *re-bending* constitutes a very small fraction of the amount of straightening that causes it and it prevails only while the tube is subjected to a given temperature gradient. The *re-bending* reverts itself with the elimination of the temperature gradient. The amount of *re-bending* (due to a temperature gradient) can be calculated, provided the (prior) *straightening* operation was numerically controlled and the residual stress distribution (left after *straightening*) has been calculated and recorded .

**References:**


1. S. Timoshenko, "Strength of Materials" part II, Third Edition Krieger Publishing Co., Huntington, NY., 1976, pp. 377-381.

2. John H. Underwood and G. Peter O'Hara, Thermal Gradient-Induced Deflection of a Thick-Walled Cylinder with Bending Residual Stresses.
Technical Report ARCCB-TR-93017, Benet Laboratories, Watervliet NY., April 1993.

3. I.G. Tadjbakhsh, Plastic Deformation and Residual Stress in Long Beams with Application to Gun Tube Straightening Process.
Technical Report-WVT-RR-5901, Watervliet Arsenal, Watervliet, NY., August 1959.

4. Leon Ru-Liang Wang, General Elastic-Plastic Analysis of Beams with Application to Straightening of Gun-Tubes.
Technical Report WVT-6811, Watervliet Arsenal, Watervliet, NY., Feb. 1968.

5. Seely and Smith, "Advance Mechanics of Materials", John Wiley and sons, New-York,1957, page 544.

6. Leon Ru-Liang Wang and Harold Goodheim, Feasibility Study of a Computer Aided Program to Guide the Straightening Process of Gun Tubes.
Technical Report WVT-7146, Watervliet Arsenal, Watervliet, NY., August 1971.

7. Boaz Avitzur, Unpublished.

8. Richard Farrara, An internal memorandum, Benet Laboratories, Watervliet NY.. 4 January 1985.

9. Boaz Avitzur, Retained Deflection in Circular and Concentrically Hollowed Beams, After Load Removal,
Proceedings of the "Third International Conference on Computer-Aided Production Engineering" June 1-3 1988. Society of Manufacturing Engineers Dearborn MI.

10. Boaz Avitzur, Retained Deflection in Circular and Concentrically Hollowed Beams after Load Removal, Not yet published.

11. Boaz Avitzur, Calculations of Bore Dilation due to Radial Temperature Gradient. Presented at the 28th Annual 'Gun and Ammunition Technical Meeting' (Sponsored by the 'American Defense Preparedness Association') Monterey, Cal. April 21-23 1993.

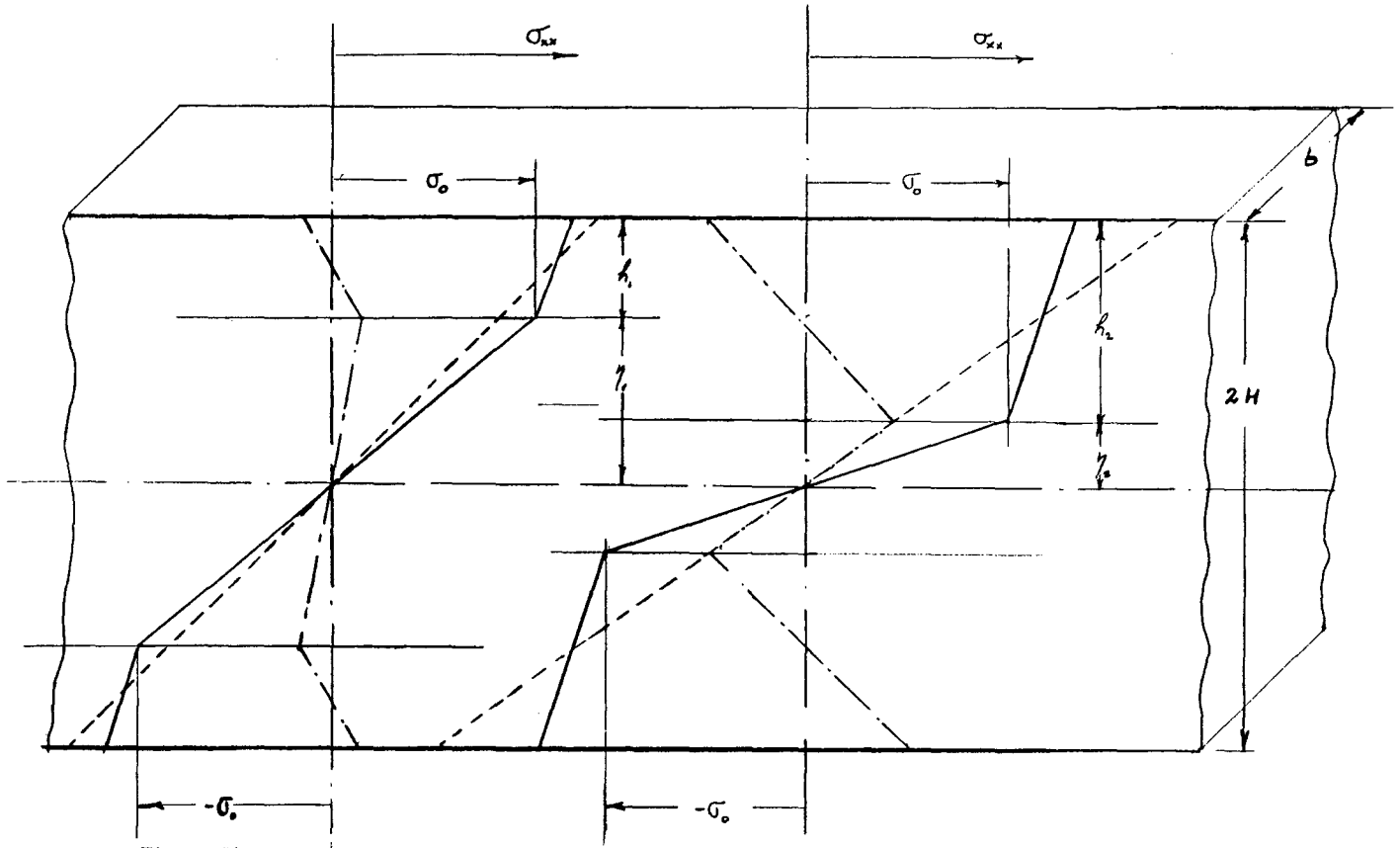



Figure #1 : Stress Distribution in an Elasto-Plastically Deformed Beam.

Stress Distribution Under Load ————————
Elastic Recovery - - - - - - -
Residual Stress Distribution —·—·—·—

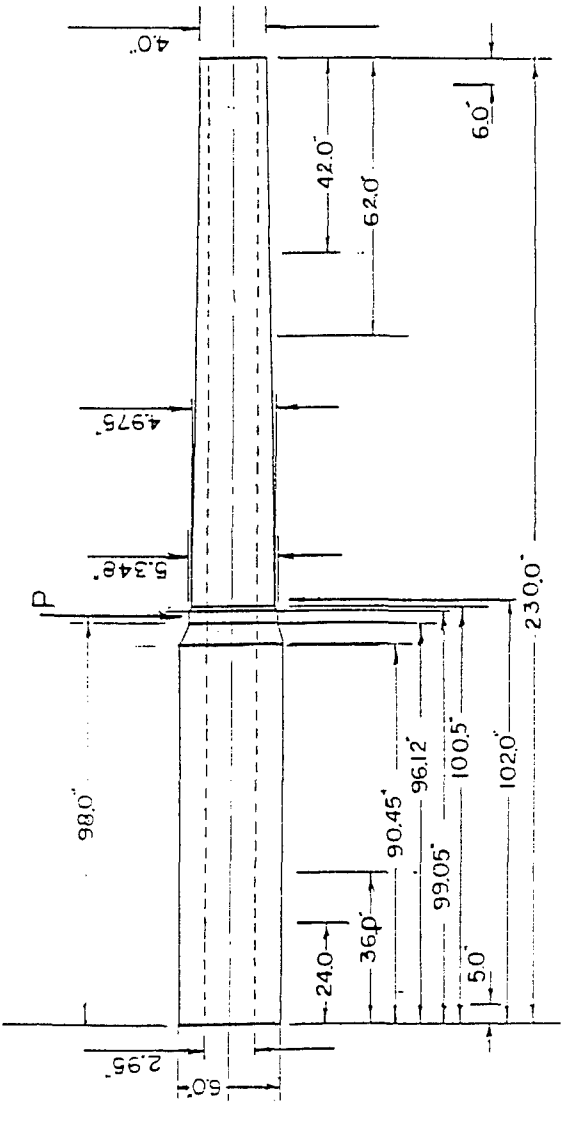



Figure #2 : Longitudinal view of Beam (with a circular cross-section)

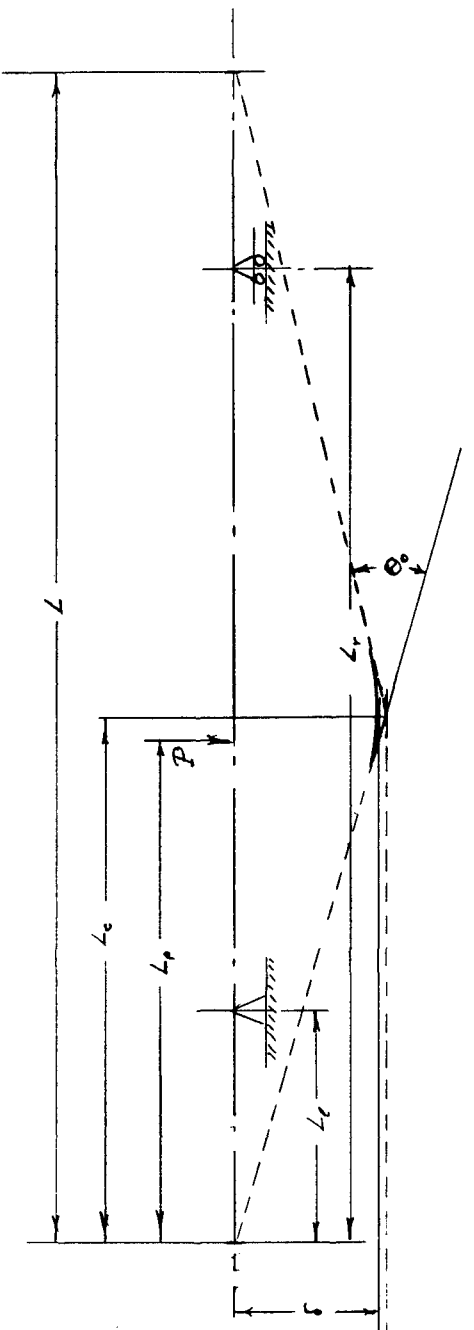



Figure #3 : Geometry of Misalignment.

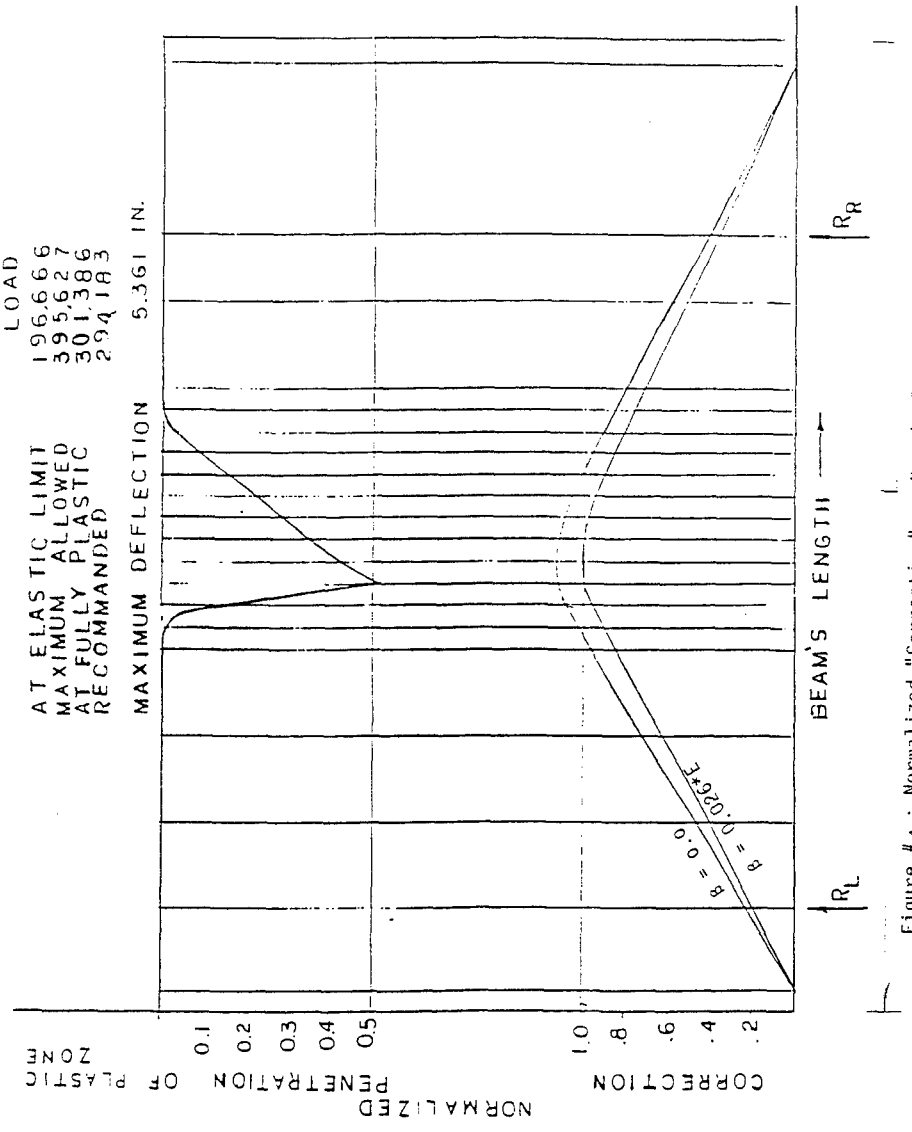



Figure #4 : Normalized "Correction" vs Beam's length, and
Normalized pentration of Plastic- Zone, vs. Beam's Length.

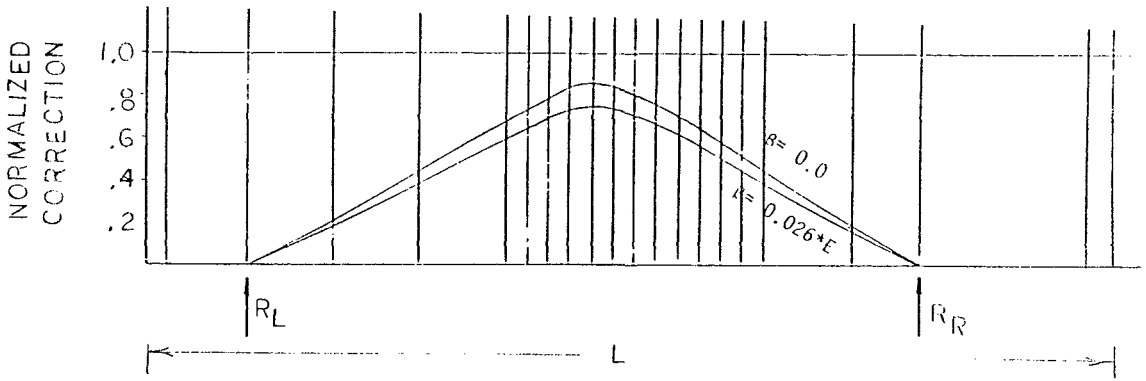



Figure #5 : Normalized "Retained Deflection", vs Beam's Length as measured between Supports.

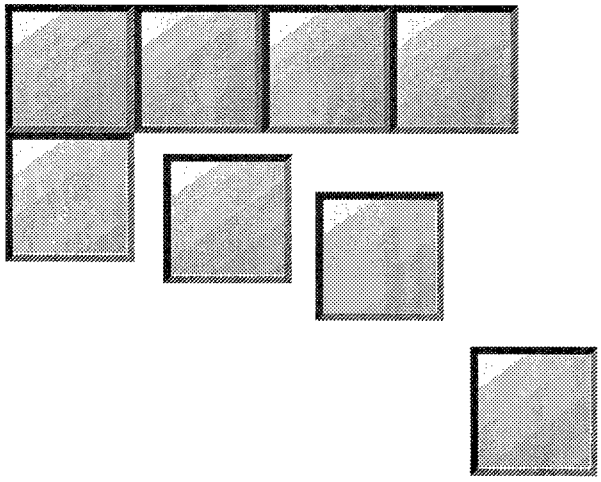
# Stress Reversal in Steel Wheels Subjected to High Performance Braking

*O. Orringer*
Volpe National Transportation System Center

"PAPER NOT AVAILABLE"

# SESSION IVB: NUMERICAL ANALYSIS

**Chairman:** *Dr. J. Wu*
**U.S. Army Research Office**



# The Micromechanical Simulation of Ductile Failure with an Eulerian Finite Element Code

Dr. David J. Benson
Dept. of AMES 0411
University of California,
San Diego
La Jolla, CA 92093-0411

## Abstract

The effects of the distribution of voids and void clustering on ductile fracture at high strain rates is studied by analyzing the response of discrete arrays of voids. The solutions of the model boundary value problems are obtained numerically with an Eulerian finite element program, which allows the generation of new free surfaces during coalescence. In contrast to previous work, the calculations are carried out until the material has fractured completely. For the small number of voids considered, the effects of the void distribution on the failure stress were equivalent to the effects of doubling the initial void fraction. Based on the preliminary calculations on the effects of clusters, it appears that the ultimate stress is largely independent of the diameter of the clusters, while the degree of material softening increases with the cluster diameter.

## Introduction

One of the major causes of ductile fracture in metals is the growth and coalescence of voids. Most phenomenological models of void growth and coalescence characterize the effects of the voids by the volume fraction of the voids. Researchers, however, realize that the distribution of the voids has a significant influence on the response of the material. Analytical studies and numerical studies using the Gurson plasticity model for quasi-static problems have shown that a non-uniform

void distribution lowers ductility. Needleman and Kushner [1] performed finite element calculations of a doubly periodic array of clusters of voids and concluded that the largest effect of void distribution was on the flow strength.

In this paper, the effect of void distribution and clustering on the failure stress of ductile metals in dynamic problems is studied. An Eulerian formulation was used to solve the model boundary value problems since the new free surfaces associated with the fracture are handled in a natural manner.

## The Eulerian Finite Element Method

A short explanation of the Eulerian finite element method is given in this section because Eulerian methods for problems in solid mechanics are not discussed in the popular texts on finite element methods. Those interested in a detailed presentation are referred to the review paper by Benson [2].

In the Eulerian formulation, the material time derivative is the sum of the rate at a spatial point and a convective term.

$$\frac{D\cdot}{Dt} = \frac{\partial\cdot}{\partial t} + \boldsymbol{u}\cdot\frac{\partial\cdot}{\partial \boldsymbol{x}} \tag{1}$$

The algorithmic strategy for an Eulerian calculation is to separate the calculation into two distinct stages: 1) a Lagrangian step, and 2) an Eulerian step. The first step is identical to the standard step for advancing time in a Lagrangian finite element program, while the second step accounts for the transport between adjacent elements.

The Lagrangian step used for the calculations in this paper is similar to those found in most explicit finite element programs such as DYNA2D [3]. Space is discretized using four node quadrilateral elements with one point integration and viscous hourglass damping [4]. The solution is advanced in time by using the explicit central difference method. A lumped mass matrix permits the solution of the accelerations without solving a system of equations. Using the standard notation in the finite element literature, the explicit time step is given by Equation 4. The Cauchy stress is $\sigma$, $B$ is the gradient operator, $V$ is the element volume, $u$ is the velocity, $F$ is the vector of applied forces and viscous hourglass forces, and $\triangle t$ is the time step. The radial return algorithm [5], [6], [7] is used to integrate the Johnson - Cook constitutive model [8] and the Jaumann rate accounts for the finite rotations.

$$\{\dot{u}\}^n = [M]^{-1}\left\{\sum_{e=1}^{ELEMENTS} -\{B_e^t \sigma_e V_e\} + \{F\}\right\} \quad (2)$$

$$\{u\}^{n+1/2} = \{u\}^{n-1/2} + \triangle t\{\dot{u}\}^n \quad (3)$$

$$\{x\}^{n+1} = \{x\}^n + \triangle t\{u\}^{n+1/2} \quad (4)$$

The transport of materials between elements is calculated by using a monotonic advection algorithm developed by van Leer [9]. In regions with a smooth solution, it is second order accurate, and where the solution is discontinuous or at an extremum, it is first order accurate and monotonic.

To minimize the cost of the calculations, several Lagrangian steps are performed and then the total transport associated with those steps is accounted for in a single Eulerian step. This strategy also minimizes the diffusion associated with the transport calculation.

## The Constitutive Model for the Matrix Material

The Johnson-Cook plasticity model [8] has been fitted to a wide variety of materials at high strain rates. OFHC copper was chosen as the matrix material because it can sustain very large plastic strain before failure.

The hardening is isotropic and the yield surface is circular in the $\pi$ plane. The yield stress, $\sigma_y$ is a function of the plastic strain, $\overline{\epsilon}^p$, the normalized strain rate, $\dot{\epsilon}^*$, and the homologous temperature, $T^*$. The upper case Roman letters $A$ through $C$ are material constants, $C_p$ is the heat capacity, $G$ is the shear modulus, and $K$ is the bulk modulus.

$$\dot{\boldsymbol{\sigma}}' = 2G(\dot{\boldsymbol{\epsilon}} - \dot{\boldsymbol{\epsilon}}^p) \quad (5)$$

$$\dot{P} = -K\,\mathrm{tr}(\dot{\boldsymbol{\epsilon}}) \quad (6)$$

$$\overline{\epsilon}^p = \int \sqrt{\frac{2}{3}\dot{\boldsymbol{\epsilon}}^p : \dot{\boldsymbol{\epsilon}}^p}\,dt \quad (7)$$

$$\sqrt{\frac{3}{2}\boldsymbol{\sigma}' : \boldsymbol{\sigma}'} = \sigma_y = [A + B(\overline{\epsilon}^p)^n][1 + C\ln\dot{\epsilon}^*][1 - T^{*m}] \quad (8)$$

$$\dot{\epsilon}^* = \frac{\dot{\epsilon}}{\dot{\epsilon}_0} \qquad \text{for } \dot{\epsilon}_0 = 1.0s^{-1} \quad (9)$$

$$T = \frac{e}{C_p} + T_{ROOM} \quad (10)$$

$$T^* = \frac{T - T_{ROOM}}{T_{MELT} - T_{ROOM}} \tag{11}$$

## The Effects of Void Distribution

*The Model Problem*

A tension wave is initiated at the upper boundary of the domain, propagates through the square test region containing a random distribution of voids, and is transmitted out through the lower boundary. The upper boundary is sufficiently remote from the test region that the uniform stress boundary condition does not prevent a non-uniform stress distribution adjacent to the voids. To avoid large numerical oscillations, the applied traction, $T$, is ramped up using a parabolic function over the first part of the calculation (typically the first one to five percent of the calculation).

$$\boldsymbol{\sigma} \cdot \boldsymbol{n} = T \min\left[1, (t/t_{blend})^2\right] \tag{12}$$

The lower boundary is a transmitting boundary, i.e., waves are transmitted through it and do not reflect back into the specimen. By the time the stress wave reaches the lower boundary, the stress is nearly uniform across the test specimen. The stress time histories are calculated by averaging the stresses in the elements adjacent to the transmitted boundary.

The left and right edges have "roller" boundary conditions so that the calculations approximate the stress states encountered at the center of a Hopkinson bar.

$$\boldsymbol{u} \cdot \boldsymbol{n} = 0 \tag{13}$$

$$\boldsymbol{t} \cdot \boldsymbol{\sigma} \cdot \boldsymbol{n} = 0 \tag{14}$$

The void distributions are taken from Needleman and Kushner [1]. They used two sets of patterns with six and three voids. Only the results for their distributions with patterns of six voids are shown here for the sake of brevity. In the current calculations, the test domain is a region 80.0 $\mu$m by 80.0 $\mu$m centered within the specimen. The standard void radius for the patterns with six voids is 2.50 $\mu$m for a void fraction of 0.0184.

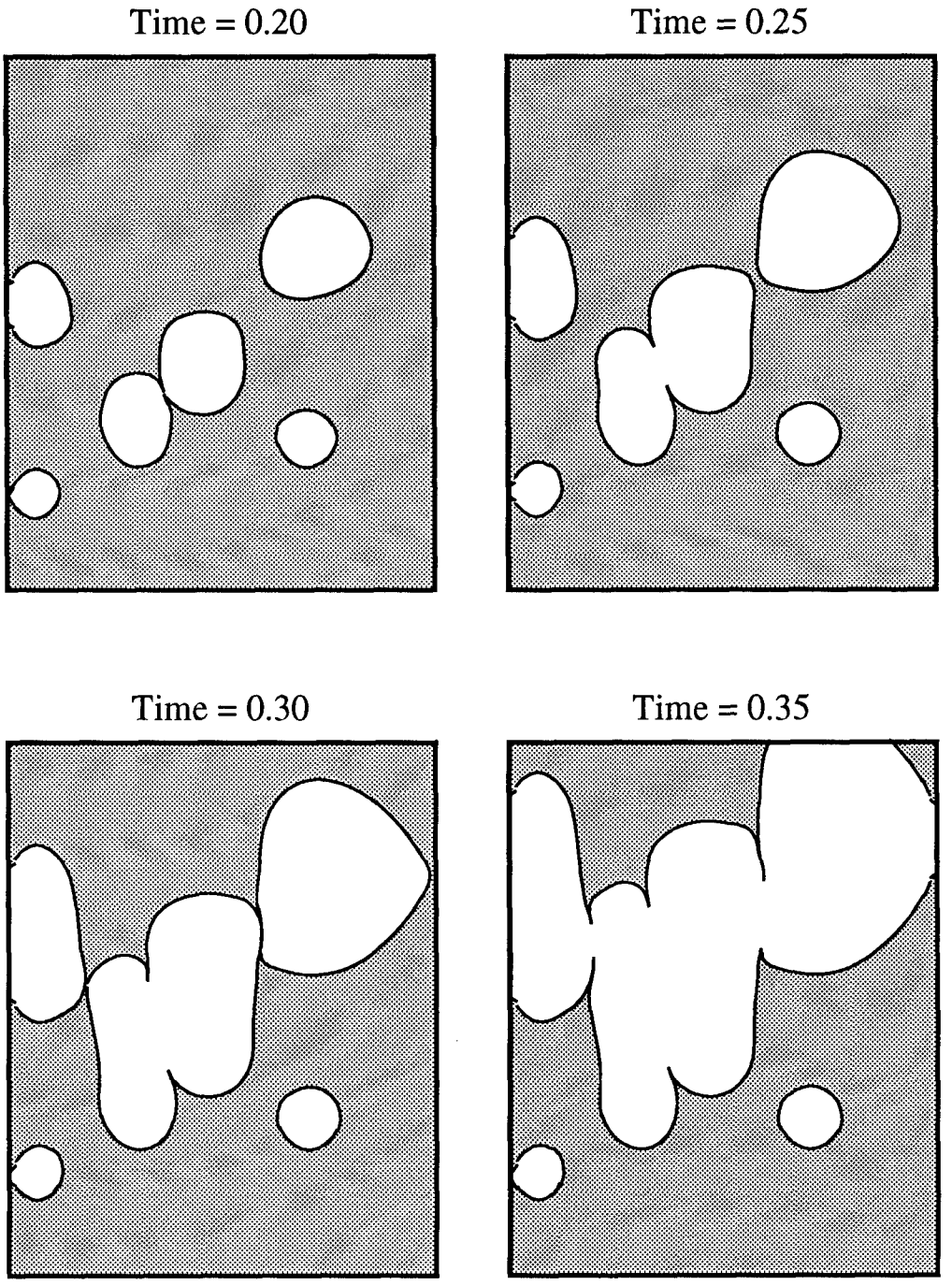



Figure 1 - The sequence of void coalescence of pattern 1 at 0.05 microsecond intervals.

*Numerical Results*

The sequence for pattern 1 with an OFHC copper matrix subjected to a tension wave of 1.24 GPa is shown at at intervals 0.05 $\mu$s in Figures 1. The most striking feature of this series of calculations is that the fracture path almost invariably consists of the first voids that the stress wave strikes regardless of their separation, and the voids that are downwind grow very little. This is contrary to the expectation that the pairs of voids that are closest together ("nearest neighbors") would coalesce first. The peak values of the transmitted stress, Figure 2, range from 450 MPa to 650 MPa, demonstrating an appreciable sensitivity to the void distribution. Although the time histories vary considerably in shape, they are roughly triangular in form, and complete failure occurs in all but one of the specimens between 0.30 $\mu$s and 0.35 $\mu$s. The only pattern that has not coalesced to failure is pattern 4, which has its voids concentrated in a triangular region at the lower left corner of the test region. Given the widely varying stress histories, it is surprising that failure occurs nearly simultaneously for four of the five void patterns.

The effect of the void fraction on the peak stress was studied by scaling the volume fraction while holding the distribution of the voids fixed. Using pattern 1, the void volume fractions were set to 0.0092, 0.0184, 0.0368, and 0.0736 while the coordinates of the centers of the voids remained unchanged. The time histories, which are shown in Figure 3, show an apparently logarithmic dependence of the peak stress on the void fraction. As would be expected, the peak stress is reduced by increasing the volume fraction. The time to fracture occurs earlier as the void fraction is reduced, but the final sizes and shapes of the voids at the time of fracture appear to be relatively independent of their initial size.

Note that the variation of the peak transmitted stress in Figure 2 is roughly the same magnitude as the change in the peak stress obtained by doubling the initial volume fraction in Figure 3.

## The Effects of Void Clusters

*The Model Boundary Value Problem*

The model problem consists of eight clusters, each consisting of four cylindrical voids, randomly distributed over a square domain 160.0 $\mu$m on a side, see Figure 4. The voids have a common diameter of 6.0 $\mu$m, resulting in an initial porosity of 3.5 percent. For an initial cluster

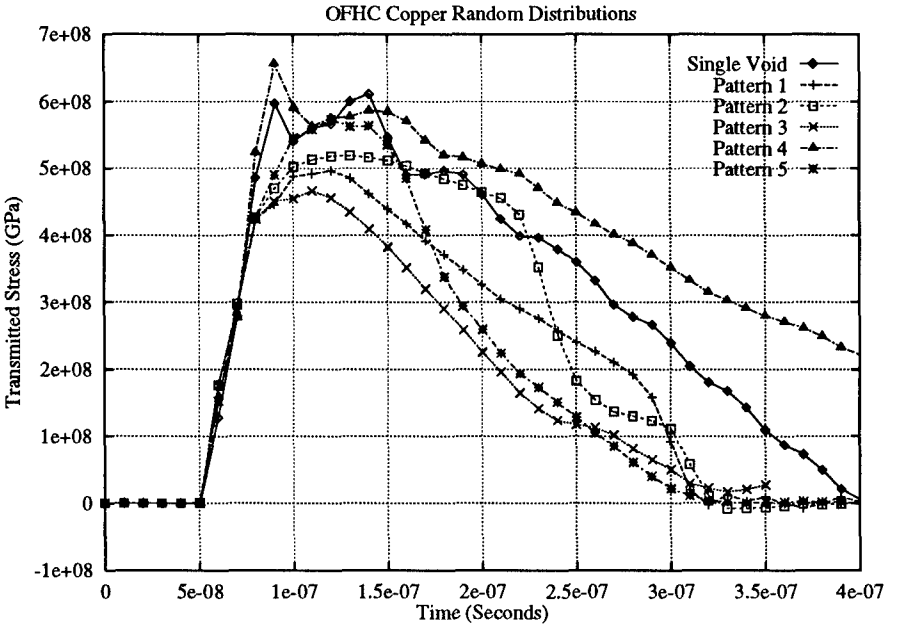



Figure 2 - The stress time histories for the random patterns and for a single void with the same void volume.

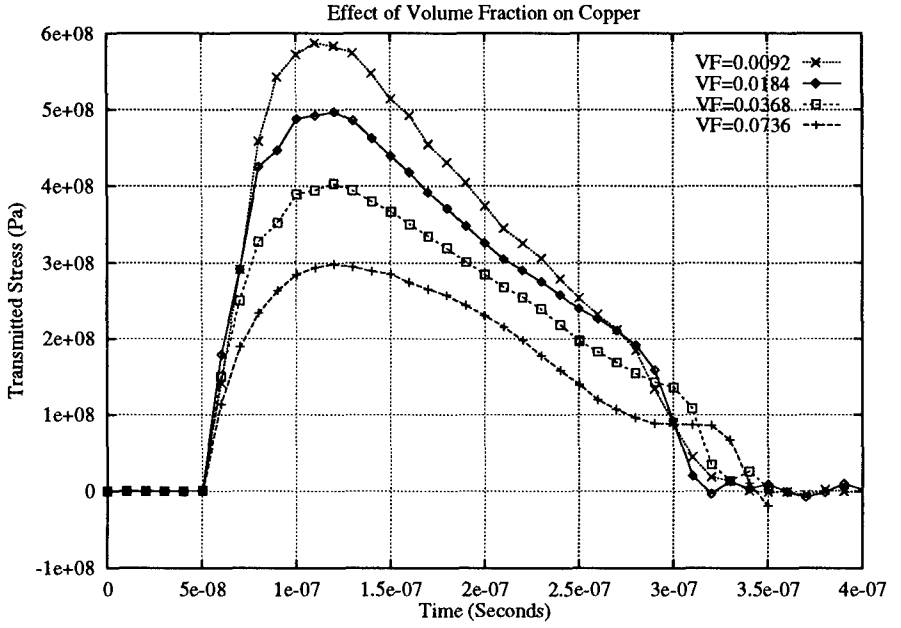



Figure 3 - The stress time histories for random pattern 1 as a function of the initial void fraction.

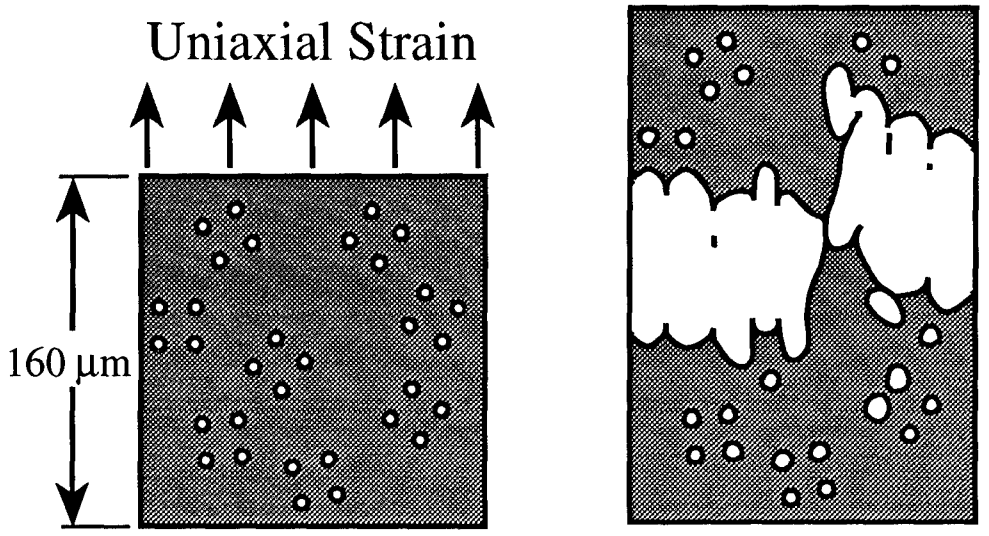



Figure 4 - The BVP for a cluster diameter of 24.0 $\mu$m and the resulting ductile fracture surface.

diameter of 24.0 $\mu$m, every void is separated from the voids in the other clusters by at least 24.0 $\mu$m. As in the previous study, the velocity of the upper boundary is defined by Equation 12, and the left and right boundaries have roller boundary conditions. The lower boundary is, however, fixed for this series of calculations.

*Numerical Results*

A parametric study with the diameters of the clusters set at 48.0, 24.0 16.0, and 8.0 $\mu$m was performed. While the voids associated with each cluster are readily identified when the cluster diameter is less than or equal to 24.0 microns, the voids appear to be randomly distributed when the cluster diameter is 48.0 $\mu$m. A "zero cluster diameter" calculation was performed by replacing each cluster with a single void having a diameter of 12.0 $\mu$m. The response of a single void with same total volume as the system of clusters was also calculated for comparison.

As shown by the stress-strain histories, Figure 5, the ultimate stress is largely independent of the cluster diameter. After reaching the ultimate stress, the magnitude of the slope of the stress-strain curve increases with the diameter of the clusters out to a nominal strain of 0.15. At higher strains, the material response is dependent on the failure of

the ligaments between the voids, and is therefore dependent on the path of the fracture. Since the fracture path varies with the cluster diameter, the fracture strain is not a simple function of the cluster diameter. The calculated stress-strain response for a single void with the same total volume provides an upper bound to the response of the clusters, with an ultimate stress that is approximately twenty percent higher than for the clusters.

A similar series of calculations for a single cluster centered in the unit cell was performed. The stress-strain response calculated for a random distribution of clusters is consistent with the response calculated for single clusters. The ultimate stress, 700 MPa, was essentially independent of the diameter of the cluster and significantly lower than the ultimate stress for a single void with the same volume as the cluster.

In a previous studies, e.g., [1], the stress-strain response was found to be a function of the distribution of the voids at small strains, and in the previous section, the variation of the ultimate stress was approximately twenty percent for the six random distributions. The variation observed in the cluster calculations is less than 3.1 percent as the diameter of the cluster varies from 1.3 to 8.0 times the diameter of the voids. When the cluster diameter of zero is included, the variation in the ultimate stress is still only 7.0 percent. Since the ultimate stress for the distribution of clusters is lower than for a single cluster, the clusters apparently interact to a significant degree. This result suggests that the details of the interactions between the voids within a cluster are relatively unimportant to the overall response.

The general trend is that an increase in the cluster diameter decreases the fracture strain. A small cluster diameter implies a greater non-uniformity in the void distribution in the sense that the ratio of the maximum to minimum separation between the voids increases as the cluster diameter decreases. Based on the previous studies, the expectation would be that fracture strain should decrease with the cluster diameter, which is contrary to the current results. These results are not, however, in disagreement with the previous studies because the void distributions considered here are not random. Fracture occurs when the neighboring voids coalesce to generate a free surface spanning the unit cell. It is reasonable to assume that the average diameter of the coalesced voids defining the fracture surface is a function of the mean distance initially separating the voids. Since the matrix material is essentially incompressible, as the average diameter required for the voids to coalesce decreases, the associated fracture strain also decreases.

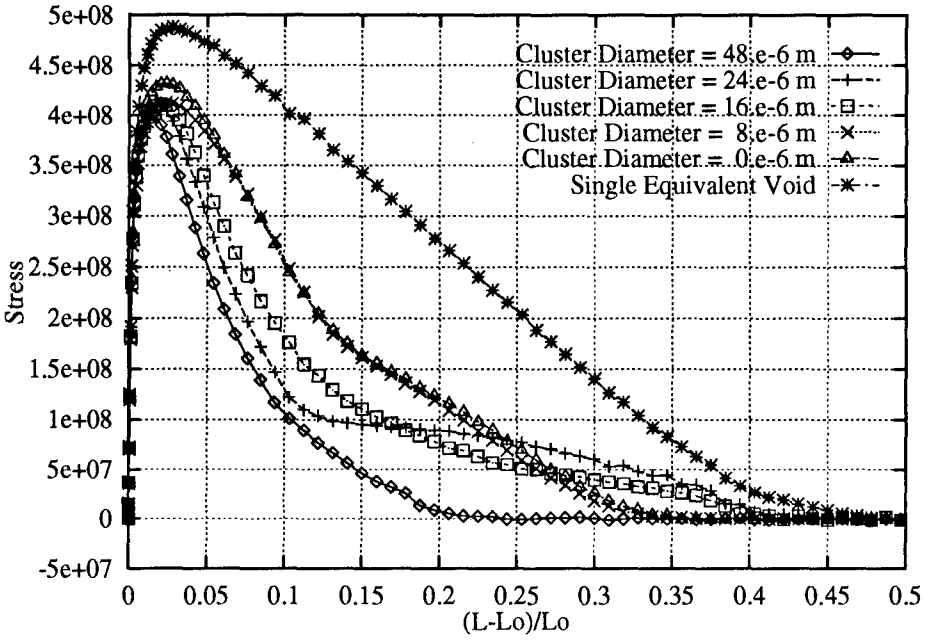



Figure 5 - The stress-strain histories as a function of the cluster diameter.

As the cluster diameter increases, the initial mean distance between the voids in this study decreases, thereby reducing the fracture strain. The relationship between the cluster diameter and the fracture strain is not monotonic because the set of voids defining the fracture changes in discrete jumps with the cluster diameter.

## Conclusions

The peak transmitted stress for a random distribution of voids was found to vary by as much as twenty percent, while the peak stress for a random distribution of void clusters varied by only three percent over a broad range of cluster diameters. This suggests that the geometrical relationships between the voids (or clusters) play a much stronger role in determining the failure stress than the details of the interactions between the voids within a cluster.

# References


[1] A. Needleman and A. S. Kushner. An analysis of void distribution effects on plastic flow in porous solids. *Eur. J. Mech., A/Solids*, 9(3):193–206, 1990.

[2] D. J. Benson. Computational methods in Lagrangian and Eulerian hydrocodes. *Computer Methods in Applied Mechanics and Engineering*, 99:235–394, 1992.

[3] J. O. Hallquist. *User's Manual for DYNA2D – An Explicit Two - Dimensional Hydrodynamic Finite Element Code with Interactive Rezoning*. Lawrence Livermore National Laboratory, 1984.

[4] G. L. Goudreau and J. O. Hallquist. Recent developments in large-scale finite element lagrangian hydrocode technology. *Computer Methods in Applied Mechanics and Engineering*, 33(1/3):725–757, 1982.

[5] G. Maenchen and S. Sack. The tensor code. In *Methods in Computational Physics*, volume 3. Academic Press, NewYork, 1964.

[6] M. Wilkins. Calculation of elastic - plastic flow. In *Methods in Computational Physics*, volume 3, pages 211–263. Academic Press, New York, 1964.

[7] R. D. Krieg and S. W. Key. Implementation of a time dependent plasticity theory into structural programs. In *Constitutive Equations in Viscoplasticity: Computational and Engineering Aspects*, volume 20, pages 125–137. ASME, 1976.

[8] G. R. Johnson and W. H. Cook. Fracture characteristics of three metals subjected to various strains, strain rates, temperatures, and pressures. *Engineering Fracture Mechanics*, 21(1):31–48, 1985.

[9] B. Van Leer. Towards the ultimate conservative difference scheme IV: A new approach to numerical convection. *Journal of Computational Physics*, 23:276–299, 1977.

# Validation of A-Posteriori Error Estimators by a Computer-Based Approach

Dr. T. Strouboulis*, C.S. Upadhyay, S.K. Gangaraj and K. Copps
Department of Aerospace Engineering, Texas A&M University,
College Station, TX 77843-3141, U.S.A.

## Abstract

A computer-based methodology which determines the quality (or robustness) of a-posteriori error estimators is described. The methodology accounts precisely for the factors which affect the quality of error estimators for finite-element solutions of linear elliptic problems, namely, the local geometry of the grid and the coefficients of the differential equation. The methodology can be employed to check the robustness of any estimator for the complex grids which are used in engineering computations.

## 1. Introduction

A-posteriori error estimation has become a key feature of practical finite-element analysis. Because of their practical importance error estimators have been the focus of intensive research; see for example [1-18] and the references in these papers. While some a-posteriori error estimators have been analyzed mathematically many estimators have been derived by purely heuristic reasoning. Usually the estimators are validated numerically on a set of *benchmarks* (example problems) which are selected in an ad-hoc manner. Most benchmark computations fail to isolate the basic factors which influence the performance of estimators and can motivate wrong conclusions. In this paper we present a clearly formulated objective *validation principle* for error estimators which takes into account the major factors influencing the performance of estimators in the case when the element is not at the boundary and the exact solution is smooth (in the neighborhood of the element). The methodology is completely numerical and can be used even when the definition of the estimator is unknown and is given only as a black-box computer program.

In practice, we are interested to have an accurate estimate of the error in a *cell* $\omega_0^h$ of the mesh $T_h$ (we will use the term cell to refer to a small patch of elements; the cell may consist of a few (possibly one) elements). The performance of any error estimator in $\omega_0^h$ depends on the local geometry of the mesh in a slightly bigger *patch* $\omega_s^h$ which includes $\omega_0^h$ in its interior (see Fig. 1) and on the local structure of the solution and no heuristic benchmarks can properly account for these factors. The methodology given below enables us to focus in the cell of interest and to study the robustness of any error estimator (even if it is only available as a black-box subroutine) for the actual geometries of the grids which are used in the engineering computations. The methodology requires the solution of relatively small problems in the regions of interest and is inexpensive. In contrast, benchmarks require global computation (which can be expensive) and do not lead to reliable conclusions.

The quality of an error estimator in the cell $\omega_0^h$ is measured by the *effectivity index*

$$\kappa_{\omega_0^h} := \frac{\mathcal{E}_{\omega_0^h}}{|||e_h|||_{\omega_0^h}}, \qquad \mathcal{E}_{\omega_0^h} := \left\{ \sum_{\substack{\tau \in T_h \\ \tau \cap \omega_0^h \neq \emptyset}} \eta_\tau^2 \right\}^{\frac{1}{2}} \tag{1}$$

where $|||e_h|||_{\omega_0^h}$ is the norm (of interest) of the error over $\omega_0^h$, $\mathcal{E}_{\omega_0^h}$ is an error estimator for this norm which is computed in terms of *element error-indicators* $\eta_\tau$, $\tau$ denotes an element in the mesh $T_h$. In this paper, we will consider estimators for the energy-norm of the error. The methodology of the paper can also be used to study the quality of estimators for other norms. Let $\Omega$ denote the domain of the problem. It has been shown (e.g. [1], [5]) that the *range* of the *global effectivity index*, $\kappa_\Omega$, exists for several estimators based on residuals, namely there exist constants $0 \leq C_L^\Omega \leq C_U^\Omega < +\infty$ such that

$$0 \leq C_L^\Omega \leq \kappa_\Omega \leq C_U^\Omega < \infty \tag{2a}$$

The two-sided inequality (2a) has been proven under very general assumptions about the exact solution (it is only required that the exact solution has finite-energy), reasonable assumptions about the regularity of the data (all practical cases are included) and under mild restrictions on the regularity of the mesh (for example see [5]). Inequality (2a) can also be written in the form

$$\frac{1}{C_U^\Omega}\,\mathcal{E}_\Omega \le |||e^h|||_\Omega \le \frac{1}{C_L^\Omega}\,\mathcal{E}_\Omega \tag{2b}$$

which expresses an *equivalence* between the global norm of the error and the estimator. Practical values for the *equivalency constants* $C_L^\Omega$ and $C_U^\Omega$ cannot be obtained for a given estimator unless further information is known about the class of solutions of interest and the finite-element meshes employed. A concrete example of how the constants can be estimated in the case of a simple residual estimator was given in [13-15]. The values of $C_L^\Omega$ and $C_U^\Omega$ depend strongly on the geometry of the grid and (relatively weakly) on the smoothness of the solution; the geometry of the grid must be understood in connection with the differential operator (see [13]).

It can also be shown (see [16-17]) that under reasonable assumptions about the grid we can determine the *asymptotic* range of the effectivity index for any estimator in any small *interior-cell* $\omega_0^h$ (a cell which is separated from the boundary by several mesh-layers) of the grid; i.e. there exist constants $0 \le C_L^{\omega_0^h} \le C_U^{\omega_0^h} < +\infty$ which depend only on the local geometry of the grid in $\omega_0^h$ and *a few mesh-layers around* it (the geometry of the grid in a sufficiently large patch $\omega_s^h$ which includes $\omega_0^h$ in its interior) such that (as the local mesh-size in $\omega_0^h$ and $\omega_s^h$ tends to zero)

$$0 \le C_L^{\omega_0^h} \le \kappa_{\omega_0^h} \le C_U^{\omega_0^h} < \infty \tag{3}$$

The constants $C_L^{\omega_0^h}$, $C_U^{\omega_0^h}$ are the best possible constants (i.e. they can be achieved) over an entire class of smooth solutions which occur in the field of application. When the values of the constants $C_L^{\omega_0^h}$, $C_U^{\omega_0^h}$ are known we can also manufacture an *upper*-(resp. *lower*-) estimator version of $\mathcal{E}_{\omega_0^h}$ denoted by $\mathcal{E}'_{\omega_0^h}$ (resp. $\mathcal{E}''_{\omega_0^h}$) defined by

$$\mathcal{E}'_{\omega_0^h} := \frac{1}{C_L^{\omega_0^h}}\,\mathcal{E}_{\omega_0^h}\,, \qquad \mathcal{E}''_{\omega_0^h} := \frac{1}{C_U^{\omega_0^h}}\,\mathcal{E}_{\omega_0^h} \tag{4a}$$

We then have

$$\left.\begin{aligned} 1 \le \kappa'_{\omega_0^h} &:= \frac{\mathcal{E}'_{\omega_0^h}}{|||e^h|||_{\omega_0^h}} \le \frac{C_U^{\omega_0^h}}{C_L^{\omega_0^h}} \\ \frac{C_L^{\omega_0^h}}{C_U^{\omega_0^h}} \le \kappa''_{\omega_0^h} &:= \frac{\mathcal{E}''_{\omega_0^h}}{|||e^h|||_{\omega_0^h}} \le 1 \end{aligned}\right\} \tag{4b}$$

The lower-estimator version of an estimator may be employed to drive adaptive-refinement algorithms in order to avoid over-refinement while the upper-estimator version may be used to guarantee a safe stopping-criterion.

Let us define the *robustness index* $\mathcal{R}_{\omega_0^h}$ $(0 \leq \mathcal{R}_{\omega_0^h} < \infty)$ which expresses the reliability of the estimator:

$$\mathcal{R}_{\omega_0^h} := \max\left\{ \left( |1 - C_U^{\omega_0^h}| + |1 - C_L^{\omega_0^h}| \right) , \left( |1 - \frac{1}{C_U^{\omega_0^h}}| + |1 - \frac{1}{C_L^{\omega_0^h}}| \right) \right\} \quad (5a)$$

The robustness index expresses the deviation of $\kappa$ and $\frac{1}{\kappa}$ (see (2a), (2b)) from the *ideal value* $\kappa = 1$. (Hence $\mathcal{R}_{\omega_0^h} = 0$ is the ideal value for the robustness index.) The robustness of an estimator for a given class of meshes $\mathcal{T} = \{T_h\}$ is given by

$$\mathcal{R}(\mathcal{T}) := \max_{T_h \in \mathcal{T}} \mathcal{R}_{T_h} , \qquad \mathcal{R}_{T_h} := \max_{\omega_0^h \in \mathcal{C}(T_h)} \mathcal{R}_{\omega_0^h} \quad (5b)$$

Here $\mathcal{C}(T_h)$ is the set of interior cells in the mesh $T_h$. The robustness index defined in (5b) characterizes the performance of the estimator for elements in the interior of the domain. Because most elements are in the interior of the domain (where the solution is smooth) the validation of the estimators has to be made especially for the case presented in this paper. The validation of the estimators for elements located at or near the boundary and singular points will be given in subsequent papers.

If an estimator does not display reasonable robustness for the interior-cells in the meshes of interest, i.e. if $\mathcal{R}(\mathcal{T})$ is too large, the estimator is unreliable and should not be used. The robustness index depends on $\mathcal{T}$, the family of meshes under consideration. (Hence restrictions placed on the mesh-generator could possibly increase the reliability of an estimator.)

The robustness index is an *objective quantitative* characterization of the reliability of an estimator. Hence, analogously as the effectivity index, the robustness index of an estimator should be reported.

This work is part of a study of the properties of local a-posteriori error estimators (see [16-18]). The objective of the study is the development of new adaptive grid methodologies for quantitative control of the local error in finite element computations. This paper summarizes the work reported in [16-17] which deals with question of checking the quality of error-estimators in the interior of the mesh for specific class of

grids employed in practical computations. In [18] a study the effect of the *pollution-error* on local error estimation is given.

Following this Introduction we present the definition of the model problems (linear elasticity and heat-conduction), we describe two types of error estimators, we present the methodology for the computation of the robustness index and we outline its theoretical justification. Finally, we give examples which demonstrate how the robustness index of error estimators for complex finite-element meshes can be computed and how it is possible to increase the reliability of an estimator by proper selection of its various parameters.

# 2. The model problems

We shall consider the vector-valued boundary-value problem

$$\left.\begin{aligned} L_i(\mathbf{u}) := -\sum_{j=1}^{2} D_j\big(\sigma_{ij}(\mathbf{u})\big) = f_i \qquad & \text{in } \Omega \\ u_i = 0 \qquad & \text{on } \Gamma_D \\ \sum_{j=1}^{2} \sigma_{ij}(\mathbf{u}) n_j = \bar{t}_i \qquad & \text{on } \Gamma_N \end{aligned}\right\} \tag{6}$$

where $i = 1, 2$.

Here $\Omega \subset \mathbf{R}^2$ is a bounded domain with boundary $\partial\Omega = \Gamma_D \cup \Gamma_N$;

$\mathbf{n} := (n_1, n_2)$ is the outward pointing unit-normal on $\Gamma_N$;

$f_i$, $i = 1, 2$ are the components of the load-vector (*body-force*);

$\bar{t}_i$, $i = 1, 2$ are the components of the normal-flux vector (*traction*) applied on $\Gamma_N$;

$\Gamma_D \neq \emptyset$, $\Gamma_D \cap \Gamma_N = \emptyset$; $\mathbf{u} = (u_1, u_2)$ is the solution-vector (*displacement*);

$$\epsilon_{ij}(\mathbf{u}) := \frac{1}{2}(D_j u_i + D_i u_j)\ , \qquad \sigma_{ij}(\mathbf{u}) := \sum_{k,\ell=1}^{2} a_{ijk\ell}\, \epsilon_{k\ell}(\mathbf{u})\ , \qquad i, j = 1, 2 \tag{7}$$

are the components of the flux (*strain, stress*);

$a_{ijk\ell}$, $i, j, k, \ell = 1, 2$, are the material-coefficients (*elastic constants*) which in the case of isotropic plane elasticity are given by $a_{ijk\ell} = \mu(\delta_{ij}\delta_{k\ell} +$

$\delta_{i\ell}\delta_{kj}) + \lambda\delta_{ik}\delta_{j\ell}$ where $\delta_{ij}$ is Kronecker's delta and $\lambda, \mu$ are Lamé's constants.

We also introduce the scalar elliptic boundary-value problem (*heat-conduction in orthotropic medium*), namely

$$\left.\begin{aligned} L'(u) := -\sum_{k,\ell=1}^{2} D_k\left(K_{k\ell}D_\ell u\right) = f \qquad & \text{in } \Omega \\ u = 0 \qquad & \text{on } \Gamma_D \\ \sum_{k=1}^{2} q_k(u)n_k = \bar{t} \qquad & \text{on } \Gamma_N \end{aligned}\right\} \tag{8}$$

Here $q_k(u) := \sum_{\ell=1}^{2} K_{k\ell}D_\ell u\,,\ k = 1,2$ are the components of the flux-vector (*heat-flux*) and $K_{k\ell},\ k,\ell = 1,2$, are the entries of the *thermal-conductivity* matrix which is symmetric, postive definite. Below we will let $K_{\min}, K_{\max}$ denote the principal values of the thermal-conductivity matrix.

Let us now cast the model problems in variational form. Let us denote the space of test-functions by

$$\mathbf{H}^1_{\Gamma_D} := \left\{ (v_1, v_2) :\ v_i \in H^1(\Omega)\,,\ v_i = 0 \text{ on } \Gamma_D \right\} \tag{9}$$

The variational form of the boundary-value problem (6) is now posed as:

Find $\mathbf{u} \in \mathbf{H}^1_{\Gamma_D}$ such that

$$\mathcal{B}_\Omega(\mathbf{u}, \mathbf{v}) = \int_\Omega \sum_{i=1}^{2} f_i v_i + \int_{\Gamma_N} \sum_{i=1}^{2} \bar{t}_i v_i \qquad \forall\, \mathbf{v} \in \mathbf{H}^1_{\Gamma_D} \tag{10}$$

where the bilinear form $\mathcal{B}_\Omega : \mathbf{H}^1_{\Gamma_D} \times \mathbf{H}^1_{\Gamma_D} \to \mathbf{R}$ is defined by

$$\mathcal{B}_\Omega(\mathbf{u}, \mathbf{v}) := \int_\Omega \sum_{i,j,k,\ell=1}^{2} a_{ijk\ell} D_\ell u_j D_k v_i\,. \tag{11}$$

The energy-norm over any subdomain $S \subseteq \Omega$ is defined by

$$|||\mathbf{v}|||_S := \sqrt{\mathcal{B}_S(\mathbf{v}, \mathbf{v})} \tag{12}$$

where $\mathcal{B}_S(\mathbf{u},\mathbf{v})$ has the obvious meaning.

In the case of the scalar elliptic problem given by (8) the bilinear form is given by $\mathcal{B}'_\Omega(u,v) := \int_\Omega \sum_{k,\ell=1}^{2} K_{k\ell} D_\ell u D_k v$. The weak-solution of (8) satisfies:

$$\text{Find } u \in H^1_{\Gamma_D} := \left\{ v \in H^1(\Omega) \ : \ v = 0 \ \text{ on } \ \Gamma_D \right\} \text{ such that}$$

$$\mathcal{B}'_\Omega(u,v) = \int_\Omega fv + \int_{\Gamma_N} \bar{t}v \qquad \forall\ v \in H^1_{\Gamma_D} \tag{13}$$

The energy-norm in any subdomain $S \subseteq \Omega$ is defined by $|||v|||_S := \sqrt{\mathcal{B}'_S(v,v)}$ .

Let $\mathcal{T} = \{T_h\}$ be a family of meshes of triangles or quadrilaterals with straight edges. It is assumed that the family is regular (i.e.: for the triangles the minimal angle of all the triangles is bounded below by a positive constant, the same for all the meshes; for the quadrilaterals see conditions (37.40) in Ciarlet [19]). The meshes are not assumed to be quasiuniform. Let us introduce the finite-element spaces

$$\mathbf{S}^p_h := \left\{ \mathbf{u} \in \mathbf{H}^1 \ : \ u_i \circ \mathbf{Q}^{(k)} \in \mathcal{P}_p(\hat{\tau}), \quad i = 1,2, \quad k = 1,\ldots,M(T_h) \right\} \tag{14}$$

where $\mathbf{Q}^{(k)}$ is the mapping function for the $k$th finite-element which maps either a standard triangular element (using an affine transformation) or a standard quadrilateral element (using a bilinear transformation) onto the $k$th finite element, $\hat{\tau}$ denotes a standard element, $M(T_h)$ is the number of elements in the mesh $T_h$, $\mathcal{P}_p(\hat{\tau})$ denotes the set of polynomials of degree $p$ over $\hat{\tau}$. We let $\mathbf{S}^p_{h,\Gamma_D} := \mathbf{S}^p_h \cap \mathbf{H}^1_{\Gamma_D}$, denote the discrete test-space. The finite element solution $\mathbf{u}^h$ (for the elasticity problem) satisfies:

$$\text{Find } \mathbf{u}^h \in \mathbf{S}^p_{h,\Gamma_D} \text{ such that}$$

$$\mathcal{B}_\Omega(\mathbf{u}^h,\mathbf{v}^h) = \int_\Omega \sum_{i=1}^{2} f_i v^h_i + \int_{\Gamma_N} \sum_{i=1}^{2} g_i v^h_i \qquad \forall\ \mathbf{v}^h \in \mathbf{S}^p_{h,\Gamma_D} \tag{15}$$

The error is $\mathbf{e}^h := \mathbf{u} - \mathbf{u}^h$ .

**Remark 2.1.** We addressed only (for simplicity) the model problems for which the differential operator $\mathbf{L}$ (or $L'$) is homogeneous with constant

coefficients. The theory and the procedure holds for the general case, for non-homogeneous operators with non-constant (but smooth) coefficients.

In the following we give two representative classes of estimators for the energy-norm of the error and we employ the model methodology to check the robustness of various versions of estimators from these classes. Below we define the estimators for the elasticity problem (the estimators for the scalar model problem (9) may be obtained by analogy; see also [16]).

# 3. Element-residual error estimators

## 3.1 Implicit element-residual estimator

We introduce notations needed for the description of the estimators. For each triangle (quadrilateral) $\tau \in T_h$, we denote by $E(\tau)$ and $N(\tau)$ the set of its edges and vertices, respectively. We define the local *bubble-spaces* of polynomials

$$\mathbf{H}_\tau := \left\{ \mathbf{w} \ : \ w_i \in \mathcal{P}_{p+1}\,, \quad \Pi^p_\tau(w_i) = 0\,, \quad i = 1,2 \right\}, \qquad \tau \in T_h \tag{16}$$

where $\Pi^p_\tau$ is a *projection-operator* defined over element $\tau$ (see [6-7]).

We define the *interior-residual* in element $\tau$ as

$$\mathbf{r}_\tau := \ -\mathbf{L}(\mathbf{u}^h) + \mathbf{f} \tag{17}$$

where $\mathbf{L}(\mathbf{u}^h) := \ \left(L_1(\mathbf{u}^h), L_2(\mathbf{u}^h)\right)$, $\mathbf{f} := \ (f_1, f_2)$,
and the *jump* or *edge-residual* associated with the edge $\epsilon := \partial\tau_{\text{in}} \bigcap \partial\tau_{\text{out}}$

$$\mathbf{J}_\epsilon := \ \left[\boldsymbol{\sigma}(\mathbf{u}^h|_{\tau_{\text{out}}}) - \boldsymbol{\sigma}(\mathbf{u}^h|_{\tau_{\text{in}}})\right]\mathbf{n} \tag{18}$$

where $\mathbf{n}$ is the unit-normal assigned to the edge $\epsilon$.

The *residual-functional* for element $\tau$ is

$$\mathcal{F}_\tau(\mathbf{v}) := \ \int_\tau \mathbf{v}\cdot\mathbf{r}_\tau + \frac{1}{2}\sum_{\epsilon\in E(\tau)} \int_\epsilon \mathbf{v}\cdot\mathbf{J}_\epsilon\,, \qquad \mathbf{v} \in \mathbf{H}^1(\tau) \tag{19}$$

We now define the element-residual estimator for the model problem (6) (we give the estimators only for elements in the interior of the domain).

The element error indicators for the implicit element-residual estimators for elements of any degree $p$ are:

$$\eta_\tau := |||\mathbf{e}_\tau|||_\tau \tag{20}$$

where

$$\mathbf{e}_\tau \in \mathbf{H}_\tau : \quad \mathcal{B}_\tau(\mathbf{e}_\tau, \mathbf{v}_\tau) = \mathcal{F}_\tau(\mathbf{v}_\tau) , \qquad \forall\ \mathbf{v}_\tau \in \mathbf{H}_\tau \tag{21}$$

In the following we will study the robustness of various versions of the implicit element-residual estimator. Of particular interest are versions based on *equilibrated residual*. Element-residual estimators which employ equilibrated data in a general setting of $h-p$ approximations have been proposed in [12].

## 3.2 Equilibrium of the residuals

The residual data for the local problems (21) are *equilibrated* if the following *consistency conditions* (*equilibrium equations*) are satisfied,

$$\left.\begin{aligned} \int_\tau \mathbf{r}_\tau + \frac{1}{2}\sum_{\epsilon\in E(\tau)}\int_\epsilon \mathbf{J}_\epsilon &= 0\,\mathbf{i}_1 + 0\,\mathbf{i}_2 \\ \int_\tau \mathbf{x}\times\mathbf{r}_\tau + \frac{1}{2}\sum_{\epsilon\in E(\tau)}\int_\epsilon \mathbf{x}\times\mathbf{J}_\epsilon &= 0\,\mathbf{i}_3 \end{aligned}\right\} \tag{22}$$

Here $\mathbf{i}_1$, $\mathbf{i}_2$ denote the unit-vectors along the global coordinate directions in $\mathbf{R}^2$ and $\mathbf{i}_3$ the out-of-plane unit-vector. The element equilibrium equations (22) will hold if

$$\left.\begin{aligned} \sum_{i=1}^{nv}\left\{\mathcal{F}_\tau(\mathbf{i}_1 N_i)\,\mathbf{i}_1 + \mathcal{F}_\tau(\mathbf{i}_2 N_i)\,\mathbf{i}_2\right\} &= 0\,\mathbf{i}_1 + 0\,\mathbf{i}_2 \\ \sum_{i=1}^{nv}\mathbf{x}_i\times\left\{\mathcal{F}_\tau(\mathbf{i}_1 N_i)\,\mathbf{i}_1 + \mathcal{F}_\tau(\mathbf{i}_2 N_i)\,\mathbf{i}_2\right\} &= 0\,\mathbf{i}_3 \end{aligned}\right\} \tag{23}$$

provided that the set of functions $\{N_i\}_{i=1}^{nv}$ satisfies $\sum_{i=1}^{nv} N_i|_\tau = 1\,,\ \forall\,\tau\in T_h\,.$ Here we let $N_i|_\tau$ be the linear (for triangles) or bilinear (for quadrilaterals)

element-shape-function which corresponds to the $i$-th vertex and $nv$ is the number of vertices for element $\tau$ ($nv = 3$ for triangles, $nv = 4$ for quadrilaterals). The equilibrium conditions for element $\tau$ will be satisfied automatically if

$$\mathcal{F}_\tau(\mathbf{i}_\ell N_i) = 0\,, \qquad \ell = 1,2, \qquad i = 1,\ldots,nv \tag{24}$$

These conditions, however, are not expected to hold for general meshes and solutions; below we discuss ways of *correcting* the definition of $\mathcal{F}_\tau$ in order to satisfy conditions (24).

### 3.2.1 Ladeveze's flux-splitting technique

The definition of $\mathcal{F}_\tau$ in (19) may to be modified in order to satisfy (24) by letting

$$\mathcal{F}_\tau^{\text{EQ}}(\mathbf{v}) := \mathcal{F}_\tau(\mathbf{v}) + \int_{\partial\tau} \mathbf{v}\cdot\boldsymbol{\theta}_\tau\,, \qquad \mathbf{v}\in\mathbf{H}^1(\tau) \tag{25}$$

Here, $\boldsymbol{\theta}_\tau$ is the *correction* of the edge-residuals for the element $\tau$.

We let

$$\boldsymbol{\sigma}_\tau|_\epsilon = \zeta_\tau^\epsilon\left(\boldsymbol{\theta}_\epsilon^1\psi_1^\epsilon + \boldsymbol{\theta}_\epsilon^2\psi_2^\epsilon\right)\,, \qquad \epsilon\in E(\tau) \tag{26}$$

where,

$$\zeta_\tau^\epsilon = \begin{cases} +1, & \text{if } \tau = \tau_{\text{in}}, \\ \\ -1, & \text{if } \tau = \tau_{\text{out}}, \end{cases}$$

where it is assumed that the edge normal $\mathbf{n}$ has been assigned to the edge $\epsilon$ in an arbitrary but unique way and $\tau_{\text{in}}$ and $\tau_{\text{out}}$ are defined as shown in Fig. 2. The linear functions $\psi_k^\epsilon$ are defined as,

$$\psi_1^\epsilon := \frac{2}{|\epsilon|}\left(2\lambda_1^\epsilon - \lambda_2^\epsilon\right)\,, \qquad \psi_2^\epsilon := \frac{2}{|\epsilon|}\left(2\lambda_2^\epsilon - \lambda_1^\epsilon\right) \qquad k = 1,2 \tag{27}$$

where $\lambda_k^\epsilon$, $k = 1,2$ are the linear shape-functions defined over the edge $\epsilon$. Using this definition of $\boldsymbol{\theta}_\tau|_\epsilon$ we can decouple the problem of determination of $\boldsymbol{\theta}_\tau|_\epsilon$ for the whole domain into small local problems involving only patches of elements connected to node $X$, as shown in Fig. 2a. We have

$$\boldsymbol{\theta}_\epsilon^k := \int_\epsilon \boldsymbol{\theta}_\tau|_\epsilon \, \lambda_k^\epsilon \,, \qquad k = 1,2 \,, \qquad \epsilon \in E(\tau) \tag{28}$$

Thus, for each patch around a node $X$ we obtain a linear system (see [3], [4], for the details)

$$\int_{\partial \tau_k^X} (\mathbf{i}_\ell \cdot \boldsymbol{\theta}_{\tau_k^X}) \, \phi_X = -\mathcal{F}_\tau(\mathbf{i}_\ell \phi_X) \,, \qquad \ell = 1,2 \qquad k = 1, \ldots, N_X \tag{29}$$

where $\phi_X$ denotes the basis function which corresponds to the vertex $X$, $\tau_k^X$ denotes the $k$-th element connected to the vertex $X$, $N_X$ is the number of elements (or edges) connected to the vertex $X$.

The linear system (29) has a one parameter family of solutions. Specific choices of solutions have been suggested in [3], [4]; in the numerical implementations we employed these choices. Below we give the definition of the edgewise-linear correction $\boldsymbol{\theta}_\tau$. Let us consider the interior-vertex $X$ and let us also denote $\epsilon_i$, $i = 1, \ldots, N_X$ the edges connected to $X$. We will determine the coefficients $\boldsymbol{\theta}_\epsilon^{\nu(\epsilon,X)}$ which is associated with the edge $\epsilon$ and the vertex $X$ and is employed in (26). Here the index $\nu(\epsilon, X)$ identifies the local enumeration of node $X$, as used in (26) for the unknowns associated with the edge; see Fig. 2b.

*a. Bank and Weiser's equilibration* [4]:

A solution of (29) can be obtained by letting

$$\left.\begin{aligned} \mathbf{i}_\ell \cdot \boldsymbol{\theta}_{\epsilon_1}^{\nu(\epsilon_1,X)} &= -\mathcal{F}_{\tau_1^X}(\mathbf{i}_\ell \phi_X) \,, \qquad \ell = 1,2 \\ \mathbf{i}_\ell \cdot \boldsymbol{\theta}_{\epsilon_i}^{\nu(\epsilon_i,X)} &= \mathbf{i}_\ell \cdot \boldsymbol{\theta}_{\epsilon_{i-1}}^{\nu(\epsilon_{i-1},X)} - \mathcal{F}_{\tau_i^X}(\mathbf{i}_\ell \phi_X) \,, \qquad \ell = 1,2; \quad i = 2, \ldots, N \end{aligned}\right\} \tag{30}$$

*b. Ladeveze's equilibration* [3]:

Here the coefficients $\boldsymbol{\theta}_{\epsilon_i}^{\nu(\epsilon_i,X)} = \sum_{\ell=1}^{2} (\mathbf{i}_\ell \cdot \boldsymbol{\theta}_{\epsilon_i}^{\nu(\epsilon_i,X)}) \mathbf{i}_\ell$, $i = 1, \ldots, N$ are selected such that

$$I_\ell^X(\boldsymbol{\theta}) := \sum_{i=1}^{N} \left[ w_i \, (\mathbf{i}_\ell \cdot \boldsymbol{\theta}_{\epsilon_i}^{\nu(\epsilon_i,X)}) \right]^2 \tag{31}$$

is minimized for $\ell = 1$ and $\ell = 2$ separately, where $w_i$ is the weight associated with each edge $\epsilon_i$. In [3] the weights $w_i$ have been taken as 1. For this choice of weights, the solution of (24) is given explicitly as,

$$\left.\begin{aligned}
&\mathbf{i}_\ell \cdot \boldsymbol{\theta}_{\epsilon_N}^{\nu(\epsilon_N,X)} = \frac{1}{N}\sum_{i=1}^{N}(N-i+1)\mathcal{F}_{\tau_i^X}(\mathbf{i}_\ell\phi_X)\ ,\ \ell = 1,2 \\
&\mathbf{i}_\ell \cdot \boldsymbol{\theta}_{\epsilon_1}^{\nu(\epsilon_1,X)} = \mathbf{i}_\ell \cdot \boldsymbol{\theta}_{\epsilon_N}^{\nu(\epsilon_N,X)} - \mathcal{F}_{\tau_1^X}(\mathbf{i}_\ell\phi_X),\ \ell = 1,2 \\
&\mathbf{i}_\ell \cdot \boldsymbol{\theta}_{\epsilon_i}^{\nu(\epsilon_i,X)} = \mathbf{i}_\ell \cdot \boldsymbol{\theta}_{\epsilon_{i-1}}^{\nu(\epsilon_{i-1},X)} - \mathcal{F}_{\tau_i^X}(\mathbf{i}_\ell\phi_X)\ ,\ \ell = 1,2;\ i = 2,3,\ldots,(N-1)
\end{aligned}\right\} \tag{32}$$

If we take the weights $w_i := |\epsilon_i|^{-1}$, we can obtain a different $\boldsymbol{\theta}_\tau$ satisfying (29).

# 4. Error estimators based on recovery techniques

Error estimators can also be based on the *superconvergent patch-recovery* technique [8-9] which is known as the *Zienkiewicz-Zhu* (Z-Z) procedure. The element error-indicators for elements of any degree $p$ are

$$\eta_\tau := ||\boldsymbol{\sigma}^* - \boldsymbol{\sigma}(\mathbf{u}^h)||_{L^2(\tau),a^{-1}} \tag{33}$$

where

$$||\boldsymbol{\sigma}||^2_{L^2(\tau),a^{-1}} := \int_\tau \sigma_{ij}\ a^{-1}_{ijk\ell}\ \sigma_{k\ell} \tag{34}$$

where $a^{-1}_{ijk\ell}$ are the entries of the compliance tensor, $\boldsymbol{\sigma}^*$ is the recovered flux.

Let $\omega_X := \bigcup_{X\in N(\tau')} \tau'$ denote the patch of elements connected to vertex $X$. For each patch $\omega_X$ we recover the *patch-projection* $\tilde{\boldsymbol{\sigma}}^X$ by solving the following least-squares problem:

$$\inf_{\substack{\sigma^X_{ij}\in\mathcal{P}_p(\omega_X)\\ i,j=1,2}} ||\boldsymbol{\sigma}(\mathbf{u}^h) - \boldsymbol{\sigma}^X||_{L^2(\omega_X),a^{-1},\{\mathbf{y}_\ell\}_{\ell=1}^{nsp}} = ||\boldsymbol{\sigma}(\mathbf{u}^h) - \tilde{\boldsymbol{\sigma}}^X||_{L^2(\omega_X),a^{-1},\{\mathbf{y}_\ell\}_{\ell=1}^{nsp}} \tag{35}$$

where $\{\mathbf{y}_\ell\}_{\ell=1}^{nsp}$ denotes a set of *sampling points* in $\omega_X$ and

$$||\boldsymbol{\sigma}||^2_{L^2(\omega_X),a^{-1},\{\mathbf{y}_\ell\}_{\ell=1}^{nsp}} := \sum_{m=1}^{nsp} \left[ \sum_{i,j,k,\ell=1}^{2} \sigma_{ij}(\mathbf{y}_m)\ a^{-1}_{ijk\ell}\ \sigma_{k\ell}(\mathbf{y}_m) \right] \tag{36}$$

$\boldsymbol{\sigma}^*$ is obtained by averaging the patch-projections $\tilde{\boldsymbol{\sigma}}^X$ over the elements (see [8], [9]).

**Remark 4.1.** Although the intention in [8], [9] was to use superconvergence points (as sampling points), the estimator performs very well (see [17] for the details) also if the sampling points are not superconvergence points. Note that the superconvergence points do not exist for the general meshes, like the meshes shown in Figs. 1, 3 which are employed in the examples of this paper.

# 5. The methodology for checking the estimators

We now describe the numerical methodology which is employed in the calculation of the robustness index for a given estimator. The robustness index depends on the following factors (see also [16-17] for further details and the complete theoretical setting of the methodology):

*a. The geometry of the grid*:

The main factor which affects any error estimator is the *geometry of the grid* namely the connectivity or topology of the grid and the geometry (*distortion*) of the elements. The element geometry has to be considered in connection with the differential operator for the boundary-value problem. For example the orthotropic heat-conduction operator can be transformed by an affine transformation to Laplace's operator on a distorted mesh which has different minimal and maximal angles.

*b. The class of solutions*:

In this paper we study the robustness of error estimators for linear elliptic equations and *interior mesh-subdomains*. It is well-known that the solutions of elliptic boundary-value problems are analytic in the interior of the domain if the coefficients of the operator and the right-hand side are analytic; for this reason we will consider the class of smooth solutions. Of particular interest is the subclass of smooth functions which satisfies the homogeneous differential equation (we will refer to such solutions as "harmonic"; if the solution satisfies Laplace's equation it is truly harmonic).

The asymptotic properties of error estimators for the class of smooth solutions can be studied by considering the class of polynomials of degree $(p+1)$.

We now give an outline of the numerical procedure which determines the robustness index $\mathcal{R}$ for any error estimator.

Let us assume that we would like to determine the robustness of an estimator for a mesh $T_h$ from a given class of meshes (the class may be defined as the class of meshes produced by a commercial mesh-generator or an adaptive code). Let $\{\omega_X\}_{X=1}^{nv}$ be the cells of elements connected to the vertices of the mesh. Let $\omega_X$ be an *interior-cell* (it is separated by several layers of elements from the boundary, singular-points and material-interfaces). Let

$$\omega_0^h := \omega_X$$

and for $s \geq 1$, integer, define the patch

$$\omega_s^h := \bigcup_{\substack{X \in \mathcal{N}(\tau') \\ \tau' \subseteq \omega_{s-1}^h}} \omega_X$$

From the analysis (given in [16] for locally-periodic meshes) and numerical experience (for more general meshes) we know that the effectivity index for any estimator in the cell $\omega_0^h$ depends practically on the geometry of the mesh in the patch $\omega_s^h$ for only a small $s$ ($s = 1$ - $4$) (more precisely increasing $s$ will change the robustness index only minimally). Given a mesh $T_h$ (resp. class of meshes $\mathcal{T}$) constructed by a mesh generator, there are patches $\omega_s^h$ of various types (topologies). We can now analyze all these patches separately and compute $\mathcal{R}_{T_h}$ (resp. $\mathcal{R}(\mathcal{T})$ ) as defined in (5b). For example, in Fig. 6 (resp. Fig. 7) we indicate the mesh-cells $\omega_0^h$ shaded gray and the patch $\omega_s^h$, for $s = 3$ (resp. $s = 4$), with its perigram shown by thick line, for various interior-cell/patch combinations from the grid shown in Fig. 3 (resp. Fig. 1). We can determine the robustness of any error-estimator in $\omega_0^h$ as follows:

*1. Completion of the mesh-cell to a periodic super-patch.*

Translate and scale the patch $\omega_s^h$ so that its image $\tilde{\omega}_s^h \subseteq \tilde{c} = [-1,1] \times [-1,1]$ (see Fig. 4b). Then employ a mesh-generator to complete the mesh in $\tilde{\omega}_s^h$ into a *periodic-mesh* $\tilde{T}$ in the super-patch $\tilde{c}$ (see Fig. 4c).

*2. Periodic boundary-value problem:*

For given exact solution $\mathbf{u}$ which is a homogeneous polynomial of degree $(p+1)$ ($\mathbf{u} \in (\hat{\mathcal{P}}_{p+1})^2$ or exact "harmonic" polynomial solution $\mathbf{u} \in (\hat{\mathcal{P}}_{p+1})^2$ such that $L_i(\mathbf{u}) = 0, \quad i = 1,2$), material properties and *mesh-pattern* (the local geometry of the grid in the cell $\omega_0^h$ and the patch $\omega_s^h$) determine

a) The finite element solution $\mathbf{u}^h$,

b) The exact error $\mathbf{e}^h$,

by solving the following *periodic boundary-value problem*:

Find $\mathbf{z}^h \in \mathbf{H}^h_{\text{per}}(\tilde{c})$ such that

$$\mathcal{B}_{\Omega_{\text{per}}}(\mathbf{z}^h, \mathbf{v}^h) = \mathcal{B}_{\Omega_{\text{per}}}(\mathbf{u} - \mathbf{u}_{\text{I}}^h, \mathbf{v}^h) \qquad \forall\ \mathbf{v}^h \in \mathbf{H}^h_{\text{per}}(\Omega_{\text{per}}) \tag{37}$$

where

$$\mathbf{H}^h_{per}(\tilde{c}) = \Big\{ \mathbf{w}^h \in \mathbf{H}^1(\tilde{c}) : \mathbf{w}^h(-1, x_2) = \mathbf{w}^h(1, x_2), \quad \mathbf{w}^h(x_1, -1) = \mathbf{w}^h(x_1, 1)$$

$$\text{and} \quad \mathbf{w}^h|_\tau \in (\mathcal{P}_p)^2, \quad \tau \in \tilde{T} \Big\},$$

$\mathbf{u}_{\text{I}}^h$ denotes a continuous piecewise $p$-degree interpolant of the exact solution $\mathbf{u}$.

Select the solution $\mathbf{z}^h$ of (37) which satisfies

$$\int_{\tilde{c}} \mathbf{z}^h = \int_{\tilde{c}} (\mathbf{u} - \mathbf{u}_{\text{I}}^h) \tag{38}$$

and define

$$\mathbf{u}^h = \mathbf{u}_{\text{I}}^h + \mathbf{z}^h \quad ; \qquad \mathbf{e}^h = (\mathbf{u} - \mathbf{u}_{\text{I}}^h) - \mathbf{z}^h \,. \tag{39}$$

Thus from (39) the finite-element solution $\mathbf{u}^h$ and the exact error $\mathbf{e}^h$ are obtained; then for a given estimator the effectivity index can be computed using $\mathbf{u}^h$, $\mathbf{e}^h$ namely

$\kappa_{\omega_0^h} = \kappa_{\omega_0^h}$ (material coeff., grid-material orientation, pattern, solution coeff.)

*3. Numerical optimization*

Let

$$C_U^{\omega_0^h} = \max_{\text{material coeff.}} \max_{\text{solution coeff.}} \kappa_{\omega_0^h} , \qquad C_L^{\omega_0^h} = \min_{\text{material coeff.}} \min_{\text{solution coeff.}} \kappa_{\omega_0^h} \tag{40}$$

The bounds $C_U^{\omega_0^h}$, $C_L^{\omega_0^h}$ for a given class of solutions and materials, a given pattern and for a given grid-material orientation can be computed using numerical optimization. The robustness of the estimator in $\omega_0^h \subseteq \omega_s^h$ is computed from

$$\left.\begin{aligned} \mathcal{R}_{\omega_0^h} &:= \max_{s=1,2,3,\ldots} \mathcal{R}^s_{\omega_0^h} , \\ \mathcal{R}^s_{\omega_0^h} &:= \max\left\{ \left( |1 - C_U^{\omega_0^h}| + |1 - C_L^{\omega_0^h}| \right) , \quad \left( |1 - \frac{1}{C_U^{\omega_0^h}}| + |1 - \frac{1}{C_L^{\omega_0^h}}| \right) \right\} \end{aligned}\right\} \tag{41}$$

The robustness of the estimator for the mesh $T_h$ can then be determined from

$$\mathcal{R}_{T_h} := \max_{\substack{\omega_0^h = \omega_X \\ X \in \mathcal{N}_{int}(T_h)}} \mathcal{R}_{\omega_0^h} \tag{42}$$

Here $\mathcal{N}_{int}(T_h)$ denotes the *interior vertices* of the mesh (the vertices must be separated by two (or more) layers of elements from the boundary of the domain and from material-interfaces).

Let us underline the reason for the optimization. In general we know *only* that the solution satisfies the differential equation, e.g. it is harmonic (when $f = 0$). Hence we wish that the effectivity index is small for the entire considered class. From the results of the theoretical study (see [16]) we can restrict the class of functions to homogeneous harmonic polynomials of degree $(p+1)$ only. Establishing the bounds for the classes of meshes and solutions of interest is essential for judging the robustness of an estimator.

**Remark 5.1.** Note that the methodology assumes that the local mesh-size $h$ is sufficiently small so that the exact solution $u$ can be replaced by its local Taylor expansion of degree $(p+1)$ (the validity of the methodology is asymptotic). However numerical studies show (see Section 6.2 below) that

the robustness index governs the performance of estimators in the range of the practical engineering computations which often employ relatively coarse grids.

# 6. Numerical studies of robustness of various error-estimators

We present examples of the application of the methodology described earlier to study the robustness of several error estimators, namely:

1. Implicit element residual (Est. 1) (Eqs. (17)-(21)).
2. Implicit element residual with equilibration (Est. 2) (Eqs. (17)-(32)).
3. Estimators based on smoothening or *Z-Z estimators* (Est. 3) (Eqs. (33)-(36)).

Note that in [16] we also studied the performance of several other estimators (explicit element-residual, subdomain-residual etc.).

We now proceed to the discussion of the numerical studies.

## 6.1 The robustness index for polynomial solutions

Here we address three questions:

1) How many layers of elements should be taken around the cell $\omega_0^h$, for the values of $C_U^{\omega_0^h}$, $C_L^{\omega_0^h}$, $\mathcal{R}_{\omega_0^h}$ to be practically independent of the surrounding mesh in the periodic super-patch $\tilde{c}$?

2) How much do $C_U^{\omega_0^h}$, $C_L^{\omega_0^h}$ and $\mathcal{R}_{\omega_0^h}$ computed from a periodic super-patch which includes $\omega_s^h$ ($s = 3$ for meshes of triangles and $s = 4$ for meshes of quadrilaterals) differ from the same quantities computed from the entire original mesh?

3) What is the robustness index for the various estimators?

We will consider the interior-patterns (cell/patch combinations) shown in Figs. 7 and 6 which occur in the meshes shown in Figs. 1 and 3, respectively.

For the scalar elliptic problem we chose the exact solution to be either a *general (homogeneous) polynomial* of degree $(p+1)$

$$Q^G(x_1, x_2) = \sum_{i,j} a_{ij}\, x_1^i x_2^j\,, \qquad i+j = p+1\,, \qquad i,j \geq 0 \tag{43}$$

or a *"harmonic" polynomial* by imposing the constraint $\sum_{k,\ell=1}^{2} D_k(K_{k\ell} D_\ell Q^H) = 0$; for example for $K_{k\ell} = \delta_{k\ell}$ we have

$$Q^H(x_1, x_2) = a_1(x_1^2 - x_2^2) + a_2\, x_1 x_2\,, \qquad \text{for } \; p+1 = 2 \tag{44a}$$

and

$$Q^H(x_1, x_2) = a_1(x_1^3 - 3x_1 x_2^2) + a_2(3x_1^2 x_2 - x_2^3)\,, \qquad \text{for } \; p+1 = 3 \tag{44b}$$

In the case of the vector-valued model problem (linear elasticity) we employed homogeneous "harmonic" polynomial solutions of degree $(p+1)$

$$\mathbf{Q}^H \in (\hat{\mathcal{P}}_{p+1})^2 \; : \quad \sum_{j=1}^{2} D_j(\sigma_{ij}(\mathbf{Q}^H)) = 0\,, \quad i = 1,2 \tag{45}$$

We determined the robustness index of the error estimators for the cells $\omega_0^h$ using the approach of the paper. In Table 1 we give the values of $C_L^{\omega_0^h}$, $C_U^{\omega_0^h}$, $\mathcal{R}_{\omega_0^h}$ for Est. 1 for the scalar elliptic problem with $p = 1$, for the pattern 1 (shown in Fig. 6a), when $s = 1, 2, 3, 4, 5$ layers of elements around $\omega_0^h$ are taken in the patch $\omega_s^h$ (see Fig. 8). In Tables 2 and 3 we give the values of $C_L^{\omega_0^h}$, $C_U^{\omega_0^h}$, and $\mathcal{R}^s_{\omega_0^h}$ ($s = 3$ for the meshes of triangles and $s = 4$ for the meshes of quadrilaterals) for the Est. 1, Est. 2, and Est. 3 for the scalar elliptic problem with $p = 1$ and 2 respectively. These are compared with the values of the effectivity indices $\bar{C}_L^{\omega_0^h}$, $\bar{C}_U^{\omega_0^h}$ and $\bar{\mathcal{R}}$ ($\bar{\mathcal{R}}$ is obtained by substituting $\bar{C}_L^{\omega_0^h}$, $\bar{C}_U^{\omega_0^h}$ into (5a)) obtained from the finite-element solution of a Dirichlet boundary-value problem using the grids shown in Figs. 1, 3 (the *big mesh*) with data consistent with the homogeneous polynomial solutions which give the extremal values $C_L^{\omega_0^h}$, $C_U^{\omega_0^h}$ of the effectivity index $\kappa_{\omega_0^h}$ in the periodic super-patch calculations. The periodic super-patches employed for the various patterns were constructed using a mesh-generator, as shown in Fig. 4. In Table 4 a similar

comparison is made for isotropic elasticity (Poisson's ratio $\nu = 0.3$) using meshes of triangles.

From the reported data we can make the following conclusions related to the questions formulated above:

1) For linear elements the values of $C_L^{\omega_0^h}$, $C_U^{\omega_0^h}$, $\mathcal{R}_{\omega_0^h}$ in the cell $\omega_0^h$ do not practically change when the patch $\omega_s^h$ has $s \geq 3$ layers of elements around the cell $\omega_0^h$. For higher order elements, a smaller $s$ can be taken, i.e. $s$ = 1-2 (thus for our numerical experiments, we considered patches with $s = 3$ for the meshes of triangles and $s = 4$ for the meshes of quadrilaterals).

2) For a given exact solution which is a homogeneous polynomial (harmonic or general) of degree $(p+1)$ the values of $C_L^{\omega_0^h}$, $C_U^{\omega_0^h}$, obtained from a periodic super-patch are very close to the values $\bar{C}_L^{\omega_0^h}$, $\bar{C}_U^{\omega_0^h}$ obtained from the approximate solution of a boundary-value problem (with data compatible with the polynomial solutions which correspond to the extrema of the effectivity index in the periodic super-patch) obtained using the big mesh. Note that we did not exactly answer question 2 because we did not perform the optimization in the big mesh; however the numerical experience from [16] indicates that $\bar{C}_L^{\omega_0^h}$, $\bar{C}_U^{\omega_0^h}$ are very close to the extremal values of the effectivity index when the optimization is performed in the big mesh.

3a) The element-residual without equilibration (Est. 1) is not robust for the general meshes (like the meshes shown in Fig. 1 and Fig. 3) and should not be used.

3b) The equilibration of the flux increases significantly the robustness of the element-residual estimators.

3c) The $Z$-$Z$ estimator appears to be the most robust.

## 6.2 The robustness index for general solutions

In Section 6.1 above, we assumed that the exact solution is a (homogeneous) polynomial of degree $(p+1)$. The following question arises:

Are the conclusions based on the assumption that the solution is a polynomial valid for general solutions?

We now give an example which shows that the results on the robustness of estimators obtained using polynomials of degree $(p+1)$ give a good indication of the local performance of the estimators for any general solution (it is assumed that the mesh is sufficiently refined near singular points so that global modes of the error (pollution-error) are controlled; see [16], [18] for the details). Let us consider the general solution

$$u(x_1,x_2) = (r_1(x_1,x_2))^{\frac{2}{3}} \sin\Big(\frac{2}{3}\theta_1(x_1,x_2)\Big) + \Big(r_2(x_1,x_2)\Big)^{\frac{1}{2}} \sin\Big(\frac{1}{2}\theta_2(x_1,x_2)\Big)$$

where

$$r_1(x_1,x_2) = \Big[(x_1-\frac{1}{2})^2 + (x_2-3)^2\Big]^{\frac{1}{2}}\,, \qquad \theta_1(x_1,x_2) = \tan^{-1}\Big(\frac{x_2-3}{x_1-\frac{1}{2}}\Big)\,,$$

$$r_2(x_1,x_2) = \Big[(x_1-3)^2 + (x_2-\frac{1}{2})^2\Big]^{\frac{1}{2}}\,, \qquad \theta_2(x_1,x_2) = \tan^{-1}\Big(\frac{x_2-\frac{1}{2}}{x_1-3}\Big)\,,$$

we let $\Omega = (0,1)\times(0,1)$ and let $T_h$ be the grid shown in Fig. 6. We solved the Neumann boundary-value problem in $\Omega$ using $T_h$ (the big mesh) and data consistent with the exact solution given above and we computed the effectivity index for Est. 1, Est. 2 and Est. 3 for five of the patterns shown in Fig. 6. We also computed the effectivity index in the cells $\omega_0^h$ by:

a) Solving the Neumann problem in $\Omega$ using the grid $T_h$ with data corresponding to the local Taylor-expansion (up to quadratic degree) about the central node $X$ of the cell $\omega_0^h \equiv \omega_X$ .

b) By using the local Taylor-expansion (about the central node of the patch) as exact solution in the periodic boundary-value problem (37) over the periodic super-patches for the patterns shown in Figs. 6a-6e (patterns 1-5).

The effectivity indices for the cells calculated from the approximate solution (which was obtained using the three different ways stated above) are given in Table 5.

We observe that the effectivity indices obtained using the approximate solution (computed from the big mesh $T_h$) of the Neumann boundary-value problem formulated using data obtained either from the general solution

or from its local Taylor series expansion are essentially identical. The results obtained using the local Taylor series expansion and the periodic boundary-value problem (37) are also very close to the values obtained from the other two types of problems; still better agreement could be obtained by increasing the number of layers $s$ in $\omega_s^h$ (here we have used $s = 3$ layers).

# 7. Summary of conclusions

1. The validation of the performance of the estimators based on the robustness index allows objective comparisons between the various error estimators.

2. A numerical methodology for computing the robustness index is given.

3. The methodology takes directly into account the factors which affect the performance of estimators namely the geometry of the grid, the differential operator and the nature of the solution. The methodology has theoretical basis (see [16]) and can be used to study the robustness of error estimators for the complex grids which are used in engineering computations.

4. The methodology allows one to check the quality of any new estimator even if it is only available as a black-box computer subroutine.

5. It is possible to use the methodology to maximize the robustness of a given estimator for a class of meshes of interest.

6. The methodology addresses the robustness index for the estimators for elements in the interior of the domain and smooth solutions. The case of unsmooth solutions and elements at the boundary will be addressed in a forthcoming paper.

7. The $Z$-$Z$ estimator seems to be the most robust and is rather insensitive to the selection at the sampling points (see also [17]).

8. The element residual estimators should be used only with equilibration.

We remark that the conclusions made above are related to the use of general meshes. Use of families of particular meshes could influence the conclusions.

## Acknowledgement

This work was supported by the U.S. Army Research Office under Grant DAAL03-G-028. This paper summarized joint work of the authors with Professor Ivo Babuška of the University of Maryland (see also [16]-[17]). The authors would like to take this opportunity to thank Professor Babuška for the advice which made this research possible.

## References

[1] I. BABUŠKA and W.C. RHEINBOLDT, "Error estimates for adaptive finite element computations", *SIAM J. Numer. Anal.*, **15**, 736-754, 1978.

[2] I. BABUŠKA and W.C. RHEINBOLDT, "Reliable error estimation and mesh adaptation for the finite element method", in: *Computational Methods in Nonlinear Mechanics*, edited by J.T. ODEN, North Holland, Amsterdam, 1980, pp. 67-108.

[3] P. LADEVEZE and D. LEGUILLON, "Error estimate procedure in the finite element method and applications", *SIAM J. Numer. Anal.* **20** (3), 485-509, 1983.

[4] R.E. BANK and A. WEISER, "Some a posteriori error estimators for elliptic partial differential equations", *Math. Comp.* **44**, 283-301, 1985.

[5] I. BABUŠKA and A. MILLER, "A feedback finite element method with a posteriori error estimation: Part I. The finite element method and some basic properties of the a posteriori error estimator", *Comput. Methods Appl. Mech. Engrg.* **61**, 1-40, 1987.

[6] J.T. ODEN, L. DEMKOWICZ, W. RACHOWICZ and T.A. WESTERMANN, "Toward a universal h-p adaptive finite element strategy: Part 2, A posteriori error estimates", *Comput. Methods Appl. Mech. Engrg.* **77**, 113-180, 1989.

[7] T.A. WESTERMANN, "A Posteriori Estimation of Errors in hp Finite Element Methods for Linear Elliptic Boundary Value Problems", *M.Sc. Thesis*, The University of Texas at Austin, Austin, Texas, 1989.

[8] O.C. ZIENKIEWICZ and J.Z. ZHU, "The superconvergent patch recovery and a posteriori error estimates. Part 1: The recovery technique", *Internat. J. Numer. Methods Engrg.* **33**, 1331-1364, 1992.

[9] O.C. ZIENKIEWICZ and J.Z. ZHU, "The superconvergent patch recovery and a posteriori error estimates. Part 2: Error estimates and adaptivity", *Internat. J. Numer. Methods Engrg.* **33**, 1365-1382, 1992.

[10] T. STROUBOULIS and K.A. HAQUE, "Recent experiences with error estimation and adaptivity, Part I: Review of error estimators for scalar elliptic problems", *Comput. Methods Appl. Mech. Engrg.* **97**, 399-436, 1992.

[11] T. STROUBOULIS and K.A. HAQUE, "Recent experiences with error estimation and adaptivity, Part II: Error estimation for h-adaptive approximations on grids of triangles and quadrilaterals," *Comput. Methods Appl. Mech. Engrg.* **100**, 359-430, 1992.

[12] M. AINSWORTH and J.T. ODEN, "A procedure for a posteriori error estimation for h-p finite element methods", *Comput. Methods Appl. Mech. Engrg.* **101**, 73-96, 1992.

[13] I. BABUŠKA, R. DURÁN and R. RODRIGUEZ, "Analysis of the efficiency of an a-posteriori error estimator for linear triangular finite elements", *SIAM J. Numer. Anal.* **29** (4), 947-964, 1992.

[14] I. BABUŠKA, L. PLANK and R. RODRIGUEZ, "Quality assessment of the a-posteriori error estimation in finite elements", *Finite Elements in Analysis and Design* **11**, 285-306, 1992.

[15] I. BABUŠKA, L. PLANK and R. RODRIGUEZ, "Basic problems of a-posteriori error estimation", *Comput. Methods Appl. Mech. Engrg.* **101**, 97-112, 1992.

[16] I. BABUŠKA, T. STROUBOULIS and C.S. UPADHYAY, "A model study of the quality of a-posteriori estimators for linear elliptic problems, Part Ia: Error estimation in the interior of patchwise uniform grids of triangles", Comput. Methods Appl. Mech. Engrg., 1994, to appear.

[17] I. BABUŠKA, T. STROUBOULIS, C.S. UPADHYAY, S.K. GANGARAJ and K. COPPS, "Validation of a-posteriori error estimators by numerical approach", Internat. J. Numer. Methods Engrg., 1994, to appear.

[18] I. BABUŠKA, T. STROUBOULIS, A. MATHUR and C.S. UPADHYAY, "Pollution error in the h-version of the finite-element method and a-posteriori error estimation", in preparation.

[19] P.G. CIARLET, *Basic error estimates for elliptic problems*, in: P.G. Ciarlet and J.L. Lions, eds., Handbook of Numerical Analysis, Vol. II, North-Holland, Amsterdam (1991), pp. 17-351.

| Laplace's Equation, Linear Triangles | | | |
|---|---|---|---|
| Element residual without equilibration (Est. 1) | | | |
| No. of layers, $s$ | Periodic Problem | | |
| | $C_L^{\omega_0^h}$ | $C_U^{\omega_0^h}$ | $\mathcal{R}_{\omega_0^h}^s$ |
| 1 | 1.084 | 1.312 | 0.396 |
| 2 | 1.079 | 1.297 | 0.376 |
| 3 | 1.080 | 1.327 | 0.407 |
| 4 | 1.080 | 1.317 | 0.397 |
| 5 | 1.080 | 1.312 | 0.392 |

**Table 1.** Influence of the size of the patch $\omega_s^h$ on the value of the robustness-index $\mathcal{R}_{\omega_0^h}$ obtained from the periodic super-patch. Laplace's equation, quadratic harmonic polynomial solution, linear elements ($p = 1$). Pattern 1 (shown in Fig. 6a) with $s = 1, 2, 3, 4, 5$ layers around the cell $\omega_0^h$ (as shown in Fig. 5) is employed in the computation of the robustness for Est. 1.

| Laplace's Equation, Linear Triangles | | | | | | |
|---|---|---|---|---|---|---|
| Pattern | Periodic Problem | | | Dirichlet BVP | | |
| Element residual without equilibration (Est. 1) | | | | | | |
| | $C_L^{\omega_0^h}$ | $C_U^{\omega_0^h}$ | $\mathcal{R}^3_{\omega_0^h}$ | $\bar{C}_L^{\omega_0^h}$ | $\bar{C}_U^{\omega_0^h}$ | $\bar{\mathcal{R}}$ |
| 1 | 1.080 | 1.312 | 0.392 | 1.080 | 1.308 | 0.388 |
| 2 | 1.041 | 1.418 | 0.459 | 1.028 | 1.413 | 0.441 |
| 3 | 0.998 | 1.011 | 0.013 | 0.999 | 1.014 | 0.015 |
| 4 | 0.996 | 1.128 | 0.132 | 0.983 | 1.116 | 0.133 |
| 5 | 0.960 | 1.701 | 0.741 | 0.954 | 1.701 | 0.747 |
| Element residual with equilibration (Est. 2) (Ladeveze's equilibration, eq. (32)) | | | | | | |
| 1 | 0.993 | 0.999 | 0.008 | 0.986 | 0.999 | 0.015 |
| 2 | 0.999 | 1.003 | 0.004 | 0.977 | 0.999 | 0.025 |
| 3 | 0.989 | 1.026 | 0.037 | 0.991 | 1.030 | 0.039 |
| 4 | 0.980 | 1.016 | 0.036 | 0.963 | 1.010 | 0.048 |
| 5 | 0.923 | 1.069 | 0.148 | 0.916 | 1.070 | 0.157 |
| 6 | 0.913 | 0.993 | 0.102 | 0.917 | 0.999 | 0.092 |
| 7 | 0.999 | 1.001 | 0.002 | 0.999 | 1.001 | 0.002 |
| $ZZ$ estimator (Est. 3) | | | | | | |
| 1 | 1.004 | 1.012 | 0.016 | 1.004 | 1.005 | 0.009 |
| 2 | 0.995 | 1.035 | 0.040 | 0.992 | 1.021 | 0.029 |
| 3 | 0.989 | 0.994 | 0.015 | 0.993 | 0.995 | 0.012 |
| 4 | 0.958 | 1.005 | 0.049 | 0.941 | 0.999 | 0.064 |
| 5 | 0.982 | 1.013 | 0.031 | 0.978 | 1.010 | 0.032 |
| 6 | 0.926 | 0.998 | 0.082 | 0.930 | 1.004 | 0.079 |
| 7 | 0.979 | 1.005 | 0.026 | 0.979 | 1.005 | 0.026 |

**Table 2a.** Accuracy of the methodology for general meshes: Laplace's equation, quadratic harmonic polynomial solution, linear elements ($p = 1$). The mesh of triangles shown in Fig. 3 and the patterns 1-7 shown in Figs. 6a-6g are employed in the computation of the robustness.

| Laplace's Equation, Bilinear Quadrilaterals | | | | | | |
|---|---|---|---|---|---|---|
| Element residual without equilibration (Est. 1) | | | | | | |
| Pattern | Periodic Problem | | | Dirichlet BVP | | |
| | $C_L^{\omega_0^h}$ | $C_U^{\omega_0^h}$ | $\mathcal{R}^4_{\omega_0^h}$ | $\bar{C}_L^{\omega_0^h}$ | $\bar{C}_U^{\omega_0^h}$ | $\bar{\mathcal{R}}$ |
| 1 | 1.096 | 1.323 | 0.420 | 1.113 | 1.298 | 0.412 |
| 2 | 1.051 | 1.577 | 0.628 | 1.053 | 1.561 | 0.616 |
| 3 | 1.114 | 1.882 | 0.996 | 1.131 | 1.896 | 1.027 |
| 4 | 1.218 | 2.240 | 1.458 | 1.189 | 2.261 | 1.450 |
| 5 | 1.340 | 2.210 | 1.550 | 1.298 | 2.224 | 1.524 |
| Element residual with equilibration (Est. 2) (Bank & Weiser equilibration, eq. (30)) | | | | | | |
| 1 | 0.819 | 0.978 | 0.243 | 0.813 | 0.979 | 0.251 |
| 2 | 0.833 | 0.999 | 0.201 | 0.852 | 1.011 | 0.185 |
| 3 | 0.776 | 0.979 | 0.310 | 0.784 | 0.988 | 0.288 |
| 4 | 0.731 | 0.953 | 0.417 | 0.749 | 0.976 | 0.360 |
| 5 | 0.702 | 0.947 | 0.480 | 0.715 | 0.965 | 0.435 |
| $ZZ$ estimator (Est. 3) | | | | | | |
| 1 | 1.010 | 1.022 | 0.032 | 1.011 | 1.029 | 0.040 |
| 2 | 1.008 | 1.017 | 0.025 | 1.008 | 1.018 | 0.026 |
| 3 | 0.991 | 1.033 | 0.042 | 0.998 | 1.033 | 0.035 |
| 4 | 0.978 | 1.016 | 0.038 | 0.980 | 1.014 | 0.034 |
| 5 | 0.938 | 0.999 | 0.067 | 0.940 | 1.001 | 0.065 |

**Table 2b.** Accuracy of the methodology for general meshes: Laplace's equation, quadratic harmonic polynomial solution, linear elements ($p = 1$). The mesh of quadrilaterals shown in Fig. 1 and the patterns 1-5 shown in Figs. 7a-7e are employed in the computation of the robustness.

| Laplace's Equation, Quadratic Triangles | | | | | | |
|---|---|---|---|---|---|---|
| Element residual with equilibration (Est. 2) (Ladeveze's equilibration, eq. (32)) | | | | | | |
| Pattern | Periodic Problem | | | Dirichlet BVP | | |
| | $C_L^{\omega_0^h}$ | $C_U^{\omega_0^h}$ | $\mathcal{R}^3_{\omega_0^h}$ | $\bar{C}_L^{\omega_0^h}$ | $\bar{C}_U^{\omega_0^h}$ | $\bar{\mathcal{R}}$ |
| 1 | 0.960 | 1.032 | 0.073 | 0.960 | 1.032 | 0.073 |
| 2 | 0.982 | 1.009 | 0.027 | 0.978 | 1.008 | 0.030 |
| 3 | 1.011 | 1.021 | 0.032 | 1.010 | 1.021 | 0.032 |
| 4 | 0.973 | 1.011 | 0.039 | 0.973 | 1.011 | 0.039 |
| 5 | 0.718 | 0.894 | 0.511 | 0.718 | 0.894 | 0.511 |
| 6 | 0.806 | 1.035 | 0.275 | 0.811 | 1.035 | 0.267 |
| 7 | 0.998 | 1.007 | 0.009 | 0.997 | 1.006 | 0.009 |
| $ZZ$ estimator (Est. 3) | | | | | | |
| Pattern | Periodic Problem | | | Dirichlet BVP | | |
| | $C_L^{\omega_0^h}$ | $C_U^{\omega_0^h}$ | $\mathcal{R}^3_{\omega_0^h}$ | $\bar{C}_L^{\omega_0^h}$ | $\bar{C}_U^{\omega_0^h}$ | $\bar{\mathcal{R}}$ |
| 1 | 0.969 | 0.995 | 0.037 | 0.969 | 0.995 | 0.037 |
| 2 | 0.919 | 0.935 | 0.158 | 0.915 | 0.933 | 0.165 |
| 3 | 1.001 | 1.060 | 0.061 | 1.001 | 1.060 | 0.061 |
| 4 | 1.006 | 1.044 | 0.050 | 1.005 | 1.043 | 0.048 |
| 5 | 0.875 | 0.933 | 0.215 | 0.875 | 0.933 | 0.215 |
| 6 | 0.854 | 0.923 | 0.254 | 0.854 | 0.923 | 0.254 |
| 7 | 0.978 | 0.979 | 0.044 | 0.977 | 0.979 | 0.045 |

**Table 3.** Accuracy of the methodology for general meshes: Laplace's equation, cubic harmonic polynomial solution, quadratic elements ($p = 2$). The mesh of triangles shown in Fig. 3 and the patterns 1-7 shown in Figs. 6a-6g are employed in the computation of the robustness.

| Isotropic Elasticity, Linear Triangles | | | | | | |
|---|---|---|---|---|---|---|
| Element residual with equilibration (Est. 2) (Ladeveze's equilibration, eq. (32)) | | | | | | |
| Pattern | Periodic Problem | | | Dirichlet BVP | | |
| | $C_L^{\omega_0^h}$ | $C_U^{\omega_0^h}$ | $\mathcal{R}^3_{\omega_0^h}$ | $\bar{C}_L^{\omega_0^h}$ | $\bar{C}_U^{\omega_0^h}$ | $\bar{\mathcal{R}}$ |
| 1 | 0.965 | 1.033 | 0.068 | 0.949 | 1.000 | 0.054 |
| 3 | 0.959 | 1.049 | 0.090 | 0.951 | 1.048 | 0.097 |
| 4 | 0.875 | 1.037 | 0.179 | 0.899 | 1.005 | 0.117 |
| 5 | 0.853 | 1.195 | 0.342 | 0.856 | 1.190 | 0.334 |
| $ZZ$ estimator (Est. 3) | | | | | | |
| Pattern | Periodic Problem | | | Dirichlet BVP | | |
| | $C_L^{\omega_0^h}$ | $C_U^{\omega_0^h}$ | $\mathcal{R}^3_{\omega_0^h}$ | $\bar{C}_L^{\omega_0^h}$ | $\bar{C}_U^{\omega_0^h}$ | $\bar{\mathcal{R}}$ |
| 1 | 0.992 | 1.054 | 0.062 | 0.992 | 1.027 | 0.035 |
| 3 | 0.943 | 1.004 | 0.064 | 0.955 | 1.004 | 0.051 |
| 4 | 0.944 | 1.002 | 0.061 | 0.931 | 0.997 | 0.077 |
| 5 | 0.948 | 1.043 | 0.096 | 0.946 | 1.002 | 0.059 |

**Table 4.** Accuracy of the methodology for general meshes: Isotropic elasticity, quadratic "harmonic" polynomial solution, linear elements ($p = 1$). The mesh of triangles shown in Fig. 3 and the patterns 1, 3, 4, 5 shown in Figs. 6a, c, d, e are employed in the computation of the robustness.

| Laplace's Equation, Linear Triangles | | | | | | | | | |
|---|---|---|---|---|---|---|---|---|---|
| Pattern | Neumann BVP | | | | | | Periodic Problem | | |
| | General solution | | | Taylor series | | | Taylor series | | |
| | $\kappa$ (Est. 1) | $\kappa$ (Est. 2) | $\kappa$ (Est. 3) | $\kappa$ (Est. 1) | $\kappa$ (Est. 2) | $\kappa$ (Est. 3) | $\kappa$ (Est. 1) | $\kappa$ (Est. 2) | $\kappa$ (Est. 3) |
| 1 | 1.219 | 0.993 | 1.006 | 1.220 | 0.993 | 1.006 | 1.228 | 0.999 | 1.013 |
| 2 | 1.293 | 0.995 | 1.006 | 1.293 | 0.995 | 1.006 | 1.298 | 0.998 | 1.009 |
| 3 | 1.007 | 1.015 | 0.992 | 1.007 | 1.015 | 0.992 | 1.006 | 1.014 | 0.991 |
| 4 | 1.085 | 1.003 | 0.990 | 1.086 | 1.003 | 0.991 | 1.098 | 1.015 | 1.003 |
| 5 | 1.316 | 1.031 | 0.983 | 1.317 | 1.031 | 0.983 | 1.316 | 1.034 | 0.987 |

**Table 5.** Applicability of the methodology for general solutions: Laplace's equation, harmonic solution, linear elements ($p = 1$). Comparison of the values of the effectivity index for the cells computed using three different approximate solutions: The solution of a Neumann boundary-value problem in the domain and mesh shown in Fig. 3 with the data taken from the exact solution (Columns 2, 3, 4); the solution of a Neumann boundary-value problem in the domain and mesh shown in Fig. 3 with the data taken from the quadratic Taylor-series expansion about the central-node of the mesh-cell $\omega_0^h$ for which the effectivity index is computed (Columns 5, 6, 7); the solution of a periodic boundary-value problem in super-patches which include the patches shown in Figs. 6a-6e with the data taken from the quadratic Taylor-series expansion about the central node of each of the mesh-cells (Columns 8, 9, 10).

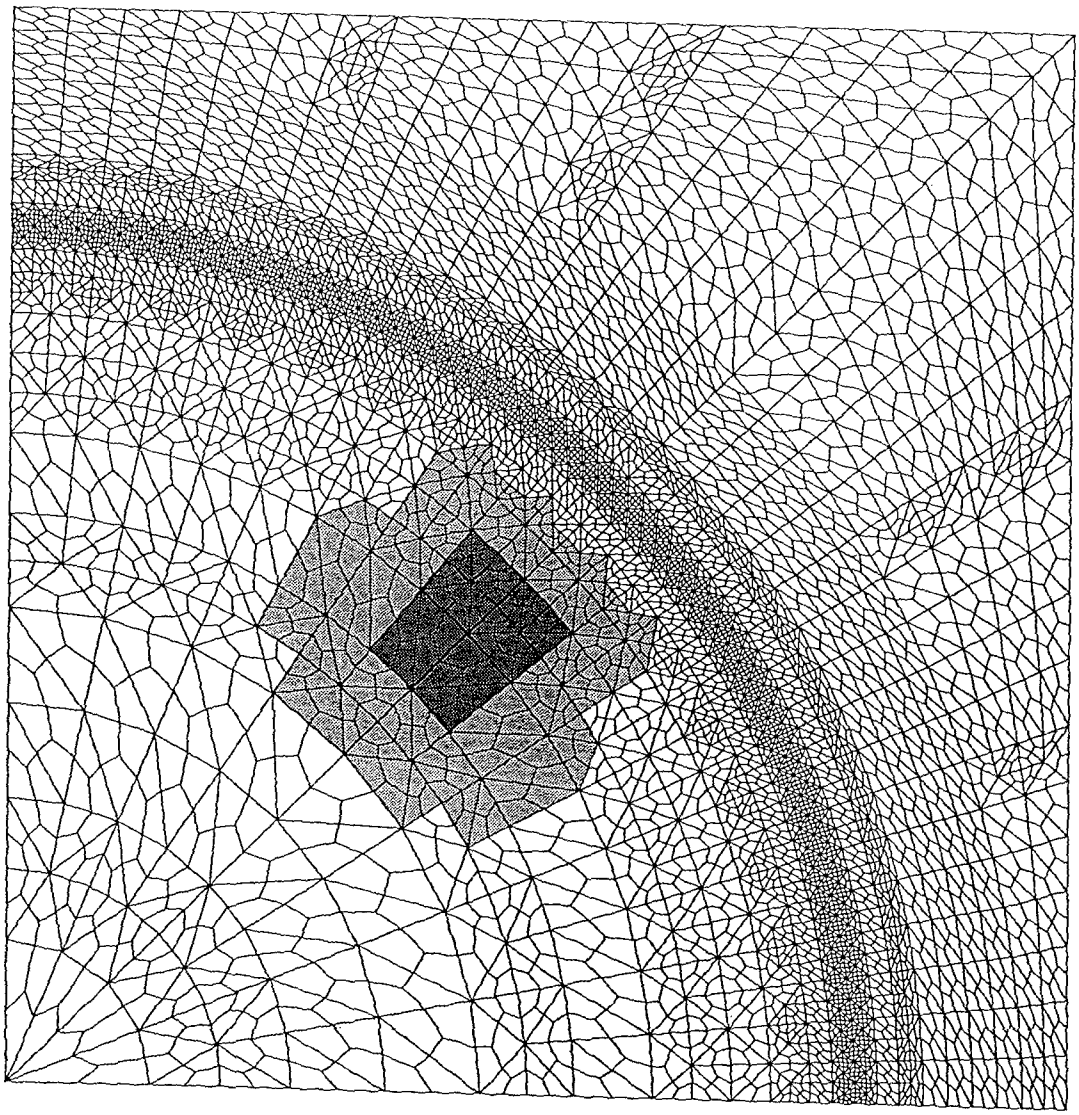
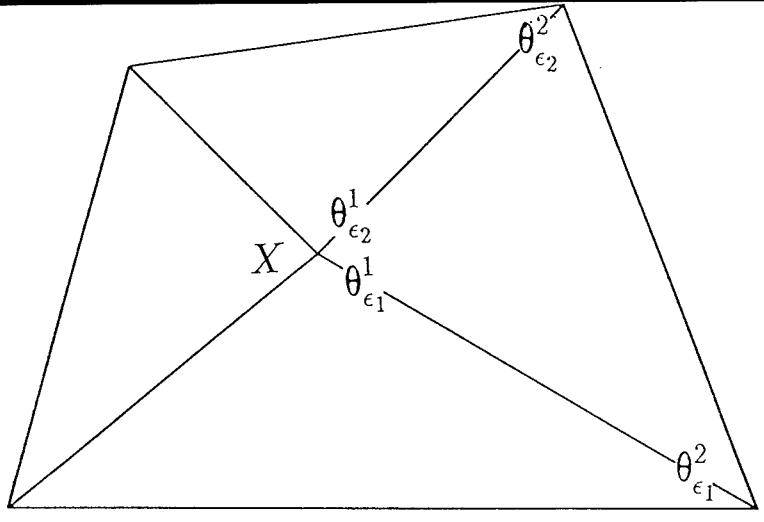
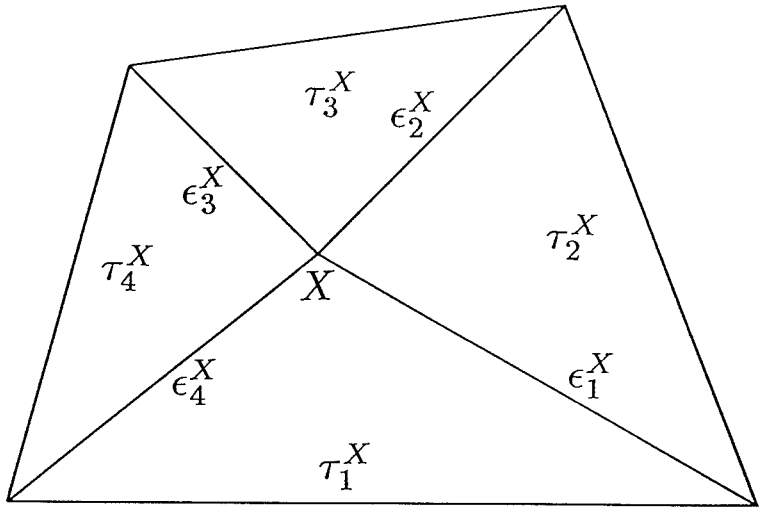


**Figure 1.** The mesh-cell $\omega_0^h$ (dark gray) and the surrounding layers of elements (light gray) which influence the error (and the error-estimator) in $\omega_0^h$.




a




b

**Figure 2.** (a) The vertex $X$ with the elements $\tau_k^X$ and the edges $\epsilon_k^X$ attached to it; (b) The local enumeration for the degrees of freedom of the correction $\boldsymbol{\theta}$ for edges connected to node $X$.

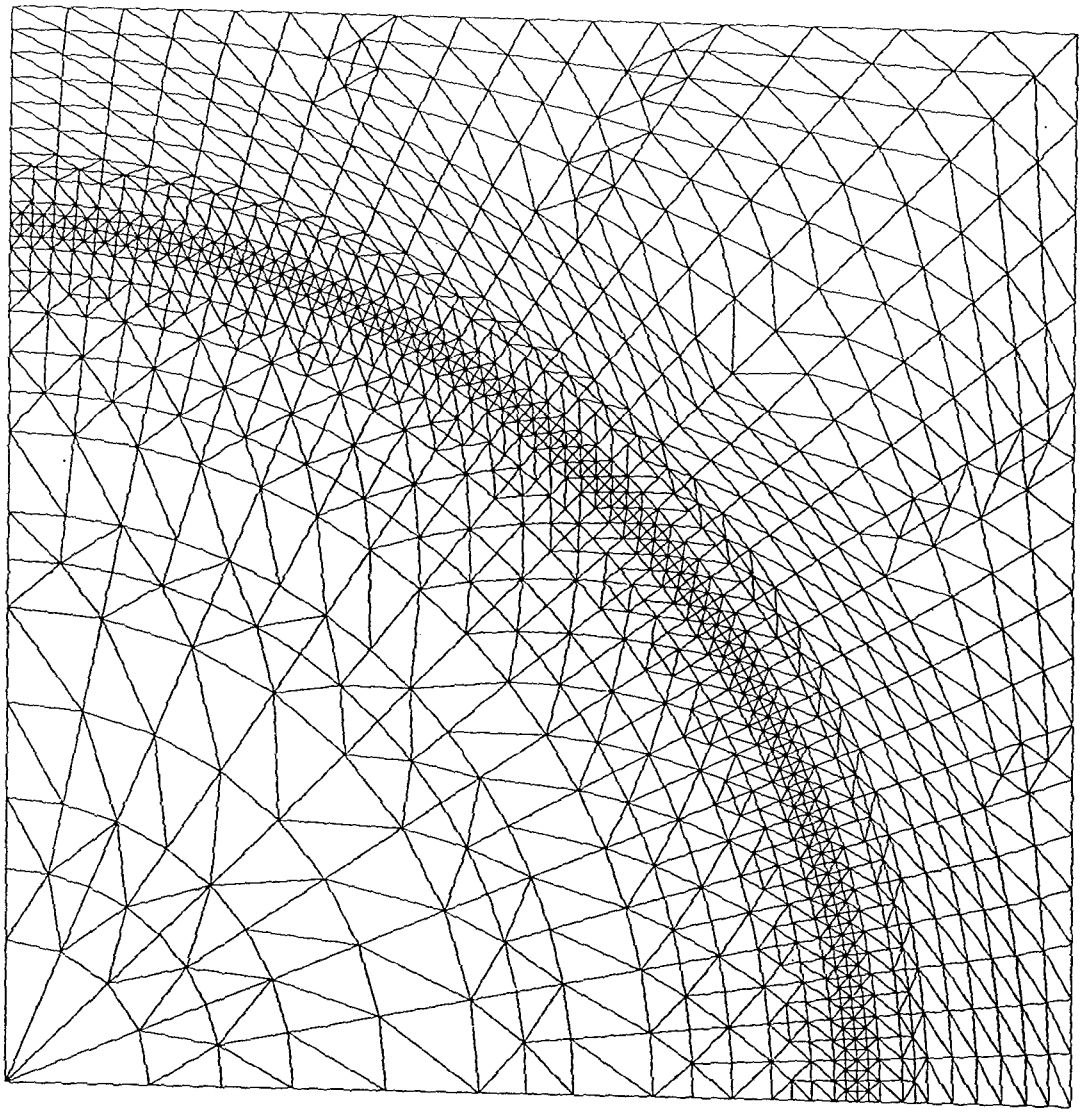
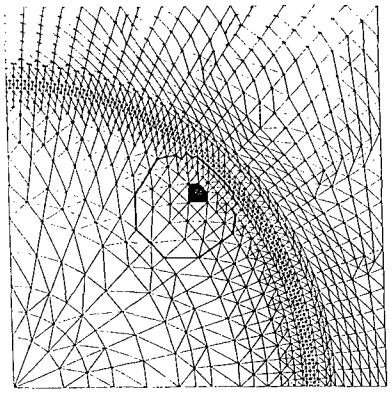
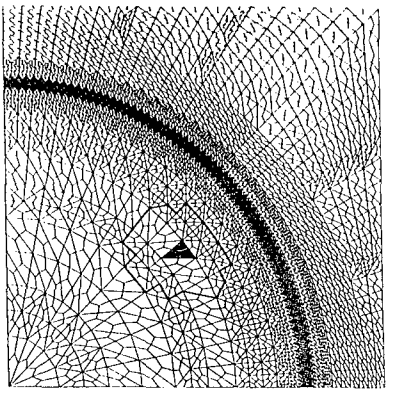


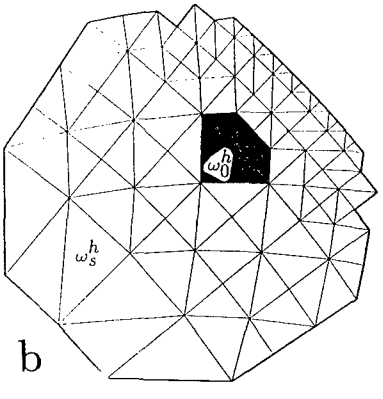
**Figure 3.** Typical example of a general finite-element grid of triangles generated by a commercial mesh-generator.



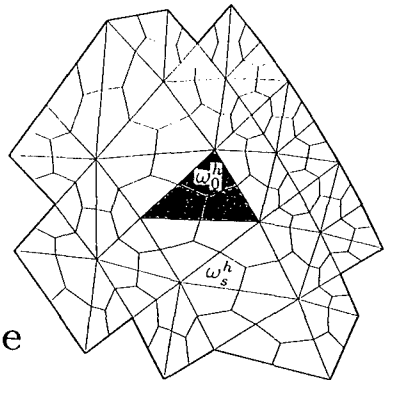
a



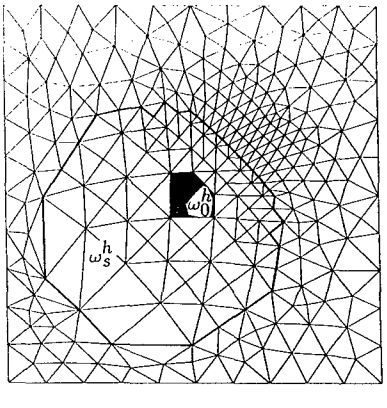
d



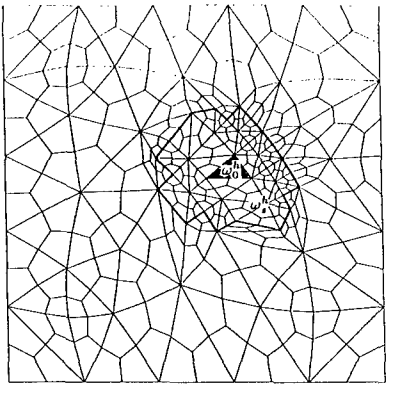

b




e




c




f

**Figure 4.** Extraction of a patch and completion to a periodic super-patch for meshes of triangles and quadrilaterals (a) The actual grid of triangles with the subdomains $\omega_0^h$, $\omega_3^h$; (b) The subdomain $\omega_s^h$ $(s = 3)$ with $\omega_0^h$ in its interior; (c) The subdomain $\omega_s^h$ embedded into a periodic super-patch; (d) The actual grid of quadrilaterals with the subdomains $\omega_0^h$, $\omega_s^h$ $(s = 4)$; (e) The subdomain $\omega_s^h$ with $\omega_0^h$ in its interior; (f) The subdomain $\omega_s^h$ embedded into a periodic super-patch.

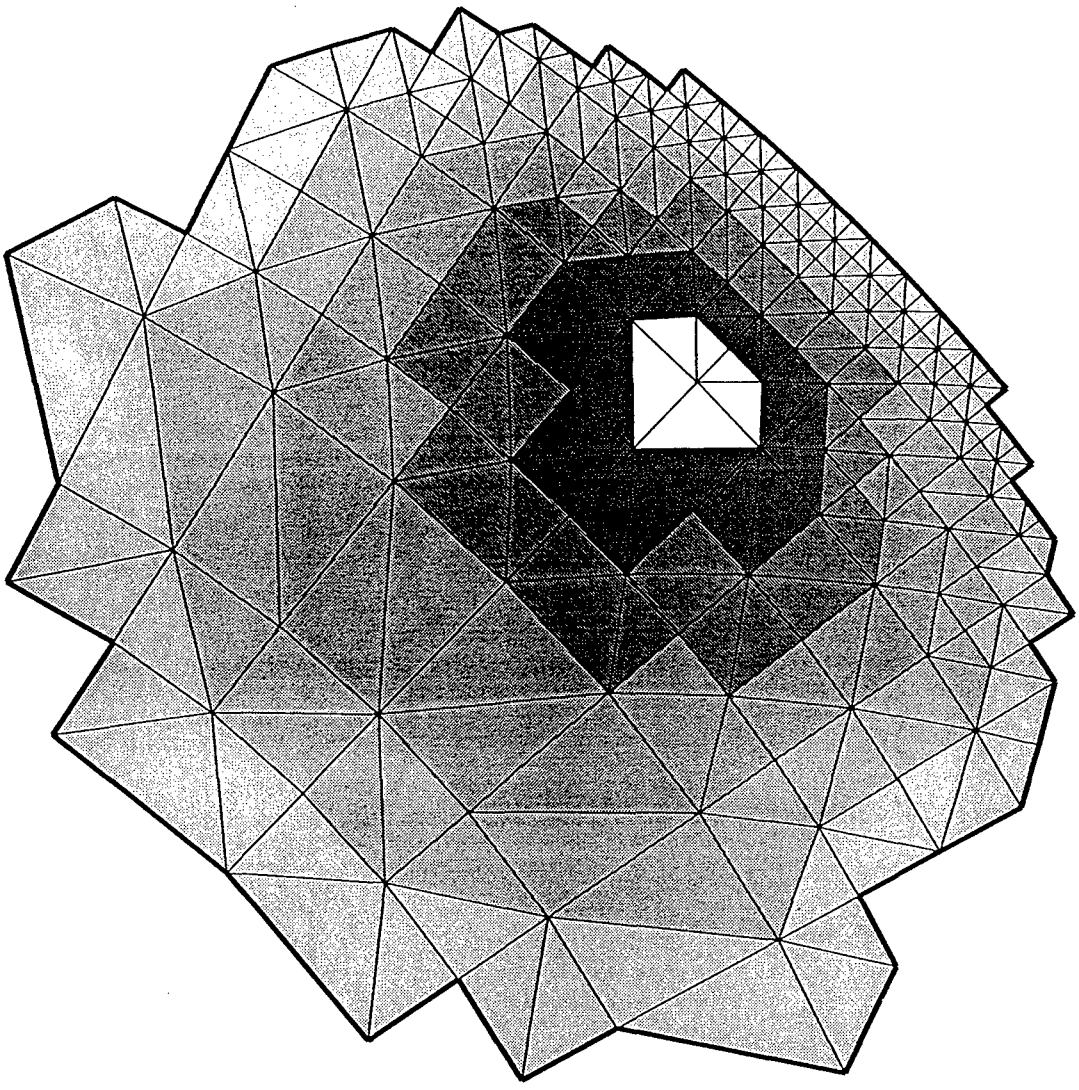


**Figure 5.** Influence of the size of the patch $\omega_s^h$ on the calculation of the robustness-index $\mathcal{R}_{\omega_0^h}$: The cell $\omega_0^h$ (shown without shading) surrounded by several mesh-layers (indicated by various tones of gray shading).

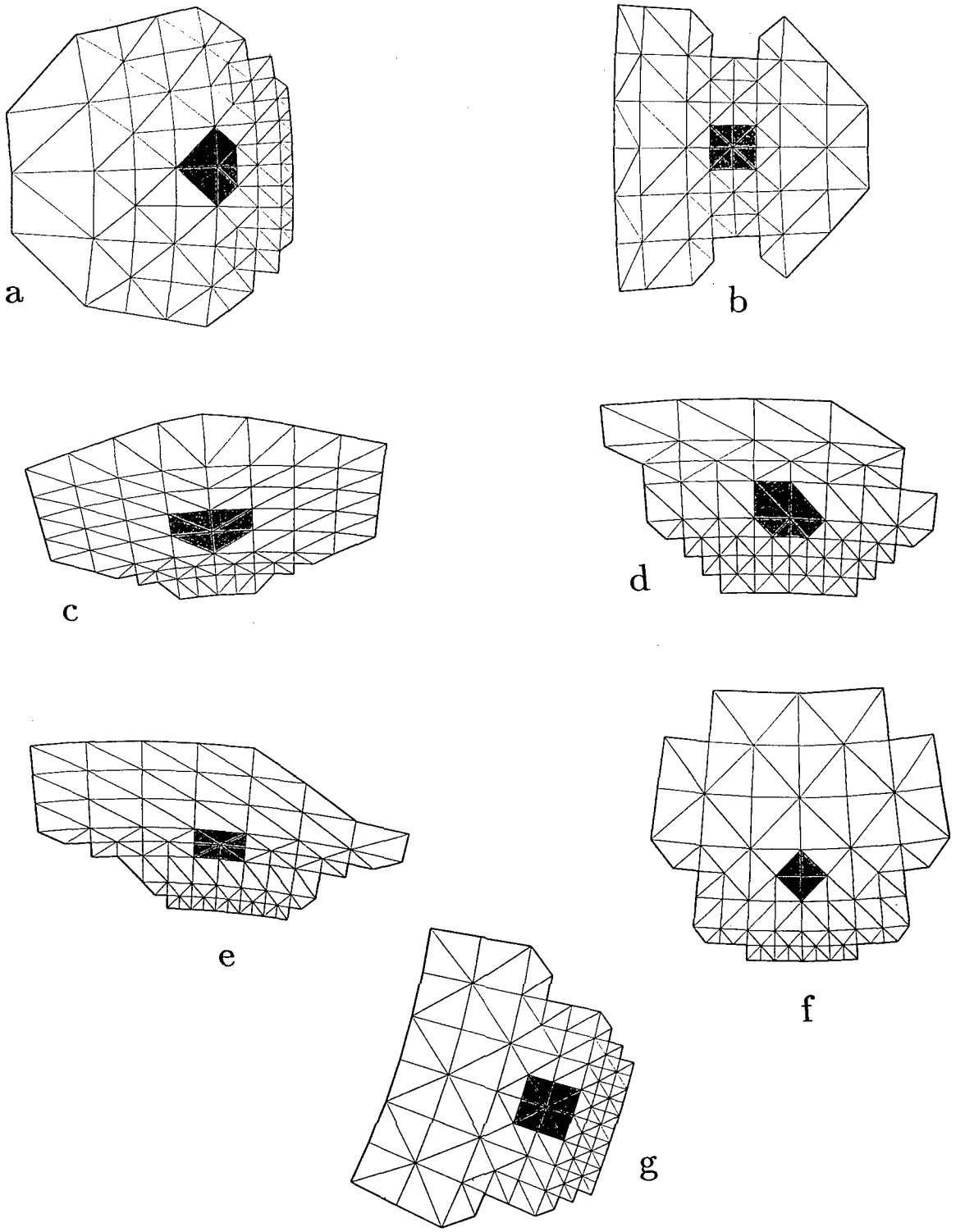



**Figure 6.** General mesh of triangles generated by a commercial mesh-generator (shown in Fig. 3): (a)-(g) Cell/patch combinations (patterns) 1-7. The cell $\omega_0^h$ is shaded gray; the perigram of the patch $\omega_s^h$ ($s = 3$) is shown in thick black line.

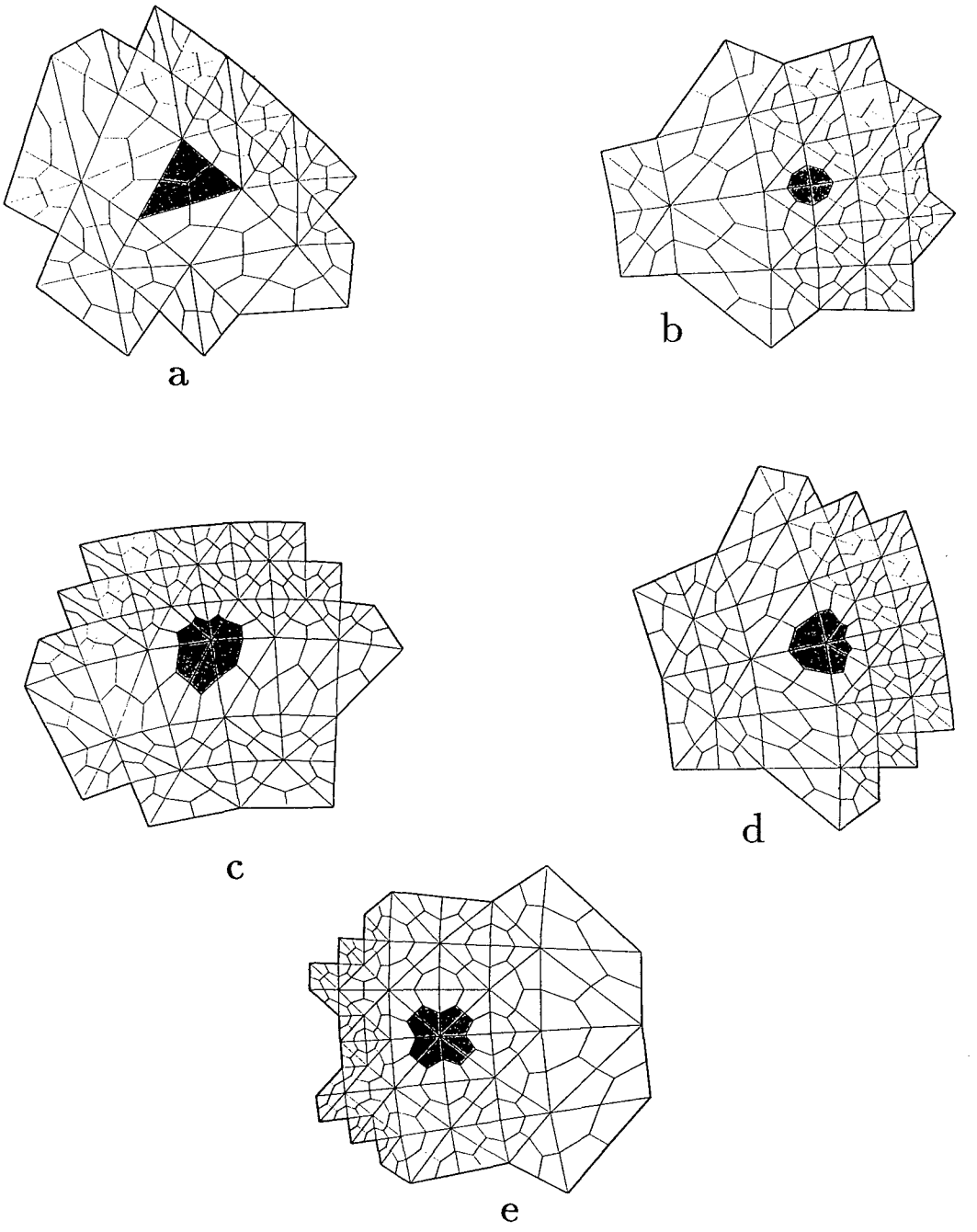



**Figure 7.** General unstructured mesh of quadrilaterals (shown in Fig. 1): Cell/patch combinations (patterns) used in the study of the robustness index for the various estimators. The cell $\omega_0^h$ consists of: (a) 3 elements, (b) 4 elements, (c) 6 elements, (d) 7 elements, (e) 8 elements connected to a node. The cell $\omega_0^h$ is shaded gray; the perigram of the patch $\omega_s^h$ $(s = 4)$ is shown in thick black line.

# Toward the Application of an Adaptive Finite Element Method to the Simulation of Adiabatic Shear Bands

John W.Walter Jr.
U. S. Army Research Laboratory
Weapons Technology Directorate
Aberdeen Proving Ground, Maryland 21005-5066

## 1 Introduction

Adiabatic shear band formation is one of several material damage mechanisms known to be critical to the performance of armor/anti-armor systems under conditions of ballistic impact. Previous experience with a non-adaptive finite element method [1] has shown that extremely large strains ($\gamma \gg 1$), strain rates ($\dot{\gamma} \approx 10^6/\mathrm{s}$) and temperatures ($T \approx T_{\mathrm{melt}}$) may occur during shear band formation. Moreover, even for the unidirectional and one-dimensional simple shearing problem considered therein, neither the severity nor the position of localization generally could be predicted in advance. These difficulties imposed unacceptable limits on the range of problems which could be simulated as well as raising questions of accuracy for those which were simulated. Similar difficulties are likely to ensue whenever one desires accurate simulations involving material models which exhibit *strain softening*, e.g., models for high rate granular flows.

This paper documents some first steps in an attempt to resolve these computational difficulties by employing an adaptive, finite element method-of-lines (MOL) code, MFEHP1 [2], generously provided to the author by Professor J. Flaherty and Dr. Y. Wang of the Scientific Computation Research Center at Rensselaer Polytechnic Institute. The general form of the system of *quasi-linear* partial differential equations (PDEs) amenable to solution by MFEHP1 is

$$\boldsymbol{M}(x, t)\, \boldsymbol{u}_t + \boldsymbol{f}(x, t, \boldsymbol{u}, \boldsymbol{u}_x) = (\boldsymbol{D}(x, t, \boldsymbol{u})\, \boldsymbol{u}_x)_x, \qquad a < x < b, \qquad t > t_0, \quad (1)$$

where $\boldsymbol{u} = \{u_1, \ldots, u_\alpha\}$, $\boldsymbol{M}$ and $\boldsymbol{D}$ are $(\alpha \times \alpha)$ matrices and (1) is *parabolic* when both are positive-definite.

The adaptive strategies and algorithms in MFEHP1 were developed for, and work well for, a variety of such parabolic systems (both regular and singularly perturbed) [2–5]. However, for application to adiabatic shear band simulation MFEHP1's problem class must be broadened to include matrices $\boldsymbol{M}$ and $\boldsymbol{D}$ which are *singular*. In particular, when $\boldsymbol{M}$ is singular (1) may contain both differential and algebraic equations with respect to time. This is significant because material models for solid dynamics problems are often stated most naturally in this form. For example, the flow law in rate-dependent thermo-visco-plasticity is an algebraic equation constraining the current values of stress, strain rate, temperature and hardening parameters.

Since MFEHP1 employs a MOL approach, its core spatial finite element discretization and time integration algorithms are decoupled so that in principle it may be applied to non-parabolic systems with little modification. Of course it is not reasonable to expect that adaptive strategies which were designed for strictly parabolic systems would work equally well for systems of mixed hyperbolic-parabolic type with embedded algebraic equations as considered here. Hence, our purpose is to explore the feasibility of this approach and identify algorithmic problems whose resolution will be reported subsequently.

## 2 Summary of Numerical Method

### 2.1 Spatial Discretization

MFEHP1 employs a finite element discretization of the form

$$\boldsymbol{U}(x, t) = \sum_{j=0}^{N} \boldsymbol{B}_j(t)\,\phi_{j,1}(x) + \sum_{j=1}^{N} \sum_{i=2}^{p_j} \boldsymbol{C}_{j,i}(t)\,\phi_{j,i}(x) \tag{2}$$

in which $\phi_{j,1}$ are node-based shape functions and $\phi_{j,i}$ are hierarchical, element-based shape functions [6], termed "hat" and "bubble" functions respectively. The latter are given by $\phi_{j,i}(x) = \phi_i(\hat{\xi}_j(x))$ in which $\hat{\xi}_j$ linearly maps the field element $\Omega_j = [x_{j-1}(t), x_j(t)]$ onto the master element $\hat{\Omega} = [-1, 1]$ and $\phi_i$ is given in terms of Legendre polynomials by

$$\phi_i(\xi) = \frac{(P_i(\xi) - P_{i-2}(\xi))}{\sqrt{2(2i-1)}}. \tag{3}$$

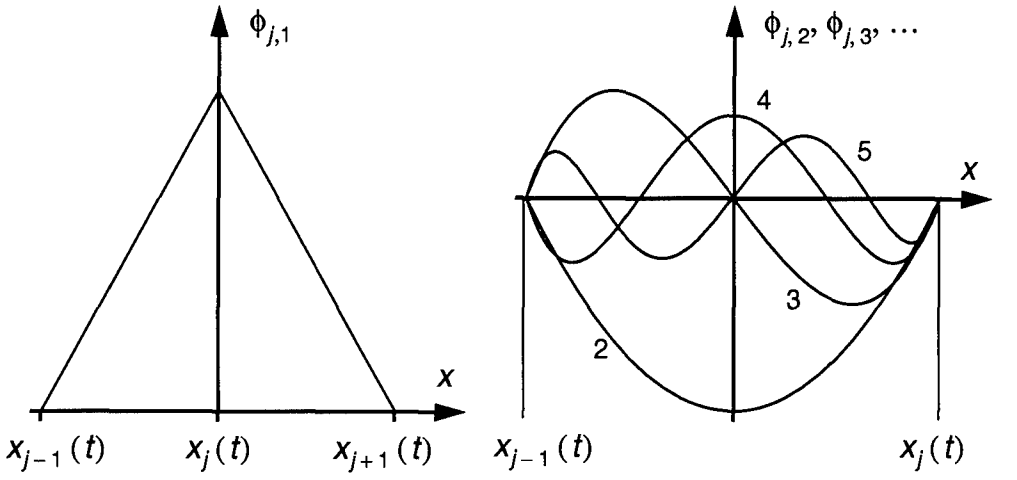



**Figure 1** Shape functions defined at the $j_{\text{th}}$ node and element.

MFEHP1 admits three different adaptive mechanisms which may be employed separately or in concert at the user's discretion.

1. *Mesh motion* (r-method) in which the position of the nodes varies continuously with time as indicated by $x_j = x_j(t)$.
2. *Spatial refinement/coarsening* (h-method) in which individual elements are subdivided or merged with adjacent elements.
3. *Spectral refinement/coarsening* (p-method) in which the polynomial order $p_j$ of each element is varied independently.

Discrete equations for the finite element degrees of freedom $\boldsymbol{B}_j(t), \boldsymbol{C}_{j,i}(t)$ are obtained from a symmetric weak formulation of (1) so that (2) is used for both trial and test functions. Except for the presence of several extra flux terms which appear due to the moving mesh, these are of fairly standard form and will not be reproduced here.

The weak formulation does not provide discrete equations for the motion of the mesh $x_j(t)$. Instead, mesh motion equations are embodied in an algorithm to approximately equidistribute a (non-negative) indicator function $\omega(x, t)$ whose value depends both on the numerical solution and the local mesh geometry. An exactly equidistributing mesh would satisfy

$$W_j(t) \equiv \int_{x_{j-1}}^{x_j} \omega(x, t)\, dx = \overline{W}(t) \equiv \frac{1}{N}\int_b^a \omega(x, t)\, dx, \qquad j = 1, \ldots, N. \quad (4)$$

Rather than solve (4) directly, MFEHP1 employs a related differential system [2] (a superposed dot indicates time differentiation)

$$\dot{x}_{j+1} - 2\dot{x}_j + \dot{x}_{j-1} = -\lambda (W_{j+1} - W_j), \qquad j = 1, \ldots, N-1, \tag{5}$$

in which $\overline{W}$ has been eliminated to preserve bandedness. The mesh relaxation parameter $\lambda$ can also be adaptively controlled so as to maintain a goodness-of-equidistribution measure within a user-specified interval.

The adaptive algorithms currently implemented in MFEHP1 are based upon a posteriori error estimates for linear parabolic problems [2,4]. The error is interpolated by the highest order "bubble" function

$$\boldsymbol{E}(x, t) = \sum_{j=1}^{N} \boldsymbol{C}_{j, p_j}(t)\, \phi_{j, p_j}(x) \tag{6}$$

with the lower order terms in (2) interpolating the solution proper. The scalar error estimates (or indicators) are the elemental and global H1-norms of $\boldsymbol{E}$

$$W_j(t) = \| \boldsymbol{E} \|_{1,j} \equiv \sqrt{\int_{\Omega_j} (\boldsymbol{E} \cdot \boldsymbol{E} + \boldsymbol{E}_x \cdot \boldsymbol{E}_x)\, dx}\,, \qquad \| \boldsymbol{E} \|_1 \equiv \sqrt{\sum_{j=1}^{N} \| \boldsymbol{E} \|_{1,j}^2}\,. \tag{7}$$

The global strategy is to adapt the mesh upon failure of the inequality

$$\frac{\mathrm{TOL}}{10} \le \| \boldsymbol{E} \|_1 \le \mathrm{TOL}. \tag{8}$$

The solution is transferred from the old mesh to the new by an H1-norm projection.

## 2.2 Temporal Integration

Application of the above FEM in space yields a system of nonlinear equations for

$$\boldsymbol{Y}(t) = \{ x_j(t), \boldsymbol{B}_j(t), \boldsymbol{C}_{j,i}(t) \}_{j,i=1,2}^{N, p_j} \tag{9}$$

of the form

$$\boldsymbol{G}(t, \boldsymbol{Y}, \boldsymbol{Y}') = \boldsymbol{0}. \tag{10}$$

For the rate-dependent visco-plastic shear band problem considered below $\boldsymbol{M}$ in (1) is singular so that (10) will generally be an index-one system of Differential/Algebraic Equations (DAEs)[1] for which special inte-

gration methods are required. MFEHP1 uses the code DASSL [8] which implements a DAE-form of the *backward difference formulae* with automatic adaptation of time step and method order to satisfy a stepwise error tolerance which is scaled by the spatial tolerance, TOL.

DASSL is robust for systems of index zero and index one modulo *consistent initialization*. That is, in addition to the initial vector $\boldsymbol{Y}_0$, DASSL also requires a vector of initial *rates* $\boldsymbol{Y}'_0$ which together must approximately satisfy $\boldsymbol{G}(t_0, \boldsymbol{Y}_0, \boldsymbol{Y}'_0) = \boldsymbol{0}$. The need to supply $\boldsymbol{Y}'_0$ in the index-one case is non-trivial because initial data for (1), $\boldsymbol{u}(x, t_0) = \boldsymbol{u}_0(x)$, contain information sufficient only to specify $\boldsymbol{Y}_0$ in (10). In the current context this may be seen by observing that because (1) is linear in $u_t$, (10) is linear in $\boldsymbol{Y}'$ so that

$$\boldsymbol{0} = \boldsymbol{G}(t_0, \boldsymbol{Y}_0, \boldsymbol{0}) + \frac{\partial \boldsymbol{G}}{\partial \boldsymbol{Y}'}(t_0, \boldsymbol{Y}_0, \boldsymbol{0}) \cdot \boldsymbol{Y}'_0 \ . \tag{11}$$

When (10) is index-one $(\partial \boldsymbol{G}/\partial \boldsymbol{Y}')_0$ is singular and (11) cannot be solved for $\boldsymbol{Y}'_0$, as would be possible if (10) were index-zero. DASSL's current initialization algorithm can handle some problems with mildly inconsistent initial data but more robust initialization methods are needed. Fortunately, a consistent initialization algorithm for a substantial class of DAEs has recently been devised [9]; implementation in DASSL is currently underway [10].

## 3 Simulation of a Parabolic Test Problem

Some algorithmic modifications and recoding of MFEHP1 were performed by the author toward its application to shear band problems. To verify that MFEHP1 continues to function properly on its original problem class and illustrate the adaptive behavior desired for shear bands, consider the following parabolic test problem (example 3.2 in [11]).

*Problem 1* Modified heat equation with Dirichlet data.

$$\begin{aligned} u_t + u_x - u_{xx} &= (x, t), \qquad 0 < x < 1, \qquad t > 0, \\ u(x, 0) &= u_0(x), \qquad 0 \le x \le 1, \\ u(0, t) &= c_0(t), \qquad u(1, t) = c_1(t), \qquad t \ge 0, \end{aligned} \tag{12}$$

1. The *index* of system (10) is the least number of times that any of the $G_k$ must be differentiated with respect to $t$ in order to obtain a purely differential (index zero) system. In particular, if $\partial \boldsymbol{G}/\partial \boldsymbol{Y}'$ is singular then the index of (10) is one or more.

where $c_0$, $c_1$, $u_0$ and $f$ are selected so that the exact solution is

$$u(x, t) = \{1 - \tanh[C_1(x - C_2 t - C_3)]\}/2; \tag{13}$$

a wave front moving to the right at speed $C_2$. Figure 2 shows an r-

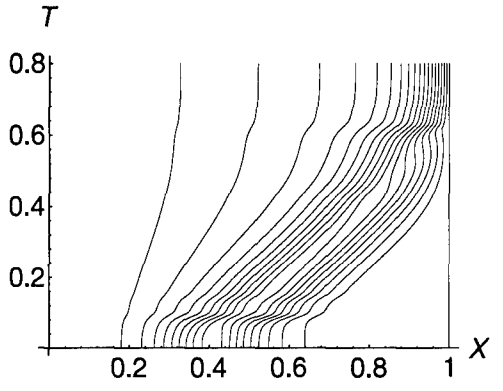



**Figure 2** Mesh history for r-method solution of Problem 1 with $C_2 = 10$.

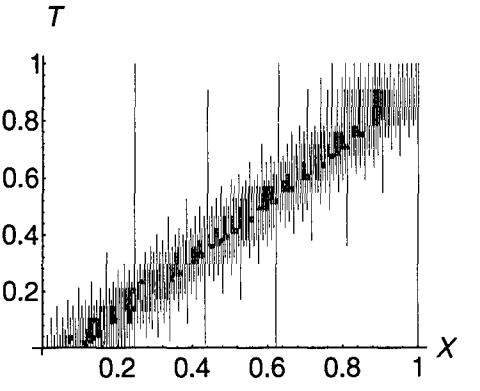



**Figure 3** Mesh history for h-method solution of Problem 1 with $C_2 = 25$.

method simulation of this problem (with $C_1 = 10$, $C_2 = 1$, $C_3 = 0.4$) using a mesh of $N = 19$ quadratic elements (i.e., $p_j = 2$ in (2), (6)) and TOL = 0.12. Note that the mesh trajectories are smooth and non-oscillatory as expected since the mesh motion equations (4), (5) are infinitesimally stability [7]; agreement with results in [11] is excellent. Figure 3 shows an h-method simulation of the same problem (with $C_1 = 25$, $C_2 = 1$, $C_3 = 0.1$) using a cubic mesh with $28 \leq N \leq 61$ elements and TOL = 0.005. Shortly after start-up the number of elements stabilizes (near 60) until the wave exits the domain near $t = 1$. This is as expected since the shape of the wave does not change. The mesh is refined near the wave's leading edge and coarsened on the trailing edge in a smooth manner. Although not shown, the maximum elemental errors are maintained in a narrow range near $\overline{\text{TOL}} = \text{TOL}/\sqrt{N}$ on the wavefront.

## 4 Shear Band Simulations

Here we attempt adaptive simulation of two of the 1-D simple shear problems considered previously on a non-uniform fixed mesh [1]; details concerning motivation and formulation appear therein.

*Problem 2* Consider the unidirectional, simple shearing of a slab of

perfectly-plastic material with a Litonski-type flow law. The boundaries $x = \pm 1$ are thermally insulated and driven at fixed speed. A temperature perturbation (symmetric about $x = 0$) is introduced at $t_0 = 0$ to initiate localization. In view of the problem's symmetry, the dimensionless field equations, side conditions and material parameters are,

$$\begin{aligned} &v_t = s_x/\rho, \qquad \theta_t = k\theta_{xx} + sv_x, \\ &s = \operatorname{sgn}(v_x)\,(1 + b|v_x|)^m e^{-a\theta}, \end{aligned} \qquad 0 < x < 1, \qquad t > 0, \tag{14}$$

$$\begin{aligned} v(0,t) &= 0, \qquad v(1,t) = 1, \\ \theta_x(0,t) &= 0, \qquad \theta_x(1,t) = 0, \end{aligned} \qquad t \geq 0, \tag{15}$$

$$\begin{aligned} &v(x,0) = x, \qquad s(x,0) = (1 + b^m)\, e^{-a\theta(x,0)}, \\ &\theta(x,0) = 0.1\,(1 - x^2)^9 e^{-5x^2}, \end{aligned} \qquad 0 \leq x \leq 1, \tag{16}$$

$$\begin{aligned} &\rho = 3.93\times10^{-5}, \qquad k = 2.20\times10^{-1}, \\ &a = 1.04\times10^{-1}, \qquad b = 5\times10^{7}, \qquad m = 2.51\times10^{-2} \end{aligned} \tag{17}$$

where $v$, $\theta$, $s$ are, respectively, the velocity, temperature and stress. The material parameters (17) are appropriate for a moderate-strength steel deforming at a nominal shear rate of 500 $s^{-1}$ (corresponding to $v_x = 1$) except that the value of $k$ has been increased by a factor of 100 to reduce the severity of localization.

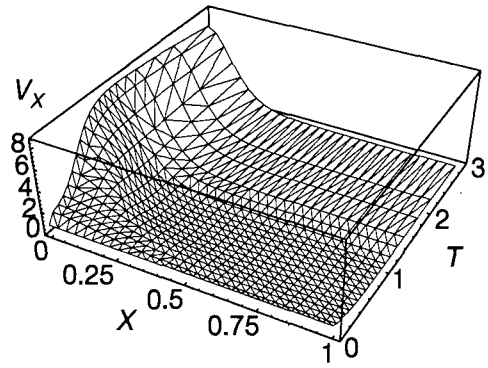



**Figure 4** $v_x$ for Problem 2 computed on a uniform, non-adaptive mesh ($p_j = 2$).

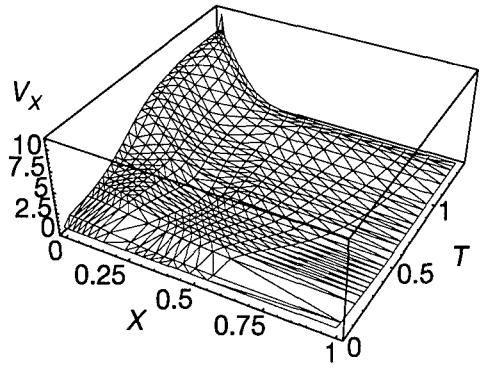



**Figure 5** $v_x$ for Problem 2 computed on an r-method adaptive mesh ($p_j = 2$).

Figure 4 shows the velocity gradient, $v_x$, for a uniform-mesh simulation of Problem 2; this result agrees qualitatively with those in [1]. Fig-

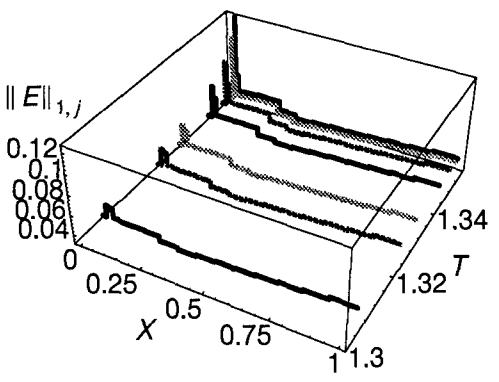



**Figure 6** Estimated elemental errors for case of Figure 5 near $t = t_f$.

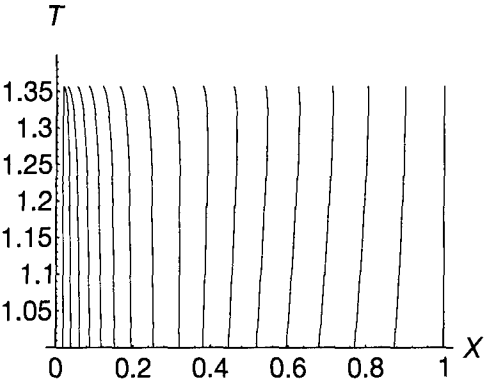



**Figure 7** Mesh trajectories for case of Figure 5 near $t = t_f$.

ures 5–7 contain results for an r-method simulation which behaved well until failing suddenly at $t_f \cong 1.36$ due to convergence of nodes two and three. The failure appears to be caused by deterioration of the error estimate (and the solution itself) rather than instability of the mesh motion equations, because the mesh trajectories, Figure 7, are appropriate for the computed evolution of elemental errors, Figure 6. Use of an alternative error estimate (which accounts for inter-element errors ignored by (5)) did not produce significant improvement. Some improvement was obtained by adding to (5) a term penalizing very short elements but such an approach is ad hoc and does not resolve the underlying difficulty.

Successful simulation of this problem on a fixed mesh suggests that the r-method failure may have occurred because the mesh motion-related fluxes were discretized in a manner inappropriate for the shear band equations. This possibility is explored by considering a variant of Problem 2 with a strain-hardening material model and simulation by the h-method.

*Problem 3* Simple shearing of a slab of rigid, strain-hardening material with the Johnson-Cook flow law [12]. The domain and balance laws are as in Problem 2. The flow law $(14)_3$ is replaced by

$$s = \operatorname{sgn}(v_x)\,(1 + \psi_0 \gamma^n)\,(1 + m \log(|b v_x|))\,(1 - (a\theta)^p), \tag{18}$$

where the total strain $\gamma$ evolves according to $\gamma_t = |v_x|$, while the side conditions are given by

$$\begin{aligned} &v(0,t) = 0, \quad v(1,t) = 1, \quad \theta_x(0,t) = 0, \quad \theta(1,t) = 0, \\ &v(x,0) = x, \quad \theta(x,0) = 0, \quad \gamma(x,0) = 0, \quad s(x,0) = 0. \end{aligned} \tag{19}$$

Material parameters appropriate for OFHC Copper deforming at a nominal shear rate of 330 $s^{-1}$ are

$$\rho = 3.56\times10^{-5}, \quad k = 1.34\times10^{-1},$$
$$a = 1.89\times10^{-2}, \quad b = 3.3\times10^{3}, \quad m = 2.5\times10^{-2}, \qquad (20)$$
$$n = 3.1\times10^{-1}, \quad \psi_0 = 3.25, \quad p = 1.09.$$

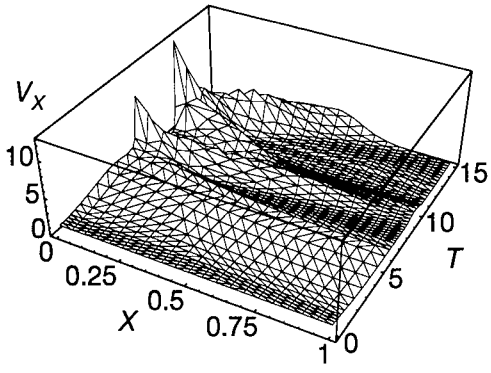



**Figure 8** $v_x$ for Problem 3 computed on a uniform, non-adaptive mesh of 20 elements ($p_j = 3$).

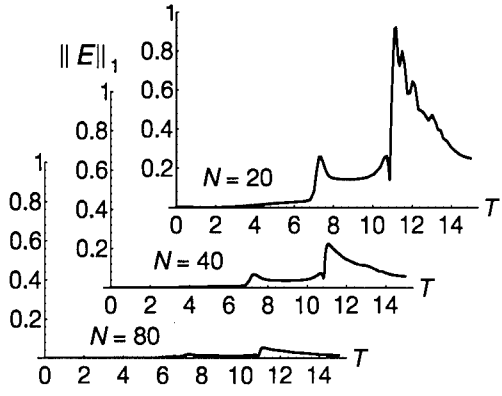



**Figure 9** Evolution of estimated global error for uniform mesh-simulations of Problem 3 with 20, 40 and 80 elements ($p_j = 3$).

In contrast with Problem 2, localization occurs here by diffusion of the thermal boundary layer at $x = 1$. Because of the low strength and high diffusivity of Copper this problem may be simulated on a fixed-mesh without modification of the material parameters. The $v_x$ surface in Figure 8 shows the same complex history observed previously [1]. Figure 9 illustrates that, at least for uniform meshes, the global error estimate appears to converge at roughly a quadratic rate. Examination of the $v_x$ and temperature surfaces for the other uniform meshes (not shown) confirms convergence.

A portion of the $v_x$ surface for an h-method simulation of Problem 3 is shown in Figure 10. The initial mesh was uniform with 30 cubic elements but because the solution is smooth for small $t$ the mesh was coarsened to $N = 8$ before refinement began at $t \cong 4$. At $t = 5$ (on the back edge of Figure 10) $N = 42$ and by $t \cong 7$, $N = 156$. In contrast with Problem 2, the simulated solution appears to be good in this case although the mesh is clearly being over-refined. Referring to Figure 11, the arrows indicate unacceptably large increases in the global error esti-

mate at each mesh adaptation. These increases evidently occur because the elemental error estimate is converging much less rapidly with refinement than would be expected in view of Figure 9; to what extent the estimate is indicative of the exact error is presently not known.This behavior may be due in part to the fact that the shear band solutions often tend to localize "in place" rather than to involve moving wavefronts typical of many of the parabolic problems to which MFEHP1 has been applied. The post-adaptation decay in $\|E\|_1$ suggests that some of the refinement-induced increase in the estimate may be due to insufficient accuracy in transferring the solution from the old to new meshes, although a high-order projection was used. It is also likely that better refinement behavior could be obtained by modifying the algorithm which calculates the density of elements in the new mesh, as it is currently based on error convergence rates for linear parabolic systems.

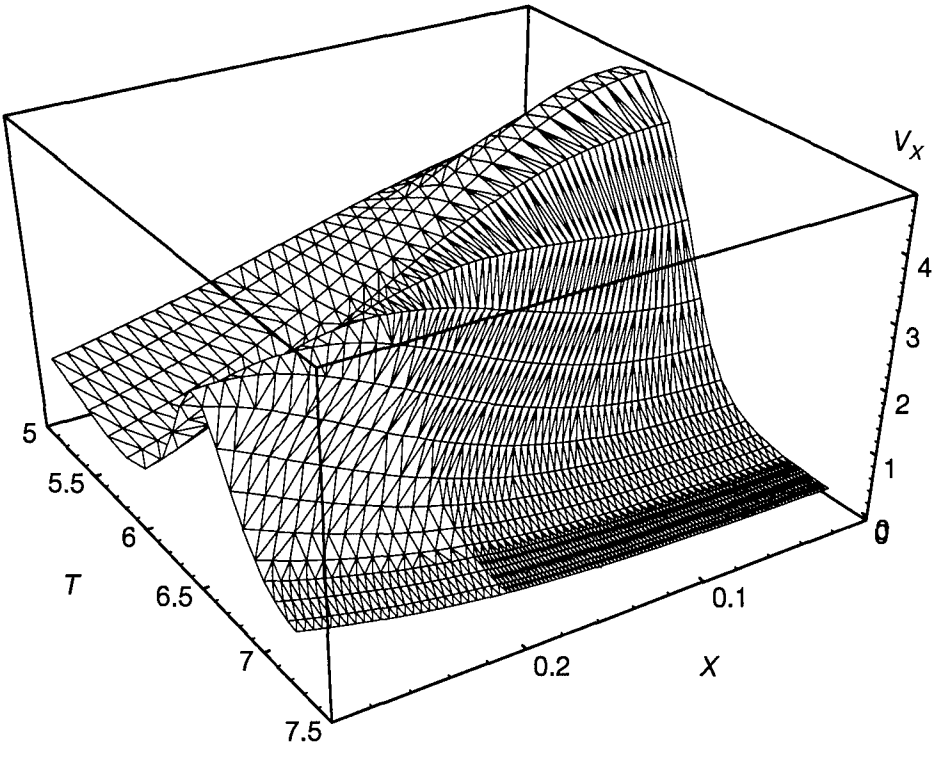



**Figure 10** $v_x$ for Problem 3 computed on an initially uniform, h-adaptive mesh. The sub-domain shown ($0 \le x \le 0.3$, $5 \le t \le 7.25$) corresponds to the first peak in Figure 8 ($p_j = 3$).

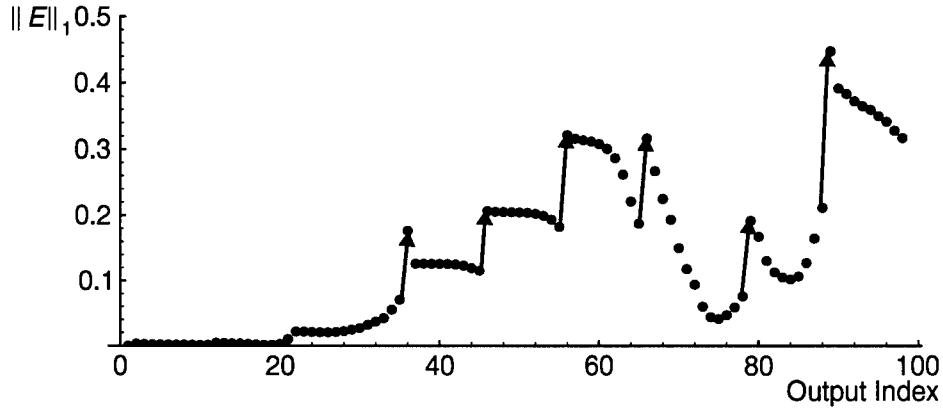



**Figure 11** Evolution of the global estimated error for the case of Figure 10.

## 5 Discussion

Clearly, much remains to be done before adaptive algorithms of the sort considered here can attain their potential performance when applied to adiabatic shear band problems. A first step toward this end is to quantify the behavior of the error indicator (6), (7) for relevant problems and implement a different indicator if necessary. To obtain acceptable performance it is not essential that the effectivity[2] remain very close to unity but it cannot deviate arbitrarily far from that value. The error indicator can be examined through a combination of the following sorts of numerical experiments.

1. *Programmed solutions.* If the exact solution to a problem is known, MFEHP1 uses it to compute the exact error and the effectivity of the error estimate. Running problems with shear band-like programmed solutions for both a simple parabolic system and for an actual shear band system such as Problem 2 will help clarify the exact nature of MFEHP1's difficulties with shear band simulation.

2. *Benchmarking and basic convergence study.* It is possible for the programmed solution approach to produce misleading results because such solutions may be different than those which the equations would admit with "usual" data. Thus, solutions should also be generated on non-adaptive, and when

2. The effectivity index is defined as $\| E \| / \| e \|$ where $e$ is the exact error.

possible uniform, meshes to obtain h, p convergence rates and benchmark solutions to be compared with adaptive solutions.

Lastly, it should be observed that adaptive strategies which do not depend on error estimates are possible. In general, an adaptive algorithm could attempt to approximately equidistribute the integral of any positive quantity related to the solution as in (4). However, such approaches are necessarily problem-specific and the connection between the *quality* of the solution and the adaptation is lost.

## References


[1] Walter, J. W. "Numerical Experiments on Adiabatic Shear Band Formation in One Dimension." *Int. J. Plast.,* **8**, 657-693, 1992.

[2] Wang, Y. J. "An Adaptive Local HPR-Refinement Finite Element Method for Parabolic Partial Differential Equations." SCOREC Report 21-1991, Sci. Comp. Res. Cen., Rensselaer Polytechnic Institute, Troy, NY, 1991.

[3] Flaherty, J. E. and Y. Wang. "Experiments with an Adaptive h-, p-, and r-Refinement Finite Element Method for Parabolic Systems." Report 90-27, Dept. of Comp. Sci., Rensselaer Polytechnic Institute, Troy, NY, 1990.

[4] Adjerid, S., J. E. Flaherty, and Y. J. Wang. "A Posteriori Error Estimation with Finite Element Methods of Lines for One-Dimensional Parabolic Systems." Report 91-1, Dept. of Comp. Sci., Rensselaer Polytechnic Institute, Troy, NY, 1991.

[5] Adjerid, S., J. E. Flaherty, P. K. Moore and Y. J. Wang. "High-order Adaptive Methods for Parabolic Systems." *Physica D*, **60**, 94-111, 1992.

[6] Szabó, B. and Babuska, I. *Finite Element Analysis.* Wiley, New York, 1991.

[7] Coyle, J. M., J.E. Flaherty and R. Ludwig. "On the Stability of Mesh Equidistribution Strategies for Time-Dependent Partial Differential Equations." *J. Comp. Phys.*, **62**, 26-39, 1986.

[8] Petzold, L. R. "A Description of DASSL: A Differential/Algebraic System Solver", in *Scientific Computing*, eds. R. S. Stepleman et al., North-Holland, Amsterdam, 65-68,1983.

[9] Leimkuhler, B., L. R. Petzold and C. W. Gear. "Approximation Methods for the Consistent Initialization of Differential-Algebraic Equations." *Siam J. Numer. Anal.*, **28**, 205-226, 1991.

[10] Petzold, L. R.,1993. Personal communication to J. Walter.

[11] Adjerid, S. and J. E. Flaherty. "A Moving-Mesh Finite Element Method with Local Refinement for Parabolic Partial Differential Equations." *Comp. Meth. Appl. Mech. Engng.*, **55**, 3-26, 1986.

[12] Johnson, G. R. et al. "Response of Various Metals to Large Torsional Strains Over a Large Range of Strain Rates—Part 1: Ductile Metals." *ASME J. Engng Mater. Technol.* **105,** 48-53, 1983.

# Finite Element Modeling of Segmental Chip Formation in High Speed Orthogonal Cutting

**Dr. Javad Hashemi,**
Department of Mechanical Engineering
Texas Tech University
Lubbock, TX 79409

**Dr. Ampere A. Tseng*, and Dr. Pei Chi Chou**
Department of Mechanical Engineering and Mechanics
Drexel University
Philadelphia, PA 19104

## SUMMARY

An explicit, lagrangian, elastic-plastic, finite element code has been modified to accommodate chip separation, segmentation, and interaction in modeling of continuous and segmented chip formation in high speed orthogonal metal cutting process. A fracture algorithm is implemented that simulates the separation of the chip from the workpiece and the simultaneous breakage of the chip into multiple segments. The path of chip separation and breakage is not assigned in advance but rather controlled by the state of stress and strain induced by tool penetration. A special contact algorithm is developed that automatically updates newly created surfaces as a result of chip separation and breakage and flags them as contact surfaces. This allows for simulation of contact between tool and newly created surfaces as well as contact between simulated chip segments. The work material is modeled as elastic perfectly plastic and the entire cutting process from initial tool workpiece contact to final separation of chip from workpiece is simulated. In this paper, the results of the numerical simulation of continuous and segmented chip formation in orthogonal metal cutting of material are presented in the form of chip geometry, stress, and strain contours in the critical regions.

## INTRODUCTION

The importance of the cutting process may be realized by the observation that nearly every device in use in our society has one or more machined surfaces or holes. In the USA, the yearly cost associated with material removal tasks has been estimated at about 10 percent of the gross national product. There are several reasons for developing a rationale approach to material removal such as improving cutting techniques, producing products with enhanced precision, and increasing the rate of production, Shaw (1984). The economics of the cutting process has made this area one of paramount importance from both a technical and an engineering economics point of view.

Attempts in understanding the mechanics of metal cutting process dates back to the work performed by Cocquilhat (1851), when he measured the work required to remove a portion of material by drilling. Other significant research investigations in the general area of metal cutting were performed by Time (1870), Treska (1873), Taylor (1906), Piispanen (1948), Ernst and Merchant (1941), and Lee and Schaffer (1951). These investigators attempted to develop a model (empirical or analytical) that predicted important machining parameters such shear plane angle. However, none of the proposed models generated consistent satisfactory results.

With the introduction of finite element techniques, many attempts have been made to model the metal cutting process through utilization of this method. One of the important goals has been to model the formation of the chip as the material is removed from the surface of the workpiece and to determine the subsequent state of deformation in the workpiece as well as the chip material. Klamecki's work (1973) is the first example of such effort. Klamecki used a three-dimensional formulation to treat the incipient chip formation process. Usui and Shirakashi (1982) developed a model based on empirical data for rate independent behavior. The model was suitable for steady state cutting conditions. Iwata, Osakada, and Terasaka (1984) simulated low speed metal cutting process based on a rigid-plastic constitutive law. The residual stresses could not be determined due to the rigid-plastic deformation behavior. Thus far, the most realistic simulations, (all plane strain simulations), have been performed by Strenkowski and Carrol (1983), Carrol and Strenkowski (1988), and most recently, Komvopoulos and Erpenbeck (1991). Strenkowski and Carrol used the Lagrangian NIKE2D code to model orthogonal metal cutting process. They simulated the formation of a continuous chip in the steady state condition and calculated the state of residual stresses according to a temperature dependent constitutive model and

adiabatic conditions. Severe distortion of the mesh due to large deformation nature of the problem presented some difficulties by reducing the integration time increment. This is a problem associated with all Lagrangian codes used to simulate large deformation problems where computationally expensive re-meshing techniques must be used. It should be mentioned that a predetermined chip separation path was utilized in Carrol's numerical scheme, i.e., whenever the tool reached the critical node on the separation path, according to the state of plastic strain surrounding the node, the node would split from the surface. The initial geometry of the chip material was distorted. This modification was made to avoid simulation complications as a result of high compressive deformations around the tool-workpiece interface.

Carrol and Strenkowski used an identical procedure and a similar constitutive equation while taking into account the effect of strain rate. Most recently, Komvopoulous and Erpenbeck utilized the finite element method to model chip formation in orthogonal metal cutting. To simulate separation of the chip from the workpiece, superposition of two nodes at each nodal location of a prearranged parting line of the initial mesh was imposed. Simply stated, the nodes on the parting line separated when the tool tip was in close, predetermined, proximity of that node. Constitutive equations of elastic-perfectly plastic and elastic-plastic with strain rate sensitivity were used in different simulations. Tool material and built-up edge (BUE) were modeled as rigid. The simulation was based on the assumption that the chip had already partially formed. The reason for that assumption, according to the authors, was to reduce the computation time. The actual simulation shape of the chip material was determined based on experimental results. The authors stated that fair agreement between experimental and numerical results was observed. It should be mentioned that their simulation included effects of friction on chip-tool contact interface as well as tool wear at the rake face. The above mentioned studies have all been related to cases where continuous chips are formed and the objective has been to gain a qualitative insight in some specific aspects of the machining process. The modeling of the machining process where segmental chips are formed has not appeared in the literature.

In summary, finite element simulation of metal machining processes has been limited to continuous chips. In addition, most studies do not utilize a systematic approach in modeling the complete process from the initial tool work contact to the chip formation and separation. For example, in some modeling attempts, the geometry of the chip has been input to the code and the simulation has been performed based on an already existing chip. Another shortcoming in

recent machining simulations has been the unavailability of an algorithm capable of simulating dynamic metal fracture, without the use of a predetermined chip separation path, as the tool penetrates the workpiece. This is specially important when simulating segmental chip formation which requires an algorithm that can handle element separation, new node creation, element reattachment, and finally sliding surface insertion and modification. The latter of which, slide line insertion and modification, is required to simulate the contact between opposite surfaces of a crack as they interact. In this paper, the theoretical formulation, related algorithms, and the simulation results of a finite element scheme capable of simulating segmental chip formation are presented.

## NUMERICAL SCHEME

The formulation of the utilized code is based on the hydro-code approach similar to that used by Chou et al (1991). In hydrocodes, where the pressure involved is very high, the material can not be simply considered as elastic-plastic. Material must be treated as a compressible material and an equation of state relating the pressure, density, and internal energy must be used in place of the elastic spherical stress-strain relation. To facilitate this, the plastic constitutive equations are expressed in terms of deviatoric stress and strain. Another point is that the numerical procedure involves the calculation of stress from the total strain rate, not the plastic strain rate, at each time increment cycle. Therefore, a constitutive relation of stress in terms of total strain rate is needed. In the numerical calculations, at time t the deviator stress and strain rate components are known, $s_{i.tr_1}^{t+\Delta t}$ is determined by first calculating a trial stress,

$$s_{i.tr_1}^{t+\Delta t} = s_i + 2G\dot{e}_i\Delta t + \omega_i\Delta t, \qquad i= 1,2,...6 \qquad (1)$$

The $\omega_i$ term represents the contribution due to element rotation. With $\omega_{\theta z} = \omega_{\theta r} = 0$, it can be shown that

$$\omega_1 = -2\sigma_4\omega_{rz}$$
$$\omega_2 = 2\sigma_4\omega_{rz}$$
$$\omega_4 = (\sigma_1-\sigma_2)\omega_{rz}$$
$$\omega_3 = \omega_5 = \omega_6=0 \qquad (2)$$

For the Von Mises yield condition, we shall use the equivalent stress, $\bar{\sigma}$,

$$\bar{\sigma} = \left[\frac{3}{2}\left(s_1^2 + s_2^2 + s_3^2\right) + 3\left(s_4^2 + s_5^2 + s_6^2\right)\right]^{1/2} \qquad (3)$$

If $\bar{\sigma}<\sigma_y$, the material is elastic, and the trial stress is the correct stress at time $t+\Delta t$. If $\bar{\sigma}>\sigma_y$ the materials has yielded and a second trial stress is calculated,

$$s_{i.tr_2}^{t+\Delta t} = s_i + 2G\dot{e}_i\Delta t - 2G(1-\alpha)\lambda s_i + \omega_i\Delta t, \qquad i=1,2,...,6 \qquad (4)$$

where $\alpha$ is the percent of the stress increment inside the yield surface.

The stress deviator increment in this trial stress deviator, not counting the rotational term, is

$$\Delta s_i = 2G\dot{e}_i\Delta t - 2G\lambda s_i \qquad (5)$$

This is exactly the Prandtl-Reuss flow rule,

$$de_i = \frac{1}{2G}\, ds_i + \lambda s_i \qquad (6)$$

Therefore, in using the trial stress in Eq. (4 ), we satisfied the von Mises yield condition and the Prandtl-Reuss flow rule. However, due to the finite increment in time, $\Delta t$, the resulting state of stress, even though following a path tangent to the yield surface, may still fall outside of it. To correct this, the final stress deviator at $t+\Delta t$ is obtained from $S_{i,tr2}$ by

$$s_i^{t+\Delta t} = s_{i,tr2}\frac{\sigma_y}{\bar{\sigma}_{tr2}} \qquad (7)$$

where $\bar{\sigma}_{tr2}$ is the equivalent stress calculated from $s_{i.tr2}^{t+\Delta t}$.

## SIMULATION RESULTS

The finite element code was applied in simulation of high speed machining of materials with the goal of simulating segmental chips. A plane strain simulation of orthogonal metal cutting processes at high cutting speeds was performed. Figure 1 shows the initial geometry of the simulation in which a cutting speed of 25 m/sec and a rake angle of $10^{o}$ were used. All surfaces were simulated as frictionless and the cutting tool was modeled as rigid. A coarse finite element mesh was utilized to minimize computational expense, however for more accurate and realistic simulations a finer mesh has to be utilized. An Elastic-perfectly plastic material constitutive equation was used to simulate the workpiece material. No attempts were made to model a specific material, however, the material constants used were that of an aluminum alloy. The simulation was primarily intended to provide numerical capability to model continuous and segmented chip formation in high speed machining of metals. The fracture criterion used for this simulation was based on the ultimate plastic strain of the material.

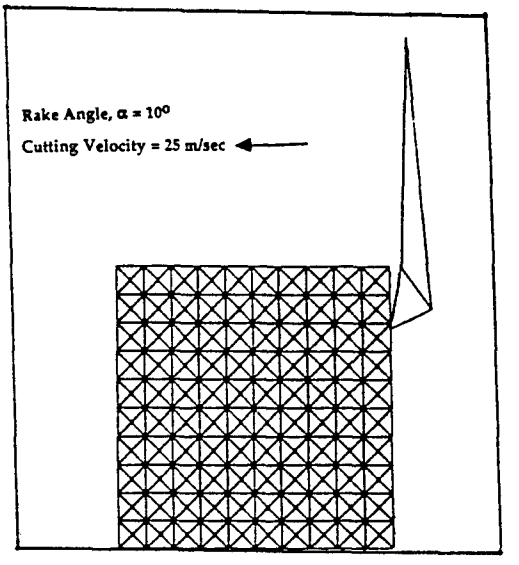



Figure 1. The initial geometry of the orthogonal cutting process. Plane strain simulation.

In the first trial, the geometry, boundary conditions, and the cutting parameters were those outlined above. A fracture criterion based on effective plastic strain was used with a critical value of 0.6. Figures 2 through 6 show the results produced in the first trial. In Figure 2(a), the initiation of the chipping process and the formation of a shear zone which starts from the tool tip and ends at the free surface is observed. Figure 2(b) shows the plastic region around the tool tip at the corresponding computational cycle. The plastic region (represented by "*") approximately represents the shear plane. The shearing stress contour of the segmented chip simulations, at the stage corresponding, is presented in Figure 2(c). It shows that the regions of high shear are located at the upper portion of the chip where the shear stress is positive and just below the tool where it is negative. The high shear contour in the chip material coincides with the approximate location of the shear plane. Figure 2(d) shows the distribution of the effective plastic strain. The same approximate distribution of effective plastic strain exists at the later computational cycles.

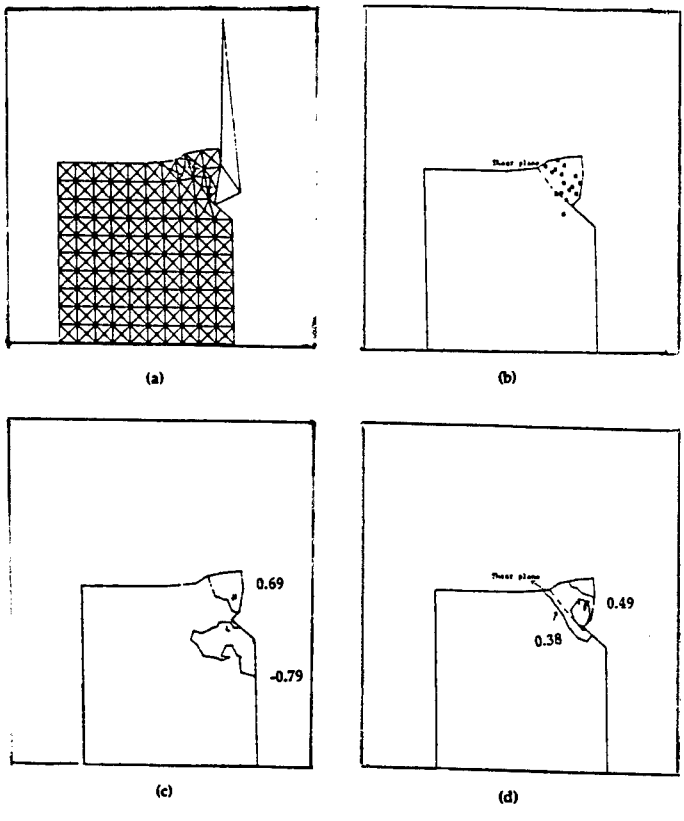



Figure 2. The chip compression and separation stage; (a) Mesh geometry, (b) Plastic zone, (c) Shear stress distribution, (d) Effective plastic strain distribution.

The first evidence of chip segmentation is observed in Figure 3(a) where the extensive shearing action on the chip material is obvious. The segmentation of the chip is clearly shown in Figure 3(b) in which a crack is initiated from the inner chip surface. It is important to note that the contact between opposite sides of the cracks is simulated adequately and no interpenetration of materials is observed. Figures 4(a) represents a later stage of the cutting process where the segmented chips are continuously forming and moving away from the cutting tool at speeds higher than the cutting speed. The results are in good qualitative agreement with those cases where the chip material breaks due to brittle fracture, Figure 4(b).

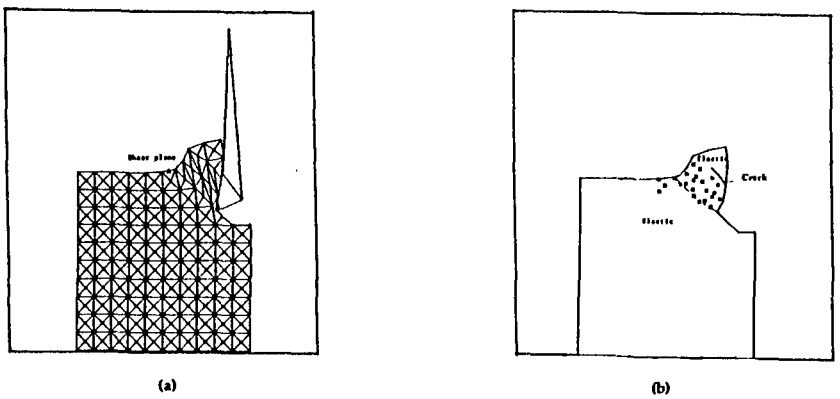



Figure 3. The development of the primary and secondary shear zone; (a) Mesh geometry, (b) Plastic zone and formation of crack in the chip material.

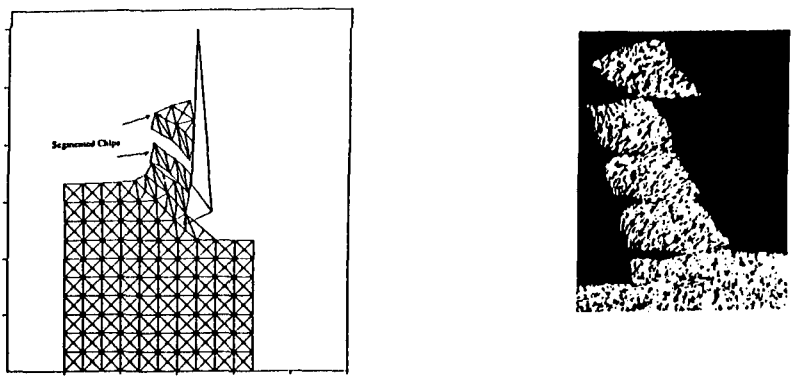


Figure 4. Comparison of finite element simulation and experimental observation of the chip formation process; (a) Code results, (b) Experimental results.

A second trial was prepared with the same geometry and cutting conditions and a fracture criterion of 1.5 was used to simulate continuous chip machining. Figures 5(a) through 5(d) show the cutting geometry at different stages of the process.

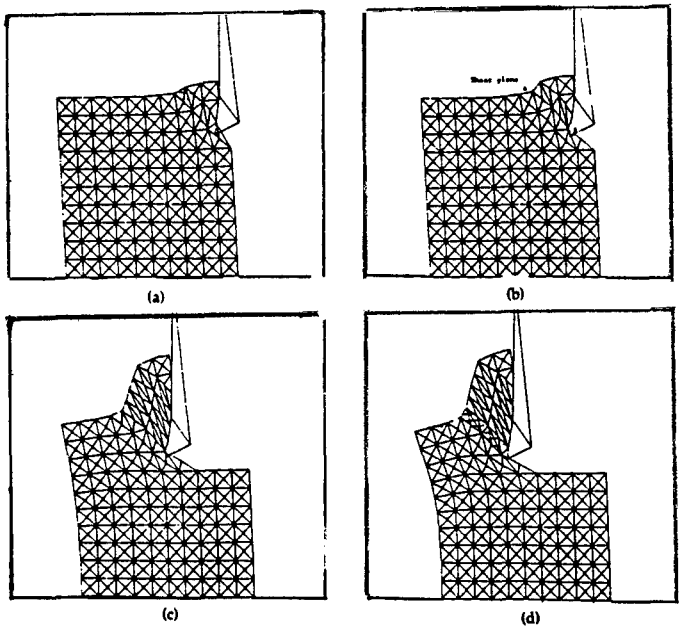



Figure 5. Different stages of the cutting process associated with continuous chip formation; (a) Initial compression of the chip material, (b) Formation of the secondary shear zone , (c) Chip separation and successive shearing of chip material entering the shear zone, (d) Final stages of the cutting process.

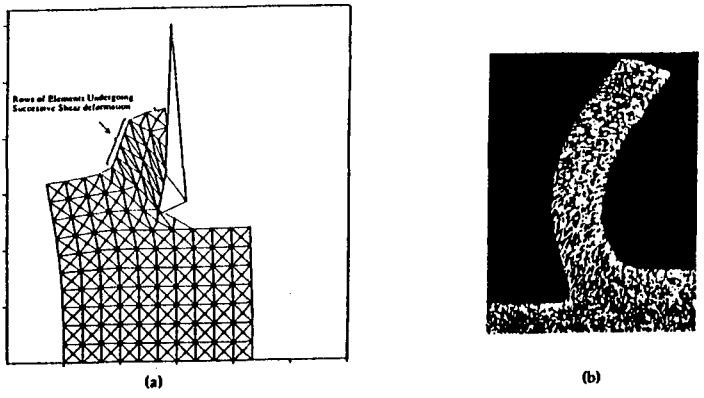



Figure 6. Comparison of finite element simulation and experimental observation of the chip formation process; (a) Code results, (b) Experimental results.

The comparison of experimental results of continuous chip formation with the numerical simulation is presented in Figure 6. Figures 7(a) through 7(c) present the results in determining the distribution of effective plastic strain at different stages. These results show high values of plastic strain at the chip along the tool face. The general chip shape also agrees with the results given by Strenkowski and others.

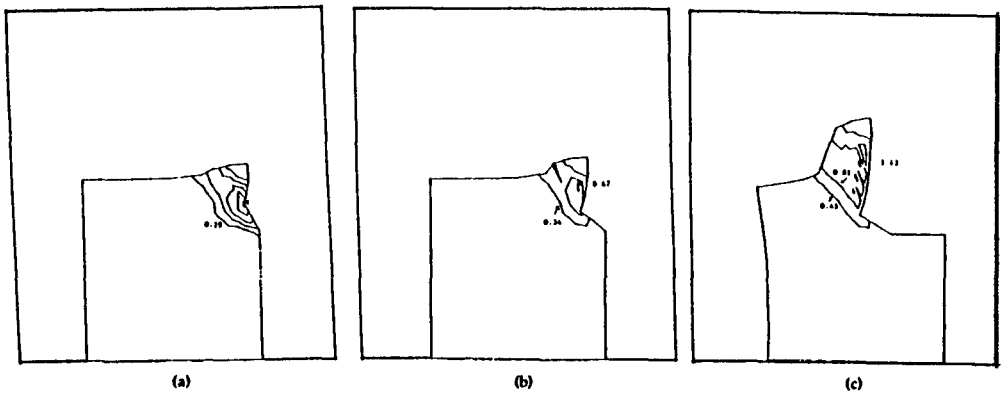



Figure 7. Effective plastic strain contours at different cutting stages; (a) Initial chip compression stage, (b) Chip separation stage, (c) The steady state cutting stage showing both the location of primary and secondary shear zone.

## CONCLUSION

The objective of this paper was to present the capability of a recently developed finite element scheme to assist in modeling of orthogonal metal cutting process with both continuous and segmental chip formation. A dynamic finite element analysis of the orthogonal metal cutting process was performed. A fracture algorithm was developed that automatically generated splitting of the elemental nodes as the cutting tool penetrated the workpiece. The splitting of the node was dependent on the state of strain of the elements attached to it while the corresponding direction of the crack was determined by a direction perpendicular to the average principal stresses at that node. In order to account for the contact between opposite sides of the crack, and in general all segments and bodies coming in contact, an automatic slide line generation algorithm was developed. The

modified code was utilized in simulation of orthogonal metal cutting with the objective of simulating continuous chip formation as well as segmental chip formation due to brittle fracture of chips. The simulation results for the prediction of the general chip geometry agreed well with the experimental results. However, a more realistic simulation requires utilization of significantly denser mesh as well as a more complete constitutive equation which includes the effects of strain, and strain rate hardening, as well as the thermal softening effects.

An important phenomenon associated with the generation of segmental chips in cutting of some metals such as titanium is the formation of adiabatic shear bands along the shear plane. In order to perform realistic simulations of the cutting processes of those metals, the method presented in this paper together with the utilization of highly fine mesh and a proper constitutive equation such as the one mentioned above should prove necessary and effective.

**ACKNOWLEDGMENTS**—This study was partially supported by a grant from Advanced Technology Center of Southeast Pennsylvania through Ben Franklin Partnership Program. The supercomputing time was furnished by a grant from National Science Foundation through Pittsburgh Supercomputing Center. The authors are greateful to Dr. William Flis for valuable discussions.

## REFERENCES

P. C. Chou, J. Hashemi, A. Chou, and H. Rogers, 1991, "Experimental and Computer Simulation of Shear Bands in Controlled Penetration Impacts,"Journal of Impact in Engineering, Vol. 11, No. 3, pp. 305-321.

Carrol, J. T., and Strenkowski, J. S., 1988, "Finite Element Models of Orthogonal Metal Cutting With Application to Single Point Diamond Turning," Int. J. Mech. Sci., Vol 30, No. 12, pp. 899-920.

Ernst, H. and Merchant, M. E., 1941, "Chip Formation, Friction, and High Quality Machined Surfaces, in Surface Treatment of Metals," American Society of Metals, Vol. 29, P. 299.

Hashemi, J., 1988, "Finite Element Simulation of Segmented Chip Formation in High-Speed Machining Process," Ph.D. Thesis, Mechanical Engineering Department, Drexel University.

Iwata, K., Osakada, K., and Terasaka, Y., 1984, "Process Modelling of Orthogonal Cutting by Rigid-Plastic Finite Element Method," ASME J. of Engng. Materials and Technology, Vol. 106, pp. 132-138.

Klamecki, B. E., 1973, " Incipient Chip Formation in Metal Cutting Processes-A three Dimentional Finite Element Analysis, "Ph.D. thesis, University of Illinois, Urbana Illinois.

Komvopoulos, K. and Erpenbeck, S. A., 1991, "Finite Element Modelling of Orthogonal Metal Cutting," ASME J. of Engng. for Industry, Vol. 113, pp. 253-267, 1991.

Lee, E. H. and Shaffer, B. W., 1951, "The Theory of Plasticity Applied to a Problem of Machining," ASME J. Applied Mech., Vol. 18, pp. 405-413.

Merchant, M. E., 1945, "Mehanics of Metal Cutting Process," J. Applied Phys., Vol 16, pp. 267-318.

Meir, G., Hashemi, J., and Chou, P. C., 1988, "Finite Element Simulation of Segmented Chip Formation in High Speed Machining," Report MR88-120, Society of Manufacturing Engineers.

Piispanen, V., 1948, "Theory of Formation of Metal Chips," J. of Appl. Phys., Vol. 19, pp. 876-881.

Shaw, M. C., 1984, Metal Cutting Principles, Oxford Series on Advanced Manufacturing.

Strenkowski, J. S., and Carrol, J. T., 1983, "A Finite Element Model of Orthogonal Metal Cutting" ASME J. of Engng. for Industry, Vol. 107, pp. 349-354.

Time, I, 1870, "Resistance of Metals and Woods to Cutting," St. Petersburg.

Tresca, H., 1873, "Writings on the Machining of Metals," Bull. Soc. d'Encouragement pour l'Industrie Nationale, pp. 585-685.

Taylor, F. W., 1906, "On the Art of Cutting Metals," Trans. ASME, Vol. 28, pp. 31-38.

Tseng, A. A., Chou, P. C., and Hashemi, J., 1991, "Thermomechanical Simulation of Adiabatic Shear Band in High Speed Forming," in Proceedings of Army Symposium on Solid Mechanics, Materials Technology Laboratory, Watertown, MA, November 4-7.

Usui, E. and Shirakashi, T., 1982, "Mechanics of Machining, From Descriptive to Predictive Theory," on the Art of Cutting Metals-75 years Later, ASME PED-Vol. 7, pp. 13-35.

Usui, E., Shirakashi, T., and Kitagawa, T., 1984, "Analytical Prediction of Cutting Tool Wear," Wear, Vol. 100, pp. 129-151.

# Heat Transfer and Thermal Stress Analysis of Railroad Car Wheels During Stop-Braking and Quenching

*Y.H. Tang*
Volpe National Transportation System Center

"PAPER NOT AVAILABLE"

# The High Capacity Artillery Projectile

**Mr. James M. Bender**
**Dr. Bruce P. Burns***
**Army Research Laboratory**
**Weapons Technology Directorate**
**Aberdeen Proving Ground MD 21005-5066**

## ABSTRACT

The High Capacity Artillery Projectile (HICAP) is a new lightweight cargo-carrying artillery shell being developed by the Army Research Laboratory (ARL) and the Army Research Development and Engineering Center (ARDEC). It is made chiefly of composite materials and is capable of carrying all submunitions currently in the Army's inventory and those under development. The weight savings afforded by the lightweight shell enable it to carry nominally twice the normal amount of payload as present shells with only a twenty percent overall weight increase. The projectile is significantly longer (78 inches) to accommodate the additional payload. Aerodynamic stabilization is provided by fins since the heavy steel shell, which normally provides the rotational inertia for spin stabilization, has been replaced by composite materials. For ease of handling, the projectile is divided into two modules, fore and aft, that can be snap-fitted together any time prior to firing or can be breech-assembled. This permits the user to mix munitions in a single round. Provisions have been made for the incorporation of a rocket module for the rear which would extend the range. This would be developed under an advanced engineering development program. The rocket module can be employed to deliver a standard payload to nominally twice the current range. The HICAP represents a major leap ahead in capability for the U.S. Army in Fire Support. This paper discusses the major technical accomplishments to date in support of the program and those challenges to be met in the near term.

## INTRODUCTION

The Army's inventory of cargo-carrying artillery shells are made of steel and typically weigh from 95 to 103 pounds, depending on payload. Approximately 65 percent of this weight is in the shell body. There are two reasons for this. First, the setback loads applied during the firing cycle call for a material with the strength of steel. Second, the mass at the shell's outer radius when spinning, serves to stabilize the round in flight. This weight limits the amount of submunitions that can be carried. The HICAP (Figure 1) has a lightweight shell that is

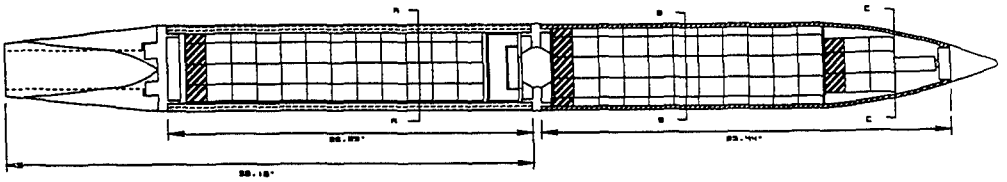


Figure 1. The High Capacity Artillery Projectile

fin stabilized and weighs less than a standard artillery shell yet can carry twice the amount of cargo. The adoption of composite materials provides HICAP with the capability to do the work of two M483-family projectiles that deliver cargo such as grenades, mines, smoke, liquid or jammers. The user can either deliver twice the payload for the same number of rounds or deliver the same amount of payload using half the number of rounds, improving his effectiveness or survivability respectively. Survivability, in this application, is defined as the reduced detection time of the firing battery. Since it will be firing significantly less rounds to achieve the same effectiveness the risk of counter-battery fire is reduced. Alternatively, the same number of projectiles can be fired with a 50 to 100 percent increase in lethality and effectiveness depending on the submunition and weapon. A propulsion option for the rear module can be selected giving the projectile equal lethality as present rounds but nominally double the range providing a greater stand-off distance.

New internal devices and shell design provide an opportunity for optimal dispersion of submunitions. The ogive, being non-metallic, creates opportunities for guidance devices such as embedded sensors and antennas not available on some metallic ogives.

## TECHNOLOGIES DEVELOPED FOR HICAP

The HICAP program requires the development of several varied and challenging technologies. First and foremost is the development of the composite shell of the rear module. Other novel technologies are the fin assembly, the special joint connecting the fore and aft modules, and the payload dispersal mechanisms.

### Composite Materials

The rear module shell must be of sufficient strength to sustain the setback loads during launch. It must not only carry its own weight but the entire weight of the forward module including the shell, payload, ogive, ejection charge and fuze. The forward payload cannot stack on top of the rear payload due to structural limitations. To illustrate this point, the M483 payload, grenades, can only be stacked eleven high. Otherwise, at peak setback, the bottom layer would be crushed. HICAP can carry 22 layers of grenades, separated into two stacks of eleven. The forward stack is supported by a deck on top of the rear module shell. The total load to be sustained by the rear shell at peak setback is nearly a million pounds (its own weight plus that of the forward shell at over 13,000 g's). This force is distributed over the cross-sectional area of the shell of 8.6 square inches producing an average axial compressive stress in the composite of 115 kpsi. This strength level has been demonstrated in a static test and is believed to be the highest strength level ever achieved for a thick graphite composite tube under axial compression.

The shell wall is a hybrid of two thermosetting composite material systems; graphite/epoxy (Hercules® IM7-8551-7/8553) and glass/epoxy (Hercules® S2/8553). To accommodate the significant axial loading at launch, the laminate stacking sequence design is such that 75 percent of the composite plies are oriented in the axial direction while the remaining 25 percent provide lateral support in the radial direction. The overall fiber volume is 65 percent. All but the first few inner layers employ IM-7 fibers. The first four inner layers contain

S-Glass fibers. The S-Glass is more compliant in compression than the graphite fibers and serve to more evenly distribute the axial stress which tends to concentrate at the inner radius of composite tubes under compression. This is illustrated by the following model. Figure 2 is an axisymmetric finite element representation of a steel endcap

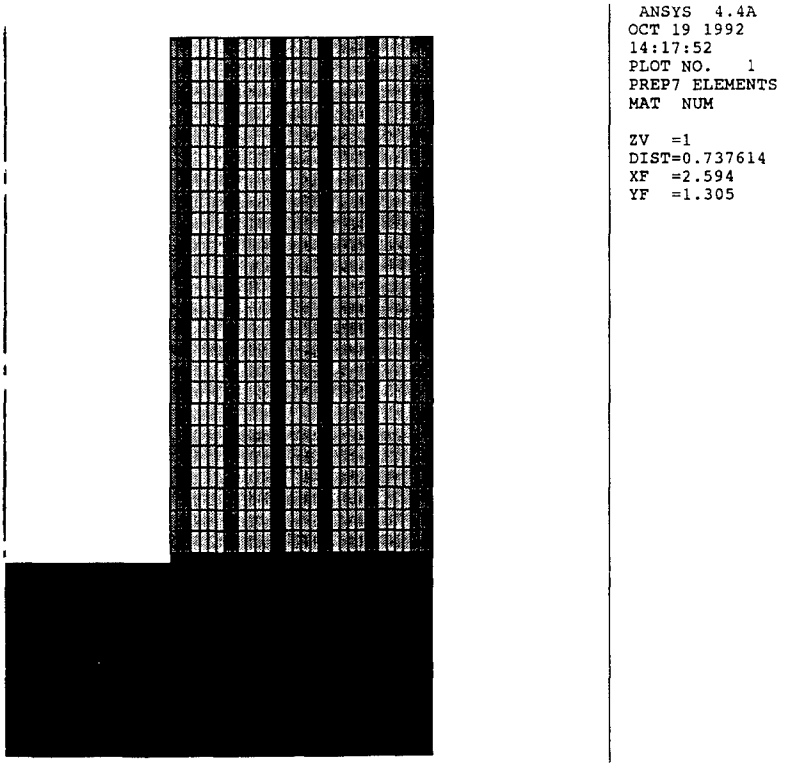



Figure 2. Axi-Symmetric Finite Element Model of a Composite Tube Butted to an End Plate

butted to a composite tube. The axial layers can be distinguished by light gray and the hoop layers by dark gray. The base of the endcap has a pressure boundary condition of 40 kpsi simulating a ballistic environment. The top of the tube is constrained from axial motion by a symmetric boundary condition. The stress plot in Figure 3 shows how the axial compressive stress is highest in the innermost axial layer. When that layer is replaced by S-Glass, a more equitable distribution of stress is achieved. Figure 4 shows the effect of a more compliant first axial layer. The stress is reduced in the glass layer and more evenly distributed to the remaining layers in the middle of the shell wall where it is contained.

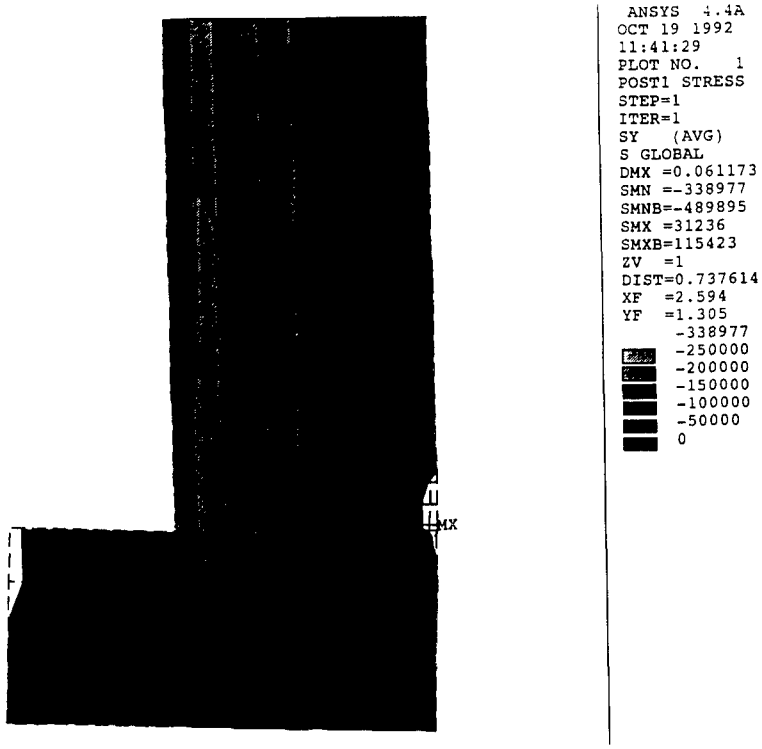



Figure 3. Compressive Stress in the Composite Tube

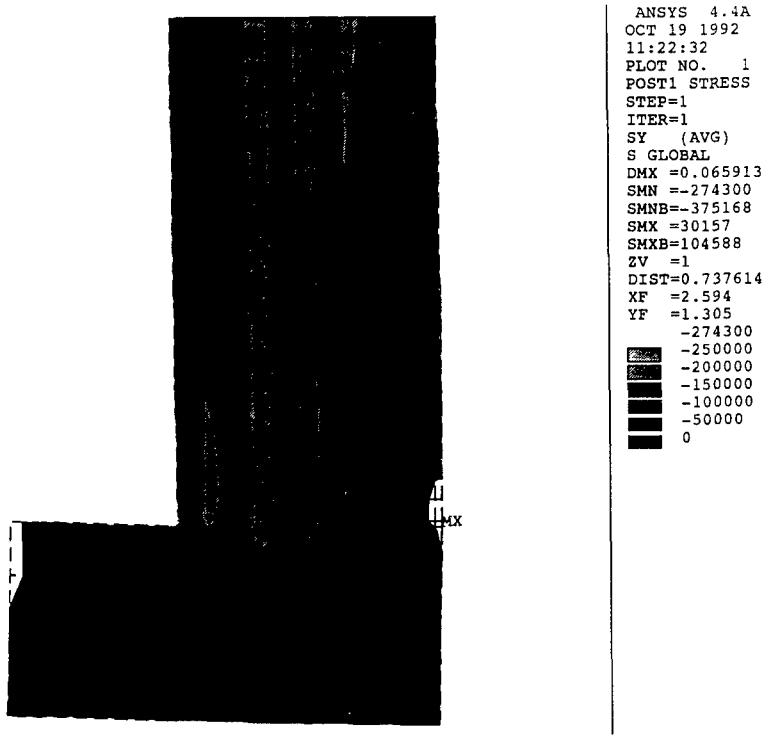



Figure 4. Compressive Stress in a Hybrid Composite Tube with More Compliant Inner Layers

Another design issue arising from the compressive loading of composite tubes is end failure. The introduction of axial load at the base of the shell has proven to be the most challenging aspect of the composite design. It is known that the majority of the load must be introduced into the shell wall through end loading. The complex state of stress that develops at the composite/metal endcap interface gives rise to various types of failure mechanisms. In all experimental tests to date these localized failures have been shown to cause premature catastrophic failure of the shell wall. This is illustrated in Figure 5 which shows the result of a static test of a full-scale tube. Figure 6 is a smear photograph of a HICAP prototype rear module with a surrogate fore module after launch from a 155-mm howitzer at zone 8 charge. The end failure has propagated forward in this case. The intrinsic strength of the tube wall has been demonstrated to be adequate. Several theories to explain this phenomenon have emerged, yet the true cause remains to be proven. Early tests of thin-walled sub-scale tubes, i.e. thickness/diameter << 0.1, result in failures in the gage section at stress levels 50 percent higher than those of thick-walled full-size tubes. The thin tube was ideally fixtured by an elaborate gripping device shown in Figure 7. Virtually all of the load is transferred into the structure through the inner and outer surfaces by traction, far different from thick-walled cylinders which are exclusively end-loaded. This type of device is not adaptable to thick cylinders in a projectile configuration. It is likely that the introduction of load on the base has some unresolved phenomenology that can only be postulated at this time. One theory is a micro-buckling effect which, due to localized shear at the interface, causes the ends of fibers to bend and initiate delamination. Another theory states that a small amount of radial tension exists when the tube is crushed also causing delamination. In a effort to respond to these effects, a special end fixture (proprietary to Custom Analytical Engineering Systems, Inc) was designed which would induce a component of radial *compressive* stress to the inside surface of the tube as axial load is applied, thus eliminating the possible failure mode. A test projectile was launched in February, 1993 which showed that the composite exceed the laboratory strength.

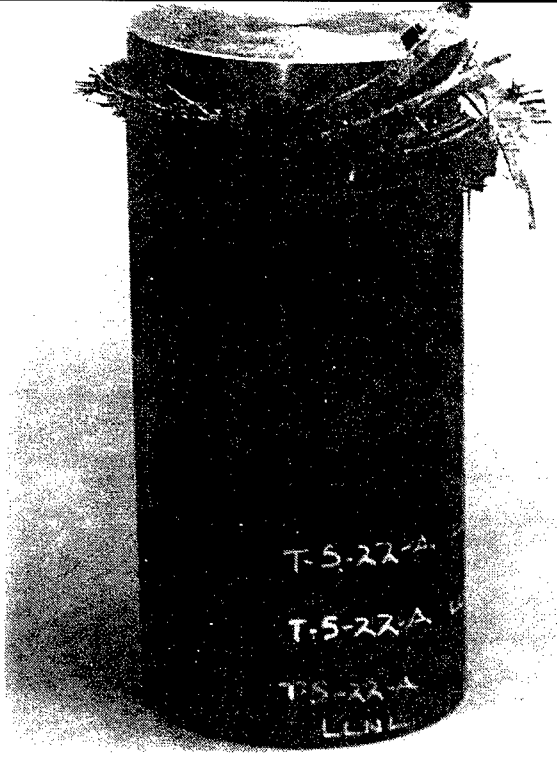



Figure 5. Static Compression Test of a Composite Tube.

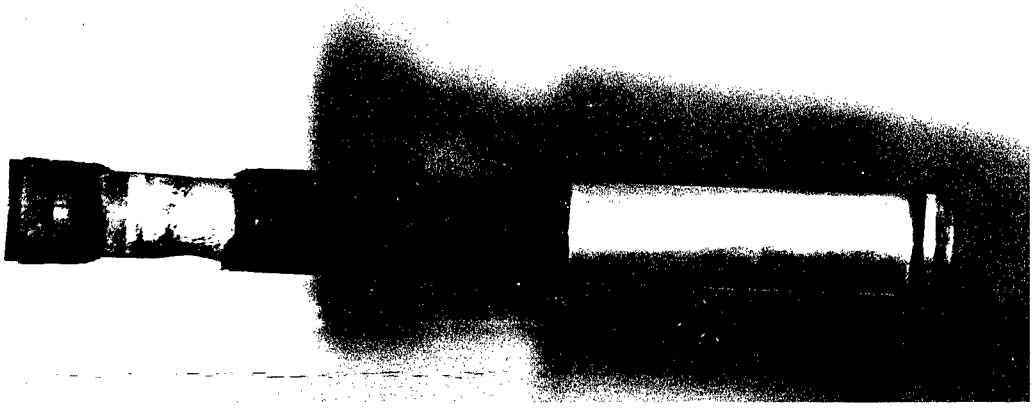


Figure 6. Gun Firing Test of Composite Tube.

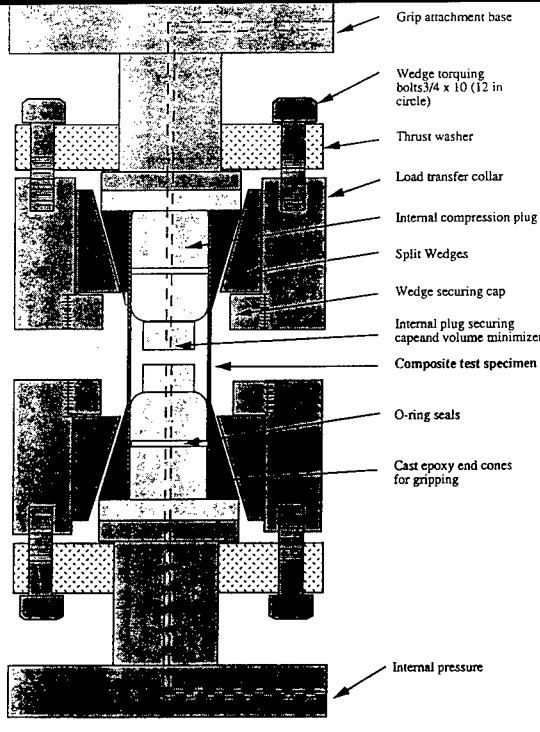



Illustration Courtesy of LLNL

Figure 7. Laboratory Fixture Used to Test Thin Composite Tubes for Determining Highest Intrinsic Strength

## HICAP Coupler

The payload is housed in two modules, one fore and one aft, which are assembled at the breech or anytime prior to ramming. The module concept has been adopted because the overall length of the assembled round would be prohibitively long for handling purposes if it were one piece, especially inside the limited working area of a self-propelled howitzer. A special joint has been designed which allows ease of assembly and has been ballistically hardened to sustain the highest propelling charge. The joint also attenuates tensile stress which can be found in long projectiles at muzzle exit due to the sudden off-load of pressure. The existence of tension has been established by computer simulation and actual gun firing tests.

A dynamic finite element analysis was employed to examine the effect of pressure off-load at muzzle exit. Figure 8 is a finite element representation of a 60-inch aluminum hollow shell with a one-inch thick steel deck midway on the structure creating two compartments for payload. Each compartment houses a simulated payload weighing 28 pounds. A typical ballistic loading cycle was applied to the base

including a monotonically decreasing pressure load at muzzle exit which decays to zero in 8 calibers of travel through the blast region. The analysis was allowed to run past muzzle exit for three milliseconds. Figure 9 is a stress history of an element near the mid

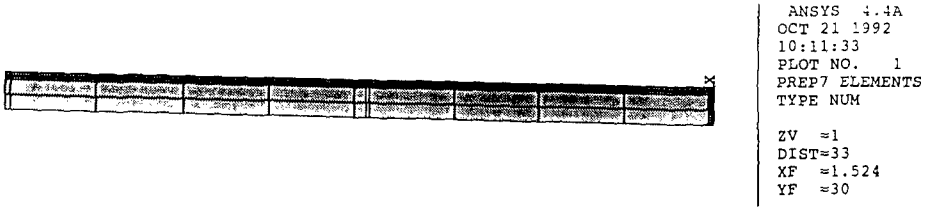



Figure 8. Finite Element Model for Wave Propagation Study

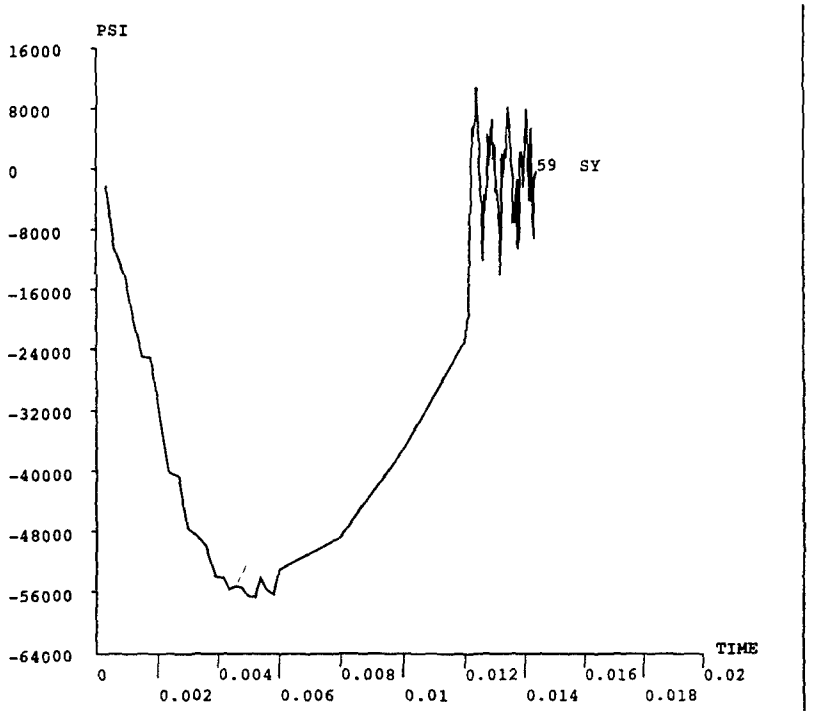



Figure 9. Axial Stress History of an Element Near the Midpoint

muzzle exit are a result of the release of compressive force much like that of a compressed spring that is suddenly unconstrained. This phenomenon was demonstrated in some early prototype tests of a composite tube. A tube was joined to a surrogate forward payload by a simple double-ended stud with no attenuation capabilities. A smear photograph (see preceding section) shows a gap at the joint indicating separation and verifying the need for a wave-attenuating joint (mechanical filter).

Although the details of the joint cannot be shown, a dynamic finite element simulation was performed on a model identical to that shown in Figure 8 with the addition of the joint. Figure 10 shows the stress histories of two elements, one above and one below the joint. It is apparent that the tensile portions of the waves have been attenuated.

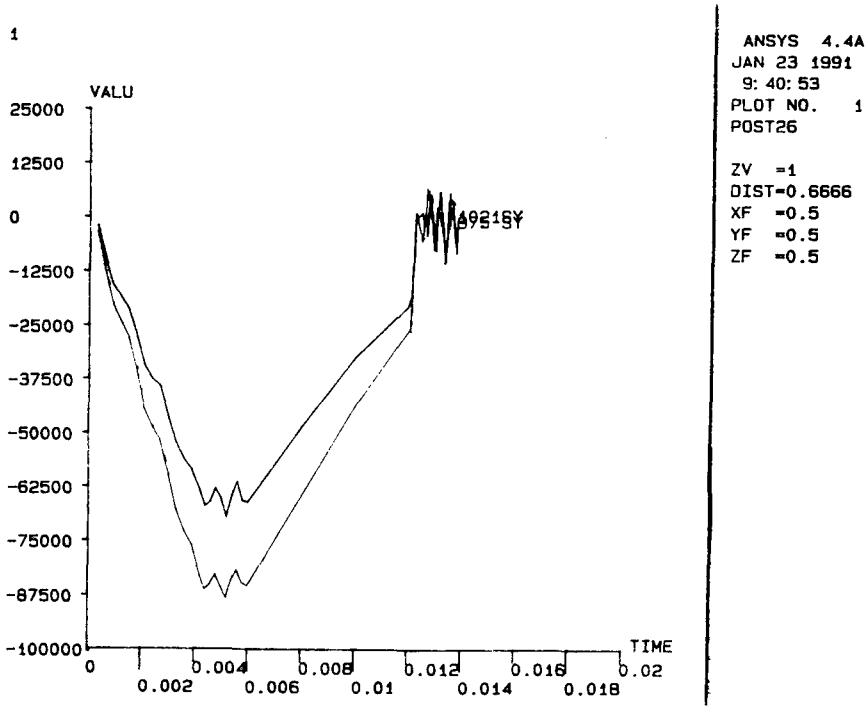



Figure 10. Axial Stress Histories of Elements above and Below the Joint Showing Attenuation of Tensile Portions of the Wave.

Cargo Dissemination

The design of HICAP provides an opportunity for advanced cargo dissemination techniques. Many current submunitions take the shape of a "hockey puck" such as implantable mines, radio frequency jammer modules and illumination submunitions. Others deploy a canister, which is burst after ejection. However, the most frequently used submunition, M42/M46 grenades, are disbursed in a circular pattern through base ejection and projectile spin. The HICAP provides this method for the rear module and employs a central burst method for the fore module much like that used in the Army's Multiple Launch Rocket System (MLRS). The fore module has a central expulsion charge to radially disburse the grenades by bursting the 1/4 inch thick composite shell. The shell wall can be designed by judicial selection of ply orientation to support setback forces during launch, yet burst easily when pressurized.

A prototype embedded fuze has been designed by the Fire Support Armaments Center of ARDEC, which will initiate two burster charges. The forward charge bursts the forward shell disseminating the cargo radially (grenades only) and creates a seismic pulse which is picked up by a sensor in the rear module. The sensor then initiates the rear burster charge which pressurizes the rear module and forces the payload through the base for conventional dispersal. The pattern on the ground should be as illustrated in Figure 11. By adjusting the amount of charge in the central burster of the fore module, the density and size of the doughnut pattern can be controlled. Tests have been performed at ARDEC to determine grenade velocity at burst. These test results were put into computer models to predict the pattern shape and density on the ground.

## CONCLUSIONS

The HICAP concept provides the soldier with many options to enhance his fire mission. If enhanced survivability is desired he will be capable of delivering double the amount of payload with a single round and cut his detection time in half. With the rocket rear module option, he can deliver the conventional payload to nominally double the range providing a greater standoff distance. If the battle plan calls for enhanced effectiveness, he can maintain his rate of fire and increase the lethality by 50 to 100 percent, depending on payload.

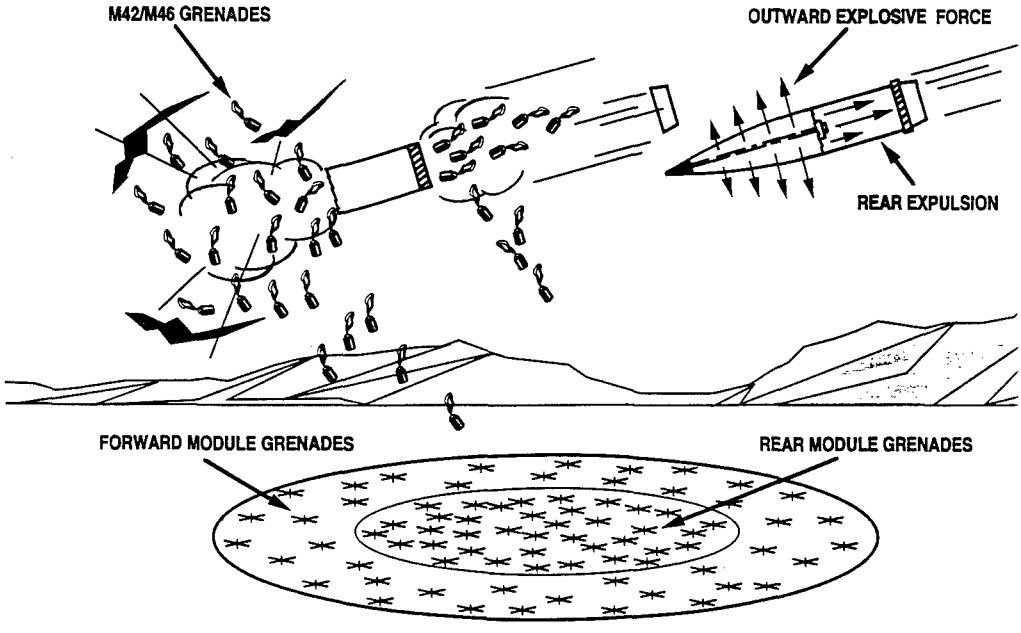



Figure 11. Cargo Dissemination Pattern of Grenades on the Ground

HICAP represents a major leap ahead in capability for the U.S. Army in Fire Support.

This advance in capability could not have been achieved without crossing several technical barriers. New manufacturing, assembly and modelling techniques were developed in support of HICAP to achieve these goals. Many challenges lie ahead such as manufacturing for affordability, guidance and control, cargo dissemination in a non-spinning mode and integration of components.

# FreeVibration and Impact Response of Laminated Composites Using a Layer-wise Theory

Dr. Asghar Nosier and Dr. Rakesh K. Kapania*
Department of Aerospace and Ocean Engineering
Virginia Polytechnic Institute and State University
Blacksburg, VA, 24061-0203
and
Dr. J. N. Reddy
Oscar S. Wyatt Chair Professor
Department of Mechanical Engineering
Texas A & M University
College Station, TX, 77843-3123

## Abstract

Reddy's layer-wise theory is used to perform free-vibration and impact response analysis of laminated plates. The results obtained from this theory are compared with those obtained from a full-fledged three-dimensional elasticity analysis and various equivalent single-layer theories that are available. These include : (i) the classical laminated plate theory (CLPT), (ii) the first-order shear deformation laminated plate theory (FSDPT), and the third-order shear deformation plate theory (THSDPT). The elasticity equations are solved by utilizing the state-space variables and the transfer matrix. The forced-vibration analysis is developed by the modal superposition technique. Six different models are introduced for representation of the impact pressure distribution. The first five models, in which the contact area is assumed to be known, result in a nonlinear integral equation similar to the one obtained by Timoshenko in 1913. The resulting nonlinear integral equation is discretized using a time-finite-element scheme. Two different interpolation functions, namely: (i) Lagrangian and (ii) Hermitian polynomials, are used to express the impact force. The sixth loading model, in which the time dependence of the contact area is taken into account according to the Hertzian contact law, resulted in a complicated but a more realistic, nonlinear integral equation. Also a simple, but accurate, numerical technique is developed for solving this nonlinear integral equation which results in the time-history of the impact force. A detailed study concerning all the response quantities, including the in-plane and interlaminar stresses, is carried out for symmetric and antisymmetric cross-ply laminates and important conclusions are reached concerning the usefulness and accuracy of the various plate theories.

## Introduction

The composite materials are widely used for space, military and commercial applications at present. due to their high strength and stiffness to weight ratios. Also these materials can be tailored to design requirements by varying the laminate scheme. Composites are used in situations involving the sudden application of loads. The dynamic response of the structure ensues after load application and a state of stress may be generated that leads to failure. One obstacle that prevents application of these materials in primary structures is the damage induced due to service or accidental loads and the consequent reduction in stiffness, strength and life of these structures. Impact by blunt objects can reduce the uniaxial tension strength of some composites by as much as 30 percent without any visible surface damage. Therefore, damage resistant and durable composite materials are essential for the design of laminated structures.

The low velocity impact response of laminated composite plates has been investigated extensively by experimental and numerical methods. Goldsmith [1] used the normal modes method to determine the dynamic response of an isotropic plate or beam to a rigid impactor. Timoshenko [2] used normal modes and a Hertzian contact law to analyze the deflections of a beam impacted by an impactor. The resulting nonlinear integral equations were solved by numerical integration. Sun and Chattopadhyay [3] extended Timoshenko's method to a laminated simply supported composite plate. Ramkumar and Chen [4] used Fourier integral transforms to find the response of an infinite anisotropic laminated plate to an experimentally determined impact force. Petersen [5] used the finite element method based on a shear deformable plate theory with rotary inertia to analyze laminated plates subjected to impact loads. Thangjitham et al. [6] obtained low-velocity impact response of orthotropic plates using a higher-order theory which incorporates the transverse normal stress and rotary inertia effects and fulfills the shear stress conditions on the bounding surfaces. Sun and Liou [7] used a three-dimensional hybrid stress finite element method to investigate laminated plates under impact loads. Cairns and Lagace [8] obtained transient response of graphite/epoxy and Kevlar/epoxy laminates subjected to impact using a Rayleigh-Ritz method. Chao, Tung, Sheu, and Chern [9] employed a 3-D laminated theory in conjunction with a modal analysis to study the impact response analysis of thick comoposites. Detailed reviews of various investigations into impact response and wave propagation studies are given by Kapania and Raciti [10] and Abrate [11].

For the study of impact response of metals and composites, many researchers [1-8] used the Hertzian contact law which relates impactor and plate motion with contact force. However, Yang and Sun [12] showed that the Hertzian contact law was not adequate by performing statical indentation tests on graphite/epoxy composite laminates using spherical steel indenters of different sizes. They found that significant permanent indenta-

tions existed. In order to account for the permanent indentation, Tan and Sun [13] proposed a modified Hertzian contact law following Yang and Sun [12]. They compared experimental results with the predictions of finite element analysis using the statically determined contact law. Sun and Chen [14] analyzed initially stressed composite plates under impact loads using this modified Hertzian contact law.

In this study, we have used Tan and Sun's law to study the impact response of laminated plates using four different theories. A model superposition approach is used and the results are obtained for natural frequencies and the impact response. A time-finite-element based approach is developed for obtaining the impact responses. It is observed that Reddy's layer-wise theory captures $3-D$ effects. While the convergence of the results with respect to number of mathematical layers in the modeling is fast, the convergence of various results with respect to the number of modes is quite slow, especially at the point of impact. However, away from that point, the convergence with respect to the number of modes is rather fast.

## Layer-wise Theory

To understand Reddy's [15] layer-wise theory, consider a two-layered plate as shown in Fig. 1. Let $u^1(x,y,t), u^2(x,y,t)$, and $u^3(x,y,t)$ represent the displacement components of all points located, respectively, at $z=-h/2, z=0$, and $z=h/2$ in the $x$-direction. Assuming that the displacement component of the plate in the $x$-direction has a linear variation within each layer, gives

$$u_1(x,y,z,t) =$$

$$\begin{cases} (1+\frac{2}{h}z)u^2(x,y,t) - \frac{2}{h}zu^1(x,y,t) & 0 \geq z \geq -h/2 \\ \frac{2}{h}zu^3(x,y,t) + (1-\frac{2}{h}z)u^2(x,y,t) & 0 \leq z \leq h/2 \end{cases} \tag{1}$$

Similar expressions can be written for the displacement components $u_2(x,y,z,t)$ and $u_3(x,y,z,t)$ of a point located at $(x,y,z)$ in the undeformed laminate in the $y$- and $z$-directions. This way the displacement field will be continuous through the laminate thickness; the transverse strain components, however, will not be continuous at the interface of the two layers. This, on the other hand, leaves the possibility of the transverse stress components becoming continuous at the interface of the two layers. This seemingly hypothetical presumption can become a reality by subdividing each physical layer into a finite number of mathematical layers. That is, by introducing more interfaces and, therefore, more unknown generalized displacement components at such mathematical interfaces. It is possible to generalize the result in Eq. (1) for a generally laminated plate by representing $u_1(x,y,z,t), u_2(x,y,z,t)$,

and $u_3(x,y,z,t)$ as

$$\begin{aligned} u_1(x,y,z,t) &= u^i(x,y,t).\ \phi^i(z) \\ u_2(x,y,z,t) &= v^i(x,y,t).\ \phi^i(z) \\ u_3(x,y,z,t) &= w^i(x,y,t).\ \phi^i(z) \qquad i = 1,2,...,N+1 \end{aligned} \tag{2}$$

where $\phi^i(z)$ are defined as:

$$\phi^i(z) = \begin{cases} 0 & z \le z_{i-1} \\ \psi_1^i = \frac{-1}{h_{i-1}}(z_{i-1} - z) & z_{i-1} \le z \le z_i \\ \psi_2^i = \frac{-1}{h_i}(z - z_{i+1}) & z_i \le z \le z_{i+1} \\ 0 & z \ge z_{i+1} \end{cases} \tag{3}$$

In Eqs. (2) the function $u^i(x,y,t), v^i(x,y,t)$, and $w^i(x,y,t)$ represent the displacement components of all points located on the $i^{th}$ plane (defined by $z = z_i$) in the $x-$, $y-$, and $z$-directions, respectively, in the undeformed laminate. Also $N$ denotes the total number of mathematical layers considered in a laminate. **Note that a repeated index indicates summation over all values of that index.** Substituting Eqs. (2) in 3D strain-displacement relations results in

$$\epsilon_{11} = \frac{\partial u^i}{\partial x}.\phi^i,\ \epsilon_{22} = \frac{\partial v^i}{\partial y}.\phi^i,\ \gamma_{12} = \left(\frac{\partial u^i}{\partial y} + \frac{\partial v^i}{\partial x}\right).\phi^i$$

$$\gamma_{13} = u^i.\frac{d\phi^i}{dz} + \frac{\partial w^i}{\partial x}.\phi^i,\ \gamma_{23} = v^i.\frac{d\phi^i}{dz} + \frac{\partial w^i}{\partial y}\phi^i, \epsilon_{33} = w^i.\frac{d\phi^i}{dz} \tag{4}$$

Using Hamilton's principle, $3(N+1)$ equations of motion corresponding to $3(N+1)$ unknowns $u^i, v^i$, and $w^i$ are derived:

$$\begin{aligned} \delta u^i &: \quad \frac{\partial M_1^i}{\partial x} + \frac{\partial M_6^i}{\partial y} - Q_1^i = I^{ij}\ddot{u}^j \\ \delta v^i &: \quad \frac{\partial M_6^i}{\partial x} + \frac{\partial M_2^i}{\partial y} - Q_2^i = I^{ij}\ddot{v}^j \\ \delta w^i &: \quad \frac{\partial K_1^i}{\partial x} + \frac{\partial K_2^i}{\partial y} - Q_3^i + \delta_{i1}P_z = I^{ij}\ddot{w}^j \end{aligned}$$

where $\delta_{i1}$ is the Kroneckar delta and $(i,j = 1,2,...,N+1)$.

For a laminated plate with a rectangular planform, the boundary conditions in LWPT at an edge parallel to $x$-axis involves the specification of $u^i$ or $M_1^i$; $v^i$ or $M_6^i$; and $w^i$ or $K_1^i$. Similarly, at an edge parallel to $y$-axis,

we can specify the required boundary conditions. The generalized stress resultants $M_1^i, M_2^i$, etc., and mass terms $I^{ij}$ are defined as

$$(M_1^i, M_2^i, M_6^i) = \int_{-h/2}^{h/2} (\sigma_{11}, \sigma_{22}, \sigma_{12}).\phi^i dz$$

$$(Q_1^i, Q_2^i, Q_3^i) = \int_{-h/2}^{h/2} (\sigma_{13}, \sigma_{23}, \sigma_{33}).\frac{d\phi^i}{dz} dz \tag{5}$$

$$(K_1^i, K_2^i) = \int_{-h/2}^{h/2} (\sigma_{13}, \sigma_{23}).\phi^i dz$$

$$I^{ij} = \int_{-h/2}^{h/2} \rho\phi^i\phi^j \, dz \tag{6}$$

where $\rho(x, y, z)$ denotes the mass density of the material point located at $(x, y, z)$ in a laminate. By substituting the three-dimensional constitutive law for each layer along with the strain-displacement relations (Eq. 4) in Eq. 5, one can obtain the $3(N+1)$ equations of motion corresponding to $3(N+1)$ unknowns $u^i, v^i$, and $w^i$. The details are given in Ref. 16.

**Free-Vibration Analysis:** By assuming the time-dependent motion of the plate to be harmonic, and assuming a spatial variation for the displacement components that satisfies the boundary conditions, we can obtain an algebraic eigenvalue problem. For the simply-supported plates considered in this study, the displacement components in the layer-wise theory (LWPT) were assumed to be:

$$\begin{Bmatrix} u^j \\ v^j \\ w^j \end{Bmatrix} = \begin{Bmatrix} A_{mnk}^j \cos\alpha_m x \sin\beta_n y \\ B_{mnk}^j \sin\alpha_m x \cos\beta_n y \\ C_{mnk}^j \sin\alpha_m x \sin\beta_n y \end{Bmatrix} \cos\omega_{mnk} t \tag{7}$$

The natural frequencies of symmetric and antisymmetric cross-ply, laminated plates $(0^o/90^o)$, $(0^o/90^o/0^o)$, $(0^o/90^o/0^o/90^o)$ were found in this study. The results obtained from LWPT were compared with those obtained from (i) the classical laminated plate theory (CLPT), (ii) the first-order shear deformation laminated plate theory (FSDPT), the third order shear deformation theory (TSDPT), and the elasticity solution obtained using a state-space approach. Note that results using the layer-wise theory (LWPT) were obtained using six layers to represent each ply. For the $(0^o/90^o/0^o/90^o)$ laminate LWPT, thus yields 75 lowest frequencies for a given mode in the $x-$ and $y-$ co-ordinate (for each $m$ and $n$ pair). This compares with 3 natural frequencies for each mode in CLPT; five natural frequencies in FSDPT and TSDPT; and infinite frequencies if we use

the theory of elasticity. Also by uncoupling the Navier Equations a detailed analysis was carried out to study various mode shapes and natural frequencies of a homogeneous transversely isotropic plate [16].

### Impact Response Analysis

The impact response of a number of laminated plates was studied next using various theories. A modal super-position approach in conjunction with a contact law suggested by Tan and Sun [20] was used. This contact law is a variation of the more famous Hertz contact law which is given as: $F = K_2 \alpha^{\frac{3}{2}}$ where $F$ is the contact force, $\alpha$ is the indentation and $K_2$ is the contact co-efficient. The Hertzian contact law, being an elastic law, does not account for permanent indentation. For composites, permanent indentation may occur at relatively low loading levels and for these materials, loading and unloading are in general, different from each other. Tan and Sun's [13] experimentally determined contact law does take into account differing loading and unloading behaviors.

To obtain the generalized forces for use in the modal superposition, six different models are introduced for representing the impact force. The first five models treat the impact force as a: (i) concentrated force, (ii) uniformly distributed pressure over a rectangular area $(a * b)$, (iii) a cosine shaped load distributed over a rectangular area, (iv) uniformly distributed over a circular area, and (v) a spherically shaped load distribution over a small circle. In all these cases, the contact area is assumed to be known and the resulting nonlinear integral equation is same as given by Timoshenko. This integral equation is descretized using a time-finite element scheme. Two different interpolation functions, namely: (i) Lagrangian or the so-called hat functions (shown in Fig. 2), and (ii) Hermitian polynomials (Fig. 3) are used to express the temporal distribution of the impact force. The details of the determination of the force are given in Ref. 17. The present approach due to its modular nature is preferrable to the existing approaches. In the sixth modeling, the time dependence of the impact force is taken into account using Hertz contact law, resulting in a more complicated but realistic integral equation. A simple and accurate, numerical technique is developed for solving this nonlinear integral equation [17].

The present developments were first applied, for verification, to study the impact response of a simply-supported isotropic beam (previously studied by Timoshenko) and subsequently to that of a number of laminated plates. The time history of the impact force and the indentation in the isotropic beam are shown in Figs. 4, and 5, respectively. In the Timoshenko's solution, the response quantities are obtained up to 1780 $\mu sec.$, and only two collisions were observed. The present results indicate the presence of a third contact at about $3000 \mu sec$. The integral equation was solved using the hat functions with a time step of $10 \mu sec$. To check the accuracy of these results, analysis was also carried out using Hermitian polynomials and it was seen that quite accurate results are obtained using hat functions.

The impact response of an anti-symmetric cross-ply, simply-supported square laminate ($0^o/90^o$) is next studied. The material properties are given in Ref. 17. Two cases with length to thickness ratio ($a/h$) of 40 and 20 were studied. Figures 6 and 7 indicate the impact force and displacement time histories (for $a/h = 20$) as obtained by various theories. Note that FSDPT and TSDPT yield very similar results. This may not be true in general as the FSDPT results may be strongly influenced by the shear correction factor. The effect of number of layers used for each physical sublayer was also studied and the results are shown in Fig. 8 for a plate with ($a/h$) of 20. To obtain these results, each physical layer was modeled using (i) one sublayer, (ii) two sublayers, and (iii) three sublayers. Clearly convergence is obtained by modeling each layer into a small number of sublayers. In addition, the effect of number of modes on the response calculation was also studied. The results from this convergenece study for the case of impact force, transverse displacement and ($\sigma_{11}$) are given in Figs. 9, 10 and 11 respectively. Note that for the case of FSDPT the convergence with respect to the number of modes is quite fast whereas it is very slow for the case of LWPT. This is due to the fact that the laminate is more precisely modeled in LWPT as a three-dimensional continuum than in FSDPT. Also note that the convergence is extremely slow at the point of impact. However, it was observed to be relatively fast for points away from the point of impact. These results along with the complete results for ($0^o/90^o/0^o$) and ($0^o/90^o/0^o/90^o/0^o$) laminates are given in Ref. 17.

## Concluding Remarks

The paper describes a recent study on the free vibration and impact response of laminated plates using four different plate theories. The first three theories belong to the class of the equivalent single-layer theories in which transverse extensibility of the plate is ignored. The fourth theory takes this into account by representing the displacements in a layerwise manner. The study demonstrates the effectiveness of this theory through several examples pertaining to the natural frequencies, the impact force, the transverse displacement and the inplane and interlaminar stress components. In the case of natural frequencies, it was observed that the CLPT yields three natural frequencies for each mode in the inplane co-ordinates. The corresponding number is infinite for three-dimensional elasticity, five for the case of FSDPT and TSDPT, and $3(N+1)$ for the case of LWPT. Here $N$ is the number of mathematical layers in which the laminate is divided into. Hence by increasing this number, one can obtain the natural frequencies given by the $3-D$ elasticity. It is observed that only through the use of the LWPT, one can capture the three-dimensional effect. But , in this theory, the modal convergence for the various response quantities (transverse displacements, impact force, inplane and interlaminar stress components) is extremely slow, especially at the point of impact.

**Acknowledgements**: The authors sincerely thank the Army Re-

search Office for the support of this research (Grant #DAAL 03-90-G-0134) with Dr. Gary Anderson as the grant monitor.

## References


1. Goldsmith, W., *Impact, The Theory and Physical Behaviour of Colliding Solids*, Edward Arnold Ltd., London, 1960.
2. Timoshenko, S. P., "Zur Frage Nach der Wirkung Eines Stosses auf Einen Balken," *ZAMP, 1913, pp. 198–209.*
3. Sun, C. T. and Chattopadhyay, S., "Dynamic Response of Anisotropic Laminated Plates under Initial Stress to Impact of a Mass," *J.of Appl. Mech., ASME*, Vol. 97, 1975, pp. 693–698.
4. Ramkumar, R. L. and Chen, P. C., "Low-Velocity Impact Response of Laminated Plates," *AIAA J.*, Vol. 21, No. 10, 1983, pp. 1448–1452.
5. Petersen, B. R., "Finite Element Analysis of Composite Plate Impacted by a Projectile," *Ph.D. dis.*, Univ. of Florida, 1985.
6. Thangjitham, S., Librescu, L. and Cederbaum, G., "Low-Velocity Impact Response of Orthotropic Plates Using a Higher-Order Theory," *Proc. 28th AIAA/ ASME/ASCE-/AHS/ASC Structures, Structural Dynamics and Materials Conference*, 1987.
7. Sun, C. T. and Liou, W. J.,"Investigation of Laminated Composite Plates Under Impact Dynamic Loading Using a Three-Dimensional Hybrid Stress Finite Element Method," *Comp. and Struct.*, Vol. 33, No. 3, 1989, pp. 879–884.
8. Cairns, D. S. and Lagace, P. A., "Transient Response of Graphite/Epoxy and Kevlar/Epoxy Laminates Subjected to Impact," *AIAA J.*, Vol. 27, No. 11, 1989, pp. 879–884.
9. Chao, C. C., Tung, T. P., Sheu, C. C., and Chern, H. J., "A 3-D Laminated Plate Theory and Nonlinear Impact Modal Analysis," *Mach. Dyn. and Element Vib.*, DE-Vol. 36, 1991, pp. 239–245.
10. Kapania, R. K., and Raciti, S., "Recent Advances in Analysis of Laminated Beams and Plates Part II: Vibration and wave Propagation", *AIAA Journal*, Vol. 27, No. 7, 1989, pp. 935–949.
11. Abrate, S., "Impact on Laminated Composite Materials", *Appl. Mech. Rev.*, Vol. 44, No. 4, 1991, pp. 155–190.
12. Yang, S. H. and Sun, C. T., "Indentation Law for Composite Laminates," *NASA CR-165460*, July 1981.
13. Tan, T. M. and Sun, C. T., "Wave Propagation in Graphite/Epoxy Laminates Due to Impact," *NASA CR-168057*, Dec. 1982.
14. Sun, C. T. and Chen, J. K., "On the Impact of Initially Stressed Composite Laminates," *J. of Comp. Mat.* , 1985, pp. 490–504.
15. Reddy, J. N., "A Generalization of Two-Dimensional Theories of Laminated Composite Plates", *Comm. Appl. Num. Meth.* ,Vol. 3, 1987, pp. 173–180.
16. Nosier, A., Kapania, R. K., and Reddy, J. N., "Free Vibration Analysis of Laminated Plates Using a Layer-Wise Theory", AIAA Paper 93-1320, to appear in *AIAA J.*
17. Nosier, A., Kapania, R. K., and Reddy, J. N., "Low-Velocity Impact Response of Laminated Plates", *CCMS-92-20*, VPI&SU, Submitted to *Computational Mechanics-an International Journal.*

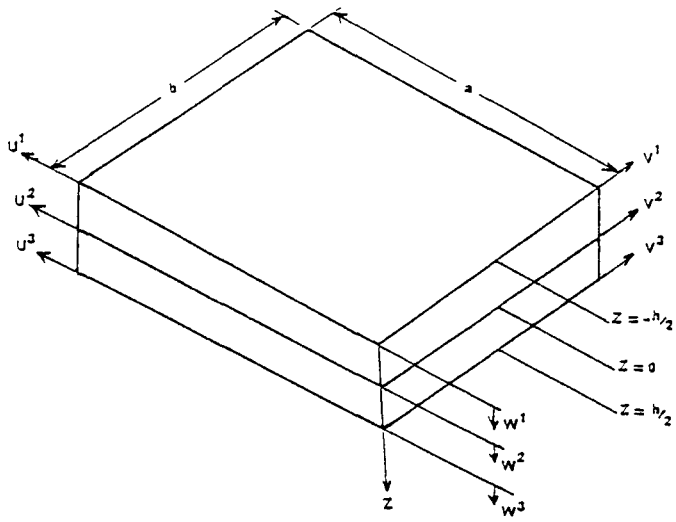



Fig. 1 Displacement components $u^j(x,y,t)$, $v^j(x,y,t)$ and $w^j(x,y,t)$ in a two-layered plate in the layerwise theory.

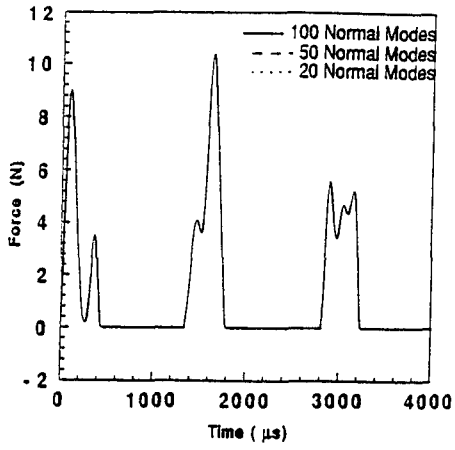



Fig. 2 The contact force history of a simply-supported beam subjected to an impact at the center.

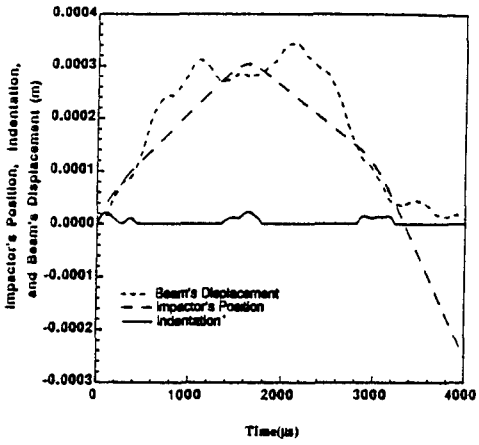



Fig. 3 The indentation and the transverse displacement of the simply-supported beam and the impactor's position.

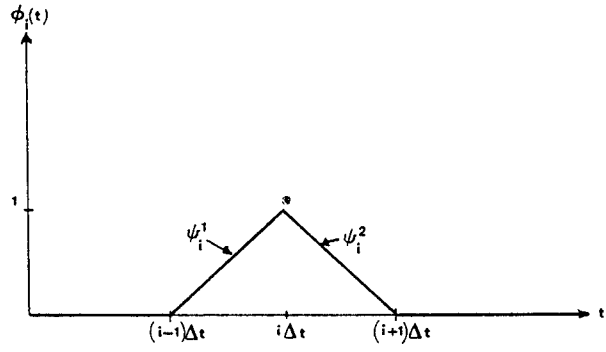



Fig. 4 The temporal linear Lagrange interpolation function (hat function).

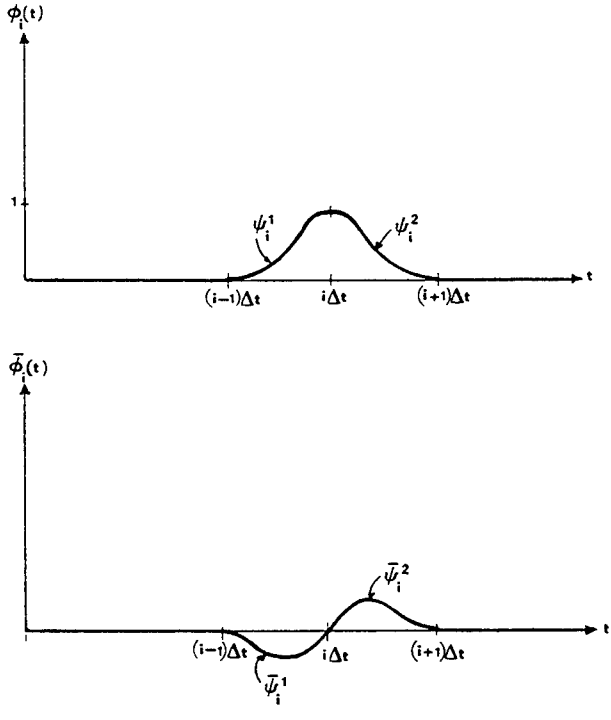



Fig. 5 The temporal Hermite cubic polynomials.

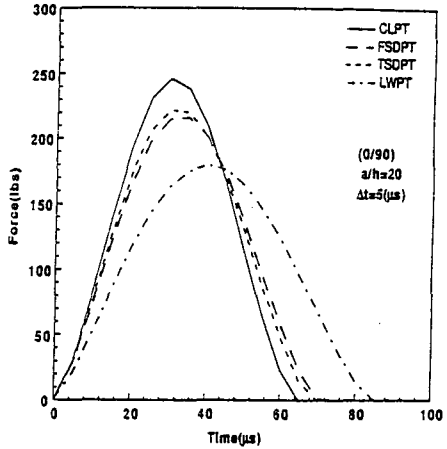



Fig. 6 Comparison of plate theories in predicting the contact force history of a ($0^o/90^o$) laminate.

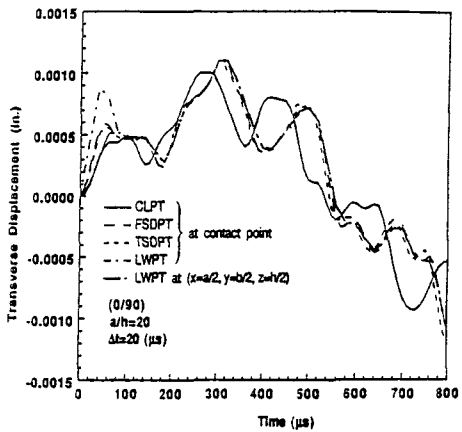



Fig. 7 The displacement time history of a ($0^o/90^o$) laminate according to various plate theories.

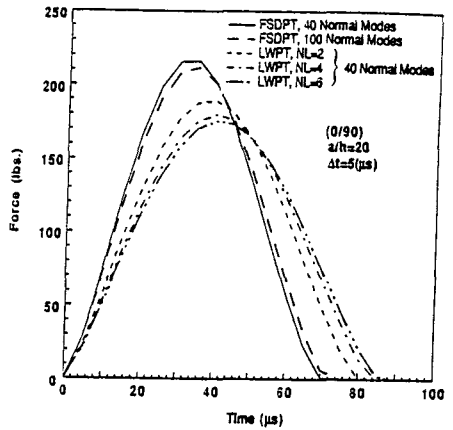



Fig. 8 Effect of modeling each physical layer into a finite number of sublayers in LWPT.

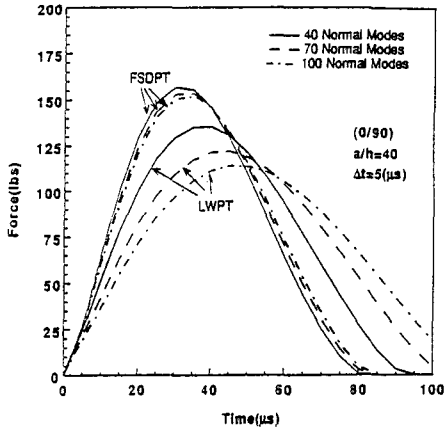



Fig. 9 Convergence study of the contact force predicted by FSDPT and LWPT with respect to the normal modes.

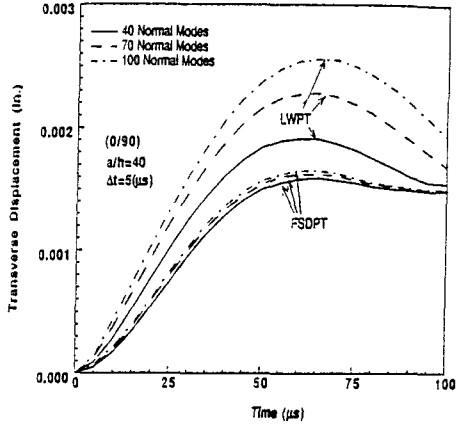



Fig. 10 Convergence study of the transverse displacement, during the contact period, predicted by FSDPT and LWPT with respect to the normal modes.

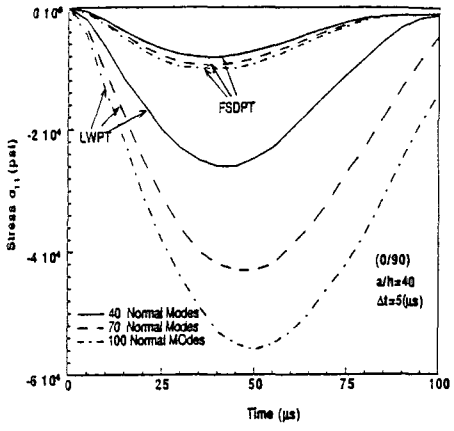
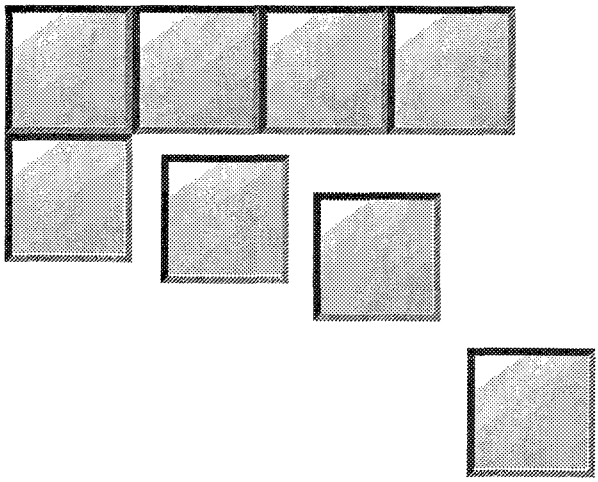



Fig. 11 Convergence study, with respect to normal modes, of the in-plane stress $\sigma_{11}$ at the contact point as predicted by FSDPT and LWPT during the contact.

# SESSION V: CERAMICS/GLASS

**Chairman:** *Dr. R. Palicka*
**Cercom Inc.**



# Determination of Material Strength in Shocked Ceramics

*Y.M. Gupta*
Washington State University

"PAPER NOT AVAILABLE"

# Dynamic Behavior of Ceramics Under Multiaxial Compression

Mr. Weinong Chen and Dr. G. Ravichandran*
Graduate Aeronautical Laboratories
California Institute of Technology
Pasadena, California 91125

## Abstract

A new experimental technique for imposing controlled, dynamic confinement on specimens subjected to high-strain-rate uniaxial compression is being developed. A brief description of the experimental technique, as well as some preliminary experimental results of the technique are presented in this paper. The results show that under dynamic confinement, the impact strength of a brittle glass ceramic increases as compared to its unconfined failure strength. It is also observed that the propensity of the ceramic to fragment is suppressed by dynamic confinement.

## Introduction

Ceramics and their composites are being increasingly used in advanced applications. Thus, there is a need to develop constitutive models to characterize their behavior and failure modes under multiaxial dynamic loading conditions. Ceramics fail typically at very small strains (<1%) under uniaxial compression, and an understanding of damage initiation and evolution is important in the analysis of such brittle materials. In brittle materials, the failure strength has been predicted to increase even under moderate amounts of confinement. This increase has been observed experimentally under static confinement in rocks and ceramics [1,2,3]. In many impact related applications, inertial confinement plays an important role in influencing the failure mode and hence the overall performance of the system. This points to the need for experimental techniques which will allow the exploration of dynamic behavior of materials under multiaxial loading conditions. Due to the transient nature of loading encountered in practical applications, the experimental technique should be able to apply both proportional

(between axial and lateral loading) and non-proportional loading paths to study failure mode transition in engineering ceramics at different strain rates and under varying amounts of confinement. In order to permit the investigation of the relation between micro structure and macroscopic behavior, the technique must allow recovery of the sample after being subjected to a known loading history. In this paper, we present a new experimental technique satisfying the above requirements. Preliminary results using this technique have been obtained on a glass ceramic.

**Experimental Technique**

The experimental setup consists of a conventional split Hopkinson (Kolsky) pressure bar (SHPB) [4,5] and an electro-magnetic force generator [6]. A schematic of the experimental setup is shown in Fig. 1. The SHPB is used for generating uniaxial compression pulses of known duration, shape and amplitude. Dynamic confinement is achieved by using an electro-magnetic force generator, which consists of a copper strip surrounding the specimen and a capacitor bank (energy capacity ~120kJ) in which capacitors are connected by inductances to discharge in a given sequence. The copper strip provides a path for high intensity electric currents flowing in opposite directions around the specimen, as shown in Fig. 2. When current passes through the copper strip, the resulting electro-magnetic force will generate pressure on the specimen surface. The outer layer tends to expand outwards but is restricted by a rigid mass. Cylindrical sample shape is preferable for evenly distributed confining pressure over the lateral surface of the sample. There are other ways to generate confinement pressure(e.g., hydro-static pressure [3]), which have been used to determine dynamic failure strength of brittle materials under static confinement. The electro-magnetic method of applying confinement has two principal advantages:

1. Pulse Tailoring: the dynamic confining pressure pulse can be tailored to the desired shape, magnitude and duration through proper design of the circuitry associated with the capacitor bank. This feature enables us to apply the multiaxial compression loading either proportionally or non-proportionally.

2. Timing: to simulate the inertial confinement effect in dynamic loading conditions, the confinement pressure should initiate and terminate with the axial loading. Therefore, the timing of the confinement pulse should be very accurate in every experiment. In the electro-magnetic technique, the timing is controlled by electric circuits and a repeatable accuracy of within one microsecond is achievable.

In the preliminary experiments presented later in this paper, the timing of the SHPB and the capacitor bank discharge system are coordinated by a photo diode(photo-interrupter) and a time delay circuit as shown in Figure 1. When the projectile passes through the photo-interrupter, the time delay circuit is triggered, which in turn will trigger the discharge system at a set delay time. The delay time is related to the transit time of the axial loading pulse to the specimen. The distance between the photo-interrupter and the incident bar is determined by the strain rate requirement of the experiment.

The SHPB has a momentum trap feature [7], which will load the sample only once, and the electro-magnetic pressure pulse can be tailored and timed to match the axial compression pulse. Therefore, the sample is loaded by a well-characterized loading history. This will enable us to relate the macroscopic behavior to the observed failure modes of the material through microscopic observations on the recovered sample.

The acquisition and interpretation of data in SHPB is well established [4,5]. If the specimen undergoes homogeneous deformation, the axial stress s in the specimen is

$$\sigma = \frac{A_o}{A_s} E\varepsilon_t \qquad (1)$$

where $A_o$ and $A_s$ are the cross-sectional area of the transmission bar and the specimen respectively. E is the Young's modulus of the bar material and $\varepsilon_t$ is the transmitted axial strain.

The rate of current flow in the copper strip can be measured by a Rogovski coil [6]. The output of the coil then is integrated by a simple integration circuit to obtain the current history. In the case of a coil with two concentric layers with currents of same amplitude but flowing in opposite directions as shown in Fig. 3, the electro-magnetic confinement pressure P is given by

$$P = \frac{\mu_0}{4}\left(\frac{i}{b}\right)^2 (\cos\alpha_1 - \cos\alpha_2) \qquad (2)$$

where $\mu_0$ is the coefficient of permeability ($4\pi x10^{-7}$ henry/m in vacuum), and i is the total current in one layer. The dimension b and the angles, $\alpha_1$ and $\alpha_2$ are shown in Fig. 3.

## Results

To check the feasibility of the experimental technique, a previously investigated machinable glass ceramic, macor, is used as a model material in the preliminary experiments. The quasi-static and dynamic behavior of the material under uniaxial compression is well established [8]. The glass ceramic has a Young's modulus of 70 GPa and a quasi-static compressive strength of 350 MPa. The cylindrical samples used in the experiments are 8.10 mm in diameter and 5.38 mm in length.

The capacitor bank is set to generate trapezoidal pressure pulses with a duration of ~400 ms and rise times of ~ 10 ms. The axial stress pulse is also trapezoidal but with shorter duration (120 ms). The confining pressure is applied before the arrival of axial pulse at the sample. In the confinement experiments, the capacitor bank was charged to 5 kV, which corresponds to a stored energy of 7.5 kJ. The preliminary experiments include two experiments with dynamic confinement (confinement pressures of 0.5 MPa and 10 MPa) and a uniaxial SHPB experiment (no confinement) for comparison. The confining pressures are estimated from Eq. (2). All the experiments were conducted at a nominal axial strain rate of 350/s.

Fig. 4 shows the strain gage signals from the transmission bar for experiments with (10 MPa) and without confinement. The impact strength can be calculated from the transmitted pulse using Eq. (1). The impact (failure) strength increases from 530 MPa to 630 MPa (17% increase) under a confinement pressure of about 10 MPa. The recovered samples are shown in Fig. 5. The sample from the experiment with no confinement is completely fragmented even though it was loaded only once by the momentum trapping SHPB. In the experiment with a small confinement (~0.5 MPa) the sample also fragmented, but the fragment sizes are larger, as can be seen from the crack density on the surface. The sample from the experiment with moderate (~10 MPa) confinement has a few cracks visible on the impact face, however the sample is completely intact. The axial stress on the sample is also the largest among the three experiments. The confinement pressure apparently reduces the tendency for crack initiation and growth, thus suppressing the axial splitting which would result in fragments.

## Conclusions

A new experimental technique capable of applying dynamic multiaxial compression is being developed. During the experiment, the specimen is subjected to a known loading history. Microscopic observations on the recovered sample can thus be related to the macroscopic behavior of the material. The applied loading history

can be either proportional or non-proportional. Preliminary experiments show that even for moderate confining pressure estimated to be about 10 MPa, an apparent increase in impact strength for machinable glass ceramic, macor. Recovered samples show that under confining pressure, the failure mode (damage) changes considerably, from complete fragmentation to little or no damage in the sample.

**Acknowledgments**

This work is being supported by the U.S. Army Research Office under Contract No. DAALO3-02-G-0192 to the California Institute of Technology. The authors would like to thank Professors W. G. Knauss and P. Washabaugh for many helpful discussions and Mr. Petros Arakelian for his technical assistance in conducting the experiments.

**References**

1. Horii, H. and Nemat-Nasser, S., Brittle Failure in Compression: splitting, faulting and ductile-brittle transition, *Phil. Trans. Roy. Soc. Lond.*, 319, 337-374, 1986.
2. Ashby, M. F. and Sammis, C. G., The damage mechanics of brittle solids in compression, *Pure Appl. Geophys.*, 133, 489-521, 1990.
3. Arrowood, R. and Lankford, J., Compressive fracture processes in an alumina-glass composite, *J. Mat.. Sci.,* 22, 3737-3744, 1987.
4. Kolsky, H., An Investigation of the Mechanical Properties of Materials at Very High Rates of Loading", *Proc. Roy. Soc., Lond* , B62, 676-700, 1949.
5. Follansbee, P.S., The Hopkinson bar, in *Mechanical Testing, Metals Handbook*, Vol. 8, 9th ed., American Society for Metals, Metals Park, Ohio, 198-217, 1985.
6. Ravi-Chandar, K. and Knauss, W. G., An experimental investigation into dynamic fracture.1.Crack initiation and arrest, *Int. J. Fract.*, 25, 247-262, 1984.
7. Nemat-Nasser, S., Isaacs, J. B. and Starrett, J. E., Hopkinson techniques for dynamic recovery experiments, *Proc. R. Soc. Lond.* A435, 371-391, 1991.
8. Ravichandran, G. and Chen, W., Dynamic failure of brittle materials under uniaxial compression, *Experiments in Micromechanics of Failure Resistant Materials*, Kim, K.-S., ed., AMD Vol. 130,ASME Press, New York, pp. 85-90, 1991.

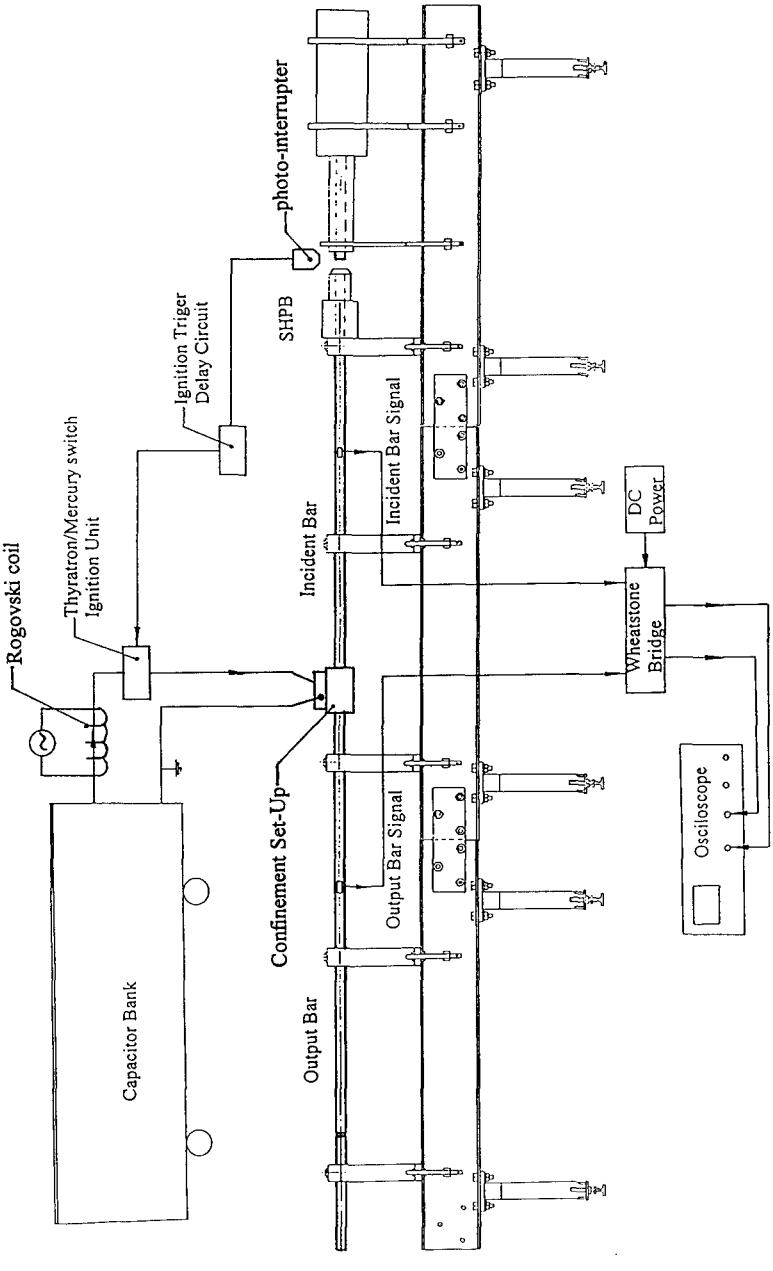



Fig. 1 Schematic of the experimental setup

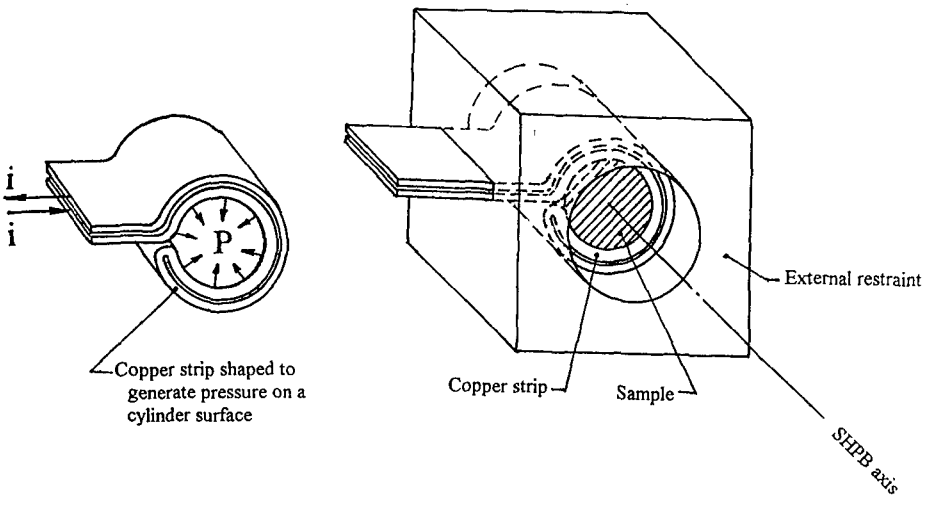



Fig. 2 Copper strip for confinement

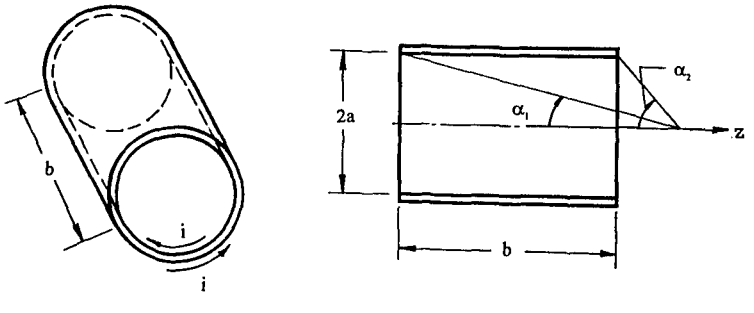



Fig. 3 Pressure estimating model

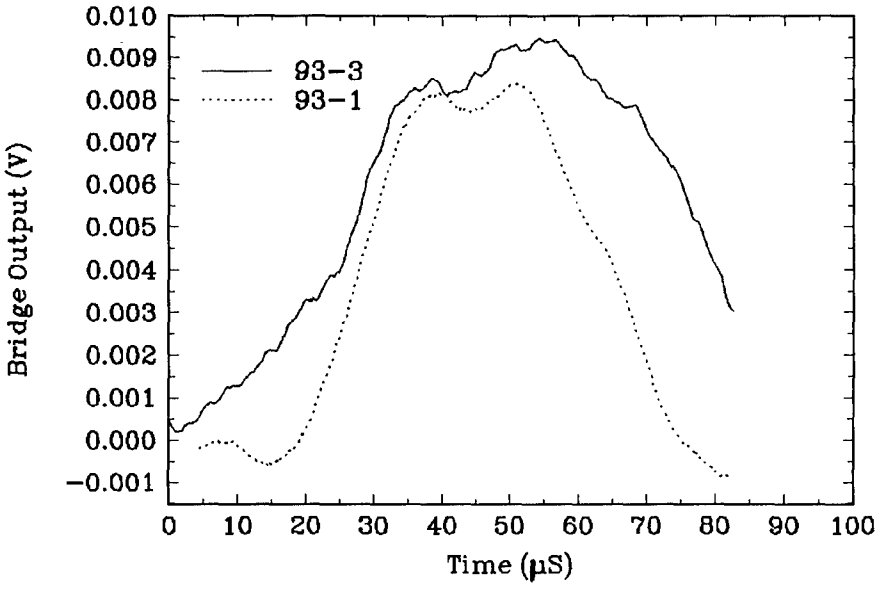



Fig. 4 Transmission bar strain gage signals
Normalized by projectile velocities

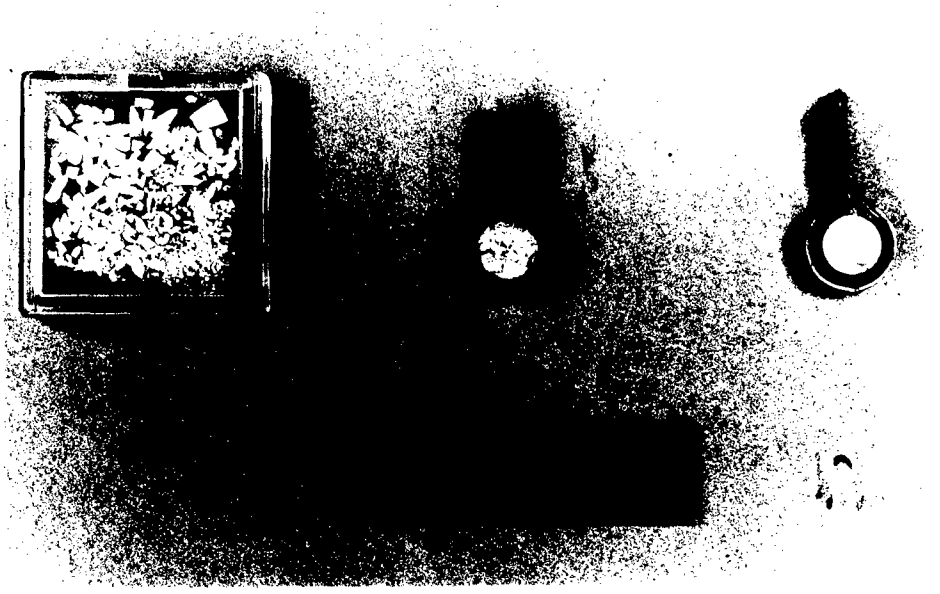


Fig. 5 Recovered samples

# Hydrodynamic Compressibility of High-Strength Ceramics*

Dr. D. E. Grady
Department 1433
Sandia National Laboratories
Albuquerque, New Mexico 87185-5800

## Introduction

Planar shock-compression experiments on monolithic ceramics provide measurements of axial-stress and specific-volume states commensurate with the high-strain-rate large-confining-pressure environment of an impact test. The large shear stresses achieved during the uniaxial-strain compression process are attested to by the Hugoniot elastic limit — an onset of softening in the axial-stress-versus-specific-volume response due to inelastic yielding in shear. Unless both longitudinal and transverse stress are measured in the shock compression experiment, complete deviatoric-stress constitutive data required to fully model the dynamic compression and flow process are not provided by the experiment. Although transverse stress measurements within the shock environment have been performed, the methods are still developmental and results in many cases are not fully satisfactory.

An alternative method commonly used to infer the deviatoric constitutive properties of the material during the shock compression process is to relate the Hugoniot or longitudinal-stress-versus-specific-volume curve to the hydrodynamic response of the material. The latter curve is usually determined indirectly by the correction of isothermal hydrostatic data for adiabatic conditions within the shock process, or by extrapolation of lower pressure ultrasonic data using accepted functional forms for the higher pressure compression behavior.

Static diamond-anvil compression data have not previously been available up to the required pressures. Recent results for ceramics with diamond-anvil methods are encouraging, however [Bassett et al., 1993, Manghnani, 1993].

Another method, and that which is explored in the present work, is to directly measures the hydrodynamic compression of the material of interest through shock-wave techniques. The method involves the immersion or mixing of the test material into a matrix

*This work sponsored by the Joint DoD/DOE Munitions Technology Development Program and conducted under the auspices of the U.S. Department of Energy under contract number DE-AC04-76DP00789.

material which is fluid like in its shock-compression behavior (unable to support deviatoric stresses). This approach was originally explored by Adadurov, *et al.* (1962). It was used by Kanel' and Pityulin (1984) to measure the hydrodynamic properties of titanium carbide. More recently, Tang and Gupta (1988) used the technique to investigate phase transformation in cadmium sulfide, and Poduretz, *et al.* (1988) have investigated the dynamic compression of silicon dioxide using similar methods.

In the present study we have developed the techniques to investigate the hydrodynamic response of high-strength ceramics by mixing powders of the ceramics with copper powder, preparing compacts, and performing shock compression tests on the metal-ceramic mixtures. Hydrodynamic properties of silicon carbide, titanium diboride, and boron carbide to approximately 30 GPa have been examined by this method, and hydrodynamic compression data for these ceramics have been determined. We have concluded, however, that the measurement method is quite sensitive to sample preparation and uncertainties in shock wave measurements. Application of the experimental technique is difficult and further efforts are needed before the method can be applied with full confidence.

Material Preparation

Mixture samples were prepared from powders of the pure ceramic and copper. Nominal grain size of the ceramic was 15-20 μm and the particle distribution was fairly narrow. Minus 325 mesh three-nines purity copper was used as the matrix material. Appropriate masses were determined to achieve a 50%-50% by volume mixture of the ceramic-copper composite.

The measured masses of ceramic and copper powder were combined, placed in a mixing vial with two 12.7 mm D tungsten carbide spheres, and mixed for two hours in a Spex Mixer/Mill. The mixture was then loaded into a graphite and grafoil lined, 40.6 mm ID, TZM die and placed in an induction-heated vacuum hot press.

After achieving a vacuum, a pressure of 166 MPa was applied to the specimen. The temperature was first increased to 900 degrees C at a rate of 30 degrees/minute and then held at 900 degrees C for one hour. The power was then shut off and the system was allowed to cool to room temperature. Pressure on the specimen was relieved at temperatures below 300 degrees C.

Samples were prepared in the form of uniform discs which were machined to approximately 5 mm in thickness and 38 mm in diameter. One sample of each type was sectioned, polished and examined by optical metallography and electron-

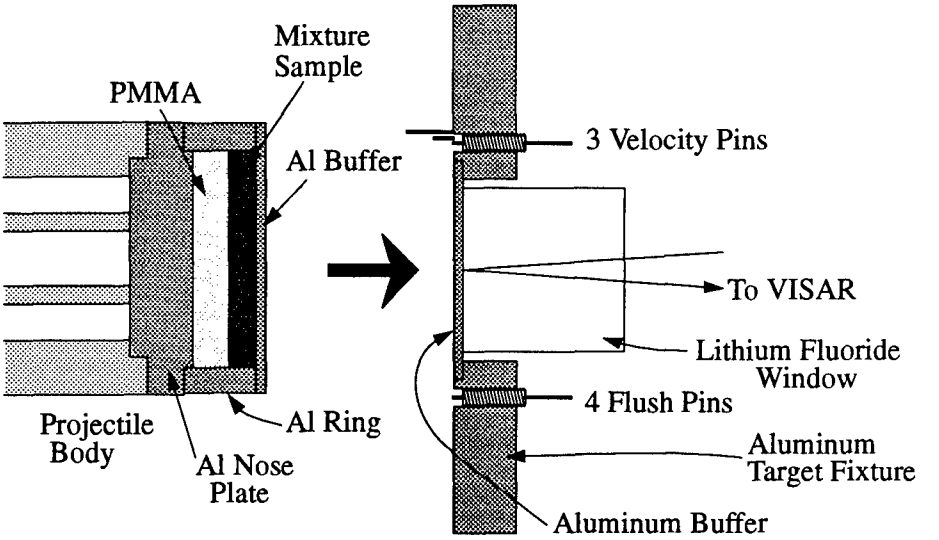



Figure 1. Experimental configuration for Hugoniot and release tests.

probe microanalysis. Negligible contaminants were found in the samples and ceramic particle distribution was judged sufficiently uniform. Ultrasound tests did not revealed any internal cracking in the specimens tested. Measured densities were within several percent of theoretical. This level of porosity was deemed acceptable for the present test method. Measured average densities, longitudinal, and shear ultrasonic velocities, and elastic moduli for the composites are provided in Table 1.

**Table 1:**
**Properties of Metal-Ceramic Composites.**

| Sample | Density $kg/m^3$ | Longitudinal Velocity km/s | Shear Velocity km/s | Bulk Modulus GPa | Poisson's Ratio |
|---|---|---|---|---|---|
| SiC/Cu | 5960 | 5.26 | 3.20 | 80 | 0.19 |
| $TiB_2$/Cu | 6560 | 6.60 | 3.82 | 158 | 0.25 |
| $B_4C$/Cu | 5670 | 5.50 | 3.49 | 69 | 0.16 |

Shock-Compression Methods

Shock-compression experiments were performed to measure both Hugoniot and release states in the metal-ceramic composite samples. The method is compatible with the laser interferometry shock-wave diagnostics use and was developed specifically for accurate Hugoniot and release state analysis [Grady and Furnish, 1988]. The experimental assembly is illustrated in Figure 1. The mixture sample is mounted on the projectile, backed by PMMA (polymethylmethacrylate) and preceded by a thin disc of aluminum (6061-T6 alloy). The stationary target consists of a thin aluminum disc followed by a lithium fluoride window.

Projectiles are accelerated to velocities between 1.0-2.4 km/s with a single-stage propellant gun and caused to undergo planar impact on the target. Diffuse-velocity interferometry or VISAR [Barker and Hollenbach, 1972] is used to monitor the time-resolved velocity at the aluminum-LiF interface in the target. A representative motion for one of the present tests is shown in Figure 2. Peripheral

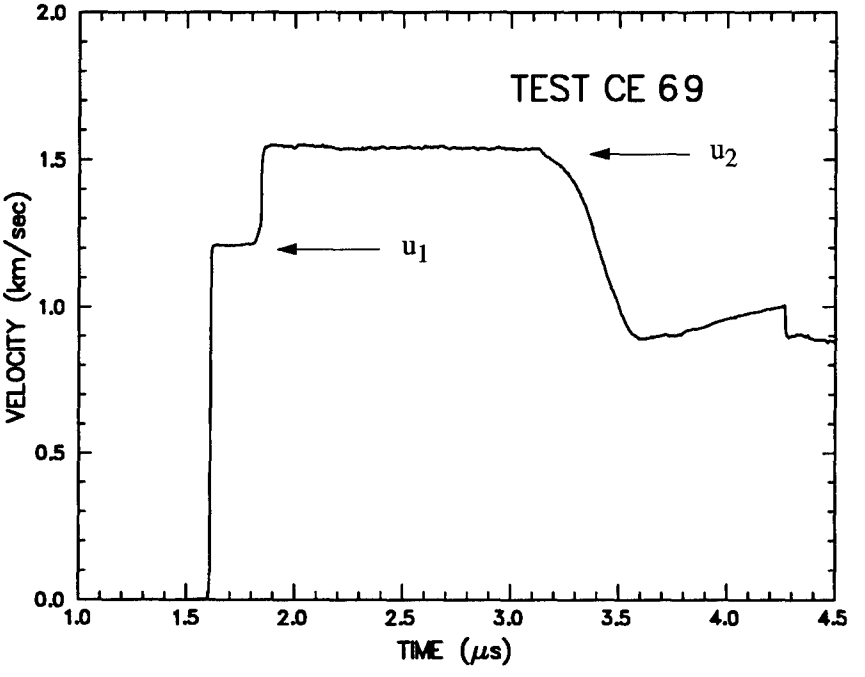



Figure 2. Interface particle velocity profile for test CE-69.

electrical shorting pins are used to measure projectile velocity and planarity of impact as shown in Figure 1.

Impact velocities were selected to achieve Hugoniot pressures within the range 15-30 GPa. Necessary experimental and Hugoniot properties are provided in Table 2. Hugoniot analysis methods for this impact configuration have been discussed previously [Grady and Furnish, 1988, 1990].

**Table 2:**
**Hugoniot Properties**

| Test No. | Material | Impact vel. | Hugoniot pressure | Hugoniot particle velocity | Hugoniot specific volume | Ceramic compression |
|---|---|---|---|---|---|---|
| | $kg/m^3$ | km/s | GPa | km/s | $m^3/kg \times 10^6$ | $m^3/kg \times 10^6$ |
| CE-69 | SiC/Cu | 2.361 | 29.7 | 0.840 | 144.7 | 144.7 |
| CE-78 | SiC/Cu | 2.027 | 24.5 | 0.715 | 146.2 | 146.2 |
| CE-76 | $TiB_2$/Cu | 1.797 | 21.1 | 0.612 | 134.7 | 203.5 |
| CE-77 | $TiB_2$/Cu | 2.347 | 29.6 | 0.801 | 131.2 | 199.4 |
| CE-92 | $B_4C$/Cu | 1.782 | 20.6 | 0.622 | 157.6 | 360.7 |
| CE-93 | $B_4C$/Cu | 2.063 | 24.5 | 0.730 | 154.6 | 352.4 |
| CE-94 | $B_4C$/Cu | 2.345 | 29.1 | 0.817 | 153.4 | 353.0 |

Mixture Analysis

To calculate the hydrodynamic compressibility of the ceramic from the Hugoniot measurements on the mixture, some simplifying assumptions are required. First, it is assumed that any initial porosity is collapsed and eliminated during the shock compression process. Second, based on the relatively low yield stress of the copper matrix it is assumed that stress deviators in the mixture at the shock state are sufficiently low that the measured Hugoniot stress can be sensibly equated to the pressure. Third, it is assumed that the compressibility of the ceramic and copper are additive. That is,

$$\upsilon(p) = \lambda \upsilon_s(p) + (1-\lambda)\upsilon_c(p), \qquad (1)$$

where $\upsilon$, $\upsilon_s$ and $\upsilon_c$ are the specific volumes of the mixture, ceramic, and copper, respectively, and $\lambda$ is the mass fraction of ceramic in the mixture.

Based on the measured masses of ceramic and copper (50%-50% volume ratio), the mass fractions of silicon carbide, boron carbide, and titanium diboride are calculated to be $\lambda$ = 0.265, 0.335, and 0.220, respectively. The compressibility of copper is calculated from its known Hugoniot properties. Linear shock-velocity versus particle-velocity parameters for copper [Marsh, 1980] are $C$ = 3.940 km/s and $S$ = 1.49. Hydrodynamic compression states for the three ceramics based on Equation 1 are compared with corresponding Hugoniot data on monolithic ceramic in Figures 3-5, and tabulated in Table 2. Horizontal error bars shown for the data are estimated from the uncertainties in Hugoniot response of the mixture, and in the initial mass fraction of components.

## Discussion

The new data provided in Figures 3-5 provide hydrodynamic (adiabatic) compression properties for several ceramics at pressures of about 20-30 GPa based on the method of shock compression of metal-ceramic mixtures. Confidence in these data

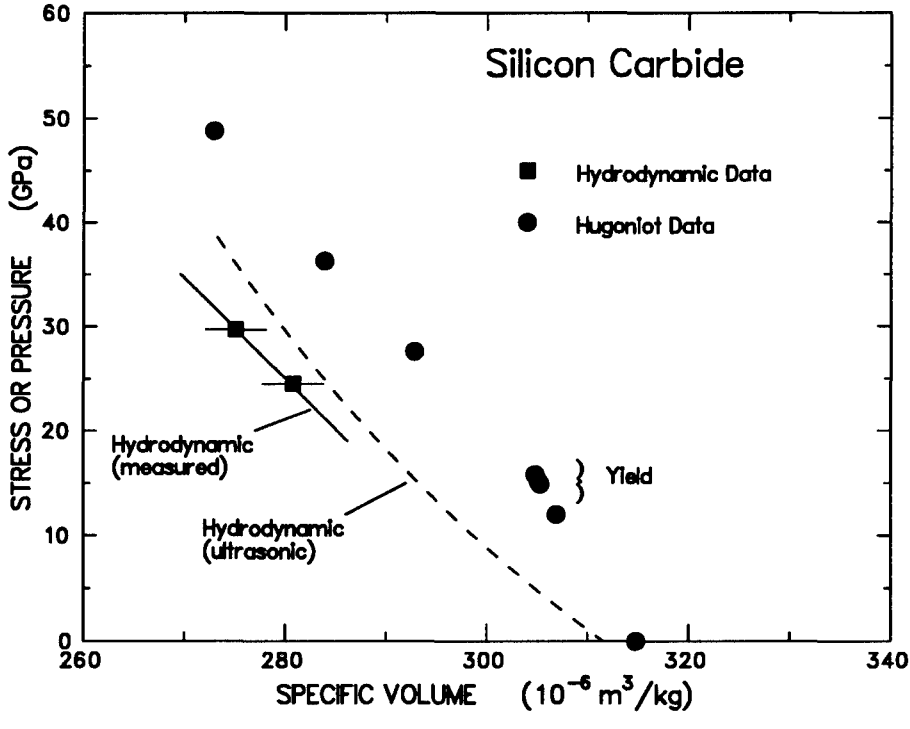



Figure 3. Hugoniot and hydrodynamic compression data for silicon carbide

are, of course, subject to the assumptions of compression additivity and negligible shear strength at the shock state which is assumed in the analysis of the wave-profile measurement needed to calculate the pressure versus volume change in the ceramic.

It has not yet been established that fully hydrodynamic conditions are achieved in the shock compressed state. Additional data on silicon carbide mixtures [Grady, 1993] suggest that deviatoric stress states may still exist in the composite samples even at these levels, and possible explanations are discussed. Compression states above 20 GPa appear to be at or very close to hydrodynamic conditions. If residual strength still persists in the mixture at these shock states then the true hydrodynamic compression state would lie even further to the left in Figures 3-5.

The measured compression values are also subject to uncertainties in sample preparation and shock-wave diagnostics. The error bars in Figure 3-5 are based on a reasonable assessment of these sources of uncertainty, but they do not account for contributions to error that may have been overlooked — a serious concern with the present method.

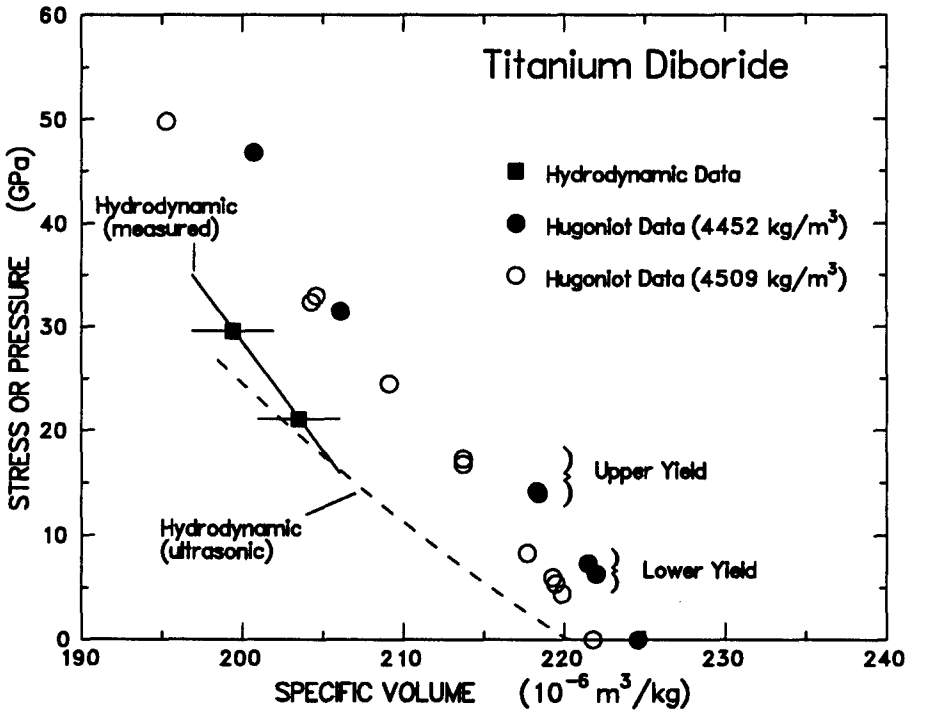



Figure 4. Hugoniot and hydrodynamic compression data for titanium diboride

The hydrodynamic data in Figure 3-5 are compared with Hugoniot data obtained on monolithic samples of the same ceramics. Hugoniot data were obtained on near-theoretical density (1%-3% porosity) ceramics. The three ceramics examined exhibit high Hugoniot elastic limits (10-20 GPa), although the actual dynamic yield stress of titanium diboride is still in question. A persistence of strength at the shock state for the monolithic ceramic requires that the measured stress state lie above the mean pressure state at the same specific volume. As seen in Figure 3-5, this is generally the case.

In Figures 3-5 calculation of the hydrodynamic compression of the theoretically dense ceramic based on ultrasonic data are also provided. Compression curves are based on the pressure versus volume relation suggested by shock wave data,

$$p = \frac{\rho_o C_o^2 \varepsilon}{(1 - S\varepsilon)^2}, \qquad (2)$$

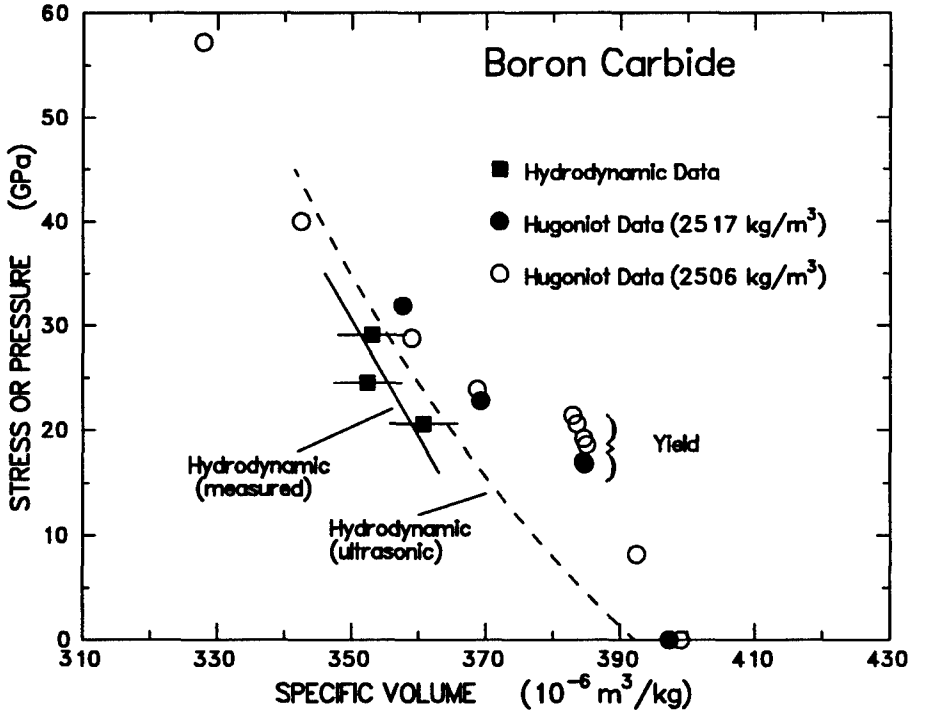



Figure 5. Hugoniot and hydrodynamic compression data for boron carbide

where $\varepsilon = 1 - \rho_o/\rho$. The near equivalence of Equation 2 to the finite strain Birch-Murnaghan equation-of-state has been demonstrated by Jeanloz (1989), while Olinger (1976) have shown the applicability of Equation 2 to describe static compression data of solids. The values used for $\rho_o$, $C_o$, and $S$ are provided in Table 3. Theoretical densities of the monolithic ceramics were estimated correcting for impurities where available. The bulk wave speeds were calculated from measured ultrasonic data. The parameter $S$ is calculated from the relation $K' = 4S - 1$ where the pressure coefficient of the bulk modulus $K'$ to approximately 2 GPa has been recently measured by Manghnani (1993) for the present ceramics.

**Table 3:**
**Properties for Ultrasonic Compression Curves**

| Material | Theoretical Density $kg/m^3$ | Bulk Velocity m/s | $S$ |
|---|---|---|---|
| SiC | 3210 | 8190 | 1.4 |
| $TiB_2$ | 4540 | 6960 | 1.0 |
| $B_4C$ | 2550 | 9570 | 1.4 |

Hydrodynamic data points in Figure 3 for silicon carbide in the range of 25-30 GPa lie near or slightly to the left of the ultrasonic compression curve. The data provides further support for the high sustained shear strength of this ceramic under the confining pressure states induced by shock compression.

Measured hydrodynamic states for titanium diboride shown in Figure 4 are also consistent with extrapolated ultrasonic compression. The slightly higher upward trend is probably not significant in considering experimental error. The data also indicates a considerable sustained shear strength in titanium diboride.

Shock compression data in Figure 5 on boron carbide and copper mixtures provide compression states for boron carbide which are in reasonable agreement with the extrapolated ultrasonic compression curves. The dramatic loss of strength on the Hugoniot is a unique characteristic of this ceramic.

Thus, to date, the new technique for measuring high-pressure hydrodynamic states of ceramics has yielded no surprises. The data are in reasonable agreement with extrapolated ultrasonic measurements. Uncertainties within the experimental method have been found to be more serious than initial analysis indi-

cated. Further efforts will focus on improving the test technique and in analysis of the release wave data which has remained largely unexplored.

References

Adadurov, G. A., A. N. Dremin, S. V. Pershin, *Zh. Prikl. Mech. Tekh. Fiz.*, **4**, 81, 1962.

Barker, L. M. and R. E. Hollenbach, *J. Appl. Phys.*, **43**, 4669, 1972.

Basset, W. A., M. S. Weathers, and T. Wu, *Proceedings of the American Physical Society Topical Group on Shock Compression of Condensed Matter*, Colorado Springs, Colorado, June 27-July2, 1993.

Grady, D. E. and M. D. Furnish, Sandia National Laboratories Technical Report SAND88-1642, December, 1988.

Grady, D. E. and M. D. Furnish, in *Shock Compression of Condensed Matter - 1989*, edited by S. C. Schmidt, J. N. Johnson, L. W. Davison (Elsevier Science Publishers, 1990) p. 621.

Grady, D. E., *J. Appl. Phys.*, (in press), 1993.

Jeanloz, R., *J. Geophys. Res.*, **94**, 5873, 1989.

Kanel', G. I. and A. N. Pityulin, *Fizika Goreniya i Vzryva*, **28**, 85, 1984.

Manghnani, M. H., *Proceedings of the American Physical Society Topical Group on Shock Compression of Condensed Matter*, Colorado Springs, Colorado, June 27-July2, 1993.

Marsh, S. P., LASL Shock Hugoniot Data., S. P. Marsh Editor, University of California Press, 1980.

Olinger, B., *J. Geophys. Res.*, **81**, 5341, 1976.

Poduretz, M. A., G. V. Simkov, R. F. Trunin, *Izvestiya, Earth Physics*, **24**, 267, 1988.

Tang and Y. M. Gupta, *J. Appl. Phys.*, **64**, 1827, 1988.

# STRENGTH OF ALUMINIUM NITRIDE

Dattatraya P. Dandekar *, A. Abbate+, and J. Frankel.+
U.S. Army Materials Technology Laboratory, Watertown, MA, 02172-0001
+ U. S. Army Armament, Munitions, and Chemical Command, Benet Weapons Laboratories, Watervliet, New York,12189.

## I. INTRODUCTION

Strengths of solids may be defined in various ways i.e., under plane shock wave propagation , magnitude of Hugoniot Elastic Limit (HEL), i.e. limit of elastic deformation, magnitudes of shear stresses maintained as a function of compressive stress, i.e shear strength, and spall threshold provide three ways of defining strength. These three definitions do not necessarily form a mutually exhaustive set. Knowledge of these three, however, are essential to tailor the use of ceramics under shock / impact loading. Shear strength of a solid under plane shock wave loading is determined through (i) measurement of of shear wave velocity under a given shock compressed stress state or shear stress - shear strain under oblique impact condition or (ii) simultaneous measurements of longitudinal and lateral stresses under normal impact or (iii) measurement of the difference between the shock Hugoniot stress and hydrodynamic pressure at a given value of strain i.e. volume change. The values of shear strength as a function of stress increase in a predictable way up to and including the HEL of a solid. The values of shear strength at stresses larger than the HEL may remain constant, or increase or decrease with an increase in the values of stress in a non-transforming solid. The present work was initiated to determine the shear strength of aluminium nitride (AIN) by means of the third type of measurements to asses the strength of AIN. This requires shock Hugoniot data and the hydrodynamic compression data for the estimation of the shear strength of AIN. Shock Hugoniot of AIN have been determined by Rosenberg et al [1] and Grady [2] on a material manufactured by Dow to 35 GPa. In the present work, the equation of state of the same material is determined through the measurements of longitudinal and shear wave velocities at high pressures to 0.7 GPa.

by an ultrasonic technique [3]. The values of shear strength estimated in this work are compared with the values of shear strength obtained from the simultaneous longitudinal and lateral stress measurements by Rosenberg et al [1]. This permits one to evaluate the consistency of these two techniques to determine the shear strength of a material under plane shock wave loading. The present work also judiciously applies this technique to determine the strengths of two other AlN under plane shock wave loading which have been investigated by Nakamura et al. [4]. It compares the deduced strengths of these AlN with the nature of deformation suggested by the authors of Ref.4.

## II. MATERIAL AND ULTRASONIC EXPERIMENTS

The composition, density and the elastic properties of AlN in this investigation are given in Table 1.

Table 1. Composition (wt. %), density ($mg/m^3$), values of elastic constants (GPa), and their pressure derivatives for AlN.

| | Present work | Manghnani Ref.5 | Gerlich et al Ref.6 | Xia et al.[a] Ref.7 |
|---|---|---|---|---|
| Composition | | | | |
| AlN | 98.62 | 98.62 | 94.97 | 99.99 |
| Oxygen | 1.0 | 1.0 | 2.0 | |
| Carbon | 0.3 | 0.3 | 0.03 | |
| $Y_2O_3$ | | | 3.0 | |
| Density | 3.23 ± 0.01 | 3.25 ± 0.06 | 3.31 | 3.255 |
| Porosity (%) | 1.0 | 1.0 | <1.5 | 0 |
| $K_0$ | 202 ± 2 | 193 -196 | 160 | 185 ± 5 |
| $\mu_0$ | 125 ± 1 | 129.5 - 130. | 131 | |
| $K'_0$ | 3.68 ± 0.62 | 4.12 - 5.0 | 5.2 ± 4.0 | 5.7 ± 1.0 |
| $\mu'_0$ | 4.24 ± 0.78 | 0.26 - 0.27 | 0.2 ± 2.0 | |

a. These are isothermal values the remaining are adiabatic.

Hydrodynamic compression of of AlN was generated from the transit time measurements of longitudinal and shear waves to 0.7 GPa. The transit times of these waves were measured by an ultrasonic technique known as pulse echo overlap technique [3]. The ultrasonic measurements were performed at 5 MHz with lithium niobate transducers. The transit times were measured with a precision of ±10 ns. A Birch - Bridgman pressure cell system manufactured by Harwood, with a 50 - 50 pentane - isopentane

pressure medium was used to generate pressure. The magnitude of hydrostatic pressure was measured by a calibrated manganin coil. The specimens of AlN were cubic in shape with a linear dimension of 1.2977 ± 0.0002 cm. The transit time measurements at high pressures were replicated five and three times for the longitudinal and the shear wave velocities, respectively. The ultrasonic transit times of longitudinal and shear waves were analyzed following an iterative scheme developed by Dandekar [8] to calculate the values of elastic constants at elevated pressures. These data yield the magnitudes of bulk and shear moduli of AlN and their pressure derivatives at room temperature.

## III. HYDRODYNAMIC COMPRESSION OF ALN

The values of relative changes in the transit times of longitudinal [$T_l$ (P)],and shear wave [$T_S$ (P)] velocities obtained from the measured transit times of longitudinal and shear wave velocities in AlN as a function of pressure [P] are shown in Fig. 1.

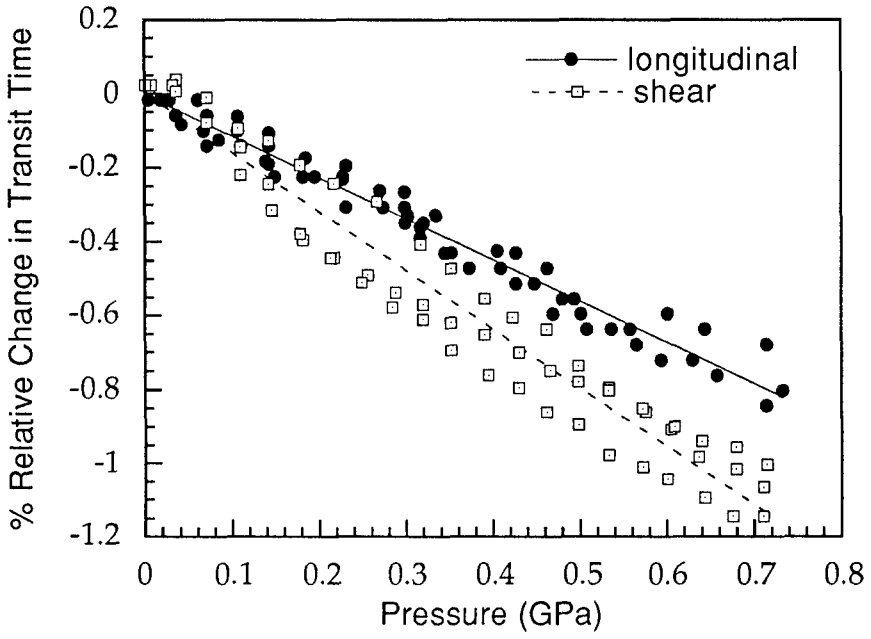



Figure 1. Relative changes in the transit times as a function of pressure in AlN.

The least squares fits to these data are represented respectively by

$$\Delta T_l = \{T_l (P) - T_l (0)\} / T_l (0)$$
$$= [- 0.1159 \pm 0.0023 ] \times 10^{-3} \times P \quad (1)$$

and

$$\Delta T_S = \{T_S (P) - T_S (0)\} / T_S (0)$$
$$= [- 0.15888 \pm 0.0102] \times 10^{-3} \times P. \quad (2)$$

In the above relations pressure P is in GPa. The values of linear correlation coefficients (r) for these modes of elastic wave propagations as represented by the above two relations are 0.9885 and 0.9712, respectively. It is obvious that the changes in transit times over a range of 0.7 GPa are very small. The relations (1) and (2) are used to estimate the transit times of longitudinal , shear and bulk sound wave velocities in AlN at various pressure to 0.7 GPa. These estimates are in turn used to calculate the values of bulk and shear moduli at high pressures by following the iterative procedure due to Dandekar [8]. The values of pressure derivatives of the bulk and the shear moduli of AlN calculated in this manner are given in Table I.

The hydrodynamic compression curve of AlN is obtained from the ultrasonic measurements by using the equation of state based on linear relationship between shock (U) and particle (u) velocities namely,

$$U = C_0 + s\, u \quad (3)$$

$$P = \rho_0 C_0^2 \eta / (1 - s \eta)^2 \quad (4)$$

and $$\eta = 1 - V / V_0. \quad (5)$$

where $\rho$, C, and V are density, bulk sound wave velocity, and volume, respectively. The subscript 0 denotes the initial values of the various parameters under the ambient condition. An additional relation required to construct the compression curve is that between s and the pressure derivative of the adiabatic bulk modulus ($K_0'$) derived by Ruoff [9] and is

$$K_0' = 4 s - 1. \quad (6)$$

There is no loss of generality in using the above equation of state since it has been shown to be equivalent to Birch - Murnaghan

equation of state based on Eulerian finite strain formalism [10]. The hydrodynamic compression curve of AlN generated in this manner is shown in Fig. 2.

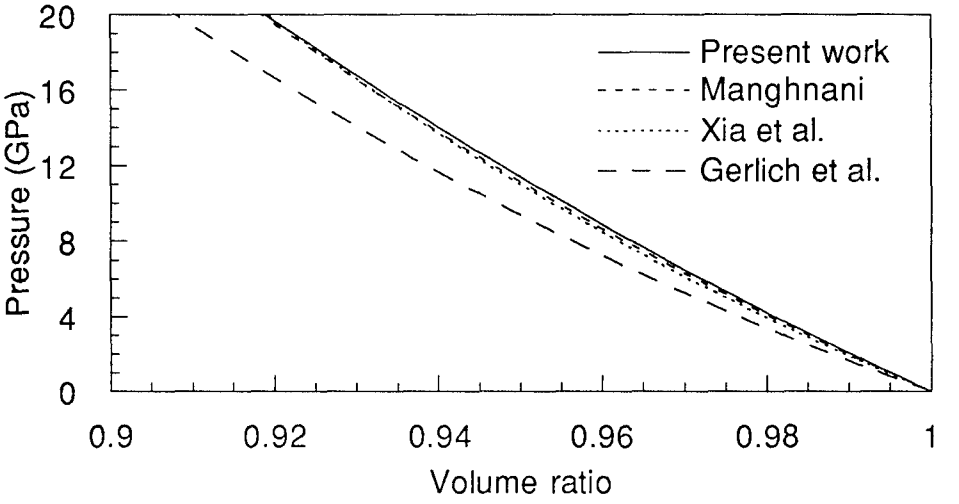



Figure 2. Hydrodynamic compression of AlN.

Gerlich et al [8] measured pressure and temperature derivatives of hot pressed AlN containing 3 % $Y_2O_3$ by weight. These authors obtained the pressure derivatives of the elastic moduli of AlN through the measurements of the variations of three sound wave velocity modes { $W_i$; i=1,3]} with uniaxial compression and the stress derivatives { $(\rho_0 W_i^2)'$; i= 1,3 } at zero stress. In the preceding W 's are the natural velocities. Mode 1 refers to longitudinal mode propagation normal to the uniaxial compression direction. Modes 2 & 3 refer to shear mode propagations normal to the uniaxial compression direction with polarization parallel and normal to the uniaxial compression direction, respectively. The three stress derivatives { $(\rho_0 W_i^2)'$; i= 1,3} are related to the three independent third-order elastic constants and the two second-order elastic constants of an isotropic solid [11]. These three third- order elastic constants are in turn related to the hydrostatic pressure derivatives of the second-order elastic constants. The explicit relations between the stress derivatives { $(\rho_0 W_i^2)'$; i= 1,3 } and third and second order elastic constants and the pressure derivatives of the second order constants are given in Ref.6, and 11. While this is a viable technique to obtain the values of third-order elastic constants it is not a preferred method to determine the pressure derivatives of the second-order elastic constants because the precision with which the values of the

three third-order elastic constants can be determined is always inferior to determinations of the second-order constants. This is reflected in the precisions of the pressure derivatives of the bulk and shear moduli of AlN reported by Gerlich et al [6] (Table I).

Recently another set of ultrasonic wave velocity measurements on AlN manufactured by Dow have been made as a function of pressure by Manghnani [5]. The properties of AlN obtained from various sources are summarized in Table I. The compression curves for AlN obtained from the ultrasonic wave velocity measurements at high pressures on Dow material and on doped material from the measurements of Gerlich et al [6], and on a pure material by in-situ high pressure X-ray diffraction measurements of Xia et al [7] are shown in Fig.2.

Fig. 2 shows that the compression curves of relatively pure AlN obtained in the present work and Refs. 5 and 7 are consistent with each other; differences are within the precision of the respective measurements on AlN . However the compression curves of pure and doped AlN do differ from one another as shown in Fig 2. The observed difference in the compression of these two AlN arise due to large differences in the magnitudes of the initial bulk modulus, 202 as compared to 160 GPa in Ref.8. The effect of the pressure derivatives of the bulk modulus (3.68 as compared to 5.2 ) is minor on the compression curves of AlN . An interesting feature discerned in Table I is that the values of shear moduli for the pure and doped AlN do not differ significantly from one another.

## IV. SHEAR STRENGTH OF ALN.

Shear strength of AlN has been determined through the simultaneous measurements of longitudinal [$\sigma_1$] and lateral [$\sigma_2$] stresses under plane shock wave loading to 18.5 GPa by Rosenberg et.al [1]. These stresses were measured by manganin foil gages. The gages used for the measurements of longitudinal stresses were around 5-10 mm in lateral dimensions. The gages used for the measurements of lateral stresses were 2 mm wide in order that a steady stress level is achieved in a shorter interval of time. The shear strength [$\tau$] is thus simply the half the value of the difference in the measured values of $\sigma_1$ and $\sigma_2$. The values of shear strength as a function of compressive stress determined by these investigators are given in Table 2.

The values of shear stress / shear strength increase as the magnitude of longitudinal stress approach the value of the Hugoniot

Table 2. Shock data on AlN from Reference 1.

| Longitudinal Stress# (GPa) | Particle Velocity# (km/s) | Lateral Stress# (GPa) | Shear Stress (GPa) | Shock Velocity* (km/s) | Volume Ratio* |
|---|---|---|---|---|---|
| 16.8 ± 0.3 | | 8.8 ± 0.1 | 4.0 ± 0.2 | | |
| 16.1 ± 0.3 | | 8.7 ± 0.1 | 3.7 ± 0.2 | | |
| 10.6 ± 0.2 | 0.296 | | | 15.25 ± 1.0 | 0.973 |
| 11.7 ± 0.2 | 0.354 | | | 8.72 ± 0.6 | 0.9651 |
| 12.5 ± 0.2 | 0.401 | | | 7.52 ± 0.5 | 0.9585 |
| 13.4 ± 0.2 | 0.43 | | | 7.91 ± 0.5 | 0.9541 |
| 14.7 ± 0.3 | 0.494 | | | 7.48 ± 0.5 | 0.9446 |
| 17.0 ± 0.3 | 0.605 | | | 7.16 ± 0.5 | 0.9275 |
| 18.5 ± 0.5 | 0.73 | | | 6.27 ± 0.4 | 0.9002 |
| 10.0 ± 0.3 | | 3.0 ± 0.1 | 3.5 ± 0.2 | | |
| 13.3 ± 0.3 | | 6.4 ± 0.2 | 3.4 ± 0.2 | | |
| 11.5 ± 0.2 | 0.335 | 4.5 ± 0.1 | 3.5 ± 0.2 | 10.31 ± 0.7 | 0.9659 |
| 6.7 ± 0.1 | | 1.7 ± 0.1 | 2.5 ± 0.1 | | 0.9819 |
| 7.5 ± 0.1 | | 2.6 ± 0.1 | 2.4 ± 0.1 | | 0.9798 |
| 8.0 ± 0.1 | | 2.2 ± 0.2 | 2.9 ± 0.2 | | 0.9784 |
| 9.4 ± 0.2 | | | | | 0.9746 |

# Table 2 in Ref. 1. * calculated from the data in Ref.1.

Elastic Limit ( HEL) i.e., 9.4 ± 0.2 GPa in AlN. The value of the shear strength at the HEL is 3.5 ± 0.2 GPa. This value of the shear stress is maintained in AlN at the higher stresses up to 16 GPa and at a stress around 16.8 GPa the shear strength increases to 4.0 ± 0.2 GPa. This increase in the shear strength at 16.8 GPa was suggested by these authors to be related to the phase transformation in AlN observed by Kondo et al [12] and Vollstadt et al [13] around 18 GPa. In other words, the results of simultaneous measurements of the longitudinal and lateral stresses in the shock wave experiments led Rosenberg et al [1] to conclude that the deformation behavior of AlN is like that of an elastic - plastic solid.

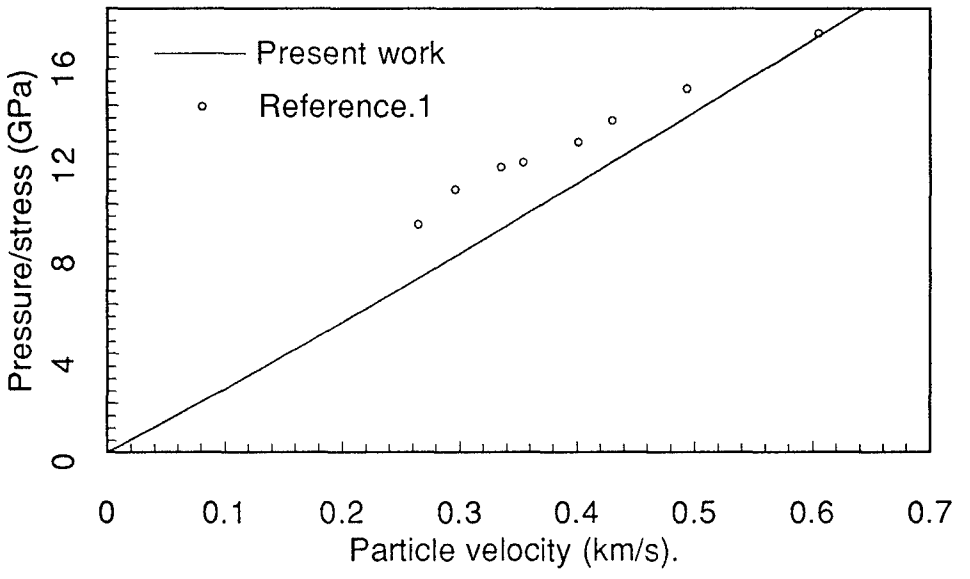



Figure 3. Pressure/Stress vs Particle velocity in AlN.

Yet another way of inferring the deformation behavior of a solid under plane shock wave loading is to estimate the value of shear stress [$\tau$] sustained by the material from the difference between the magnitudes of shock Hugoniot stress i.e., longitudinal stress and hydrodynamic pressure at a given value of strain i.e. volume change. This can be qualitatively inferred by plotting the measured values of Longitudinal stress versus particle velocity for AlN from Ref. 1 and the pressure-particle velocity locus obtained from our ultrasonic measurements. The advantage of such a comparison is that one does not have to perform any calculations on the data given in Ref. 1. The locus for AlN, i.e., pressure [P] - particle velocity [u] coordinates are obtained by using the density and the bulk sound wave speed measured by these researchers (Table I) and the value of s derived from the ultrasonic measurements discussed above. This yields the following relation between the pressure and the particle velocity for the material .

$$P = \rho_0 U u = \rho_0.(C_0 + s u) u. \qquad (7)$$

This, then, represents the hydrodynamic states of AlN in pressure - particle velocity coordinates. Fig. 3 shows a plot of the measured values of longitudinal stress versus particle velocity in AlN reported in Ref 1 and the hydrodynamic pressure -particle velocity locus for AlN obtained from our ultrasonic measurements and through

the use of Eq. (7). If the stress-particle velocity coordinates of AlN reported in Ref. 1 converge towards the hydrodynamic loci it implies that AlN is sustaining a smaller magnitude of shear stress with an increase in the compressive stress. This result is consistent with the calculated magnitudes of the shock velocities above its HEL i.e. 9.4 GPa because these values of the velocities are smaller than the bulk sound wave velocity of AlN (Table 2). It has been shown by Graham and Brooks [14] that in a material undergoing a significant loss of shear strength under plane shock wave loading the values of shock velocity will be smaller than its bulk sound wave velocity. Thus the constancy of constancy of the shear strength estimates above the HEL calculated from the difference between the measured longitudinal and lateral stresses are inconsistent with the shock Hugoniot of AlN reported in Ref. 1.

Grady [2] provided his shock data in AlN to 36 GPa. Estimates of shear strength [$\tau$] of AlN from the shock Hugoniot reported in Ref.2 and the hydrodynamic compression curve obtained in the present work at a given compression/strain ($\eta$ ) is given by Eq. (8) .

$$\tau = 0.75 \times [\sigma(\eta) - P(\eta)] \qquad (8)$$

The results of these calculations (Fig.4 ) show that shock Hugoniot data of Ref.1 and 2 when used in conjunction with the hydrodynamic compression yield two radically different trends in the the variation of shear strength with impact stress. Data obtained in Ref.2 show that values of shear strength of AlN up to around 22 GPa remain constant at around 2.8 $\pm$ 0.2 GPa i.e approximately the same value as at its HEL. Data of Ref. 1 on the other hand shows a decline in the shear strength but shows a trend similar to one observed in Ref.2 if the shear strength is calculated from the difference between their shock Hugoniot and the lateral stress measurements.

This observed discrepancy illustrates the pitfall of lateral stress measurements when they are not checked for their consistency by some independent set of measurements. The reasons for the above mentioned discrepancies in the estimates of the values of shear stress sustained in AlN may be rooted in the problems related to the measurements of lateral stresses by means of piezoresistive gauges like the manganin gages which have been investigated and reported by Wong [15]. The reliability of the measurements of lateral stresses especially above the HEL of a material is subject to uncertainty arising from the fact that conservation relations of mass, momentum, and internal energy for the one dimensional plane shock wave propagation do not include the lateral stresses as a variable. Hence,

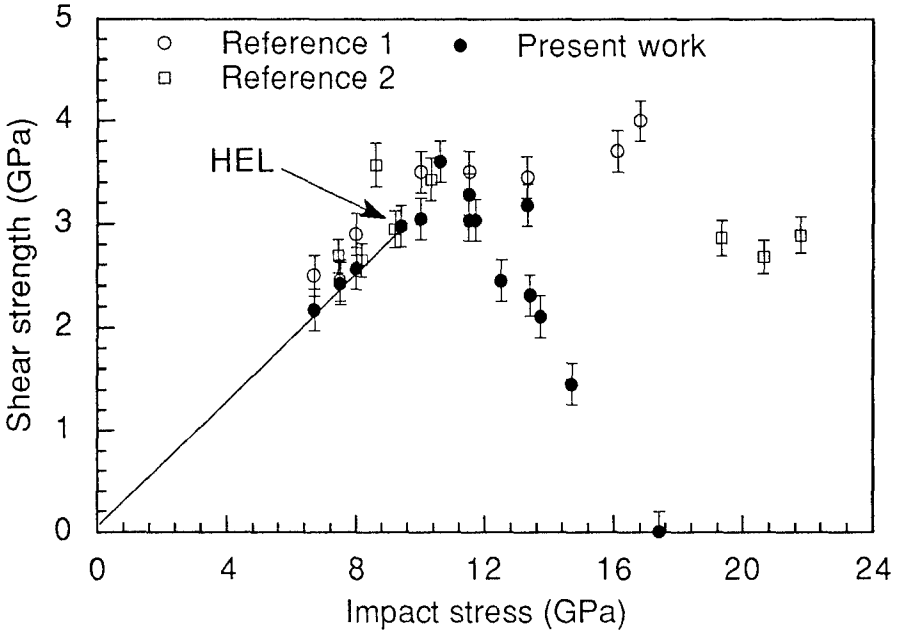



Figure 4. Shear strength vs. impact stress in AlN.

above the HEL it is not possible to verify the accuracy or fidelity of lateral stress measurements without knowing the properties of the material a priori. In addition, Wong [15] has shown that the response of a lateral stress gauge is affected by the property of the matrix material in which the gauge is embedded and the emplacement technique used to bond the gauge to the material being investigated. Finally , Rosenberg and Partom [16,17] in analyzing and calibrating the response of a lateral gauge assumed that the gauge material deforms like an elastic-plastic material. It is clear that such an assumption will not be valid if the matrix material deforms like a hydrodynamic material i. e. fluid material because in such a situation the calibration of the gauge based on its elastic - plastic behavior is not applicable. Difference in the estimates of the shear stress sustained by AlN as shown in Fig. 4 may be due to computational scheme followed to calculate the value of the stress obtained from the response of lateral stress gauge in the experiments conducted on AlN and reported by Rosenberg et al. [1].

Nakamura et al. [4] reported results of their plane shock wave experiments conducted on pure and $Y_2O_3$ (6.2 % by weight ) doped polycrystalline samples of AlN to approximately 35 GPa. They summarize the results of their experiments as follows:

(i) The HEL of the pure and the doped AlN lie between 7.6 - 9.4 GPa and 7.8 - 9.8 GPa, respectively.

(ii) Whereas the pure AlN suffers a loss of comparatively large shear strength above its HEL , the doped material maintains a fair amount of shear strength above its HEL.

(iii) These materials do not show any evidence of the reported phase transformation around 20 GPa reported by other investigators [2,12,13].

(iv) the shock data of the pure and the doped AlN above their respective HEL's are best represented by the following two linear relations between the shock [U] and particle [u] velocities

$$U = 5.22 \pm 2.11\ u : \text{pure material} \qquad (9)$$

$$U = 7.04 \pm 1.29\ u : \text{doped material} \qquad (10)$$

The conclusions pertaining to the shear strengths of the pure and the doped AlN are based on the the values of shock velocities for these two materials given in Eqs. (9) and (10) compared to their respective measured values of bulk sound wave velocities under the ambient condition, i.e. 7.93 and 7.82 km/s. The pressure derivatives of the bulk modulus of a material when a linear relation is found to exist between shock and particle velocity can be obtained from Eq. (6). The estimated values of the pressure derivatives of the bulk modulus $[K_0']$ of the pure and the doped materials obtained from the values of the slopes i.e., s in Eqs. (9) and (10) are 4.16 and 7.44, respectively. The value of $[K_0']$ for the doped material is similar in magnitude to the value determined from the ultrasonic measurements i.e., 3.7 - 5.2. On the other hand a value of 7.44 for the pressure derivative of the bulk modulus of the pure material is very large. Such a large value for the pressure derivative of the bulk modulus for a material is unusual unless it is undergoing a drastic change in its compressive behavior as for example in the case of a phase transformation under pressure. However, these investigators did not observe any evidence of phase transformation to 35 GPa in their experiments. Figure 5 and 6 show the measured values of stress vs. volume ratios and the hydrodynamic compression curves for these two materials calculated by using the the value of the pressure derivative of the bulk modulus obtained in the present work and the respective values of densities and bulk sound wave speeds measured by Nakamura et. al. [4].

Fig. 5 shows that the pure material does lose a significant amount of its shear strength above the HEL. Also the

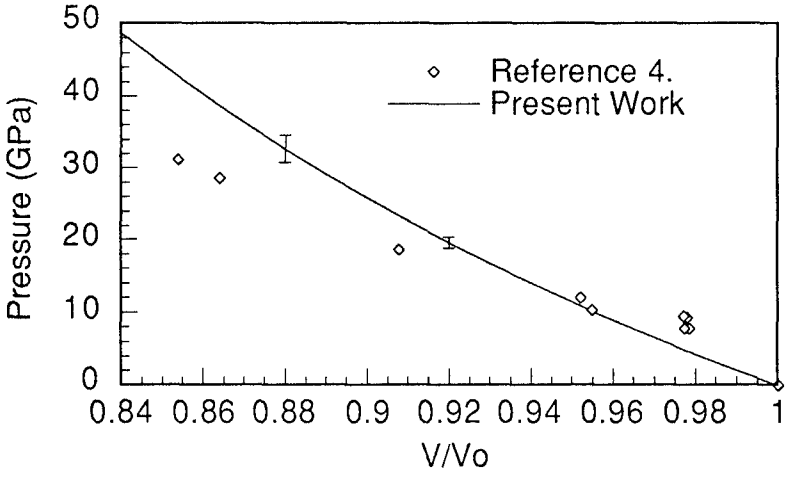



Figure 5. Stress vs. Volume Ratio of Pure AlN

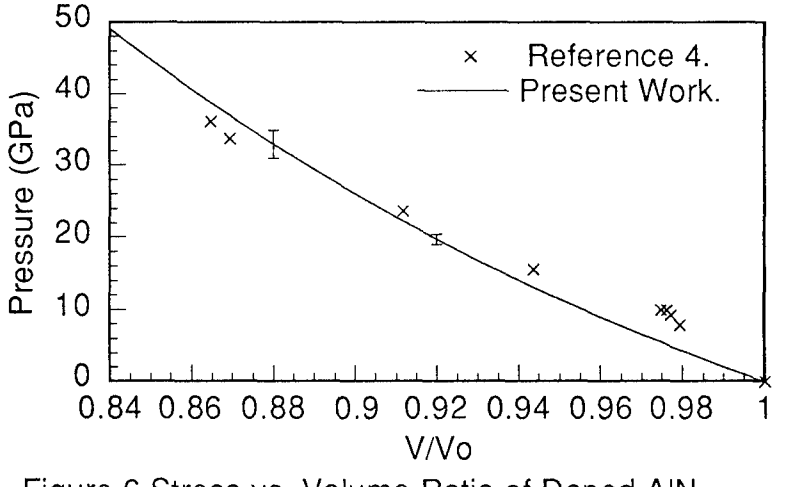



Figure 6.Stress vs. Volume Ratio of Doped AlN

observed stress - volume ratio coordinates above 12 GPa lies below the hydrodynamic compression curves of AlN obtained from the ultrasonic data as well as from the shock wave data generated by these investigators. In view of the above it is intriguing that the Nakamura et al.[4] did not observe the massive phase transition in their experiments observed by Kondo et al. [12]. The deformation behavior of the doped material is initially like that of an elastic - plastic material (Fig.6). However, this material also crosses the hydrodynamic compression curve around 20-24 GPa. This crossover pressure is larger but is suggestive of the occurrence of phase transition in AlN even though these investigators did not observe the

suggested phase transition in their experiments. The above is very puzzling and remains inexplicable at present. However, if the assumption that these crossover coordinates represent the pressure at which the reported transformation in AlN is occurring then one may say that the effect of doping AlN with Yittria is to change the deformation behavior of AlN above its HEL and also change the pressure of transition. This conjecture needs to be validated.

## V. CONCLUSIONS

The present work shows that :

(1) Whereas shock Hugoniot of AlN manufactured by Dow determined by Rosenberg et al. [1] indicate a loss of shear strength above its HEL the Hugoniot of this material determined by Grady [2] does not indicate such a loss.

(2) The magnitudes of shear stress sustained by this material obtained from the simultaneous measurements of longitudinal and lateral stresses by means of manganin gages in Ref.1 show that the material has not suffered any loss of its shear strength above its HEL.

(3) The results of shock wave experiments on pure and doped AlN by Nakamura et al. [4] show that whereas the pure material suffers a loss of its shear strength the doped material does not above their respective HELs.

(4) The conclusions of (1) and (3) are also substantiated when these shock data are analyzed in conjunction with the hydrodynamic compression curve of AlN obtained through ultrasonic wave velocity measurements at moderate pressures in the present work.

(5) The analysis presented in this work indicates that the existing shock wave data on AlN manufactured by Dow are not conclusive to determine shear strength of this material above its HEL thereby its nature of deformation above the HEL remains unclear.

## ACKNOWLEDGEMENT

The authors appreciate the assistance of P. Bartkowski and P. Moy in preparation of the manuscript.

## REFERENCES

1. Z. Rosenberg, N. S. Brar, and S. J. Bless, J. Appl. Phys.**70**, 167 (1991).
2. D. Grady, Private Communication
3 E. P. Papadakis, J. Acoust. Soc. Am.**42**, 1045 (1967).

4. A. Nakamura, T. Mashimo, and M. Kodama, *Mechanical Behaviour of Materials - VI* , edited by M. Jono and T. Inoue (Pergamon, New York, 1992) pp. 395 - 400.
5. M. Manghnani, Private Communication.
6. D. Gerlich, S. L. Dole, G. A. Slack, J. Phys. Cem. Solids. **47**, 437 (1986).
7. Q.Xia, H. Xia, and A. L. Ruoff, J. Appl. Phys.**73**, 8198 (1993).
8. D. P. Dandekar, J. Appl. Phys.**41**, 667 (1970).
9. A. L. Ruoff, J.Appl. Phys.**38**, 4976 (1967).
10. R. Jeanloz and R. Grover,*Shock Waves In Condensed Matter-1987*, edited by S. C. Schmidt and N. C. Holms (North-Holland, Amsterdam, 1988) pp 69 - 72.
11.R. N. Thurston and K. Brugger , Phys. Rev.**133**, A1604 (1964).
12. K. Kondo, A. Sawaoka, K. Sato, and M. Ando, *Shock Waves In Condensed Matter-1981*, edited by W. J. Nellis, L. Seaman, and R. A. Graham (American Institute of Physics, New York, 1982) pp 325 - 329.
13. H. Vollstadt, E. Ito, M. Akaishi, S. Akimoto, and O. Fukunaga,Proc. Japan Acad.**66**, Ser.B 7 (1990).
14. R. A. Graham and W. P. Brooks, J. Appl. Phys. **32**, 2311 (1971).
15. M. K. W. Wong, Ph.D thesis (unpublished) Washington State University (1991). Unpublished.
16. Z. Rosenberg and Y. Partom,J. Appl. Phys. **58**, 1814 (1985).
17. Z. Rosenberg and Y. Partom,J. Appl. Phys. **58**, 3072 (1985).

# The Mechanical Behavior of a High-Purity Alumina Over the Strain Rate Range $10^{-4}$ - $10^{6}$ $sec^{-1}$

Mr. J.M. Staehler*, Dr. W.W. Predebon

Dept. of Mechanical Engineering-Engineering Mechanics

Dr. B.J. Pletka

Dept. of Metallurgical & Materials Engineering
Michigan Technological University
1400 Townsend Dr.
Houghton, MI 49931-1295

## Abstract

The strain rate dependence of the compressive strength of two high purity aluminas produced by vacuum hot pressing and hot isostatic pressing a 99.99% pure $Al_2O_3$ powder has been investigated. Previous results by the authors have suggested a strong rate dependence of the compressive strengths of both of these aluminas over a strain rate range from $10^{-4}$ to $10^{3}$ $sec^{-1}$. One of these aluminas, designated JS-I, has exhibited a uniaxial compressive strength which rose from 5.5 GPa at $10^{-4}$ $sec^{-1}$ to 8.3 GPa at $10^{3}$ $sec^{-1}$. Although the compressive strengths were lower in magnitude for the coarser grained alumina, designated as JS-II, it exhibited a similar rise in strength with strain rate. Recent results from flyer-plate impact tests indicate that the Hugoniot elastic limit for the JS-I alumina is about 11.9 GPa. Conversion to a dynamic uniaxial yield strength suggests that yielding occurs at about 8.3 GPa for a strain rate between $10^{5}$ to $10^{6}$ $sec^{-1}$. Of particular interest for the JS-I alumina was its spall strength of 1.2 GPa after a peak precompression of three times the HEL (36 GPa).

## Introduction

The importance of strain rate on the compressive fracture strength of alumina has been the subject of several recent studies. One key question in this work has been the contribution of plastic deformation to the fracture process of alumina. Lankford[1] studied the commercial alumina Lucalox, produced by General Electric, over a strain rate range from $10^{-5}$ to $10^{3}$ $sec^{-1}$. He observed a moderate strain rate dependence of the uniaxial compressive strength over this strain rate range. Based on his observation of deformation twins in this material, he came to the conclusion that the uniaxial compressive fracture strength of alumina at room temperature is closely related to the initiation of plastic deformation in the material, similar to Rice's[2] conclusion with regards to the fracture of ceramics. Because alumina does not have readily activated slip systems at room temperature under conditions of uniaxial stress to accommodate any appreciable amount of plastic deformation, the initiation of plastic flow quickly progresses to microcracking and subsequent failure.

Cosculluela et al[3] recently tested two commercially available French aluminas and found a more pronounced strain rate dependence than that observed by Lankford[1] in Lucalox. They used dumb-bell shaped specimen geometries as opposed to the right circular cylinders used by Lankford. However, contrary to Lankford's results, they observed no evidence of plastic deformation.

The existence of plastic deformation in alumina under conditions of uniaxial strain, such as are encountered in flyer-plate impact testing, is gaining more widespread acceptance. There is, however, some disagreement concerning some of the behavior of alumina under these loading conditions. One area of controversy concerns the meaning of the Hugoniot elastic limit (HEL) and whether it represents the onset of widespread microcracking or widespread plastic deformation. A second area of controversy which appears to be linked to the first concerns whether a spall strength exists above the HEL in alumina. Munson and Lawrence[4] tested Lucalox using flyer-plate impact techniques. They observed negligible spall strength in this alumina at peak stresses above the HEL and suggested that the HEL was therefore associated with the onset of widespread microcracking. The argument they used was that if the material did not contain extensive microcracks it should have been able to sustain some tensile stresses as the material went into tension due to the release waves. The lack of a spall strength suggests it was extensively microcracked.

However, recent work by Longy and Cagnoux[5] has shown that aluminas can exhibit spall strengths when shocked by as much as twice the HEL. They looked at four different aluminas with purities of 99.7% and another of 94% purity. In each material a spall strength was observed above the HEL.

The lack of a general consensus on these issues may be a direct consequence of the wide variations in the microstructures of the aluminas being tested. The results presented in the present paper describe the strain rate dependence of the compressive strength for two high purity aluminas produced at Michigan Technological University (MTU). One is a fine grained alumina called JS-I and the second is a coarser, less isometric grained material called JS-II. Since these aluminas have controlled variations in their microstructure, the influence of the microstructure on some of the issues presented earlier will be discussed.

## Materials

Both of the MTU aluminas were produced by first vacuum hot pressing a 99.99% pure alumina powder in graphite dies. No additions of any kind were made to the powder. For the material called JS-I, the vacuum hot pressing was followed by a hot isostatic pressing cycle in high purity argon. The JS-II material was subjected to a heat treatment to induce grain growth before the hot isostatic pressing cycle. More details with regards to the processing are presented in Staehler et al.[6]

Image analysis techniques were used to determine average grain sizes and grain isometry. The JS-I alumina has an average grain size of 1.48 μm with a shape parameter of 1.41. The JS-II material has an average grain size of 4.0 μm and a shape parameter of 2.15. The shape parameter used to describe grain isometry was that suggested by Kibbel and Heuer[7]. The value of 1.41 for JS-I is comparable to a rectangle with a length to width ratio of 3:2. Using immersion techniques, the densities of JS-I and JS-II were determined to be 3.974 g/cc and 3.96 g/cc, respectively. Transmission electron microscopy observations suggest that the porosity in JS-I is predominantly within the grain interiors. JS-II includes some additional porosity on the grain boundaries.

## Experimental Setup

The specimen preparation and experimental procedure for the quasi-static and intermediate strain rate testing were presented in

Staehler et al.[6] The flyer-plate impact tests which were conducted on JS-I are divided into two types; tests above the HEL to measure the HEL and spall strengths, and tests to recover the specimens intact after being subjected to shock loading. Tests of each type were conducted at Sandia National Laboratory and at the University of Dayton Research Institute (UDRI). Velocity interferometer techniques (VISAR) were used in the non-recovery tests at Sandia. A simple schematic of the test configuration is shown in Fig. 1. The UDRI non-recovery tests were performed using manganin pressure gauges and are shown in Fig. 2. More details on each of these techniques can be found in references by Barker and Hollenbach[8] and Rosenberg et al,[9] respectively.

Recovery tests both above and below the HEL were conducted on the MTU JS-I alumina with the former being performed at Sandia and the latter at UDRI. The recovery testing at either laboratory used only velocity pins to measure projectile velocities. A simple schematic of the Sandia recovery test setup is shown in Fig. 3. The specimen is encased in a steel cylinder with a rear copper backing plate followed by a low density foam. The steel cylinder served to contain the test specimen and hopefully minimize the amount of fragmentation.

The recovery tests at UDRI used the configuration shown in Fig. 4. The design incorporated a rear surface momentum trap, star shaped flyers, and a rag filled catch tube to stop the specimen.

Specimen and flyer plate dimensions are listed in Table 1 along with some additional test parameters on the flyer-plate impact tests.

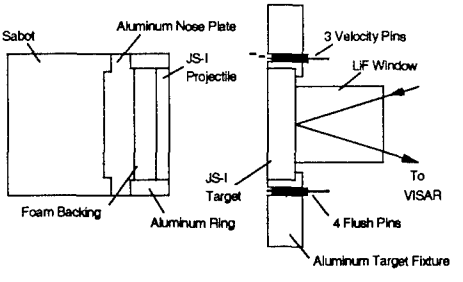



Figure 1. Sandia VISAR test schematic.

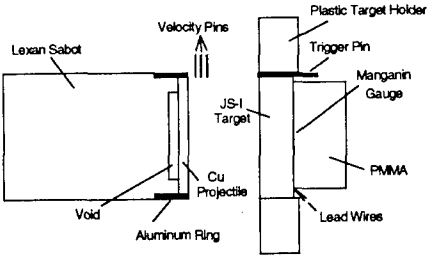



Figure 2. UDRI manganin gauge test schematic.

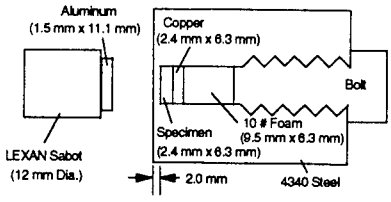



Figure 3. Sandia shock recovery assembly.

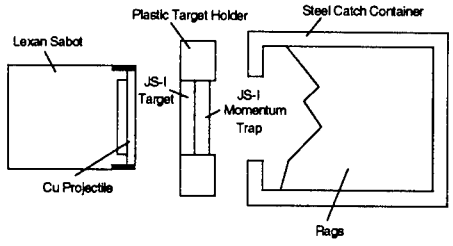



Figure 4. UDRI shock recovery schematic.

## Results

The uniaxial stress compression test results as a function of strain rate for JS-I and JS-II were presented in Staehler et al[6] but are repeated in Fig. 5 for convenience. Included in the figure are the quasi-static and intermediate strain rate results of Lankford[1] and the flyer-plate impact results of Munson and Lawrence[4] for Lucalox. Also included are the results of Cosculluela et al[10] for the French alumina AL23. The plate impact data for AL23 obtained from Cagnoux and Cosculluela[10] indicates an HEL of about 6.5 GPa for this alumina compared with the value of 9.1 GPa found for Lucalox.[4] The HEL data was converted into an equivalent dynamic uniaxial yield stress using the relationship

$$\sigma_y = 2\frac{C_s^2}{C_l^2}\sigma_{HEL}$$

where $C_s$ and $C_l$ are the shear and longitudinal sound speeds, respectively, and $\sigma_{HEL}$ is the measured HEL.

The quasi-static compressive fracture strengths of JS-I and JS-II are shown in Fig. 6 as a function of grain size. Included in the figure are comparable data for some commercially pure (99.5%) aluminas taken from a report by Weyand.[11] The JS-I and JS-II aluminas do not appear to follow the same general trend exhibited by the commercial aluminas, suggesting that a different Hall-Petch type relationship applies.

Following the proposal of Rice,[2] the theoretical yield strengths deduced using Knoop microhardness indentations were measured for

JS-I and JS-II. Figure 7 shows the uniaxial compressive strength of each of these aluminas as a function of their respective theoretical yield strengths. If the proposal of Rice is true, the upper limit to the compressive yield strength should be the theoretical yield strength of the material and the points should fall on the line in the figure. This is approximately the case for JS-I, but JS-II falls well below the line, suggesting that the strength of this material is controlled by factors other than the yield strength.

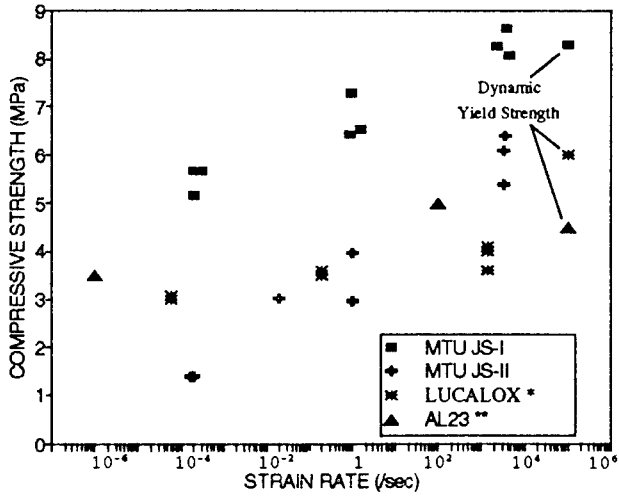



Figure 5. Uniaxial compressive strength versus strain rate.
(* data taken from ref 1 and 4, ** data taken from ref 3 and 10)

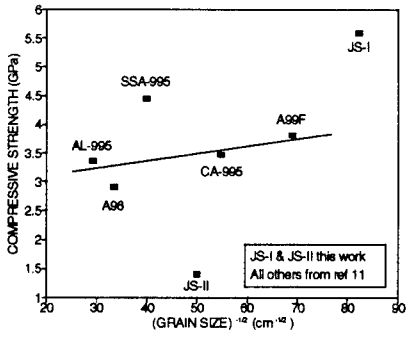



Figure 6. Compressive strength as a function of grain size.

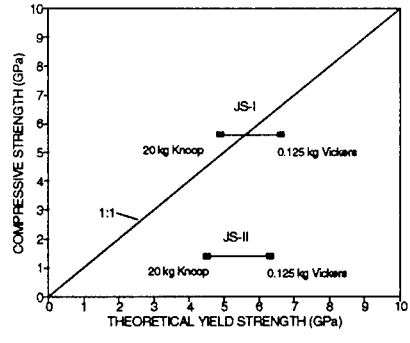



Figure 7. Uniaxial compressive strength versus the theoretical yield strength.

The VISAR data for the two Sandia HEL tests are shown in Fig. 8. For specimen B44 the HEL is about 11.9 GPa and the peak stress is about 36 GPa. Besides the high HEL, the interesting aspect of these data is the spall signal which is significant for a ceramic prestressed to three times its HEL. This signal corresponds to a spall strength of about 1.2 GPa. Specimen B45 was subjected to a peak stress just above the HEL. In contrast to B44, it exhibited a lower spall strength (≈0.5 GPa).

The HEL type flyer-plate impact tests at UDRI were intended to measure the HEL of the JS-I alumina and the decay, if any, of the HEL with specimen thickness. Three different specimen thicknesses were used; 6, 9, and 12 mm. The results are summarized in Fig. 9 and indicate a slight decay (<8%) of the HEL in going from 6 mm to 9 mm.

The Sandia recovery specimen was shocked to a peak stress of about 25 GPa. The specimen was extensively fragmented despite the steel confinement. It was possible, however, to make TEM foils from some of these fragments. These foils showed evidence of enhanced plastic deformation through the presence of dislocation structures within the microstructure.

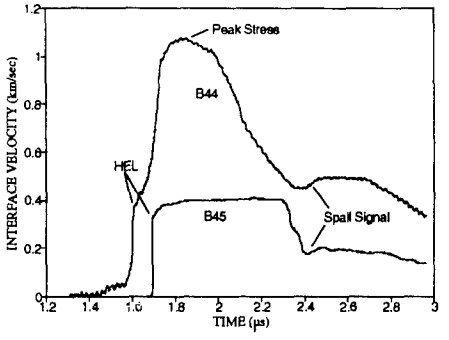



Figure 8. Sandia interface velocity data.

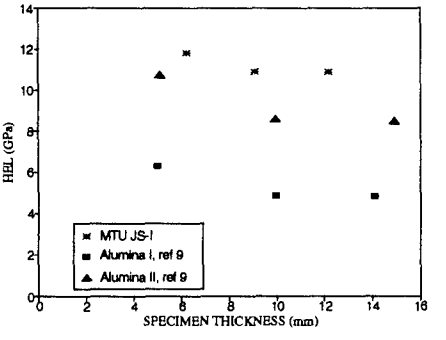



Figure 9. HEL decay with propagation distance.

The UDRI recovery specimen, which was shocked to a stress level below about half of the HEL, was also fragmented. However, the fragments themselves were fairly well intact compared to the Sandia recovery test specimen. The fragmentation that did occur is believed to be a consequence of the recovery technique used and is therefore not thought to be representative of the material response to the initial compressive loading. TEM foils made from the UDRI test fragments revealed no noticeable increase in dislocations or twinning over undeformed material. This is not surprising due to the relatively low compressive stresses encountered in the test (<½HEL).

## Discussion

The high strength of the JS-I alumina is attributed to its controlled microstructure. Microstructural characteristics known to be important for high strength include the high purity, fine, isometric grain structure, and high density exhibited by JS-I. Other microstructural characteristics that control the strength may be less obvious and include the distribution of the porosity, the relative orientation of adjacent grains, and the lack of any glassy phases on the grain boundaries. Krell and Blank[12] have used replicating techniques to carefully study the grain boundaries of high purity aluminas they produced by sintering. They found that there were fine micropores on the grain boundaries which they believe controlled the strength of the material. Although similar work on the nature of the grain boundaries in JS-I has not been completed, it is believed that the presence of such fine grain boundary micropores has been greatly reduced as a result of the processing techniques used to produce JS-I. The reduced grain boundary porosity results in a much higher grain boundary toughness between adjacent grains which translates into the greater observed macroscopic strengths. The lack of any impurities at the grain boundaries further increases the grain boundary toughness.

Another microstructural feature that may be important concerns the number of special grain boundaries in the material. It is known that two adjacent grains can form a stronger interface if the lattice structures have certain favorable relative orientations across the grain boundaries. If more of these special boundaries exist in the JS-I alumina compared to the commercial aluminas, it may also account for the higher strengths. The greater incidence of special grain boundaries in JS-I may result from the fine grain size and "clean" grain boundaries maintained throughout the processing scheme. However, additional work to confirm this hypothesis is necessary.

The reduced strength of JS-II relative to JS-I results from the fact that the microstructure of JS-II is more similar to commercial aluminas than it is to JS-I. For example, the lower density of JS-II may lead to an increase in the porosity along the grain boundaries which will reduce the grain boundary toughness. The coarser, less isometric grain structure of JS-II, combined with its lower density relative to JS-I, may outweigh any gains from its high purity and the presence of special grain boundaries.

The magnitude of the spall strength in the JS-I alumina at three times the HEL was not expected. Similarly, the very low spall strength of the JS-I alumina tested at a peak stress just above the HEL was a surprise in view of the very high spall strength observed at three times the HEL. These results suggest that the spall strength is a function of the peak stress to which the specimen has been subjected. Recently Longy and Cagnoux[5] have conducted plate impact tests on alumina to study the influence of peak stress on spall strength. They reported that within their experimental uncertainty the spall strength was found to be constant from the threshold value out through twice the HEL. It is worthwhile to review these results again and the data of Longy and Cagnoux are included in Fig. 10 along with the JS-I data. Despite experimental uncertainty, the spall strengths for both of the aluminas they tested consistently show a drop near the HEL. The drop is as much as 50% for the one alumina and about 25% for the other. If such a drop is real, the data suggest that the lower confining stresses to which the specimen is subjected when the peak stress is near the HEL is not sufficient to prevent microcracking within the specimen.

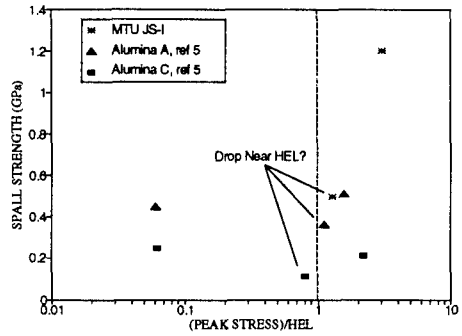



Figure 10. Spall strength with peak stress.

In the past the HEL of alumina has been associated with the onset of widespread microcracking. This was based on the apparent lack of a spall strength above the HEL in alumina such as Lucalox[4]. However, Longy and Cagnoux[5] argued that the presence of a non zero spall strength above the HEL was evidence that the HEL was associated with the onset of plastic deformation. Their X-ray diffraction studies on deformed specimens showed that an increased dislocation density was

present. Also, using the star shaped plate impact design of Kumar and Clifton[13], Longy and Cagnoux were able to recover specimens intact with no evidence of microcracking in their higher purity specimens tested at stresses up to twice the HEL.

Our results support the contention that the HEL is associated with the onset of plastic deformation rather than a state of general microcracking. The TEM results of the JS-I recovery specimens showed no evidence of plastic deformation below the HEL but there was dislocation activity above the HEL. This is consistent with previous studies in which plasticity was observed in shock loaded sapphire[14] and polycrystalline alumina[15]. The presence of the large spall strength of the JS-I at three times the HEL also supports the argument that the material has not undergone a state of general microcracking. The low spall strength near the HEL is not fully understood at this time.

The data in Fig. 9 indicate a decay of the HEL. This is consistent with the results of several recent investigations on alumina but is in disagreement with the findings of Cagnoux and Longy[16]. A decay of the HEL is reasonable if the HEL is indeed associated with plastic deformation. Furthermore, because of the high stresses around localized stress concentrations such as voids, plastic deformation or microcracking may occur at these locations at a lower applied stress, so that as the elastic wave front encounters these defects, a portion of the elastic energy is lost.

## Conclusions

The higher purity JS-I and JS-II aluminas show a greater strain rate sensitivity of the uniaxial compressive strength than the commercial aluminas shown in Fig. 5. In the case of JS-I the strengths are also significantly higher than those of the commercial aluminas. For JS-II the strength at the lowest strain rates was below those of the commercial aluminas and is not well understood. It may be a consequence of the increased porosity present in JS-II plus a more anisometric grain structure.

The observed dependence of the spall strength upon the peak stress, shown in Fig. 10, suggests that two competing processes may be involved in the deformation mechanisms of alumina in flyer-plate impact tests. At peak stresses in excess of the HEL, the high spall strength combined with TEM observations of dislocation activity substantiates the conclusion that plastic deformation dominates. The high pressures associated with these peak stresses suppress the

formation of microcracks, enhance the tendency for dislocation activity, and results in a high spall strength. When the peak stresses are comparable to the HEL, there is an increased tendency for the formation of microcracks due to the reduced confining pressures, as evidenced by the significantly reduced spall strength. The JS-I data in Fig. 9 combined with the data of Rosenberg et al[9] demonstrates the existence of a precursor decay. This can be explained by localized plasticity or microcracking near defects even though the macroscopic response is elastic. The decay of the HEL with propagation distance appears to reach a stable value at about 9 mm.

Table 1. Specimen, flyer and test parameters for JS-I plate impact tests.

| JS-I Spec. ID | Spec. Width (mm) | Spec. Diam. (mm) | Flyer Type | Flyer Width (mm) | Flyer Vel. (km/s) | Test Type | Peak Stress (GPa) |
|---|---|---|---|---|---|---|---|
| B44 | 6.261 | 51 | JS-I | 2.802 | 1.855 | HEL[a] | 36 |
| B45 | 6.230 | 51 | JS-I | 2.804 | 0.587 | HEL[a] | 13 |
| B46 | 6.220 | 51 | Cu | 3.17 | 0.765 | HEL[b] | 31 |
| B49 | 9.108 | 51 | Cu | 3.17 | 0.789 | HEL[b] | 29 |
| B50 | 12.192 | 51 | Cu | 3.17 | 0.790 | HEL[b] | 29 |
| B47a | 2.4 | 6.3 | Al | 1.5 | 2.00 | Rec[c] | 25 |
| B40B | 2.906 | 38 | Cu | 2.0 | 0.098 | Rec[d] | <6 |

[a] at Sandia, [b] at UDRI, [c] recovery test at Sandia, [d] recovery test at UDRI

## References


1 J. Lankford, J. Mater. Sci., **12** [4], pp. 791-796, (1977).

2 R.W. Rice, in *Ceramics in Severe Environments*, W.W. Kriegel and H. Palmer (eds.), Materials Science Research, Plenum Press, NY, **5**, pp. 195-229, (1971).

3 A. Cosculluela, J. Cagnoux, and F. Collombet, J. Phys. IV, Colloque **C3**, suppl. J. Phys. III, **1**, pp. 109-116, (1991).

4 D.E. Munson and R.J. Lawrence, J. Appl. Phys., **50** [10], pp. 6272-6282, (1979).

5 F. Longy and J. Cagnoux, J. Am. Ceram. Soc., **72** [6], pp. 971-979, (1989).
6 J.M. Staehler, W.W. Predebon, and B.J. Pletka, in Proc. 1991 Army Symposium on Solid Mechanics, S. Chow (ed.), Plymouth, MA, Nov. 4-7, pp. 221-235, (1991).
7 B.W. Kibbel and A.H. Heuer, J. Am. Ceram. Soc., **72** [3], pp.517-519, (1989).
8 L.M. Barker and R.E. Hollenbach, J. Appl. Phys., **43** [11], pp. 4669-4675, (1972).
9 Z. Rosenberg, N.S. Brar, and S.J. Bless, J. Phys. (Fr.), Colloque **C3**, suppl. n9, 49, pp. 707-711, (1988).
10 J. Cagnoux and A. Cosculluela, in *Dynamic Failure of Materials*, H.P. Rossmanith and A.J. Rosakis (eds.), Elsevier, 1991, pp.73-84.
11 J.D. Weyand, in Alcoa Laboratories Technical Report, No. 03-88-01, (1988).
12 A. Krell and P. Blank, J. Eur. Ceram. Soc., **9**, pp. 309-322 (1992).
13 P. Kumar and R.J. Clifton, J. Appl. Phys., **48** [11], pp. 4850-4852, (1977).
14 Y. Wang and D.E. Mikkola, Mater. Sci. Eng., A148, pp. 25-32, (1991).
15 J.A. Brusso, D.E. Mikkola, J.E. Flinn, and P.V. Kelsey, Scr. Metall., **22** [1], pp. 47-52, (1988).
16 J. Cagnoux and F. Longy, in Proceedings of the Am. Phys. Soc., *Shock Waves In Condensed Matter 1987*, S.C. Schmidt and N.C. Holmes (eds), Amsterdam, Elsevier, 1988, pp. 293-296.

# Plate Impact Investigation of Failure Waves in Glass

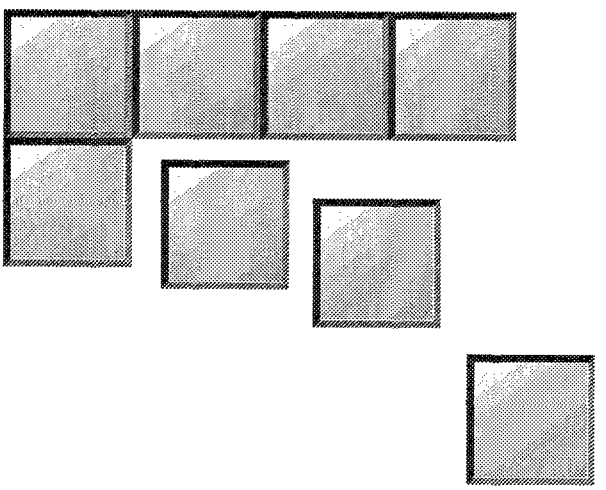
*G.F. Raiser and R.J. Clifton*
Brown University

*J.L. Wise, D.E. Grady and D.E. Cox*
Sandai National Laboratories

"PAPER NOT AVAILABLE"

# SESSION VIA: ANISTROPY AND HETEROGENIETY

**Chairman:** *Dr. R. Kohn*
**Courant Institute of**
**New York University**



# Degree-of-Freedom Based Deterministic Model Reduction: Application to Laminates

Dr. L. D. Flippen, Jr.
Naval Research Laboratory, Code 6386, 4555 Overlook Ave., S.W., Washington, D. C. 20375-5343

## Introduction

The need to predict the macroscale behavior of composite materials has led to the development of multiple-scales homogenization [1-2], effective medium and self-consistent theories [3], variational-bounds theories [4], the differential scheme [5], the method-of-cells [6], and others. An alternative to these methods will be demonstrated which is based on the idea of degree-of-freedom (DOF) reduction in spatially-discretized models of the heterogeneous material. This approach avoids both the periodic-media and the global boundary-layer restrictions which plague current deterministic-material-oriented methods of homogenization/smoothing, such as multiple-scales. It has the additional advantage that computer implementations of the method are both straightforward (involving only matrix manipulations) and independent of the microgeometry, with no requirement of homogenization/smoothing methodology expertise. To use the method to smooth the dynamic mechanical behavior of a composite material, one would discretize the mathematical model of the composite spatially, using standard finite element techniques and sufficiently fine resolution so as to fully "capture" the heterogeneity of the composite. This produces a finite, but large number of spatial degrees-of-freedom, with time left as continuous. In the case of linear-response systems with nonevolving-microgeometries the resulting spatially-discretized model will have the universal form of a matrix differential equation in time with a mass, possibly a damping, and a stiffness matrix. The method smooths by eliminating most of the degrees-of-freedom, producing for such cases much smaller mass, damping (if initially present), and stiffness matrices. This reduced-DOF model can be interpreted as a coarse-mesh, spatially-discretized model of an equivalent single-phase material whose predictions are smoothed versions of the

corresponding original (fine-mesh) model's predictions. The method is one of the products of a new theory of condensation model reduction [7] which itself evolved from earlier model reduction work [8]. (A model reduction process mathematically produces a simpler model from the original complex model such that the simpler model contains only the "essential physics" of the physical system. In the special case of composites the complexity arises from the intricate spatial heterogeneity.) The methodology is so recent that no computational results based on the approach have yet been carried out other than the preliminary laminate cases presented in this paper. One of the three laminates chosen is the same as that used by Randles [9] so that comparisons with his results are possible.

## Method Description

The introduction of more generality than is needed to understand the specific cases considered later in this paper seems counter to brevity and clarity. The methodology of [7] will hence be correspondingly specialized in its reproduction here. The method will be described for the special case of the linear, mechanical response of a system with negligible body forces, a nonevolving microgeometry, and a boundary consisting of prescribed-load-history (and possibly load-free) regions. The spatial discretization of the model of such a system leads to the generic form

$$M\ddot{u} = Su + f, \tag{1}$$

where the constant mass and stiffness matrices are given by $M$ and $S$ respectively, the dots signify time derivatives, $u$ represents the displacement response, and $f$ represents the (global-boundary) loads driving the system. The nodes of the spatial discretization are divided into "master" and "slave" nodes, the degrees-of-freedom of the slave nodes being the ones targeted for elimination. (The master nodes must include all the loaded boundary nodes.) Let the rows and columns of $M$ and $S$, and the rows of $f$, be permuted and the results then partitioned as

$$\begin{bmatrix} M_{11} & M_{12} \\ M_{21} & M_{22} \end{bmatrix} \tag{2}$$

$$\begin{bmatrix} S_{11} & S_{12} \\ S_{21} & S_{22} \end{bmatrix} \tag{3}$$

$$\begin{bmatrix} f_1 \\ f_2 \end{bmatrix} \tag{4}$$

such that $M_{11}$, $S_{11}$, and $f_1$ are the submatrices associated with the master nodes. The mass and stiffness matrices of the reduced-DOF system are given in terms of the above submatrices as

$$M_{red} = M_{11} + M_{12}B_0 - S_{12}B_1 \tag{5}$$

$$S_{red} = S_{11} + S_{12}B_0 , \tag{6}$$

where the matrices $B_0$ and $B_1$ are defined as

$$B_0 = -(S_{22})^{-1}S_{21} \tag{7}$$

$$B_1 = (S_{22})^{-1}(M_{21} + M_{22}B_0) \tag{8}$$

The reduced-DOF model takes the form

$$M_{red}\ddot{v} = S_{red}v + f_1 , \tag{9}$$

where $v$ is defined at the master nodes. A smooth interpolation, such as a cubic spline for one-dimensional cases, of $v$'s components onto the slave nodes provides a smoothed version of the solution to the original problem (1). More importantly, the method has the solution-reconstruction attribute, similar to multiple-scales homogenization, whereby one can recover the fluctuations as well. Solutions $u$ for (1) can be approximately *reconstructed* from solutions $v$ for (9) by

$$u_{perm} = \begin{bmatrix} v \\ C_0 f_1 + C_1 v \end{bmatrix} , \tag{10}$$

where $u_{perm}$ is the permuted version of $u$. The matrices $C_0$ and $C_1$ are defined by

$$C_0 = B_1 (M_{red})^{-1} \tag{11}$$

$$C_1 = B_0 + C_0 S_{red} \,. \tag{12}$$

The process of validating the method for the cases of this paper consists of comparisons of "brute force" solutions to (1) with those, to be referred to as "reconstructed" solutions, which are obtained from solving (9) and using (10).

## Alternating-Steel-Polystyrene Laminate Results

Dynamic laminate-response predictions were obtained for three laminates, each consisting of alternating layers of 304 stainless steel and polystyrene, starting with steel at the extreme left layer (spatial origin) and ending up with polystyrene at the extreme right layer (backface). As in [9], 304 stainless steel was taken to have a mass density of 7.9 gm/cm$^3$ and an acoustic wave velocity of 0.57 cm/microsecond, the modulus value being density times wave velocity squared, and the polystyrene was taken to have a mass density of 1.05 gm/cm$^3$ and a wave velocity of 0.299 cm/microsecond. (The polystyrene wave velocity value used was the readjusted one from [9].) The one dimensional response transverse to the layers was computed for a load-free right side and a left side with load history of zero load for times less than zero and a constant load of 0.001 gm/cm-microsecond$^2$ for times greater than or equal to zero. (Body forces were ignored.) Initial displacements and velocities were taken to be zero.

The solutions to (1) and (9) for each of the laminate cases were obtained using a fourth order Runge-Kutta method. The $M$ and $S$ matrices were obtained, for each of the laminate cases, by control-volume-integration based finite difference methods [10] of spatial discretization. Five nodes per laminate layer (spaced evenly within the layer interior) and, additionally, one node at each boundary, were used. All programming was implemented in Mathematica.

### *Six-Layer Periodic Laminate*

The case studied in [9] is that of a six layer periodic laminate, three layers each of steel and polystyrene, where the steel layer thickness is 0.1524 cm and the polystyrene layer thickness is 0.08 cm. A plot

of layer thickness versus layer number (numbered from left to right) is given in Figure 1.

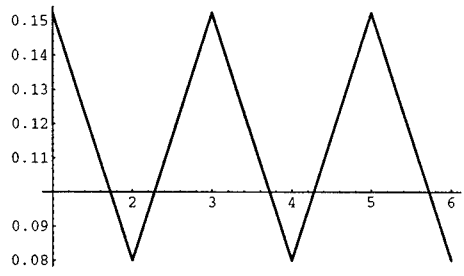



*Figure 1. Layer thickness (cm) vs. layer number for six-layer periodic case.*

The spatially-discrete model resolving the spatial heterogeneity has 32 DOF, one DOF per node. Reduced models were obtained from this which had 8 and 4 DOF, respectively. Master nodes consisted of the central node for each of the six layers and the two boundary nodes for the 8 DOF case. Master nodes consisted of the central node for each of layers 2 and 5, and the two boundary nodes, for the 4 DOF case. A constant time step value of 0.0126 microseconds was used in this case.

The backface (right boundary) velocity history predicted by the 32 DOF model is given by Figure 2. The signal arrival time is quantitatively correct and the response shape is in general qualitative agreement with that of [9] except for the dips in the "steps" of the "staircase".

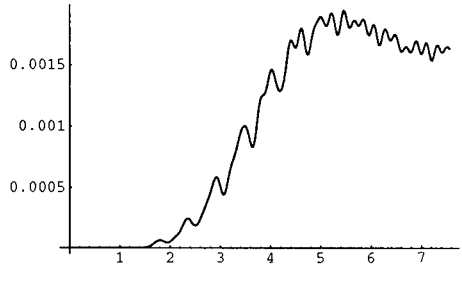
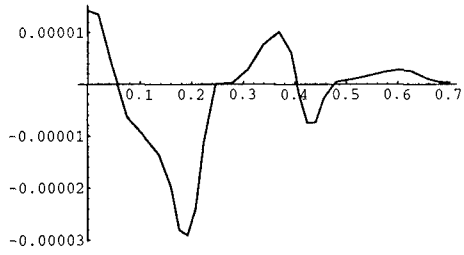
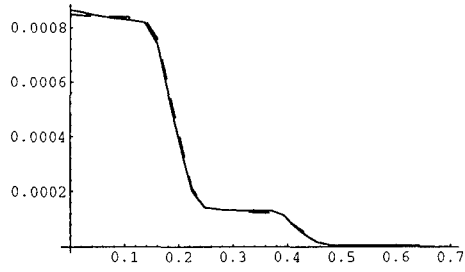



*Figure 2. Backface velocity (cm/microsecond) vs. time (microseconds) for 32 DOF model of six-layer periodic laminate.*

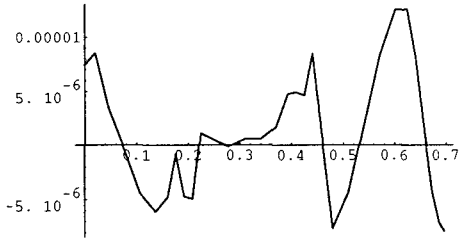
The transient was taken to 600 time steps. Early, middle, and later times were chosen from Figure 2 for plotting the six-layer transient cases. The case for the reduction to 8 DOF is given by Figure 3.



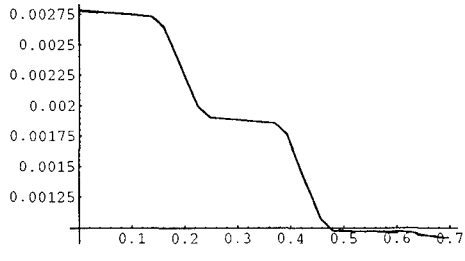

*a) Difference for time = 1.563.*



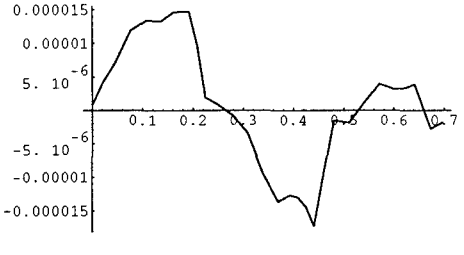

*b) Full/reduced DOF for time = 1.563.*



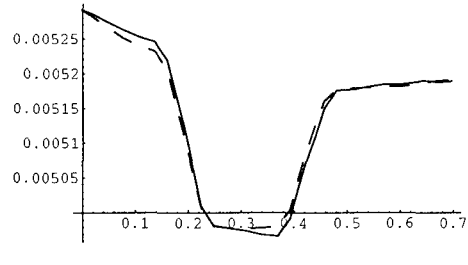

*c) Difference for time = 3.781.*




*d) Full/reduced DOF for time = 3.781.*




*e) Difference for time = 6.302.*

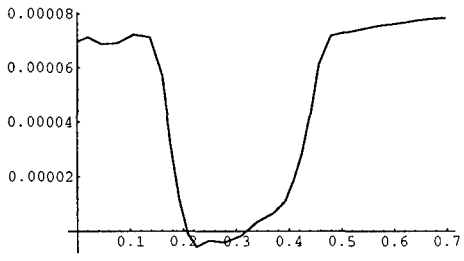



*f) Full/reduced DOF for time = 6.302.*

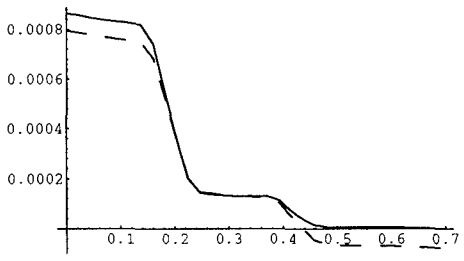
*Figure 3. 6 LAYER PERIODIC. Plots a, c, and e: Full (32) DOF model solution minus reconstructed solution of reduced (8) DOF model. Plots b, d, and f: reconstructed solution (dashed) and full DOF model solution (solid). Time is in microseconds.*

The placement and number of DOF retained in this case allowed for good accuracy in the reconstructed solution in comparison to the full DOF solution. The infinity norm of the difference between the full DOF solution and the reconstructed solution fluctuated, its largest value of about $4 \times 10^{-5}$ being obtained once, but its value more typically being $1.5 \times 10^{-5}$ to $3 \times 10^{-5}$ (sometimes smaller). The fluctuations in time of the norm included times for which its value actually decreased.

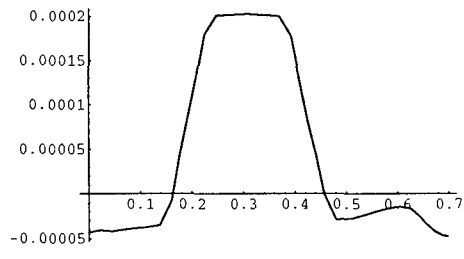
The plots at the same three time values as above for the reduction to 4 DOF is given in Figure 4. There is a drop in accuracy for the reconstructed solution from the 4 DOF model in comparison to the previous 8 DOF model, as is to be expected.



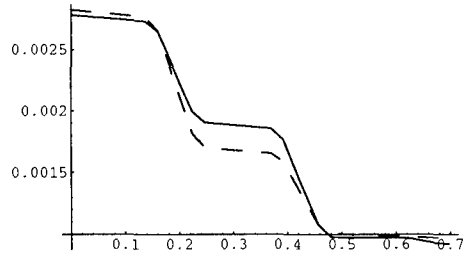

*a) Difference for time = 1.563.*



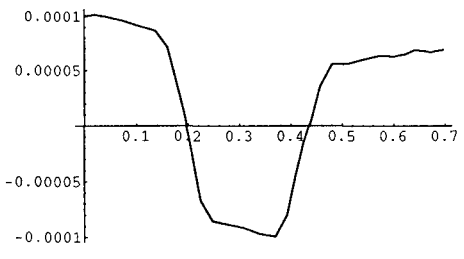

*b) Full/reduced DOF for time = 1.563.*



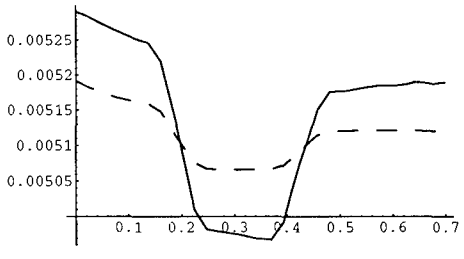

*c) Difference for time = 3.781.*




*d) Full/reduced DOF for time = 3.781.*




*e) Difference for time = 6.302.*




*f) Full/reduced DOF for time = 6.302.*

*Figure 4. 6 LAYER PERIODIC. Plots a, c, and e: Full (32) DOF model solution minus reconstructed solution of reduced (4) DOF model. Plots b, d, and f: reconstructed solution (dashed) and full DOF model solution (solid). Time is in microseconds.*

The results of these, and other cases not reproduced here, seem to indicate that the reconstructed solution accuracy is sensitive to retained-DOF (master node) placement, especially when the number of master

nodes is small, as one might expect. The placement choice probably determines which modes are accurately "captured" by the process. In a few trial cases where the master nodes were "bunched" and few in total number, the accuracy was good in the "bunched" region, but quite poor elsewhere.

### *Six-Layer Non-periodic Laminate*

The response of a six layer non-periodic laminate, three layers each of steel and polystyrene, was calculated using 32 degrees-of-freedom. The layer thicknesses of the laminate varied with layer number according to the plot in Figure 5. Reduced models were obtained from this which had 8 and 4 DOF, respectively. Master nodes consisted of the central node for each of the six layers and the two boundary nodes for the 8 DOF case. Master nodes consisted of the central node for each of layers 2 and 4, and the two boundary nodes, for the 4 DOF case. A constant time step value of 0.00988 microseconds was used in this case.

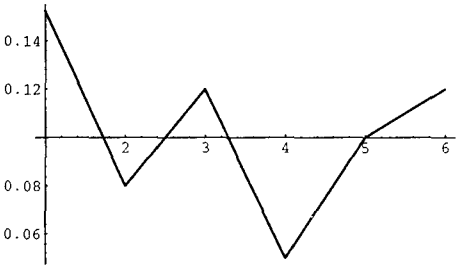



*Figure 5. Layer thickness (cm) vs. layer number for six-layer non-periodic case.*

The backface velocity history predicted by the 32 DOF model is given by Figure 6. The lack of periodicity has resulted in a much smoother "staircase".

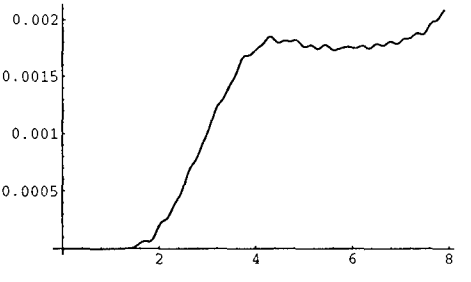
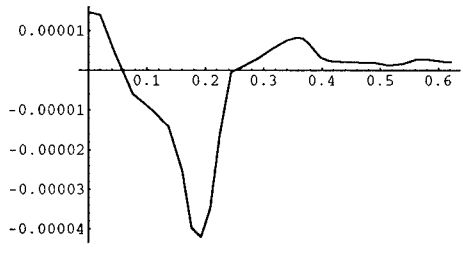
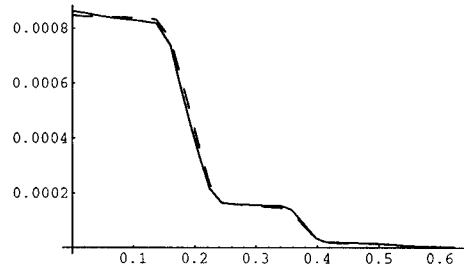



*Figure 6. Backface velocity (cm/microsecond) vs. time (microseconds) for 32 DOF model of six-layer non-periodic laminate.*

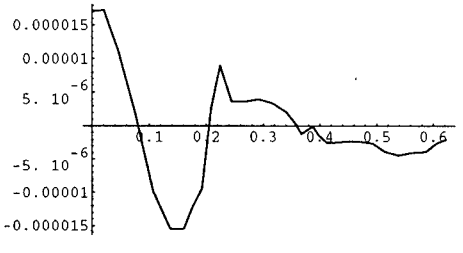
The transient was taken to 800 time steps. The six-layer, non-periodic 32-to-8-DOF reduction case is plotted at the previous three time values in Figure 7.



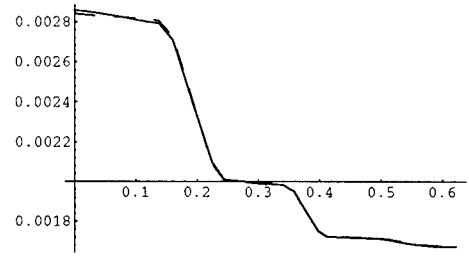

*a) Difference for time = 1.561.*



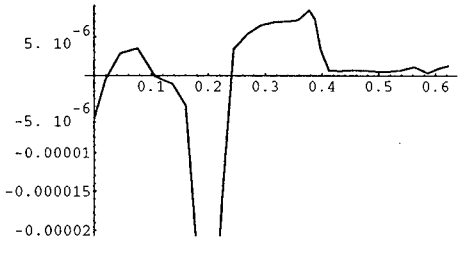

*b) Full/reduced DOF for time = 1.561.*



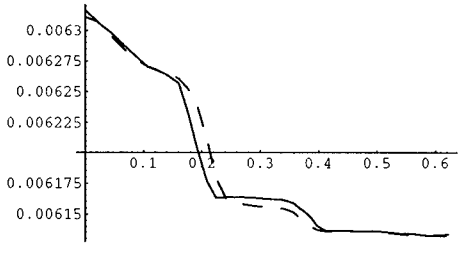

*c) Difference for time = 3.785.*




*d) Full/reduced DOF for time = 3.785.*



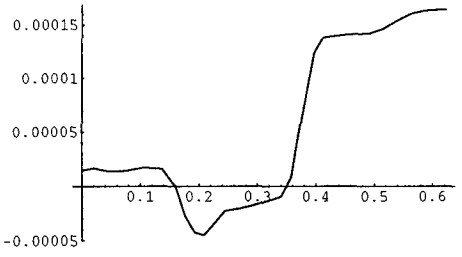

*e) Difference for time = 6.305.*



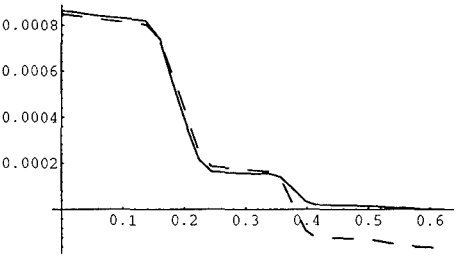

*f) Full/reduced DOF for time = 6.305.*

*Figure 7. 6 LAYER NON-PERIODIC. Plots a, c, and e: Full (32) DOF model solution minus reconstructed solution of reduced (8) DOF model. Plots b, d, and f: reconstructed solution (dashed) and full DOF model solution (solid). Time is in microseconds.*

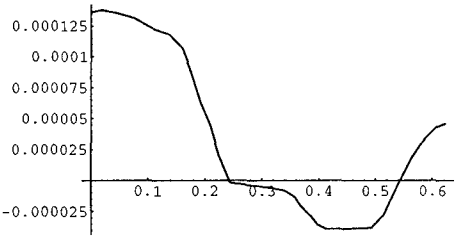
The three corresponding plots for the reduction to 4 DOF are given in Figure 8.



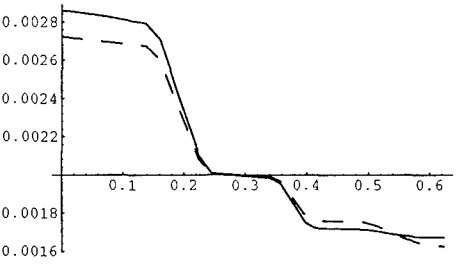

*a) Difference for time = 1.561.*



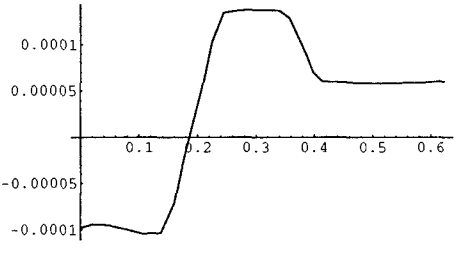

*b) Full/reduced DOF for time = 1.561.*



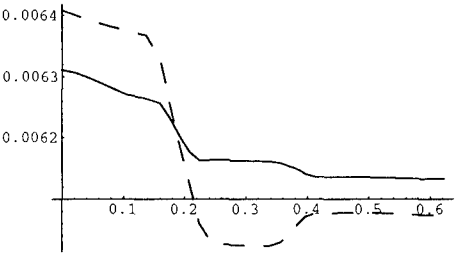

*c) Difference for time = 3.785.*




*d) Full/reduced DOF for time = 3.785.*




*e) Difference for time = 6.305.*




*f) Full/reduced DOF for time = 6.305.*

*Figure 8. 6 LAYER NON-PERIODIC. Plots a, c, and e: Full (32) DOF model solution minus reconstructed solution of reduced (4) DOF model. Plots b, d, and f: reconstructed solution (dashed) and full DOF model solution (solid). Time is in microseconds.*

The 8 DOF reconstructed solution's accuracy, as measured by the infinity norm of the difference between the full DOF solution and the reconstructed solution, behaved very similarly to that for the 8 DOF periodic case. The 4 DOF reconstructed solution lost accuracy, from that of the 8 DOF, to a level comparable to the 4 DOF periodic case.

### *Twelve-Layer Non-periodic Laminate*

Figure 9 gives a plot of the layer thicknesses of a twelve layer non-periodic laminate versus layer number. The response of this

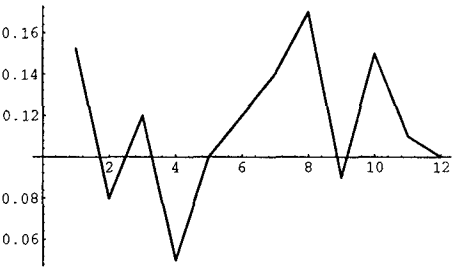



*Figure 9. Layer thickness (cm) vs. layer number for twelve-layer non-periodic case.*

laminate, with six layers each of steel and polystyrene, was calculated using 62 DOF. The reduced model obtained from the 62 DOF model has 5 DOF. Master nodes consisted of the central node for each of layers 3, 7, and 10, and the two boundary nodes, for this case. A constant time step value of 0.00988 microseconds was used in this case.

The backface velocity history predicted by the 62 DOF model is given by Figure 10. The "staircase" is totally absent.

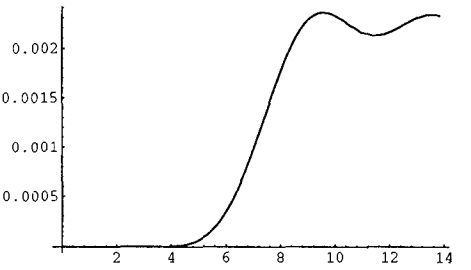
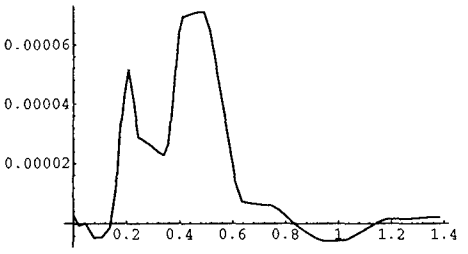
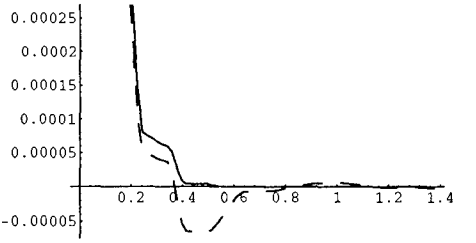



*Figure 10. Backface velocity (cm/microsecond) vs. time (microseconds) for 62 DOF model of twelve-layer non-periodic laminate.*

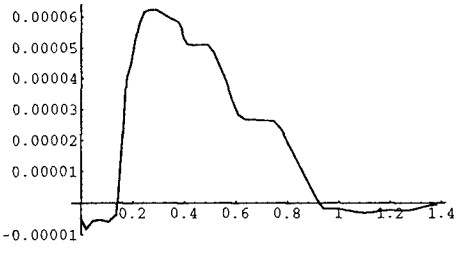
The transient was taken to 1400 time steps. Figures 11 and 12 contain plots for six times from the history of the laminate response. The undershoot of Figure 15b (and earlier) has disappeared by the 1.887 microsecond value of Figure 16b. The infinity norm of the difference between the full DOF solution and the reconstructed solution fluctuated in time, attaining its largest value of about $4.5 \times 10^{-4}$ only once; its value more typically being less than $4 \times 10^{-4}$ (sometimes much smaller). As in the



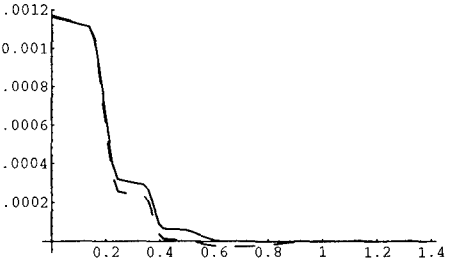

*a) Difference for time = 1.265.*



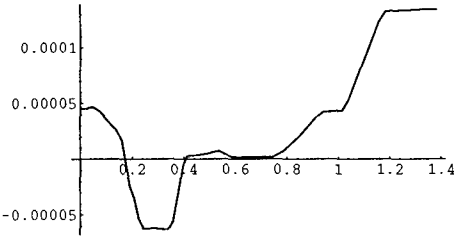

*b) Full/reduced DOF for time = 1.265.*



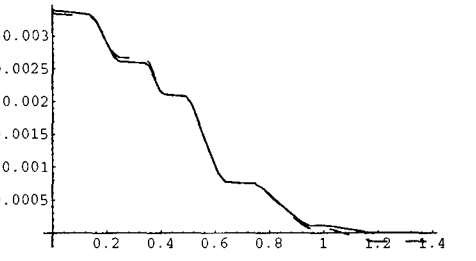

*c) Difference for time = 1.887.*



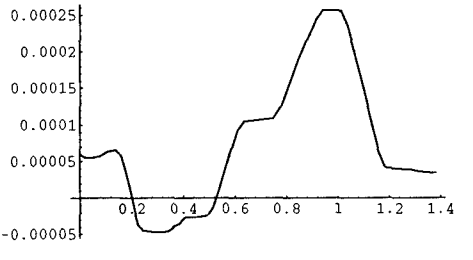

*d) Full/reduced DOF for time = 1.887.*



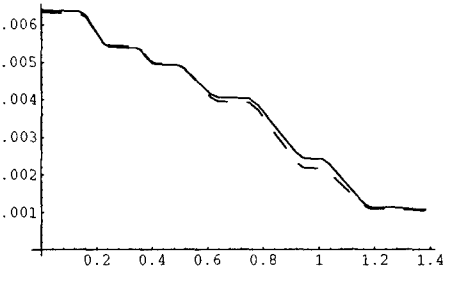

*e) Difference for time = 4.407.*




*f) Full/reduced DOF for time = 4.407.*



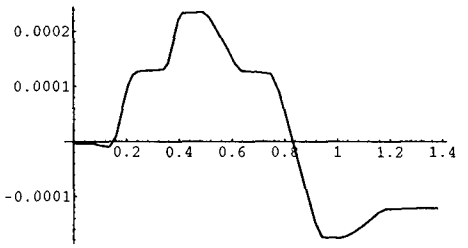

*g) Difference for time = 7.233.*



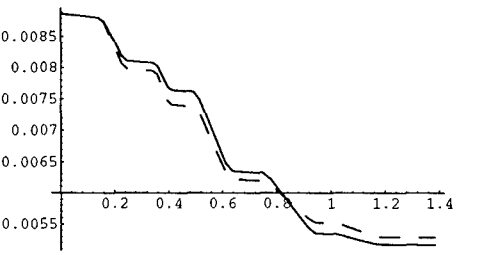

*h) Full/reduced DOF for time = 7.233.*

*Figure 11. 12 LAYER NON-PERIODIC. Plots a, c, e, and g: Full (62) DOF model solution minus reconstructed solution of reduced (5) DOF model. Plots b, d, f, and h: reconstructed solution (dashed) and full DOF model solution (solid). Time is in microseconds.*

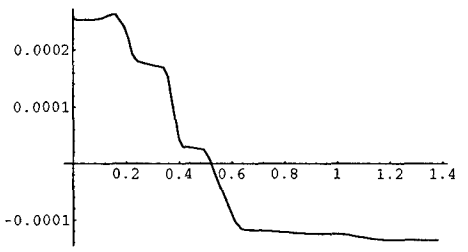
previous cases, the fluctuations in time of the norm of the difference included times for which its value decreased.



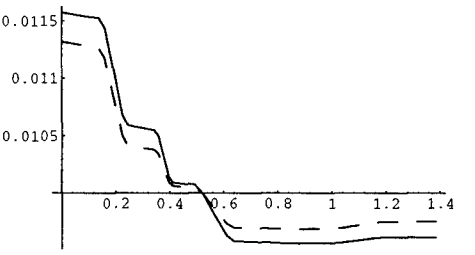

*a) Difference for time = 9.388.*




*b) Full/reduced DOF for time = 9.388.*




*c) Difference for time = 11.364.*




*d) Full/reduced DOF for time = 11.364.*

*Figure 12. 12 LAYER NON-PERIODIC. Plots a and c: Full (62) DOF model solution minus reconstructed solution of reduced (5) DOF model. Plots b and d: reconstructed solution (dashed) and full DOF model solution (solid). Time is in microseconds.*

The 12 layer laminate results show that 5 DOF, reasonably positioned, can maintain a high degree of fidelity to the predictive capability of a 62 DOF model. Hence, for this case, only 8.1% of the original DOF is required for reasonable accuracy. If this could be extrapolated to two dimensions, so that a 5 by 5 grid of nodes could accurately replace a 62 by 62 grid of nodes, then only 0.65% of the original DOF would be required. The savings in three dimensions, assuming the validity of extrapolation, would be even greater, requiring only 0.05% of the original DOF. Such extrapolations are probably highly optimistic, but they do at least provide the incentive for exploring what DOF reductions are actually possible in the dynamic-response modeling of composites in two and three dimensions.

## Concluding Remarks

As the next step, this methodology is currently being coupled to two dimensional finite element discretization/modeling capability so as to enable the exploration of the method's accuracy, as a function of master node choice, in predicting two dimensional responses of composites. As stated in [7], there are at least three implementation strategies available for the method: perform the reduction either 1) once globally (entire model) with a large degree-of-freedom reduction, or 2) recursively and globally with a small degree-of-freedom reduction per recursion, or 3) locally (as in substructuring) wherever it is needed most in the model. The efforts of this paper, and the capability-upgrade to two dimensions mentioned above, fall under the first strategy. For large enough problems, in terms of number of DOF, the latter two strategies will probably be more practical. In fact, an implementation in terms of substructuring offers the additional potential benefit of parallel computing; that is, the DOF reduction of each substructure could be performed in parallel. This provides incentive to place the exploration of the method's accuracy as a substructure-reduction method in one and two dimensions at higher priority than moving directly on to global reduction in three dimensions, (as the step following global reduction in two dimensions).

## References


1. A. Maewal, "Homogenization for Transient Heat Conduction", *J. Appl. Mech.*, 46: 945-946, 1979.

2. E. Sanchez-Palencia and A Zaoui (Ed.), Homogenization Techniques for Composite Media, Lecture Notes in Physics No. 272, Springer-Verlag, Berlin, 1987.

3. J. E. Gubernatis, "Scattering Theory and Effective Medium Approximations to Heterogeneous Materials", AIP Conf. Proc., No. 40 (1978), pp. 84-98.

4. J. R. Willis, "Variational and related methods for the overall properties of composites", Advances in Applied Mechanics, Vol. 21, Academic Press, New York (1981), pp. 1-78.

5. Z. Hashin, "The Differential Scheme and its Application to Cracked Materials", *J. Mech. Phys. Solids*, 36: 719-734, 1988.

6. Jacob Aboudi, Mechanics of Composite Materials: A Unified Micromechanical Approach, Studies in Applied Mechanics 29. Elsevier, Amsterdam (1991).

7. L. D. Flippen, "A Theory of Condensation Model Reduction", accepted by *Comput. Math. Appl.*

8. L. D. Flippen, "Abstract Zwanzig Model Reduction Theory with Application to Discretized Linear Systems", *Mathl. Comput. Modelling*, 16(10): 121-134, 1992.

9. P. W. Randles, "Synthesis of Equivalent Dynamic Laminate Behavior by Homogenization Techniques", *Wave Motion*, 16: 229--247, 1992.

10. S. V. Patankar, Numerical Heat Transfer and Fluid Flow, Hemisphere, Washington (1980), pp. 25-52.

# Modeling Anisotropic Response of Titanium Polycrystalline Aggregates

*V.C. Prantil, J.T. Jenkins and P.R. Dawson*
Cornell University

"PAPER NOT AVAILABLE"

# VORONOI CELL FINITE ELEMENT MODEL FOR RANDOM MICROPOLAR ELASTIC-PLASTIC HETEROGENEOUS MEDIA

Dr. Somnath Ghosh *, Assistant Professor of Engineering Mechanics
Mr. Suresh Moorthy and Mr. Yunshan Liu, Graduate Students
The Ohio State University, Columbus, OH 43210

**ABSTRACT** A Voronoi finite element model has been developed for analysis of heterogeneous media, in which second phase inclusions are arbitrarily dispersed within a matrix. Finite element formulations have been developed for thermo-elasticity, micropolar elasticity and elasto-plasticity.

## INTRODUCTION

A number of analytical micromechanical models have evolved for heterogeneous materials such as composites assuming small deformation linear elasticity theory. These models predict effective constitutive response at the macroscopic level from characteristics of microstructural behavior. Notable among them are models based on : variational approach using extremum principles [1], probabilistic approach [2], self-consistent schemes [3], and generalized self consistent model [4]. Extensions of linear elastic models to the elastic-plastic domain for small strains have been accomplished by the use of Mori-Tanaka mean-stress theory in [5]. Though these analytical models are reasonably effective in predicting equivalent material properties for relatively simple geometries, arbitrary distribution of shapes, sizes and location of the second phase are difficult to deal with these models. Constitutive response of the constituent phases are also somewhat restricted and predictions with large property mismatches are not reliable. Also, these models are not capable of depicting evolution of stresses and strains in the microstructure, thereby limiting their use to the study of macroscopic behavior only. Consequently, *Unit Cell* models e.g. [6], that generate material response through detailed discretization of a representative volume element of the composite microstructure, have been increasingly implemented. Macroscopic periodicity conditions are generally assumed on the Unit Cells. Most of these models also make assumptions on local periodicity, thereby making the unit cells very simple. Despite their overall success, the unit cell methods suffer from a few drawbacks. While periodic spatial distribution is often useful to predict optimum properties, the fact remains that real

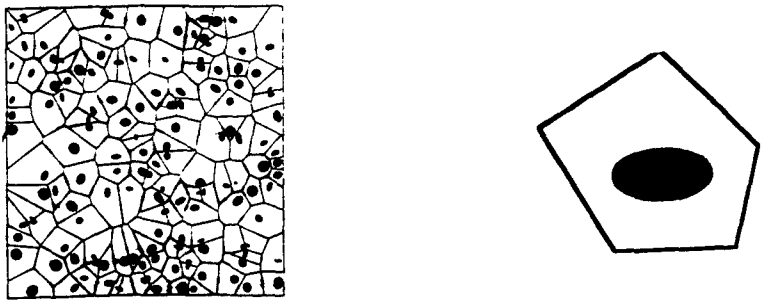


Figure 1: (a) A representative material element (RME) and (b) A basic structural element (BSE)

microstructures are seldom periodic. Additionally, these models utilize conventional mesh generators for finite element analysis. For arbitrary or random microstructures, morphological incompatibility of the generated mesh with the physical domain may arise with these generators and also tremendous efforts are required to adequately represent the microstructure.

The present method is aimed at establishing a direct correlation between techniques of quantitative metallography for arbitrary composite microstructures and their stress/deformation analysis. Results can be used to establish a scientific basis for determining the relationship between overall material response and spatial distribution of location, size, shape, local volume fraction and mechanical properties of constituent phases. The finite element model developed, evolves naturally from a heterogeneous microstructure by *Dirichlet Tessellation* of the domain. Tessellation methods have been used by Richmond and coworkers in [7] in conjunction with quantitative characterization of micrographs obtained by automatic image analysis systems. In this paper, a tessellated two-dimensional microstructural domain is directly cast into finite element analysis without any further discretization. Tessellation of a representative material element (RME) discretizes a heterogeneous domain into basic structural elements (BSE) as shown in figure 1. BSE's are multi-sided convex "Voronoi"polygons containing one second phase inclusion at most. Ghosh and Mukhopadhyay [8] have innovated a finite element formulation for BSE's, where Voronoi polygons act as composite elements in a FEM formulation. In this paper, the above work has been extended to incorporate (a) non-polar and micropolar thermoelasticity problems and (b) elasto-plasticity problems.

## DIRICHLET TESSELLATION AND VORONOI ELEMENTS

Dirichlet tessellation is defined as the subdivision of a plane, determined by a set of points. Each point has associated with it, a region of the plane that is closest to it than to any other. Mathematically speaking, let $\mathbf{P}_1(\mathbf{x}_1), \mathbf{P}_2(\mathbf{x}_2), \ldots$

$\mathbf{P}_n(\mathbf{x}_n)$ be a set of $n$ distinct random points in plane. Then the interior of the Voronoi polygon associated with the i-th labeled point $\mathbf{P}_i$ is the region $\mathbf{D}_i$ defined as

$$\mathbf{D}_i = \{\mathbf{x} : \mid \mathbf{x} - \mathbf{x}_i \mid < \mid \mathbf{x} - \mathbf{x}_j \mid, \forall \ j \neq i\} \tag{1}$$

The aggregate of all such regions $\mathbf{D}_i$ constitute the Dirichlet tessellation in plane. Based on these principles, a two dimensional mesh generator to create convex elements within for plane sections of multiphase materials, has been developed by Ghosh and Mukhopadhyay [9]. Starting from information on the boundary of the domain, locations, shapes and sizes of the inclusions, discretization takes place automatically by *Dirichlet tessellation* of a domain to yield a network of convex "Voronoi polygons", containing one inclusion each, at most.

## VORONOI CELL FINITE ELEMENT FORMULATION

Different Voronoi cells in a tessellated domain can have different number of sides. Application of the displacement finite element method is difficult because it is impossible to ensure interelement displacement compatibility. Additionally, rank deficiencies in the stiffness matrix may result. To avoid these difficulties and represent Voronoi cells as conforming elements, an assumed stress hybrid method introduced by Pian [10], is invoked.

### Elasticity

The complimentary energy functional for a Voronoi element is of the form :

$$\Pi_e^E = -\int_{\Omega_e} \frac{1}{2}\{\boldsymbol{\sigma}\}^T[\mathbf{S}]\{\boldsymbol{\sigma}\}\mathbf{d}\Omega + \int_{\partial\Omega_\mathbf{e}} \boldsymbol{\sigma}.\mathbf{n}.\mathbf{u}\mathbf{d}\partial\Omega + \int_{\Gamma_{\mathbf{t_e}}} \bar{\mathbf{t}}.\mathbf{u}\mathbf{d}\Gamma \tag{2}$$

where $\{\boldsymbol{\sigma}\}$ is the equilibriated stress field in the element domain $\Omega_e$, $\mathbf{u}$ is the compatible displacement field on the element boundary $\partial\Omega_e$ with an outward normal $\mathbf{n}$, $\bar{\mathbf{t}}$ is prescribed traction field on $\Gamma_{t_e}$, the element boundary that coincides with global traction boundary and $S_{ijkl}$ are components of the elastic compliance tensor for linear elasticity. In the application of variational principles, the equilibrating stress field is expressed as a polynomial in the interior of the element as :

$$\{\boldsymbol{\sigma}\} = [\mathbf{P}]\{\boldsymbol{\beta}\} \ \mathbf{in} \ \boldsymbol{\Omega_e} \tag{3}$$

where $\{\boldsymbol{\beta}\}$ is a column of $m$ undetermined stress coefficients $\beta_1, \beta_2 \cdots \beta_m$ and $[\mathbf{P}]$ is a $m$ x $m$ matrix containing functions of coordinates $x$,$y$ corresponding to the chosen polynomial. The prescribed boundary displacements $\{\mathbf{u}\}$ can be interpolated from generalized displacement $\{\mathbf{q}\}$ at the nodes, in the form

$$\{\mathbf{u}\} = [\mathbf{L}]\{\mathbf{q}\} \ \mathbf{in} \ \partial\boldsymbol{\Omega_e} \tag{4}$$

where elements of the matrix [**L**] are functions of boundary coordinates. Stationarity of $\Pi_e^E$ with respect to stress coefficients yields,

$$[\mathbf{H}]\{\boldsymbol{\beta}\} = [\mathbf{G}]\{\mathbf{q}\} \tag{5}$$

where [**H**] and[**G**] are detailed in [8]. Substitution of $\{\boldsymbol{\beta}\}$ in the expression for complementary strain energy $\Pi^E = (\sum_e \Pi_e^E)$ for the entire domain and setting the first variation $\delta\Pi^E = 0$ gives

$$[\mathbf{K}]\{\mathbf{q}\} = [\mathbf{G}]^{\mathbf{T}}[\mathbf{H}]^{-1}[\mathbf{G}]\{\mathbf{q}\} = \int_{\Gamma_{t_e}} \{\bar{\mathbf{t}}\}^{\mathbf{T}}\{\mathbf{u}\}\mathbf{d}\Gamma = \{\bar{\mathbf{f}}\} \tag{6}$$

The stiffness matrix [**K**] will be rank deficient if it's rank is less than *n-l* where $n$ is the number of degrees of freedom and $l$ is the number of rigid body modes. The necessary condition for [**K**] to have sufficient rank is $m \geq n\text{-}l$, where $m$ is the number of independent $\beta$-stress coefficients. The effectiveness of this formulation has been elucidated by numerical examples in [8].

**Thermo-Elasticity**

When thermo-elasticity is included in the problem, the complimentary energy density in equation (2) should be modified for $\Pi_e^{TE}$ as :

$$B(\boldsymbol{\sigma},\boldsymbol{\theta}) = \frac{1}{2}\{\boldsymbol{\sigma}\}^T[\mathbf{S}]\{\boldsymbol{\sigma}\} + \alpha\theta\sigma^H \tag{7}$$

where $\theta$ denotes the temperature field, $\alpha$ is the coefficient of thermal expansion and $\sigma^H$ denotes the trace of the stress tensor. Stationarity of $\Pi_e^{TE}$ with respect to $\{\boldsymbol{\beta}\}$ yields :

$$[\mathbf{H}]\{\boldsymbol{\beta}\} = [\mathbf{G}]\{\mathbf{q}\} - \int_{\Omega_e} [\mathbf{P}]^{\mathbf{T}}\alpha\theta\{\mathbf{I}\}^{\mathbf{T}}\mathbf{d}\Omega = [\mathbf{G}]\{\mathbf{q}\} - \{\boldsymbol{\Theta}\} \tag{8}$$

Substituing $\{\boldsymbol{\beta}\}$ in $\Pi^{TE} = (\sum_e \Pi_e^{TE})$ and setting the first variation to zero yields

$$[\mathbf{G}]^{\mathbf{T}}[\mathbf{H}]^{-1}[\mathbf{G}]\{\mathbf{q}\} = \{\bar{\mathbf{f}}\} + [\mathbf{G}]^{\mathbf{T}}[\mathbf{H}]^{-1}\{\boldsymbol{\Theta}\} \tag{9}$$

It is seen that once the temperature field is known, equation ( 9) can be solved for nodal displacements and element stresses.

*A homogeneous thermo-elasticity example*

A thick cylinder is analyzed under the conditions of plane strain thermo-elasticity. It is subjected to an internal temperature of $\theta_{internal}$= 30° C and an external temperature of $\theta_{external}$= 50° C and an internal presure of 500 psi. The internal and external radii of the pressure vessel are assumed to be 100 in and 200 in respectively. Material properties are Young's Modulus (E) = 3.x $10^7$ psi, Poisson Ratio ($\nu$)=0.3 and coefficient of thermal expansion ($\alpha$)=0.124

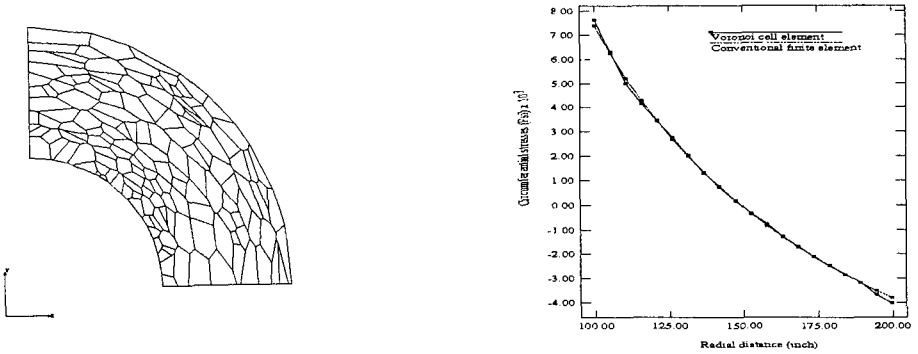



Figure 2: (a) Voronoi mesh for the pressure vessel problem (b)Variation of radial stress

x $10^{-4}$ 0 $c^{-1}$. Figure 2(a) shows a Voronoi mesh for the problem. Figure 2(b) shows a comparison of the variation of radial stress with the radial distance between the Voronoi cell finite element method and a conventional FEM analysis.

**Micropolar Elasticity**

Heterogeneous microstructures often develop differential polarity due to the presence of second phase. This leads to micro-couples, and micropolar representation is beneficial especially in regions of severe strain gradients. In addition to the equations of linear momentum balance, Cosserat micropolar theory introduces the balance of angular momentum, which, in the absence of body couples and inertia effects is stated as :

$$div(\boldsymbol{\mu}) + \mathbf{e} : \boldsymbol{\sigma} = 0 \tag{10}$$

where $\boldsymbol{\mu}$ corresponds to couple stresses and $\mathbf{e}$ is the permutation symbol. The infinitesimal strain tensor is assumed to consist of two independent components, viz.,

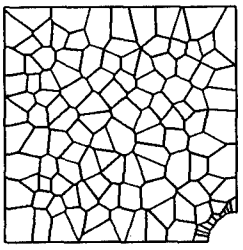
$$\boldsymbol{\epsilon} = grad(\mathbf{u}) + \mathbf{e} : \boldsymbol{\omega} \tag{11}$$

In equation (11), $\boldsymbol{\omega}$ represents micro-rotations at each material point. For isotropic linear elasticty, the constitutive equations are given as :

$$\boldsymbol{\sigma} = (2\mu \mathbf{1}_4^{sym} + 2\mu_c \mathbf{1}_4^{skw} + \lambda \mathbf{I} \otimes \mathbf{I}) : \boldsymbol{\epsilon} \tag{12}$$

$$\boldsymbol{\mu} = (l_c^2 \mu \mathbf{I}) : \boldsymbol{\kappa} \tag{13}$$

where $\mathbf{I}$, $\mathbf{1}_4^{sym}$ and $\mathbf{1}_4^{skw}$ denote identity tensors of second and fourth order respectively, $\lambda$ and $\mu$ are *Lame* constants, $\mu_c$ is the Cosserat shear modulus, $l_c$ represents a characteristic length scale of the Cosserat continuum and $\boldsymbol{\kappa}$ is the local curvature. Implementation of micropolar elasticity in the Voronoi cell finite element formulation takes place in the same fashion as for non-polar elasticity with the exception that the **[P]** matrix needs to be modified appropriately to account for couple stresses.



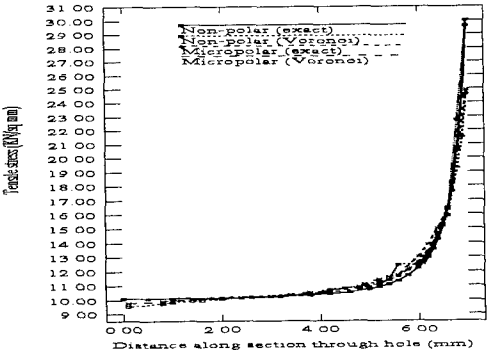



Figure 3: (a) Voronoi mesh for the plate with a hole (b)Stress distribution along the axis of symmetry

*Example of a plate with a hole*

A $8in$ x $8in$ square domain with a 1 $in$ radius circular hole is subjected to a uniform tension field of 10 $psi$. The material parameters are assumed to be Young's Modulus (E) = 200 $psi$, Poisson Ratio ($\nu$)=0.3, Cosserat Shear modulus ($\mu_c$)= 100 $psi$ and characteristic length $l_c$=1 $in$. Exact solutions for the stress distribution are available for both non-polar as well as micropolar elasticity. Results of the Voronoi cell finite element analysis are compared with the exact solutions in figure 3(b).

**Elasto-Plasticity**

Only small deformation elasto-plasticity, governed by $J_2$ flow theory with isotropic hardening, has been considered in this paper. It is evident that the elastic compliance matrix [S] in equation ( 2) should be changed to the elastic-plastic tangent compliance matrix [$S^{EP}$] to incorporate the effects of of state and internal variables. A rate form of the constitutive relations for isotropic hardening can be expressed as:

$$\dot{\boldsymbol{\epsilon}} - \dot{\boldsymbol{\epsilon}}^p = \dot{\boldsymbol{\epsilon}} - \frac{9}{4}\frac{\boldsymbol{\sigma}' \otimes \boldsymbol{\sigma}'}{H\bar{\sigma}^2} : \dot{\boldsymbol{\sigma}} = \mathbf{S} : \dot{\boldsymbol{\sigma}} \tag{14}$$

where $\dot{\boldsymbol{\epsilon}}^p$ is the plastic strain rate, $\mathbf{S}$ is the fourth order elastic compliance tensor, $\boldsymbol{\sigma}'$ is the deviatoric Cauchy stress tensor, $H$ is the plastic hardening modulus and $\bar{\sigma}$ is the current effective stress. In an incremental finite element method, the increments of the strain tensor $\Delta\boldsymbol{\epsilon}$ for a given stress increment $\Delta\boldsymbol{\sigma}$ can be obtained by integrating equation (14) within a step. Variational and hybrid methods for application to nonlinear problems have been extensively studied by Atluri and Murakawa [11]. The complimentary energy functional for an element in equation (3) is modified for the elastic-plastic case to yield :

$$\Pi_e^{EP}(\boldsymbol{\sigma}, \mathbf{u}) = -\int_{\Omega_e} \frac{1}{2}\boldsymbol{\epsilon}(\boldsymbol{\sigma}) : \boldsymbol{\sigma} d\Omega + \int_{\partial\Omega_e} \boldsymbol{\sigma} \cdot \mathbf{n} \cdot \mathbf{u} d\partial\Omega - \int_{\partial\Omega_\Gamma} \bar{\mathbf{t}} \cdot \mathbf{u} d\Gamma_t \tag{15}$$

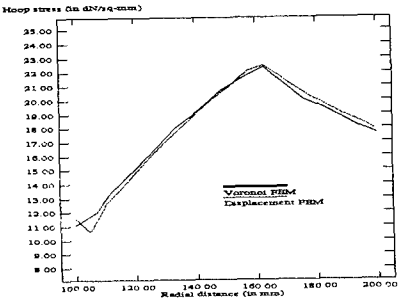



Figure 4: Hoop stress vs radial location for the pressure vessel elasto-plasticity problem

where $\epsilon(\boldsymbol{\sigma}) = \frac{1}{2}(\nabla \mathbf{u} + \nabla^T \mathbf{u})$ *in* $\Omega_e$ is not satisfied apriori. In an incremental formulation, stationarity is sought for the incremented complimentary energy functional $\Pi^{ep}(\boldsymbol{\sigma} + \Delta\boldsymbol{\sigma}, \mathbf{u} + \boldsymbol{\Delta}\mathbf{u})(= \sum_e \Pi_e^{EP}(\boldsymbol{\sigma} + \Delta\boldsymbol{\sigma}, \mathbf{u} + \boldsymbol{\Delta}\mathbf{u})$ under the assumptions of equilibriated stress field $\boldsymbol{\sigma} + \Delta\boldsymbol{\sigma}$ in $\Omega_e$ and compatible displacement fields $\mathbf{u} + \boldsymbol{\Delta}\mathbf{u}$ on $\partial\Omega_e$. The *increments* of stresses and boundary displacements are now expressed in the polynomial forms as for elasticity. The stationarity condition with respect to $\Delta\boldsymbol{\sigma}$ at the end of an increment, yields

$$\begin{aligned} \int_{\Omega_e} [\mathbf{P}]^T [\mathbf{S^T}] \{\delta\Delta\boldsymbol{\sigma}\} d\Omega &= \int_{\partial\Omega_e} [\mathbf{P}]^T \{\mathbf{n}\}\{\mathbf{L}\} d\partial\Omega \{\mathbf{q} + \boldsymbol{\Delta}\mathbf{q}\} - \int_{\Omega_e} [\mathbf{P}]^T \{\epsilon(\boldsymbol{\sigma})\} d\Omega \\ &- \int_{\Omega_e} [\mathbf{P}]^T \{\Delta\epsilon(\Delta\boldsymbol{\sigma})\} d\Omega = \{\mathbf{f}_1\} \; in \; \Omega_e \end{aligned} \tag{16}$$

where $\{\delta\Delta\boldsymbol{\sigma}\}$ can be interpreted correction to the stress increment tensor in an iterative process. The first variation of the global complimentary energy functional $\Pi^{ep}(\boldsymbol{\sigma} + \Delta\boldsymbol{\sigma}, \mathbf{u} + \boldsymbol{\Delta}\mathbf{u})$ with respect to $\Delta\mathbf{q}$, when set to zero yields an equation, which should then be solved for nodal displacements.

*A homogeneous elastic-plastic problem*

The same thick cylinder as for thermo-elasticty problem (figure 2) is now solved for elasto-plasticity. The cylinder is subjected to an internal presure that is increased from zero to 18 dN/mm$^2$. The internal and external radii of the pressure vessel are assumed to be 100 mm and 200 mm respectively. Material properties are Young's Modulus (E) = 21000 dN/mm$^2$, Poisson Ratio ($\nu$)=0.3, Yield stress ($\sigma_Y$)=24 dN/mm$^2$ and Plastic Modulus (H)=0. Results are compared with Owen and Hinton [12]. Figure 4 plots the hoop stress as a function of the radial distance at the final increment.

## COMPOSITE VORONOI ELEMENTS WITH SECOND PHASE

A composite Voronoi element formulation for incorporating the effect of the

second phase materials in the matrix is now developed. Two alternative approaches are discussed. The first is based on the introduction of a transformation strain in the regions of material discontinuity. The second approach is a direct implementation of the heterogeneity through introduction of traction continuity constraint at the interface.

**Transformation Strain Method**

Subject to a prescribed stress field $\boldsymbol{\sigma}$ in a heterogeneous domain, the inclusion occupying an domain $\Omega_c \subset \Omega_e$ (figure 1), exhibits an additional non-stress causing *eigenstrain* $\boldsymbol{\epsilon}^*$, given by,

$$[\mathbf{S(x)}] : \{\boldsymbol{\sigma}\} = [\mathbf{S^0}] : \{\boldsymbol{\sigma}\} + \{\boldsymbol{\epsilon}^*\} \tag{17}$$

where $[\mathbf{S(x)}]$ is the location dependent elastic compliance of the inhomogeneous composite material and $[\mathbf{S^0}]$ is the elastic compliance of the homogeneous matrix material. For the composite element, the element complimentary energy functional in equation (2) is modified as

$$\begin{aligned} \Pi_e^{C1} &= -\int_{\Omega_e} B(\boldsymbol{\sigma}) d\Omega + \int_{\partial\Omega_e} \boldsymbol{\sigma}.\mathbf{n}.\mathbf{u} d\partial\Omega + \int_{\Gamma_{te}} \bar{\mathbf{t}}.\mathbf{u} d\Gamma \\ &- \int_{\Omega_c} \boldsymbol{\sigma} \cdot \boldsymbol{\epsilon}^* d\Omega + \int_{\Omega_c} \frac{1}{2} \boldsymbol{\epsilon}^* \cdot \Delta\mathbf{S}^{-1} \cdot \boldsymbol{\epsilon}^* \end{aligned} \tag{18}$$

$\boldsymbol{\epsilon}^*$ is defined only in the composite domain $\Omega_c$. In addition to the approximating functions for the stress and displacement variables defined earlier, the *eigen strain* is interpolated as,

$$\{\boldsymbol{\epsilon}^*\} = [\mathbf{R}]\{\boldsymbol{\lambda}\} \tag{19}$$

Setting the first variation of $\Pi_e^{c1}$ to zero at the element level followed by the variation of the global equation yields a global matrix equation, which is solved for displacements and eigen-strains.

**Direct implementation of interface constraint**

Along a bonded composite interface $\partial\Omega_c$, the stress and strain fields are discontinuous, while the displacement and traction fields are continuous. A discontinuous stress field is introduced into the modified complimentary energy. Traction continuity along the composite boundary is ensured by introducting this constraint into the modified complimentary energy $\Pi_e$ through the use of Lagrange multipliers. Consider a discontinuous stress field $\boldsymbol{\sigma}$ and a displacement field $\mathbf{u}'$ on $\partial\Omega_c$ satisfying *apriori*, equilibrium conditions of $\boldsymbol{\sigma}$ in $\Omega_c$ and $\Omega_e - \Omega_c$ but not necessarily in $\partial\Omega_c$. The complimentary energy functional in equation ( 2) is modified to accommodate the constraint as,

$$\Pi_e^{C2} = \Pi_e - \int_{\partial\Omega_c} (\boldsymbol{\sigma}^m - \boldsymbol{\sigma}^c) \cdot \mathbf{n} \cdot \mathbf{u}' \mathbf{d}\Omega \tag{20}$$

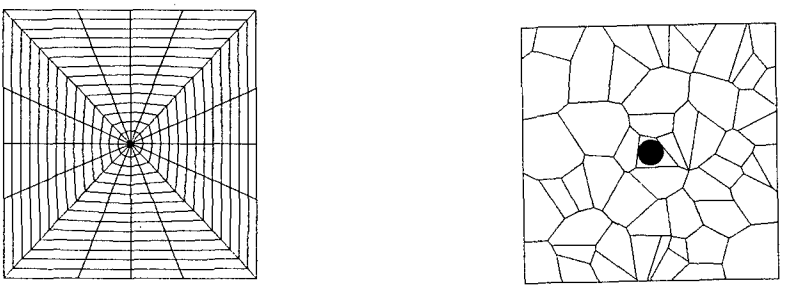


Figure 5: (a) ANSYS mesh and (b) Voronoi mesh for square domain with inclusion

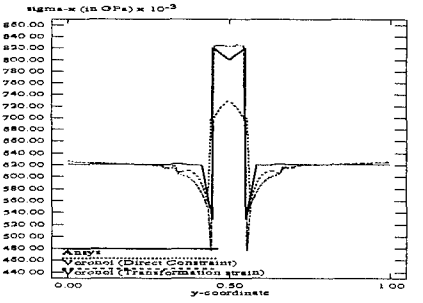



Figure 6: Stress variation along a section through the inclusion

$\boldsymbol{\sigma}^m$ and $\boldsymbol{\sigma}^c$ designate stresses in the matrix and second phase respectively and $\mathbf{n}$ is the unit normal on $\partial\Omega_c$ out of the composite domain. Variation of $\Pi_e^{C2}$ yields the *aposteriori* traction continuity condition,

$$(\boldsymbol{\sigma}^m - \boldsymbol{\sigma}^c) \cdot \mathbf{n} = \mathbf{0} \; on \; \partial\Omega_c$$

The discontinuous stress field in an element is expressed as,

$$\{\boldsymbol{\sigma}\} = [\mathbf{P}]\{\boldsymbol{\beta} + L(\mathbf{x})\boldsymbol{\beta}'\} \; \mathbf{on} \; \boldsymbol{\Omega}_\mathbf{e} \tag{21}$$

where $L(\mathbf{x}) = 0 \; for \; \mathbf{x} \subset \Omega_e - \Omega_c$ and $L(\mathbf{x}) = 1 \; for \; \mathbf{x} \subset \Omega_c$. The displacement field $\mathbf{u}'$ written as,

$$\{\mathbf{u}'\} = [\mathbf{L}]\{\mathbf{q}'\} \; in \; \partial\Omega_c \tag{22}$$

*Composite Voronoi Cell analysis for Elasticity*

A 1m x 1m square domain with a circular inclusion is subjected to uniform stretching of 0.05 m. The matrix material has properties ($E_m$=69 GPa, $\nu_m$=0.33) and the inclusion has properties ($E_c$=133 GPa, $\nu_c$=0.285). Calculations are performed for plane stress conditions. Results with the eigen-strain

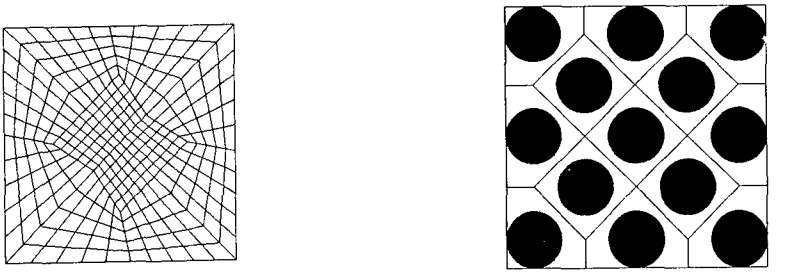


Figure 7: (a) Conventional Unit cell mesh and (b) Voronoi mesh for a square diagonal packing RME

and direct constraint approaches in the composite Voronoi cell analysis are compared with displacement based FEM results, generated by ANSYS Software package. Figure 5 shows the ANSYS mesh and a tessellated Voronoi cell mesh. Figure 6 shows the variation of longitudinal stress along a section through the middle of the inclusion. The comparison convincingly demonstrates the improved accuracy of the direct constraint method with respect to the eigen strain method, especially within the second phase.

*Numerical experiments with different distributions*

In this example, effective properties and stress/strain distributions are computed for a representative material element (RME) with different distributions of the second phase. The volume fraction of the second phase is approximately 46%. The microstructures considered are : (i) a square edge packing composite (ii) a square diagonal packing composite and (iii) random packing composite. Two approaches are considered for verifying results. The first is the conventional Unit cell approach where a part of the RME is modeled with periodicity boundary conditions. Figure 7(a) show this mesh for square diagonal packing composites. The second approach is the composite Voronoi cell analysis where a RME is subjected to similar boundary conditions. Voronoi meshes for square diagonal packing and random packing composites are shown in figures 7(b) and 8 respectively. Various numerical experiments involving uniaxial tension, simple shear and thermal expansion have been conducted with these models.The material parameters for the matrix are ($E_m$=69 GPa, $\nu_m$=0.33, $\sigma_Y$ =43 MPa) and for the inclusion are ($E_c$=410 GPa, $\nu_c$=0.2). The post-yield stress-strain law for the matrix material is $\bar{\sigma} = 0.043 + 0.14\bar{\epsilon}^{0.3333}$ $GPa$. For elasticity and thermo-elasticity problems, the effective values of material properties are tabulated in table I. For small deformation elasto-plasticty, tension tests have been conducted to determine the effective uniaxial stress-strain curves for the heterogeneous materials shown in figures 7 and 8. Tests have been conducted to upto .5 % strain and the results have been compared with unit cell models

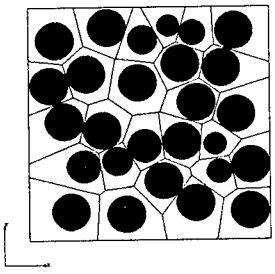


Figure 8: Voronoi mesh for a random packing RME

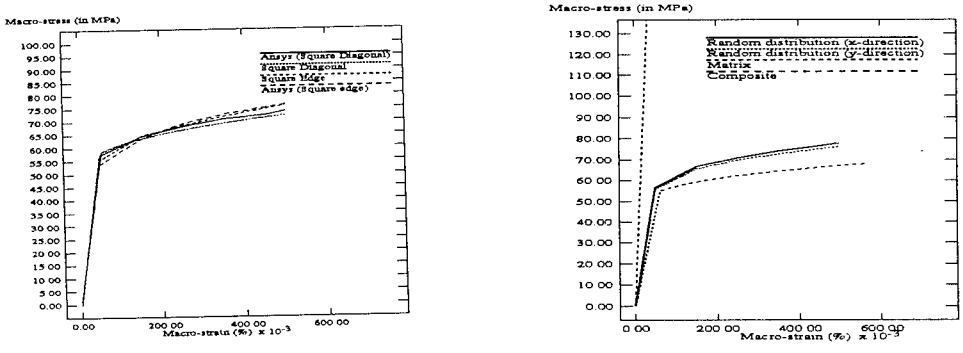



Figure 9: Effective elastic-plastic stress-strain curves for (a) square edge and square diagonal packing composite and (b) random packing composite

on ANSYS. Figure 9 depicts the effective elastic/plastic stress-strain curves for the square edge and square diagonal packing composite. It is generally seen that predictions with the Voronoi cell analysis match well with ANSYS unit cell predictions. For a random packing composite only Voronoi cell analysis has been conducted. The effective stress-strain plots in the x- and y- directions are depicted in figure 9(b). It is observed that there is some difference in the curves for the x- and y- directions.

Table I: **Thermo-Elastic Properties**

| | Square Edge Packing | | Square Diagonal Packing | |
|---|---|---|---|---|
| Properties | Voronoi Cell | Unit Cell | Voronoi Cell | Unit Cell |
| Young's Modulus | 135.58 GPa | 129.1 GPa | 116.97 GPa | 118.35 GPa |
| Poisson Ratio | 0.2929 | 0.2914 | 0.3211 | 0.3105 |
| Shear Modulus | 37.24 GPa | 36.63 GPa | 52.99 GPa | 50.96 GPa |
| Coef. Ther. Expan. | 16.06 | 16.26 | 15.02 | 15.85 |

## CONCLUSION

A Voronoi cell finite element method is developed for two-dimensional heterogeneous materials with arbitrary microstructures for thermo-elasticity, microp-

olar elasticity and small deformation elasto-plasticity. The direct constraint method is observed to perform better than the tranformation strain method in terms of accuracy. Overall the Voronoi cell FEM offers an excellent natural basis for analysis of heterogeneous microstructures.

## ACKNOWLEDGEMENTS

Sponsorship of this work by the US Army Research Office through grant DAAL03-91-G-0168 (Program Director : Dr. K.R. Iyer) is gratefully acknowledged.

## REFERENCES

1. Hashin Z and Strikman S, A variational approach to the theory of the elastic behavior of multiphase materials, *J. Mech Phys. Solids* **11**, 127-140 (1963).
2. Chen HS and Acrivos A, The effective elastic moduli of composite materials containing spherical inclusions at non-dilute concentrations *Int. J. Solids and Structures* **14**, 349-364 (1978).
3. Hill R, A self consistent mechanics of composite materials *J. Mech Phys. Solids*, **13**, 213-222 (1965).
4. Christensen RM and Lo KH, Solutions for effective shear properties in three phase sphere and cylinder models *J. Mech. Phys. Solids*, **27**, 315-330 (1979).
5. Teply JL and Dvorak GJ, Bounds on overall instantaneous properties of elastic-plastic composites *J. Mech. Phys. Solids*, **36**, 29-58 (1988).
6. Tvergaard V, Analysis of tensile properties for a whisker-reinforced metal matrix composite *Acta Metall. et Mater.*, **38**, 185-194 (1990).
7. Spitzig WA, Kelly JF and Richmond O, Quantitative characterization of second phase populations *Metallography*, **18**, 235-261 (1985).
8. Ghosh S and Mukhopadhyay SN, A material based finite element analysis of heterogeneous media involving Dirichlet Tessellations *Computer Meth. in Applied Mechanics and Engineering*, **104**, 211-247 (1993).
9. Ghosh S and Mukhopadhyay SN, A two dimensional automatic mesh generator for finite element analysis of random composites *Computers and Structures*, **41(2)**, 245-256 (1991).
10. Pian THH, Derivation of element stiffness matrices by assumed stress distribution *AIAA Journal*, **2**, 1333-1336 (1964).
11. Atluri S and Murakawa H, On hybrid finite element models in nonlinear solid mechanics, in *Finite Elements in Nonlinear Mechanics* ( eds P.G. Bergan et.al. ), Tapir, vol. 1, pp. 3-41 (1977).
12. Owen DRJ and Hinton E, *Finite elements in plasticity, Theory and Practice*, Pineridge Press Ltd., Swansea, UK, 1980.

# On the Coupling of Pressure and Deviatoric Stress in Hyperelastic Materials

Mike Scheidler
US Army Research Laboratory
Weapons Technology Directorate
Aberdeen Proving Ground, MD 21005-5066

## 1 Introduction

The *Cauchy stress tensor* $\mathbf{T}$ can be decomposed into a spherical part,[1] $-p\mathbf{I}$, and a deviatoric part, $\mathbf{T}^*$:

$$\mathbf{T} = -p\mathbf{I} + \mathbf{T}^*, \qquad t_i = -p + t_i^*. \tag{1.1}$$

The *pressure* $p$ is given by

$$p \equiv -\tfrac{1}{3}\mathrm{tr}\,\mathbf{T} = -\tfrac{1}{3}(t_1 + t_2 + t_3), \tag{1.2}$$

and the *deviatoric stress tensor* $\mathbf{T}^*$ is given by

$$\mathbf{T}^* \equiv \mathbf{T} - \tfrac{1}{3}(\mathrm{tr}\,\mathbf{T})\mathbf{I}, \qquad t_i^* = t_i - \tfrac{1}{3}(t_1 + t_2 + t_3), \tag{1.3}$$

so that $\mathrm{tr}\,\mathbf{T}^* = t_1^* + t_2^* + t_3^* = 0$. The *principal stresses* $t_i$ and *principal deviatoric stresses* $t_i^*$ are the principal values of $\mathbf{T}$ and $\mathbf{T}^*$, respectively. For an isotropic elastic material the linear theory predicts that the pressure depends only on the volumetric strain, whereas $\mathbf{T}^*$, which is a tensorial measure of shear stress, depends only on the shear strain.

The object of this paper is to study those aspects of the nonlinear elastic response of polycrystalline metals and ceramics which are relevant for high velocity impacts, where large elastic increases in density are encountered.

[1] Second-order tensors are denoted by boldface uppercase Roman letters. The *identity tensor* is denoted by $\mathbf{I}$, and tr denotes the *trace* function. The *deviatoric part* and the *transpose* of any tensor $\mathbf{A}$ are denoted by $\mathbf{A}^*$ and $\mathbf{A}^{\mathrm{T}}$, respectively. The *norm* of $\mathbf{A}$ is $\|\mathbf{A}\| \equiv \mathrm{tr}\,(\mathbf{A}^{\mathrm{T}}\mathbf{A})$.

As is well-known, a nonlinear pressure/density relation is generally required for such applications. Here we focus on other nonlinear effects which are often ignored or treated incorrectly. In particular, we study the coupling of the pressure and deviatoric stress which results from the dependence of shear stress on volumetric strain and the dependence of pressure on shear strain.

We begin with a brief review of relevant results from the theory of hyperelastic materials.[2] Let $\mathbf{F}$ denote the *deformation gradient* relative to some fixed reference configiration. An *elastic* (or *Cauchy-elastic*) material is one for which $\mathbf{T}$ is a function of $\mathbf{F}$ only. A *hyperelastic* (or *Green-elastic*) material is an elastic material for which the *first Piola-Kirchhoff stress tensor* $(\det \mathbf{F})\mathbf{T}(\mathbf{F}^{-1})^{\mathrm{T}}$ is the gradient of some real valued function $\varepsilon$ of $\mathbf{F}$, in which case $\varepsilon$ is called the *strain energy* or the *stored energy* per unit reference volume.[3] We consider only hyperelastic materials here. For simplicity we also assume the material is isotropic. This condition, together with the requirement that constitutive equations be properly invariant under changes of frame, yields various reduced forms (see below) for the strain energy and the Cauchy stress tensor.

The *left stretch tensor* $\mathbf{V}$ is the unique symmetric positive-definite tensor occurring in the *left polar decomposition* of the deformation gradient:

$$\mathbf{F} = \mathbf{V}\mathbf{R}\,, \qquad \mathbf{V}^2 = \mathbf{B} \equiv \mathbf{F}\mathbf{F}^{\mathrm{T}}\,, \tag{1.4}$$

where $\mathbf{R}$, the *rotation tensor*, is proper orthogonal, and $\mathbf{B}$, the *left Cauchy-Green tensor*, is symmetric positive-definite. The tensors $\mathbf{V}$ and $\mathbf{B}$ share a common set of principal axes, called the *principal axes of strain in the deformed state* or the *Eulerian strain axes*. The *principal stretches* $\lambda_i$ $(i = 1, 2, 3)$ are the principal values of $\mathbf{V}$, the *principal strains* are $\lambda_i - 1$, and the principal values of $\mathbf{B}$ are $b_i = \lambda_i^2$. Let $J$ denote the *Jacobian* of the deformation, and let $\bar{\rho}$ denote the ratio of the densities $\rho$ and $\rho_0$ in the deformed and reference configurations, respectively:

$$J \equiv \det \mathbf{F} = \det \mathbf{V} = \lambda_1\lambda_2\lambda_3 \quad \text{and} \quad \bar{\rho} \equiv \rho/\rho_0 = 1/J\,. \tag{1.5}$$

Then relative to an undistorted reference configuration of an isotropic hyperelastic material, $\varepsilon$ and $\mathbf{T}$ may be expressed as isotropic functions of

[2] A standard reference is Truesdell and Noll[1].

[3] This restriction on the constitutive equation is motivated by the restrictions imposed on thermoelastic materials by the second law of thermodynamics. A thermoelastic material reduces to a hyperelastic material for isentropic deformations, provided we take $\varepsilon$ to be the internal energy per unit reference volume. The same thermoelastic material reduces to a (generally different) hyperelastic material for isothermal deformations, provided take $\varepsilon$ to be the free energy per unit reference volume.

$\mathbf{V}$ or $\mathbf{B}$; $\varepsilon$ may also be expressed as a symmetric function of $\lambda_1, \lambda_2, \lambda_3$ or $b_1, b_2, b_3$; the Eulerian strain axes are principal axes for $\mathbf{T}$; and[4]

$$\mathbf{T} = \bar{\rho}\,\mathbf{V}\frac{\partial \varepsilon}{\partial \mathbf{V}} = 2\bar{\rho}\,\mathbf{B}\frac{\partial \varepsilon}{\partial \mathbf{B}}, \quad t_i = \bar{\rho}\lambda_i \frac{\partial \varepsilon}{\partial \lambda_i} = 2\bar{\rho}\, b_i \frac{\partial \varepsilon}{\partial b_i}. \tag{1.6}$$

Note that the summation convention is not used here or elsewhere.

# 2 The Logarithmic Strain Tensor

The *principal logarithmic strains* $l_i$ are the logarithms of the principal stretches, and the *(Eulerian) logarithmic strain tensor* $\mathbf{L}$ is the tensor coaxial with $\mathbf{V}$ and $\mathbf{B}$ but with corresponding principal values equal to the principal logarithmic strains:

$$l_i \equiv \ln \lambda_i = \tfrac{1}{2} \ln b_i, \quad \mathbf{L} = \ln \mathbf{V} = \tfrac{1}{2} \ln \mathbf{B}. \tag{2.1}$$

Then the strain energy function $\varepsilon$ of an an isotropic hyperelastic material can be expressed as an isotropic function of $\mathbf{L}$ or, equivalently, as a symmetric function of the principal logarithmic strains. From $(1.6)_3$ and $(2.1)_1$ it follows that

$$t_i = \bar{\rho}\frac{\partial \varepsilon}{\partial l_i}, \quad \mathbf{T} = \bar{\rho}\frac{\partial \varepsilon}{\partial \mathbf{L}}. \tag{2.2}$$

The logarithmic strain tensor has several interesting properties. By (1.5) we have

$$\operatorname{tr} \mathbf{L} = l_1 + l_2 + l_3 = \ln(\lambda_1 \lambda_2 \lambda_3) = \ln J = -\ln \bar{\rho}. \tag{2.3}$$

Hence $\operatorname{tr} \mathbf{L}$ is a measure of the volumetric strain. The deviatoric part $\mathbf{L}^*$ of $\mathbf{L}$ has principal values

$$\begin{aligned} l_i^* &= l_i - \tfrac{1}{3}(l_1 + l_2 + l_3) = l_i - \tfrac{1}{3} \ln J \\ &= \ln\left(\frac{\lambda_i}{J^{1/3}}\right) = \frac{1}{3}\left[\ln\left(\frac{\lambda_i}{\lambda_j}\right) + \ln\left(\frac{\lambda_i}{\lambda_k}\right)\right], \end{aligned} \tag{2.4}$$

[4]If $\varepsilon$ is a scalar-valued function of a symmetric tensor $\mathbf{A}$ then the gradient of $\varepsilon$ at $\mathbf{A}$ is the symmetric tensor $\partial\varepsilon/\partial\mathbf{A}$ with the property $\operatorname{tr}[(\partial\varepsilon/\partial\mathbf{A})\mathbf{S}] = d/dt\ \varepsilon(\mathbf{A} + t\mathbf{S})|_{t=0}$, where $\mathbf{S}$ is any tensor such that $\mathbf{A} + t\mathbf{S}$ lies in the domain of $\varepsilon$ for sufficiently small $t$. Furthermore, $\varepsilon$ is an isotropic function of the symmetric tensor $\mathbf{A}$ iff $\varepsilon$ is a symmetric function of the principal values $a_i$ of $\mathbf{A}$, in which case $\partial\varepsilon/\partial\mathbf{A}$ is coaxial with $\mathbf{A}$ and has corresponding principal values $\partial\varepsilon/\partial a_i$.

where $i, j, k$ always denotes a permutation of $1, 2, 3$. Now consider another deformation which differs from the given one by a superimposed dilatation and rotation, so that this second deformation has left stretch tensor $a\mathbf{V}$ and principal stretches $a\lambda_1, a\lambda_2, a\lambda_3$ for some $a > 0$. Then $\mathbf{L}^*$ is the same for both deformations, since the factor $a$ cancels out in $(2.4)_4$. Hence the *deviatoric logarithmic strain tensor* $\mathbf{L}^*$ is independent of the dilatational part of the deformation gradient, i.e., it is independent of the volumetric stretch or strain as measured by (1.5) or (2.3). Therefore $\mathbf{L}^*$ is a tensorial measure of shear strain only.

From the results above it follows that $\varepsilon$, $\mathbf{T}$, $\mathbf{T}^*$, and $p$ may be regarded as a function of the independent variables $\mathbf{L}^*$ and $J$ (or $\bar{\rho}$), with each function isotropic in $\mathbf{L}^*$ for fixed $J$ (or $\bar{\rho}$). Then it can be shown that $(2.2)_2$ is equivalent to the conditions[5]

$$p = -\left(\frac{\partial \varepsilon}{\partial J}\right)_{\mathbf{L}^*} \quad \text{and} \quad J\,\mathbf{T}^* = \left(\frac{\partial \varepsilon}{\partial \mathbf{L}^*}\right)_J, \tag{2.5}$$

where a subscript denotes the variable held constant during differentiation. Equivalently,

$$p = \bar{\rho}^2 \left(\frac{\partial \varepsilon}{\partial \bar{\rho}}\right)_{\mathbf{L}^*} \quad \text{and} \quad \mathbf{T}^* = \bar{\rho}\left(\frac{\partial \varepsilon}{\partial \mathbf{L}^*}\right)_{\bar{\rho}}. \tag{2.6}$$

In terms of the *pressure response functions* $p = \hat{p}(J, \mathbf{L}^*) = \bar{p}(\bar{\rho}, \mathbf{L}^*)$, equations $(2.5)_1$ and $(2.6)_1$ may be integrated to yield

$$\varepsilon = \int_J^1 \hat{p}(\xi, \mathbf{L}^*)\, d\xi + \hat{\varepsilon}(\mathbf{L}^*) = \int_1^{\bar{\rho}} \bar{p}(\xi, \mathbf{L}^*)\xi^{-2}\, d\xi + \hat{\varepsilon}(\mathbf{L}^*) \tag{2.7}$$

for some isotropic function $\hat{\varepsilon}$ of $\mathbf{L}^*$ only. From (2.7) we see that *the pressure response function of an isotropic hyperelastic material determines the strain energy function to within an arbitrary function of* $\mathbf{L}^*$ *only.* Also note that *for an isotropic elastic material, the existence of a strain energy function places no restrictions on the pressure response function.* That is, given any isotropic function $\hat{p}$ of $J$ and $\mathbf{L}^*$, there exist infinitely many strain energy functions, namely those given by $(2.7)_1$, for which the corresponding

[5]To prove $(2.5)_1$, for example, note that since $l_i^*$ is independent of $J$, (2.4) yields $\partial l_i/\partial J = 1/3J$. Then

$$\frac{\partial \varepsilon}{\partial J} = \sum_{i=1}^{3} \frac{\partial \varepsilon}{\partial l_i}\frac{\partial l_i}{\partial J} = \frac{1}{3J}\sum_{i=1}^{3} \frac{\partial \varepsilon}{\partial l_i}.$$

But from (1.2), (2.2), and $\bar{\rho} = 1/J$, we see that the expression on the right above is equal to $-p$.

pressure response function is $p = \hat{p}(J, \mathbf{L}^*)$; then the response function for the deviatoric stress tensor is determined from $(2.5)_2$.

In practice we are usually faced with a somewhat different situation, i.e., we have a limited amount of experimental data on the response functions for both the pressure and the deviatoric stress, and we need to determine any additional restrictions imposed on these response functions due to the existence of a strain energy function. We will address this problem in the next section for small shear strains. The following result, which requires no restrictions on the magnitude of the shear strain, is an immediate consequence of (2.5) or (2.6). *For an isotropic hyperelastic material the following conditions are equivalent:*

(i) *The strain energy decouples additively into a function of density only and a function of shear strain only, i.e.,* $\varepsilon = \bar{\varepsilon}(\bar{\rho}) + \hat{\varepsilon}(\mathbf{L}^*)$;

(ii) *The pressure depends only on the density, i.e.,* $p = \bar{p}(\bar{\rho})$;

(iii) $J\mathbf{T}^*$ *is independent of the density;*

If these conditions hold then $\bar{p}(\bar{\rho}) = \bar{\rho}^2 d\bar{\varepsilon}/d\bar{\rho}$ and $\mathbf{T}^* = \bar{\rho}\,\partial\hat{\varepsilon}/\partial\mathbf{L}^*$. In particular, either (i) or (ii) implies $\mathbf{T}^*$ is proportional to the density ratio $\bar{\rho}$. As we will see in Section §4, these properties are generally inconsistent with experimental data.

In the remainder of this section we consider some relations involving the invariants of $\mathbf{L}^*$. These results will be utilized in the next section. Let $\gamma^*$ and $\delta^*$ denote the *second* and *third moments* of $\mathbf{L}^*$:

$$\begin{aligned}\gamma^* &\equiv \operatorname{tr}[(\mathbf{L}^*)^2] = \|\mathbf{L}^*\|^2 = (l_1^*)^2 + (l_2^*)^2 + (l_3^*)^2 \\ &= -2(l_1^* l_2^* + l_2^* l_3^* + l_3^* l_1^*) = 2[(l_i^*)^2 + l_i^* l_j^* + (l_j^*)^2] \\ &= \tfrac{1}{3}[(l_1^* - l_2^*)^2 + (l_2^* - l_3^*)^2 + (l_3^* - l_1^*)^2], \qquad (2.8)\end{aligned}$$

and

$$\begin{aligned}\delta^* &\equiv \operatorname{tr}[(\mathbf{L}^*)^3] = (l_1^*)^3 + (l_2^*)^3 + (l_3^*)^3 \\ &= 3\det\mathbf{L}^* = 3l_1^* l_2^* l_3^* = -\sum_{m\neq n}(l_m^*)^2 l_n^*, \qquad (2.9)\end{aligned}$$

where we have used the fact that

$$\operatorname{tr}\mathbf{L}^* = l_1^* + l_2^* + l_3^* = 0. \qquad (2.10)$$

Both $\gamma^*$ and $\delta^*$ are isotropic scalar measures of shear strain which are independent of the dilatational part of the deformation.[6] Note that $\gamma^* \geq 0$ and that $\sqrt{\gamma^*} = \|\mathbf{L}^*\|$ is the norm of $\mathbf{L}^*$, which may be interpreted as the *equivalent shear strain*; it is zero iff the deformation gradient is a dilatation superimposed on a rotation:

$$\gamma^* = 0 \;\Leftrightarrow\; \|\mathbf{L}^*\| = 0 \;\Leftrightarrow\; \mathbf{L}^* = \mathbf{0} \;\Leftrightarrow\; \mathbf{V} = J^{1/3}\mathbf{I} \;\Leftrightarrow\; \mathbf{F} = J^{1/3}\mathbf{R}. \quad (2.11)$$

[6] Alternate expressions for $\gamma^*$ follow from $(2.8)_6$ and $l_i^* - l_j^* = l_i - l_j = \ln(\lambda_i/\lambda_j)$.

Of course, $\gamma^* = 0 \Rightarrow \delta^* = 0$, but the converse does not hold.[7] Let $\mathbf{L}^{**}$ denote the deviatoric part of the square of the deviatoric part of $\mathbf{L}$:

$$\mathbf{L}^{**} \equiv [(\mathbf{L}^*)^2]^* = (\mathbf{L}^*)^2 - \tfrac{1}{3}\gamma^*\mathbf{I}. \tag{2.12}$$

Then the principal values $l_i^{**}$ of $\mathbf{L}^{**}$ are given by

$$l_i^{**} = (l_i^*)^2 - \tfrac{1}{3}\gamma^* = \tfrac{1}{3}[(l_i^*)^2 + 2l_j^* l_k^*] = l_j^* l_k^* + \tfrac{1}{6}\gamma^*. \tag{2.13}$$

From (2.3), $(2.4)_1$, (2.8)–(2.10), and (2.13), we find that[8]

$$\frac{\partial \bar{\rho}}{\partial l_i} = -\bar{\rho}, \quad \frac{\partial \gamma^*}{\partial l_i} = 2l_i^*, \quad \frac{\partial \delta^*}{\partial l_i} = 3l_i^{**}. \tag{2.14}$$

As observed above, any function of $\mathbf{L}$ can be regarded as a function of $\bar{\rho}$ and $\mathbf{L}^*$. Therefore any scalar-valued isotropic function of $\mathbf{L}$ can be expressed as a function of $\bar{\rho}$ and the second and third moments of $\mathbf{L}^*$. In particular, this applies to the strain energy $\varepsilon$ and the pressure $p$:

$$\varepsilon = \varepsilon(\bar{\rho}, \gamma^*, \delta^*) \quad \text{and} \quad p = p(\bar{\rho}, \gamma^*, \delta^*) = \bar{\rho}^2 \left(\frac{\partial \varepsilon}{\partial \bar{\rho}}\right)_{\gamma^*, \delta^*}, \tag{2.15}$$

where $(2.6)_1$ has been used. Then from (1.1), $(2.2)_1$, $(2.15)_3$, and (2.14), we obtain the following formula for the principal deviatoric stresses in an isotropic hyperelastic material:

$$t_i^* = 2\bar{\rho}\left(\frac{\partial \varepsilon}{\partial \gamma^*}\right)_{\bar{\rho}, \delta^*} l_i^* + 3\bar{\rho}\left(\frac{\partial \varepsilon}{\partial \delta^*}\right)_{\bar{\rho}, \gamma^*} l_i^{**}; \tag{2.16}$$

equivalently,

$$\mathbf{T}^* = 2\bar{\rho}\left(\frac{\partial \varepsilon}{\partial \gamma^*}\right)_{\bar{\rho}, \delta^*} \mathbf{L}^* + 3\bar{\rho}\left(\frac{\partial \varepsilon}{\partial \delta^*}\right)_{\bar{\rho}, \gamma^*} \mathbf{L}^{**}. \tag{2.17}$$

Note that the coefficients of $\mathbf{L}^*$ and $\mathbf{L}^{**}$ in (2.17) generally depend on all three of the strain variables $\bar{\rho}$, $\gamma^*$, and $\delta^*$.

[7] If the principal stretches are ordered so that $\lambda_1 \le \lambda_2 \le \lambda_3$, then

$$\delta^* = 0 \Leftrightarrow l_2^* = 0 \Leftrightarrow l_1^* = -l_3^* \Leftrightarrow l_2 = \tfrac{1}{2}(l_1 + l_3) \Leftrightarrow \lambda_2 = \sqrt{\lambda_1 \lambda_3}.$$

In particular, $\delta^* = 0$ for a simple shear (where $\lambda_1 = 1/\lambda_3$ and $\lambda_2 = 1$) and also for a simple shear with superimposed dilatation (where $\lambda_1 = J^{2/3}/\lambda_3$ and $\lambda_2 = J^{1/3}$).

[8] In deriving $(2.14)_{2,3}$ it is useful to first establish the following results: $\partial l_i^*/\partial l_i = \frac{2}{3}$, $\partial l_i^*/\partial l_j = -\frac{1}{3}$, $\partial l_i^{**}/\partial l_i = \frac{2}{3}l_i^*$, and $\partial l_i^{**}/\partial l_j = \frac{2}{3}l_k^*$.

# 3 Approximate Formulas

In this section we consider approximate formulas for the strain energy, pressure and deviatoric stress which are valid for sufficiently small shear strains and arbitrarily large changes in density. From $(2.15)_1$, (2.8), and (2.9), it follows that

$$\begin{aligned} \varepsilon &= \bar{\varepsilon}(\bar{\rho}) + \varepsilon_2(\bar{\rho})\,\gamma^* + \mathcal{O}_{\bar{\rho}}(\|\mathbf{L}^*\|^3) \\ &= \bar{\varepsilon}(\bar{\rho}) + \varepsilon_2(\bar{\rho})\,\gamma^* + \varepsilon_3(\bar{\rho})\,\delta^* + \mathcal{O}_{\bar{\rho}}(\|\mathbf{L}^*\|^4) \end{aligned} \tag{3.1}$$

for some functions $\bar{\varepsilon}$, $\varepsilon_2$, and $\varepsilon_3$ of $\bar{\rho}$ only. Here $\mathcal{O}_{\bar{\rho}}(\|\mathbf{L}^*\|^n)$ denotes a function of $\bar{\rho}$ and $\mathbf{L}^*$ which is of order $n$ in $\mathbf{L}^*$, i.e., there is a function $M(\bar{\rho})$ such that $\mathcal{O}_{\bar{\rho}}(\|\mathbf{L}^*\|^n) \le M(\bar{\rho})\,\|\mathbf{L}^*\|^n$ for $\mathbf{L}^*$ sufficiently close to $\mathbf{0}$. Similarly, from $(2.15)_2$ we have

$$\begin{aligned} p &= \bar{p}(\bar{\rho}) + \mathcal{O}_{\bar{\rho}}(\|\mathbf{L}^*\|^2) \\ &= \bar{p}(\bar{\rho}) + p_2(\bar{\rho})\,\gamma^* + \mathcal{O}_{\bar{\rho}}(\|\mathbf{L}^*\|^3) \\ &= \bar{p}(\bar{\rho}) + p_2(\bar{\rho})\,\gamma^* + p_3(\bar{\rho})\,\delta^* + \mathcal{O}_{\bar{\rho}}(\|\mathbf{L}^*\|^4) \end{aligned} \tag{3.2}$$

for some functions $\bar{p}$, $p_2$, and $p_3$ of $\bar{\rho}$ only. Since $\gamma^*$ and $\delta^*$ are independent of $\bar{\rho}$, $(2.15)_3$ and (3.1) imply

$$\bar{p}(\bar{\rho}) = \bar{\rho}^2 \frac{d\bar{\varepsilon}}{d\bar{\rho}}, \quad p_2(\bar{\rho}) = \bar{\rho}^2 \frac{d\varepsilon_2}{d\bar{\rho}}, \quad p_3(\bar{\rho}) = \bar{\rho}^2 \frac{d\varepsilon_3}{d\bar{\rho}}. \tag{3.3}$$

We call $\bar{p} = \bar{p}(\bar{\rho})$ the *hydrostatic pressure* at the density ratio $\bar{\rho}$. It is the pressure the material would experience if the shear strain were zero, i.e., if the conditions in (2.11) hold, in which case (1.1) and (2.17) require that $\mathbf{T} = -p\mathbf{I} = -\bar{p}\mathbf{I}$. In accordance with experimental data we assume $d\bar{p}/d\bar{\rho} > 0$. Then the *bulk modulus* $\kappa$ is positive:

$$0 < \kappa \equiv \bar{\rho}\,\frac{d\bar{p}}{d\bar{\rho}} = \rho\,\frac{d\bar{p}}{d\rho} = -J\,\frac{d\bar{p}}{dJ}. \tag{3.4}$$

Also, $\bar{\rho}$ may be regarded as a function of the hydrostatic pressure $\bar{p}$. Hence any function of $\bar{\rho}$, such as $\kappa$ and the functions $\mu$ and $\omega$ below, may also be regarded as a function of $\bar{p}$.

From (2.16) and (3.1), the principal deviatoric stresses satisfy

$$\begin{aligned} t_i^* &= 2\mu(\bar{\rho})\,l_i^* + \mathcal{O}_{\bar{\rho}}(\|\mathbf{L}^*\|^2) \\ &= 2\mu(\bar{\rho})\,l_i^* + 3\,\omega(\bar{\rho})\,l_i^{**} + \mathcal{O}_{\bar{\rho}}(\|\mathbf{L}^*\|^3), \end{aligned} \tag{3.5}$$

where $\mu(\bar{\rho})$, the *shear modulus* at density ratio $\bar{\rho}$, is given by

$$\mu(\bar{\rho}) = \bar{\rho}\,\varepsilon_2(\bar{\rho}) = \bar{\rho}\left(\frac{\partial \varepsilon}{\partial \gamma^*}\right)_{\bar{\rho},\delta^*}\Bigg|_{\gamma^*=\delta^*=0}, \tag{3.6}$$

and

$$\omega(\bar{\rho}) = \bar{\rho}\,\varepsilon_3(\bar{\rho}) = \bar{\rho}\left(\frac{\partial \varepsilon}{\partial \delta^*}\right)_{\bar{\rho},\gamma^*}\Bigg|_{\gamma^*=\delta^*=0}. \tag{3.7}$$

The relations (3.5) are equivalent to

$$\begin{aligned} \mathbf{T}^* &= 2\mu(\bar{\rho})\mathbf{L}^* + \mathcal{O}_{\bar{\rho}}(\|\mathbf{L}^*\|^2) \\ &= 2\mu(\bar{\rho})\mathbf{L}^* + 3\,\omega(\bar{\rho})\mathbf{L}^{**} + \mathcal{O}_{\bar{\rho}}(\|\mathbf{L}^*\|^3). \end{aligned} \tag{3.8}$$

The constitutive relations (3.2) for the pressure and (3.5) or (3.8) for the deviatoric stress, clearly demonstrate the dependence of pressure on shear strain and the dependence of deviatoric stress on volumetric strain. Furthermore, these dependencies are coupled. Indeed, from $(3.3)_{2,3}$, $(3.6)_1$ and $(3.7)_1$, it follows that the coefficients $p_2(\bar{\rho})$ and $p_3(\bar{\rho})$ in the expansion (3.2) for the pressure are related to $\mu$ and $\omega$ by

$$p_2(\bar{\rho}) = \bar{\rho}^2 \frac{d}{d\bar{\rho}}\left(\frac{\mu}{\bar{\rho}}\right) = \bar{\rho}\,\frac{d\mu}{d\bar{\rho}} - \mu = \kappa\left(\frac{d\mu}{d\bar{p}} - \frac{\mu}{\kappa}\right), \tag{3.9}$$

$$p_3(\bar{\rho}) = \bar{\rho}^2 \frac{d}{d\bar{\rho}}\left(\frac{\omega}{\bar{\rho}}\right) = \bar{\rho}\,\frac{d\omega}{d\bar{\rho}} - \omega = \kappa\left(\frac{d\omega}{d\bar{p}} - \frac{\mu}{\kappa}\right). \tag{3.10}$$

This coupling of the pressure and deviatoric stress may be made more explicit as follows. First, note that from (2.8) and either (3.8) or (3.5), we have

$$\|\mathbf{T}^*\|^2 = (t_1^*)^2 + (t_2^*)^2 + (t_3^*)^2 = [2\mu(\bar{\rho})]^2\gamma^* + \mathcal{O}_{\bar{\rho}}(\|\mathbf{L}^*\|^3). \tag{3.11}$$

Then on solving (3.11) for $\gamma^*$ and substituting into $(3.2)_2$, we obtain the following relation between the pressure $p$, the hydrostatic pressure $\bar{p} = \bar{p}(\bar{\rho})$, the shear modulus $\mu$, and the *equivalent shear stress* $\|\mathbf{T}^*\|$:

$$\begin{aligned} p &= \bar{p}(\bar{\rho}) + \frac{1}{4\mu^2}\left(\bar{\rho}\,\frac{d\mu}{d\bar{\rho}} - \mu\right)\|\mathbf{T}^*\|^2 + \mathcal{O}_{\bar{\rho}}(\|\mathbf{T}^*\|^3) \\ &= \bar{p} + \frac{1}{4\mu}\left(\frac{\kappa}{\mu}\frac{d\mu}{d\bar{p}} - 1\right)\|\mathbf{T}^*\|^2 + \mathcal{O}_{\bar{p}}(\|\mathbf{T}^*\|^3), \end{aligned} \tag{3.12}$$

where in $(3.12)_1$ the coefficient of $\|\mathbf{T}^*\|^2$ is regarded as a function of $\bar{\rho}$, and in $(3.12)_2$ it is regarded as a function of $\bar{p}$.

The above results may be expressed in terms of the deviatoric parts $\mathbf{E}^*$, $\mathbf{G}^*$, and $\mathbf{H}^*$ of the *(Eulerian) finite strain tensors*

$$\mathbf{E} \equiv \mathbf{V} - \mathbf{I}, \quad \mathbf{G} \equiv \tfrac{1}{2}(\mathbf{B} - \mathbf{I}), \quad \mathbf{H} \equiv \tfrac{1}{2}(\mathbf{I} - \mathbf{B}^{-1}); \tag{3.13}$$

in particular, $\mathbf{H}$ is known as the *Almansi-Hamel* strain tensor. Some care must be taken here since, unlike $\mathbf{L}^*$, the tensors $\mathbf{E}^*$, $\mathbf{G}^*$, and $\mathbf{H}^*$ are not independent of the volumetric strain. Analogous to the definition (2.12) of $\mathbf{L}^{**}$, for any tensor $\mathbf{A}$ let $\mathbf{A}^{**} \equiv [(\mathbf{A}^*)^2]^* = (\mathbf{A}^*)^2 - \frac{1}{3}\mathrm{tr}\,[(\mathbf{A}^*)^2]\mathbf{I}$. Then it can be shown that

$$\mathbf{L}^* \approx \bar{\rho}^{1/3}\mathbf{E}^* - \tfrac{1}{2}\bar{\rho}^{2/3}\mathbf{E}^{**} \approx \bar{\rho}^{2/3}\mathbf{G}^* - \bar{\rho}^{4/3}\mathbf{G}^{**} \approx \bar{\rho}^{-2/3}\mathbf{H}^* + \bar{\rho}^{-4/3}\mathbf{H}^{**} \tag{3.14}$$

$$\mathbf{L}^{**} \approx \bar{\rho}^{2/3}\mathbf{E}^{**} \approx \bar{\rho}^{4/3}\mathbf{G}^{**} \approx \bar{\rho}^{-4/3}\mathbf{H}^{**} \tag{3.15}$$

$$\gamma^* \approx \bar{\rho}^{2/3}\|\mathbf{E}^*\|^2 \approx \bar{\rho}^{4/3}\|\mathbf{G}^*\|^2 \approx \bar{\rho}^{-4/3}\|\mathbf{H}^*\|^2, \tag{3.16}$$

where the error in each of these approximations is of order $\|\mathbf{L}^*\|^3$. Substitution of (3.14)–(3.16) into $(3.1)_1$, $(3.2)_2$, and $(3.8)_2$ yields alternate formulas for $\varepsilon$, $p$, and $\mathbf{T}^*$ to within an error of order $\|\mathbf{L}^*\|^3$. Also note that if the $\mathbf{E}^{**}$, $\mathbf{G}^{**}$, and $\mathbf{H}^{**}$ terms are omitted in (3.14), then the error in (3.14) is of order $\|\mathbf{L}^*\|^2$, and $(3.8)_1$ and $(3.2)_1$ yield

$$\mathbf{T}^* \approx 2\mu(\bar{\rho})\mathbf{L}^* \approx 2\bar{\rho}^{1/3}\mu(\bar{\rho})\mathbf{E}^* \approx 2\bar{\rho}^{2/3}\mu(\bar{\rho})\mathbf{G}^* \approx 2\bar{\rho}^{-2/3}\mu(\bar{\rho})\mathbf{H}^* \tag{3.17}$$

and $p \approx \bar{p}(\bar{\rho})$, all to within an error of order $\|\mathbf{L}^*\|^2$. Thus when terms of second order in the shear strain are neglected, the pressure depends only on the density whereas the deviatoric stress depends on both the shear strain and the density through the density dependence of the shear modulus.[9] As we will see in the next section, for many materials the shear modulus changes substantially over the range of densities encounterd in high velocity impacts.

# 4 Material Properties

Let $U_L$ and $U_S$ denote the *longitudinal* and *shear wave speeds* in an isotropic hyperelastic material in a state of dilatational strain (cf. (2.11)) under

[9]The reader who prefers to work with the strain tensor $\mathbf{G}$, for example, may be tempted to use the term "shear modulus" for the coefficient $\bar{\rho}^{2/3}\mu(\bar{\rho})$ of $2\mathbf{G}^*$ in (3.17). However, as we will see in the next section this would be in conflict with the terminology used in much of the wave propagation literature.

hydrostatic stress $\mathbf{T} = -\bar{p}\mathbf{I}$. These wave speeds are related by the well-known formula (cf. [1, (75.4)]) $U_L^2 = \frac{4}{3}U_S^2 + U_B^2$, where $U_B \equiv \sqrt{d\bar{p}/d\rho}$ is referred to as the *bulk wave speed*. Then from (3.4) we have $\kappa = \rho U_B^2$. Similarly, it is customary to define the *shear modulus* $\mu$ by $\mu \equiv \rho U_S^2$. Then $\frac{4}{3}\mu = \rho U_L^2 - \bar{\rho}\, d\bar{p}/d\bar{\rho}$, and by use of the well-known formula (cf. [1, (74.7)]) $\rho U_L^2 = \partial t_i/\partial l_i$, it can be verified that the shear modulus as defined here agrees with the definition used in the previous section. The shear and bulk moduli as a function of density or hydrostatic pressure are usually obtained from measurements of ultrasonic longitudinal and shear wave speeds, together with the above relations. From $\mu = \rho U_S^2$, (3.9), and (3.4), we see that the coefficient $p_2$ of $\gamma^*$ in the expansion (3.2) for $p$ is also given by

$$p_2 = 2\rho\kappa U_S \frac{dU_S}{d\bar{p}}. \tag{4.1}$$

Then from (3.9) and (4.1) it follows that

$$p_2 > 0 \;\Leftrightarrow\; \bar{\rho}\frac{d\mu}{d\bar{\rho}} > \mu \;\Leftrightarrow\; \frac{d\mu}{d\bar{p}} > \frac{\mu}{\kappa} \;\Leftrightarrow\; \frac{dU_S}{d\bar{p}} > 0\,. \tag{4.2}$$

In particular, $dU_S/d\bar{p} > 0$ implies $d\mu/d\bar{p} > 0$. Also, since $\gamma^* > 0$ for any nonzero shear strain, from (4.2) and $(3.2)_2$ we see that shear strain at constant density results in an increase in pressure, whereas shear strain at zero pressure results in bulking (since $\bar{p}(\bar{\rho}) < 0$ in this case), provided that terms of order three in the shear strain can be neglected and $dU_S/d\bar{p} > 0$. For most isotropic elastic materials the shear wave speed does in fact increase with pressure.[10]

The elastic moduli and their pressure derivatives evaluated at $\bar{p} = 0$ (equivalently, $\bar{\rho} = 1$) will be denoted with a zero subscript. Values for a few materials are listed in Table 1 on the next page.[11] Table 1 shows that polycrystalline zinc oxide and fused silica are anomalous in that their shear modulus decreases with increasing pressure. For these materials the inequalities in (4.2) are reversed, and (3.2) implies shear induced compaction (for sufficiently small shear strains) at zero pressure. This is indeed

[10]This statement requires some qualification in the adiabatic case, since the shear modulus and the shear wave speed should increase with pressure to some peak values and then decay to zero as the material melts. Also note that (4.2) remains valid if all inequalities are replaced by equality, in which case we have $\mu = \mu_0\bar{\rho}$; thus for the typical case where $dU_S/d\bar{p} > 0$, the shear modulus cannot be proportional to the density.

[11]The data for Al, Cu, U, and W are taken from [2], $TiB_2$ from [3], ZnO from [4], and fused silica from [5].

a well-known phenomenon in fused silica. Observe that

$$\mu = \mu_0 + \left.\frac{d\mu}{d\bar{p}}\right|_0 \bar{p} + \mathcal{O}(\bar{p}^2) \quad \text{and} \quad \frac{\mu - \mu_0}{\mu_0} = \frac{1}{\mu_0}\left.\frac{d\mu}{d\bar{p}}\right|_0 \bar{p} + \mathcal{O}(\bar{p}^2)\,. \tag{4.3}$$

Thus $(d\mu/d\bar{p})_0/\mu_0$ measures the relative change in the shear modulus due to hydrostatic pressure.

| Material | $\kappa_0$ | $\mu_0$ | $\left.\frac{d\kappa}{d\bar{p}}\right\|_0$ | $\left.\frac{d\mu}{d\bar{p}}\right\|_0$ | $\left.\frac{1}{\mu_0}\frac{d\mu}{d\bar{p}}\right\|_0$ | $\left.\frac{d\mu}{d\bar{p}}\right\|_0 - \frac{\mu_0}{\kappa_0}$ |
|---|---|---|---|---|---|---|
| Al | 76.0 | 26.1 | 4.4 | 1.8 | 0.069 | 1.5 |
| Cu | 137 | 47.7 | 5.5 | 1.4 | 0.028 | 1.0 |
| U | 113 | 84.4 | 5.9 | 3.0 | 0.036 | 2.3 |
| W | 310 | 160 | 3.9 | 2.3 | 0.014 | 1.8 |
| $TiB_2$ | 237 | 246 | 2.0 | 9.0 | 0.036 | 7.9 |
| ZnO | 139 | 44.2 | 4.8 | −0.69 | −0.016 | −1.0 |
| Fused $SiO_2$ | 36.7 | 31.3 | −6.3 | −3.2 | −0.10 | −4.1 |

Table 1: Elastic Moduli and Their Pressure Derivatives ($\kappa_0$ and $\mu_0$ in GPa, $(d\mu/d\bar{p})_0/\mu_0$ in $\text{GPa}^{-1}$, other quantities dimensionless).

Expansion of the hydrostatic pressure $\bar{p}$ in powers of $\bar{\rho}$ yields

$$\bar{p}(\bar{\rho}) = \kappa_0(\bar{\rho} - 1) + \frac{\kappa_0}{2}\left(\left.\frac{d\kappa}{d\bar{p}}\right|_0 - 1\right)(\bar{\rho} - 1)^2 + \mathcal{O}((\bar{\rho} - 1)^3)\,. \tag{4.4}$$

Now consider the case where $\|\mathbf{L}^*\| = \mathcal{O}(\bar{\rho} - 1)$, i.e., where the shear strain and the volumetric strain are of the same order. Then

$$\gamma^* = a\,(\bar{\rho} - 1)^2 + \mathcal{O}((\bar{\rho} - 1)^3) \tag{4.5}$$

for some constant $a$ which depends on the particular deformation in question, and from $(3.2)_2$ and (4.4) we have

$$\frac{p - \bar{p}}{\bar{p}} = a\left(\left.\frac{d\mu}{d\bar{p}}\right|_0 - \frac{\mu_0}{\kappa_0}\right)(\bar{\rho} - 1) + \mathcal{O}((\bar{\rho} - 1)^2)\,, \tag{4.6}$$

$$\begin{aligned}\frac{p}{\kappa_0} &= (\bar{\rho} - 1) + \left[\frac{1}{2}\left(\left.\frac{d\kappa}{d\bar{p}}\right|_0 - 1\right) + a\left(\left.\frac{d\mu}{d\bar{p}}\right|_0 - \frac{\mu_0}{\kappa_0}\right)\right](\bar{\rho} - 1)^2 \\ &\quad + \mathcal{O}((\bar{\rho} - 1)^3)\,.\end{aligned} \tag{4.7}$$

Equation (4.6) gives an estimate for the relative increase in the pressure due to shear strain. Equation (4.7) is useful for comparing the second-order contributions to the total pressure: the first group of terms inside the square brackets is the contribution due volumetric strain; the second group is the contribution due to shear strain. These results apply in particular to *uniaxial strain* where $\lambda_2 \equiv \lambda_3 \equiv 1$, in which case $\gamma^* = \frac{2}{3}(\ln \bar{\rho})^2$ and $a = 2/3$ in (4.5)–(4.7). We will apply the above results to uniaxial strain of the polycrystalline titanium diboride tested in [3]. From the data in Table 1 we find that the contributions of volumetric strain and shear strain to the second-order term in the expansion (4.7) for the total pressure are 0.5 and 5.27, respectively, i.e., the shear strain contribution is an order of magnitude greater than that of the volumetric strain. And from (4.6) we have $(p - \bar{p})/\bar{p} \approx 5.27\,(\bar{\rho} - 1)$. Of course, these results are valid only within the elastic range of this material. At the Hugoniot elastic limit (HEL), $\bar{\rho} - 1$ is approximately equal to 0.03 (cf. [6]), so that $(p - \bar{p})/\bar{p} \approx 0.16$. In other words, at the HEL the relative increase in pressure due to shear strain is about 16%. If not taken into account this increase would lead to an overestimation of the shear stress at the HEL (obtained by subtracting $p$ from the longitudinal stress).

# References


[1] C. Truesdell and W. Noll. The Non-Linear Field Theories of Mechanics. In S. Flügge, editor, *Handbuch der Physik*, volume III/3. Springer, Berlin, 1965.

[2] M. W. Guinan and D. J. Steinberg. Pressure and temperature derivatives of the isotropic polycrystalline shear modulus for 65 elements. *J. Phys. Chem. Solids*, 35:1501–1512, 1974.

[3] A. Abbate, J. Frankel and D. Dandekar. Pressure dependence of the elastic constants of pollycrystalline titanium diboride. *XIII AIRAPT Proceedings*, 1991.

[4] N. Soga and O. L. Anderson. Anomalous behavior of the shear-sound velocity under pressure for polycrystalline ZnO. *J. Appl. Phys.*, 38:2985–2988, 1967.

[5] E. H. Bogardus. Third-order elastic constants of Ge, MgO, and fused $SiO_2$. *J. Appl. Phys.*, 36:2504–2513, 1965.

[6] M. E. Kipp and D. E. Grady. Shock compression and release in high-strength ceramics. Technical Report SAND89-1461, Sandia National Laboratories, 1989.

# Modelling Substructural and Textural Anisotropy at Finite Strain

Dr. M.P. Miller[1], Dr. D.L. McDowell[2*], and Dr. D.J. Bammann[3]

[1]Research Assistant and [2]Professor, The George W. Woodruff
School of Mechanical Engineering,
Georgia Institute of Technology, Atlanta, GA 30332-0405
[3] Senior Staff Scientist, Sandia National Labs,
Livermore, CA 94551

Dominant inelastic deformation processes of metal polycrystals at large strain include the nucleation and evolution of dislocation substructures, deformation twinning, phase transformations, and the evolution of crystallographic texture. Due to its technological importance, crystallographic texture has been the focus of much of the current research in large strain (cf. [1-5]). Strain-hardening theories which incorporate deformation substructure, such as the mesh length theory of Kuhlmann-Wilsdorf [6,7], have been largely ignored in large strain deformation model development, however. Accounting for strain-hardening processes either directly in the case of micro-scale models or indirectly in the case of macro-scale models is necessary for a more complete theory.

The mesh length theory proposes that clusters of stress-screened dislocation arrays, which are lower energy structures than uniform or statistically predictable distributions, will prevail [8]. These clusters are low energy dislocation structures (LEDS). This means that there will be areas of sparse dislocation population interspersed with densely packed dislocation arrays. The most common example of an LEDS is the dislocation cell which forms in materials with higher stacking fault energies (SFE). The cell is the dominant LEDS in these materials during the linear, stage II strain hardening regime. The evolution of certain cell walls into geometrically necessary boundaries (GNBs) in the form of dense dislocation walls (DDWs) and microbands (MBs) signals the onset of the non-linear stage III strain-hardening regime. These GNBs divide the grain into regions of cells of common slip called cell blocks (CBs). The cell block becomes the dominant LEDS during the large strain stage IV regime and its refinement defines the strain-hardening

character. The GNBs are often macroscopically oriented near the plane of maximum shear stress [9]. This being the case, one can envisage more possible orientations for GNBs in compression or tension as compared to torsion due to the conceptually infinite number of maximum shear stress planes which exist in pure compression or tension. In materials of lower SFE or of higher frictional stress, cross-slip becomes more difficult and the dominant LEDS during stage II becomes the Taylor lattice typified by alternating rows of edge dislocations differing by sign along the primary slip plane. Much less is known about the details of the strain hardening processes in these materials, but it has generally been observed that GNBs form and the grain is again segmented into subgrains in a manner similar to cell forming materials [10].

Plastic deformation is a continuous process consisting of different modes of deformation. Deformation by twinning can occur simultaneously and subsequently to slip [11] in many materials of low stacking fault energy and can alter the basic substructure observed within these materials. This complicated scenario can be augmented by phase transformations such as the strain-induced $\gamma \rightarrow \alpha'$ martensite transformation which occurs during plastic deformation in austenitic stainless steels [12-14]. The strain-induced $\alpha'$ martensite uses intersections of stacking faults and/or twinning planes which result from slip and twinning processes, respectively, as nucleation sites. The dislocation substructure which forms in these materials at lower strains, therefore, can have a strong effects on the density of $\alpha'$ martensite nucleation sites.

Metals at large strains develop a preferred orientation or crystallographic texture in which certain crystallographic planes tend to orient themselves in a preferred manner in response to the applied loads or displacements. The bulk material response is a result of both texture evolution and strain-hardening processes as well as the complex interactions which naturally arise between them. Very fundamental questions regarding the effect of dislocation microstructure on texture development as well as the relative importance of both to the bulk material response remain largely unanswered [15].

The development of deformation-induced anisotropy during large strain deformation has long been attributed to the evolution of texture and its importance has been demonstrated in many experiments [16-18]. Comparisons between experimental observations and theoretical predictions show, however, that texture can only account for part of the observed deformation-induced anisotropy. For example, if deformation-induced anisotropy results only from the formation of texture during a rolling process, then its effect on the subsequent yield stress of specimens taken at various orientations with respect to the rolling direction could be accounted for by the

modification of the stress level by the Taylor factor, M. The M factor is the ratio of the sum of the crystallographic shear strains to the macroscopic axial strain in uniaxial tension using Taylor's assumption of generalized minimum work [19,20]. It has been observed, however, that this modification can only account for part of the flow stress discrepancies. In recent work by Hansen and Jensen [21], the observed orientation and spacing of GNBs in the form of DDWs and MBs were taken into account to accurately predict the flow stress distribution as a function of angle from the rolling axis for tensile tests conducted on cold-rolled aluminum. These GNBs are structures of immobile dislocations which provide directional resistance to motion of mobile dislocations. They altered the Petch-Hall relationship for the grain size contribution to flow stress according to

$$\sigma_{GNB} = K_h \sqrt{\frac{Gb}{D_{GNB}}} \qquad (1)$$

where $D_{GNB}$ is the distance between geometrically necessary boundaries. Crystallographic slip is assumed to take place on planes which form an angle of 45° with respect to the tensile axis. For a given orientation, the normals to all of these planes will form a cone with its altitude direction along the tensile axis and with a half-cone angle of 45°. This model is referred to as the conical slip model. These results are very significant. As proposed by Teodosiu [15], these results confirm that the bulk deformation behavior of a material is dependent on **both** the development of crystallographic texture and the development and evolution of dislocation substructure. The results also confirm that the stress-state dependent macroscopic orientation of the large strain GNBs plays a strong role in their evolution as well as affecting continued slip processes and strain-hardening.

Due to inherent instabilities in tension, finite strain experiments have been largely confined to uniaxial [22] and biaxial [23] compression as well torsion (cf. [2,22]) tests. Traditionally, torsion tests comprise the majority of experiments due to frictional complexities which arise at the test machine - specimen interface during a compression test. Torsion tests have been conducted on both solid circular bars [2] and very short thin-walled tubes (cf. [22]). An assessment of path history dependence can be made by conducting tests involving sequences of compression (or tension) and torsion. Due to experimental complexities, however, few experiments of this type have been reported (cf. [22]).

One of the most consistently observed experimental phenomena is the softening behavior of torsion relative to compression. This effect has been

attributed to differences in crystallographic textures and, to a lesser extent, heightened strain-hardening in compression over torsion due to more slip activity in compression [24]. In light of the earlier discussion concerning the profusion of dislocation substructures in compression, the latter explanation seems more plausible, especially within the moderate strain regime. During free-end torsion, an axial strain develops as a manifestation of the evolution of deformation-induced anisotropy. During fixed-end tests an axial stress is induced. Monitoring and correlation of such "secondary" effects is an important aspect of the performance of large strain theories [25,26].

**Experimental Program**

Motivated by the above observations, large strain experiments involving pure torsion, pure compression, and sequences between compression / torsion and torsion / tension were conducted on type 304 stainless steel (SS 304L). The equivalent stress versus equivalent plastic strain response is depicted in Fig. 1a with $\bar{\sigma} = (3J_2)^{1/2}$ and $\bar{\epsilon}^p = \sqrt{2/3}\,\| \int \mathbf{D}^p dt \|$. The second invariant of deviatoric stress, $J_2$, is defined by $J_2 = 1/2 \mathrm{tr}\, \mathbf{s}^2$ and $\mathbf{D}^p$ is the plastic rate of deformation tensor.

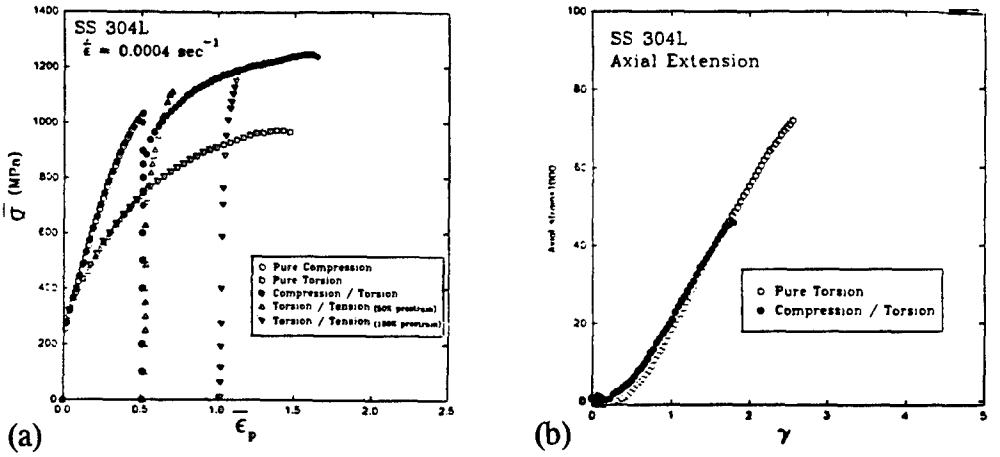



Fig. (1) - Experimental results for compression, free-end torsion, compression followed by free-end torsion, and free-end torsion followed by tension tests conducted on SS 304L: (a) the equivalent stress-strain response for all tests and (b) the axial strain response during the free-end torsion test and the torsional component of the compression/torsion test.

The expected torsional softening can be observed in Fig. 1a. In addition, the compressively prestrained material appears to yield between the pure torsion and pure compression curves and subsequently hardens in a

manner similar to torsion; the torsionally prestrained material appears to yield near the pure torsion stress level, then hardens towards the pure compression curve. In Figure 1b, the induced axial strain as a function of shear strain is plotted for both the pure torsion test and for the torsion episode of the compression/torsion sequence test. The induced axial strain appears to be independent of compressive prestrain; since the sequence test involves a much higher shear stress level, its relation to non-linear elastic effects (cf. [27]) is doubtful.

The strain induced $\gamma \rightarrow \alpha'$ martensite transformation which occurs in SS 304L has a significant impact on its strain-hardening character [14]. To investigate the occurrence of the $\alpha'$ transformation and to characterize the overall deformation substructure of this material, a transmission electron microscopy (TEM) study as well as magnetization measurements were conducted. Figure 2 is a bright field TEM micrograph which shows representative deformation substructure at $\bar{\epsilon}^p = 50\%$ compression. The plane of the page is normal to a radius of the cylindrical specimen. The compression axis is noted by the arrow on the figure. The light-colored features trending horizontally are $\alpha'$ martensite as determined by the diffraction pattern of this area. Twinning planes run roughly from the lower right corner of the figure to the upper left. Some of the planar features become so fine that distinguishing between twins, stacking faults and $\epsilon$ martensite (hcp) is not possible. Consistent with the terminology of Murr et al. [13], these areas are simply referred to as faulted regions. The $\epsilon$ martensite, twinning planes, and stacking fault intersections serve as nucleation sites for the $\alpha'$ martensite. These $\alpha'$ embryos grow and eventually coalescence, resulting in the polyhedral-shaped $\alpha'$ evident in Figure 2.

While the martensite transformation is extremely important, dislocation substructures are also evident. Figure 3a is from an $\bar{\epsilon}^p = 100\%$ torsion experiment. Twinning planes are apparent in this figure, but superimposed on the twin structure is a Taylor lattice. The positions of these features are shown schematically in Figure 3b. Dislocation cells and dense dislocation walls were also seen in other micrographs. One can conclude that the deformation substructure of this material is indeed extremely complicated.

The volume fraction of $\alpha'$ determined from the magnetization measurements for various loading histories is shown in Table 1. Upon examination of Figure 1a, it can be seen that the fraction of $\alpha'$ is related to the stress level as well as the accumulated plastic strain. Since there is a slight volume increase during the transformation, a positive hydrostatic stress aids the process and more $\alpha'$ is produced during tension than compression [14]. The increased $\alpha'$ production in compression compared to torsion, however, likely results from a heightened density of nucleation sites

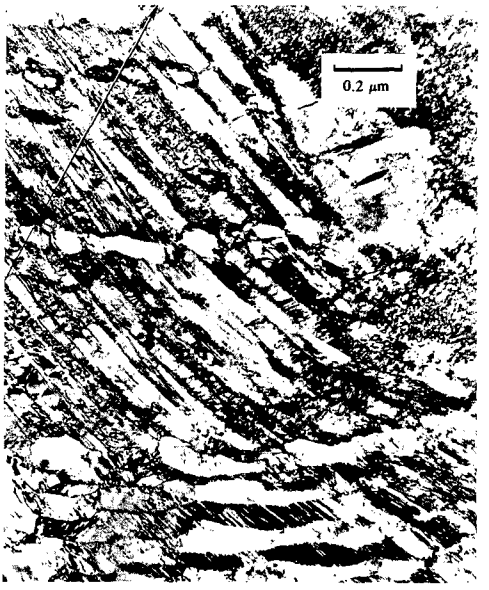



Fig (2) - TEM micrograph of SS 304L deformed to $\bar{e}^p = 50\%$ in compression. The compression axis is depicted by an arrow.

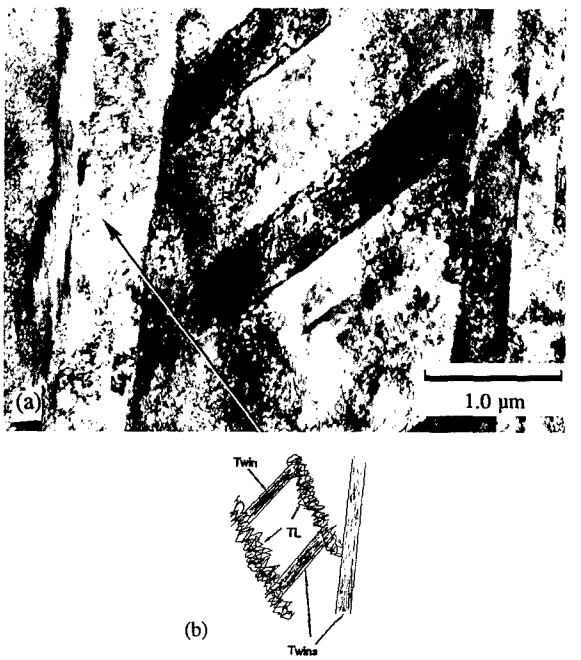



Fig. (3) - (a) TEM micrograph of SS 304L deformed in torsion to $\bar{e}^p = 100\%$. The torsional axis is depicted with an arrow. (b) Schematic depicting the position of the twins and the Taylor lattice (TL) shown in (a).

(intersections of twinning planes, $\epsilon$ martensite, and stacking faults) due to the higher number of planes of maximum shear stress in compression compared to torsion. One can conclude, therefore, that both the evolution of deformation substructures and the production of $\alpha'$ contribute to the strain-hardening character of SS 304L, and that these processes can be highly coupled.

Table 1. Volume fractions of $\alpha'$ determined from magnetization measurements

| Deformation History | Volume Fraction $\alpha'$ (%) |
|---|---|
| Torsion, $\bar{\epsilon}^p = 50\%$ | 2.8 |
| Compression, $\bar{\epsilon}^p = 50\%$ | 5.1 |
| Torsion, $\bar{\epsilon}^p = 100\%$ | 10.0 |
| Compression $\bar{\epsilon}^p = 50\%$ / Torsion $\bar{\epsilon}^p = 50\%$ | 12.4 |

**Deformation models for large strain**

Large strain models are generally micro-scale (formulated on the size scale of a slip system/grain) or macro-scale (formulated on the size scale of the test specimen or structural member) in nature. Micro-scale models are also referred to a crystal plasticity or micromechanical models and are based on the pioneering work of Taylor [19]. The philosophy of micro-scale polycrystal models is to formulate the problem at the slip system level and then to use the geometry of the crystal class to construct a grain. Then the polycrystalline solid is constructed by assembling an ensemble of grains using an appropriate constraints (cf. [28]), a self-consistent method (cf. [29]), or by assigning each grain as a finite element [30-32]. One of the inherent strengths of these models is their ability to track the development of crystallographic texture. In an earlier subsection, the development of macro-oriented geometrically necessary boundaries like dense dislocation walls and microbands was presented. Evidence was presented which substantiated the claim that the development and evolution of these structures can have an influence on the overall aggregate deformation on the same order as the

development of crystallographic texture. Microscale models have no explicit manner for dealing with such deformation substructure. While the structure of the crystal lattice which is explicitly present in crystal plasticity formulations allows for direct monitoring of the motion of the lattice itself, accountance for the nucleation and evolution of dislocation substructures has not yet been made. Crystal plasticity formulations assume deformation by crystallographic slip, and the focus of these formulations is the slip plane. Specific details of dislocation generation, motion and interaction do not appear explicitly. Hence, dislocation substructure must be accounted for in a phenomenological manner, i.e. through expressions for the instantaneous hardening modulus for each slip system. Hardening which results from phase transformations may be treated in analogous fashion. The introduction of realistic constraints on dislocation interaction and hardening processes within the crystal to reflect formation of LEDS is presently beyond the scope of crystal plasticity theory.

As the name implies, macro-scale formulations involve constitutive assumptions on the scale of a representative volume element consisting of an ensemble of grains. Such models typically assume material homogeneity but can include elastic and plastic anisotropy. In reality, the philosophy of macro-scale models is really quite similar to that of micro-scale models except, as was shown in the previous section, micro-scale models make the "phenomenological" constitutive assumption at the slip system level whereas similar assumptions are manifested in the macro-scale models through evolution equations of internal variables such as the kinematic hardening variable, $\alpha$, and the isotropic hardening variable, R. The macro-scale model framework has the flexibility to reflect physical processes on all size scales of the material. In theory, the inclusion of the effects of processes such as the evolution of dislocation substructure, phase transformations, etc. is possible. This flexibility also presents a great challenge since such effects must be included implicitly through the evolution equations of the internal variables, as well as within the structure of other elements of the theory such as the flow potential.

**Proposed Model Framework**

A simple framework is discussed here within the framework of rate-independent, incompressible plasticity which incorporates the third invariant of overstress, $J_3^* = 1/3 \text{ tr } (\mathbf{s}\text{-}\boldsymbol{\alpha})^3$. The framework permits dependence on $J_2$ and the third invariant, $J_3 = 1/3 \text{ tr } \mathbf{s}^3$, of deviatoric stress. If kinematic hardening is employed, the second, $J_2^* = 1/2 \text{ tr } \mathbf{s}^2$, and third, $J_3^*$, invariant of overstress, $\boldsymbol{\Sigma} = \mathbf{s}\text{-}\boldsymbol{\alpha}$ are permitted. Within the present model, $J_3^*$ appears explicitly in the yield function and in the evolution equations of the hardening

variables $\alpha$ and R as a means of delineating stress states effects on both initial yielding and work hardening. For example, in a free-end torsion test, $J_3^* = 0$, while for a uniaxial tension test, $J_3^* = \Sigma_{11}^3/4$, and for a uniaxial compression test, $J_3^* = -\Sigma_{11}^3/4$. It becomes apparent that an even power of $J_3^*$ can be used to delineate torsion from tension and compression, and an odd power of $J_3^*$ delineates compression from tension.

It has long been hypothesized that $J_3^*$ reflects a change of constraint on slip as a function of stress state [33]. Slip occurs on planes oriented most closely to the plane of maximum shear stress. As discussed previously, there are an infinite number of such planes during uniaxial compression or tension, and only two during a torsion test. It therefore seems reasonable to include $J_3^{*2}$ as a means of accounting for heightened slip and subsequent accelerated hardening which occurs in tension and compression compared to torsion.

In light of the discussion on substructure presented in the previous section, this interpretation implies that the $J_3^*$ level present during a particular stress state may have a direct impact on the nucleation, evolution, and orientation of dislocation substructures such as microbands, dense dislocation walls and other deformation substructures such as twin planes which can influence such processes as phase transformations. It is not, however, intended for use in representation of textural anisotropy.

A yield function of the form

$$f(J_2^*, J_3^*) = 3J_2^* \Psi(J_2^*, J_3^*) - R^2 \tag{2}$$

is introduced where

$$\Psi = 1 - 27\Phi\kappa J_3^{*2} / 16J_2^{*3} - 3\sqrt{3}(1-\Phi)\kappa J_3^* / 8J_2^{*3/2} \tag{3}$$

with the limits $0 < \kappa < 1$ and $1/2 < \Phi < 1$. The form with $\Phi = 1$ has been employed [33] in the context of isotropic hardening to correlate tests on thin walled tubes under axial tension and internal pressure subjected to varying ratios of axial stress to circumferential stress. For $\Phi = 1$, tension and compression are equivalent on the basis of $J_2^*$, while for $\Phi = 1/2$, compression and shear are equivalent but tension has a higher effective stress based on $J_2^*$. The yield function reduces to that of von Mises for $\kappa = 0$, and lies in-between the von Mises and Tresca criteria for nonzero $\kappa$ with $\Phi = 1$. Experimental observations (cf. [34,35]) often reveal that $\kappa$ is zero initially, and develops with cumulative plastic strain, if at all. In general, it is necessary to change the direction of the loading path in the deviatoric stress plane at several values of finite prestrain to assign values of $\kappa$ and $\Phi$ necessary to model abrupt (nearly instantaneous) changes in flow stress based on $J_2^*$.

We assume the following evolution equation for $\kappa$:

$$\dot{\kappa} = C_{\kappa}(\bar{\kappa} - \kappa)\dot{p} \tag{4}$$

The normality flow rule is given by

$$\mathbf{D}^{p} = \frac{1}{H}\langle \overset{\circ}{\mathbf{s}}:\mathbf{n}\rangle \mathbf{n} \tag{5}$$

The Macaulay brackets are defined as $<g> = g$ for $g>0$ and $<g> = 0$ for $g \leq 0$. The unit normal vector $\mathbf{n}$ is given by

$$\mathbf{n} = \frac{\partial f/\partial \boldsymbol{\sigma}}{\|\partial f/\partial \boldsymbol{\sigma}\|} = \left(3(\Psi + J_2^{*}\eta\kappa)\boldsymbol{\Sigma} - 3J_2^{*}\xi\kappa\mathbf{t}\right)/\|\partial f/\partial \boldsymbol{\sigma}\| \tag{6}$$

where $\Sigma_{ij} = s_{ij} - \alpha_{ij}$ and $t_{ij} = \Sigma_{ik}\Sigma_{kj} - 2J_2^{*}\delta_{ij}$. The parameters $\eta$ and $\xi$ are given by

$$\begin{aligned} \eta &= 81\Phi J_3^{*2}/16J_2^{*4} + 9\sqrt{3}(1-\Phi)J_3^{*}/16J_2^{*5/2} \\ \xi &= 27\Phi J_3^{*}/8J_2^{*3} + 3\sqrt{3}(1-\Phi)/8J_2^{*3/2} \end{aligned} \tag{7}$$

A total of N multiple hardening sets are employed using an Armstrong-Frederick hardening/recovery format for the backstress, $\alpha$, i.e.

$$\boldsymbol{\alpha} = \sum_{i=1}^{N} \boldsymbol{\alpha}_i \tag{8}$$

where the co-rotational rate of $\alpha_i$ is given by

$$\overset{\circ}{\boldsymbol{\alpha}}_i = C_i(B_i\mathbf{n}_{\alpha} - G_i\boldsymbol{\alpha}_i)\dot{p} \tag{9}$$

where $\mathbf{n}_{\alpha} = \boldsymbol{\Sigma}/\|\boldsymbol{\Sigma}\|$, $G_i$ is a nonlinear dynamic recovery function and $\dot{p} = \|\mathbf{D}^{p}\|$. The evolution of the isotropic hardening variables are given by

$$\dot{R}_i = C_i H_i\left(\bar{R}_i - R_i\right)\dot{p} \tag{10}$$

Here, the function $H_i(f) = f$ for "reversible" isotropic hardening and $H_i(f) = <f>$ for irreversible hardening (e.g. martensite formation).

We consider N hardening variable sets, representative of intermediate

and long range components which account for the post-yield behavior. Saturation values for the hardening variables contain an explicit dependence on $J_3^*$ i.e.

$$B_i = B_i^o g_i^{\alpha} \qquad \text{and} \qquad \bar{R}_i = \bar{R}_i^o g_i^{R} \qquad i = 1,...,N \tag{11}$$

where

$$g_i^j = 1 + m_i^j 27 J_3^{*2} / 4 J_2^{*3} + n_i^j 3\sqrt{3} J_3^* / 2 J_2^{*3/2} \qquad i=1,...,N;\ j = \alpha, R \tag{12}$$

This representation renders the following conditions for i = 1,...,N and j = $\alpha$, R: pure tension; $g_i^j = (1 + m_i^j + n_i^j)$, pure compression; $g_i^j = (1 + m_i^j - n_i^j)$, and pure torsion; $g_i^j = 1$. All rates are taken corotationally with the intermediate configuration. Under a small elastic strain assumption these rates are given by

$$\overset{\circ}{\boldsymbol{\alpha}} = \dot{\boldsymbol{\alpha}} - (\mathbf{W} - \mathbf{W}^p)\cdot\boldsymbol{\alpha} + \boldsymbol{\alpha}\cdot(\mathbf{W} - \mathbf{W}^p) \tag{13}$$

An expression similar to that derived by Dafalias (cf. [36,37]) for the component of plastic spin associated with each backstress is written as

$$\mathbf{W}_i^p = \rho_i^D (\boldsymbol{\alpha}_i \cdot \mathbf{D}^p - \mathbf{D}^p \cdot \boldsymbol{\alpha}_i) \tag{14}$$

where

$$\rho_i^D = \zeta_i e^{C_i p} \tag{15}$$

The total plastic spin in (13) is given by

$$\mathbf{W}^p = \sum_{i=1}^{N} \mathbf{W}_i^p \tag{16}$$

The plastic spin is the only feature of the present framework which may reflect texturing processes, albeit indirectly.

The experimental data of the compression and torsion data was correlated using the above framework. These correlations are depicted in Figures 4a and 4b. The sequence effects observed in Figure 1 for compression followed by torsion and torsion followed by tension tests, were

not adequately correlated using this preliminary model framework, however. It is likely that the rate coefficients, $C_i$, are also history dependent, a feature not considered here. The correlation parameters are given in Table 2.

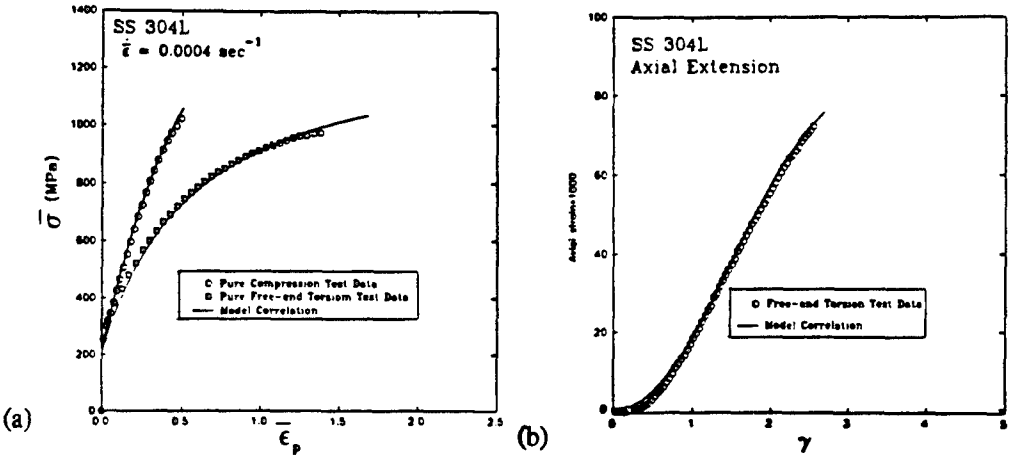



Figure 4 Model correlation of SS 304L compression and free-end torsion experimental data (a) equivalent stress versus equivalent plastic strain (b) axial stress versus shear strain.

## Discussion and Conclusions

Finite compression, shear and finite strain sequences of compression/shear and shear/tension have been performed on SS 304L. It has been shown that the dislocation substructure and the degree of strain-induced martensitic transformation for this material depends on the stress state during finite deformation. Based on this result and on the findings for other fcc materials that textural anisotropy must be augmented by anistropy induced by substructure (cf. Hansen and Jensen [21]), it is argued to include in the macro-scale theory the influence of the third invariant of the overstress in the flow potential and in the evolution equations for internal variables which represent material hardening. Likewise, micro-scale theories such as continuum crystal plasticity should be developed to include appropriate sub-grain scale constraints to represent formation of LEDS and associated anisotropy; in this case, it may be necessary to partition the dislocation density into mobile and immobile parts, permitting formation of low energy structures of the latter.

It should be noted that the only source of anisotropy in the macro-scale theory presented here is the backstress, $\alpha$. More sophisticated forms of

anisotropy may be introduced, for example, in the flow potential and in terms of elastic anisotropy associated with texture effects. In so doing, however, care must be taken to introduce evolution of the anisotropy consistent with the physics of texture development and the formation of LEDS. As is the case of representing LEDS in crystal plasticity theory, the introduction of evolving anisotropy in macro-scale models requires further developments likely rooted in micromechanics.

Table 2. Parameters used to correlate experimental data

| Parameter | Value | Parameter | Value |
|---|---|---|---|
| $\Phi$ | 1.0 | $\bar{R}_2^o$ | 690 MPa |
| $C_\kappa$ | $4.6 = C_1$ | $m_1^\alpha$ | 0.25 |
| $\bar{\kappa}$ | 0.44 | $m_2^\alpha$ | 0.25 |
| $R_o$ | 210 MPa | $m_1^R$ | 0.25 |
| N | 2 | $m_2^R$ | 0.667 |
| $C_1$ | 4.6 | $G_1$ | 1.0 |
| $C_2$ | 1.2 | $G_2$ | 1.0 |
| $B_1^o$ | 8.0 MPa | $\zeta_1$ | 0.0 $MPa^{-1}$ |
| $B_2^o$ | 160 MPa | $\zeta_2$ | 0.002 $MPa^{-1}$ |
| $\bar{R}_1^o$ | 112 MPa | | |

**Acknowledgements**

The authors would like to acknowledge the U.S. Army Research Office (ARO Grant No. DAAL 03-92-6-0103; K. Iyer, Monitor) for support of this work. Dr. D.A. Hughes of Sandia National Laboratories is acknowledged for the TEM and magnetization results. Sandia National Laboratories is gratefully acknowledged for conducting the compression experiments and support of other experimental aspects of the program.

## References


[1] Chin, G.Y., 1973, in The Inhomogeneity of Plastic Deformation, The American Society of Metals, Metals Park, Ohio.

[2] Montheillet, F., Cohen, M., and Jonas, J.J, 1984, Acta Metall., **32**, No. 11, pp. 2077-2089.

[3] Dawson, P.R., 1987, Int. J. Solids and Structures, **23**, No. 7, pp. 947-968.

[4] Mathur, K.K., and Dawson, P.R., 1989, Int. J. Plasticity, **5**, pp. 67-94.

[5] Kalidindi, S.R., and Anand, L., 1991, in Advances in Finite Deformation Problems in Materials Processing and Structures, AMD **125**, ASME, New York, NY.

[6] Kuhlmann-Wilsdorf, D., 1962, Trans. Metall. Soc. AIME, **224**, pp. 1047-1061.

[7] Kuhlmann-Wilsdorf, D. and Comins, N.R., 1983, Mater. Sci. Eng., **60**, pp. 7-24.

[8] Hansen, N., and Kuhlmann-Wilsdorf, D., 1986, Mater. Sci. Eng., **8**, pp 141-161.

[9] Hughes, D.A. and Nix, W.D., 1989, Mater. Sci. Eng. **A122**, pp. 153-172.

[10] Hughes, D.A., 1993, Acta Metall. et Mater. **41**, pp. 1421-1430.

[11] Meyers, M.A., and Chawla, K.K., 1984, Mechanical Metallurgy, Principles and Applications, Prentice Hall, Englewood Cliffs, N.J.

[12] Olson, G.B., and Cohen, M., 1972, Journal of the Less Common Metals, **28**, pp. 107-118.

[13] Murr, L. E., Staudhammer, K.P., and Hecker, S.S., 1982, Met. Trans. A, **13A**. pp. 627-635.

[14] Stout, M.G., and Follansbee, P.S., 1983, ASME J. Eng. Mater. Tech.,

**108**, pp. 344-353.

[15] Teodosiu, C., 1991, in Anisotropy and Localization of Plastic Deformation, J.-P. Boehler and A.S. Khan eds, pp. 179-182.

[16] Bunge, H.-J., and Roberts, W.T., 1969, , J. Appl. Cryst., **2**, pp. 116-128.

[17] Kallend, J.S., and Davies, G.J., 1971, J. Inst. Metals, **5**, pp. 252-273.

[18] Juul Jensen, D., and Hansen, N., 1990, Acta Metall. et Mater., Vol. 38, pp. 1369-1380.

[19] Taylor, G.I., 1938, J. Inst. Metals, **62**, pp. 307-324.

[20] Chin, G.Y., and Mammel, W.L., 1967, Trans. of Met. Soc. AIME, **239**, pp. 1400-1405.

[21] Hansen, N. and Jensen, J., 1991, Acta Metall. et Mater. (In press).

[22] Hecker, S.S., and Stout, M.G., 1984, in Deformation Processing and Structures, George Krauss, Editor, American Society of Metals, Metals Park, Ohio, pp. 1-46.

[23] Khan, A.S., and Wang, X., 1990, Int. J. Plasticity, **6**, pp. 485-504.

[24] Jonas, J.J, Canova, G.R., Shrivistava, S.C., and Christodoulou, N., 1982, in Proceedings of The Workshop on Plasticity of Metals at Finite Strain: Theory, Experiment and Computation, Division of Applied Mechanics, Stanford University, Stanford, CA., pp. 206-222.

[25] Bammann, D.J. and Aifantis, E.C., 1987, Acta Mech. **69** pp. 97-117.

[26] Paulun, J.E., and Pecherski, R.B., 1987, Int. J. Plasticity, **3**, pp. 303-314.

[27] Khen, R., and Rubin, M.B., 1992, Int. J. Plasticity, **29**, No. 18, pp. 2235-2258.

[28] Asaro, R.J.,and Needleman, A., 1985, Acta Metall., **33**, pp. 923-953.

[29] Iwakuma, T., and Nemat-Nasser, S., 1984, Proc. Roy. Soc. Lond. **A394**, pp. 87-119.

[30] Harren, S.V., and Asaro, R.J., 1989, J. Mechs. Phys. Solids, **37**, pp. 191-232.

[31] McHugh, P.E., Varias, A.G., Asaro, R.J., and Shih, C.F., 1989, Future Generation Computer Systems, Vol. 5, pp. 295-318.

[32] Havliček, F., Tokuda, M., Hino, S., and Kratochvil, J., 1992, Int. J. Plasticity, **8**, pp. 477-499.

[33] Drucker, D.C., 1949, ASME J. Appl. Mech., **16**, pp. 349-357.

[34] Shrivastava, S.C., Jonas, J.J. and Canova, G., 1982 J. Mech. Phys. Solids, **30**, No.1/2, pp. 75-90.

[35] Miller, M.P. and McDowell, D.L., in Microstructural Characterization in Constitutive Modeling of Metals and Granular Media, ASME MD **32**, G.P. Voyiadjis, Editor, 1992, pp 27-44.

[36] Dafalias, Y.F., 1984, , Mech. Mat., **3**, pp. 223-233.

[37] Dafalias, Y.F., 1985, ASME J. of Appl. Mech., **107**, pp. 865-871.

# END EFFECTS IN ANISOTROPIC AND COMPOSITE STRUCTURES

Dr. C. O. Horgan* and Dr. J. G. Simmonds*
Department of Applied Mathematics
School of Engineering & Applied Science
University of Virginia
Charlottesville, VA 22903-2442

## Abstract

Thin-walled structures of interest to the U. S. Army, such as rifle barrels, rocket casings, helicopter blades and containment vessels are often constructed of layers of anisotropic, filament or fiber-reinforced materials which must be designed to remain elastic. A proper assessment of end or edge effects in such structures is of fundamental importance to U. S. Army technology. The extent to which *local* stresses, such as those produced by fasteners and at joints, can penetrate girders, beams, plates and shells must be understood by the designer. Thus a distinction must be made between *global* structural elements (where Strength of Materials or other approximate theories may be used) and *local* elements which require more detailed (and more costly) analyses based on exact elasticity. The neglect of end effects is usually justified by appeals to some form of Saint-Venant's principle and years of experience with *homogeneous isotropic elastic structures* has served to establish this standard procedure. Saint-Venant's principle also is the fundamental basis for static mechanical tests of material properties. Thus property measurements are made in a suitable *gage section* where *uniform* stress and strain states are induced and local effects due to clamping of the specimen are neglected on invoking Saint-Venant's principle. Such traditional applications of Saint-Venant's principle require major modifications when strongly anisotropic and composite materials are of concern. For such materials, local stress effects may persist over distances *far greater* than is typical for isotropic metals. In this paper, we describe plane elastostatic problems where anisotropy induces such extended Saint-Venant end zones. The paper is a review and a comprehensive list of references is given to original work where details of the analyses may be found. The

implications of such extended end zones due to anisotropy are far reaching in the proper analysis and design of structures using advanced composite materials.

## 1. Introduction

A proper assessment of end or edge effects in structures is of fundamental importance in structural engineering analysis and design. The extent to which *local* stresses, such as those produced by fasteners and at joints, can penetrate girders, beams, plates and shells must be understood by the designer. Thus a distinction must be made between *global* structural elements (where Strength of Materials or other approximate theories may be used) and *local* elements which require more detailed (and more costly) analyses based on exact elasticity. The neglect of end effects is usually justified by appeals to some form of Saint-Venant's principle and years of experience with *homogeneous isotropic elastic structures* has served to establish this standard procedure. Saint-Venant's principle also is the fundamental basis for static mechanical tests of material properties. Thus property measurements are made in a suitable *gage section* where *uniform* stress and strain states are induced and local effects due to clamping of the specimen are neglected on invoking Saint-Venant's principle. For recent reviews of Saint-Venant's principle, see [1,2].

Such traditional applications of Saint-Venant's principle require major modifications when strongly anisotropic and composite materials are of concern. For such materials, local stress effects persist over distances *far greater* than is typical for isotropic metals. The implications of such extended end zones due to anisotropy are far reaching in the proper analysis and design of structures using advanced composite materials.

In this paper, we describe *plane elasticity problems* where anisotropy induces such extended Saint-Venant zones and we provide results for the characteristic decay lengths in terms of geometric and material parameters. The paper is a review and gives a comprehensive list of references to original work where details of the analyses may be found.

## 2. Plane deformations of rectangular strips

Let *OXYZ* denote a fixed, right-handed Cartesian reference frame. We consider an homogeneous elastic body which, if undeformed,

occupies the region $0 \le X$, $|Y| \le H$, $|Z| \le T$. We shall regard the thickness, $T$, of the body as either infinitesimal or infinite and we shall assume that the deformation of the body is governed by the equations of static linear elasticity. All faces of the body are traction free except $X=0$ on which any combination of stress and/or displacement may be prescribed which induce stresses in the body that decay as $X \to \infty$. (Thus, the stresses on the end $X=0$, whether known or not, must, necessarily, be self-equilibrating.) We shall assume that the infinitesimally thin body is in a state of plane stress with the Cartesian components $\tau_{xz}, \tau_{yz}$, and $\tau_{zz}$ of the stress tensor all zero; we shall assume that the infinitely thick body is in a state of plane strain with the Cartesian components $\varepsilon_{xz}, \varepsilon_{yz}$, and $\varepsilon_{zz}$ of the strain tensor all zero. Except for different values of the elastic constants, the governing equations are identical mathematically. In both cases, we assume that the body is fully anisotropic in the $XY$-plane in the sense that $\varepsilon_{xx}, \varepsilon_{yy}$, and $2\varepsilon_{xy}$, regarded as the components of a column vector $e \equiv [e_1, e_2, e_3]^T$ are related to $\tau_{xx}, \tau_{yy}$, and $\tau_{xy}$, regarded as a column vector $s \equiv [s_1, s_2, s_3]^T$, by the relation

$$e = Bs \ , \ \text{that is,} \ \begin{bmatrix} e_1 \\ e_2 \\ e_3 \end{bmatrix} = \begin{bmatrix} \beta_{11} & \beta_{12} & \beta_{16} \\ \beta_{12} & \beta_{22} & \beta_{26} \\ \beta_{16} & \beta_{26} & \beta_{66} \end{bmatrix} \begin{bmatrix} s_1 \\ s_2 \\ s_3 \end{bmatrix} , \tag{1}$$

where $B$ is the (symmetric) compliance matrix and where we have followed the usual subscript notation. We henceforth refer to the problem of computing the stresses in either case (plane stress or plane strain) as the *anisotropic strip problem.*

If the dimensionless Airy stress function $\phi(x, y)$ is introduced, where

$$x = X/H \ , \ y = Y/H \, , \tag{2}$$

and

$$\tau_{xx} = \phi_{,yy} \ , \ \tau_{yy} = \phi_{,xx} \ , \ \tau_{xy} = -\phi_{,xy} \tag{3}$$

(the comma denoting partial differentiation), then $\phi$ satisfies

$$\begin{aligned} \beta_{22}\phi_{,xxxx} - 2\beta_{26}\phi_{,xxxy} + (2\beta_{12} + \beta_{66})\phi_{,xxyy} \\ - 2\beta_{16}\phi_{,xyyy} + \beta_{11}\phi_{,yyyy} = 0 \, , \ 0 < x \, , \ |y| < 1 \, . \end{aligned} \tag{4}$$

If the material is *transversely isotropic* (or *orthotropic*) so that

$$\beta_{16} = \beta_{26} = 0 , \tag{5}$$

then (4) simplifies considerably. For an *isotropic* material, in addition to (5), we have

$$\beta_{11} = \beta_{22} = (1 - \nu^2)/E \ , \ \beta_{12} = -\nu(1 + \nu)/E \ , \ \beta_{66} = 2(1 + \nu)/E , \tag{6}$$

where the constants $E$ and $\nu$ are Young's modulus and Poisson's ratio, respectively, and (4) reduces to the biharmonic equation

$$\phi_{,xxxx} + 2\phi_{,xxyy} + \phi_{,yyyy} = 0 . \tag{7}$$

The classic approach to analyzing Saint-Venant's principle in the isotropic case is to seek solutions of (7) of the form

$$\phi = e^{-\gamma x} F(y) , \tag{8}$$

where $\gamma$ is a constant. This leads to a fourth-order eigenvalue problem for $F(y)$ on $|y| < 1$, where the eigenvalues $\gamma$ are complex. This gives rise to the celebrated Fadle-Papkovich eigenfunctions with associated eigencondition

$$\sin 2\gamma = \pm 2\gamma . \tag{9}$$

The decay rate for Saint-Venant end effects is given by the real part of the root of (9) of *smallest* real part and so

$$\mathcal{R}\gamma \approx 2.1 . \tag{10}$$

(See [1], [3, p.62]). Thus the stresses $\tau$ decay exponentially from the end $X = 0$ as

$$\tau \sim Ke^{-kX} \tag{11}$$

where

$$k \approx \frac{2.1}{H} \tag{12}$$

is the decay rate. Thus the characteristic decay length $\lambda \equiv 1/k \approx H/2.1$. If, instead, we use the characteristic decay length $\lambda^* \equiv (\ln 100)\lambda$ (the distance over which the right side of (11) decays to 1% of its value at $X=0$), we find that

$$\lambda^* \approx 2H\,. \tag{13}$$

This result mathematically substantiates the engineering rule of thumb that Saint-Venant end effects in the isotropic case are "negligible" *at a distance of approximately one strip width from the end.*

The preceding approach was used by Choi & Horgan [4] for a fully anisotropic strip governed by equation (4). The eigencondition analogous to (9)—see equation (18) of [4]—is considerably more complicated. In particular, this condition involves the elastic constants $\beta_{ij}$. For a specially orthotropic (or transversely isotropic) material where (5) holds, the results simplify somewhat. Of special interest in [4] was the case of strongly anisotropic materials (modeling fiber-reinforced composites) where the longitudinal Young's modulus $E_L \gg E_T$ or $G_{LT}$. It was shown in [4,5] that the exponential *rate* of stress decay from the loaded end is then given by

$$k \approx \frac{\pi}{H}\,(G_{LT}/E_L)^{1/2} \tag{14}$$

and so the characteristic *decay length* $\lambda = 1/k$ is

$$\lambda \approx \frac{H}{\pi}\,(E_L/G_{LT})^{1/2}\,. \tag{15}$$

For a graphite-epoxy composite, for example, where $E_L/G_{LT} \approx 33.3$, (14) yields

$$k \approx 0.5442/H \tag{16}$$

which is *four times* slower than the corresponding decay rate (12) for isotropic materials (see, e.g., [4,5] for a discussion). Thus the Saint-Venant end zone for plane deformations of this composite material is approximately *four* specimen widths. Consequently, in mechanical testing of material properties for composites with this order of magnitude for the $E_L/G_{LT}$ ratio, specimen *aspect ratios* of at least 10:1 would be required.

The asymptotic result (14) was derived from the appropriate eigencondition in [4] and provides a remarkably accurate estimate for the exact decay rate. For example, for a graphite-epoxy composite,

the estimate (16) is very close to the exact decay rate

$$k \approx 0.5640/H \tag{17}$$

computed numerically in [4]. Illustrative examples involving extension and bending of strips which show the significant difference in stress decay between isotropic and anisotropic materials are discussed in [4] and [5].

The design formulas (14) and (15) were established in the course of studies [4,5,6] on plane orthotropic elasticity. The results have been widely adopted in the literature on composite materials. For example, the role of such results in designing test specimen geometries for mechanical testing of fiber-reinforced composites is discussed in the SESA monograph by Whitney et al. [7] and in the text by Carlsson and Pipes [8] on experimental characterization of advanced composite materials. A finite element study by Carlsson et al [9] on end effects in graphite/epoxy bolted joints has shown very good agreement with (14) and (15). Further finite element analyses are reported in Arridge and Folkes [10], Holt and Hope [11], Dong and Goetschel [12], and Goetschel and Hu [13]. The presence of extended Saint-Venant edge zones in composites has led to a modification of the ASTM test D198 to measure the shear modulus of anisotropic beams by flexural methods (Gromala [14]); see also Sandorff [15] and Sullivan and Van Oene [16]. The implications of (14) and (15) for the ASTM D3410 specimen geometries recommended for the IITRI Compression Test Method is discussed by Bogetti et al [17] who use a finite element approach, in conjunction with (14) and (15), to evaluate the appropriateness of test methods for strongly anisotropic composite laminates.

From (9) it is seen that, in the isotropic case, the eigencondition is independent of the two elastic moduli $E$ and $\nu$. (It is well known that the stresses are also independent of the elastic constants in this case.) Likewise, although an orthotropic (or transversely isotropic) strip ($\beta_{16} = \beta_{26} = 0$) depends on *four* elastic constants, Horgan & Simmonds [18] have shown that the analogous eigencondition depends only on *one* combined elastic parameter,

$$\varepsilon = \frac{\sqrt{\beta_{11}\beta_{22}}}{2\beta_{12} + \beta_{66}} \,. \tag{18}$$

This facilitates the presentation of results for whole classes of specially

orthotropic materials as shown in Fig. 1, where $h=2H$. The characteristic decay length (i.e., the distance over which end effects decay to 1% of their end values) versus a nondimensional material parameter is plotted and the results for various materials are indicated by the dots shown on the curves. The decay length for an isotropic material is shown by the dark square. It is seen that the latter has the *smallest* decay length and that this is approximately equal to the width of the strip. Fig. 1 can be used directly in the design process to account for anisotropic end effects. (We are grateful to Dr. M. P. Nemeth of NASA Langley Research Center for his collaboration in generating Fig. 1.)

In recent work [19] we have returned to the fully anisotropic material governed by (1) and (4) where *six* elastic constants are involved. It is shown in [19] that the associated eigencondition depends now on *two* dimensionless elastic parameters only. This has allowed us to numerically determine the Saint-Venant decay length for the fully anisotropic strip. The results in [19] are presented in a form immediately accessible to designers. Thus, *for any arbitrary degree of anisotropy*, (or, equivalently, for any off-axis orientation of a fiber-reinforced strip), the numerical data allow one to determine the Saint-Venant decay length precisely. The results should have widespread application to structural mechanics issues such as assessing end constraint effects in mechanical testing (in particular, for the off-axis tension test), determining the influence of fasteners, joints, cut-outs, etc., in composite structures and in the evaluation of the limits of strength-of-materials formulas when applied to composites.

Plane problems for symmetric sandwich laminates have also been investigated. Choi & Horgan [20] have studied exact decay rates for two phase sandwich strips, with isotropic layers, subject to self-equilibrated end loads. For a relatively soft inner core, slow decay of end effects was again established. Asymptotic formulas for the estimated decay rate similar to (14) were obtained. (See also [5].) Related experimental and finite element calculations have been reported (see the references in [2]). An interesting study of the decay of Saint-Venant end effects for plane deformations of a laminate composite subject to (partial) interface debonding has been carried out by Benveniste [21] who showed that debonding has the effect of *reducing* the exponential decay rate.

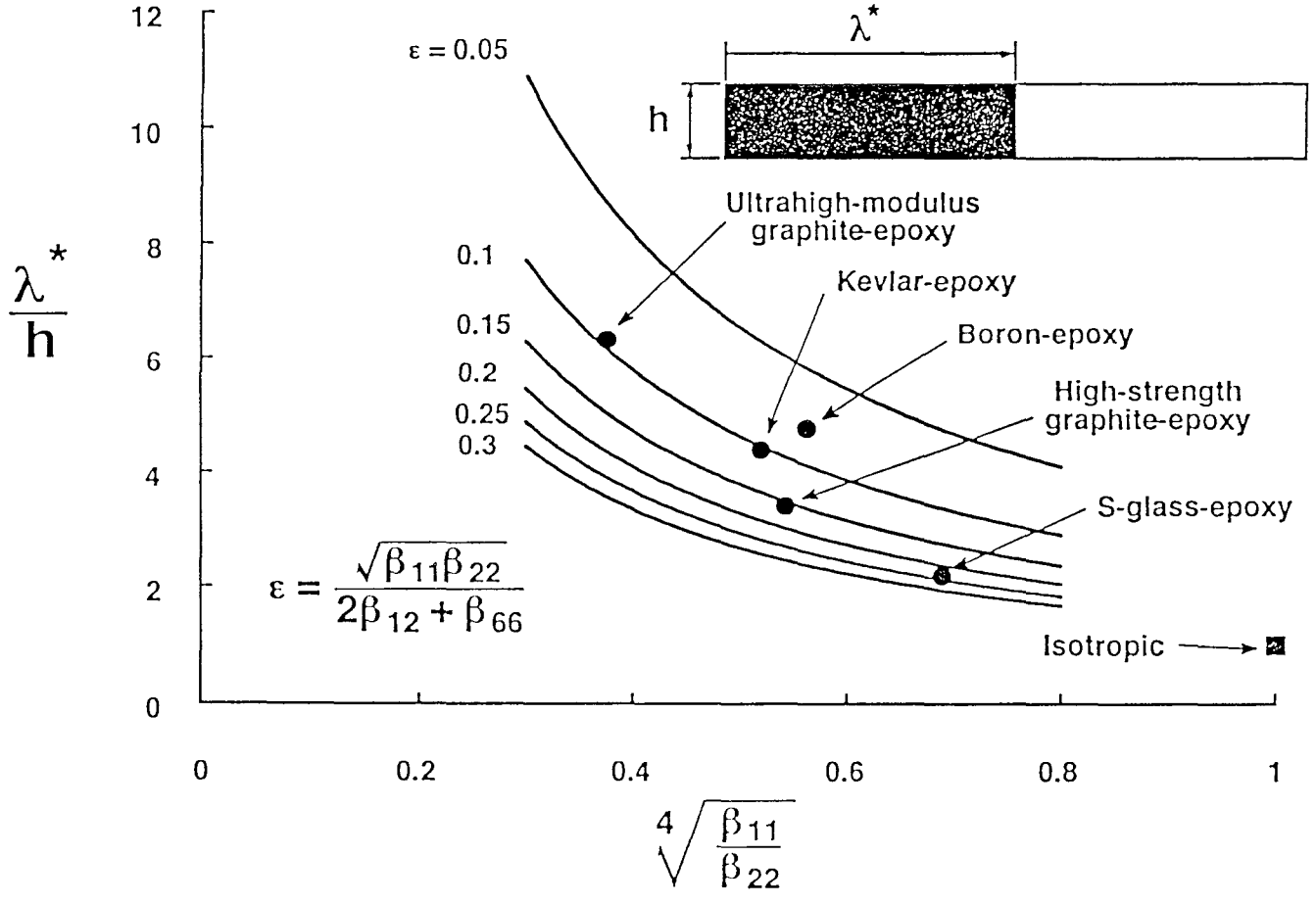



Fig. 1. Decay Lengths For Semi-Infinite Orthotropic Strips Subjected To Self-Equilibrated Edge Loads

## 3. Concluding remarks

For illustrative purposes, we have confined attention in the preceding to plane linear elastostatics. Extended end effects due to anisotropy also occur in three-dimensional problems such as axisymmetric deformations of solid or hollow circular cylinders (see, e.g., [5], [22], [23] and the references cited therein and in [1,2]). Slow stress decay for strongly anisotropic materials has also been observed experimentally. In the course of conducting torsional pendulum tests designed to measure the longitudinal shear modulus of a polymeric composite, Folkes and Arridge [24] encountered difficulties (because of end effects) in obtaining values of this modulus which are independent of specimen aspect ratios (length/width ratio). Meaningful results were obtained only for samples whose aspect ratios exceeded 100. The data in [24] for polystyrene fibers in a matrix of polybutadiene indicate that $E_L/G_{LT}$ is about 280 and so characteristic decay lengths of the order of several specimen widths are predicted by the theoretical results. Further tests are described in Arridge et al. [25] and Arridge and Folkes [10]. A review of this work is given by Arridge and Barham [26]. See also Section 4 of [2] for further discussion of the application of (14) and (15) in the polymer physics literature. Experimental work by Stubbs [27] on Saint-Venant end effects in cruciform fabric specimens shows qualitative agreement with (14) and (15). Of course, many of the applications of Saint-Venant's principle to highly-drawn polymers and fabric materials may well require consideration of *inelastic* and *nonlinear* effects. While some progress has been made in this direction (see, e.g., [1,2,28-32] and the references cited therein), the consideration of additional effects due to anisotropy and material inhomogeneity remains a formidable challenge.


## Acknowledgements

This work was supported by the U. S. Army Research Office under Grant DAAL-03-91-G-0022. We are grateful to Dr. M. P. Nemeth, NASA Langley Research Center, for many helpful discussions, in particular in connection with Fig. 1


## References


1. Horgan, C. O., and Knowles, J. K., Recent developments concerning Saint-Venant's principle, *Advances in Applied Mechanics* (T. Y. Wu and J. W. Hutchinson eds.), **23** 179-269, Academic Press,

New York, 1983.

2. Horgan, C. O., Recent developments concerning Saint-Venant's principle: an update, *Appl. Mech. Rev.* **42** (1989), 295-303.
3. Timoshenko, S. P., and Goodier, J. N., *Theory of Elasticity*, 3rd ed, McGraw-Hill, New York, 1970.
4. Choi, I., and Horgan, C. O., Saint-Venant's principle and end effects in anisotropic elasticity, *J. Appl. Mech.* **44** (1977), 424-430.
5. Horgan, C. O., Saint-Venant end effects in composites, *J. Composite Materials,* **16** (1982), 411-422.
6. Horgan, C. O., Some remarks on Saint-Venant's principle for transversely isotropic composites, *J. Elasticity* **2** (1972), 335-339.
7. Whitney, J. M., Daniel, I. M., and Pipes, R. B., *Experimental Mechanics of Fiber-Reinforced Composite Materials,* SESA Monograph 4, SESA (1982).
8. Carlsson, L. A., and Pipes, R. B., *Experimental Characterization of Advanced Composite Materials,* Prentice-Hall, New Jersey, 1987.
9. Carlsson, L. A., Sindelar, P., and Nilsson, S., Decay of end effects in graphite/epoxy bolted joints, *Composites Science and Technology,* **26** (1986), 307-322.
10. Arridge, R. G. C., and Folkes, M. J., Effect of sample geometry on the measurement of mechanical properties of anisotropic materials, *Polymer* **17** (1976), 495-500.
11. Holt, J. S., and Hope, P. S., Displacement oscillation in plane quadratic isoparametric elements in orthotropic situations. *Int. J. for Numerical Methods in Engineering,* **14** (1979), 913-920.
12. Dong, S. B., and Goetschel, D. B., Finite element analysis of edge effects in laminated composite plates, *J. Appl. Mech.* **49** (1982), 129-135.
13. Goetschel, D. B., and Hu, T. H., Quantification of Saint-Venant's principle for a general prismatic member, *Computers and Structures,* **21** (1985), 869-874.
14. Gromala, D. S., Determination of modulus of rigidity by ASTM D198 flexural methods, *J. of Testing and Evaluation* **13,** (1985), 352-355.
15. Sandorff, P. E., Saint-Venant effects in an orthotropic beam, *J. of Composite Materials,* **14** (1980), 199-212.

16. Sullivan, J. L., and Van Oene, H., An elasticity analysis for the generally and specially orthotropic beams subjected to concentrated loads, *Composites Science and Technology,* **27** (1986), 133-155.

17. Bogetti, T. A., Gillespie, J. W., and Pipes, R. B., Evaluation of the IITRI compression test-method for stiffness and strength determination, *Composites Science and Technology,* **32** (1988), 57-76.

18. Horgan, C. O., and Simmonds, J. G., Asymptotic analysis of an end-loaded, transversely isotropic, elastic, semi-infinite strip weak in shear, *Int. J. Solids Structures* **27** (1991), 1895-1914.

19. Crafter, E. C., Heise, R. M., Horgan, C. O., and Simmonds, J. G., The eigenvalues for a self-equilibrated, semi-infinite, anisotropic elastic strip, *J. Appl. Mech.* (in press).

20. Choi, I., and Horgan, C. O., Saint-Venant end effects for plane deformation of sandwich strips. *Int. J. Solids Struct.,* **14** (1978), 187-195.

21. Benveniste, Y., On the effect of debonding on the overall behavior of composite materials, *Mech. of Materials* **3** (1984), 349-358.

22. Horgan, C. O., The axisymmetric end problem for transversely isotropic circular cylinders, *Int. J. Solids Struct.* **10** (1974), 837-852.

23. Simmonds, J. G., An asymptotic analysis of end effects in the axisymmetric deformation of elastic tubes weak in shear: higher order shell theories are inadequate and unnecessary, *Int J. Solids Struct.* **29** (1992), 2441-2461.

24. Folkes, M. J., and Arridge, R. G. C., The measurement of shear modulus in highly anisotropic materials: the validity of St. Venant's principle, *J. Phys. D: Appl. Phys.,* **8** (1975), 1053-1064.

25. Arridge, R. G. C., Barham, P. J., Farrell, C. J., and Keller, A, The importance of end effects in the measurement of moduli of highly anisotropic materials, *J. Materials Sci.,* **11** (1976), 788-790.

26. Arridge, R. G. C., and Barham, P. J., Polymer elasticity: discrete and continuum models, *Advances in Polymer Science,* **46** (1982), 67-117.

27. Stubbs, N., Experimental estimation of Saint-Venant's end effects for cruciform fabric specimens, *J. Reinforced Plastics and Composites,* **3** (1984), 181-192.

28. Horgan, C. O., and Knowles, J. K., The effect of nonlinearity on a principle of Saint-Venant type, *J. Elasticity* **11** (1981), 271-291.

29. Horgan, C. O., and Payne, L. E., On Saint-Venant's principle in finite anti-plane shear: An energy approach, *Arch. Ration. Mech. Anal.*, **109** (1990), 107-137.

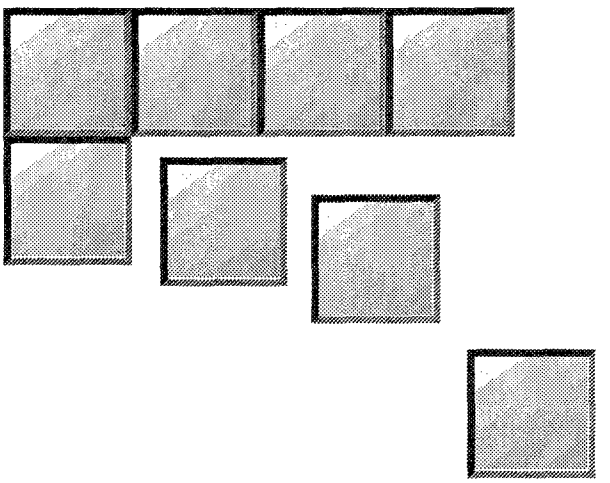
30. Abeyaratne, R., Horgan, C. O., and Chung, D.-T., Saint-Venant end effects for incremental plane deformations of incompressible nonlinearly elastic materials, *J. Appl. Mech.*, **52** (1985), 847-852.

31. Horgan, C. O., Payne, L. E., and Simmonds, J. G., Existence, uniqueness and decay estimates for solutions in the nonlinear theory of elastic, edge-loaded, circular tubes, *Quart. Appl. Math.* **48** (1990), 341-359.

32. Horgan, C. O., and Payne, L. E., A Saint-Venant principle for a theory of nonlinear plane elasticity, *Quart. Appl. Math.* **50** (1992), 641-675.

# SESSION VIB: DYNAMIC BEHAVIOR

**Chairman:** *Dr. T. Nicholas*
**AF Materials Laboratory**



# Experimental Evaluation of Strain, Strain-Rate and Temperature Dependance of Flow Stress at High Strain Rate

*S. Nemat-Nasser*
University of California, San Diego

"PAPER NOT AVAILABLE"

# EFFECT OF GAS-PRODUCING AND POLYMORPHIC REACTIONS ON STRESS WAVE PROPAGATION

Prof. Thomas J. Ahrens* and Mr. Guangqing Chen
Lindhurst Laboratory of Experimental Geophysics,
Seismological Laboratory, California Institute of Technology
Pasadena, CA 91125

Abstract

Both solid to gas ($CaSO_4 + SiO \rightarrow CaSiO3 + SO_2$ and $Si_3N_4 + 3C$ (diamond) $\rightarrow$ and $3SiC + 2\ N_2$) and polymorphic reactions, e.g. GeO (glass, 3.7 g/cm$^3$) to $GeO_2$ (rutile, 6.3 g/cm$^3$) can be shock-induced at ballistic velocities. Because of the endothermic nature of the gas- producing reactions, the extent of reactions observed are limited to interfaces. Moreover, polymorphic reactions (such as the $GeO_2$ reaction) occur upon dynamic compression and not only upon isentropic release. The transformation of $GeO_2$ from glass to rutile appears, upon analogy with similar reactions in the $SiO_2$ system, to be a highly energy hysterectic material which merits study as a stress wave mitigating material.

## 1. INTRODUCTION

Shock-induced endothermic solid-solid phase changes and gas-producing reactions have been studied in material consolidation and synthesis, especially starting with powdered materials (e.g. Boslough, [1]; Tan et al.[6]; Erskine and Nellis [2]; Yang et al. [7]). Although thermal effects induced by shock compression is the major factor inducing chemical reactions under dynamic stress loading, unloading within the time scale of microseconds can be expected to proceed very differently than under equilibrium conditions. Gas-producing reactions, as well as solid-solid phase changes involving large density changes with their potential effects on partitioning of linear momentum, may

have some ballistic application. Particularly, we have examined the following four reactions:

$$Si_3N_4 + 3C \text{ (diamond)} \rightarrow 3SiC + 2N_2 \uparrow \quad (1)$$

$$CaSO_4 \text{ (anhydrite)} + SiO_2 \rightarrow CaSiO_3 \text{ (wollastonite)} + SO_3 \uparrow \quad (2)$$

$$CaSO_4 + SiO \rightarrow CaSiO_3 + SO_2 \uparrow \quad (3)$$

$$GeO_2 \text{ (glass)} \rightarrow GeO_2 \text{ (rutile)} \quad (4)$$

## 2. GAS-PRODUCING REACTIONS

A series of recovery experiments and bulk chemical analyses were conducted on the recovered samples. No (solid) reaction products are found for reactions (1) and (2), but reaction (3) is discovered to take place to a varied extent in different shots. These results contradict Gibbs' formation energy calculations, which allow all three reactions to proceed below calculated after-shock temperatures.

The shock experiments utilize a 20 mm gun at Caltech's Shock Wave Lab. Reactants (in powder form, particle sizes ~10-30 μm, except $Si_3N_4$ is whisker shaped) are mixed and pressed in 304 stainless steel containers. The sample chambers are usually evacuated to ~30 millitorr until just before the shots are fired. The shot parameters are listed in Table 1. Flyer plates are tantalum unless specified otherwise in parentheses. Hugoniot pressures are calculated following the formulation outlined by Yang et al. [7] assuming 100% crystal density, actual reflected pressures are higher, but non-uniform.

Using reactant Hugoniots as release paths (assuming the main part of the reaction takes place during the late stage of release), the calculated average after-shock temperatures are 2700-3000°C; for shot 1100, because of the inverted mass ratio, the same temperature for shot 1106 is 1200°C. Recovered samples are analyzed with SEM, electron microprobe, and x-ray diffraction. The SEM micrographs of shots for which reaction (1) was studied (Fig. 1) show $Si_3N_4$ is molten under compression, but diamond is intact. Although in some small regions near boundaries of the two reactants decrease in nitrogen $K_\alpha$ x-ray intensity relative to silicon intensity is detected, it is believed to be an effect of geometric absorption by neighboring carbon atoms. All prominent peaks in XRD spectra are identified with diamond/$Si_3N_4$ peaks, therefore the reaction product must be lower than the detection limit (about 2%), and gas production is not enough to account for the sample holder explosions reported by Yang et al. For shot 1066, reaction (2) does not happen, but an interesting feature is discovered

in the sample: quartz grains were apparently molten but anhydrite was not (Fig. 2) despite $SiO_2$'s higher melting point (1500°C vs. $CaSO_4$'s 1400°C).

Table 1: Recovery experiments on three gas-producing reactions

| Starting mix (wt. %) | | Initial density (%) | Shot number | Flyer plate velocity (km/s) | Pressure (GPa) |
|---|---|---|---|---|---|
| $Si_3N_4$ | diamond | | | | |
| 16 | 84 | 65 | 953 | 1.93 | 41.9 |
| 16 | 84 | 70 | 961 | 1.95 | 42.5 |
| 20 | 80 | 66.6 | 962 | 1.97 | 43.0 |
| 16 | 84 | 65.5 | 968 | 1.96 | 42.9 |
| 16 | 84 | 60 | 971 | 1.90 (SS 304) | 43.5 |
| 16 | 84 | 65 | 1095 | 1.90 | 41.2 |
| 16 | 84 | 65 | 1096 | 1.69 | 35.9 |
| 16 | 84 | 65 | 1097 | 1.98 | 43.2 |
| 80 | 20 | 60 | 1100 | 1.82 | 35.8 |
| $CaSO_4$ | $SiO_2$ | | | | |
| 69 | 31 | 83 | 1106 | 1.87 | 34.9 |
| $CaSO_4$ | SiO | | | | |
| 67 | 33 | 89 | 1098 | 2.06 (W) | |
| 67 | 33 | 82 | 1099 | 1.58 | |

In comparison to the inert reactions (1) and (2), reaction (3) is quite active. The bulk reaction product ($CaSiO_4$) yield is estimated at about 30% for shot 1098. Reduction of a factor of 4-5 in sulfur content is seen while calcium is unchanged, and the deficit in atomic number is approximately made up with incorporation of silicon which demonstrates the importance of SiO participation. To find the initiation of the reaction, shot 1099 was conducted at a lower pressure. Clearly separated reaction and no-reaction zones are seen in the SEM micrographs (Figs. 3a, b). Both materials appear to have been molten. In the no-reaction zones, there may be some melting in SiO, especially at grain boundaries, but $CaSO_4$ remains solid during compression. Like quartz, SiO also has a higher melting point (~1700°C) than $CaSO_4$.

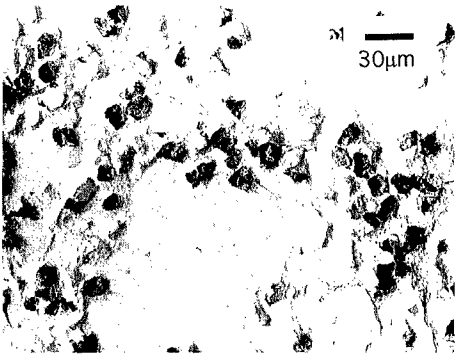



Fig. 1: SEM micrograph of shot 1100. Light area is $Si_3N_4$, voids where diamond grains plucked out indicate weak bonding.

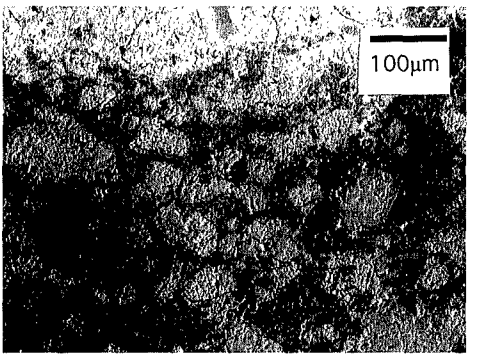



Fig. 2: SEM micrograph of shot 1106. Darker area is quartz, lighter area anhydrite.

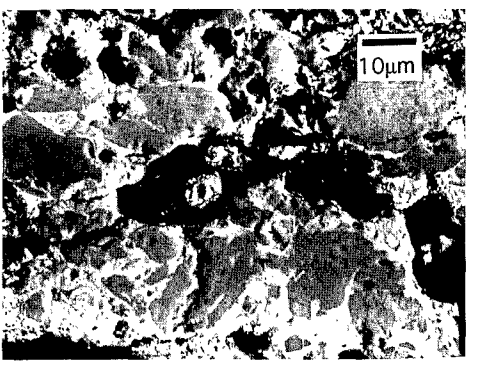



Fig. 3a: SEM micrograph of shot 1099 near sample edge. Dark gray area is SiO, light gray area is ~$Ca_4Si_3SO_{13}$. Black area is epoxy.

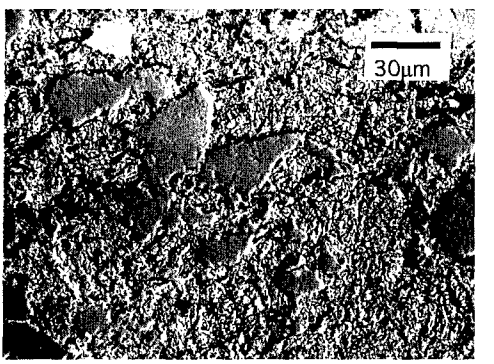



Fig. 3b: Shot 1099 away from edge. Large grains are SiO, fine-grained material is $CaSO_4$.

The SEM electron beam spot is less than 1μm, but the dimension of x-ray emitting volume could be larger due to electron scattering in the sample. A "fuzziness" function is assumed to convolve with the "true" chemical composition to give the observed composition. The function form is taken to be

$$f(x) = \frac{1}{\sqrt{\pi}a} e^{-x^2/a^2} \qquad (5)$$

$$\int_{-\infty}^{\infty} f(x)dx = 1 \qquad (6)$$

where 2a is a measure of distance scale of the SEM analytic resolution. A comparison was made between a pressed boundary of calcium sulfate and quartz and calculation (convolution of the above function and a step function), a $\simeq 0.53$ μm was found to provide the best fit. Denote g(x) as the ratio of (Ca+S)/O, and the general solution of one dimensional diffusion is

$$g(x) = \frac{1}{2}\,\mathrm{erfc}\,(x/b) \qquad \text{when } x>0, \qquad (7)$$

for the boundary condition $g(x \leq 0) = 1/2$.

A fit to the shocked sample profile (solid curve) (convolved with f(x)) gives the diffusion length $b \simeq 1.5$ μm (Fig. 4).

The molar ratio experimentally observed resulting from devolatilization shows some scatter. For simplicity, we assume an average of 20% devolatilization in the $x > 0$ half space, in which the ratios of S/O, Ca/O are:

$$g_S(x) = 1/2 \times \frac{0.8}{1.0 + 0.8}\,\mathrm{erfc}(x/b), \qquad (8a)$$

$$g_{Ca}(x) = 1/2 \times \frac{1}{1.0 + 0.8}\,\mathrm{erfc}(x/b), \qquad (8b)$$

$$g_S + g_{Ca} = g(x) \qquad (9)$$

$$(S/Ca)(x) = \frac{\int_{-\infty}^{\infty} g_S(x')e^{-(x'-x)^2/a^2}dx'}{\int_{-\infty}^{\infty} g_{Ca}(x')e^{-(x'-x)^2/a^2}dx'}, \qquad (10)$$

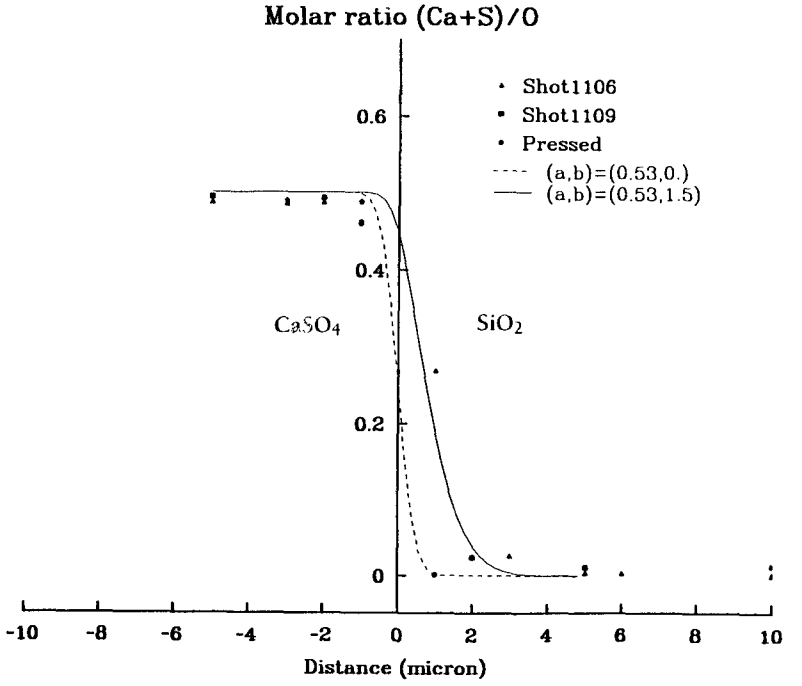



Fig. 4. Chemical composition versus distance as determined with a JEOL Scanning Electron, Camscan #2, Microscope with Tracor Model Th 3/54-6901 energy dispersive analyser. Molar ratio of (Ca+S)/O versus distance across $CaSO_4$-$SiO_2$ interfaces. Length parameters a and b are indicated for dashed and solid curves. The dashed curve is theoretical curve Eq. 5 fit to data obtained from a cold pressed $CaSO_4 \rightarrow SiO_2$ interface. The solid curve is the convolution of Eqs. 5 and 7 for shock-induced reaction (2) occuring across $CaSO_4$ - $SiO_2$ interfaces in two shock recovery experiments.

Moreover, we observe an indication of S loss as the ratio of S/Ca decreases upon going into the $SiO_2$ from the $CaSO_4$-$SiO_2$ interface.

Overall, devolatilization, DV, the mass fraction of total $CaSO_4$ is given by

$$DV = \frac{3\int_0^\infty (g_{Ca} - g_s)dx}{g_{Ca}(x \leq 0)R}, \qquad (11)$$

where R is the average anhydrite grain size ($\simeq$ 100 μm). The factor 3 takes into account the three dimensional effect. Evaluation of the formula yields DV = 0.006.

Gibbs' formation energy calculations for reactions (1) and (2) give initiation temperatures of 1800°C and 900°C, respectively, and reaction (3) is allowed under STP or higher temperatures.

## 3. $GeO_2$ PHASE TRANSITION FROM GLASS TO RUTILE STRUCTURE

During the last two decades a number of experimental shock wave studies of silicates demonstrated that large (typically 30%) increases in density due to phase transitions occurred during compression. Upon release, much of the mechanical work (energy) expended in compressing material within the phase transition regime remains irreversibly in the material (Figs. 5 and 6). Both in the regime of phase change, the so-called mixed phase regime and the stress regime where the material has been completely driven into the high pressure phase gives rise to excess stress wave attenuation in silicate material [5]. We initially discuss shock properties of quartz because a considerable amount of research has been done in this area. However, we believe the shock pressures in $SiO_2$ are too high to be of ballistic interest, whereas $GeO_2$ transforms in a stress range achievable at ballistic velocities.

The fraction of the shock wave energy remaining in material upon isentropic release is given by

$$f' = (E_{RH} - E_{Rel}) / E_{RH} \qquad (12)$$

In Eq. 12, $E_{RH}$ is the usual Rankine-Hugoniot internal energy increase across a shock front and $E_{Rel}$ is the internal energy transformed to kinetic energy upon isentropic release from high shock to zero pressure. Explicitly,

$$E_{RH} = P_1 (V_0 - V_1) / 2 \qquad (13)$$

and

$$E_{Rel} = \int_0^{P_1} P dV|_{isentrope} \qquad (14)$$

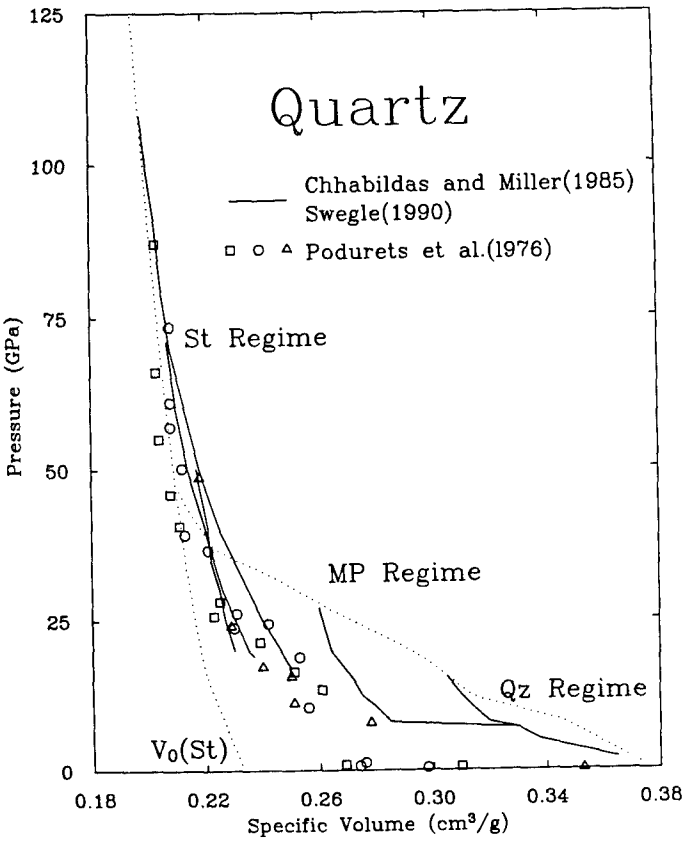



Fig. 5. Pressure-volume data for quartz and related release paths. Locus of compression states define Hugoniot in 3 regimes: Qz is quartz regime, MP is quartz plus stishovite regime, and St is stishovite or high pressure phase regime. Release paths are indicated. Initially steep unloading and then flattening at ~10 GPa gives rise to very hysteretic behavior (after Sekine et al. [4]).

TJA91115SFD

where $P_1$ is the shock pressure, $V_1$ is specific volume, and $V_0$ is the initial (unshocked) specific volume of the material. Using a model in which successively greater quantities of high pressure phases are induced with shock pressure upon shocking $SiO_2$ (either) starting with quartz or fused quartz as a lower pressure phase, complete transformation to the high pressure phase, stishovite, is believed to occur at 30 GPa. As shown in Fig. 5, upon unloading from the MP regime, the shocked material initially unloads as a mixture of high pressure and low-pressure phase. Upon reaching a pressure of ~8

GPa transformation to low density (high specific volume) quartz or glass occurs. As indicated in Fig. 6, the fraction of shock internal energy deposited in the material is 0.4 to 0.7 of the total energy in going from 20 to 100 GPa.

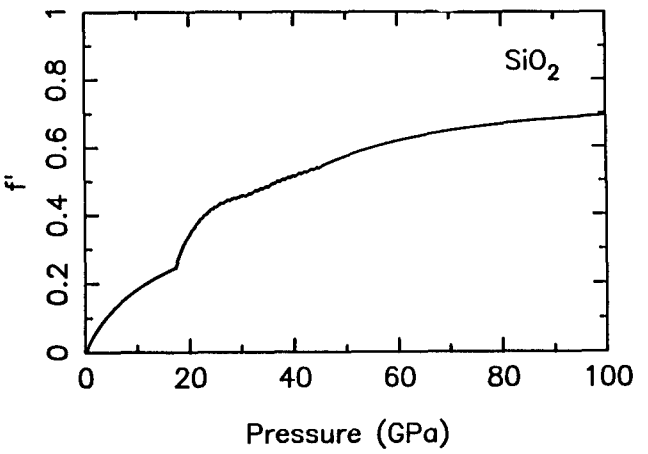



Fig. 6. Fraction f' of Rankine Hugoniot energy irreversibly deposited in silicate as a function of shock pressure. TJA93013SFD

We believe $SiO_2$ can be demonstrated to be a very attenuative material for hypervelocity impact because of the strong irreversibility of the $SiO_2$ quartz to stishovite (rutile) transition. However, that transition occurs at 14 GPa, a pressure achieved only in a small volume (on the order of the projectile volume) at ordnance speeds (of 1 km/sec). In contrast, $GeO_2$, which has a very similar phase diagram, (Ge is immediately below Si in the standard periodic table of the elements) this transition has been demonstrated to occur at ~4 GPa [3] (Fig. 7). It is expected that $GeO_2$, like $SiO_2$, will be very attenuative for all the same reasons in the ballistically important 4-10 GPa stress range.

Note that upon achieving pressures of 20 GPa, the $GeO_2$ glass (3.6 g/cm$^3$) achieves density of rutile structure (6.3 g/cm$^3$).

Acknowledgments: Supported under DAAL0G-92-G-0218 and DAAL03-92-G-0192. Contribution # 5293, Division of Geological and Planetary Sciences.

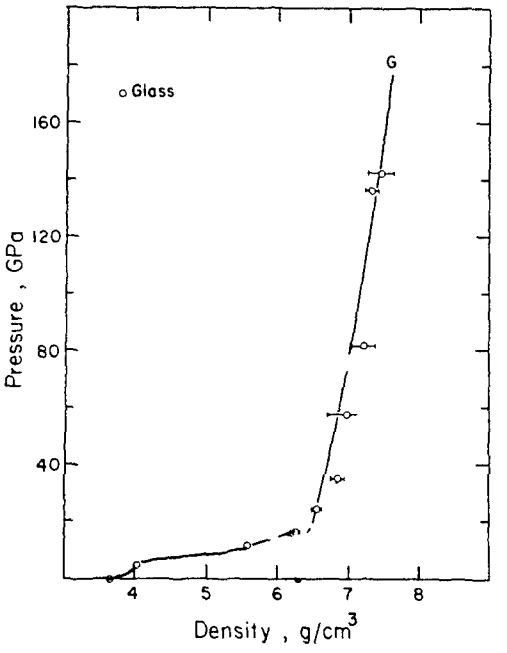



Fig. 7. Hugoniot data for vitreous $GeO_2$ in density-pressure space. Previous data of Jackson and Ahrens [3] do not resolve expected difference between dynamic yield stress (HEL) and onset of phase change at ~4 GPa. TJA93015SFD

REFERENCES


1 Boslough, M. B., A thermochemical model for shock-induced reactions (heat detonations) in solids, *J. Chem. Phys.*, *92*, 1839-1848, 1990.

2 Erskine, D. J., and W. J. Nellis, *Nature*, *349*, 317, 1991.

3 Jackson, I., and T. J. Ahrens, Shock-wave compression of vitreous and rutile-type $GeO_2$: A comparative study, *Phys. Earth Planet. Int.*, *20*, 60-70, 1979.

4 Sekine, T., A. M. Rubin, T. S. Duffy, and T. J. Ahrens, Shock compression and isentropic release of granite, *Geophys. J. Intl.*, submitted, 1993.

5 Swegle, J. W., Irreversible phase transition and wave propagation in silicate materials, *J. Appl. Phys.*, *68*, 1563-1579, 1990.

6 Tan, H., and T. J. Ahrens, Shock-induced polymorphic transition in quartz, carbon, and boron nitride, *J. Appl. Phys.*, *67*, 217-224, 1990.

7 Yang, W., G. M. Bond, H. Tan, T. J. Ahrens, and G. Liu, Dynamic consolidation of super hard materials, *J. Mater. Res.*, *7*, 1501-1518, 1992.

# On the Strain and Strain-Rate Dependence of the Fraction of Plastic Work Converted to Heat and Full Field Measurements of the Dynamic Deformation Field Around a Growing Adiabatic Shear Band

**Dr. James J. Mason, Dr. Ares J. Rosakis and Dr. G. Ravichandran***

*California Institute of Technology, 105-50, Pasadena, CA 91125*

**Abstract**

A summary of two experimental measurements of parameters pertaining to adiabatic shear band formation is made. First, the rate of conversion of plastic work to heat in metals is examined using a Kolsky (split Hopkinson) pressure bar and a high-speed infrared detector array. Several experiments are performed, and the work rate to heat rate conversion fraction, the relative rate at which plastic work is converted to heat, is reported for 2024 aluminum and Ti-6Al-4V titanium alloys undergoing high strain and high strain rate deformation. The functional dependence of this quantity upon strain and strain rate is also reported for these metals. This quantity represents the strength of the coupling term between temperature and mechanical fields in thermomechanical problems involving plastic flow such as shear band formation. Next, the method of Coherent Gradient Sensing (CGS) is used to record the deformation field around an adiabatic shear band emanating from a pre-crack or pre-notch tip in C-300 steel loaded dynamically in mode-II. The experimental fringe patterns are fitted to the theoretical Dugdale crack deformation field by using a least squares fitting scheme. This results in values for the shear band length and the average shear stress acting on the shear band as functions of time. The shear stress on the shear band decreases from 1.6 GPA at initiation to 1.3 GPa during this propagation. An estimate of the stress-strain behavior of the shear band material is made.

## 1. Introduction

The formation of adiabatic shear bands has recently received renewed attention following the experimental measurements of the temperature rise in adiabatic shear bands by Duffy (1984). In the past ten years these measurements have helped motivate a considerable amount of modelling of adiabatic

shear band growth which has recently appeared in the open literature. Without presenting an extensive review, it is helpful to recall some of the salient and common features of the many models that have been made available.

Commonly, the formation or growth of an adiabatic shear band is modelled as the competition between thermal softening and strain and/or strain-rate hardening of a material under shear loading. Usually an approximate model of thermal softening is added to the constitutive equation for a material, the temperature is treated as an additional unknown and the heat conduction equation is added to the field equations. This additional equation provides a link between mechanical deformation fields and the temperature field, $T(\mathbf{x}, t)$, and is given by

$$k\nabla^2 T - \dot{T} = -\frac{\beta \boldsymbol{\sigma} \cdot \dot{\boldsymbol{\epsilon}}^p}{\rho c_p} \tag{1}$$

where the dot refers to differentiation with respect to time, $k$ is the thermal conductivity, $\rho$ is density, $c_p$ is the heat capacity, $\beta$ is defined below, $\boldsymbol{\sigma}$ is the stress, and $\dot{\boldsymbol{\epsilon}}^p$ is the plastic strain-rate. The term on the right represents heating due to irreversible plastic deformation (Taylor and Quinney, 1934; Bever et al., 1973) If adiabatic conditions prevail, then the heat conduction equation takes a more simple form, i.e.;

$$\rho c_p \dot{T} = \beta \boldsymbol{\sigma} \cdot \dot{\boldsymbol{\epsilon}}^p \tag{2}$$

where

$$\beta = \frac{\rho c_p \dot{T}}{\dot{W}^p}. \tag{3}$$

and

$$\dot{W}^p = \boldsymbol{\sigma} \cdot \dot{\boldsymbol{\epsilon}}^p. \tag{4}$$

Note that even for simple adiabatic conditions it is necessary to know the material parameters such as $\beta$, the work rate to heat rate conversion fraction, before useful solutions to shear band problems can be obtained. Also note that the constitutive behavior of the shear band material should be accurately obtained before the results of models can be compared to experimental measurements.

The net effect of the assumptions of the shear band model is the introduction of a mathematical mechanism by which instabilities in the deformation can be formed. When thermal softening is greater than strain and/or strain-rate hardening, the material deforms, heats and becomes softer. Then, further deformation occurs due to the lower strength generating more heat which in turn softens the material more producing a "self-feeding" mechanism by which an instability is formed. The purpose of this work is to examine both the mechanism by which plastic work is converted to heat, or, more specifically, the material parameter $\beta$, as well as the deformation field around an adiabatic shear band as it forms in order to extract more information about the shear band formation process itself.

## 2. Experimental Apparatus

### *2.1 The Conversion of Plastic Work to Heat*

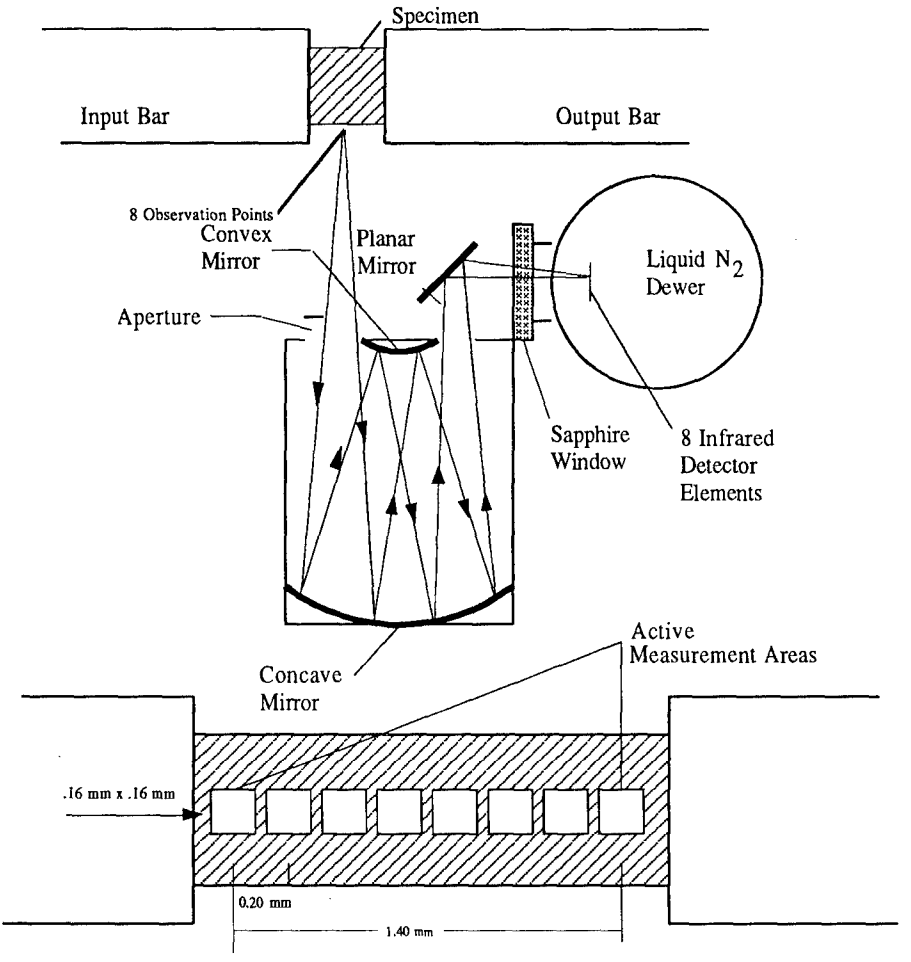
To investigate the conversion of plastic work to heat, the Kolsky pressure bar is used to deform the materials at high strain-rates ($\approx$1000–3000 $s^{-1}$) in this investigation. By assuming that the specimen deforms *homogeneously*, the stress, strain-rate, strain and average velocity of the deforming specimen can be determined from the recorded incident, reflected and transmitted pulses in the Kolsky bar (Kolsky, 1949). For further details of the pressure bar technique the reader is referred to Lindholm (1965) and Follansbee (1985).

The temperature rise in the Kolsky pressure bar experiments is recorded using a stationary, focused, high-speed, infrared (IR) detector array. A schematic of the apparatus is shown in Figure 1. The detectors measure the amount of incident IR radiation over a range of wavelengths and a calibration curve is used to determine temperature from the voltage output. The detectors are calibrated by heating a sample—with controlled surface finish—of the specimen material to a known temperature while simultaneously recording the detector output voltage. The calibration procedure precludes the need for any knowledge of the specimen emissivity and, thus, greatly simplifies the temperature measurement procedure. Calibration curves are evaluated for every material investigated, and the resulting curves are invariably qualitatively very similar to each other. Further details of the high-speed infrared measurement technique can be found in Duffy (1984) and in Zehnder and Rosakis (1991 and 1993) and Mason (1993).

Assuming that homogeneous deformation of the specimen occurs, one may easily calculate the plastic work rate density from the Kolsky bar using equation (4). By measuring the temperature and differentiating it with respect to time, $\dot{T}(t)$ is estimated, and by assuming that adiabatic conditions apply during the experiment, $\beta$ is calculated from Eq (3). The density and heat capacity (with its dependence upon temperature) may be found in the literature (e.g., Aerospace Structural Materials Handbook, 1985). Fortunately, it is seen that the heat capacity for each of these materials does not change significantly over the range of material temperatures anticipated during the experiments (20-130°C).

### *2.2 The Formation of Shear Bands*

Kalthoff (1987) and Kalthoff and Winkler (1987) have observed the formation of adiabatic shear bands at the tip of dynamically loaded, stationary, pre-manufactured notches in plates made of C-300 steel. The pre-manufactured notches are loaded dynamically in nearly pure mode-II loading conditions by an asymmetric impact in the area between the two pre-notches on the edge of the plate. See Figure 2(a). When sufficient impact velocity




(Specimen, bars and detector array not drawn to scale.)

FIGURE 1 A schematic representation of the high-speed I-R detector array focussed on a specimen in a Kolsky pressure bar. The detector array size and orientation as focussed on the specimen is also shown.

is used, an adiabatic shear band is formed directly ahead of the pre-notch as shown schematically in the figure. In the work described here, a similar configuration is used. This configuration involves the dynamic asymmetric loading of only *one* pre-notch and is schematically shown in Figure 2(b). The use of only one pre-notch provides a simple loading geometry by which one may observe the formation of adiabatic shear bands. The method of Coherent Gradient Sensing (CGS) is used here in conjunction with high speed photography to measure the deformation field around an adiabatic shear band as it forms. For the sake of brevity the method may be described as an interfer-

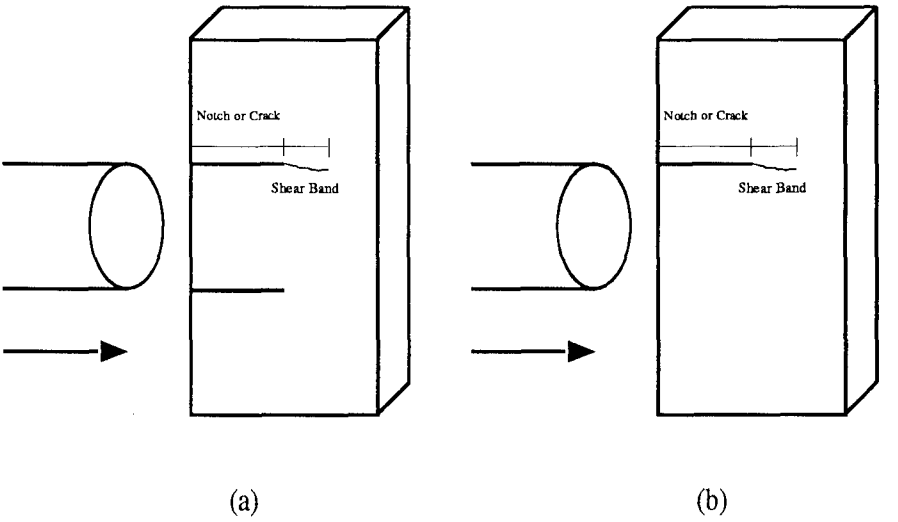



FIGURE 2 (a) The loading geometry observed by Kalthoff (1987) and Kalthoff and Winkler (1987) to generate shear bands in C-300 steel at a pre-notch or pre-crack tip. (b) The modified pre-notched geometry used in the present investigation.

ometer producing fringe patterns that are equivalent to a contour map of the hydrostatic stress in plane-stress loading situations. The fringe patterns may be digitized and fit to known, expected solutions to produce measurements of the important parameters of the experiment, one example being the stress intensity factor in dynamic fracture experiments. The quality of the fits gives indication of the validity of any assumptions made in the analysis. Complete discussions of the method of CGS may be found in Tippur et al. (1989a) and (1989b) and Rosakis (1993).

It is proposed here that the shear band formation at a dynamically loaded mode-II pre-notch may be modelled by the Dugdale strip yield model. In such a model the shear band is assumed to be a one-dimensional line of yielded material extending directly ahead of the stationary pre-notch or pre-crack with a uniform shear stress acting upon it. Implicit in this approach to modelling are a number of assumptions about the mechanisms of the nucleation and growth of adiabatic shear bands. For example, it is assumed, among other things,that the length of the shear band is determined by the far field $K_{II}^{d}(t)$ that is acting on the pre-notch (small scale yielding is implied and the magnitude of the shear stress on the yielded zone is chosen to nullify the highest order stress singularity at the shear band tip). This assumption is

perhaps the most restrictive, however it is useful because it gives a relation between the stress intensity factor, the shear stress on the yield zone and the length of the yield zone. In addition it is also motivated by numerical investigations of dynamic shear band growth [Lee (1990)] where no singularity is found to exist at the growing shear band tip.

Although the assumptions and approximations of the model are somewhat limiting, the model is used here as a first attempt at analyzing the results, and it should be emphasized that the quantitative conclusions are reported as *first estimates* .

## 3. Results and Discussion

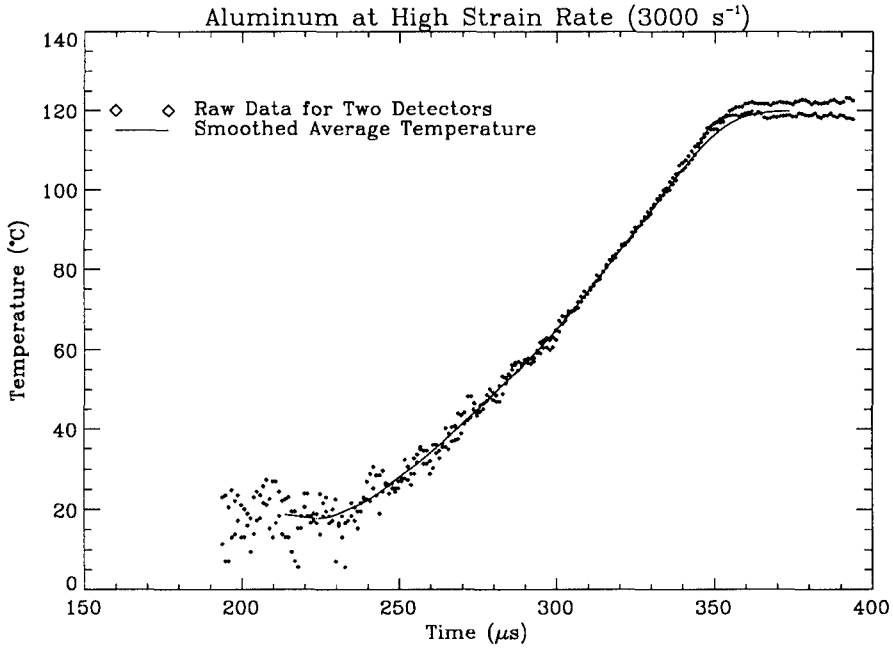



FIGURE 3 The temperature data for 2024 aluminum. The solid line represents the smoothed function which is differentiated to calculate $\beta$.

### *3.1 The Conversion of Plastic Work to Heat*

The measured temperature for 2024 aluminum deforming in the Kolsky bar is plotted in Figure 3. The most significant difficulty in calculating $\beta$ is due to the problems associated with differentiation of the measured temperature. Differentiation of a noisy signal has inherent instabilities, and usual numerical schemes do not work because they are formulated for numerically exact functions. For that reason the measured temperature is smoothed before

differentiation. An example of the smoothed temperature signal may be seen in Figure 3 plotted with both noisy signals. Multiplying the derivative of the smoothed temperature by $\rho c_p$ and using equation (3) results in the evaluation of $\beta$ as seen in Figure 4. It can be seen in the figure that $\beta$ for 2024 aluminum is strongly strain dependent; initially the relative rate at which work is converted to heat is approximately 0.5 rising with strain to the traditionally accepted 0.85-1.00 range for metals (Taylor and Quinney, 1934; Bever et al., 1973).

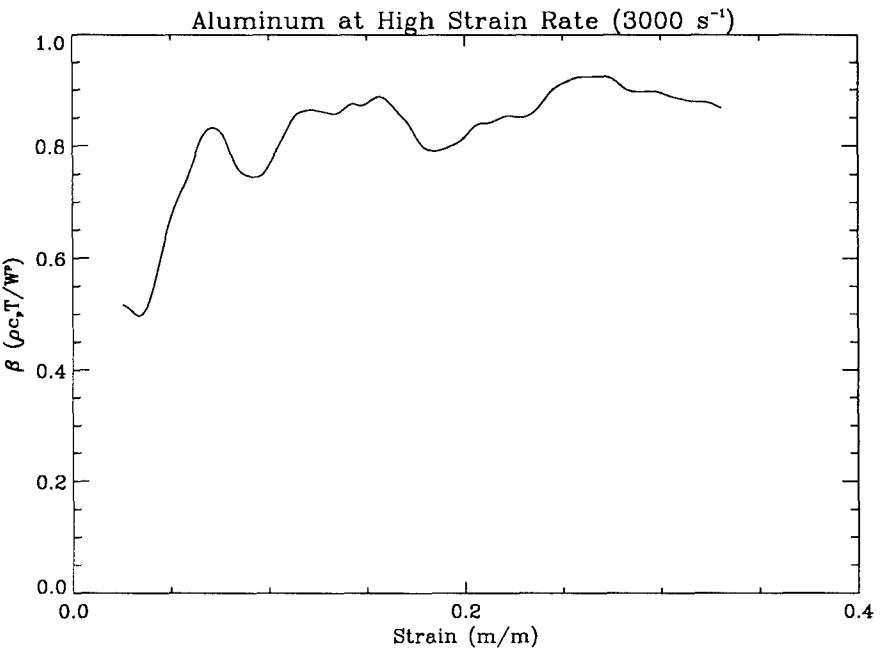



FIGURE 4 The work rate to heat rate conversion fraction for 2024 aluminum.

In contrast, the results of measurements of $\beta$ in Ti-6Al-4V are seen in Figure 5. Note that the form of $\beta$ for Ti-6Al-4V titanium is different than that of 2024 aluminum. Since quasi-static measurement of the stress-strain behavior of Ti-6Al-4V titanium by the authors shows this alloy to be strain-rate sensitive while 2024 is not strain-rate sensitive over this range of strain-rates, this difference between the behavior of Ti-6Al-4V and the behavior of 2024 aluminum—in the same strain-rate range—may be connected to the strain-rate sensitivity of the Ti-6Al-4V titanium. It is known that twinning occurs in titanium alloys at high strain rates (Follansbee and Gray, 1989); that type of change in deformation mechanism may explain the observed difference in the conversion of plastic work to heat. Further work is needed to shed more light on this issue.

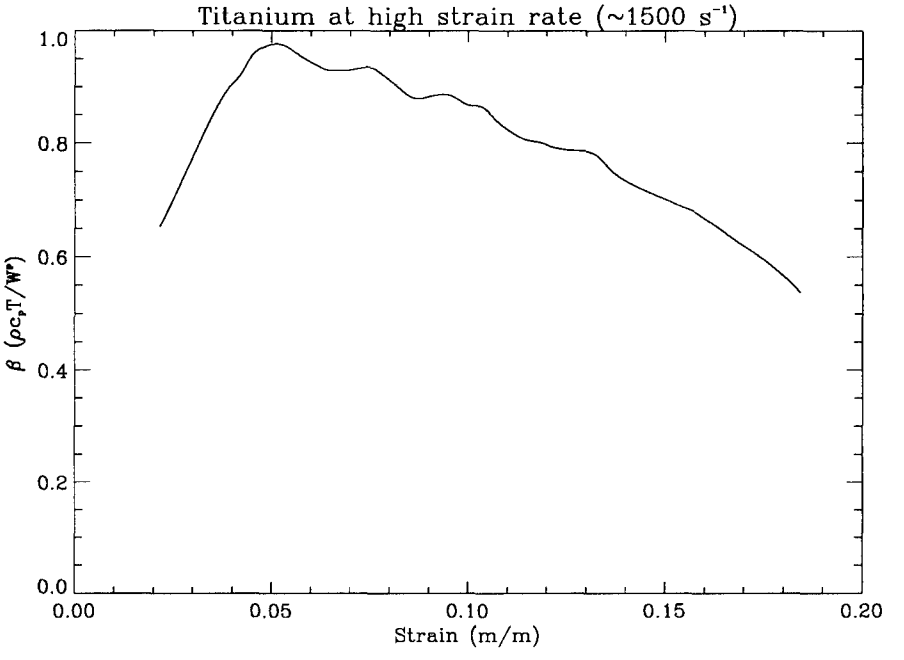
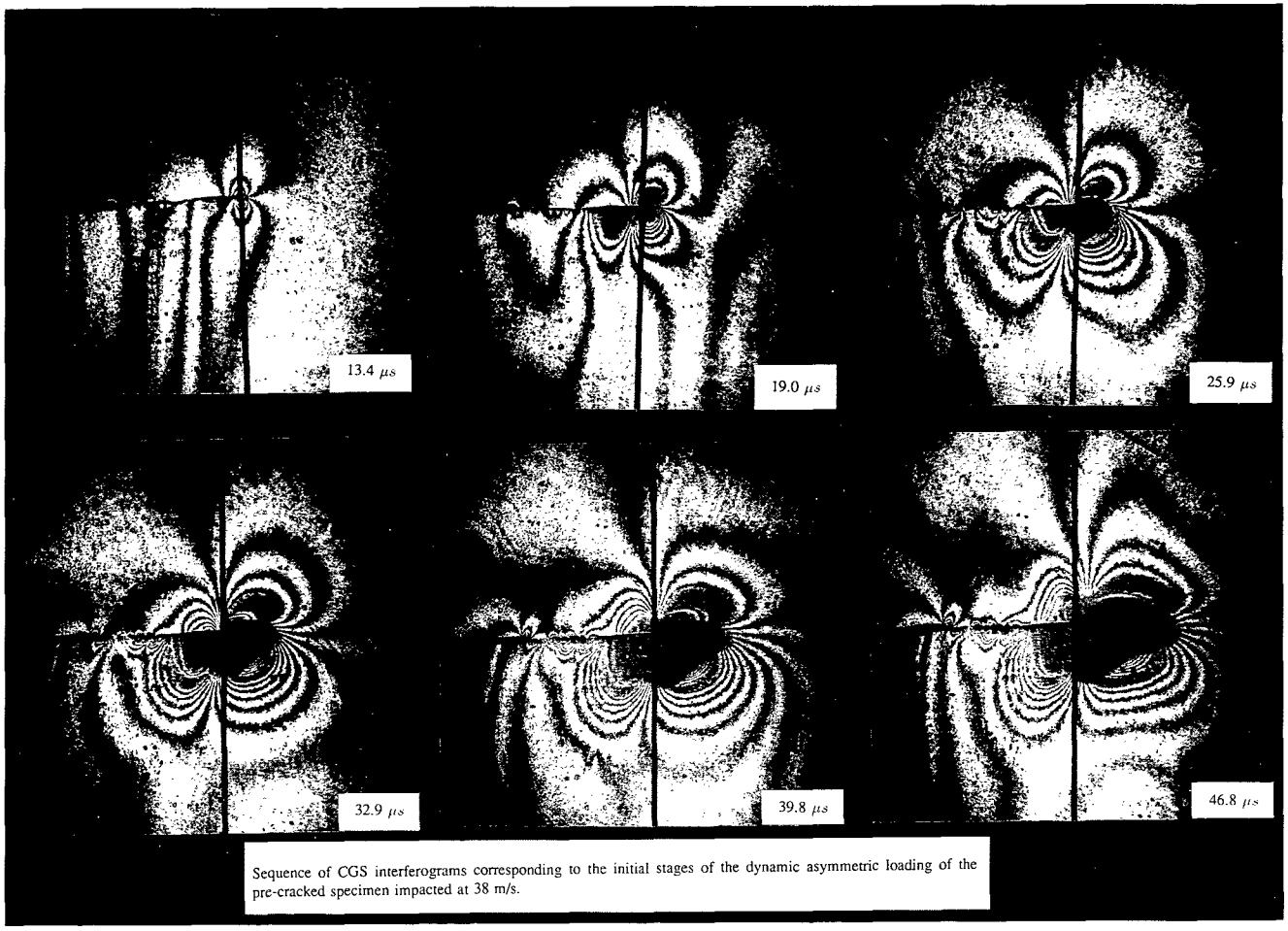



FIGURE 5 The work rate to heat rate conversion fraction is calculated for Ti-6Al-4V titanium using the average of the temperature of the two detectors.

### *3.2 The Formation of Shear Bands*

Fringe patterns are recorded using high speed photography after the impact of the plate and the shear band formation is recorded in successive stages of growth after the pre-crack tip is loaded as shown in Figure 6. For the sake of brevity the actual photographs are not shown here (see Mason, 1993). Fits of the theoretical fringe patterns to recorded fringe patterns were performed assuming that $\mathrm{K}_{\mathrm{II}}^{\mathrm{d}}(\mathrm{t})$ followed the solution of Lee and Freund (1990). An example of one of the fits (performed at 31.5 $\mu s$) can be found in Figure 7. Acceptable agreement between the theoretical Dugdale field and the experimentally measured field is seen.

The results of the fit for the shear stress on the shear band, $\tau_0(t)$, and for the shear band length, $R_{sb}(t)$ are plotted in Figure 8. The shear band length increases with time, and a linear fit of the growth provides an estimate of the shear band growth velocity of 320 m/s. The initiation occurs at approximately 26 $\mu s$ after impact, well within the domain of the Lee and Freund (1990) solution. At this time the stress intensity is roughly 140 $MPa\sqrt{m}$. The shear stress increases initially with time from 0.6 GPa to 1.6 GPa before the shear band initiation. It is assumed that this effect is due to increasing load on the pre-crack faces that are already in contact. After the shear band is initiated, the shear stress decreases from 1.6 GPa to 1.3 GPa. This type of behavior is expected since thermal softening is the acting mechanism by which the




Sequence of CGS interferograms corresponding to the initial stages of the dynamic asymmetric loading of the pre-cracked specimen impacted at 38 m/s.

FIGURE 6

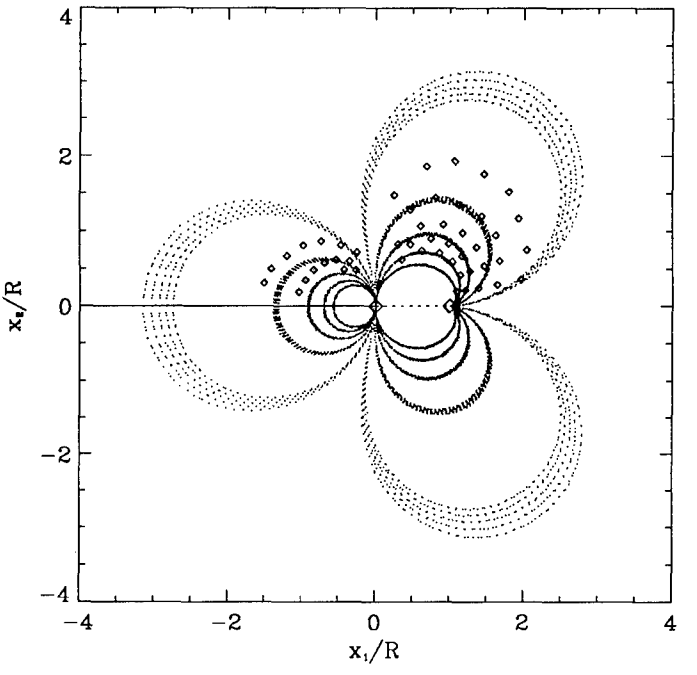



FIGURE 7 A check of the fitting procedure for t=31.5 $\mu s$. Data points should fall alternately on light and dark fringes in the figure. It can be seen that the fit is reasonably good for the forward fringe with less agreement found for the rear fringe.

shear band forms. As the shear band grows it is expected that the shear stress decreases due to thermal softening. The value of the shear band length obtained from the fit is compared to the estimated shear band length as measured by the authors directly from interferograms. This estimated length is found by qualitatively comparing the recorded CGS fringe patterns to the predicted fringe patterns. Acceptable agreement is seen.

The stress-strain behavior of the material in the shear band may be estimated by using the reported stress in Figure 8 and by estimating the strain from the crack opening displacement. Assuming that the shear band has fixed thickness, $t_{sb}$, and that the shear displacement decreases linearly from the crack opening displacement to zero along the length of the shear band, the average strain is given as

$$\epsilon = \frac{K_{II}^2}{2E\tau_o t_{sb}}.$$

This combined with the known values of shear stress in Figure 8gives a stress-strain relationship for the shear band material For comparison, the constitutive behavior of this material was measured using the Kolsky bar and are shown

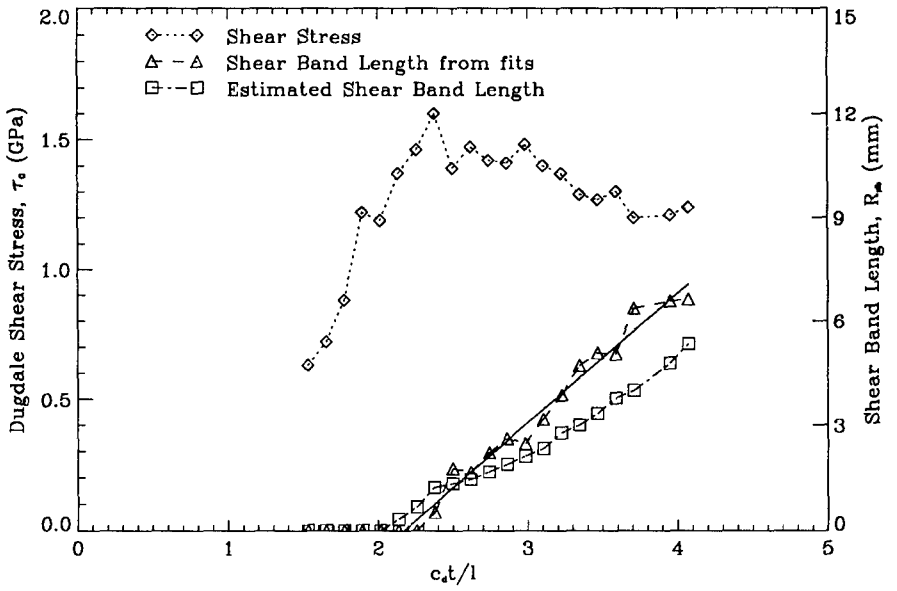



FIGURE 8 A plot of $\tau_0(t)$ and $R(t)$ as found from the fitting procedure. The shear band length is compared to the length as estimated by comparing the fringe patterns to the theoretical fringe pattern. $l \approx 2$ inches.

in Figure 9 along with the stress-strain behavior of the material in the shear band. When necessary the equivalent *shear* stress is plotted using the Von Mises criterion. Good agreement is found between the measured shear stress for the shear band emanating from a pre-crack tip and the measured shear stress for a shear band formed in uniaxial dynamic compression. Note that in the high strain rate tests using the Kolsky bar, shear bands formed in the specimen resulting in evidence of softening in the measured stress-strain response.

## 4. Conclusions

For nominally strain-rate independent solids like 2024 aluminum, the dependence of $\beta$ upon strain at high strain-rate (1000–3000 $s^{-1}$) roughly follows the dependence expected at low strain-rates. However, strain-rate sensitive Ti-6Al-4V titanium exhibited interesting behavior at high strain-rates. The measured dependence of $\beta$ upon strain for this material did not follow the qualitative trends observed in strain-rate insensitive 2024 aluminum. This difference may be connected to the strain-rate sensitivity of the material and twinning at high strain-rate. Further investigation is required.

The formation of a shear band at the tip of a pre-crack loaded dynamically in mode-II has been recorded using high-speed photography and the

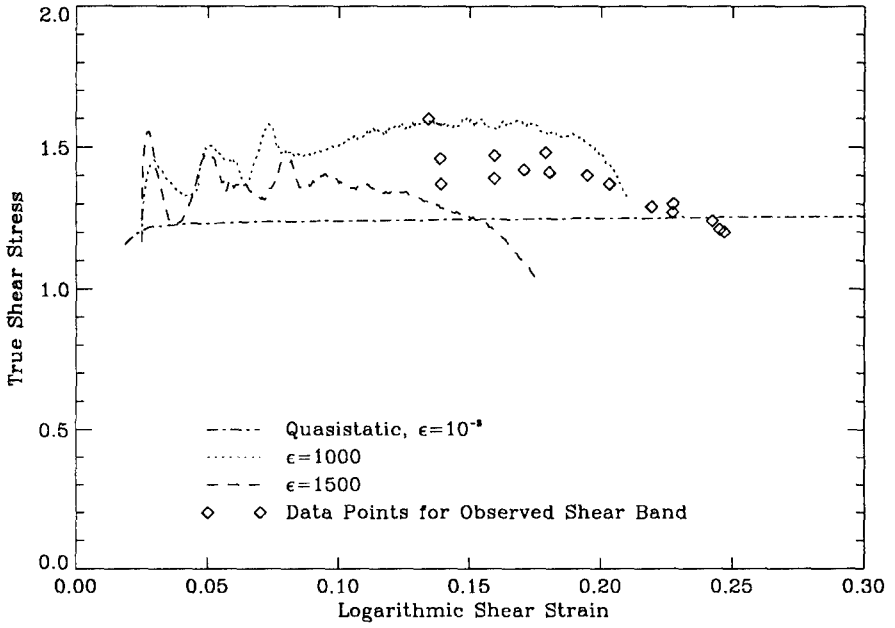



FIGURE 9 The constitutive behavior of C-300 at various strain rates as measured in compression. High strain rate data was measured using a Kolsky bar apparatus. The data plotted for an observed shear band at a crack tip is seen to agree well with the Kolsky bar experiments.

method of CGS is used to examine the stress field around the pre-crack tip. A fit of the digitized experimental fringe field is made to the Dugdale crack solution with the shear stress on the shear band as a variable parameter. The stress intensity factor is assumed to follow the model of Lee and Freund (1990). The results of the fits are used to extract the time evolution of the shear stress on the shear band and the length of the shear band with the following results:

It is seen that the shear band initiates within the regime of the Lee and Freund (1990) solution for this problem. However, it does not initiate at the first loading of the pre-notch tip. There is a time delay of approximately 11 $\mu s$ before shear band growth is observed. The shear band initiates when $\mathrm{K}_{\mathrm{II}}^{\mathrm{d}} = 140 MPa\sqrt{m}$.

The shear band propagates into the material with a speed of roughly 320 m/s while at the same time the shear stress on the shear band decreases from 1.6 GPa at initiation to 1.3 Gpa. The arrest of the shear band is not recorded.

The stress-strain relationship for the shear band material is estimated, and it agrees well with the Kolsky bar test of the same material. Softening is observed in the material as plastic work increases.

**Acknowledgements**

The support of the Army Research Office under grant # DAAH04-93-G0037 and the support of the Office of Naval Research under grant # N00014-90-J-1340 is greatly appreciated.

**References**

1. M.B. Bever, D.L. Holt and A.L. Titchener, *Prog. Mat. Sci.,* **17,** 1
2. J.Duffy (1984), *Mechanics of Material Behavior,* G.J. Dvorak and R.T. Shields, eds., Elsevier Science Pub. B.V., Amsterdam, 75
3. P.S. Follansbee (1985), *Metals Handbook; 9th Edition,* American Society for Metals, Metals Park OH, **8,** 198
4. P.S. Follansbee and G.T. Gray, III (1989), *Met. Trans. A,* **20A,** 863
5. J.F. Kalthoff (1987), in: *SPIE Vol. 814 Photomechanics and Speckle Metrology,* 531
6. J.F. Kalthoff and S. Winkler (1987), in: *Impact Loading and Dynamic Behaviour of Materials,* C.Y. Chiem, H.-D. Kunze and L.W. Meyer, eds., Verlag, Vol. 1, 185
7. H.Kolsky (1949), *Proc. Royal Soc. B,* **62,** 676
8. Y.J. Lee (1990), Ph.D. Thesis, Division of Engineering, Brown University, Providence, RI
9. Y.J. Lee and L.B. Freund (1990), *J. Applied Mechanics,* **57,** 104
10. U.S. Lindholm (1964), *J. Mech. Phys. Sol.,* **12,** 317
11. J.J. Mason (1993), Ph.D. Thesis, California Institute of Technology, Pasadena CA
12. A.J. Rosakis (1993), in *Experimental Techniques in Fractures III,* J.S. Epstein, Ed., Society for Experimental Mechanics, Inc., Bethel, CT, Ch. 10
13. G.I. Taylor and M.A. Quinney, *Proc. Roy. Soc. London A,* **143,** 307
14. H.V. Tippur, S. Krishnaswamy and A.J. Rosakis (1989a), Caltech SM-Report 89-1, (*Int. J. Fracture,* **48,** 193)
15. H.V. Tippur, S. Krishnaswamy and A.J. Rosakis (1989b), Caltech Report SM89-11, (*Int. J. Fracture,* **52,** 91).

# Considerations in the Experimental Determination of Constitutive Parameters for Finite Strain Plasticity

Dr. Norris J. Huffington, Jr.
Weapons Technology Directorate
U.S. Army Research Laboratory
Aberdeen Proving Ground, Maryland 21005-5066

## ABSTRACT

Various experimental procedures for measurement of quasi-static constitutive parameters for finite strain elastoplasticity are discussed in relation to counterpart finite element analyses of specimen deformation. It is concluded that the usefulness of such analyses is limited by the assumptions made in the formulations of current computer codes.

## INTRODUCTION

There remain significant difficulties in the measurement of elastoplastic parameters for use in analysis of finite straining of relatively ductile materials. Ideally, one would prefer use of tests in which a single stress component (at a time) could be varied as a function of an associated strain component, during which measurements of applied loads and corresponding deformations could be made on a test section of reasonable size and in which a state of homogeneous stress exists. However, conventional uniaxial tests have shortcomings which limit their usefulness. Tension tests are limited to relatively modest strains by the inception of necking. Compression testing involves overcoming friction problems on end surfaces in order to obtain uniform axial stresses on these surfaces and avoid "barreling" (or interrupted testing of re-machined specimens). The torsion test is attractive in that shearing strains of 600% and greater have been reported for thin-walled tube specimens, but also presents experimental and interpretational problems which will be discussed.

It may be recalled that Poynting [1] studied finite torsion of wires while Swift [2] performed tests on solid and hollow rods. Both reported an elongation of their specimens under finite twisting. Subsequently, Lindholm and Johnson et al. [3,4] employed a torsion specimen of the form shown in Figure 1, in particular for determination of material parameters for use with the Johnson-Cook [5] constitutive model. White [6] recently published a report in which the limitations on use of elementary analysis for interpretation of torsion test results were assessed by comparison with finite element calculations. It was found necessary to apply a correction factor to the rotation of the grips to allow for the deformation which occurs in the shoulder section of the Lindholm-type specimen. Unfortunately, this factor is a function of the specimen geometry and the flow stress function. Also, finite element calculations have revealed a tendency for tubes to decrease in diameter as the twist increases. When this is inhibited by the massive shoulder regions of the Lindholm specimen, longitudinal bending develops. Another concern with torsion testing of thin-walled tubes is the possibility of torsional buckling. To mitigate these problems, the gauge length of the Lindholm specimen is made quite short, making accurate optical measurements of strains almost impossible. Perhaps a more serious drawback is that there is essentially no portion of the gauge section which is in a homogeneous stress state.

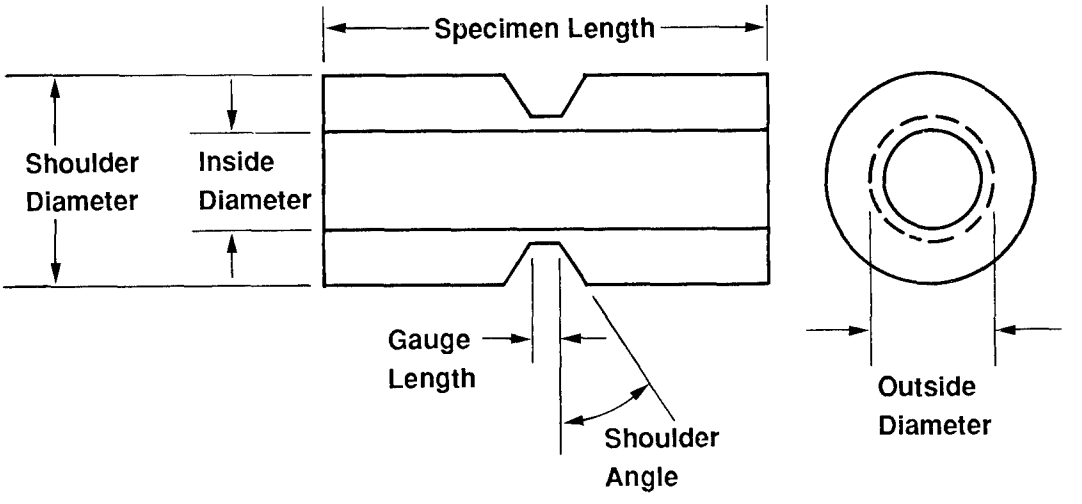



Figure 1. Geometry of the thin-walled torsion specimen.

In an effort to circumvent at least some of the problems cited above, the author has studied designs of torsion specimens in which a longer

gauge section can be employed, but which would have to be thick-walled or even solid in order to avoid buckling. There is a severe penalty associated with this approach. Whereas for the thin-walled tube a mean shearing stress can be related to the applied torque by equilibrium considerations, it now becomes necessary to calculate the elastoplastic variation of stresses with the radius, and this requires selection of a specific plasticity model. It was decided to perform the necessary calculations using rate-independent isothermal elastoplasticity, the von Mises yield function, and the associated flow rule.

The widely employed Lagrangian hydrocode DYNA3D [7] provides these features in several of its material models. In particular, Model 10 accepts input of discrete data pairs representing points on an effective stress vs. effective plastic strain curve and interpolates for intermediate values as needed. This model originally only provided for isotropic work hardening but the author has modified it to feature mixed isotropic/kinematic hardening as suggested by Hodge [8]. Also, the DYNA3D code has been altered to offer a choice between use of the Jaumann [9] stress rate or the Green-Naghdi [10,11] rate (polar decomposition of the deformation gradient). In the following, this code is employed to treat several boundary value problems pertaining to the torsion of hollow tubes and solid rods.

## HOLLOW CYLINDERS

Consider the problem of a moderately thick ring composed of "brick" elements: 5 elements in the radial direction, 72 in the circumferential direction, and 1 in the axial direction (see Figure 2). The undeformed inner and outer radii of the ring are 0.315 in and 0.465 in, respectively, and the axial dimension is 0.030 in. The radial dimensions of each element are initially equal. The material data to be employed in Model 10 were derived from the quasi-static tests on annealed OFHC copper reported by Weerasooriya and Swanson [12], sixteen points on the effective stress vs. effective plastic strain curve being used as input. The density was taken to be 0.000837 lb sec/in$^4$. The nodes are constrained to not move in the axial direction, but are free to move radially. The two z = constant faces rotate in contrary directions at 1 radian/sec and are given appropriate initial velocities to avoid a starting transient. Clearly, the solution of this idealized problem also applies to an infinitely long cylinder made of many such rings all

subjected to the same loading. It also applies to the central portion of a finite fixed-ended cylinder sufficiently removed from the ends where torques are applied that a homogeneous state of stress exists. Except when it is desired to analyze the possibility of torsional buckling of the cylinder, it is possible to focus on the stresses and deformation of a single "wedge" of five radial elements, since all such wedges have the same deformation history (see Figure 3). Since the DYNA3D code does

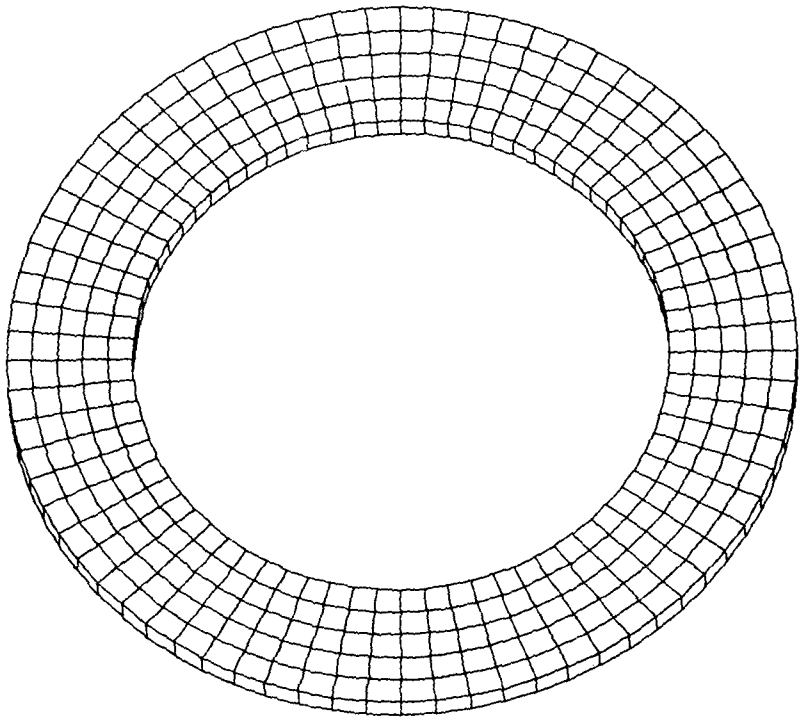


Figure 2. Ring-torsion problem gridding.

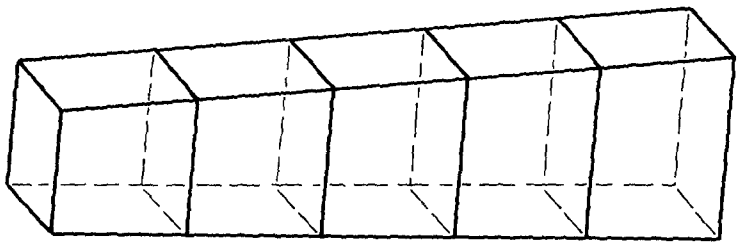


Figure 3. Wedge of five radial elements.

not have input options suitable for modeling the wedge problem, a special subroutine, T5RFIX, was introduced to apply the appropriate nodal constraints to duplicate the results of the ring calculations. Consequently, the rather voluminous results for the ring problem will not be shown, but were used to check the validity of the wedge constraints.

## WEDGE PROBLEMS

A matrix of fixed-ended wedge problems was then studied for the possible combinations of isotropic and kinematic hardening and the Jaumann and Green-Naghdi stress rates, all run to a final torsional shear strain of $\varepsilon_{z\theta} \approx 2.0$ (tensor component). In the course of a convergence study it was found that the major stress $\sigma_{z\theta}$ is insensitive to the size of the wedge angle, but that computed values of the circumferential stresses $\sigma_{\theta\theta}$ in the five elements were inconsistent with the requirement that the hoop force on any radial section should be zero in a statics problem. This cast doubt on the validity of all predicted normal stresses induced by the torsional loading. The difficulty appears to be associated with the brick element employed by DYNA3D. This element uses a single integration point located at its center; when the element experiences large shearing and warping, the stresses computed at the integration point are inappropriate for evaluating nodal forces since the actual stresses in the neighborhood of the nodes would vary significantly from those at the center of the element. This difficulty can be somewhat alleviated by reducing the thickness of the elements in the z-direction (which reduces the amount of circumferential stretch required to reach the desired shearing strain). Some effort was made to optimize the element thickness to minimize the hoop force, and the results which follow are based on this concept.

Results from DYNA3D calculations for the fixed-ended wedge using the Jaumann stress rate for both isotropic and kinematic hardening are shown in Figure 4 for the middle element of the wedge. The isotropic hardening curve for the shearing stress is in good agreement with experimental data [12] and the induced normal stresses, while not zero, are too small to be visible with the scale employed. For the pure kinematic hardening case, the shear stress exhibits the widely noted sinusoidal behavior associated with the Jaumann rate, as do the induced normal stresses. The magnitudes of the latter stresses are unrealistically large, and these stresses would significantly affect the effective stress function if actually present. The experimental curve for

the induced axial stress is also shown in this figure. Calculations for a free-ended wedge were also made using the Jaumann stress rate for the isotropic case; the results were indistinguishable from the isotropic curves shown in Figure 4. Of course, there was an axial extension of the wedge, and the magnitudes of the axial stresses were further reduced.

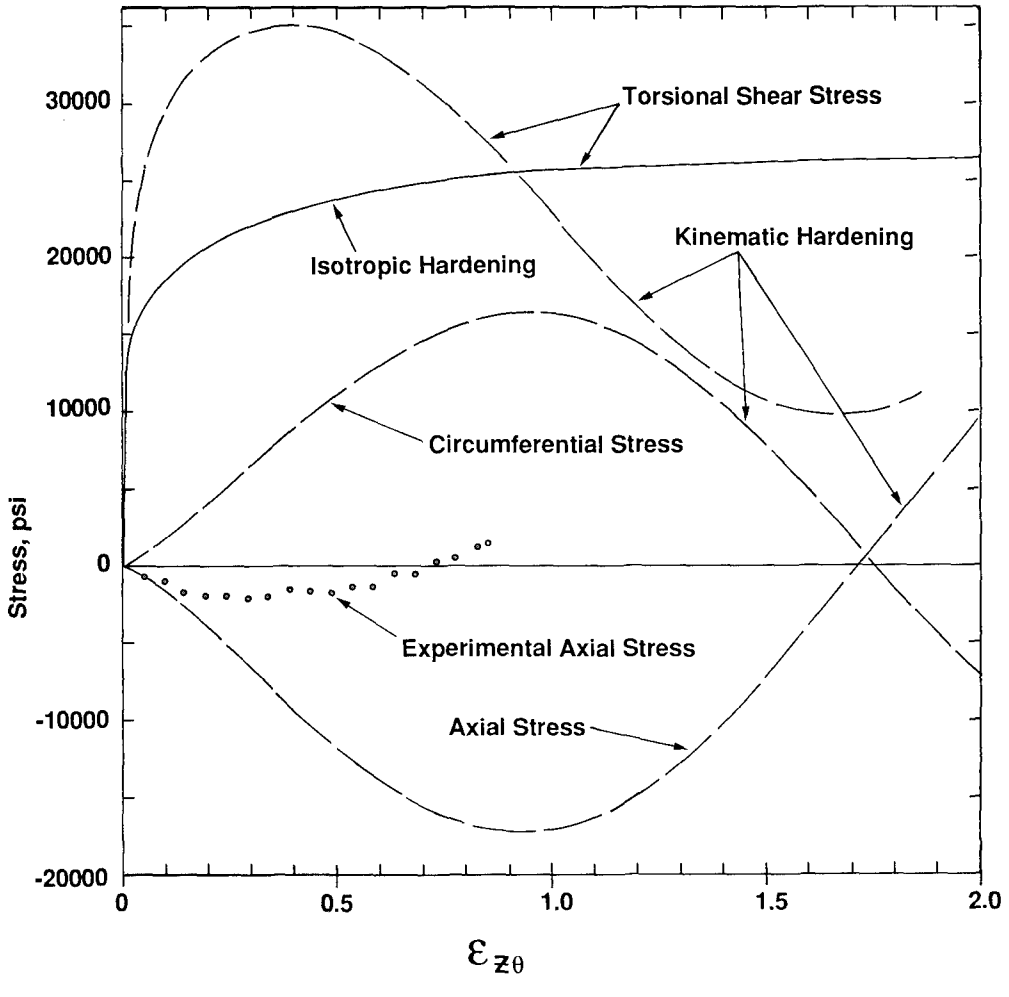



Figure 4. Stresses computed using the Jaumann stress rate.

Calculations similar to those described above were also performed using the Green-Naghdi stress rate, and the results for a fixed-ended wedge are shown in Figure 5. For the isotropic case, the curves shown in this figure are essentially the same as those obtained using the

Jaumann rate. In the kinematic hardening case the early oscillatory behavior was avoided, but the magnitudes of the induced normal stresses are still large.

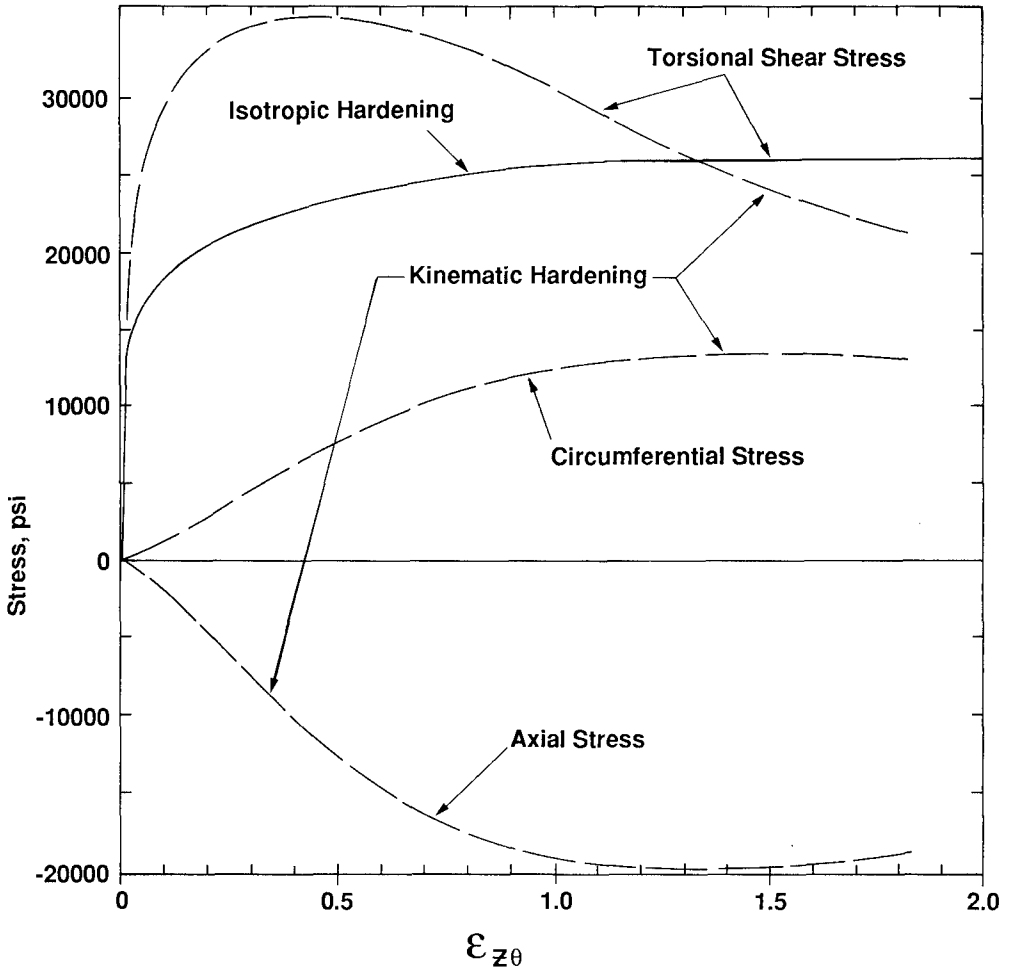



Figure 5. Stresses computed using the Green-Naghdi stress rate.

## SOLID SPECIMENS

In anticipation that torsional buckling of hollow cylindrical specimens might preclude successful material characterization tests at large shear strains, a study of the feasibility of using DYNA3D calculations for test data interpretations (up to incipient buckling) was conducted. Again, it is not necessary to model the entire cross section but only a

"pie-shaped" wedge with appropriate constraints. To accomplish this, the DYNA3D code was modified to include subroutines TWED and TWED2 which apply to the geometry indicated in Figure 6.

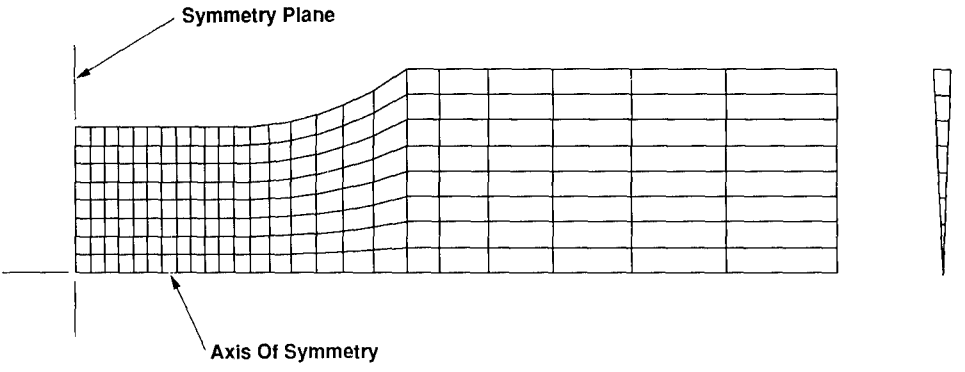



Figure 6. Geometry for the solid wedge calculations.

A series of calculations were performed in which the nodes on the outer surface in the "grip" region were inhibited from moving in the axial direction and constrained to rotate about the Z-axis at specified angular velocities. The results of these calculations are too complex to report in this paper. However, it is worth noting certain new phenomena which arise in these calculations.

One of these is what may be termed isothermal shear banding, which entails a spontaneous rapid increase in plastic strain in an element or in all the elements at some axial location. This phenomenon is unrelated to thermal softening of materials since the mathematical model has no provision for thermal effects. Although this behavior is observed to a very limited extent during calculations using isotropic hardening, it has a serious destabilizing effect when kinematic hardening is employed. This banding is triggered in the most critically loaded element when the sinusoidally varying shear stress decreases from its first peak. Figure 7 shows end views of the twisting wedge before and after the appearance of the first band. Unlike adiabatic shear bands which progress to extreme localization, these isothermal bands tend to broaden as the banding spreads to adjacent elements.

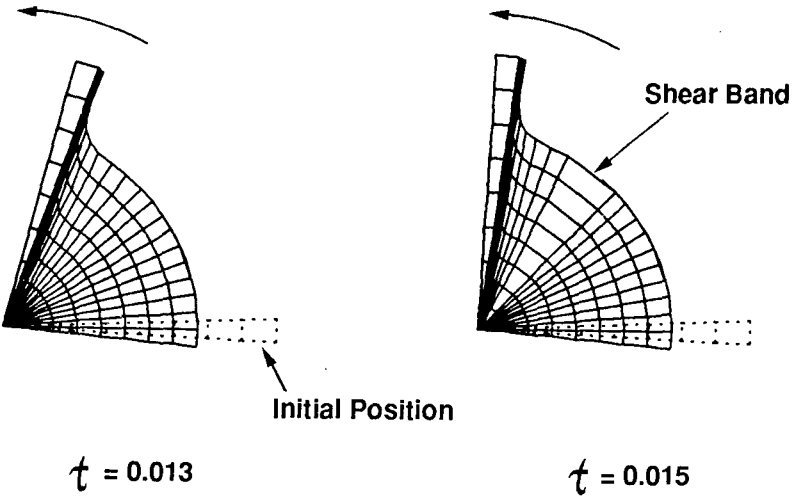



Figure 7. End views of wedge before and after shear banding.

Another phenomenon occurred during a mixed isotropic/kinematic calculation using the Green-Naghdi stress rate (made to assess the Bauschinger effect) in which the "grip" end was programmed to twist through 280° and then twist back to 120°. During the latter part of the reversed loading, the wedge was observed to buckle (computationally, but this may also occur in a physical experiment).

## CONCLUDING REMARKS

It is the uncertainties regarding modeling plastic flow, work hardening, evolution of anisotropy, and objective stress rates which impede successful finite element modeling of experimental specimen configurations and motivate experimentalists to adopt simple shapes such as the thin-walled tube for which stress can be related to strain through equilibrium and geometric considerations.

The feasibility of modeling the torsion of hollow cylinder and solid rod specimens has been demonstrated in this paper, but the results are conditioned by material modeling decisions. In view of this, the writer does not feel that the tedious and expensive calculations required for a converged solution for the solid rod can be justified. Further study of

modeling the hollow tube using various material representations and alternate finite elements may be worthwhile.

Where it is desired to use the thin-walled tube specimen, the configuration shown in Figure 8 may be considered. This configuration, which is very similar to that employed by Professor Swift [2], consists of a straight cylindrical tube with snugly fitted plugs of a high modulus material inserted in each end. The grips of a torsion tester would be applied in the region of the plugs. The gauge section of the tube must be relatively short to inhibit torsional buckling. Swift attempted to resist buckling by introducing a small clearance solid rod into the gauge section as part of one of the end plugs, but had problems with binding between the rod and specimen. It would appear preferable to introduce a "free floating" solid rod and use today's super lubricants. Another method for delaying the onset of buckling would be to apply a uniform axial tension to the test specimen.

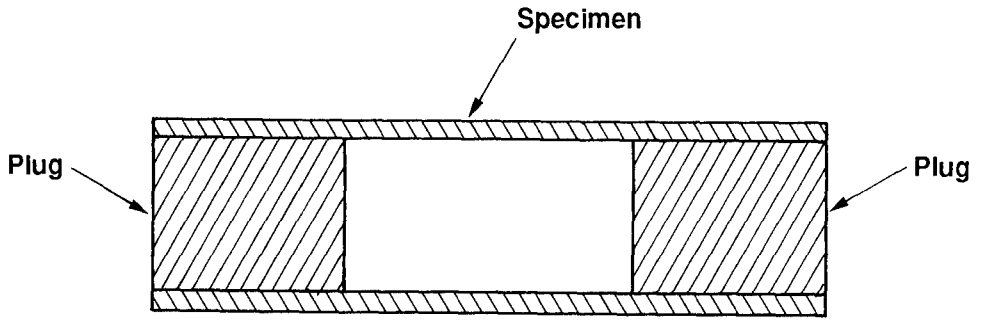



Figure 8. Suggested torsion test configuration.

It should be remarked that elastoplastic parameters obtained by finite shearing or compression tests may no longer pertain to an isotropic material. It would be extremely valuable to be able to map the current yield surface to assess induced anisotropy, preferably in the same experimental apparatus.

ACKNOWLEDGEMENT

The author wishes to express his appreciation for many stimulating discussions with Dr. Joseph M. Santiago during the course of this investigation.

## REFERENCES


1. Poynting, J. H., "On Pressure Perpendicular to the Shear Planes in Finite Pure Shears, and on the Lengthening of Loaded Wires when Twisted." Proceedings of the Royal Society of London, vol. A82, pp. 546–559, 1909.
2. Swift, H. W., "Length Changes in Materials under Torsional Overstrain." Engineering, vol. 163, pp. 253–257, 1947.
3. Lindholm, U. S., Nagy, A., Johnson, G. R., and Hoegfeldt, J. M., "Large Strain, High Strain Rate Testing of Copper." ASME Journal of Engineering Materials and Technology, pp. 376–381, 1980.
4. Johnson, G. R., Hoegfeldt, J. M., Lindholm, U. S., and Nagy, A., "Response of Various Metals to Large Torsional Strains Over a Large Range of Strain Rates—Part 1: Ductile Metals." ASME Journal of Engineering Materials and Technology, pp. 42-53, 1983.
5. Johnson, G. R., and Cook, W. H., "A Constitutive Model and Data for Metals Subjected to Large Strains, High Strain Rates and High Temperatures." Seventh International Symposium on Ballistics, The Hague, April 1983.
6. White, C. S., "Use of the Thin-Walled Torsion Specimen." U.S. Army Materials Technology Laboratory, TR 92-49, 1992.
7. Hallquist, J. O., "Theoretical Manual for DYNA3D," University of California, Lawrence Livermore National Laboratory, Rept. UCID-19401, I983.
8. Hodge, Jr., P. G., Discussion of Prager (1956), Journal of Applied Mechanics, vol. 24, no. 3, pp. 482–483, 1957.
9. Jaumann, G., "Grundlagen der Bewegungslehre," Leipzig, 1905.
10. Green, A. E., and Naghdi, P. M., "A General Theory of an Elastic-Plastic Continuum," Arch. Rat. Mech. Anal., vol. 18, pp. 251–281, 1965.
11. Green, A. E., and McInnis, B. C., "Generalized Hypo-Elasticity," Proceedings of the Royal Society of Edinburgh, A57, p. 220, 1967.
12. Weerasooriya, T., and Swanson, R. A., "Experimental Evaluation of the Taylor-Type Polycrystal Model for the Finite Deformation of an FCC Metal (OFHC Copper)." U. S. Army Materials Technology Laboratory, TR 91-20, 1991.

# High Strain Rate Behavior and Localization in Hafnium

**Dr. Ghatuparthi Subhash***
Assistant Professor
Department of Mechanical Engineering-Engineering Mechanics
Michigan Technological University
Houghton, Michigan 49931

and

**Dr. Guruswami Ravichandran**
Assistant Professor
Graduate Aeronautical Laboratories
California Institute of Technology
Pasadena, California 91125

Constitutive behavior of polycrystalline hafnium is investigated at various strain rates in the range $10^{-5}$-$10^{4}$/s in uniaxial compression. It is found that hafnium exhibits shear banding at all the strain rates employed in this study. The inelastic stress-strain response reveals a three stage hardening which is typical of several h.c.p. metals. As the strain accumulates, the slope of the hardening regime gradually falls to zero and the material experiences instability. The instability leads to localization and failure along a plane at $45^{o}$ to the compression axis. Multiple shear bands were observed when the thickness of the specimen was small. SEM observations of the fractured surfaces revealed extensive void formation, growth and coalescence along the shear bands. Temperature measurements using high speed infrared detectors revealed a rise of 320 $^{o}$C for a strain of 0.42 on cylindrical specimens tested at high strain rate under uniaxial compression.

## Introduction

Hafnium (Hf) is a refractory metal with hexagonal close packed structure (h.c.p.). It has many desirable engineering properties like high density, good ductility and excellent resistance to corrosion, irradiation and mechanical damage. It has been used in nuclear reactors as a control material due to its high capture cross-sectional area for thermal

neutrons. Hf is also widely used as a solid solution strengthener. Addition of 10% hafnium to columbium (Niobium) increases its hot strength, weldability and formability. The columbium alloys, C-103 (Cb-10Hf-1Ti) and C-129Y (Cb-10W-10Hf-0.07Y) have wide applications in jet engines and missile systems. Inspite of its many potential engineering applications, little is known about its mechanical response, plastic behavior, and its ability to undergo localized shear deformation. Experiments were done on commercially available pure hafnium to investigate its plastic response at various strain-rates under uniaxial compression.

Recently there have been a number of studies on the plastic deformation of h.c.p metals, particularly on computer simulations of various twin, dislocation and vacancy properties and their interactions using atomic potentials (Vitek and Igarashi (1991), Serra and Bacon (1991), Serra *et al.*, (1991), Johnson (1991) and De Diego and Bacon(1991)). Simulations are extremely important to characterize and understand the atomic configurations. Some early experimental studies on mechanisms of plastic flow on Ti at low and high temperature were reported by Rosi *et al.*(1953, 1956), Rosi (1954), Levine (1966), De Crecy *et al.* (1983) and recently, by Naka *et al.* (1991), Meyers *et al.* (1993) and on zirconium by Rapperport and Hartley (1960), Akhtar and Teghtsoonian (1971) and Numakura (1991). These studies focussed on identifying the dominant mechanisms which govern the low and/or high temperature plasticity. Other mechanisms of plastic deformation like prismatic glide and interaction of point defects with dislocations and grain boundaries in h.c.p. metals were studied by Couret *et al.* (1991) and Monti et al (1991). Importance of deformation twinning in h.c.p. metals and alloys was well described by Yoo (1981) and by Yoo and Lee (1991). Stress-state dependence of slip in Ti-6Al-4V and other h.c.p. metals is investigated by Jones and Hutchinson (1981). Analysis of low temperature, low and high strain rate deformation of Ti-6Al-4V was investigated by Follansbee and gray (1989). It is obvious from the above studies that majority of the work is focussed on computer simulation of the deformation mechanisms in h.c.p. structures. Experimental investigations into their mechanical behavior under various loading conditions can yield valuable information in enhancing our understanding of the plastic behavior and kinetics of deformation. Lack of experimental data can hinder the progress in theoretical modelling of constitutive behavior and the efforts in understanding the micromechanisms of dislocation interactions using the above computer simulations. Such data is abundantly available for f.c.c. metals but is very limited for h.c.p. metals, and especially for hafnium. Our extensive literature search has yielded two early references on this subject. One on the microstructure of hafnium by Vahldiek (1969) and the other on mechanical properties of hafnium single crystals by Das and Mitchell (1973). Recent advances in processing technology has made it possible to obtain ultra pure metals with excep-

tional mechanical properties. In light of these advances and also due to the necessity of more experimental data to understand the fundamental mechanisms of plastic deformation, and associated microstructural changes in hafnium, the present study is undertaken.

The objective of this study to investigate the constitutive behavior of hafnium under uniaxial compression and its ability to form shear bands at various strain rates. The study is also aimed at identifying the deformation and failure modes, the active slip and twin systems and the dominant dislocation mechanisms that contribute to the observed overall behavior. Temperature rise during the dynamic deformation is also investigated using high speed infrared detectors. The effect of temperature rise on the over all plastic behavior and the resulting dislocation substructure is also under investigation.

## Experimental

### I. Materials

Commercially available pure hafnium is obtained from Teledyne Wah Chang, Huntsville, Alabama, in the form of a rod. Chemical analysis for gaseous and metallic impurities was performed at Teledyne Wah Chang Analytical Laboratories, Albany, Oregon. The results of the analysis are given below.

**Table 1: Gaseous Impurities**

| Element | C | H | N | O |
|---|---|---|---|---|
| ppm | 30 | <3 | 34 | 270 |

**Table 2: Metallic Impurities**

| Element | Al | Cr | Cu | Fe | Mg | Mo |
|---|---|---|---|---|---|---|
| ppm | 29 | <20 | 195 | 215 | <10 | <10 |

| Element | Nb | Ta | Ti | U | W | Zr |
|---|---|---|---|---|---|---|
| ppm | <50 | <100 | 25 | <1 | <20 | 2.05% |

The effect of impurities on the mechanical behavior of hafnium and several other h.c.p. metals has been given considerable attention in the literature. It is known that Hf is extremely reactive. It is also well established that, in h.c.p. metals with less than ideal c/a ratio (Hf, Ti and

Zr), prismatic slip is preferred and this is found to be more strongly affected by impurities as compared to basal slip. Levine (1966) found that the yield stress is strongly affected by oxygen impurities in Ti, especially at low temperatures. Interstitial impurities also have strong hardening effect. When oxygen impurity is beyond 1500 ppm, it hardens Ti through chemical interaction with screw dislocations (Naka *et al.*, 1991).

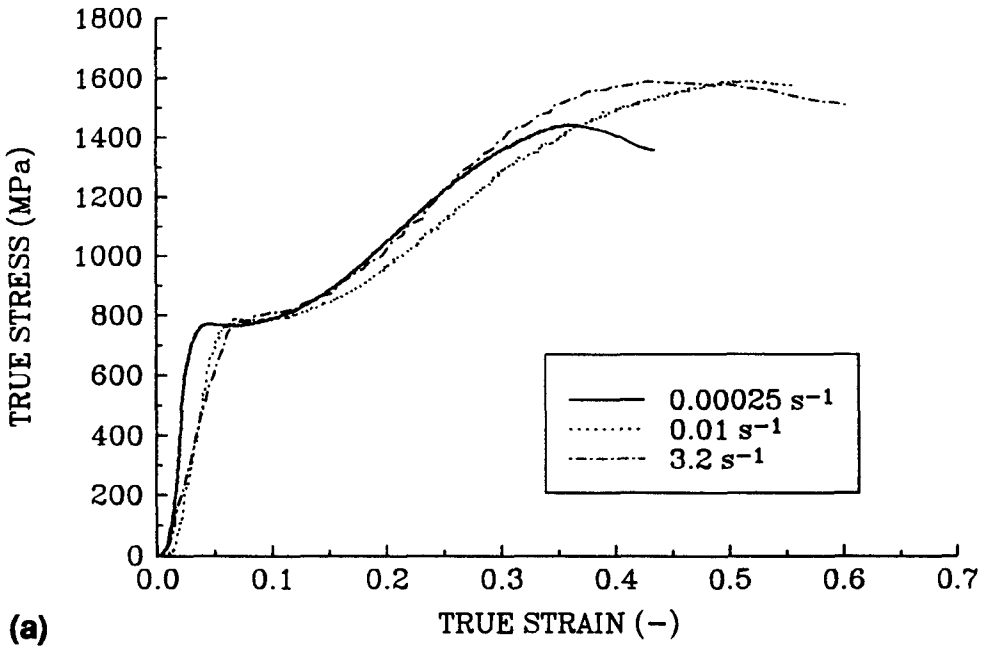
## II. Procedure

Polycrystalline specimens were cut from the rod into cylindrical shapes in sizes of 5mm length x 5mm diameter and into 2mm length x 4mm diameter. These sizes were chosen due to the limited amount of available material. The specimens were subjected to various strain rates at room temperature. Low strain rate experiments ($10^{-5}$-3.2 $s^{-1}$) were performed on a MTS servohydraulic machine and high strain rate experiments ($10^{2}$-$10^{4}$ $s^{-1}$) were performed on a split Hopkinson pressure bar (SHPB).

## Results and Discussion

The complete summary of the experimental results are presented in Table 3. The stress-strain response of specimens tested at quasi static and dynamic strain rates is given in Fig. 1. It can be seen that the compressive response of hafnium can be divided into three regimes. There is an initial flat (perfectly plastic) response followed by a hardening regime. The slope of this curve gradually decreases and falls to zero. At this stage, the load carrying capacity of the specimen falls to zero and the specimen fails along a plane at $45^{o}$ to the compression axis. This effect is seen as a load drop in the stress-strain response. It is interesting to note from the stress-strain response of hafnium that there is no strain rate dependence of yield stress in this material. It has been well established that h.c.p. materials, especially Ti and Zr (with c/a ratio less than ideal) are extremely strain rate sensitive (Meyers *et al.* (1993)). It is not clear at this stage why hafnium behaves differently. Das and Mitchell (1973) have observed temperature dependency of yield stress in single crystal hafnium and they attributed this behavior to impurity contents like oxygen and nitrogen. Goodwin and Trout (1966) also observed that substitutional impurities like Cd and Zr (beyond 2%) and interstitial impurities like oxygen (beyond 300 ppm) significantly affect the mechanical behavior. In the present case, it is speculated that the low strain rate sensitivity of hafnium could be due to the high purity of the material.

Irrespective of the strain rate of the test, all the specimens exhibited shear failure (after accumulating certain strain) along a plane approximately $45^{o}$ to the compression axis. The critical strain for shear failure was around 0.3 - 0.35. When loading rates were very low, it was



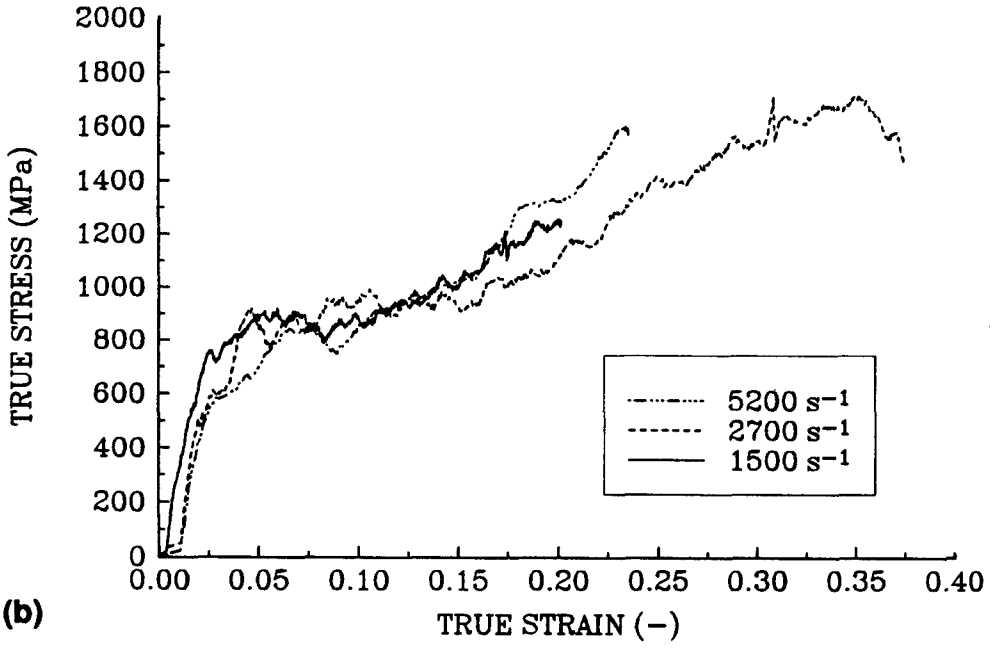




Fig. 1. Stress-strain response of hafnium at (a) quasistatic strain rates and (b) high strain rates.

possible to stop the test at the onset of shear localization (see Hf-O3 in Table 3). The number of shear bands formed in each specimen varied from 1-4 depending on the thickness of the specimen, strain and the strain rate. Multiple shear bands were observed in thin specimens. The micrographs in Fig. 2 reveal the shear bands formed in the specimens Hf-N3 and Hf-O4 and failure along these bands during the experiment.

**Table 3: Summary of Experimental Results**

| Specimen No | Dimension L x D ($mm^2$) | Strain Rate ($s^{-1}$) | No. of Shear Bands |
|---|---|---|---|
| Hf-N1 | 5 x 5 | 0.004 | None |
| Hf-N2 | 5 x 5 | 0.00009 | None |
| Hf-N3 | 5 x 5 | 1.4 | 1 |
| Hf-N4 | 5 x 5 | 0.001 | 1 |
| Hf-O1 | 2 x 4 | 0.013 | 2 |
| Hf-O2 | 2 x 4 | 3.2 | 3 |
| Hf-O3 | 4.1 x 6.3 | 0.00025 | 1 (Initiated) |
| Hf-N5 | 5 x 5 | 1500 | None |
| Hf-N6 | 5 x 5 | 2700 | 1 (Fractured) |
| Hf-N8 | 5 x 5 | 5200 | 1 |
| Hf-O4 | 2 x 4 | 4000 | 3 |
| Hf-O5 | 2 x 4 | 2800 | Spec. Lost |
| Hf-O6 | 2 x 4 | 10000 | 4 |

## Microscopic Observations

At high strain rates, the specimens fractured along the shear band in to two pieces. The fractured surfaces were observed under a scanning electron microscope. Figure 3 reveals the microstructure of the fracture surface of the specimen Hf-N6. The microstructure consists of number of elongated voids along the direction of shear failure. It is clear from the micrograph that the failure occurs by generation of voids, their growth and coalescence. But whether the voids initiate the shear band or the shear band (or the localization) initiates the voids which then grow to cause failure is under investigation.

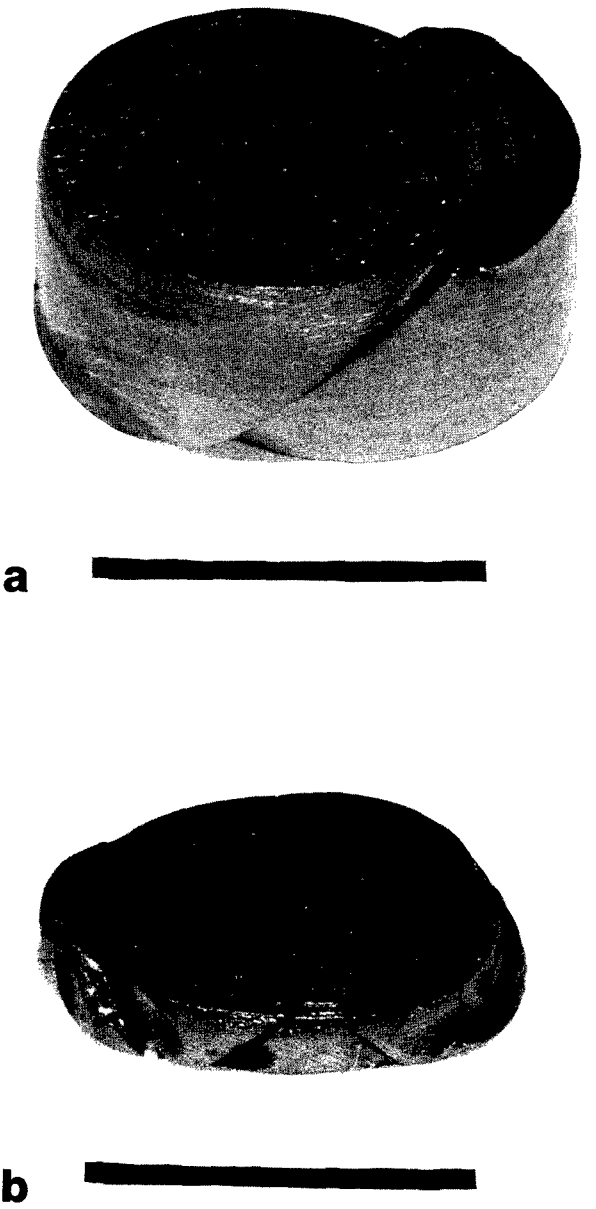



Fig. 2. Photographs of deformed and fractured specimens (a) Hf-N3 and (b) Hf-O4. The marker is 5 mm long.

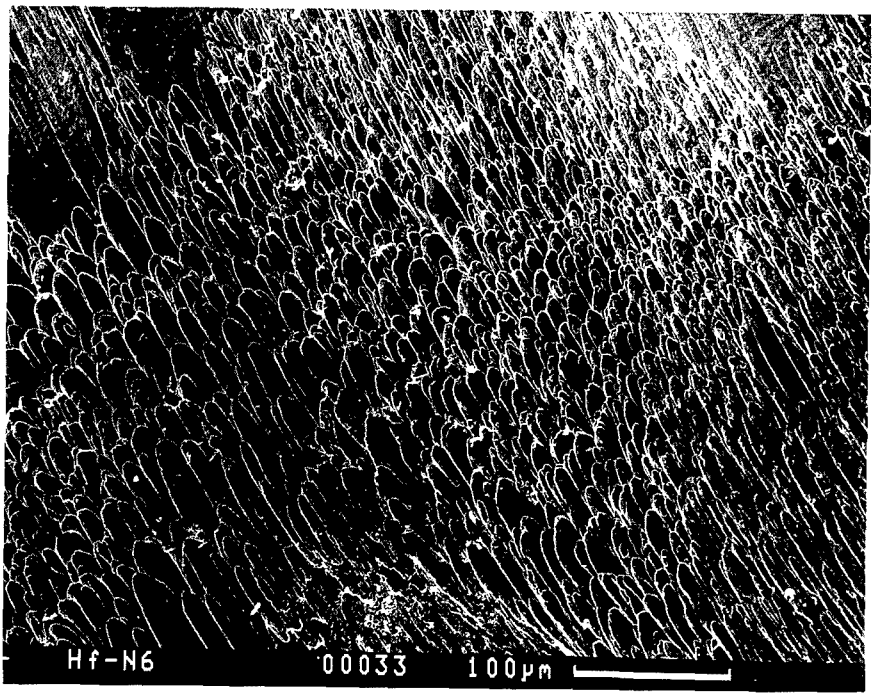


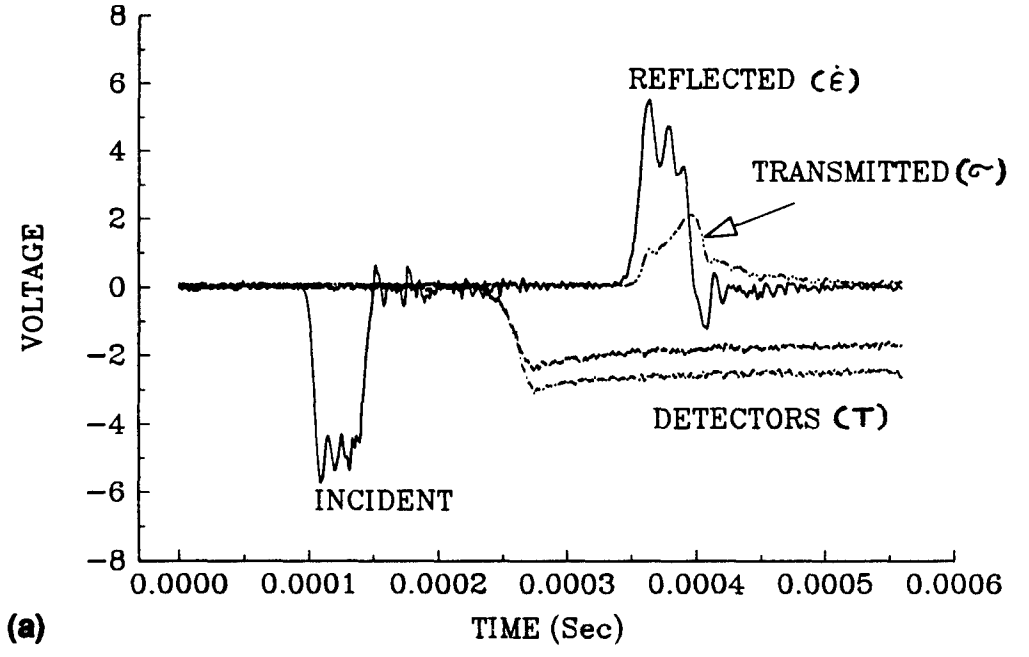

Fig. 3. SEM micrograph of fractured surface revealing elongated voids in the plane of shear failure.

## Temperature Measurements

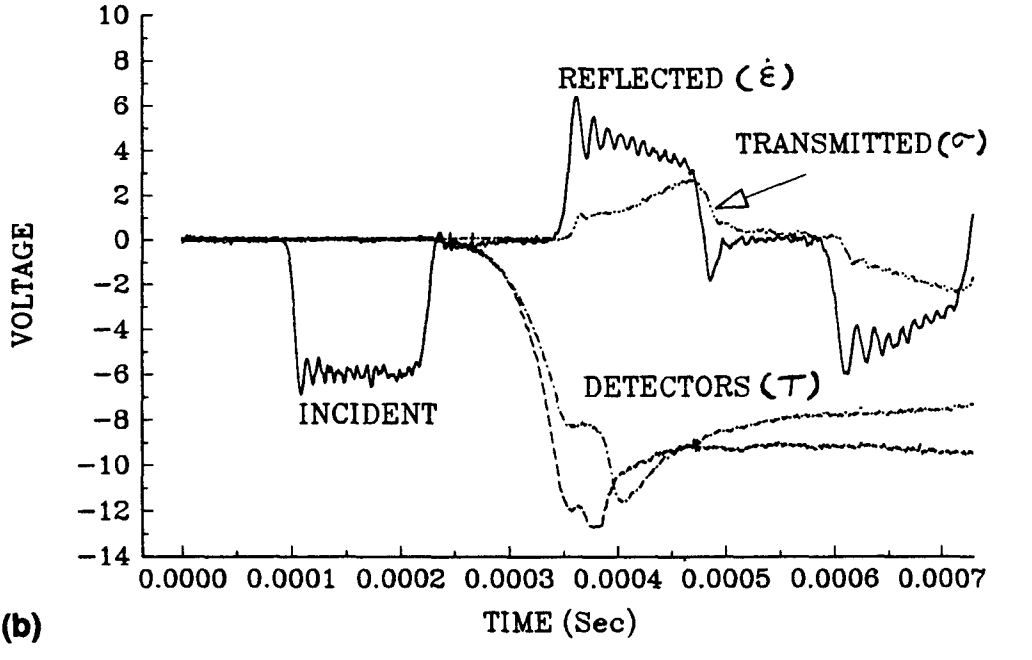
During dynamic testing, there is considerable rise in temperature of the specimen due to adiabatic nature of the deformation. This rapid rise in temperature significantly affects the flow and fracture behavior of metals and the resulting dislocation substructure. Hence it is very important to measure the temperature rise during the deformation and assess its influence on the deformation behavior of the metal. To measure the temperature rise in the specimen during the deformation in the SHPB, high speed infrared detectors are focussed on to the specimen and the voltage signal obtained from the detectors is recorded along with the transmitted and reflected signals in the SHPB. The technique of measuring temperature rise using infrared detectors has been successfully used to measure the rise in temperature at the tip of a dynamically propagating crack (Zhender and Rosakis, 1991). Typical voltage signals obtained during the high strain rate testing of specimens Hf-N8 and Hf-N6 are shown in Fig. 4. In Fig. 4(a) the detectors were focussed on to a small region on the specimen and the shear band did form with in this area and hence the signal obtained shows a uniform rise in temperature in that region during the test. When the focussed area is close to the region where the shear band propagates, then there is a rapid rise in the temperature in that region and the signal obtained from the detectors is as shown in Fig. 4(b). The rapid rise is due to the high temperature associated with the intense localized shear deformation and associated fracture in the band. Due to the movement of the incident bar in SHPB, the specimen also moves forward during the deformation and hence the area under focus also changes. Now the focussed region on the specimen has shifted away on to a region which is under a homogeneous deformation and this area obviously has a lower rise in temperature as compared to the shear band and hence there is a fall in voltage signal obtained from the detectors. The temperature rise corresponding to the signal in Fig. 4(a) is around 320 $^{o}$C for a strain of 0.42 and the maximum temperature in the Fig. 4(b) is approximately 560 $^{o}$C. The effect of this temperature rise can be seen in the resulting dislocation substructure in the material. A systematic study of the deformed specimens using transmission electron microscopy is under progress to evaluate these effects.

## Conclusions

The experiments on polycrystalline hafnium show high propensity for shear banding under a range of strain rates. Extensive void generation, growth and coalescence lead to fracture along the shear bands. There is a significant temperature rise in the material during the deformation, especially with in the shear bands. Microscopic studies are




(a)




(b)

Fig. 4. Voltage signals corresponding to stress, strain rate and temperature in the specimen during high-strain rate testing. (a) The focussed region of the detectors is under homogeneous deformation and the signal corresponds to a temperature rise of about 320 °C. (b) The focussed region is close to a shear band and the maximum temperature rise is about of 560 °C.

under progress at this time to identify the various slip, twin and dislocation mechanisms that are responsible for the observed constitutive behavior. These results will be reported in future publications.

## References


Akhtar, A., and Teghtsoonian, A., 1971, *Acta Metall*, **19**, 655.

Couret, A., Calliard, D., Puschl, W., Schoeck, G., 1991, *Phil Mag A*, **63**, 1045.

Das, G., and Mitchell, 1973, *Metall. Trans*, **4**, 1405.

De Crecy, A., Bourret, A., Naka, S., and Lasalmonie, M. A., 1983, *Phil. Mag A*, **47**, 245.

De Diego, N., and Bacon, D. J., 1991, *Phil Mag A*, **63**, 873.

Follansbee, P. S., and Gray III, G. T., 1989, *Metall Trans.*, **20A**, 863.

Goodwin, J. G., and Trout Jr., H. E., 1966, *Trans ASM*, **59**, 384.

Griffiths, 1991, *Phil mag A*, **63**, 835.

Johnson, R. A., 1991, *Phil. Mag A*, **63**, 865.

Jones and Hutchinson, 1981, *Acta Metall* **29**, 951.

Levine, E.D., 1966, *Trans. Metall. Soc. AIME*, **236**, 1558.

Meyers, M. A., Subhash, G., Kad, B., and Prasad, L., *Mechanics of Materials*, submitted.

Monti, A. M., Sarce, A., Smetniansky-De Grande, N., Savino, E. J., Tome, C. N., 1991, *Phil Mag.*, **63**, 925.

Naka, S., Kubin, L. P., and Perrier, C., *Phil mag.* A, 1991,**63**, 1035.

Numakura, H., Minonishi, Y., and Koiwa, M., 1991, *Phil mag A*, **63**, 1077.

Rapperport, E. J., and Hartley, C. S., 1960, *Trans Metall Soc AIME*, **218**, 869.

Rosi, F. D., Dube, C. A., and Alexander, B. H., 1953, *Trans. AIME, J of Metals*, 257.

Rosi, F. D., 1954, *Trans AIME, J of Metals*, 58.

Rosi, F. D., Perkins, F. C., and Siegel, L. L., 1956, *Trans AIME, J of Metals*,115.

Serra, A., and Bacon, D. J., 1991, *Phil mag A*, **63**, 1001.

Serra, A., Pond R. C., and Bacon, D. J., 1991, *Acta Metall Mater.* **39**, 1469.

Vahldiek, 1969, *J Less Comm Metal*, **19**, 83.

Vitek, V., and Igarashi, G., 1991, *Phil Mag A*, **63**, 1059.

Yoo 1981, *Metall trasns, A* **12**, 409.

Yoo, M. H., and Lee, J. K., 1991, *Phil Mag A*, **63**, 987.

Zhender, A. T., and Rosakis, A. J., 1991, *J Mech Phys Solids.*, **39** [3] 385.

# Split Hopkinson Bar Compression Screening Tests of High Density Penetrator Materials

Lee S. Magness, Jr.*
Army Research Laboratory
Weapons Technology Directorate
Aberdeen, MD 21005-5066
and
Craig Lopatin
AlliantTech Systems Inc.
600 Second Street Northeast
Hopkins, MN 55343

## Background

As a high velocity long rod projectile burrows a cavity in armor, its high density penetrator core is also inverted and eroded. Due to the relatively slow propagation rates of plastic strains, the deformation to both penetrator and armor materials is localized to regions on either side of the penetrator-target interface. Both materials therefore undergo the large plastic strains at extremely high strain rates, estimated to exceed 10^6 per second, (WRIGHT, [1982]).

These deformations also occur under conditions of high hydrostatic pressure generated by the inertia of each material and the confinement of the surrounding volume of armor material that is resisting the expansion of the penetration cavity. The pressures can exceed 5 GPa (MESCALL, [1983]) on either side of the moving penetrator-target interface (see Fig. 1). The hydrostatic pressures act to suppress fracture failures in these immediate regions. For example, even nominally brittle penetrator materials such as polycrystalline tungsten will be back-extruded from the interface in a ductile manner (GERLACH, [1986]).

The high rates at which these deformations occur allow little time for the dissipation of the heat generated by plastic work. Thermo-mechanical instabilities and subsequent plastic localizations

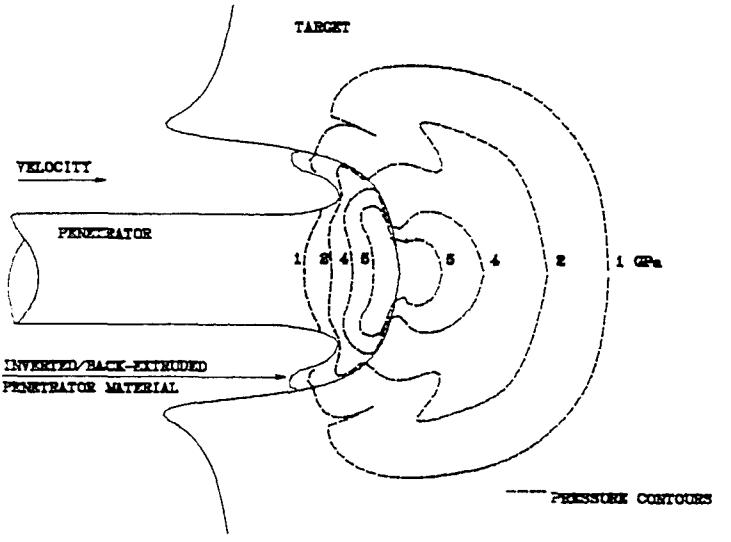



Figure 1. Hydrostatic Pressure Contours Surrounding the Penetrator-Target Interface, from Mescall, (1983).

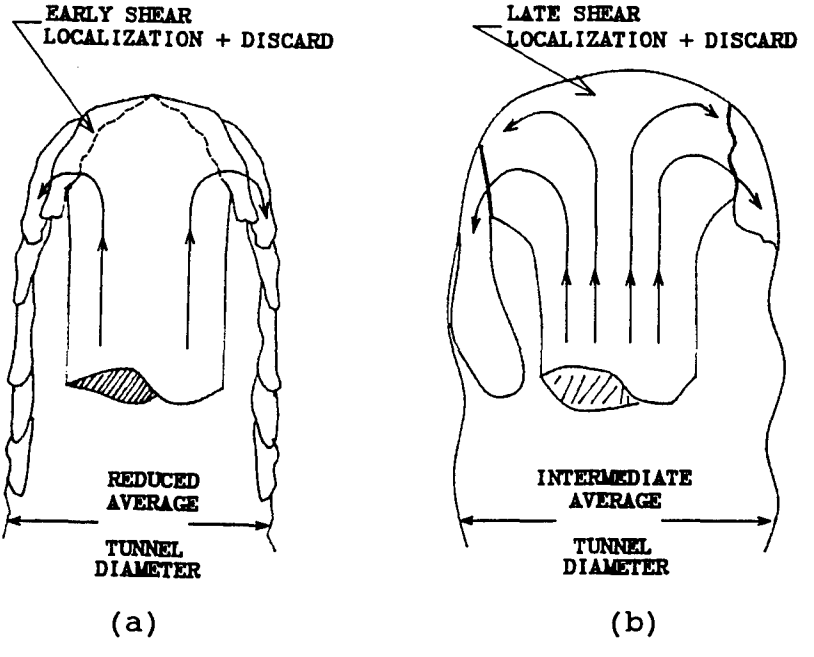



Figure 2. Behaviors of High Density Materials During Penetration, (a) U-3/4Ti, (b) Conventional WHA.

(adiabatic shear bands) often develop in both armor and penetrator materials. How quickly (at what critical value of plastic strain) this occurs is determined by a balance between the thermal softening of the material, a function of its heat capacity, softening rate with temperature, etc., and the strengthening of the material with the strain and strain rate (ROGERS, [1979]). Differences in the dynamic flow-softening and subsequent adiabatic shear susceptibility of tungsten heavy alloys (WHA) and depleted uranium (DU) alloys are responsible for their differing performances as penetrator materials (MAGNESS and FARRAND, [1990]). Uranium alloy penetrators quickly develop adiabatic shear failures during penetration and rapidly discard the back-extruded material from the head of the projectile (Fig. 2a). In WHA penetrators, the shear localizations develop only after extensive plastic deformation, resulting in the build up of a large mushroomed head on the projectile (Fig. 2b). As a result, the WHA projectiles must displace larger diameter penetration cavities in the armor and cannot achieve penetration depths as great as those achieved by equivalent uranium penetrators.

Several efforts to improve the ballistic performance of WHA, by promoting a similar thermomechanical instability and localization behavior in novel tungsten-based composites, are now under way. A primary approach being explored in these efforts is the replacement of the nickel-based matrix of conventional WHA materials with a matrix composition that is thermomechanically less stable (for example, a titanium alloy). An instrumented dynamic test, whose output can be correlated to the ballistic behavior and performance relationship described above, would aid both fundamental understanding, and serve as a screening methodology for candidate matrix materials and the overall tungsten-matrix composites.

## Selection of a Split Hopkinson Bar Compression Test

Ideally, the loading environment in the instrumented test should resemble that seen by the penetrator material during the penetration process. Of particular concern is the ability to distinquish between shear fractures and adiabatic shear localizations. This issue is illustrated in the results of dynamic tubular torsion tests by JOHNSON et

al. (1983), comparing a 90% tungsten-7% nickel-3% iron composite and the U-3/4Ti alloy used in large caliber U.S. tank ammunition. The shear strains at which maximum stress levels were recorded, and at which shear failures occurred, were lower for the WHA composite than for the U-3/4Ti alloy. This is an apparent reversal of the ballistic observations and likely is due to the torsion test's lack of high superimposed hydrostatic pressures. The lack of hydrostatic pressure allows the operation of other strain-softening mechanisms (COWIE and TULER, [1987]), particularly microcracking and void nucleation and growth mechanisms important in composite materials. These mechanisms are suppressed during the inversion of the material at a penetrator's head. (As an aside, this also suggests that the eventual appearance of the shear localizations in the mushroomed head of a WHA penetrator may be as much a function of its position in the pressure field drawn in Figure 1, as it is of the achievement of some critical strain value.)

The relatively simple, split Hopkinson bar (SHB) compression test deforms specimens at strain rates of 10^3 to 10^4 per second. Although the rates of deformation are still a couple of orders of magnitude lower than those in ballistic events, the loading of the specimens more closely simulate that seen at the head of the penetrator than that found in pure or simple shear tests.

A sudden drop in the load-displacement or force-time records is often observed in these dynamic compression tests and is associated with the development of an adiabtic shear failure (CIMPOERU and WOODWARD, [1990]). The strain-to-load-drop (STLD) measure may provide an easily recordable quantification of adiabatic shear susceptibility. Its value in a particular test, however, is a function of the geometry of the compression specimens (length-to-diameter [L/D] ratio) and the friction between the anvils and the ends of the specimen, as well as the fundamental dynamic flow-softening behavior of the material (O'DONNELL and WOODWARD, [1988]). In tests of conventional WHAs (BELK et al., [1992]), catastrophic load drops did not occur for both L/D = 0.5 and 1.0 specimens, but did appear at true strains exceeding 60% in L/D = 2 specimens. The shear localizations can be "forced" in WHA materials at still lower strain values, if the specimen ends are left unlubricated (BOSE et al., [1992]). Reflecting

a true difference in dynamic flow-softening response, tests of uranium alloy, using L/D = 0.5 specimens with lubricated ends, have exhibited load drops at moderate true strains (SEMIATIN et al., [1982]).

For this evaluation of the dynamic compression test, well-lubricated L/D = 0.5 specimens were used. The specimens were 0.250 inches in diameter by 0.125 inches in height, and the ends of the specimens were grooved and lubricated with Molylube to minimize friction at the anvil surfaces (Fig.3). The test set-up was a conventional SHB, with strain gages on the elastic input and output bars on either side of the specimen.

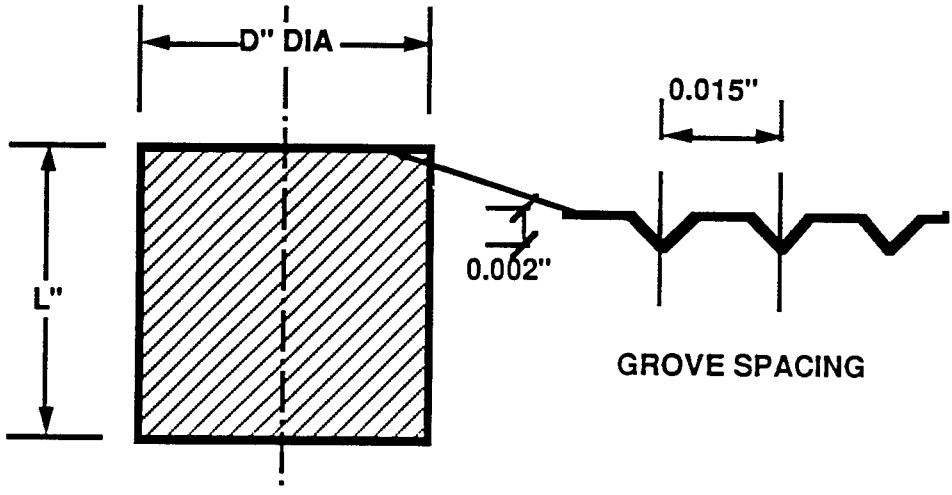



Figure 3. Geometry of Split Hopkinson Bar Compression Specimens.

To examine a possible correlation between the dynamic compression test results and penetration performance, a selection of penetrator materials with demonstrated differences in ballistic performance was required. To date, the basic penetration performance of conventional (nickel-base matrix) WHA penetrator materials has been quite insensitive to changes in properties and has been shown to be a function of alloy density only (MEYER et al., [1990]). This is not the case for uranium alloys. The ballistic performances of equidensity uranium alloys can vary significantly (MAGNESS and FARRAND, [1990]). Nine DU alloys, of differing chemistries, crystallographic structures, processing histories and properties were selected for the series of SHB tests (Table 1).

Table 1. Chemistry and Properties of Selected Uranium Alloys.

| Alloy | Density (g/cc) | Tensile Properties Elong. (%) | Y.S.(0.2%) (MPa) | U.T.S. (MPa) | Compressive Y.S.(0.2%) (MPa) |
|---|---|---|---|---|---|
| U-6Nb | 17.3 | 30 | 600 | 896 | --- |
| (metastable monoclinic structure) | | | | | |
| U-8Mo | 17.2 | 17 | 936 | 938 | 910 |
| (body-centered cubic structure) | | | | | |
| U-1Mo-3/4Ti | 18.4 | 7 | 1396 | 1821 | 1572 |
| (orthorhombic, gamma-quenched and aged, Rc 49) | | | | | |
| U-3/4Ti | 18.6 | 20 | 848 | 1489 | 952 |
| (ortho., gamma-quenched & aged, Rc 40) | | | | | |
| U-3/4Ti | 18.6 | 6 | 1089 | 1689 | 1389 |
| (ortho., gamma-quenched &>aged, Rc 49) | | | | | |
| U-3/4Ti | 18.6 | 8 | 1276 | 1593 | 862 |
| (ortho., gamma-quenched, swaged 28%) | | | | | |
| U-3/4Ti | 18.6 | 6 | 1351 | 1717 | 965 |
| (ortho., gamma-quenched, swaged 28%, aged) | | | | | |
| U-3/4Ti | 18.6 | 24 | 676 | 1241 | 1434 |
| (ortho., gamma-quenched, upset 12%) | | | | | |
| U-3/4Ti | 18.6 | 15 | 945 | 1338 | 1441 |
| (ortho., gamma-quenched, upset 12% & aged) | | | | | |

Seven of the alloys have the orthorhombic crystal structure, martensitic microstructure of the standard U-3/4Ti alloy used in U.S. tank munitions. The U-6Nb alloy has a metastable monoclinic structure (WOOD et al., [1983]). The high temperature phase (body-centered cubic structure) of uranium was stabilized at room temperature by an 8% molybdenum addition for the ninth alloy. The ballistic performances, measured as limit velocities of constant mass, fixed geometry (65 g, L/D of 15) penetrators, against a fixed, finite thickness armor steel plate, are ranked in Table 2. Since the densities of three of the alloys were lower than the 18.6 g/cc of the U-3/4Ti alloys, the ballistic performances of all the alloys were normalized by the limit velocities obtained for equal-density WHA penetrators, thus separating the effects of alloy density and material response. Note that only one alloy, U-6 Niobium(Nb), performed as poorly as an equal-density WHA, (V/Vwha = 1.0). This was also the only uranium alloy that did not exhibit extensive adiabatic shear failures during the penetration process.

## Results of Split Hopkinson Bar Tests

Most of the tests were conducted at a strain rate of approximately 1500/sec. In most of the tests, thermal softening was apparent in the calculated true stress - true strain curves (Fig. 4 and 5). In all the SHB tests, save those done with the U-6Nb alloy (Fig. 5), a sudden load drop was observed (Fig. 4). The true strain values at which these drops occurred, listed in Table 2, ranged from 14% to 42%, and were quite reproducible for each of the materials tested.

Table 2. SHB and Ballistic Test Results

| Alloy | Tensile Elong. (%) | Compressive Y.S.(0.2%) (MPa) | Aver. SHB STLD (%) | Normalized V/Vwha |
|---|---|---|---|---|
| U-6Nb (metastable monoclinic) | 30 | --- | none | 1.00 |
| U-8Mo (body-centered cubic) | 17 | 910 | 30 | 0.95 |
| U-3/4Ti (orthorhombic, gamma-quenched & aged) | 20 | 952 | 28 | 0.93 |
| U-3/4Ti (ortho., gamma-quenched, swaged 28%) | 8 | 862 | 42 | 0.91 |
| U-3/4Ti (ortho., gamma-quenched, swaged 28%, aged) | 6 | 965 | 32 | 0.91 |
| U-3/4Ti (ortho., gamma-quenched &>aged, Rc 49) | 6 | 1389 | 19 | 0.90 |
| U-3/4Ti (ortho., gamma-quenched, upset 12%) | 24 | 1434 | 18 | 0.89 |
| U-1Mo-3/4Ti (ortho., gamma-quenched and aged, Rc 49) | 7 | 1572 | 15 | 0.89 |
| U-3/4Ti (ortho., gamma-quenched, upset 12% & aged) | 15 | 1441 | 14 | 0.89 |

A greater STLD value would suggest that more "mushrooming" of the head of the penetrator would be required before a shear localization and discard occurred. The resulting ballistic performance therefore should be poorer (greater normalized limit velocity). Consistent with this hypothesis, the three uranium alloys exhibiting the lowest STLD values, ranging from 14% to 18%, delivered the lowest normalized limit velocities (V/Vwha = 0.89). The results were more mixed for the remaining uranium alloys exhibiting a load drop, but the general trend of increasing limit velocity with increasing STLD is generally consistent. Note that the U-6Nb alloy,

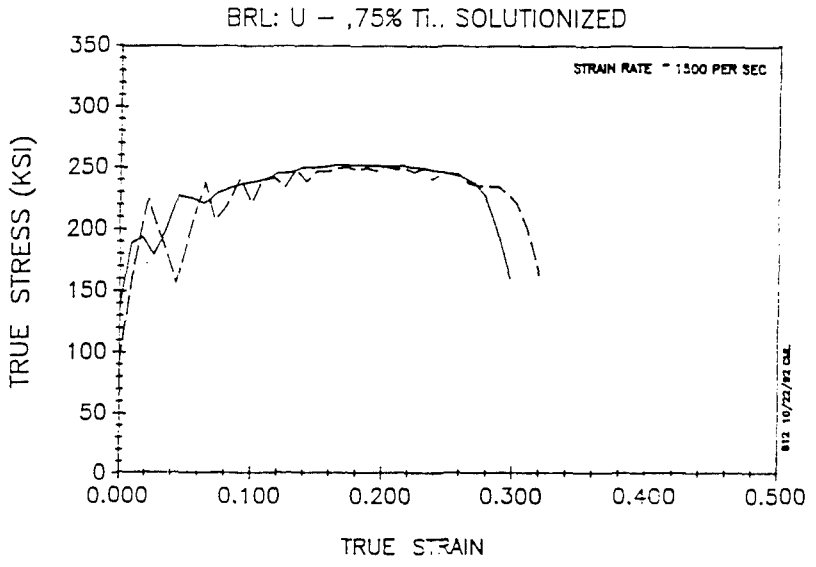



Figure 4. SHB Compressive True Stress - True Strain Curve for U-3/4Ti Alloy, Quenched and Aged, Exhibiting Load Drop Behavior (STLD = 0.28).

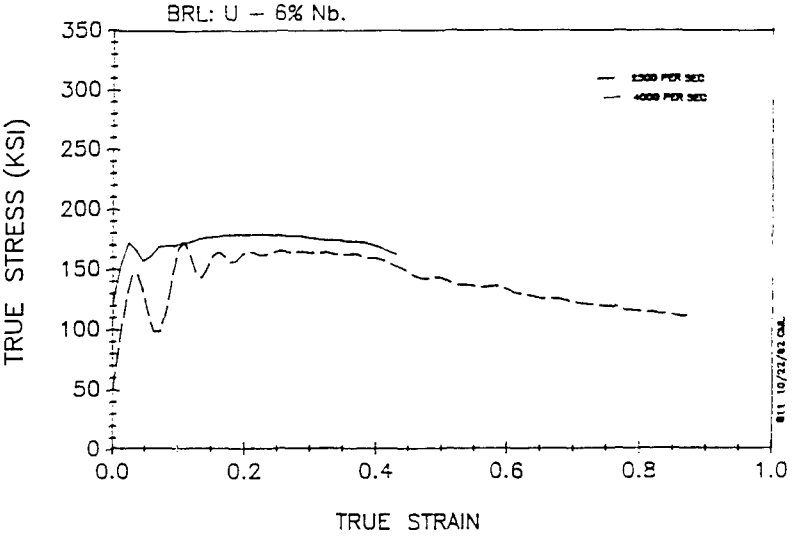



Figure 5. SHB Compressive True Stress - True Strain Curve for U-6Nb Alloy, Exhibiting No Load Drop Behavior.

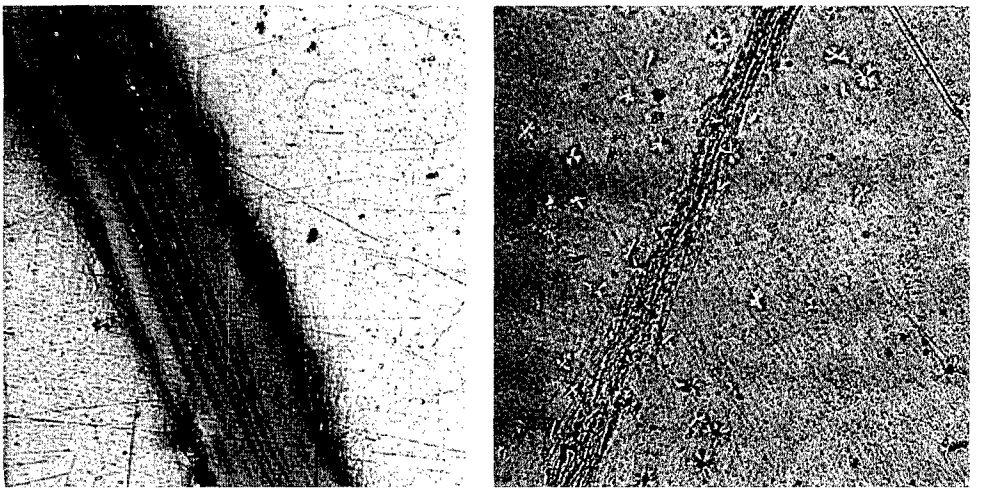
which performed no better than conventional WHA and did not exhibit any shear localizations during the penetration process, did not exhibit a load drop, even when deformed to strains exceeding 80%. This result is consistent with the lack of a load drop in tests of lubricated, low aspect ratio WHA compression specimens.

One should also note the inverse relationship between the compressive yield strength of the DU alloys (listed again in Table 2) and the STLD values. Similar relationships between strength and critical strain to adiabatic shear failure are often observed for steels and other metals (ROGERS, [1979]).

Optical metallographic examinations of the specimens, which had failed via a sudden load drop, revealed that the failures occurred in a ductile manner (Fig. 6a). This is indicative of a plastic localization (adiabatic shear) failure rather than fracture. To examine earlier stages of the shear band propagation, steel washers of the required thicknesses were placed between the input and output bars in subsequent tests to try to stop the compression at a strain below the critical STLD. These specimens were then sectioned and examined. With only one exception, the metallographic examinations did not reveal a shear band in the process of propagation, even in those specimens arrested at strains just below the critical STLD. This suggests that once a shear band initiates, it propagates very quickly across the specimen.

The sole exception was a U-8Mo specimen, #869 (Fig. 6b), in which a shear band nearly traversed the specimen, starting at one corner and propagating to the opposite corner. Note that the U-8Mo shear band does not have the classic "white-etching" characteristic of "transformed" adiabatic shear bands in high-strength steels or orthorhombic uranium alloys (STELLY and DORMEVAL, [1986]). Since the U-8Mo alloy already has the high temperature, body-centered cubic structure of uranium at room temperature, it will not undergo a phase transformation upon adiabatic heating in the shear band. This may explain the lack of the white-etching feature that is characteristic of transformation bands. It is also interesting to note that the shape of the dynamic true stress - true strain curves for the U-8Mo alloy were somewhat different from those of the orthorhombic uranium alloys. Thermal softening was more pronounced for the U-8Mo alloy than for the martensitic uraniums, yet the

final load drop was more gradual. Although many features of the U-8Mo compression tests remain difficult to explain, the U-8Mo alloy clearly exhibited adiabatic shear failures in both the ballistic and SHB tests, and its superior ballistic performance corresponded to its STLD value of 0.30.



(a) (b)

Figure 6. Adiabatic Shear Bands Observed in Sectioned SHB Specimens, (a) White-Etching Band Found in U-3/4Ti Samples Exhibiting Load Drop, (b) Non-White-Etching Band Found in U-8Mo Sample. (Oxalic Acid Etch, 300X).

## Conclusions

In these initial split Hopkinson bar compression tests of DU alloys, the strain-to-load-drop (STLD) measure appears to be a good indicator of each alloy's relative ballistic performance. The STLD value indicates the critical strain required for the development of an adiabatic shear failure in the specimen. The STLD values can also be viewed as a measure of the amount of "mushrooming" of the head of the penetrator required before a shear localization and discard will develop, and thus the penetrator material's performance. Adiabatic shear failures have proven difficult to model in two- and three-dimensional hydrocode simulations of the penetration process. However, in recent simulations by Silling (1993) using an ad hoc shear band model, a similar relationship between strain-to-shear-failure and

ballistic performance was demonstrated.

The usefulness of this SHB compression test as a screening technique for novel WHA composites has yet to be demonstrated. However, load drops have not been observed in equivalent compression tests of conventional WHAs, a result consistent with WHA's poorer performance and the results (both SHB and ballistic) for the U-6Nb alloy. Further testing using additional uranium alloy samples and novel WHA composites is planned.

## References


Belk, J., Hogwood, M., Bentley, A., and Watson, C., "The Incidence of Shear Instabilities in Tungsten Heavy Alloys," Proc. Int. Conf. Tungsten & Tungsten Alloys - 1992, eds. Bose and Dowding, p.379, (1992).

Bose, A., Couque, H. and Lankford, J., "Influence of Microstructure on Shear Localization in Tungsten Heavy Alloys," Proc. Int. Conf. Tungsten & Tungsten Alloys - 1992, eds. Bose and Dowding, p.291, (1992).

Cimpoeru, S.J. and Woodward, R.L., "High Strain Rate Properties of Three Liquid Phase Sintered Tungsten Alloys," J. Mater. Sci. Letters, Vol.9, p.87, (1990).

Cowie, J.G. and Tuler, F.R., "Flow Localization Models - A Review," Mat. Sc.& Eng., Vol.95, pp.93-99, (1987).

Gerlach, U., "Microstructural Analysis of Residual Projectiles - A new Method to Explain Penetration Mechanisms," Met. Trans., Vol.17, pp.435-442, (1986).

Johnson, G.R., Hoegfeldt, J.M., Lindholm, U.S., and Nagy, A., "Response of Various Metals to Large Torsional Strains Over a Large Range of Strain Rates - Part 2: Less Ductile Metals", J. Eng. Matrls. & Tech., Vol.105, p.48-53, (1983).

Magness, L. and Farrand, T. "Deformation Behavior and Its Relationship to the Penetration Performance of High-Density KE Penetrator Materials", Proc. 1990 Army Sc. Conf., Rayleigh-Durham, NC, p.465 (1990).

Mescall, J., "Materials Issues in Computer Simulations of Penetration Mechanics," Computational Aspects of Penetration Mechanics, eds. Chandra and Flaherty, pp.47-62, (1983).

Meyer, L.W., Behler, F.-W., Frank, K., and Magness, L., "Interdependencies Between the Dynamic Mechanical Properties and the Ballistic Behavior of Materials," Proc. 12th Int. Symp. Ballistics, San Antonio, TX, (1990).

O'Donnell, R.G. and Woodward, R.L., "Instability During High Strain Rate Compression of 2024 T351 Aluminum," J.Mater. Sci., Vol. 23, p.3578, (1988).

Rogers, H.C., "Adiabatic Plastic Deformation," Ann. Rev. Mater. Sci., Vol. 9, pp.283-311, (1979).

Semiatin, S.L., Lahoti, G.D., and Oh, S.I., "The Occurence of Shear Bands in Metalworking," Material Behavior Under High Stress and Ultrahigh Loading Rates, Proc. 29th Sagamore Army Res. Conf., eds. Mescall & Weiss, p.119, (1982).

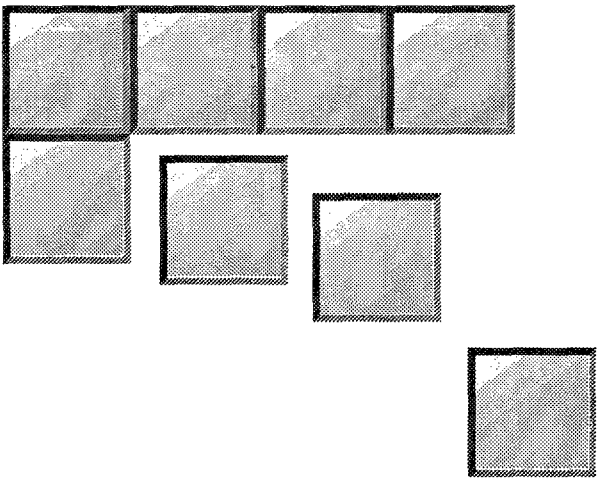
Silling, S.A., "Shear Band Formation and Self-Sharpening in Penetrators," Sandia Rep. SAND92-2692, (1993).

Stelly, M. and Dormeval, R., "Adiabatic Shearing," Met. Appl. of Shock Waves and High Strain Rate Phen., eds. Murr, Staudhammer,& Meyers, pp.607-632, (1986).

Wood, D.H., Dini, J.W., and Johnson, H.R., "Tensile Testing of U-5.3%Nb and U-6.8%Nb Alloys," J. Nuclear Mat., Vol. 114, pp.199-207, (1983).

Wright, T.W., "A Survey of Penetration Mechanics for Long Rods," Proc. ARO/BRL Symp. on Comp. Aspects of Penetration Mech., Aberdeen Proving Grd., MD, (1982).

# ATTENDANCE LIST



DR CHARLES E ANDERSON JR
MGR BALLISTIC SCI SEC
SOUTHWEST RES INST
6220 CULEBRA RD
SAN ANTONIO TX 78238-5166
(210)-522-2313
FAX: (210)-522-5122

PROF GANG BAO
THE JOHNS HOPKINS UNIV
DEPT OF MECH ENGRG
34TH AND CHARLES ST
BALTIMORE MD 21218-0001
(410)-516-8637
FAX: (410)-516-7254

MR PETER BARTKOWSKI
MECH ENGR
US ARMY RES LAB
AMSRL-MA-DA
ARSENAL ST
WATERTOWN MA 02172-0001
(617)-923-5705

MR F D BARTLETT
CHIEF STR MECH DIR
US ARMY
LANGLEY RES CNTR
M/S 266
HAMPTON VA 73681-0001
(804)-864-3952
FAX: (804)-864-3970

DR ROMESH C BATRA
UNIV OF MISSOURI-ROLLA
MECH & AEROSPACE ENGRG
125 ME ANNEX
ROLLA MO 65401-0249
(314)-341-4589
FAX: (314)-341-4607

MS TRISH BEAULIEU
MECH ENGR
US ARMY RES LAB
AMSRL-MA-DA
409 ARSENAL ST
WATERTOWN MA 02172-0001
(617)-923-5703
FAX: (617)-923-5065

DR DAVID J BENSON
UNIV OF CA AT SAN DIEGO
DEPT APPLIED MECH & ENGRG
M/S 0411
95000 GILMAN
LA JOLLA CA 92093-0001

WAYNE BETHONEY
US ARMY RES LAB
AMSRL-MA-DB
WATERTOWN MA 02172-0001
(617)-923-5203

MR RAYMOND S BLAJDA
CHF MATLS BR
US ARMY
SMCAR-AET-M
BLDG 335
PICATINNY ARSENAL NJ 07806-5000
(201)-724-2879
FAX: (201)-361-7378

DR STEVE J BLESS
INST FOR ADV TECH
UNIV OF TEXAS AT AUSTIN
4030-2 W BRAKER LANE
AUSTIN TX 78759-0001

DR N S BRAR
UNIV OF DAYTON RES INST
M/S SPC-0182
300 COLLEGE PARK
DAYTON OH 45469-0182
(513)-229-3546
FAX: (513)-229-3869

DR BRUCE P BURNS
US ARMY RES LAB
AMSRL-WT-PD
ABERDENN PROVING GRD MD 21005-5066
(407)-278-6132

PROF FU-KUO CHANG
ASSOC PROF
STANFORD UNIV
DEPT OF AERONAUTICS
& ASTRONAUTICS
MC 4035
STANFORD CA 94305-4035
(415)-723-3466
FAX: (415)-725-3377

DR ADITI CHATTOPADHYAY PHD
ASST PROF
ARIZ STATE UNIV
MECH & AERO ENG
TEMPE AZ 85287-6106
(602)-965-9342
FAX: (602)-965-1384

DR PETER CHEN
LOUISIANA STATE UNIV
COATES HALL RM 257
COMPUTER SCIENCE DEPT
BATON ROUGE LA 70803-0001
(518)-266-5907
FAX: (518)-266-5227

DR WING L CHENG
FMC CORPORATION
CORP TECH CTR
1205 COLEMAN AVE
SANTA CLARA CA 95052-0001

H P CHERUKURI
RES ASSIS
UNIV OF ILLINOIS
104 S WRIGHT ST
URBANA IL 61801-0001
(217)-244-4373

PROF FU-PEN CHIANG
MECH ENGRG
STATE UNIV OF NEW YORK
DEPT OF MECH ENGRG
STONY BROOK NY 11794-2300
(516)-632-8311
FAX: (516)-632-8720

MS LUNA H CHIU
MECH ENGR
US ARMY RES LAB
AMSRL-MA-DA
ARSENAL ST
WATERTOWN MA 02172-0001
(617)-923-5067
FAX: (617)-923-5065

DR SHUN-CHIN CHOU
CHF MATLS DYNAMICS BRCH
US ARMY RES LAB
AMSRL-MA-DA
405 ARSENAL ST
WATERTOWN MA 02172-0001
(617)-923-5115
FAX: (617)-923-5065

MR WILLIAM L CRENSHAW
US ARMY RES LAB
AMSRL-MA-DB
ARSENAL ST
WATERTOWN MA 02172-0001
(617)-923-5274

MR PHILIP M CUNNIFF
RES MECH ENGR
US ARMY NATICK RD&E CTR
SATNC-ITF
KANSAS ST
NATICK MA 01760-5019
(508)-651-5463
FAX: (508)-651-5223

DR DATTATRAYA P DANDEKAR
US ARMY RES LAB
AMSRL-MA-DA
ARSENAL ST
WATERTOWN MA 02172-0001
(617)-923-5704

DR PIYUSH K DUTTA
MAT RES ENGR
US ARMY
CRREL
COLD REGIONS RES & ENGRG
72 LYME RD
HANOVER NH 03755-1290
(603)-646-4212
FAX: (603)-646-4640

DR LUTHER D FLIPPEN JR
NAVAL RES LAB
CODE 6380
4555 OVERLOOK AVE SW
WASHINGTON DC 20375-5343
(202)-404-7182
FAX: (202)-404-7176

DR MICHAEL J FORRESTAL
SANDIA NATL LABS
DIV 9723
PO BOX 5800
ALBUQUERQUE NM 87185-0001
(505)-844-8854
FAX: (505)-845-9319

PROF L B FREUND
BROWN UNIV
DIV OF ENGRG
BOX D
PROVIDENCE RI 02912-0001
(401)-863-1476
FAX: (401)-863-1157

MR ABRAHAM M FRYDMAN
US ARMY RES LAB
AMSRL-WT-PD (ALC)
2800 POWDER MILL RD
ADELPHI MD 20783-1145
(202)-394-2804

MS SONIA M F GARCIA
ASST PROF
US NAVAL ACADEMY
M/S 9E
USNA NAVY MIL
ANNAPOLIS MD 21402-0001
(410)-647-0611

PROF SOMNATH GHOSH
ASSIS PROF
OHIO STATE UNIV
DEPT OF ENGRG MECHANICS
(BOYD LAB)
155 W WOODRUFF AVE
COLUMBUS OH 43210-1181
(614)-292-2599
FAX: (614)-292-9021

MR THOMAS GODFREY
GEN ENGR
US ARMY NATICK RD&E CTR
M/S SATNC-UE
KANSAS ST
NATICK MA 01760-5017
(508)-651-4697
FAX: (508)-660-1187

MR MARTIN A GOLDBERG
SR ENGR
GRUMMAN AIRCRAFT CORP
M/S B44-35
STEWART AVE
BETHPAGE NY 11714-0001
(516)-346-3105
FAX: (516)-575-8828

DR DENNIS GRADY
SANDIA NATL LABS
DIV 1433
PO BOX 5800
ALBUQUERQUE NM 87185-5800

MR JOHN L GREEN
MECH ENGRG
US ARMY RES LAB
AMSRL-MA-DA
ARSENAL ST
WATERTOWN MA 02172-0001
(617)-961-3441
FAX: (617)-923-5065

MR ROBERT GREIF
MECH ENGR
US DOT/VOLPE CTR
DTS-76
KENDALL SQ
CAMBRIDGE MA 02142-0001
(617)-494-2103
FAX: (617)-494-3066

MR DAVID J GROVE
ASSIS PROG/ANALYST
UNIV OF DAYTON RES INST
300 COLLEGE PARK
DAYTON OH 45469-0120
(513)-229-4417
FAX: (513)-229-4251

MR JOHN W GROVE
ASSOC PROF
UNIV AT STONY BROOK
DEPT OF APPL MATH
STONY BROOK NY 11794-3600
(516)-632-8375
FAX: (516)-632-8490

MR WILLIAM E HASKELL III
MATLS ENGR
US ARMY MATLS TECH LAB
AMSRL-MA-PA
ARSENAL ST
WATERTOWN MA 02172-0001
(617)-923-5172
FAX: (617)-923-5154

DR G E HAUVER
US ARMY RES LAB
AMSRL-WT-TA
ABERDEEN PROVING GRD MD 21005-5066

DR DAVID HOPKINS
US ARMY RES LAB
AMSRL-WT-PD
ABERDEEN PROVING GRD MD 21005-5066

DR NORRIS J HUFFINGTON JR
US ARMY RES LAB
AMSRL-WT-TD
ABERDEEN PROVING GRD MD 21005-5066
(401)-278-6556

DR KAILASAM R IYER
STAFF SCI
US ARMY RES OFC
AMSRO-MS
PO BOX 12211
RES TRIANGLE PK NC 27709-2211
(919)-549-4258
FAX: (919)-549-4310

DR KAREN E JACKSON
AEROSPACE ENGR
US ARMY VSD/ARL
NASA LANGLEY RES CTR
M/S 495
HAMPTON VA 23681-0001
(804)-864-4147
FAX: (804)-864-8547

DR DAVID Y JEONG
MECH ENG
US DEPT OF TRANS
M/S DTS-76
KENDALL SQ
CAMBRIDGE MA 02142-1093
(617)-494-3654
FAX: (617)-494-3066

DR P W KINGMAN
METALLURGIST
US ARMY RES LAB
AMSRL-WT-TD
1115 HIGH COUNTRY
TOWSON MD 21286-0001
(410)-278-6088

PROF DUSAN KRAJCINOVIC
ARIZONA STATE UNIV
MECH & AEROSPACE ENGRG
M/S 6106
TEMPE AZ 85287-6106
(602)-965-8656
FAX: (602)-965-1384

DR EDWARD LENOE
WEST POINT MIL ACADEMY
DEPT OF MECH ENGRG
114 G WASHINGTON RD
WEST POINT NY 10996-1792
(914)-938-3131

PROF DAVID L MCDOWELL
DIR MECH PROP RES LAB
GEORGIA INST OF TECH
302 COON BLDG MECH ENGRG
ATLANTA GA 30332-0405
(404)-894-5128
FAX: (404)-894-8336

PROF SIA NEMAT-NASSER
DEPT OF APP MECH & ENGRG SCI
UCSD-DEPT OF AMES
M/S 0411 RM 4207 EBU1
9500 GILMAN DR
LA JOLLA CA 92093-0411
(619)-534-4772
FAX: (619)-534-2727

PROF JAMES JENKINS
CORNELL UNIV
DEPT OF THEORETICAL
& APPLIED MECH
KIMBALL HALL
ITHACA NY 14853-0001
(607)-255-7185
FAX: (607)-255-2011

PROF RAKESH K KAPANIA
ASSOC PROF
VPI & SU VA TECH
M/S 0203
215 RANDOLPH HALL
BLACKSBURG VA 24061-0219
(703)-231-4881
FAX: (703)-231-9632

PROF ROBERT V KOHN
COURANT INST
251 MERCER ST
NEW YORK NY 10012-0001
(212)-998-3217
FAX: (212)-995-4121

DR DAVID H LASSILA
LAWRENCE LIVERMORE NATL LAB
M/S L-342
PO BOX 808
LIVERMORE CA 94550-0001
(510)-423-9537
FAX: (510)-422-2438

DR LEE S MAGNESS JR
US ARMY RES LAB
AMSRL-WT-TD
ABERDEEN PROVING GRD MD 21005-5066

MR PAUL MOY
MECH ENG
US ARMY RES LAB
AMSRL-MA-DA
ARSENAL ST
WATERTOWN MA 02172-0001

DR THEODORE NICHOLAS
SR SCIENTIST
US AIR FORCE
WL/MLLN
2230 TENTH ST STE 1
WRIGHT-PATTERSON AFB OH 45433-6533
(513)-255-1347
FAX: (513)-476-4840

DR T KEVIN O'BRIEN
SR RES SCI
US ARMY RES LAB/VSD
NASA LANGLEY RES CTR
M/S 188E
HAMPTON VA 23681-0001
(804)-864-3465
FAX: (804)-864-7729

DR OSCAR ORRINGER
MECH ENGR
US DOT/VOLPE CTR
DTS-76
KENDALL SQ
CAMBRIDGE MA 02142-0001
(617)-494-2303

MR RICHARD J PALICKA
PRES
CERCOM INC
PO BOX 70
1960 WATSON WAY
VISTA CA 92083-0001
(619)-727-6200
FAX: (619)-727-6209

DR FORREST T PATTERSON
MASS INST OF TECH
REL RM 1-008
77 MASSACHUSETTS AVE
CAMBRIDGE MA 02139-0001
(617)-253-2318
FAX: (617)-258-5802

DR WILLIAM W PREDEBON
PROF OF ENGRG MECH
MICHIGAN TECH UNIV
1400 TOWNSEND DR
HOUGHTON MI 49931-1295
(906)-487-2158
FAX: (906)-487-2822

MRS CLAUDIA J QUIGLEY
US ARMY RES LAB
AMSRL-MA-DB
ARSENAL ST
WATERTOWN MA 02172-0001
(617)-923-5152
FAX: (617)-923-5154

DR MARTIN N RAFTENBERG
US ARMY RES LAB
BLDG 309
AMSRL-WT-TD
ABERDEEN PROVING GRD MD 21005-5066
(410)-278-6075
FAX: (410)-278-6952

DR ANISUR RAHMAN
DREXEL UNIV
M/S 27-438
32ND AND CHESTNUT
PHILADELPHIA PA 19104-0001
(215)-895-2382
FAX: (215)-895-6684

DR A M RAJENDRAN
US ARMY RES LAB
AMSRL-MA-DA
ARSENAL ST
WATERTOWN MA 02172-0001
(617)-923-5260

PROF K T RAMESH
ASSOC PROF
THE JOHNS HOPKINS UNIV
DEPT OF MECH ENGRG
34TH AND CHARLES ST
BALTIMORE MD 21218-0001
(410)-516-7735
FAX: (410)-516-7254

PROF G RAVICHANDRAN
CA INST OF TECH
M/S 105-50
1201 E CALIFORNIA BLVD
PASADENA CA 91125-0001
(818)-395-4525
FAX: (818)-449-2677

PROF JOHN M ROSSETTOS
NORTHEASTERN UNIV
DEPT OF MECH ENGRG
360 HUNTINGTON AVE
BOSTON MA 02115-5096
(617)-437-3809
FAX: (617)-437-2921

MR KARL SALOMAN
US ARMY RES LAB
AMSRL-MA-DA
ARSENAL ST
WATERTOWN MA 02172-0001
(617)-923-5233

PROF BHAVANI V SANKAR
ASSOC PROF
UNIV OF FLORIDA
DEPT OF AERO ENGRG
231 AEROSPACE
GAINESVILLE FL 32611-2031
(904)-392-6749
FAX: (904)-392-7303

DR MICHAEL SCHEIDLER
MATHEMATICIAN
US ARMY RES LAB
AMSRL-WT-TD
ABERDEEN PROVING GRD MD 21005-5066
(301)-278-6836
FAX: (301)-278-6952

DR MARK J SHUART
ASST CHF STRUC MECH DIV
NASA LANGLEY RES CTR
M/S 244
HAMPTON VA 23681-0001
(804)-864-2902
FAX: (804)-864-8318

PROF JAMES G SIMMONDS
UNIV OF VIRGINIA
DEPT OF APPLIED MATH
THORNTON HALL
CHARLOTTESVILLE VA 22903-2422
(804)-924-1041

PROF JAMES M STAEHLER
MICHIGAN TECH UNIV
DEPT MECH ENGRG
1400 TOWNSEND DR
HOUGHTON MI 49931-1295
(906)-487-2009
FAX: (906)-487-2822

PROF THEOFANIS STROUBOULIS
TEXAS A&M UNIV
DEPT OF AERO ENGRG
COLLEGE STATION TX 77843-0001

DR GHATUPARTHI SUBHASH
CALIFORNIA INST OF TECH
GRAD AERO LAB
M/S 105-50
PASADENA CA 91125-0001

PROF C T SUN
PURDUE UNIV
SCHOOL OF AERO & ASTRO
GRISSOM HALL 325
W LAFAYETTE IN 47907-1282
(317)-494-5130
FAX: (317)-494-0309

MISS YIM HAR TANG
MECH ENGR
US DOT/VOLPE CTR
DTS-76
KENDALL SQ
CAMBRIDGE MA 02142-0001
(617)-494-2356
FAX: (617)-494-3066

DR JEROME TZENG
MECH ENGR
US ARMY RES LAB
AMSRL-WT-PD
ABERDEEN PROVING GRD MD 21005-5066
(410)-278-6805

MR RICHARD VITALI
DIR
US ARMY RES LAB
AMSRL-D
2800 POWDER MILL RD
ADELPHI MD 20783-1145
(301)-394-1600
FAX: (301)-394-1496

DR JOHN W WALTER
MECH ENGR
US ARMY RES LAB
AMSRL-WT-TD
ABERDEEN PROVING GRD MD 21005-5066
(410)-278-6051
FAX: (410)-278-6952

DR TUSIT WEERASOORIYA
US ARMY RES LAB
AMSRL-MA-DA
ARSENAL ST
WATERTOWN MA 02172-0001
(000)-923-5069

MR CRAIG WITTMAN
STAFF ENGR
ALLIANT TECHSYSTEMS INC
M/S MN11-1812
600 2ND ST NE
HOPKINS MN 55343-0001
(612)-931-6983
FAX: (612)-931-6512

DR THOMAS W WRIGHT
SR RES SCIENTIST
US ARMY RES LAB
WTD
AMSRL-WT-TD
ABERDEEN PROVING GRD MD 21210-0001
(410)-278-6046
FAX: (410)-278-6952

DR JULIAN J WU
US ARMY RES OFC
MATH SCIENCE DIV
AMSRO-MA
PO BOX 12211
RES TRIANGLE PARK NC 27709-2211

MR MIN ZHOU
BROWN UNIV
DIV OF ENGRG
PO BOX D
PROVIDENCE RI 02912-0001
(401)-863-3034
FAX: (401)-863-1157